BİNGÖL ÜNİVERSİTESİ

e-ISSN 2149-6366

Cilt 14, Sayı 3, Eylül 2025
Volume 14, Issue 3, September 2025

TDFD
TÜRK DOĞA ve FEN DERGİSİ

TURKISH JOURNAL OF NATURE AND SCIENCE

TJNS

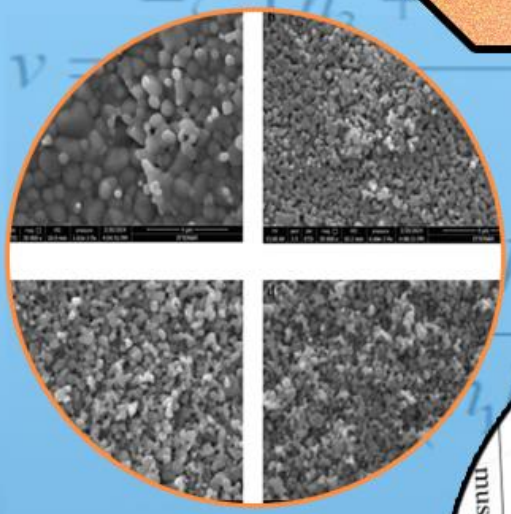

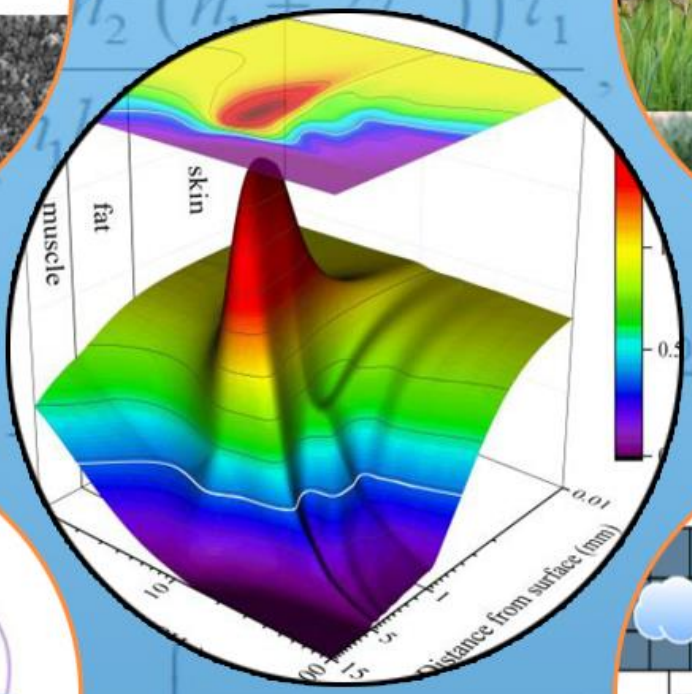

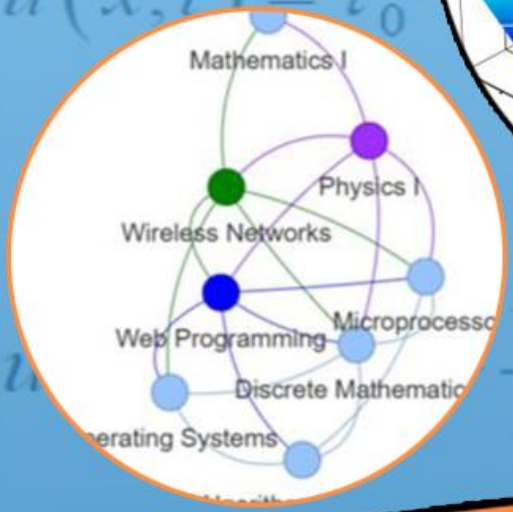

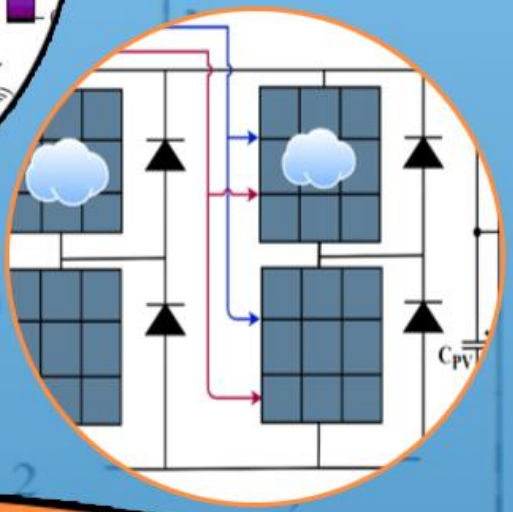

www.dergipark.gov.tr/tdfd

Bingöl Üniversitesi Fen Bilimleri Enstitüsü tarafından yayımlanmaktadır.
Published by Bingol University Institute of Science

ULAKBİM TR DİZİN

TÜRK DOĞA VE FEN DERGİSİ

Amaç

Türk Doğa ve Fen Dergisi, Dergipark tarafından yayınlanan Bingöl Üniversitesi Fen Bilimleri Enstitüsüne ait ulusal ve hakemli bir dergidir. Türk Doğa ve Fen Dergisi, Türkiye ve dünyanın her yerinden gelen doğa ve fen bilimlerinin her alanında özgün, yayımlanmamış, yayımlanmak üzere başka yere gönderilmemiş makale, derleme ve sempozyum değerlendirmesi gibi çalışmaların bilim alemine sunulması amacıyla kurulmuştur.

Kapsam

Türk Doğa ve Fen Dergisinde Mühendislik, Ziraat, Veterinerlik, Fen ve Doğa Bilimleri alanlarından olmak üzere Türkçe ve İngilizce hazırlanmış orijinal makale, derleme ve sempozyum değerlendirmesi gibi çalışmalar yayımlanır. Türk Doğa ve Fen Dergisi sadece online sistemde yayınlanmakta olup ayrıca kağıt baskısı bulunmamaktadır.

Merhaba…

Türk Doğa ve Fen Dergisi, Dergipark tarafından yayınlanmakta olup Bingöl Üniversitesi Fen Bilimleri Enstitüsüne aittir. Bahar ve güz dönemi olmak üzere yılda iki defa çıkarılan ulusal hakemli bir dergi olarak ilk sayısını 2012 bahar döneminde yayımlamıştır. Türk Doğa ve Fen Dergisi, Türkiye ve dünyanın her yerinden gelen doğa ve fen bilimlerinin her alanında özgün, yayımlanmamış, yayımlanmak üzere başka yere gönderilmemiş makale, derleme ve sempozyum değerlendirmesi gibi çalışmaların bilim alemine sunulması amacıyla kurulmuştur. İlk sayısından bugüne kesintisiz olarak faaliyetlerini sürdürmektedir.

Türk Doğa ve Fen Dergisi sadece online sistemde yayınlanmakta olup ayrıca kağıt baskısı bulunmamaktadır. Dergimize gelen her çalışma öncelikle Turnitin intihal programında taranmaktadır. Dergimizde editörlerin, hakemlerin ve yazarların, uluslararası yayım etik kurallarına uyması ve makalelerin yazım kurallarına uyumlu olması zorunluluğu vardır.

Yazarlar yayımlanmak üzere dergimize gönderdikleri çalışmaları ile ilgili telif haklarını zorunlu olarak Bingöl Üniversitesi Türk Doğa ve Fen Dergisi'ne devretmiş sayılırlar. Yazarlardan herhangi bir ücret talep edilmemektedir. Yazarların değerlendirmeleri, dergimizin resmi görüşü olarak kabul edilemez. Çalışmaların her türlü sorumluluğu yazarlarına aittir. Araştırma ürünleri için etik kurul raporu gerekli ise, çalışma üzerinde bu raporun alınmış olduğu belirtilmeli ve kurul raporu sisteme kaydedilmelidir. Araştırma ile ilgili intihal, atıf manipülasyonu, sahte veri uydurma vb. suistimallerin tespit edilmesi halinde yayım ve etik ilkelerine göre davranılır. Bu durumda çalışmanın yayımlanmasını önlemek, yayımdan kaldırmak ya da başka işlemler yapmak için gerekli işlemler takip edilmektedir.

Dergimizde, kaynak gösteriminde uluslararası Vancouver sistemine geçilmiştir. Ayrıca dergimiz, Creative Commons ile lisanslanmak suretiyle dergimizde yayımlanan makalelerin paylaşımı, kaynak gösterimi ve yayımlanmasında dergi ve yazar haklarını korumaya almıştır. 2018 yılı güz döneminden itibaren makaleler, uluslararası yazar kimlik numarası ORCID No'su ile yayımlanmaktadır.

Dergi ekibi, dergimizin ulusal ve uluslararası indekslerce taranan bir dergi olması yönünde çalışmalarını titizlikle sürdürmektedir. Dergimize gösterilen ilgi bu yönde bizleri teşvik etmeye devam edecektir.

Bingöl Üniversitesi Fen Bilimleri Enstitüsü tarafından yayımlanmaktadır

EDİTÖRLER (YAYIN) KURULU

BAŞEDİTÖR

Dr. Öğr. Üyesi Mücahit ÇALIŞAN

Bingöl Üniversitesi, Mühendislik-Mimarlık Fakültesi, Bilgisayar Mühendisliği
E-Mail: mcalisan@bingol.edu.tr

EDİTÖR YARDIMCILARI

Doç. Dr. Ekrem DARENDELİOĞLU

Bingöl Üniversitesi, Fen-Edebiyat Fakültesi, Moleküler Biyoloji ve Genetik Bölümü
E-Mail: edarendelioglu@bingol.edu.tr

Doç. Dr. Adnan AYNA

Bingöl Üniversitesi, Fen-Edebiyat Fakültesi, Kimya Bölümü
E-Mail: aayna@bingol.edu.tr

EDİTÖRLER

Fen ve Doğa Bilimleri

Prof. Dr. İkram ORAK

Bingöl Üniversitesi, Sağlık Hizmetleri Meslek Yüksekokulu, Tıbbi Hizmetler ve Teknikler
E-Mail: iorak@bingol.edu.tr

Prof. Dr. Selami SELVİ

Balıkesir Üniversitesi, Altınoluk Meslek Yüksekokulu, Bitkisel ve Hayvansal Üretim Bölümü
E-Mail: sselvi2000@yahoo.com

Prof. Dr. Refik KESKİN

Sakarya Üniversitesi, Fen-Edebiyat Fakültesi, Matematik Bölümü
E-Mail: rkeskin@sakarya.edu.tr

Prof. Dr. Halim ÖZDEMİR

Sakarya Üniversitesi, Fen-Edebiyat Fakültesi, Matematik Bölümü
E-Mail: hozdemir@sakarya.edu.tr

Prof. Dr. Zafer ŞİAR

Bingöl Üniversitesi, Fen-Edebiyat Fakültesi, Matematik Bölümü
E-Mail: zsiar@bingol.edu.tr

Prof. Dr. Uğur ÇAKILCIOĞLU

Munzur Üniversitesi, Pertek Sakine Genç Meslek Yüksekokulu, Bitki Morfolojisi ve Anatomisi Bölümü
E-Mail: ucakilcioglu@yahoo.com

Prof. Dr. Kamuran DİLSİZ

Bingöl Üniversitesi, Fen-Edebiyat Fakültesi, Fizik Bölümü
E-Mail: kdilsiz@bingol.edu.tr

Doç. Dr. Şükran KONCA

Bakırçay Üniversitesi, Mühendislik ve Mimarlık Fakültesi, Temel Bilimler, Matematik Bölümü
E-Mail: sukran.konca@bakircay.edu.tr

Doç. Dr. İdris YAZGAN

Kastamonu Üniversitesi, Fen Edebiyat Fakültesi, Biyoloji

E-Mail: idrisyazgan@gmail.com

Doç. Dr. Abdulcabbar YAVUZ

Gaziantep Üniversitesi, Mühendislik Fakültesi, Metalurji ve Malzeme Mühendisliği
E-Mail: ayavuz@gantep.edu.tr

Doç. Dr. Bünyamin ALIM

Bayburt Üniversitesi, Teknik Bilimler Meslek Yüksekokulu, Elektrik ve Enerji Bölümü
E-Mail: balim@bayburt.edu.tr

Doç. Dr. Mustafa Şükrü KURT

Erzurum Teknik Üniversitesi, Fen Fakültesi, Temel Bilimler
E-Mail: mustafa.kurt@erzurum.edu.tr

Doç. Dr. Sinan SAĞIR

Karamanoğlu Mehmetbey Üniversitesi, Fizik

E-Mail: sinansagir@kmu.edu.tr / sinan.sagir@cern.ch

Doç. Dr. Murat AYDEMİR

Erzurum Teknik Üniversitesi, Fen Fakültesi, Temel Bilimler

E-Mail: murat.aydemir@erzurum.edu.tr

Mühendislik Bilimleri

Prof. Dr. Figen KOREL

İzmir Yüksek Teknoloji Enstitüsü, Gıda Mühendisliği Bölümü
E-Mail: figenkorel@iyte.edu.tr

Prof. Dr. Kubilay ASLANTAŞ

Afyon Kocatepe Üniversitesi, Teknoloji Fakültesi, Makine Mühendisliği Bölümü
E-Mail: aslantas@aku.edu.tr

Prof. Dr. Hamit Özkan GÜLSOY

Marmara Üniversitesi, Teknoloji Fakültesi, Metalurji ve Malzeme Mühendisliği Bölümü
E-Mail: ogulsoy@marmara.edu.tr

Prof. Dr. Ali Adnan HAYALOĞLU

İnönü Üniversitesi, Mühendislik Fakültesi, Gıda Mühendisliği Bölümü
E-Mail: adnan.hayaloglu@inonu.edu.tr

Prof. Dr. Barbara SAWICKA

University of Life Sciences in Lublin, Department of Plant Production Technology and Commodities Sciences
E-Mail: barbara.sawicka@gmail.com

Prof. Dr. İbrahim GÜNEŞ

Giresun Üniversitesi, Mühendislik Fakültesi, İnşaat Mühendisliği Bölümü
E-Mail: ibrahim.gunes@giresun.edu.tr

Doç. Dr. Serhat ŞAP

Bingöl Üniversitesi, Teknik Bilimler Meslek Yüksekokulu, Elektrik ve Enerji Bölümü
E-Mail: ssap@bingol.edu.tr

Doç. Dr. Sırma YEĞİN

Ege Üniversitesi, Mühendislik Fakültesi, Gıda Mühendisliği Bölümü
E-Mail: sirma.yegin@ege.edu.tr

Doç. Dr. Hasan OĞUL

Sinop Üniversitesi, Mimarlık ve Mühendislik Fakültesi, Nükleer Enerji Mühendisliği
E-Mail: hogul@sinop.edu.tr

Doç. Dr. Murat YILMAZTEKİN

İnönü Üniversitesi, Mühendislik Fakültesi, Gıda Mühendisliği Bölümü
E-Mail: murat.yilmaztekin@inonu.edu.tr

Doç. Dr. Ferhat AYDIN

Sakarya Uygulamalı Bilimler Üniversitesi, Teknoloji Fakültesi, İnşaat Mühendisliği Bölümü
E-Mail: ferhata@subu.edu.tr

Dr. Öğr. Üyesi Nurullah DEMİR

Bingöl Üniversitesi, Mühendislik ve Mimarlık Fakültesi, Gıda Mühendisliği Bölümü
E-Mail: ndemir@bingol.edu.tr

Doç. Dr. Ahmet GÜNER

Bingöl Üniversitesi, Mühendislik ve Mimarlık Fakültesi, Elektrik ve Elektronik Mühendisliği Bölümü
E-Mail: aguner@bingol.edu.tr

Dr. Öğr. Üyesi Tahir AKGÜL

Sakarya Uygulamalı Bilimler Üniversitesi, Teknoloji Fakültesi, İnşaat Mühendisliği Bölümü
E-Mail: tahirakgul@subu.edu.tr

Dr. Öğr. Üyesi Yavuz Selim TARİH

Bingöl Üniversitesi, Teknik Bilimler Meslek Yüksekokulu, Mekatronik Bölümü
E-Mail: ystarih@bingol.edu.tr

Dr. Erhan Sulejmani

University of Tetova, Faculty of Food Technology and Nutrition
E-Mail: erhan.sulejmani@unite.edu.mk

Dr. Hacène Medjoudj

Larbi Ben M'Hidi University of Oum El Bouaghi, Food Science Department
E-Mail: medjoudjh@yahoo.com

Dr. Avinash Lakshmikanthan

Nitte Meenakshi Institute of Technology, Department of Mechanical Engineering, Karnataka, India
E-Mail: avinash.laks01@gmail.com

Dr. Manjunath Patel GC

PES Institute of Technology and Management, Department of Mechanical Engineering, Karnataka, India
E-Mail: manju09mpm05@gmail.com

Sağlık Bilimleri

Prof. Dr. Aydın Şükrü BENGÜ

Bingöl Üniversitesi, Sağlık Hizmetleri Meslek Yüksekokulu, Tıbbi Hizmetler ve Teknikler
E-Mail: abengu@bingol.edu.tr

Dr. Öğr. Üyesi Dilhun Keriman ARSERİM UÇAR

Bingöl Üniversitesi, Sağlık Bilimleri Fakültesi, Beslenme ve Diyetetik Bölümü
E-Mail: dkucar@bingol.edu.tr

Dr. Öğr. Üyesi Abdullah TUNÇ

Bingöl Üniversitesi, Sağlık Bilimleri Fakültesi, İş Sağlığı ve Güvenliği Bölümü
E-Mail: atunc@bingol.edu.tr

Dr. Öğr. Üyesi Ramazan GÜNDOĞDU

Bingöl Üniversitesi, Sağlık Hizmetleri Meslek Yüksekokulu, Eczane Hizmetleri
E-Mail: rgundogdu@bingol.edu.tr

Dr. Alexander HERGOVICH

UCL Cancer Institute, Faculty of Medical Sciences, Department of Cancer Biology, UCL, London, UK
E-Mail: a.hergovich@uc.ac.uk

Dr. Valenti GOMEZ

UCL Cancer Institute, Faculty of Medical Sciences, Department of Oncology, UCL, London, UK
E-Mail: valentin.gomez@ucl.ac.uk

Veterinerlik Bilimleri

Prof. Dr. Fatih Mehmet KANDEMİR

Atatürk Üniversitesi, Veteriner Fakültesi, Veteriner Hekimliği Temel Bilimler
E-Mail: fmehmet.kandemir@atauni.edu.tr

Doç. Dr. Akın KIRBAŞ

Bozok Üniversitesi, Veteriner Fakültesi, Klinik Bilimler Bölümü
E-Mail: akindahiliye55@yahoo.com

Doç. Dr. Emrah Hicazi AKSU

Atatürk Üniversitesi, Veteriner Fakültesi, Klinik Bilimler Bölümü
E-Mail: emrahaksu@atauni.edu.tr

Ziraat Bilimleri

Doç. Dr. Zeynep DUMANOĞLU

Bingöl Üniversitesi, Ziraat Fakültesi, Biyosistem Mühendisliği Bölümü
E-Mail: zdumanoglu@bingol.edu.tr

Prof. Dr. Kağan KÖKTEN

Bingöl Üniversitesi, Ziraat Fakültesi, Tarla Bitkileri Bölümü
E-Mail: kahafe1974@yahoo.com

Prof. Dr. Mustafa SÜRMEN

Adnan Menderes Üniversitesi, Ziraat Fakültesi, Tarla Bitkileri Bölümü
E-Mail: mustafa.surmen@adu.edu.tr

Prof. Dr. Banu YÜCEL

Ege Üniversitesi, Ziraat Fakültesi, Hayvan Yetiştirme Anabilim Dalı, Zootekni Bölümü
E-Mail: banu.yucel@ege.edu.tr

Prof. Dr. Hakan İNCİ

Bingöl Üniversitesi, Ziraat Fakültesi, Zootekni Bölümü
E-Mail: hinci@bingol.edu.tr

TEKNİK EDİTÖRLER

Dr. Nimetullah KORKUT

Bingöl Üniversitesi, BİNUZEM, Bilgisayar Teknolojileri
E-Mail: nkorkut@bingol.edu.tr

DİL EDİTÖRÜ

Dr. Öğr. Üyesi Ahmet KESMEZ
Bingöl Üniversitesi, Yabancı Diller Yüksekokulu, İngilizce Bölümü
E-Mail: akesmez@bingol.edu.tr

BİNGÖL ÜNİVERSİTESİ

Türk Doğa ve Fen Dergisi
Turkish Journal of Nature and Scienc
www.dergipark.gov.tr/tdfd

CONTENTS

Molecular Biological Effects of *Gundelia tournefortii* (Kenger Herb) Extract on Oxidative Stress and Cellular Responses in *Saccharomyces cerevisiae*

Batuhan YILMAZ[1], Hacı FIRAT[1], Seda BEYAZ[1], Nasrullah CELAYİR[1], Abdullah ASLAN[1*]

[1] Fırat University, Faculty of Science, Biology Department, Elazığ, Türkiye
Batuhan YILMAZ ORCID No: 0009-0009-9391-1367
Hacı FIRAT ORCID No: 0009-0007-9146-8598
Seda BEYAZ ORCID No: 0000-0003-0436-8112
Nasrullah CELAYİR ORCID No: 0009-0006-9391-1613
Abdullah ASLAN ORCID No: 0000-0002-6243-4221
**Corresponding author: aaslan@firat.edu.tr*

1

(Received: 17.04.2025, Accepted: 16.06.2025, Online Publication: 26.09.2025)

Solitary Wave Solution of the Third Order Gilson-Pickering Equation Via the Abel's Equation with Variable Coefficients

Harun BİÇER[1*]

[1*]Bingöl University, Genç Vocational School, Department of Electric and Energy, Bingöl, Türkiye
Harun BİÇER ORCID No: 0000-0002-9854-0595

10

**Corresponding author: hbicer@bingol.edu.tr*

(Received: 04.02.2025, Accepted: 18.06.2025, Online Publication: 26.09.2025)

Protective Effects of Morin Against Paracetamol-Induced Nephrotoxicity via Modulation of Oxidative Stress, Inflammation, and Apoptosis Pathways

Özge KANDEMİR[1*], Fatih Mehmet KANDEMİR[2], Nurhan AKARAS[3], Hasan ŞİMŞEK[4]

[1] Aksaray University, Aksaray Technical Sciences Vocational School, Department of Food Processing, Aksaray, Türkiye
[2] Aksaray University, Faculty of Medicine, Department of Medical Biochemistry, Aksaray, Türkiye
[3] Aksaray University, Faculty of Medicine, Department of Histology and Embryology, Aksaray, Türkiye
[4] Aksaray University, Faculty of Medicine, Department of Physiology, Aksaray, Türkiye
Özge KANDEMİR ORCID No: 0000-0001-8884-4168
Fatih Mehmet KANDEMİR ORCID No: 0000-0002-8490-2479
Nurhan AKARAS ORCID No: 0000-0002-8457-9448
Hasan ŞİMŞEK ORCID No: 0000-0001-5573-4923

30

**Corresponding author: ozgekandemir@aksaray.edu.tr*

(Received: 04.05.2025, Accepted: 23.06.2025, Online Publication: 26.09.2025)

Assessment of Real Confectionery Industry Wastewater: Characterisation and Treatability with Coagulation-Flocculation

Inci Karakas[1*]

[1] Uskudar University, Vocational School of Health Services, Department of Environmental Health, İstanbul, Türkiye
Inci KARAKAS ORCID No: 0000-0002-3590-3395

**Corresponding author: inci.karakas@uskudar.edu.tr*

(Received: 10.02.2025, Accepted: 06.07.2025, Online Publication: 26.09.2025)

40

Graph-Based Course Scheduling Using the Malatya Vertex Coloring Algorithm for Constraint Optimization

Cezayir KARACA[1*], Selman YAKUT[2]

[1] İnönü University, Faculty of Engineering, Department of Computer Engineering, Malatya, Türkiye
[2] İnönü University, Faculty of Engineering, Department of Software Engineering, Malatya, Türkiye
Cezayir KARACA ORCID No: 0009-0007-9250-2612
Selman YAKUT ORCID No: 0000-0002-0649-1993

**Corresponding author: cezayirkaraca0242@gmail.com*

(Received: 29.01.2025, Accepted: 10.07.2025, Online Publication: 26.09.2025)

46

Performance Evaluation of a Nature-Inspired Three-Particle Swarm Optimization Algorithm in PV Systems with a Modified SEPIC Converter

Muhammed MAHHO[1], Mehmet YILMAZ[1], M. Fatih ÇORAPSIZ[1*]

[1] Ataturk University, Engineering Faculty, Electrical-Electronics Engineering, Erzurum, Türkiye
Muhammed MAHHO ORCID No: 0009-0005-0938-7031
Mehmet YILMAZ ORCID No: 0000-0001-7624-4245
M. Fatih ÇORAPSIZ ORCID No: 0000-0001-5692-8367

**Corresponding author: corapsiz@atauni.edu.tr*

(Received: 11.06.2025, Accepted: 14.07.2025, Online Publication: 26.09.2025)

57

Determination of Turkey Meat Adulteration in Cooked Ground Beef Using Fluorescence Spectroscopy with Machine Learning

Ali SOYUÇOK[1], Samet UÇAK[2*]

[1]Burdur Mehmet Akif Ersoy University, Department of Food Processing, Burdur Food Agriculture and Livestock Vocational School, Burdur, Türkiye
[2*]Istanbul Aydin University, School of Medicine, Department of Medical Biology, Istanbul, Türkiye
Ali SOYUÇOK ORCID No: 0000-0003-2626-5827
Samet UÇAK ORCID No: 0000-0002-3461-2481

**Corresponding author: sametucak@aydin.edu.tr*

(Received: 26.05.2025, Accepted: 14.07.2025, Online Publication: 26.09.2025)

67

Performance Analysis of Four Metaheuristic Algorithms on Benchmark Functions

Sibel ARSLAN[1*], Muhammed Furkan GÜL[2]

[1] Sivas Cumhuriyet University, Faculty of Engineering, Department of Software Engineering, Sivas, Türkiye
[2]Sivas University of Science and Technology, Faculty of Engineering and Natural Sciences, Department of Computer Engineering, Sivas, Türkiye
Sibel ARSLAN ORCID No: 0000-0003-3626-553X
Muhammed Furkan GÜL ORCID No: 0009-0007-0486-0525

*Corresponding author: sibelarslan@cumhuriyet.edu.tr

(Received: 31.12.2024, Accepted: 15.07.2025, Online Publication: 26.09.2025)

73

Determination of Earthquake Performance of Existing RC Buildings According to FEMA-356 and TBEC-2018

Mohamed Omar HIRABE[1*], Elif BORU[2]

[1] Sakarya University of Applied Science, Faculty of Engineering, Department of Civil Engineering, Sakarya, Türkiye
[2] Sakarya University of Applied Science, Faculty of Engineering, Department of Civil Engineering, Sakarya, Türkiye
Mohamed Omar Hirabe ORCID No: 0000-0003-1605-732X
Elif Boru ORCID No: 0000-0003-1661-7673

*Corresponding author: hiraabe171@gmail.com

(Received: 18.02.2025, Accepted: 22.07.2025, Online Publication: 26.09.2025)

90

The Campus Flora of Bingöl University (Bingöl/Türkiye)

Mihriban AHISKALI [1*], Deniz CANLI [1,2]

[1] Bingöl University Vocational School of Food, Agriculture and Livestock, Bingöl, Türkiye
[2] Bingol University Bee and Natural Products R&D and P&D Application and Research Center, Bingöl, Türkiye
Mihriban AHISKALI ORCID No: 0000-0003-0580-7594
Deniz CANLI ORCID No: 0000-0001-9794-8911

Corresponding author: mahiskali@bingol.edu.tr

(Received: 29.04.2025, Accepted: 05.08.2025, Online Publication: 26.09.2025)

101

Effect of GFRP Anchor on the Performance of Reinforced Concrete Beams to Mitigate The Debonding Failure

Yusuf SÜMER[1*], M. Nawar ZAKOUR[1], Wael ALDHABIR[1]

[1] Sakarya University of Applied Sciences, Faculty of Technology, Department of Civil Eng. Sakarya, Türkiye
Yusuf SÜMER ORCID No: 0000-0002-9314-1640
M.Nawar ZAKOUR ORCID No: 0000-0002-9454-3406
Wael ALDHABİR ORCID No: 0000-0002-5220-7041
Corresponding author: ysumer@subu.edu.tr

(Received: 07.05.2025, Accepted: 05.08.2025, Online Publication: 26.09.2025)

109

A New Model for Transmission Line Modelling Method to Investigate Frequency-Dependent Bioelectromagnetic Interactions **120**

Burak ARICIOĞLU[1*], Abdullah FERİKOĞLU (Retired)[1]

[1] Sakarya University of Applied Sciences, Faculty of Technology, Electrical & Electronics Engineering Department, Sakarya, Türkiye
Burak ARICIOĞLU ORCID No: 0000-0001-9526-7629
Abdullah FERİKOĞLU ORCID No: 0000-0002-5907-1845

**Corresponding author: baricioglu@subu.edu.tr*

(Received: 08.01.2025, Accepted: 09.08.2025, Online Publication: 26.09.2025)

Synthesis and Characterization of (Sn, Al) Co-doped ZnO Semiconductors

Özlem BİLGİLİ[1*]

[1] Dokuz Eylul University, Science Faculty, Physics Department, Izmir, Turkey
Özlem BİLGİLİ ORCID No: 0000-0002-6334-2513

**Corresponding author: ozlem.bilgili@deu.edu.tr*

130

(Received: 26.03.2025, Accepted: 10.08.2025, Online Publication: 26.09.2025)

Fabrication and Characterisation of TiO_2 Thin Film Methanol Vapor Sensor

Ömer ÇOBAN[1*]

[1] Atatürk University, Engineering Faculty, Electrical and Electronic Engineering Department, Erzurum, Türkiye
Ömer ÇOBAN ORCID No: 0000-0003-4312-9026

**Corresponding author: omercoban@atauni.edu.tr*

139

(Received: 03.07.2025, Accepted: 10.08.2025, Online Publication: 26.09.2025)

Strength Performance of 304 Series Steels Welded by Plasma Arc Method

Tanju TEKER[1*], Sinan AYDIN[2]

[1] Sivas Cumhuriyet University, Technology Faculty, Manufacturing Engineering Department, Sivas, Türkiye
[2] Sivas Cumhuriyet University, Technology Faculty, Mechatronics Engineering Department, Sivas, Türkiye
Tanju TEKER ORCID No: 0000-0001-7293-0723
Sinan AYDIN ORCID No: 0000-0003-2285-0906

**Corresponding author: tanjuteker@cumhuriyet.edu.tr*

145

(Received: 05.05.2025, Accepted: 12.08.2025, Online Publication: 26.09.2025)

Investigation of the Joining of SiC-Reinforced Copper Matrix Composites via Friction Welding

İhsan KIRIK[1], Ömer BARAÇ[2], Anıl İMAK[2*], Serhat ŞAP[3]

[1] Bingol University, Technical Sciences Vocational School, Department of Machinery, Bingöl, Türkiye
[2] Bingol University, Faculty of Engineering and Architecture, Department of Mechanical Engineering, Bingöl, Türkiye
[3] Bingol University, Technical Sciences Vocational School, Department of Electricity and Energy, Bingöl, Türkiye
İhsan KIRIK ORCID No: 0000-0002-8361-319X

151

Ömer BARAÇ ORCID No: 0000-0003-2624-0224
Anıl İMAK ORCID No: 0000-0001-6091-1584
Serhat ŞAP ORCID No: 0000-0001-5177-4952

*Corresponding author: aimak@bingol.edu.tr

(Received: 09.05.2025, Accepted: 02.09.2025, Online Publication: 26.09.2025)

Formulation and Evaluation of a Peel-off Gel Mask Containing Macerate St. John's Wort Oil and Activated Carbon Derived from Pine Cones

Hatice KARAER YAĞMUR[1*], Hatice Kübra ÖZER [2]

[1] Dicle University, Faculty of Science, Chemistry Department, Diyarbakır, Türkiye
[2] Dicle University, Science and Technology Application and Research Center, Diyarbakır, Türkiye
Hatice KARAER YAĞMUR ORCID No: 0000-0002-3728-1825
Hatice Kübra ÖZER ORCID No: 0009-0003-5666-5538

*Corresponding author: profhatice23@hotmail.com

156

(Received: 21.01.2025, Accepted: 02.09.2025, Online Publication: 26.09.2025)

Investigation of the Effects of CNC Nanoparticle-Added Nanofluids on the Machinability of Cupral 4M Alloy

Üsame Ali USCA[1*]

[1] Selçuk University, Akşehir Faculty of Engineering and Architecture, Mechanical Engineering Department, Konya, Türkiye
Üsame Ali USCA ORCID No: 0000-0001-5160-5526

*Corresponding author: ali.usca@selcuk.edu.tr

165

(Received: 09.07.2025, Accepted: 03.09.2025, Online Publication: 26.09.2025)

Combined Humic Acid and Lichen-Derived Endophytic Bacteria Application Alleviates Salt Stress-Induced Oxidative Damage in Alfalfa (*Medicago sativa* L.)

Aytekın MAMMADOVA[1] , Ökkeş ATICI[1*], Özlem GÜLMEZ[1]

[1]Department of Biology, Faculty of Science, Atatürk University, 25240 Erzurum, Türkiye
Aytekın MAMMADOVA ORCID: 0009-0008-6108-1221
Ökkeş ATICI ORCID: 0000-0001-6256-5101
Özlem GÜLMEZ ORCID: 0000-0002-7199-4634

Corresponding author: oatici@atauni.edu.tr

172

(Received: 28.05.2025, Accepted: 03.09.2025, Online Publication: 26.09.2025)

Phytochemical contents and *in vitro* activities of *Berberis thunbergii* hydroethanolic extract

Elif Ceren KARAKUS[1], Tevfik OZEN[1*], Semiha YENIGUN[1], Yunus BASAR[2], Ibrahim DEMIRTAS[3], Ilyas YILDIZ[4]

[1] Ondokuz Mayis University, Faculty of Science, Chemistry, Samsun, Türkiye
[2] Igdir University, Research Laboratories Application and Research Center (ALUM), Iğdır, Türkiye
[3] Ondokuz Mayis University, Faculty of Pharmacy, Pharmaceutical Chemistry, Samsun, Türkiye
[4] Tokat Gaziosmanpaşa University, Faculty of Arts and Sciences, Molecular Biology and Genetics, Tokat, Türkiye
Elif Ceren KARAKUS ORCID No: 0009-0004-5082-7919
Tevfik OZEN ORCID No: 0000-0003-0133-5630

183

Semiha YENIGUN ORCID No: 0000-0002-1979-5427
Yunus BASAR ORCID No: 0000-0002-7785-3242
Ibrahim DEMIRTAS ORCID No: 0000-0001-8946-647X
Ilyas YILDIZ ORCID No: 0000-0003-1254-1069

*Corresponding author: tevfikoz@omu.edu.tr

(Received: 16.04.2025, Accepted: 05.09.2025, Online Publication: 26.09.2025)

Non-Destructive Prediction of Maturity from the Sound of Hand Hitting a Watermelon Using Machine Learning

Savaş KOÇ[1*], Ferit AKBALIK[2]

[1] Batman University, Faculty of Engineering and Architecture, Department of Mechanical Engineering, Batman, Türkiye
[2] Batman University, Vocational School of Social Sciences, Batman, Türkiye
Savaş KOÇ ORCID No: 0000-0002-5257-3287
Ferit AKBALIK ORCID No: 0000-0002-9791-1809

*Corresponding author: savas.koc @batman.edu.tr

191

(Received: 06.03.2025, Accepted: 12.09.2023, Online Publication: 26.09.2025)

Spatial Evaluation of Urban Green Space-Population Relationship Using Sentinel-2 Satellite Data and Object-Based Image Analysis: A Case Study Antalya

Mesut ÇOŞLU[1*]

[1] Burdur Mehmet Akif Ersoy University, Science and Letters Faculty, Precision Agriculture and Agricultural Robots Department, Burdur, Türkiye
Mesut ÇOŞLU ORCID No: 000-0003-3952-6563

*Corresponding author: mcoslu@mehmetakif.edu.tr

202

(Received: 26.05.2025, Accepted: 14.09.2025, Online Publication: 26.09.2025)

Investigation of Water Quality and Molecular Analysis (16s rRNA) of Bacterial Community Structure in a Rural Geothermal Spring: Ucler Hill (Azat Village), Kars, Türkiye

Orhan ULUÇAY[1*]

[1] Kafkas University, Faculty of Engineering and Architecture, Department of Bioengineering, Kars, Türkiye
Orhan ULUÇAY ORCID No: 0000-0002-0820-5372

*Corresponding author: orhanulucay@gmail.com

218

(Received: 29.07.2025, Accepted: 16.09.2025, Online Publication: 26.09.2025)

Considering the Health Effects of Climate Change: A Scoping Review

Emine Didem EVCİ KİRAZ[1], Kübra Ecem TURGUTKAYA[1*], Eda ÇELİK[1], Onur TOPÇU[1], İsmail ÇEVİK[1], Dilara ŞAHİN[1], Murat EĞİLMEZ[1], Kübra SOFUOĞLU[1], Tolga Hüseyin ATIŞ[1]

[1] Aydın Adnan Menderes University, Faculty of Medicine, Public Health Department, Aydın, Türkiye
Emine Didem EVCİ KİRAZ ORCID No: 0000-0003-0090-5590
Kübra Ecem TURGUTKAYA ORCID No: 0000-0002-0697-336X

226

Eda ÇELİK ORCID No: 0009-0009-1942-7921
Onur TOPÇU ORCID No: 0009-0003-6479-2967
İsmail ÇEVİK ORCID No: 0000-0002-3797-4461
Dilara ŞAHİN ORCID No: 0000-0002-4499-8533
Murat EĞİLMEZ ORCID No: 0000-0002-9279-2038
Kübra SOFUOĞLU ORCID No: 0009-0000-9710-2326
Tolga Hüseyin ATIŞ ORCID No: 0000-0002-1533-4877

*Corresponding author: kturgutkaya@adu.edu.tr

(Received: 20.11.2024, Accepted: 02.08.2025, Online Publication: 26.09.2025)

Melatonin: The Multifaceted Hormone

Beyzanur ŞİMŞEK[1], Esra AYDEMİR[1], Bülent KAYA[1*]

[1] Department of Biology, Faculty of Science, Akdeniz University, Antalya TR-07058, Turkey
Beyzanur ŞİMŞEK ORCID No: 0000-0003-3086-6836
Esra AYDEMİR ORCID No: 0000-0002-5206-7333
Bülent KAYA ORCID No : 0000-0002-0491-9781

*Corresponding author: bkaya@akdeniz.edu.tr

(Received: 07.05.2025, Accepted: 05.09.2025, Online Publication: 26.09.2025)

Volume 14, Issue 3, Page 1-9, 2025 https://doi.org/10.46810/tdfd.1675603 Research Article

BİNGÖL UNIVERSITY

Türk Doğa ve Fen Dergisi
Turkish Journal of Nature and Science
www.dergipark.gov.tr/tdfd

Molecular Biological Effects of *Gundelia tournefortii* (Kenger Herb) Extract on Oxidative Stress and Cellular Responses in *Saccharomyces cerevisiae*

Batuhan YILMAZ[1], Hacı FIRAT[1], Seda BEYAZ[1], Nasrullah CELAYİR[1], Abdullah ASLAN[1*]

[1] Fırat University, Faculty of Science, Biology Department, Elazığ, Türkiye
Batuhan YILMAZ ORCID No: 0009-0009-9391-1367
Hacı FIRAT ORCID No: 0009-0007-9146-8598
Seda BEYAZ ORCID No: 0000-0003-0436-8112
Nasrullah CELAYİR ORCID No: 0009-0006-9391-1613
Abdullah ASLAN ORCID No: 0000-0002-6243-4221

**Corresponding author: aaslan@firat.edu.tr*

(Received: 17.04.2025, Accepted: 16.06.2025, Online Publication: 26.09.2025)

Keywords
Gundelia tournefortii (Kenger plant), Hydrogen peroxide, Oxidative damage, Protein synthesis, *Saccharomyces cerevisiae*

Abstract: *Gundelia tournefortii* (Kenger plant) is traditionally used for liver diseases, diabetes, chest pain, heart failure, stomach pain, vitiligo, diarrhea, and bronchitis. Additionally, it is known for its purgative, sedative, anti-inflammatory, antiparasitic, antiseptic, and antiemetic properties. This study investigates whether *Gundelia tournefortii* has a protective role against hydrogen peroxide (H_2O_2)-induced oxidative damage in *Saccharomyces cerevisiae*. In this study, four groups were established: Control group; H_2O_2 group (15 millimolar); *G. tournefortii* group (10%); *G. tournefortii* (10%) + H_2O_2 (15 millimolar) group. *S. cerevisiae* cultures were grown at 30°C for 1, 3, 5, and 24-hour intervals. Cell growth periods, lipid peroxidation malondialdehyde (MDA) analysis, glutathione (GSH) levels, and catalase activity (CAT) were measured using a spectrophotometer. The total protein concentration changes of *S. cerevisiae* cultures were determined by SDS-PAGE electrophoresis and calculated using the Bradford method. As a result, in the H_2O_2 group, MDA levels increased, while GSH levels and CAT activity decreased, indicating increased oxidative stress. In the *G. tournefortii* group, MDA levels decreased, while GSH levels and CAT activity increased, suggesting that this plant has a protective effect. The results suggest that *G. tournefortii* extract enhances cellular defense mechanisms by mitigating oxidative stress and promoting protein synthesis in yeast cells.

Gundelia tournefortii (Kenger Otu) Ekstresinin *Saccharomyces cerevisiae'de* Oksidatif Stres ve Hücresel Tepkiler Üzerindeki Moleküler Biyolojik Etkileri

Anahtar Kelimeler
Gundelia tournefortii (Kenger bitkisi), Hidrojen peroksit, Oksidatif hasar, Protein sentezi, *Saccharomyces cerevisiae*

Öz: *Gundelia tournefortii* (Kenger bitkisi), geleneksel olarak karaciğer hastalıkları, diyabet, göğüs ağrısı, kalp yetmezliği, mide ağrısı, vitiligo, ishal ve bronşit için kullanılır. Ayrıca müshil, yatıştırıcı, iltihap giderici, antiparaziter, antiseptik ve kusma önleyici özellikleriyle de bilinir. Bu çalışma, *Gundelia tournefortii'nin Saccharomyces cerevisiae'de* hidrojen peroksit (H_2O_2) kaynaklı oksidatif hasara karşı koruyucu bir rolü olup olmadığını araştırmaktadır. Bu çalışmada dört grup oluşturuldu: Kontrol grubu; H_2O_2 grubu (15 milimolar); *G. tournefortii* grubu (%10); *G. tournefortii* (%10) + H_2O_2 (15 milimolar) grubu. *S. cerevisiae* kültürleri 30°C'de 1, 3, 5 ve 24 saat boyunca büyütüldü. Hücre büyüme periyotları, lipid peroksidasyon malondialdehit (MDA) analizi, glutatyon (GSH) seviyeleri ve katalaz aktivitesi (CAT) bir spektrofotometre kullanılarak ölçüldü. *S. cerevisiae* kültürlerinin toplam protein konsantrasyonundaki değişimler SDS-PAGE elektroforezi ile belirlendi ve Bradford yöntemi kullanılarak hesaplandı. Sonuç olarak, H_2O_2 grubunda MDA seviyeleri artarken, GSH seviyeleri ve CAT aktivitesi azaldı ve bu da oksidatif stresin arttığını gösterdi. *G. tournefortii* grubunda ise MDA seviyeleri azalırken, GSH seviyeleri ve CAT aktivitesi arttı ve bu da bu bitkinin koruyucu etkiye sahip olduğunu gösterdi. Sonuçlar, *G. tournefortii* özütünün oksidatif stresi azaltarak maya hücrelerinde protein sentezini teşvik ederek hücresel savunma mekanizmalarını güçlendirdiğini göstermektedir.

1. INTRODUCTION

For centuries, humans have used compounds derived from plants to treat or prevent diseases. The use of medicinal plants and the identification of their roles in treatment processes have continued to gain importance, with their significance steadily increasing over time. Traditionally used plants continue to inspire new ideas and important research in today's pharmaceutical industry. The plants used for treating various ailments and the specific disorders for which they are used have been passed down orally from generation to generation. Recently, there has been a growing interest in herbal supplements and functional food products due to their nutritional and health benefits. The subject of this project, *Gundelia tournefortii*, is an endemic, edible plant belonging to the Asteraceae family, commonly known by various names, including "kenger otu," "haskenger," "akub," and "kanger." It is a plant with well-known health benefits and has a long history of traditional uses. *Gundelia tournefortii* (Kenger plant) is a therapeutic plant known for its antibacterial, anti-inflammatory, hepatoprotective, antiplatelet, and hypolipidemic activities [1,2].

In Turkish folk medicine, it has been used to treat diabetes, act as a painkiller, relieve cramps, treat indigestion, manage hypoglycemia, strengthen nerves, and alleviate migraines. Its stem is particularly known for its hepatoprotective and blood-purifying properties, while its fruit is used to treat vitiligo [2]. *G. tournefortii* is a perennial plant that grows to about 60 cm in height, with branched stems that are almost hairless and spiny, resembling thistles. Its leaves are leathery and tough, with distinct yellow, red, or purple veins arranged alternately. Its flowers can be white, yellow, purple, red, or green. The stems, flowers, leaves, and seeds of *G. tournefortii* can be used as food. In Turkey, the dried plant is stored as winter food. The latex sap of *G. tournefortii* is used for various traditional purposes, while its seeds are considered a coffee alternative and consumed [3].

Figure 1. *Gundelia tournefortii* (Kenger plant) [4]

Saccharomyces cerevisiae (*S. cerevisiae*) is a species of yeast known as the simplest eukaryotic model organism. Yeast cells are exposed to various stresses, and each stress factor has the potential to cause cellular damage. Oxidative stress is one of these stress factors. *S. cerevisiae* cells must cope with the toxic effects of reactive oxygen species (ROS) derived from molecular oxygen. These reactive oxygen species include superoxide anion ($O_2^{\bullet -}$), singlet oxygen ($^1O_2$), hydroxyl radical (OH•), and hydrogen peroxide (H_2O_2). Particularly, hydrogen peroxide (H_2O_2) is a harmful oxidative stress factor for *S. cerevisiae* cells. It accumulates within the cell and targets cellular structures, especially proteins, lipids, and DNA, leading to oxidative damage and disrupting normal cellular functions. Hydrogen peroxide (H_2O_2), as a strong reactive oxygen species (ROS), causes oxidative effects on proteins, lipids, and DNA, leading to oxidative damage in these biomolecules. This damage results in the disruption of cellular functions, harm to genetic material, and imbalance in biological systems. Oxidative damage can prevent cells from performing their normal functions and contribute to the development of pathological conditions such as aging, cancer, cardiovascular diseases, and neurological disorders. H_2O_2 is commonly used in both in vivo and in vitro conditions for modeling oxidative stress, making it a valuable research tool to study the effects of oxidative stress on biological systems [5].

Oxidative stress arises from the imbalance between free radicals and antioxidant defense mechanisms in cells. This imbalance results in the damage caused by reactive oxygen species (ROS) targeting cellular structures. Biomolecules such as DNA, proteins, lipids, and carbohydrates are among the structures most affected by this damage. To counteract the effects of oxidative stress, organisms rely on protective mechanisms such as antioxidant enzymes and reduced glutathione. Lipid oxidation is considered an indicator of cellular stress, and in association with this process, levels of malondialdehyde (MDA) increase [6]. This study aims to investigate the protective effects of *Gundelia tournefortii* (Kenger plant) against hydrogen peroxide (H_2O_2)-induced oxidative damage in the *S. cerevisiae* cell model. Furthermore, the study will evaluate the effects of *G. tournefortii* extracts on antioxidant and oxidative stress parameters, such as cellular development, malondialdehyde (MDA) levels, glutathione (GSH) levels, catalase (CAT) activity, and total protein concentration.

2. MATERIAL AND METHOD

2.1. Material

In this study, MDA, GSH, catalase activity (CAT) analyses were performed using a spectrophotometer device, and protein electrophoresis was performed using an SDS-PAGE mini protein device. Some of the chemical consumables used are as follows; glucose, tryptone, yeast extract, hydrogen peroxide (H_2O_2).

2.2. Experimental Groups

In this study, the therapeutic effects of *Gundelia tournefortii* (Kenger plant) extract against hydrogen peroxide (H_2O_2)-induced damage in *S. cerevisiae* were investigated. Four different groups were established, as follows: 1) Control group, 2) H_2O_2 group (15 millimolar),

3) *G. tournefortii* group (10%), 4) *G. tournefortii* (10%) + H_2O_2 (15 millimolar) group.

2.3. Application of *Gundelia tournefortii* (Kenger plant) Extract and Hydrogen Peroxide (H_2O_2) to the Culture

Preparation of *S. cerevisiae* Culture Medium: The medium required for yeast growth was prepared using YEPD medium. For this medium, 7.5 g of yeast extract, 7.5 g of tryptone, and 7.5 g of glucose were mixed per 250 mL solution. The prepared medium was transferred into five Erlenmeyer flasks, 50 mL each, and sterilized in an autoclave at 121°C for 1 hour. After sterilization, the flasks were allowed to cool at room temperature. Once cooled, 800 µl of yeast was added to each flask, and the cultures were incubated in an incubator for 20 min. After the incubation period, yeast development was assessed by optical density measurements. Preparation of 10% *Gundelia tournefortii* (Kenger plant) Extract: 10 g of *G. tournefortii* (Kenger plant) was added to 100 mL of boiling distilled water and left to steep for 15-20 min. After the steeping process, the mixture was filtered through a sterile cloth and was ready to be added to the culture medium.

Figure 2. *Gundelia tournefortii* (Kenger plant) and Extract

2.4. Malondialdehyde (MDA) Analysis

Malondialdehyde (MDA) reacts with TBA to form a pink-colored compound. The concentration of MDA is determined by measuring the absorbance of this compound at 535 nm using a spectrophotometer. 0.4 mL of supernatant was mixed with 1.6 mL of Tris-KCl buffer, and 0.5 mL of 30% TCA was added. After 0.5 mL of 0.75% TBA was added and boiled, then centrifuged at 4000 rpm. The clear supernatant was collected, and the absorbance was measured at 532 nm [7,8].

2.5. Glutathione (GSH) Analysis

The GSH analysis was performed according to the Ellman [9] method. Reduced glutathione reacts with 5,5'-dithiobis 2-nitrobenzoic acid to form a yellow-green colored compound. The light intensity of this compound was spectrophotometrically measured at 412 nm [9,10].

2.6. Catalase (CAT) Activity Assay

The method developed by Aebi was used to measure CAT (catalase) activity. The measurement principle is based on the light absorption properties of hydrogen peroxide (H_2O_2) at a wavelength of 240 nm [11,12].

2.7. Total Protein Concentration Measurements (Bradford Method)

Total protein concentration was determined spectrophotometrically at 595 nm using the Bradford method. The protein amount in S. cerevisiae groups was calculated comparatively using BSA protein standards [13,14].

2.8. Protein Isolation for SDS-PAGE (Sodium Dodecyl Sulfate-Polyacrylamide Gel Electrophoresis)

After taking 1 mL of the culture sample, it was centrifuged at 13,000 rpm for 5 min. The resulting pellet was resuspended with 500 µl of TEA (Tris-EDTA Acetic Acid) buffer (pH: 7.5). The cells were disrupted using a Bandelin Sonopuls sonicator (Germany) at power level 2, with two rounds of sonication, each lasting 10 seconds. After sonication, the sample was incubated on ice for 5 min. and then centrifuged again at 13,000 rpm for 10 min. The resulting pellet was mixed with an equal amount of sample buffer (Sample Amplification Buffer) to prepare the sample for SDS-PAGE [15,16].

2.9. SDS-PAGE (Sodium Dodecyl Sulfate–Polyacrylamide Gel Electrophoresis) Analysis

Before loading the protein samples from *Saccharomyces cerevisiae* cultures into the wells, they were boiled for 5 min. after the addition of an equal amount of SDS-PAGE Sample Amplification Buffer (SAB) dye. A 1x tank buffer was used for electrophoresis. Afterward, a 30 mA current was applied until the blue band of bromophenol blue (tracking dye) reached the end of the gel, allowing the movement of proteins in the gel to be tracked. After electrophoresis, the gel was stained with Coomassie Brilliant Blue for 30 min. to 1 hour at room temperature. The gel was then washed with a stain remover solution until the protein bands became visible. Gel images were taken, and the protein bands between the groups were analyzed [17, 18].

2.10. Statistical Analysis

The statistical data of the study were presented as mean ± standard error (Mean ± Sd). The analyses were repeated 3 times. Comparisons between the groups were made using One-Way Analysis of Variance (ANOVA), and the analyses were performed using the Statistical Package for Social Sciences (SPSS, SPSS Inc., Chicago, IL, USA) software version 25.0. Statistical significance was determined at $p<0.05$.

3. RESULTS

In this study, the protective effects of *Gundelia tournefortii* (Kenger otu) extract against H_2O_2-induced oxidative stress were investigated through biochemical parameters such as malondialdehyde (MDA), catalase (CAT), glutathione (GSH) levels, cell growth, and protein concentration. The obtained results show that *G. tournefortii* significantly reduced the oxidative damage

caused by H_2O_2 and played an effective role in protecting the cells. The findings are as follows:

As presented in Table 1 and Figure 3, the H_2O_2-treated group exhibited significantly lower cell growth at all time points compared to the control group ($p<0.05$). This result supports the hypothesis that H_2O_2 inhibits cell growth. However, the *G. tournefortii* + H_2O_2 group showed significantly higher cell growth compared to the H_2O_2-only group ($p<0.05$). The data in Table 1 demonstrate that while H_2O_2 inhibits cell growth significantly, *G. tournefortii* extract mitigates this inhibition and preserves cell viability.

Table 1. Cell Growth (1h, 3h, 5h, 24h)

Groups	1h	3h	5h	24h (Overnight)
Control	0.624 ± 0.04[a]	0.743 ± 0.06[b]	0.935 ± 0.07[b]	1.266 ± 0.04[b]
G. tournefortii	0.697 ± 0.03[c]	0.808 ± 0.05[d]	1.263 ± 0.05[d]	1.615 ± 0.05[d]
H_2O_2	0.515 ± 0.02[a]	0.558 ± 0.01[a]	0.596 ± 0.03[a]	1.013 ± 0.02[a]
G. tournefortii + H_2O_2	0.585 ± 0.03[b]	0.579 ± 0.02[c]	0.644 ± 0.05[c]	1.135 ± 0.03[c]

[a,b,c,d] The differences between the groups carrying different letters are statistically significant ($p<0.05$). One-way ANOVA Post Hoc Tukey Test.

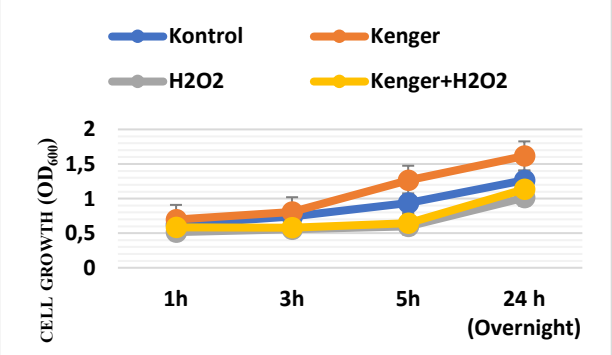

Figure 3. Time-Based Changes in *S. cerevisiae* Cell Development (1, 3, 5, and 24 Hours)

MDA is a marker of oxidative stress as an indicator of lipid peroxidation. As shown in Table 2 and Figure 4 the H_2O_2 group exhibited significantly higher MDA levels compared to the Control group (0.44 ± 0.06 nmol/mL vs. 0.33 ± 0.02 nmol/mL, $p<0.05$). This confirms that H_2O_2 increases oxidative stress. The *G. tournefortii* + H_2O_2 group, however, showed significantly lower MDA levels compared to the H_2O_2 group (0.37 ± 0.04 nmol/mL vs. 0.44 ± 0.06 nmol/mL, $p<0.05$). This indicates that *G. tournefortii* significantly reduced the H_2O_2-induced MDA increase, demonstrating a protective effect against lipid peroxidation. This suggests that *G. tournefortii* reduces H_2O_2-induced oxidative stress and prevents lipid peroxidation.

Table 2. Malondialdehyde (MDA) Level

Groups	MDA Level (nmol/mL)
Control	0.33 ± 0.02[c]
G. tournefortii	0.31 ± 0.03[c]
H_2O_2	0.44 ± 0.06[a]
G. tournefortii + H_2O_2	0.37 ± 0.04[b]

a–c: The differences between the groups carrying different letters in the same column are statistically significant ($p<0.05$). One-way ANOVA Post Hoc Tukey Test

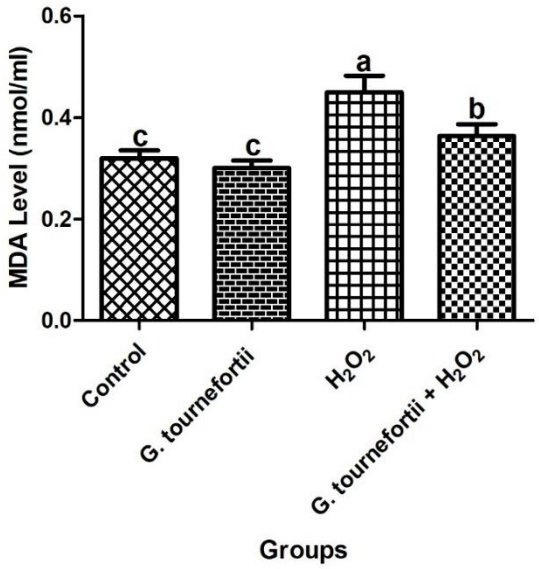

Figure 4. MDA results

Glutathione (GSH) is an important molecule that neutralizes free radicals in cells, preventing oxidative damage, and contributes to the body's defense system.

According to the data presented in Table 3 and Figure 5 the H_2O_2 group exhibited significantly lower glutathione levels compared to the Control group (1.61 ± 0.05 µg/mL vs. 2.08 ± 0.12 µg/mL, $p<0.05$). This confirms that H_2O_2 increases oxidative stress by decreasing glutathione levels. On the other hand, the *G. tournefortii* + H_2O_2 group showed significantly higher glutathione levels compared to the H_2O_2 group (2.09 ± 0.10 µg/mL vs. 1.61 ± 0.05 µg/mL, $p<0.05$). These findings suggest that *G. tournefortii* supports antioxidant defense mechanisms by preventing the reduction of glutathione induced by H_2O_2.

Table 3. Glutathione (GSH) Level

Groups	**GSH Seviyesi (µg/mL)**
Control	2.08 ± 0.12[a]
G. tournefortii	2.09 ± 0.10[a]
H_2O_2	1.61 ± 0.05[c]
***G. tournefortii* + H_2O_2**	1.92 ± 0.06[b]

a–c: The differences between the groups carrying different letters in the same column are statistically significant ($p<0.05$). One-way ANOVA Post Hoc Tukey Test

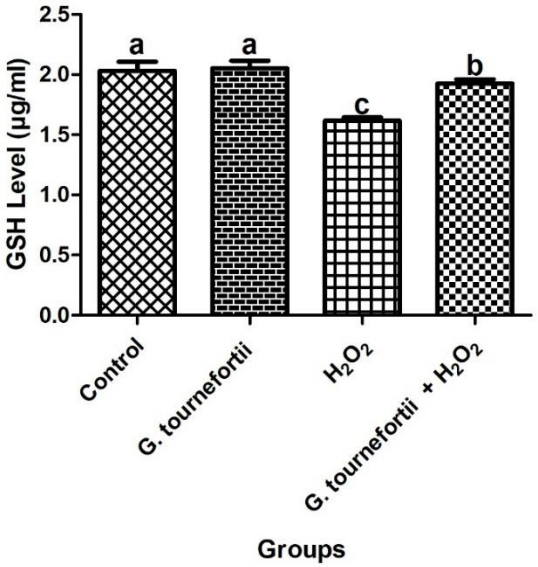

Figure 5. GSH results

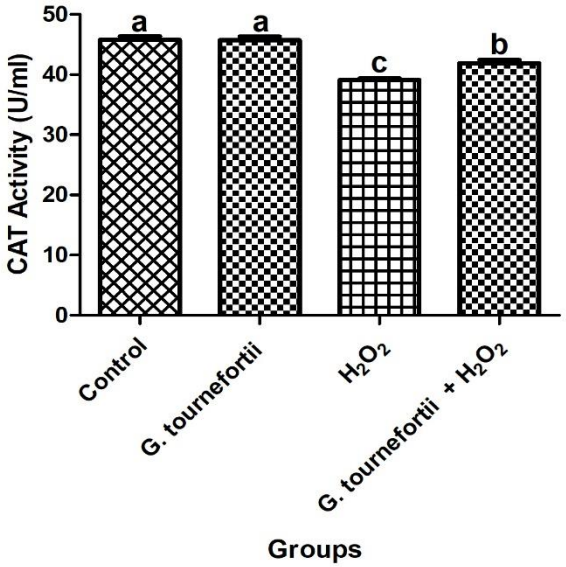

Figure 6. CAT results

Catalase is an important enzyme that converts hydrogen peroxide, which can accumulate in cells and cause oxidative damage, into water and oxygen. According to the data presented in Table 4 and Figure 6, the H_2O_2 group exhibited significantly lower catalase activity compared to the Control group (39.32 ± 0.56 U/mL vs. 45.76 ± 1.05 U/mL, $p<0.05$).

This result indicates that H_2O_2 suppresses antioxidant defense. In the *G. tournefortii* + H_2O_2 group, however, significantly higher catalase activity was observed compared to the H_2O_2 group (45.68 ± 1.03 U/mL vs. 39.32 ± 0.56 U/mL, $p<0.05$). These findings suggest that *G. tournefortii* supports antioxidant defense by preventing the reduction of catalase activity caused by H_2O_2. *G. tournefortii* significantly reversed the decrease in catalase (CAT) and glutathione (GSH) levels induced by H_2O_2, thereby strengthening cellular defense.

Table 4. Catalase (CAT) Activity

Groups	CAT Seviyesi (U/mL)
Control	45.76 ± 1.05[a]
G. tournefortii	45.68 ± 1.03[a]
H_2O_2	39.32 ± 0.56[c]
***G. tournefortii* + H_2O_2**	41.89 ± 0.95[b]

a–c: The differences between the groups carrying different letters in the same column are statistically significant ($p<0.05$). One-way ANOVA Post Hoc Tukey Test

As shown in Table 5, 6 and Figures 7, 8, and 9 the H_2O_2 group exhibited significantly lower protein density in both the supernatant and pellet images compared to the control group ($p<0.05$). This confirms that H_2O_2 inhibits protein synthesis. The *G. tournefortii* + H_2O_2 group, however, showed significantly higher protein density in both the supernatant and pellet images compared to the H_2O_2 group ($p<0.05$). This suggests that *G. tournefortii* reduces the inhibition of protein synthesis caused by H_2O_2 and supports protein synthesis.

Table 5. Protein Density Level (Supernatant)

Groups (Supernatant)	Total Protein Level (nmol/mL)
Control	4.50 ± 0.17[b]
G. tournefortii	4.57 ± 0.18[a]
H_2O_2	3.19 ± 0.08[d]
***G. tournefortii* + H_2O_2**	3.93 ± 0.12[c]

a–d: The differences between the groups carrying different letters in the same column are statistically significant ($p<0.05$). One-way ANOVA Post Hoc Tukey Test

Table 6. Protein Density Level (Pellet)

Groups (Pellet)	Total Protein Level (nmol/mL)
Control	5.37 ± 0.07[a]
G. tournefortii	5.42 ± 0.06[a]
H_2O_2	4.32 ± 0.03[c]
***G. tournefortii* + H_2O_2**	4.95 ± 0.05[b]

a–c: The differences between the groups carrying different letters in the same column are statistically significant ($p<0.05$). One-way ANOVA Post Hoc Tukey Test

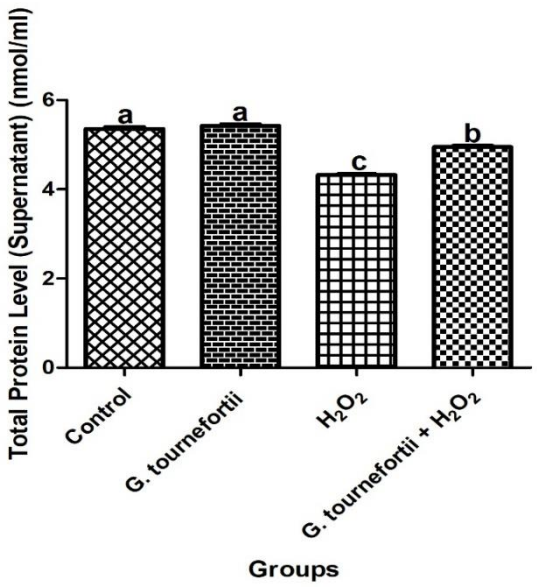

Figure 7. Supernatant Protein Density

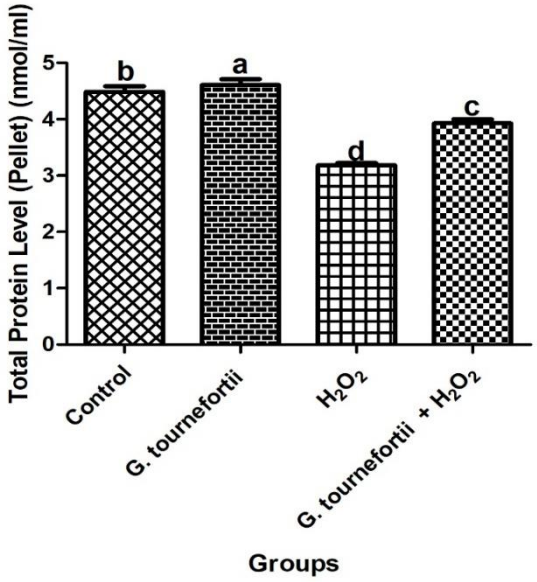

Figure 8. Pellet Protein Density

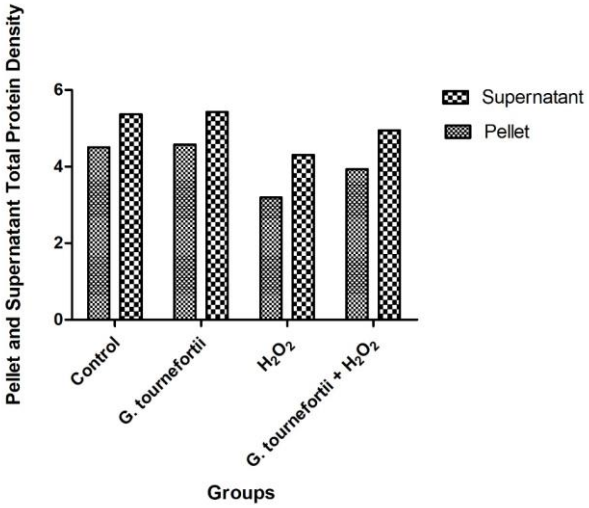

Figure 9. Pellet anad Supernatant Protein Density

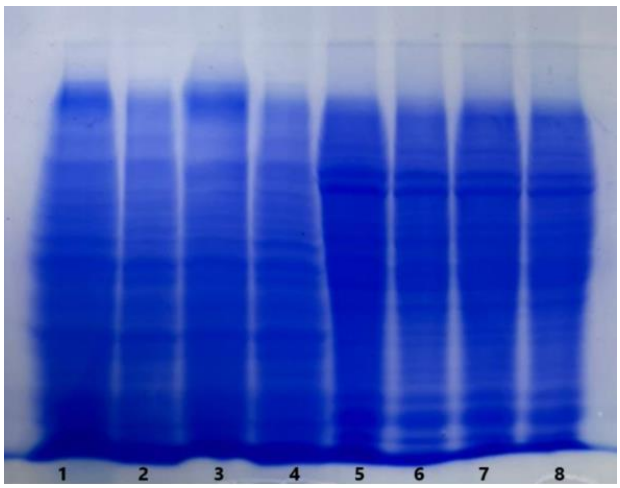

Figure 10. Groups (Supernatant); 1: Control; 2: *G. tournefortii*; 3: H2O2; 4: *G. tournefortii* + H2O2; Groups (Pellet); 5: Control; 6: *G. tournefortii*; 7: H2O2; 8: *G tournefortii* + H2O2

The SDS-PAGE gel image of the supernatant and pellet proteins obtained after subjecting *S. cerevisiae* cells to different Groups was examined (Figure 10):

Band-1; Control-Supernatant: In the Control group, distinct bands corresponding to proteins normally produced by the cells under normal conditions were observed at different molecular weights. This indicates normal protein expression.

Band-2; *G. tournefortii*-Supernatant: In the cells treated with *G. tournefortii*, a band similar to the Control group was observed. This shows that *G. tournefortii* has no effect on extracellular protein secretion.

Band-3; H_2O_2-Supernatant: A significant decrease in band intensity was observed in the cells treated with H_2O_2. This indicates that H_2O_2 inhibits extracellular protein secretion and the cells secrete fewer proteins in response to stress.

Band-4; *G. tournefortii* + H_2O_2-Supernatant: An increase in band intensity was observed in cells treated with both *G. tournefortii* and H_2O_2. This indicates that *G. tournefortii* protects cells from the harmful effects of H_2O_2.

Band-5; Control-Pellet: In the pellet image of the Control group, distinct bands corresponding to intracellular proteins were observed. This represents the intracellular proteins produced by the cells under normal conditions.

Band-6; *G. tournefortii*-Pellet: In the cells treated with *G. tournefortii*, a band similar to the Control group was observed. This indicates that *G. tournefortii* has no effect on intracellular protein expression.

Band-7; H_2O_2-Pellet: A significant decrease in band intensity was observed in the cells treated with H_2O_2. This shows that H_2O_2 inhibits intracellular protein expression and that the cells produce fewer proteins in response to stress. The decrease in low molecular weight proteins is particularly notable.

Band-8; *G. tournefortii* + H_2O_2-Pellet: An increase in band intensity was observed in the cells treated with both *G. tournefortii* and H_2O_2. This indicates that *G. tournefortii* partially reverses the decrease in protein expression caused by H_2O_2 and protects the cells.

4. DISCUSSION

Recent studies have shown that *G. tournefortii* possesses anticancer, anti-inflammatory, antioxidant, anti-cholesterolemic, antibacterial, hepatoprotective, and hypoglycemic effects [19].

Abu Lafi et al. [20] examined the anticancer effects of the *Gundelia tournefortii* plant on human colon cancer HCT-116 cell lines. The study found that the methanol and hexane extracts exhibited significant antitumor effects on cancer cells, while the aqueous extract was ineffective. Additionally, the phytochemical profiles of these extracts were analyzed using gas chromatography-mass spectrometry, and it was determined that 6 out of 27 natural compounds were active against cancer cells. Among these compounds were sitosterol, stigmasterol, lupeol, gitoxigenin, α-amyrin, and artemisinin. These findings suggest that *Gundelia tournefortii* may be a potential source for cancer treatment. Bati et al.[6] investigated the effects of *G. tournefortii* extract on DNA damage, biochemical parameters, and antioxidant activities in rats fed a high-calorie diet. The study was conducted by dividing Wistar albino male rats into four groups and monitoring them for 12 weeks. The results indicated that *G. tournefortii* extract positively reduced DNA damage in brain tissue and improved MDA levels by affecting lipid peroxidation in liver tissue. Furthermore, the plant extract was found to significantly improve antioxidant parameters and demonstrated potential anti-obesity effects by targeting obesity. Vazquez et al. [21] investigated the effects of melatonin on cellular defense against oxidative stress in *S. cerevisiae* cells. The aim of the study was to understand how melatonin affects endogenous cellular defense systems by examining cell viability, glutathione levels (reduced GSH and oxidized GSSG), reactive oxygen species (ROS) production, and the expression of genes related to antioxidant defense systems. The study observed changes in glutathione levels after melatonin was applied to the cells; GSH levels decreased, while GSSG levels increased. Furthermore, melatonin-activated genes are related to the antioxidant defense system, leading to a stronger cellular defense against oxidative stress. In cells subjected to oxidative stress with H_2O_2, melatonin treatment reduced ROS accumulation and increased GSSG levels, thereby reducing cell damage. As a result, melatonin was found to exhibit antioxidant properties in *S. cerevisiae* cells and strengthen cellular defense systems. Aslan [15] studied the protective effects of goji berry against oxidative damage induced by chromium ($K_2Cr_2O_7$) in *S. cerevisiae*. The study showed that goji berry extract reduced $K_2Cr_2O_7$-induced oxidative stress, preserved cell viability, and increased antioxidant enzyme activity. Amer et al. [3] investigated the effects of *G. tournefortii* on hepatocellular carcinoma (HCC). They found that *G. tournefortii* treatment increased tumor size in HCC mice, inhibited cell proliferation, reduced inflammation, and increased antioxidant levels. Furthermore, the treatment inhibited the p53 and phosphorylated PI3K/AKT/mTOR signaling pathways, leading to significant changes in HCC cells. The study suggested that *G. tournefortii* exhibited anticancer and antiproliferative effects and could be a potential therapeutic option for liver cancer.

Hachem et al. [22] examined the effects of *G. tournefortii* extract on liver and kidney damage induced by PCOS. PCOS is an endocrine disorder that increases the risk of kidney and liver damage, and the long-term use of current treatment methods can lead to undesirable side effects. The study explored the potential of *G. tournefortii* to improve liver and kidney damage by regulating oxidative stress pathways. The researchers found that *G. tournefortii* modulated oxidative stress and inflammation, alleviating damage in these organs. In an experiment conducted on mice, the extract treatment reduced ALT and AST levels by 50% and decreased the oxidant marker MDA by 65%. Additionally, superoxide dismutase (SOD) and catalase (CAT) activities returned to normal. Pro-inflammatory cytokines IL-1β and TNF-α were reduced by 80% and 68%, respectively. The study concluded that *G. tournefortii* reduced inflammation in the kidneys by regulating the NLRP3 inflammasome and improved liver and kidney health by reducing oxidative stress. These findings suggest that *G. tournefortii* has complementary potential in the treatment of PCOS.

Karatas [23] evaluated the antioxidant compounds and oxidative stress-related parameters in *G. tournefortii* (thistle). The study determined the levels of vitamin A, vitamin E, vitamin C, MDA, reduced GSH, and oxidized glutathione (GSSG) in the plant. These analyses revealed that the thistle plant exhibited healthy development and was particularly rich in vitamin C and reduced GSH. Additionally, the low MDA level suggested that the plant had not encountered oxidative stress, further indicating healthy growth. The results showed that *G. tournefortii* possesses antioxidant properties, and these properties could provide potential health benefits.

Beyaz et al. [24] evaluated the effects of black mulberry (*Morus nigra* L.) and cornelian cherry (*Cornus mas* L.) fruits on oxidative damage, focusing on molecular biological and biochemical parameters. The study examined parameters such as cell development, MDA levels, reduced GSH, and total protein synthesis. They found that both black mulberry and cornelian cherry fruits played a significant role in reducing oxidative stress. Specifically, in the *Black Mulberry + Cornelian Cherry* + H_2O_2 group, cell development was enhanced, and MDA levels were reduced compared to the H_2O_2-only group. Since MDA is a marker of oxidative stress, this finding suggests that black mulberry and cornelian cherry fruits reduce cellular oxidative damage. Additionally, GSH levels were significantly higher in the black mulberry and cornelian cherry groups compared to the H_2O_2 group. In addition, Aslan [25], Aslan et al. [26] and Beyaz et al. [27] indicated that Mulberry Juice, kiwi fruit juice and epigallocatechin-3 gallate have protective effect against

oxidative stress. In conclusion, black mulberry and cornelian cherry fruits were found to have protective properties against oxidative stress and support cellular growth and protein synthesis, providing beneficial effects on health.

5. CONCLUSION

In conclusion, it has been determined that *G. tournefortii* extract exhibits a strong protective effect against H_2O_2-induced oxidative stress. This extract significantly reduced MDA levels, which are the end product of lipid peroxidation caused by H_2O_2, while showing a significant increase in antioxidant enzyme markers, such as GSH and CAT levels. Furthermore, *G. tournefortii* extract alleviated the detrimental effects of H_2O_2 on protein synthesis and had a positive effect on cell development by increasing cell density. These findings suggest that *G. tournefortii* extract could be an effective natural compound in preventing biological damage caused by oxidative stress and may be considered a potential therapeutic option.

Acknowledgement
I gratefully acknowledge the support provided by the Scientific and Technological Research Council of Turkiye (TUBITAK) for this study.

Financial Disclosure. This study was supported by the Scientific and Technological Research Council of Turkiye (TUBITAK) 2209-A University Students Research Projects Support Program.

Conflict of Interest
No potential conflict of interest was reported by the author(s).

Data Availability Statement
All data from the present study were inserted in this manuscript.

REFERENCES

[1] Rakotondramasy-Rabesiaka, L., Havet, J.L., Porte, C., Fauduet, H. Solid–liquid extraction of protopine from Fumaria officinalis L.—analysis determination, kinetic reaction and model building. Separation and purification technology. 2007; 54(2), 253-261.

[2] Gezici, S., Sekeroglu, N. Comparative biological analyses on kenger and kenger coffee as novel functional food products. Journal of Food Science and Technology. 2021; 59(6), 2328–2338.

[3] Amer, J., Salhab, A., Jaradat, N., Abdallah, S., Aburas, H., Hattab, S., Ghanim, M., Alqub, M. *Gundelia tournefortii* inhibits hepatocellular carcinoma progression by lowering gene expression of the cell cycle and hepatocyte proliferation in immunodeficient mice. Biomedicine & Pharmacotherapy. 2022; 156, 113885.

[4] Mansi, K., Tabaza, Y., Aburjai, T. The iron chelating activity of *Gundelia tournefortii* in iron overloaded experimental rats. Journal of Ethnopharmacology. 2020; 263, 113114.

[5] Cheng, C.H., Ma, H.L., Liu, G.X., Deng, Y.Q., Feng, J., Jie, Y.K., Guo, Z.X. Oxidative stress, DNA damage, and cellular response in hydrogen peroxide-induced cell injury of mud crab (*Scylla paramamosain*). Fish & Shellfish Immunology. 2021; 114, 82-89.

[6] Bati, B., Celik, I., Vuran, N.E., Turan, A., Alkan, E.E., Zirek, A.K. Effects of *Gundelia tournefortii* L. on biochemical parameters, antioxidant activities and DNA damage in a rat model of experimental obesity. Brazilian Journal of Biology. 2021; 83, e251198.

[7] Ohkawa, H., Ohishi, N., Yagi, K. Assay for lipid peroxides in animal tissues by thiobarbituric acid reaction. Analytical Biochemistry. 1979; 95(2), 351-358.

[8] Gbaranor, K.B., Maakai, B., Olatunbosun, T.H., Ben, E.E., Otobo, B.M., Enebeli, K.S., Saronee, F., Etim, D.N., Ovili-Odili, B.Z, Daka, I.R. Effects of smoothies on oxidative stress markers following administration of monosodium glutamate in male wistar rats. Sch Int J Anat Physiol. 2024; 7(8), 129-134.

[9] Ellman, G.L. Tissue sulphydryl groups. Archives of biochemistry and biophysics. 1959; 195982(1), 70-77.

[10] Malayeri, A., Birgani, S.M., Basir, Z., Kalantar, H. Protective effects of diosmin on doxorubicin-induced testicular toxicity in rat. Naunyn-Schmiedeberg's Archives of Pharmacology. 2024; 397(10), 7881-7890.

[11] Aebi, H. Catalase in vitro. Methods in Enzymology. 1984; 105, 121-126.

[12] Kandemir, O., Kucukler, S., Comakli, S., Gur, C., İleriturk, M. Docetaxel-induced liver and kidney toxicity in rats can be alleviated by suppressing oxidative stress, endoplasmic reticulum stress, inflammation, apoptosis and autophagy signaling pathways after Silymarin treatment. Food and Chemical Toxicology. 2025; 196, 115202.

[13] Bradford MM. A rapid and sensitive methof for the quantitation of microgram quantities of protein utilizing the principle of protein-dye binding, Analytical Biochemistry. 1976; 72, 248–254.

[14] Nili-Ahmadabadi, A., Abdpour, S., Omidifar, N., Hashemi, S.A., Mousavi, S.M., Ahmadabadi, M.N. Therapeutic potentials of N-acetylcysteine immobilized polyrhodanine nanoparticles toward acetaminophen-induced acute hepatotoxicity in rat. Chemical Biology & Drug Design. 2024; 103(1), e14430.

[15] Aslan, A. Protective effects of goji berry on oxidative damage induced by chromium ($K_2Cr_2O_7$) in *Saccharomyces cerevisiae*. Bitlis Eren University Journal of Science. 2021; 10, 784-795.

[16] Nergiz, M.A., Beyaz, S., Gok, O., Aslan, A. Evaluation of the antioxidative effects of *Hibiscus sabdariffa* l. extract on *Saccharomyces cerevisiae* with molecular biological and biochemical biomarkers. Journal of Applied Biological Sciences. 2024; 18(3), 342-354.

[17] LaemmLi, U.K. Cleavage of structural proteins during the assembly of the head of bacteriophage T4. Nature. 1970; 227, 680–685.
[18] Beyaz, S. Investigation of antioxidant activities of *Melissa officinalis* and *Lavandula angustifolia* extracts against chromium induced oxidative damage in *Saccharomyces cerevisiae* with molecular biological and biochemical biomarkers. Progress in Nutrition. 2022; 24(3), 2-11.
[19] Yuksel, A., Celayir, D.N., Yenilmez Tunoglu, E.N., Tutar, L., Tutar, Y. Metabolite-induced apoptosis by *Gundelia tournefortii* in A549 lung cancer cells: A cytotoxic and gene expression study. Nutrients. 2025; 17(3), 374-388.
[20] Abu-Lafi, S., Rayan, B., Kadan, S., Abu-Lafi, M., Rayan, A. Anticancer activity and phytochemical composition of wild *Gundelia tournefortii*. Oncology Letters. 2019; 17(1), 713–717.
[21] Vázquez, J., Muñiz-Calvo, S., González, J. Melatonin reduces oxidative stress damage ınduced by hydrogen peroxide in *Saccharomyces cerevisiae*. Frontiers in Microbiology. 2017; 8, 1066.
[22] Hachem, S., Al Battal, M., Dakdouk, H., Natour, D.E., Borjac, J. Anti-inflammatory and antioxidant effects of *Gundelia tournefortii* aqueous extract on the liver and kidney of pcos mice. Journal of Evidence-Based Integrative Medicine. 2025; 30, 2515690X241304519.
[23] Karatas, F. Investigation of A, E, and C vitamins, malondialdehyde, and glutathione levels in kenger (*Gundelia tournefortii*) plant. Erzincan University Journal of Science and Technology. 2014; 7(2), 159-168.
[24] Beyaz, S., Dalkılıc, L.K., Gok, O., Aslan, A. The effect of black mulberry (*Morus nigra* L.) and cornelian cherry (*Cornus mas* L.) on some molecular biological and biochemical parameters against hydrogen peroxide-induced oxidative damage in *Saccharomyces cerevisiae*. Bitlis Eren University Journal of Science. 2020; 9(3), 1134-1144.
[25] Aslan, A. Cell culture development and the imaging of total protein product changing with SDS-PAGE in *Saccharomyces cerevisiae.* Progress in Nutrition. 2018; 20(1), 128-132.
[26] Aslan, A., Gok, O., Erman, O. The protective effect of kiwi fruit extract against to chromium effect on protein expression in *Saccharomyces cerevisiae.* Progress in Nutrition. 2017; 19(4), 472-476.
[27] Beyaz, S., Gok, O., Aslan, A., The therapeutic effects and antioxidant properties of epigallocatechin-3 gallate: A new review, International Journal of Secondary Metabolite. 2018; 9(2), 125-136.

Volume 14, Issue 3, Page 10-29, 2025 https://doi.org/10.46810/tdfd.1633095 Research Article

BİNGÖL UNIVERSITY

Türk Doğa ve Fen Dergisi
Turkish Journal of Nature and Science
www.dergipark.gov.tr/tdfd

Solitary Wave Solution of the Third Order Gilson-Pickering Equation Via the Abel's Equation with Variable Coefficients

Harun BİÇER[1*]

[1*]Bingöl University, Genç Vocational School, Department of Electric and Energy, Bingöl, Türkiye
Harun BİÇER ORCID No: 0000-0002-9854-0595

**Corresponding author: hbicer@bingol.edu.tr*

(Received: 04.02.2025, Accepted: 18.06.2025, Online Publication: 26.09.2025)

Keywords
The Gilson Pİckering equation, Exact solution, Variable Coefficient Generalized Abel's equation (VCAEM)

Abstract: A novel analytical method, termed the Variable Coefficient Second Degree Generalized Abel Equation Method, is presented in this paper. It has been specifically developed to address the complexities of the Gilson Pickering equation—an important nonlinear partial differential equation encountered in various physical applications. This equation is recognized as a general case of several significant nonlinear partial differential equations, including the Fornberg Whitham, Rosenau Hyman, and Fuchssteiner-Fokas-Camassa-Holm equations. Unlike conventional approaches, which are typically based on constant coefficient ordinary differential equations (ODEs) or auxiliary equations, a unique framework based on variable coefficient ODEs integrated within a subequation structure is introduced by this method.. By applying the method to the Gilson Pickering equation, new exact analytical solutions are derived. The correctness of the technique is validated, and its superior efficiency and robustness are highlighted through these results. The intricate dynamics of the equation are effectively captured, demonstrating the method's suitability for modeling phenomena in fluid dynamics, nonlinear optics, and wave propagation. Furthermore, the potential application of the method to a broader class of nonlinear partial differential equations across mathematical physics is implied by its generalizability. The importance of advancing analytical tools to better understand and resolve complex physical systems is emphasized by the findings, thereby marking a significant contribution to the analytical study of nonlinear differential equations. Ultimately, an expansion of the repertoire of solution strategies available to researchers in applied mathematics and theoretical physics is achieved through this work.

Üçüncü Mertebe Gilson-Pickering Denkleminin Değişken Katsayılı Abel Denklemi Yoluyla Soliter Dalga Çözümü

Anahtar Kelimeler
Gilson Pickering denklemi, Tam çözüm, Değişken katsayılı genelleştirilmiş Abel denklemi

Öz: Bu makalede, Değişken Katsayılı İkinci Derece Genelleştirilmiş Abel Denklemi Yöntemi olarak adlandırılan yeni bir analitik yöntem sunulmaktadır. Bu yöntem, çeşitli fiziksel uygulamalarda karşılaşılan önemli bir doğrusal olmayan kısmi diferansiyel denklem olan Gilson Pickering denkleminin karmaşıklıklarını ele almak için özel olarak geliştirilmiştir. Bu denklem, Fornberg-Whitham, Rosenau-Hyman ve Fuchssteiner-Fokas-Camassa-Holm denklemleri de dahil olmak üzere, diğer bazı önemli doğrusal olmayan kısmi diferansiyel denklemlerin genel bir durumu olarak kabul edilmektedir. Genellikle sabit katsayılı adi diferansiyel denklemlere (ADD) veya yardımcı denklemlere dayanan geleneksel yaklaşımların aksine, bu yöntem alt denklem yapısına entegre edilmiş değişken katsayılı ADD'lere dayanan benzersiz bir çerçeve sunmaktadır. Yöntem, Gilson Pickering denklemine uygulanarak yeni, tam analitik çözümler elde edilmiştir. Bu sonuçlar, tekniğin doğruluğunu kanıtlamakta ve üstün verimliliğini ve sağlamlığını ortaya koymaktadır. Yöntemin denklemin karmaşık dinamiklerini etkin şekilde yakalaması, akışkanlar dinamiği, optik ve dalga yayılımı gibi alanlardaki olguları modellemede uygunluğunu göstermiştir. Genel geçerliliği sayesinde, yöntem daha geniş bir doğrusal olmayan diferansiyel denklem sınıfına uygulanabilir. Bu çalışma, karmaşık fiziksel sistemleri çözmek için analitik araçların geliştirilmesinin önemine dikkat çekerek, ilgili alanlardaki çözüm stratejilerini genişletmektedir.

1 Introduction

Nonlinear partial differential equations (PDEs) hold a profound significance in understanding and modeling various real-world phenomena across diverse fields such as physics, engineering, biology, and finance. Unlike their linear counterparts, these equations encompass intricate relationships where the effects are not proportional to the causes, leading to complex and often unexpected behaviors. From describing fluid dynamics and electromagnetism to population dynamics and wave propagation, nonlinear PDEs capture the intricate interplay of multiple factors, making them indispensable in modeling phenomena exhibiting nonlinearity, chaos, and emergent behavior. However, solving nonlinear PDEs presents formidable challenges due to their inherent complexity, often requiring sophisticated numerical methods, computational techniques, and mathematical analysis [1, 2, 3, 4, 5]. Despite these challenges, mastering nonlinear PDEs unlocks a deeper understanding of the rich tapestry of phenomena that shape our world, enabling scientists and engineers to tackle some of the most pressing challenges facing humanity.

Analytical methods for solving nonlinear PDEs play a pivotal role in understanding the fundamental behavior and properties of complex systems in various fields of science and engineering. Unlike numerical techniques which rely on approximations and computational power, analytical methods aim to derive exact solutions or obtain insightful approximations that offer profound insights into the underlying mechanisms governing nonlinear phenomena. These methods not only provide a deeper understanding of the system's behavior but also serve as the foundation for developing numerical algorithms and computational models. Furthermore, analytical solutions offer invaluable benchmarks for validating numerical simulations and experimental observations, ensuring the accuracy and reliability of predictive models. Moreover, analytical approaches often reveal hidden symmetries, conservation laws, and qualitative features of solutions, shedding light on the underlying physics and guiding the design of efficient algorithms and control strategies. In essence, the importance of analytical methods for solving nonlinear PDEs lies in their ability to unveil the intricate dynamics of complex systems, enabling scientists and engineers to make informed decisions and advance our understanding of the world around us [6, 7, 8, 9, 10, 11].

This paper examines the nonlinear Gilson Pickering (GP) equation of third order [12]:

$$u_t + 2ku_x - \alpha u u_x - \beta u_x u_{xx} - \omega u_{xxt} - \varpi u u_{xxx} = 0. \tag{1}$$

The nonlinear GP equation holds significant physical relevance due to its ability to model complex wave phenomena in various real-world systems. It serves as a generalized framework that encompasses several well-known nonlinear partial differential equations, making it applicable in diverse fields such as fluid dynamics, nonlinear optics, and plasma physics. In particular, it captures the evolution of nonlinear wave structures, including solitary waves and dispersive shock waves, which are essential in understanding water wave propagation, optical pulse dynamics in fiber optics, and wave interactions in plasmas. Its versatility and rich mathematical structure make it a valuable tool for describing and predicting behaviors in systems where nonlinearity and dispersion play crucial roles.

The GP equation was chosen due to its general form, which encompasses several important nonlinear partial differential equations frequently appearing in physical models. Topological properties and wave structures of Eq. (1) are studied in [13]. Some parametric wave solutions which are periodic, solitary, and unbounded wave solutions are reported in [14]. In [15], approximate solutions of GP equation are considered by a meshless method base on the thin plate radial basics functions. The sine Gordon expansion method utilized to contract some exact solution in the form of shock wave, topological, compound topological and nontopo-

logical soliton solutions in [16].

For arbitrary real constants, namely α, β, k, ϖ, and ω, the equation (1) transforms into well known nonlinear PDEs under specific parameter selections:

(1) Fornberg-Whitham (FW) equation [17, 18]:

$$u_t + u_x + uu_x - 3u_xu_{xx} - u_{txx} - \varpi uu_{xxx} = 0, \quad (\alpha = -1,\ \beta = 3,\ k = 0.5,\ \omega = 1). \tag{2}$$

(2) Rosenau-Hyman (RH) equation [19, 20]:

$$u_t - uu_x - 3u_xu_{xx} - \varpi uu_{xxx} = 0, \quad (\alpha = 1,\ \beta = 3,\ k = 0,\ \omega = 0). \tag{3}$$

(3) Fuchssteiner-Fokas-Camassa-Holm (FFCH) equation [21, 22]:

$$u_t + 2ku_x + uu_x - 2u_xu_{xx} - u_{txx} - \varpi uu_{xxx} = 0, \quad (\alpha = -1,\ \beta = 2,\ \omega = 1). \tag{4}$$

By employing the substitution:

$$u(x,t) = U(\xi), \quad \xi = x - \nu t, \tag{5}$$

and substituting this transformation (5) into Eq. (1), we derive the subsequent equation:

$$(2k - \nu)U' + \omega\nu U''' - \varpi UU''' - \alpha UU' - \beta U'U'' = 0. \tag{6}$$

Integrating equation (6) once, we get

$$(2k - \nu)U + \omega\nu U'' - \frac{\alpha}{2}U^2 + \Big(\frac{\varpi - \beta}{2}\Big)(U')^2 - \varpi UU'' = c, \tag{7}$$

where c is a constant of integration.

The remainder of this paper is organized as follows: In Section 2, we introduce the VCAEM and detail the analytical framework developed for solving the GP equation. Section 3 presents the main analytical results obtained using the proposed method, including explicit solutions and their derivations. In Section 4, we discuss the physical and mathematical implications of the results, highlighting the method's effectiveness. Finally, Section 5 concludes the paper with a summary of findings and a discussion on the broader impact and potential future applications of the method in nonlinear science and mathematical physics.

2 Methodology

In this article, we present an innovative method inspired by Hashemi's work in [23, 24], which relies on the VCAEM. Let us explore:

$$\Omega\left(\xi, \mathcal{P}, \mathcal{P}', \ldots, \mathcal{P}^{(n)}\right) = 0.$$

Here, $\Omega\left(\xi, \mathcal{P}, \mathcal{P}', \ldots, \mathcal{P}^{(n)}\right)$ denotes a polynomial w.r.t. $\mathcal{P}, \mathcal{P}', \ldots, \mathcal{P}^{(n)}$, where the coefficients vary according to the ξ.

In this research, we introduce a technique in which the solutions to the specified second order Abel's equation are also solutions to the equation represented in (7), as outlined below:

$$\mathcal{P}' = \vartheta_2(\xi)\mathcal{P}^2 + \vartheta_1(\xi)\mathcal{P} + \vartheta_0(\xi), \tag{8}$$

where $\vartheta_j(\xi) \in \mathcal{C}^n (0 \le j \le 2)$.

For different types of differential equations, it is possible to utilize a generalized Abel's equation with different order. In general, an n^{th} order Abel's equation has the following form:

$$\mathcal{P}' = \sum_{i=0}^{n} \vartheta_i(\xi)\mathcal{P}^i, \tag{9}$$

where $\vartheta_j(\xi) \in \mathcal{C}^n (j \in \{0, 1, ..., n\})$.

We begin by introducing a method to derive equations (8) from the initial equation (7). Letting $\mathcal{P} = \mathcal{P}(\xi)$ represent any solution of (8), differentiating w.r.t. ξ yields:

$$\mathcal{P}''(\xi) = \vartheta_2'\mathcal{P}^2 + \vartheta_1'\mathcal{P} + \vartheta_0' + \mathcal{P}'\left[2\vartheta_2\mathcal{P} + \vartheta_1\right] \quad (10)$$

Moreover, in the general case from the Eq. (9), we have

$$\mathcal{P}'' = \sum_{j=0}^{n}\left[\vartheta_j'(\xi)\mathcal{P}^j + \mathcal{P}'\left(j\vartheta_j(\xi)\mathcal{P}^{j-1}\right)\right], \quad (11)$$

and therefore

$$\mathcal{P}'' = \sum_{j=0}^{n}\left[\vartheta_j'(\xi)\mathcal{P}^j + \left(j\vartheta_j(\xi)\mathcal{P}^{j-1}\right)\sum_{i=0}^{n}\vartheta_i(\xi)\mathcal{P}^i\right]. \quad (12)$$

Therefore, in the second order case, from (8) we have

$$\mathcal{P}''(\xi) = 2\vartheta_2^2\mathcal{P}^3 + \left(\vartheta_2' + 3\vartheta_1\vartheta_2\right)\mathcal{P}^2 + \left(\vartheta_1' + \vartheta_1^2 + 2\vartheta_0\vartheta_2\right)\mathcal{P} + \left(\vartheta_0' + \vartheta_0\vartheta_1\right). \quad (13)$$

The core concept of this new approach is explained as follows. By inserting polynomial expressions for $\mathcal{P}', \mathcal{P}'', \ldots, \mathcal{P}^{(n)}$ into $\Xi\left(\xi, \mathcal{P}, \mathcal{P}', \ldots, \mathcal{P}^{(n)}\right)$, one obtains a polynomial $\Omega(\mathcal{P})$ in terms of $\mathcal{P}$. Setting the coefficients of $\Omega(\mathcal{P})$ to zero leads to an overdetermined system of algebraic and ordinary differential equations (ODEs) for $\vartheta_i(\xi)$, $0 \le i \le 2$. If this system admits solutions in the form of $\vartheta_0(\xi), \vartheta_1(\xi), \vartheta_2(\xi)$, then any solution to (8) will also satisfy (7).

3 Main results

In this present investigation, we employ the subsequent generalized Abel's equation to solve Eq. (7):

$$\frac{d}{d\xi}\mathcal{P}(\xi) = \vartheta_2(\xi)\mathcal{P}^2(\xi) + \vartheta_1(\xi)\mathcal{P}(\xi) + \vartheta_0(\xi). \quad (14)$$

Inserting (14) into Eq. (7) results in a fifth degree polynomial with respect to $\mathcal{P}$, expressed as:

$$\sum_{i=0}^{4} S_i\mathcal{P}^i = 0,$$

where

$$S_0 = 2\nu\omega\left(\frac{d}{d\xi}\vartheta_0(\xi)\right) + 2\nu\omega\vartheta_0(\xi)\vartheta_1(\xi) + (\varpi - \beta)\vartheta_0^2(\xi) - 2c,$$

$$S_1 = 4\omega\nu\,\vartheta_0(\xi)\vartheta_2(\xi) + 2\omega\nu\vartheta_1^2(\xi) - 2\beta\vartheta_0(\xi)\vartheta_1(\xi) + 2\omega\nu\left(\frac{d}{d\xi}\vartheta_1(\xi)\right) - 2\varpi\left(\frac{d}{d\xi}\vartheta_0(\xi)\right) + 4k - 2\nu,$$

$$S_2 = -2\varpi\left(\frac{d}{d\xi}\vartheta_1(\xi)\right) + 2\omega\nu\left(\frac{d}{d\xi}\vartheta_2(\xi)\right) - 2\left(-3\omega\nu\vartheta_1(\xi) + \vartheta_0(\xi)(\beta + \varpi)\right)\vartheta_2(\xi) - (\beta + \varpi)\vartheta_1^2(\xi) - \alpha,$$

$$S_3 = -2\varpi\left(\frac{d}{d\xi}\vartheta_2(\xi)\right) + 4\omega\nu\,\vartheta_2^2(\xi) - 2(\beta + 2\varpi)\vartheta_1(\xi)\vartheta_2(\xi),$$

$$S_4 = -(\beta + 3\varpi)\vartheta_2^2(\xi).$$

Considering $S_i = 0,\ i = 0, \ldots, 4$, leads to a system of differential algebraic equations with the subsequent sets of solutions:

Family 1:

$$\vartheta_0(\xi) = -\frac{3\left(\beta - 3\omega\alpha\right)c}{4\left(9c\,\omega^2\alpha^2 - 18k^2\omega^2\alpha - 6c\beta\omega\alpha + c\,\beta^2\right)\beta\sqrt{\frac{-3}{72c\beta\,\omega^2\alpha^2 - 144\beta\,k^2\omega^2\alpha - 48c\,\beta^2\omega\alpha + 8c\,\beta^3}}},$$

$$\vartheta_1(\xi) = 12\omega k\sqrt{\frac{-3}{72c\beta\,\omega^2\alpha^2 - 144\beta\,k^2\omega^2\alpha - 48c\,\beta^2\omega\alpha + 8c\,\beta^3}}\,\alpha,$$

$$\vartheta_2(\xi) = \sqrt{\frac{-3}{72c\beta\,\omega^2\alpha^2 - 144\beta\,k^2\omega^2\alpha - 48c\,\beta^2\omega\alpha + 8c\,\beta^3}}\,\left(-3\omega\alpha + \beta\right)\alpha,$$

$$\nu = \frac{2\beta k}{\beta - 3\omega\alpha},\ \varpi = -\frac{\beta}{3}.$$

In this scenario, (14) transforms to

$$\frac{d}{d\xi}\mathcal{P}(\xi) = \sqrt{\frac{-3}{72c\beta\,\omega^2\alpha^2 - 144\beta\,k^2\omega^2\alpha - 48c\,\beta^2\omega\alpha + 8c\,\beta^3}}\,\left(-3\omega\alpha + \beta\right)\alpha\,\mathcal{P}^2\left(\xi\right) \tag{15}$$

$$+12\omega k\sqrt{\frac{-3}{72c\beta\,\omega^2\alpha^2 - 144\beta\,k^2\omega^2\alpha - 48c\,\beta^2\omega\alpha + 8c\,\beta^3}}\,\alpha\,\mathcal{P}\left(\xi\right)$$

$$-\frac{3\left(\beta - 3\omega\alpha\right)c}{4\left(9c\,\omega^2\alpha^2 - 18k^2\omega^2\alpha - 6c\beta\omega\alpha + c\,\beta^2\right)\beta\sqrt{\frac{-3}{72c\beta\,\omega^2\alpha^2 - 144\beta\,k^2\omega^2\alpha - 48c\,\beta^2\omega\alpha + 8c\,\beta^3}}}, \tag{16}$$

with exact solution:

$$\mathcal{P}(\xi) = \frac{-\sqrt{18}\,\tan\left(\frac{\sqrt{9}\,\sqrt{\alpha\Phi}\,(C_1+\xi)\sqrt{3}}{2(9c\,\omega^2\alpha^2 - 18k^2\omega^2\alpha - 6c\beta\omega\alpha + c\,\beta^2)\beta\sqrt{\frac{-1}{9\beta\Phi}}}\right)\sqrt{\alpha\Phi} - 6k\omega\alpha}{\alpha\left(-3\omega\alpha + \beta\right)}, \tag{17}$$

where C_1 is an arbitrary constant, and $\Phi = \left(\omega\alpha - \frac{\beta}{3}\right)^2 c - 2k^2\omega^2\alpha$. Hence, based on (7), and (17), the first exact solution in the form of a Kink soliton solution can be articulated as follows:

$$u(x,t) = \frac{-\sqrt{18}\,\tan\left(\frac{\sqrt{9}\,\sqrt{\alpha\Phi}\left(C_1 + x - \left(\frac{2\beta k}{\beta - 3\omega\alpha}\right)t\right)\sqrt{3}}{2(9c\,\omega^2\alpha^2 - 18k^2\omega^2\alpha - 6c\beta\omega\alpha + c\,\beta^2)\beta\sqrt{\frac{-1}{9\beta\Phi}}}\right)\sqrt{\alpha\Phi} - 6k\omega\alpha}{\alpha\left(-3\omega\alpha + \beta\right)}. \tag{18}$$

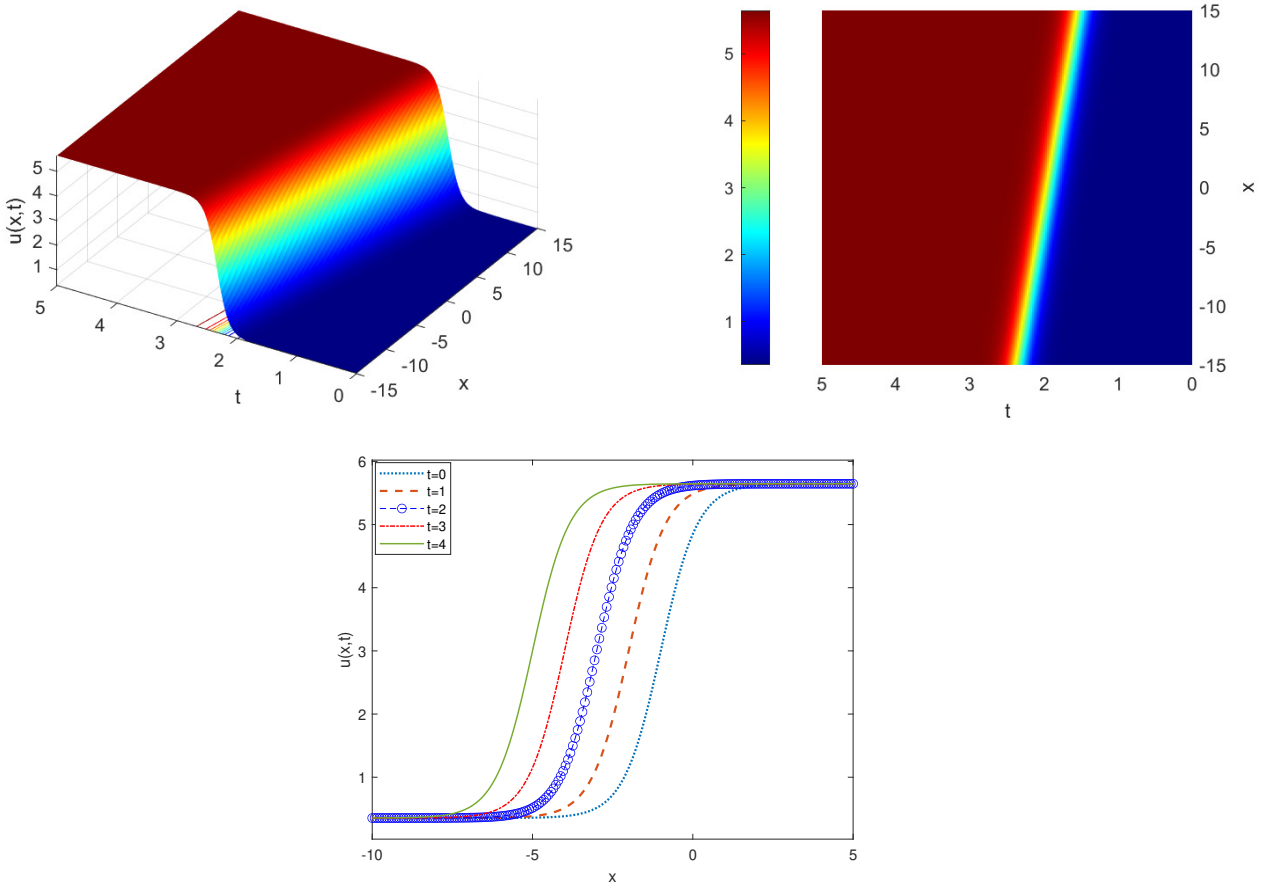

Figure 1: 2D, 3D and contour plots of (18).

Family 2:

$$\vartheta_0(\xi) = -\frac{4k\sqrt{-\frac{3\alpha}{2\beta}}}{3\alpha},\ \vartheta_1(\xi) = \sqrt{-\frac{3\alpha}{2\beta}},\ \vartheta_2(\xi) = 0,\ \nu = \frac{16k^2 - 9\alpha c}{12k},\ \varpi = -\frac{\beta}{3}.$$

Here, the ODE (14) can be written as:

$$\frac{d}{d\xi}\mathcal{P}(\xi) = \sqrt{-\frac{3\alpha}{2\beta}}\mathcal{P}(\xi) - \frac{4k\sqrt{-\frac{3\alpha}{2\beta}}}{3\alpha}, \quad (19)$$

Undoubtedly, a exact solution to (19) also serves as a solution to (7). The exact solution for (19) can be represented as follows:

$$\mathcal{P}(\xi) = \frac{4k}{3\alpha} + C_1\, \mathrm{e}^{\frac{\sqrt{-\frac{6\alpha}{\beta}}\,\xi}{2}}, \quad (20)$$

where C_1 is an arbitrary constant. Therefore, from (7), and (20), a solitary wave solution of the GP equation has the following form:

$$u(x,t) = \frac{4k}{3\alpha} + C_1\, \mathrm{e}^{\frac{\sqrt{-\frac{6\alpha}{\beta}}\left(x - \frac{16k^2 - 9\alpha c}{12k}t\right)}{2}}. \quad (21)$$

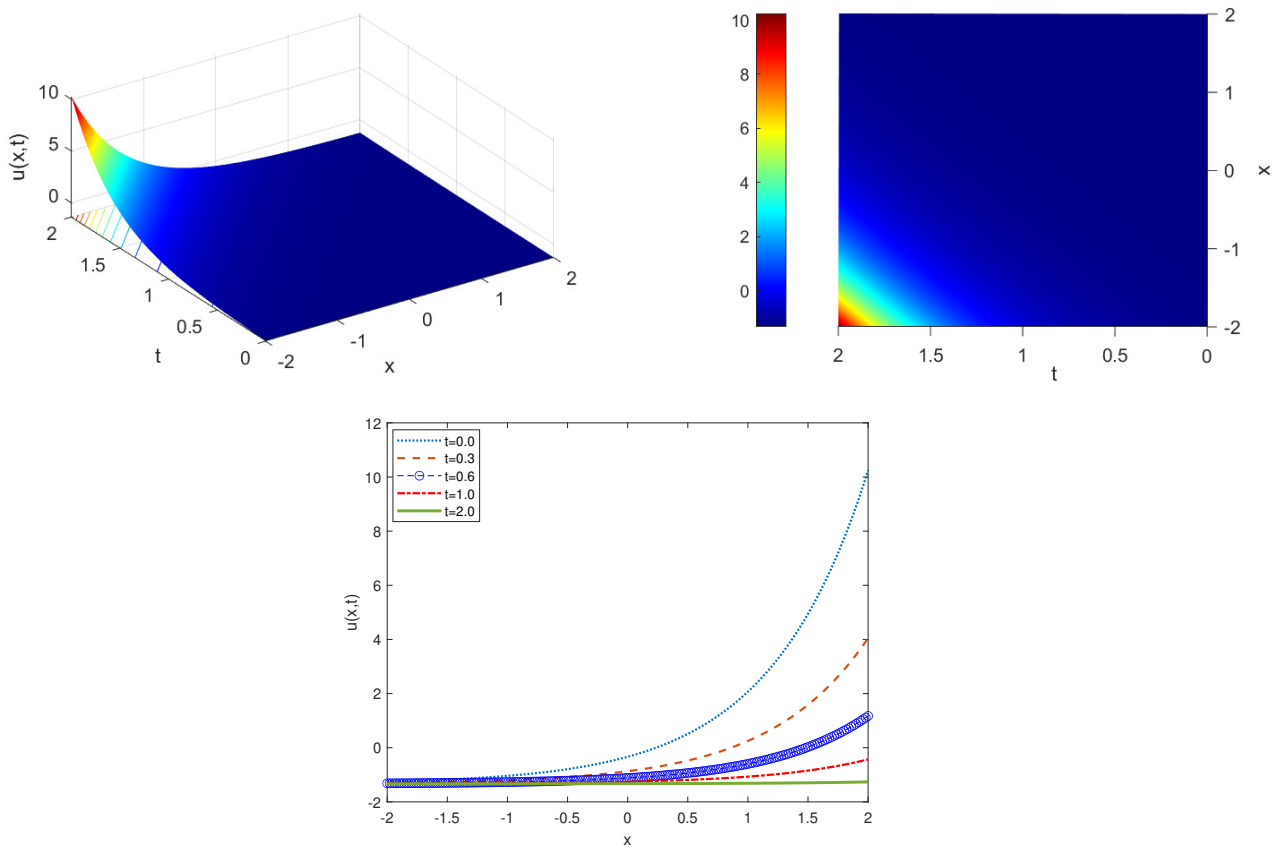

Figure 2: 2D, 3D and contour plots of (21).

Family 3:

$$\vartheta_0(\xi) = -\frac{6\sqrt{-\frac{3\alpha}{2\beta}}\left(\frac{3(6k\omega\alpha+16k\beta+3\Psi)k\,\omega^2\alpha}{-9\alpha^2\omega^2+6\omega\alpha\beta+8\beta^2}+\frac{2(6k\omega\alpha+16k\beta+3\Psi)\beta k\omega}{-9\alpha^2\omega^2+6\omega\alpha\beta+8\beta^2}+3c\omega\alpha-4k^2\omega-c\beta\right)}{\frac{9(6k\omega\alpha+16k\beta+3\Psi)\omega^2\alpha^2}{-9\alpha^2\omega^2+6\omega\alpha\beta+8\beta^2}-\frac{15(6k\omega\alpha+16k\beta+3\Psi)\beta\omega\alpha}{-9\alpha^2\omega^2+6\omega\alpha\beta+8\beta^2}+\frac{4(6k\omega\alpha+16k\beta+3\Psi)\beta^2}{-9\alpha^2\omega^2+6\omega\alpha\beta+8\beta^2}+6k\omega\alpha-8k\beta},$$

$$\vartheta_1(\xi) = \sqrt{-\frac{3\alpha}{2\beta}},\ \vartheta_2(\xi) = 0,\ \nu = \frac{(6k\omega\alpha+16k\beta+3\Psi)\,\beta}{-9\alpha^2\omega^2+6\omega\alpha\beta+8\beta^2},\ \varpi = -\frac{\beta}{3},$$

where $\Psi = \sqrt{-18c\,\omega^2\alpha^3+36k^2\omega^2\alpha^2+12c\beta\omega\,\alpha^2+16c\alpha\,\beta^2}$. In this family, (14) transforms to

$$\frac{d}{d\xi}\mathcal{P}(\xi) = \sqrt{-\frac{3\alpha}{2\beta}}\mathcal{P}(\xi) - \frac{6\sqrt{-\frac{3\alpha}{2\beta}}\left(\frac{3(6k\omega\alpha+16k\beta+3\Psi)k\,\omega^2\alpha}{-9\alpha^2\omega^2+6\omega\alpha\beta+8\beta^2}+\frac{2(6k\omega\alpha+16k\beta+3\Psi)\beta k\omega}{-9\alpha^2\omega^2+6\omega\alpha\beta+8\beta^2}+3c\omega\alpha-4k^2\omega-c\beta\right)}{\frac{9(6k\omega\alpha+16k\beta+3\Psi)\omega^2\alpha^2}{-9\alpha^2\omega^2+6\omega\alpha\beta+8\beta^2}-\frac{15(6k\omega\alpha+16k\beta+3\Psi)\beta\omega\alpha}{-9\alpha^2\omega^2+6\omega\alpha\beta+8\beta^2}+\frac{4(6k\omega\alpha+16k\beta+3\Psi)\beta^2}{-9\alpha^2\omega^2+6\omega\alpha\beta+8\beta^2}+6k\omega\alpha-8k\beta}, \tag{22}$$

with exact solution:

$$\mathcal{P}(\xi) = \frac{9\left(\alpha\omega-\frac{4\beta}{3}\right)\left(\frac{\Theta\,(3\alpha\omega-\beta)\sqrt{2}}{3}+6\omega\beta k\alpha\right)C_1 e^{\frac{\sqrt{6}\sqrt{-\frac{\alpha}{\beta}}\,\xi}{2}}}{9\left(\alpha\omega-\frac{4\beta}{3}\right)\left(\frac{\Theta\,(3\alpha\omega-\beta)\sqrt{2}}{3}+6\omega\beta k\alpha\right)} + \frac{18\left(\sqrt{2}\,\Theta\,k\omega-3c\,\omega^2\alpha^2+\left(6k^2\omega^2+5c\beta\omega\right)\alpha-\frac{4c\,\beta^2}{3}\right)\left(\alpha\omega+\frac{2\beta}{3}\right)}{9\left(\alpha\omega-\frac{4\beta}{3}\right)\left(\frac{\Theta\,(3\alpha\omega-\beta)\sqrt{2}}{3}+6\omega\beta k\alpha\right)}, \tag{23}$$

where C_1 is an arbitrary constant, and $\Theta = \sqrt{\alpha\left(-9c\,\omega^2\alpha^2 + 18k^2\omega^2\alpha + 6\omega\beta\alpha c + 8c\,\beta^2\right)}$. Therefore, another solitary wave solution can be written as:

$$u(x,t) = \frac{9\left(\alpha\omega - \frac{4\beta}{3}\right)\left(\frac{\Theta\,(3\alpha\omega-\beta)\sqrt{2}}{3} + 6\omega\beta k\alpha\right)C_1 \mathrm{e}^{\frac{\sqrt{6}\sqrt{-\frac{\alpha}{\beta}}\left(x - \frac{(6k\omega\alpha+16k\beta+3\Psi)\beta}{-9\alpha^2\omega^2+6\omega\alpha\beta+8\beta^2}t\right)}{2}}}{9\left(\alpha\omega - \frac{4\beta}{3}\right)\left(\frac{\Theta\,(3\alpha\omega-\beta)\sqrt{2}}{3} + 6\omega\beta k\alpha\right)}$$
$$+\frac{18\left(\sqrt{2}\,\Theta\,k\omega - 3c\,\omega^2\alpha^2 + \left(6k^2\omega^2 + 5c\beta\omega\right)\alpha - \frac{4c\,\beta^2}{3}\right)\left(\alpha\omega + \frac{2\beta}{3}\right)}{9\left(\alpha\omega - \frac{4\beta}{3}\right)\left(\frac{\Theta\,(3\alpha\omega-\beta)\sqrt{2}}{3} + 6\omega\beta k\alpha\right)}. \tag{24}$$

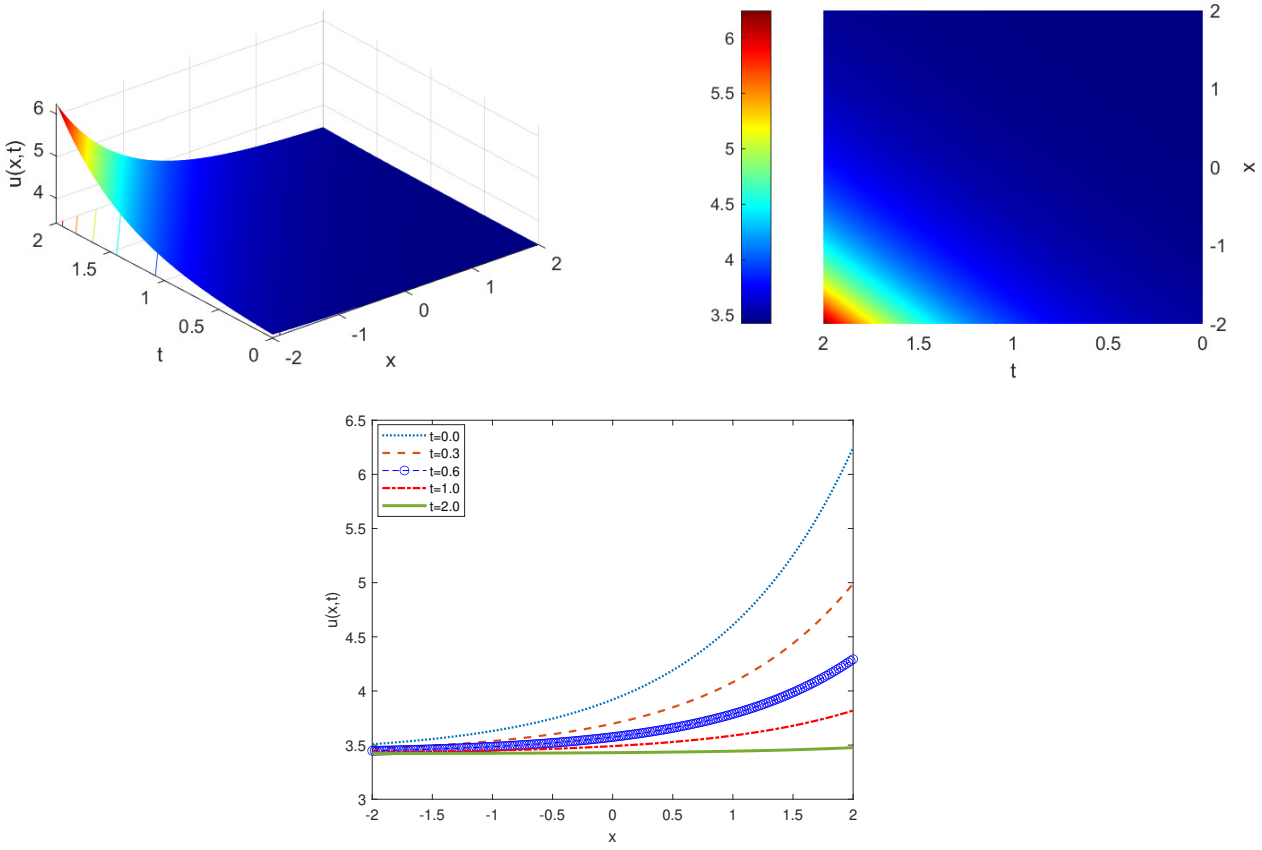

Figure 3: 2D, 3D and contour plots of (24).

Family 4:

$$\vartheta_0(\xi) = \frac{c\,(\alpha\omega+2\beta)\left(2\omega k+\sqrt{2}\,\sqrt{-\omega\,(c\omega\alpha-2k^2\omega+2c\beta)}\right)(C_1+C_2\sin(K\xi)+\cos(K\xi))}{\sqrt{\alpha}\,\sqrt{\beta}\,\omega\left(\sqrt{2}\,\alpha c\omega+2\sqrt{2}\,\beta c-4\sqrt{2}\,k^2\omega-4k\sqrt{-\omega\,(c\omega\alpha-2k^2\omega+2c\beta)}\right)(-\cos(K\xi)\,C_2+\sin(K\xi))},$$

$$\vartheta_1(\xi) = \frac{\omega\left(\left(C_2^2-1\right)\left(\cos^2(K\xi)\right)+(-2C_2\sin(K\xi)-C_1)\cos(K\xi)-\sin(K\xi)\,C_1C_2-C_2^2\right)}{\sqrt{\beta}\,\left(\sin(K\xi)\cos(K\xi)\left(C_2^2-1\right)+2\left(\cos^2(K\xi)\right)C_2+\cos(K\xi)\,C_1C_2-\sin(K\xi)\,C_1-C_2\right)}$$

$$\times\frac{\sqrt{\alpha}\,\left(-4k\sqrt{-\omega\,(c\omega\alpha-2k^2\omega+2c\beta)}+\sqrt{2}\,\left(\left(\alpha c-4k^2\right)\omega+2c\beta\right)\right)}{\left(2\omega k+\sqrt{2}\,\sqrt{-\omega\,(c\omega\alpha-2k^2\omega+2c\beta)}\right)^2},$$

$$\vartheta_2(\xi)=0,\ \nu=\frac{\left(2\omega k+\sqrt{-2c\,\omega^2\alpha+4\omega^2k^2-4c\beta\omega}\right)\beta}{\omega\,(\alpha\omega+2\beta)},\ \varpi=\beta.$$

where $K=\frac{\sqrt{\alpha}}{\sqrt{2\beta}}$. In this Family, the ODE (14) can be written as:

$$\frac{d}{d\xi}\mathcal{P}(\xi)=\frac{2\sqrt{2}\,\left(\left(-\frac{\mathcal{P}(\xi)\alpha}{2}+k\right)\cos(K\xi)+C_2\left(-\frac{\mathcal{P}(\xi)\alpha}{2}+k\right)\sin(K\xi)+kC_1\right)}{\sqrt{\beta}\,\sqrt{\alpha}\,\left(2\cos(K\xi)\,C_2-2\sin(K\xi)\right)},\tag{25}$$

by assuming $\omega=-\frac{2c\beta}{\alpha c-2k^2}$. Definitely, any solution that satisfies (25) also meets the criteria of (7). Expressing the solution to (25) can be done as:

$$\begin{aligned}\mathcal{P}(\xi)=\quad&\Big((4\alpha C_2^3C_3+8kC_1C_2^2+8kC_2^2-4\alpha C_2C_3-8k)\cos^4(K\xi)\\&+(-8\alpha C_2^2C_3-8kC_1C_2-16kC_2)\cos^3(K\xi)\sin(K\xi)\\&+(4\alpha C_2C_3-4\alpha C_2^3C_3-8kC_1C_2^2-4kC_2^2+8k)\cos^2(K\xi)\\&+(4\alpha C_2^2C_3+4kC_1C_2+4kC_2)\cos(K\xi)\sin(K\xi)+C_3\alpha C_2^3+2kC_1C_2^2\Big)\\&\times\frac{1}{\alpha C_2\,(-2C_2\cos^2(K\xi)+2\sin(K\xi)\cos(K\xi)+C_2)},\quad C_1\in\mathbb{R}.\end{aligned}\tag{26}$$

Therefore

$$\begin{aligned}u(x,t)=&\Big((4\alpha C_2^3C_3+8kC_1C_2^2+8kC_2^2-4\alpha C_2C_3-8k)\cos^4(K(x-\nu t))\\&+(-8\alpha C_2^2C_3-8kC_1C_2-16kC_2)\cos^3(K(x-\nu t))\sin(K(x-\nu t))\\&+(4\alpha C_2C_3-4\alpha C_2^3C_3-8kC_1C_2^2-4kC_2^2+8k)\cos^2(K(x-\nu t))\\&+(4\alpha C_2^2C_3+4kC_1C_2+4kC_2)\cos(K(x-\nu t))\sin(K(x-\nu t))+C_3\alpha C_2^3+2kC_1C_2^2\Big)\\&\times\frac{1}{\alpha C_2\,(-2C_2\cos^2(K(x-\nu t))+2\sin(K(x-\nu t))\cos(K(x-\nu t))+C_2)}.\end{aligned}\tag{27}$$

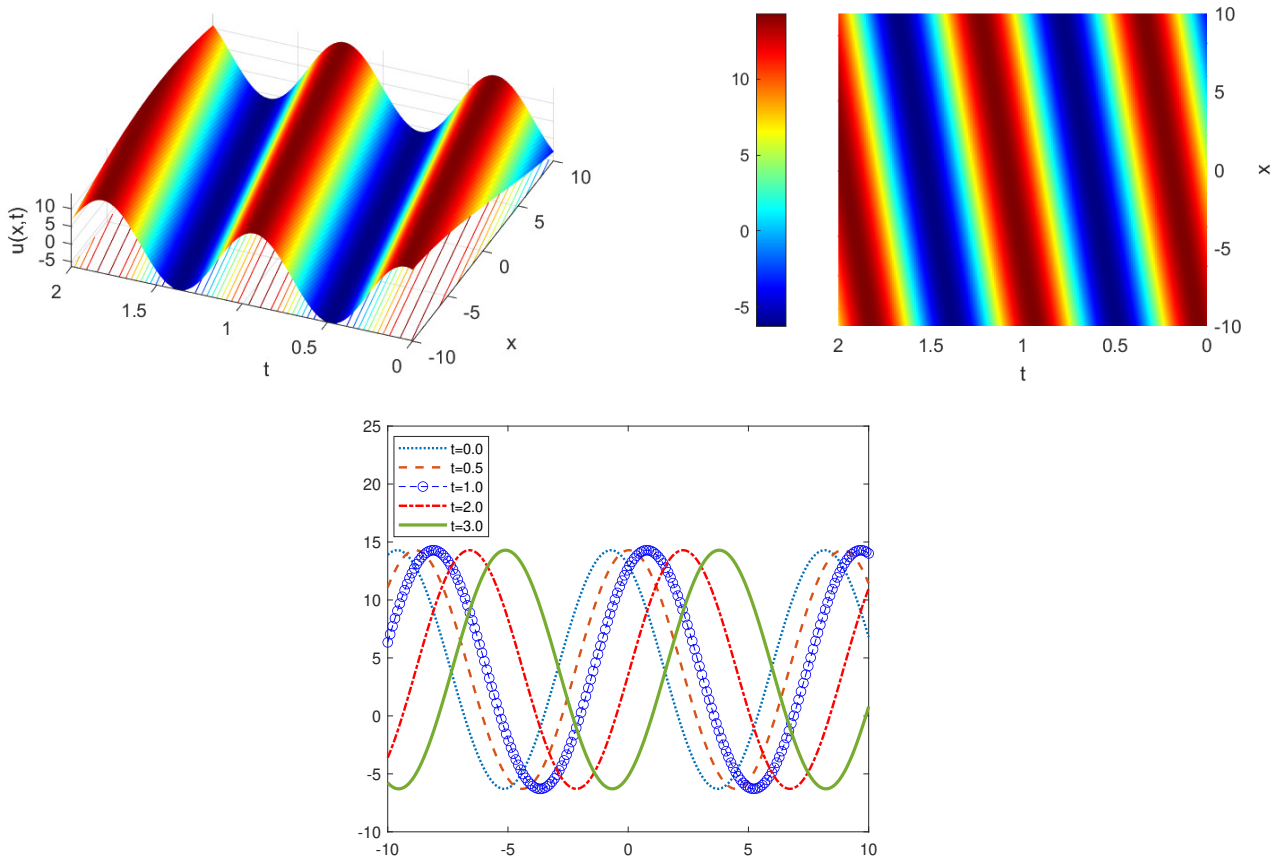

Figure 4: 2D, 3D and contour plots of (27).

Family 5:

$$\vartheta_0(\xi) = -\frac{\tan\left(\frac{\alpha\sqrt{c(\beta+\varpi)}\,(C_1+\xi)}{2\sqrt{\alpha c}\,\varpi}\right)\sqrt{c\,(\beta+\varpi)}\,\sqrt{2}}{\beta+\varpi},$$

$$\vartheta_1(\xi) = -\frac{\sqrt{\alpha c}\,\tan\left(\frac{\alpha\sqrt{c(\beta+\varpi)}\,(C_1+\xi)}{2\sqrt{\alpha c}\,\varpi}\right)\sqrt{c\,(\beta+\varpi)}}{(\beta+\varpi)\,c},$$

$$\vartheta_2(\xi) = 0,\ \nu = 2\sqrt{2\alpha c},\ \omega = -\frac{\varpi}{2\alpha},\ ,\ k = \frac{\sqrt{2}\,\sqrt{\alpha c}}{2}.$$

Here, the ODE (14) takes the following form:

$$\frac{d}{d\xi}\mathcal{P}(\xi) = -\frac{\tan\left(\frac{\alpha\sqrt{c(\beta+\varpi)}\,(C_1+\xi)}{2\sqrt{\alpha c}\,\varpi}\right)\sqrt{c\,(\beta+\varpi)}\,\left(\mathcal{P}(\xi)\,\sqrt{\alpha c}+\sqrt{2}\,c\right)}{c\,(\beta+\varpi)}, \tag{28}$$

with exact solution

$$\mathcal{P}(\xi) = \left(-\frac{\sqrt{2}\left(\frac{2}{\cos\left(\frac{\alpha\sqrt{c(\beta+\varpi)}\,(C_1+\xi)}{\sqrt{\alpha c}\,\varpi}\right)+1}\right)^{\frac{\varpi}{\beta+\varpi}}\sqrt{\alpha c}}{\alpha} + C_3 \right) \times \left(1+\tan^2\left(\frac{\alpha\sqrt{c\,(\beta+\varpi)}\,(C_1+\xi)}{2\sqrt{\alpha c}\,\varpi}\right)\right)^{-\frac{\varpi}{\beta+\varpi}}, \quad C_1 \in \mathbb{R}. \tag{29}$$

Thus, a periodic wave solution can be expressed in the following manner:

$$u(x,t) = \left(-\frac{\sqrt{2}\left(\frac{2}{\cos\left(\frac{\alpha\sqrt{c(\beta+\varpi)}\,(C_1-2\sqrt{2}\sqrt{\alpha c}\,t+x)}{\sqrt{\alpha c}\,\varpi}\right)+1}\right)^{\frac{\varpi}{\beta+\varpi}}\sqrt{\alpha c}}{\alpha} + C_3 \right) \times \left(1+\tan^2\left(\frac{\alpha\sqrt{c\,(\beta+\varpi)}\,\left(C_1-2\sqrt{2}\sqrt{\alpha c}\,t+x\right)}{2\sqrt{\alpha c}\,\varpi}\right)\right)^{-\frac{\varpi}{\beta+\varpi}}, \quad C_3 \in \mathbb{R}. \tag{30}$$

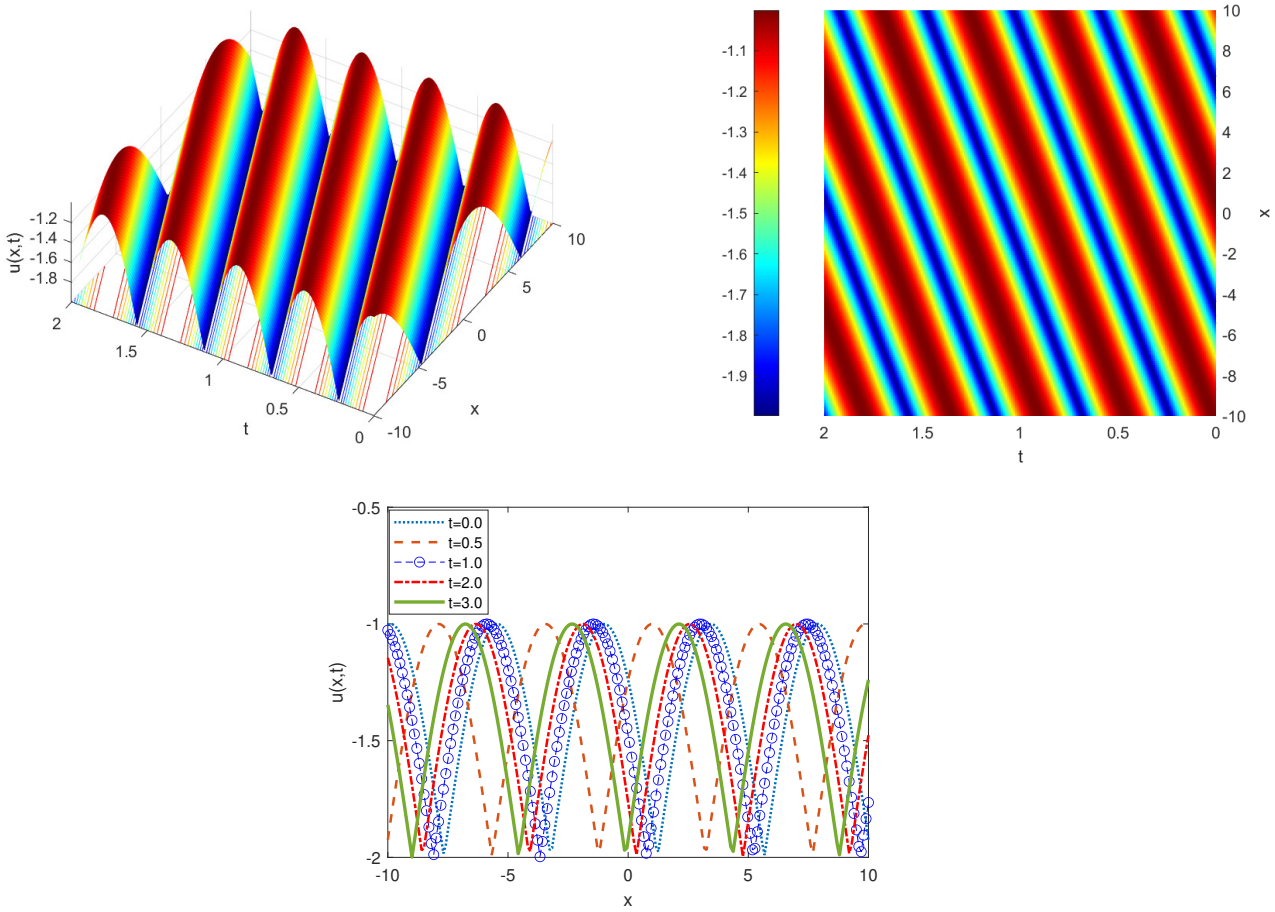

Figure 5: 2D, 3D and contour plots of (30).

Family 6:

$$\vartheta_0(\xi) = \frac{\sqrt{-\frac{\alpha}{\beta+\varpi}}\,(\alpha\omega+\beta+\varpi)}{(\alpha\omega-\beta+\varpi)\left(k\varpi\,\omega^2\alpha^2+2\alpha\left(k\,\varpi^2+\frac{\Phi}{4}\right)\omega-\varpi\left(k\,\beta^2-k\,\varpi^2-\frac{1}{2}\Phi\right)\right)}$$
$$\times\left(\left(-2k^2\varpi+\beta\left(\alpha c-2k^2\right)\right)\alpha\,\omega^2+\left(-\alpha\,\beta^2 c+2c\beta\varpi\alpha+2k^2\beta^2-2k^2\varpi^2-k\Phi\right)\omega-c\beta\varpi\,(\beta-\varpi)\right),$$
$$\vartheta_1(\xi) = \sqrt{-\frac{\alpha}{\beta+\varpi}},\ \vartheta_2(\xi) = 0,$$
$$\nu = \frac{-2\alpha k\varpi\omega+2k\,\beta^2-2k\,\varpi^2+\sqrt{-2c\,\beta^2\omega^2\alpha^3+4\beta^2k^2\omega^2\alpha^2-4c\,\beta^2\varpi\omega\,\alpha^2+2c\,\beta^4\alpha-2c\,\beta^2\varpi^2\alpha}}{-\alpha^2\omega^2-2\alpha\varpi\omega+\beta^2-\varpi^2},$$

where

$$\Phi = -2\alpha k\varpi\omega+2k\,\beta^2-2k\,\varpi^2+\sqrt{-2c\,\beta^2\omega^2\alpha^3+4\beta^2k^2\omega^2\alpha^2-4c\,\beta^2\varpi\omega\,\alpha^2+2c\,\beta^4\alpha-2c\,\beta^2\varpi^2\alpha}.$$

In this instance, the Eq. (14) transforms into

$$\frac{d}{d\xi}\mathcal{P}(\xi) = \sqrt{-\frac{\alpha}{\beta+\varpi}}\,\mathcal{P}(\xi)+\frac{\sqrt{-\frac{\alpha}{\beta+\varpi}}\,(\alpha\omega+\beta+\varpi)}{(\alpha\omega-\beta+\varpi)\left(k\varpi\,\omega^2\alpha^2+2\alpha\left(k\,\varpi^2+\frac{\Phi}{4}\right)\omega-\varpi\left(k\,\beta^2-k\,\varpi^2-\frac{1}{2}\Phi\right)\right)}$$
$$\times\left(\left(-2k^2\varpi+\beta\left(\alpha c-2k^2\right)\right)\alpha\,\omega^2+\left(-\alpha\,\beta^2 c+2c\beta\varpi\alpha+2k^2\beta^2-2k^2\varpi^2-k\Phi\right)\omega-c\beta\varpi\,(\beta-\varpi)\right), \quad (31)$$

with exact solution

$$\mathcal{P}(\xi) = -\mathrm{e}^{\sqrt{-\frac{\alpha}{\beta+\varpi}}\,\xi}\Big[\mathrm{e}^{-\sqrt{-\frac{\alpha}{\beta+\varpi}}\,\xi}\big(-2c\beta\,\omega^3\alpha^3+4\beta\,k^2\omega^3\alpha^2-6c\beta\varpi\,\omega^2\alpha^2+4\beta^2k^2\omega^2\alpha+4\beta\,k^2\varpi\,\omega^2\alpha$$
$$+2c\,\beta^3\omega\alpha-6c\beta\,\varpi^2\omega\alpha+2c\,\beta^3\varpi-2c\beta\,\varpi^3\big)+2\beta^2k\,\omega^2\alpha^2C_1-2\beta^3k\omega\alpha C_1+2\beta^2k\varpi\omega\alpha C_1$$
$$+\sqrt{2}\,\sqrt{\beta^2\alpha\,(-c\,\omega^2\alpha^2+2k^2\omega^2\alpha-2\alpha\varpi\omega c+\beta^2c-\varpi^2c)}\big(2\,\mathrm{e}^{-\sqrt{-\frac{\alpha}{\beta+\varpi}}\,\xi}\,k\,\omega^2\alpha+\omega^2\alpha^2C_1-\beta\varpi C_1$$
$$+2\varpi\omega\alpha C_1-\beta\omega\alpha C_1+2\,\mathrm{e}^{-\sqrt{-\frac{\alpha}{\beta+\varpi}}\,\xi}\beta k\omega+2\,\mathrm{e}^{-\sqrt{-\frac{\alpha}{\beta+\varpi}}\,\xi}k\varpi\omega+\varpi^2C_1\big)\Big]$$
$$\times(-\alpha\omega+\beta-\varpi)^{-1}\Big(2k\omega\,\beta^2\alpha+\sqrt{2}\,\sqrt{\beta^2\alpha\,(-c\,\omega^2\alpha^2+2k^2\omega^2\alpha-2\alpha\varpi\omega c+\beta^2c-\varpi^2c)}\,(\omega\alpha+\varpi)\Big)^{-1}, \quad (32)$$

where $C_1 \in \mathbb{R}$. Therefore, an additional exact solution in the shape of a solitary wave solution can be expressed as follows:

$$u(x,t) = -\mathrm{e}^{\sqrt{-\frac{\alpha}{\beta+\varpi}}\,(x-\nu t)}\Big[\mathrm{e}^{-\sqrt{-\frac{\alpha}{\beta+\varpi}}\,(x-\nu t)}\big(-2c\beta\,\omega^3\alpha^3+4\beta\,k^2\omega^3\alpha^2-6c\beta\varpi\,\omega^2\alpha^2+4\beta^2k^2\omega^2\alpha+4\beta\,k^2\varpi\,\omega^2\alpha$$
$$+2c\,\beta^3\omega\alpha-6c\beta\,\varpi^2\omega\alpha+2c\,\beta^3\varpi-2c\beta\,\varpi^3\big)+2\beta^2k\,\omega^2\alpha^2C_1-2\beta^3k\omega\alpha C_1+2\beta^2k\varpi\omega\alpha C_1$$
$$+\sqrt{2}\,\sqrt{\beta^2\alpha\,(-c\,\omega^2\alpha^2+2k^2\omega^2\alpha-2\alpha\varpi\omega c+\beta^2c-\varpi^2c)}\big(2\,\mathrm{e}^{-\sqrt{-\frac{\alpha}{\beta+\varpi}}\,(x-\nu t)}\,k\,\omega^2\alpha+\omega^2\alpha^2C_1-\beta\varpi C_1$$
$$+2\varpi\omega\alpha C_1-\beta\omega\alpha C_1+2\,\mathrm{e}^{-\sqrt{-\frac{\alpha}{\beta+\varpi}}\,(x-\nu t)}\beta k\omega+2\,\mathrm{e}^{-\sqrt{-\frac{\alpha}{\beta+\varpi}}\,(x-\nu t)}k\varpi\omega+\varpi^2C_1\big)\Big]$$
$$\times(-\alpha\omega+\beta-\varpi)^{-1}\Big(2k\omega\,\beta^2\alpha+\sqrt{2}\,\sqrt{\beta^2\alpha\,(-c\,\omega^2\alpha^2+2k^2\omega^2\alpha-2\alpha\varpi\omega c+\beta^2c-\varpi^2c)}\,(\omega\alpha+\varpi)\Big)^{-1}. \quad (33)$$

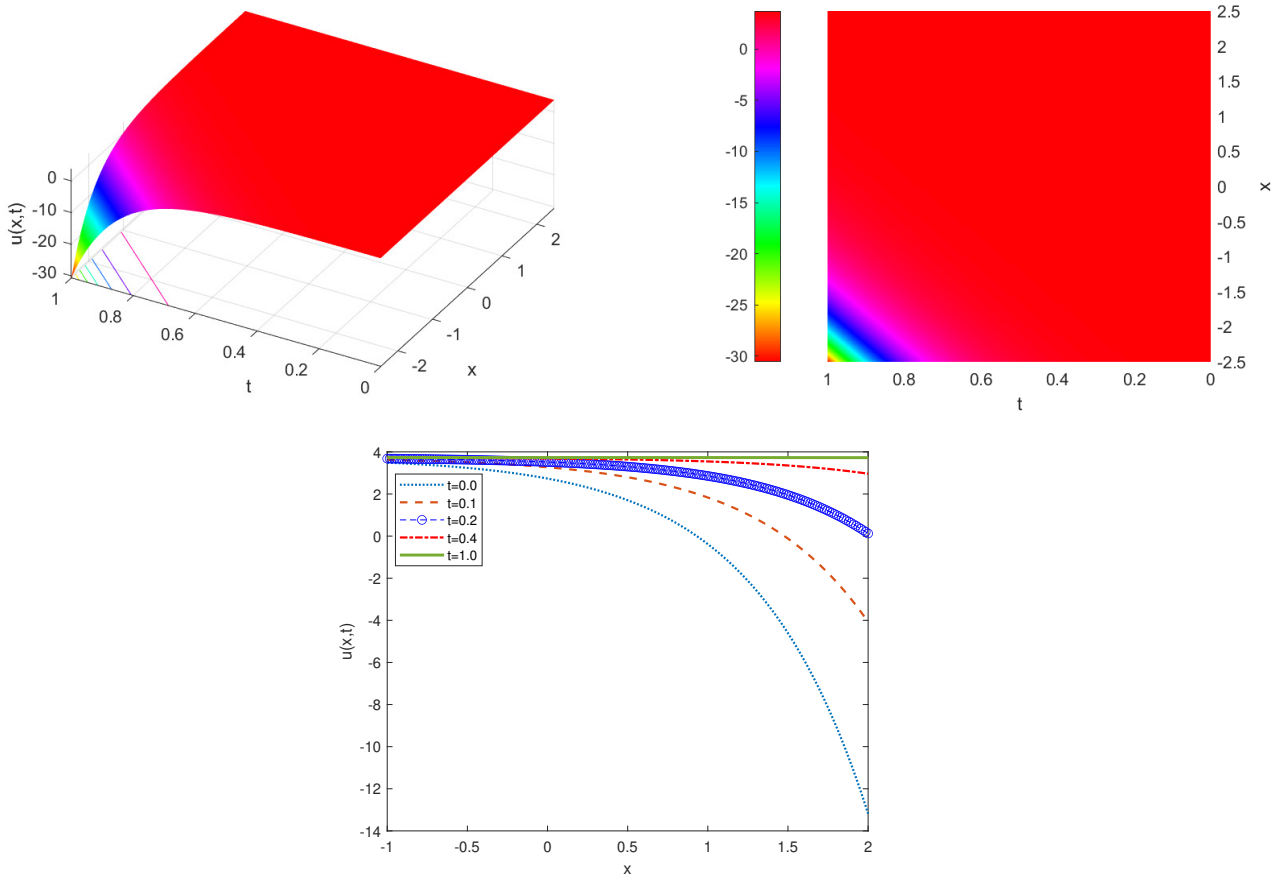

Figure 6: 2D, 3D and contour plots of (33).

To discover further exact solutions for the FW equation (2), by substituting (14) into Eq. (7) (with parameters $\alpha = -1$, $\beta = 3$, $k = 0.5$, and $\omega = 1$), we obtain a fifth degree polynomial in terms of $\mathcal{P}$, formulated as:

$$\sum_{i=0}^{4} S_i \mathcal{P}^i = 0,$$

where

$$S_0 = \nu \left(\frac{d}{d\xi} \vartheta_0(\xi) \right) + \vartheta_1(\xi)\, \vartheta_0(\xi)\, \nu + \frac{(\varpi - 3)\, \vartheta_0^2(\xi)}{2} - c,$$

$$S_1 = 2\nu \vartheta_0(\xi)\, \vartheta_2(\xi) + \nu \vartheta_1^2(\xi) + \nu \left(\frac{d}{d\xi} \vartheta_1(\xi) \right) - 3\vartheta_0(\xi)\, \vartheta_1(\xi) - \varpi \left(\frac{d}{d\xi} \vartheta_0(\xi) \right) - \nu + 1,$$

$$S_2 = -\varpi \left(\frac{d}{d\xi} \vartheta_1(\xi) \right) + \nu \left(\frac{d}{d\xi} \vartheta_2(\xi) \right) + \frac{(-\varpi - 3)\, \vartheta_1^2(\xi)}{2} + 3\nu \vartheta_2(\xi)\, \vartheta_1(\xi) + \frac{1}{2} - (\varpi + 3)\, \vartheta_0(\xi)\, \vartheta_2(\xi),$$

$$S_3 = -\varpi \left(\frac{d}{d\xi} \vartheta_2(\xi) \right) + 2 \left(\nu \vartheta_2(\xi) - \left(\varpi + \frac{3}{2} \right) \vartheta_1(\xi) \right) \vartheta_2(\xi),$$

$$S_4 = -\frac{3\,(\varpi + 1)\, \vartheta_2^2(\xi)}{2}.$$

Considering $S_i = 0,\ i = 0, \ldots, 4$, leads to a system of differential algebraic equations with the subsequent sets of solutions:

Case 1:

$$\vartheta_0(\xi) = \frac{C_1\sqrt{2}\,\mathrm{e}^{\frac{\sqrt{2}\xi}{2}}}{8C_2\mathrm{e}^{\sqrt{2}\xi} - 8} - \frac{\sqrt{2}\left(C_1 + C_2\mathrm{e}^{\frac{\sqrt{2}\xi}{2}} + \mathrm{e}^{-\frac{\sqrt{2}\xi}{2}}\right)}{2\left(2C_2\mathrm{e}^{\frac{\sqrt{2}\xi}{2}} - 2\,\mathrm{e}^{-\frac{\sqrt{2}\xi}{2}}\right)}, \quad \vartheta_1(\xi) = -\frac{\sqrt{2}\left(C_1 + C_2\mathrm{e}^{\frac{\sqrt{2}\xi}{2}} + \mathrm{e}^{-\frac{\sqrt{2}\xi}{2}}\right)}{2C_2\mathrm{e}^{\frac{\sqrt{2}\xi}{2}} - 2\,\mathrm{e}^{-\frac{\sqrt{2}\xi}{2}}},$$

$$\vartheta_2(\xi) = -\frac{C_1\sqrt{2}\,\mathrm{e}^{\frac{\sqrt{2}\xi}{2}}}{2C_2\mathrm{e}^{\sqrt{2}\xi} - 2}, \quad \nu = \frac{1}{2}, \quad \varpi = -1, \quad c = -\frac{1}{8}.$$

Here, from the ODE (14) we have

$$\frac{d}{d\xi}\mathcal{P}(\xi) = -\frac{\sqrt{2}\left(C_1\left(\mathcal{P}(\xi) + \frac{1}{2}\right)\mathrm{e}^{\frac{\sqrt{2}\xi}{2}} + C_2\mathrm{e}^{\sqrt{2}\xi} + 1\right)\left(\mathcal{P}(\xi) + \frac{1}{2}\right)}{2C_2\mathrm{e}^{\sqrt{2}\xi} - 2}, \tag{34}$$

with exact solution

$$\mathcal{P}(\xi) = \frac{-C_1\left(C_3 - 1\right)\mathrm{e}^{-\frac{\sqrt{2}\xi}{2}} - C_1\left(C_3 + 1\right)\mathrm{e}^{\frac{\sqrt{2}\xi}{2}} + \left(-4C_2 - 4\right)C_3 + 4C_2 - 4}{4C_1\left(C_3\cosh\left(\frac{\sqrt{2}\xi}{2}\right) + \sinh\left(\frac{\sqrt{2}\xi}{2}\right)\right)}. \tag{35}$$

Therefore, utilizing (7) and (35), the ensuing dark soliton can be expressed as:

$$u(x,t) = \frac{-C_1\left(C_3 - 1\right)\mathrm{e}^{-\frac{\sqrt{2}\left(-\frac{t}{2}+x\right)}{2}} - C_1\left(C_3 + 1\right)\mathrm{e}^{\frac{\sqrt{2}\left(-\frac{t}{2}+x\right)}{2}} + \left(-4C_2 - 4\right)C_3 + 4C_2 - 4}{4C_1\left(\cosh\left(\frac{\sqrt{2}\left(-\frac{t}{2}+x\right)}{2}\right)C_3 + \sinh\left(\frac{\sqrt{2}\left(-\frac{t}{2}+x\right)}{2}\right)\right)}. \tag{36}$$

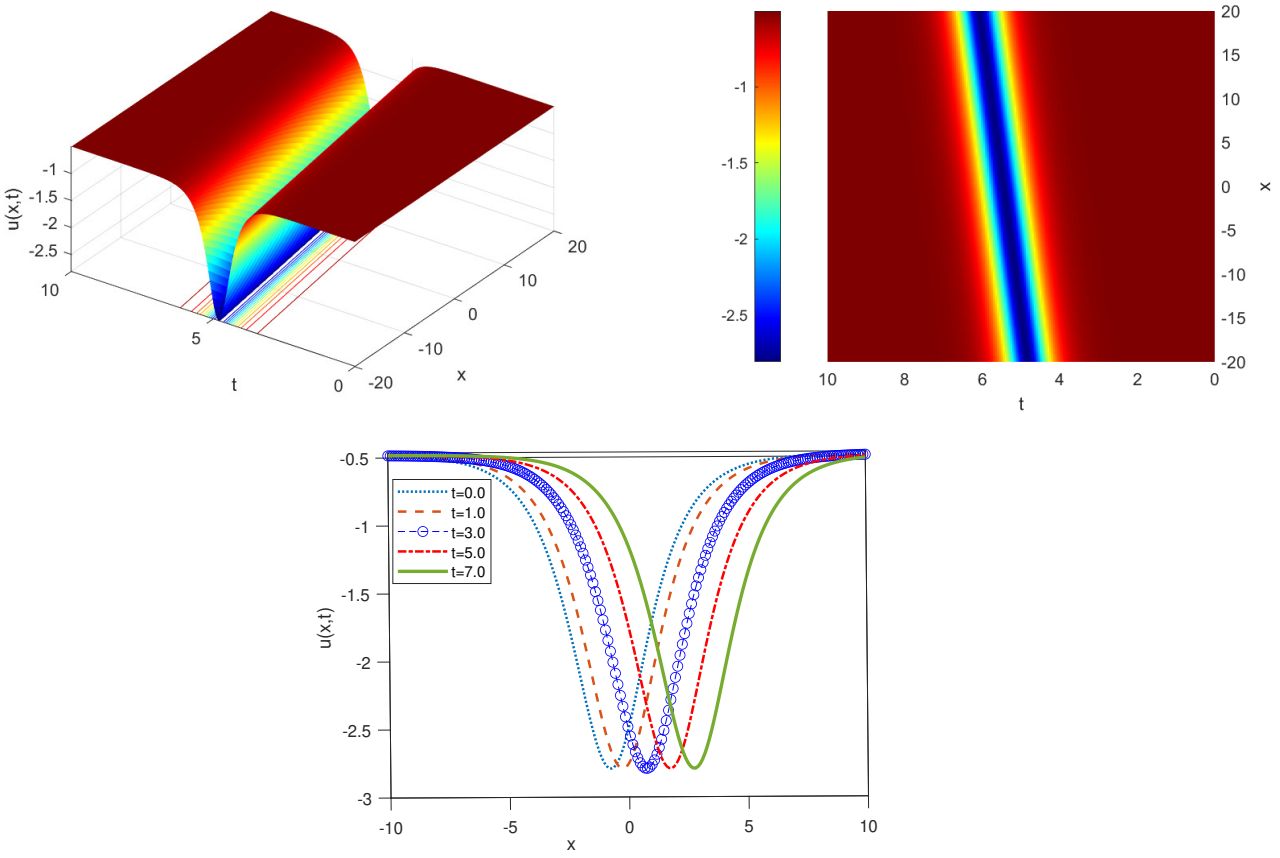

Figure 7: 2D, 3D and contour plots of (36).

Case 2:

$$\vartheta_0(\xi) = -2c\sqrt{-\frac{1}{8c+1}}, \quad \vartheta_1(\xi) = \vartheta_2(\xi) = \sqrt{-\frac{1}{8c+1}}, \quad \nu = \frac{1}{2}, \quad \varpi = -1.$$

Eq. (14) in the current case can be written as

$$\frac{d}{d\xi}\mathcal{P}(\xi) = \sqrt{-\frac{1}{8c+1}}\left(\mathcal{P}^2(\xi) + \mathcal{P}(\xi) - 2c\right). \tag{37}$$

The solution of equation (37) can be formulated as:

$$\mathcal{P}(\xi) = -\frac{\tanh\left(\frac{\sqrt{-\frac{1}{8c+1}}\sqrt{8c+1}\,(C_1+\xi)}{2}\right)\sqrt{8c+1}}{2} - \frac{1}{2}, \quad C_1 \in \mathbb{R}. \tag{38}$$

Hence, based on (7), and (38), we obtain the following periodic singular solution:

$$u(x,t) = -\frac{\tanh\left(\frac{\sqrt{-\frac{1}{8c+1}}\sqrt{8c+1}\,(C_1-\frac{t}{2}+x)}{2}\right)\sqrt{8c+1}}{2} - \frac{1}{2}. \tag{39}$$

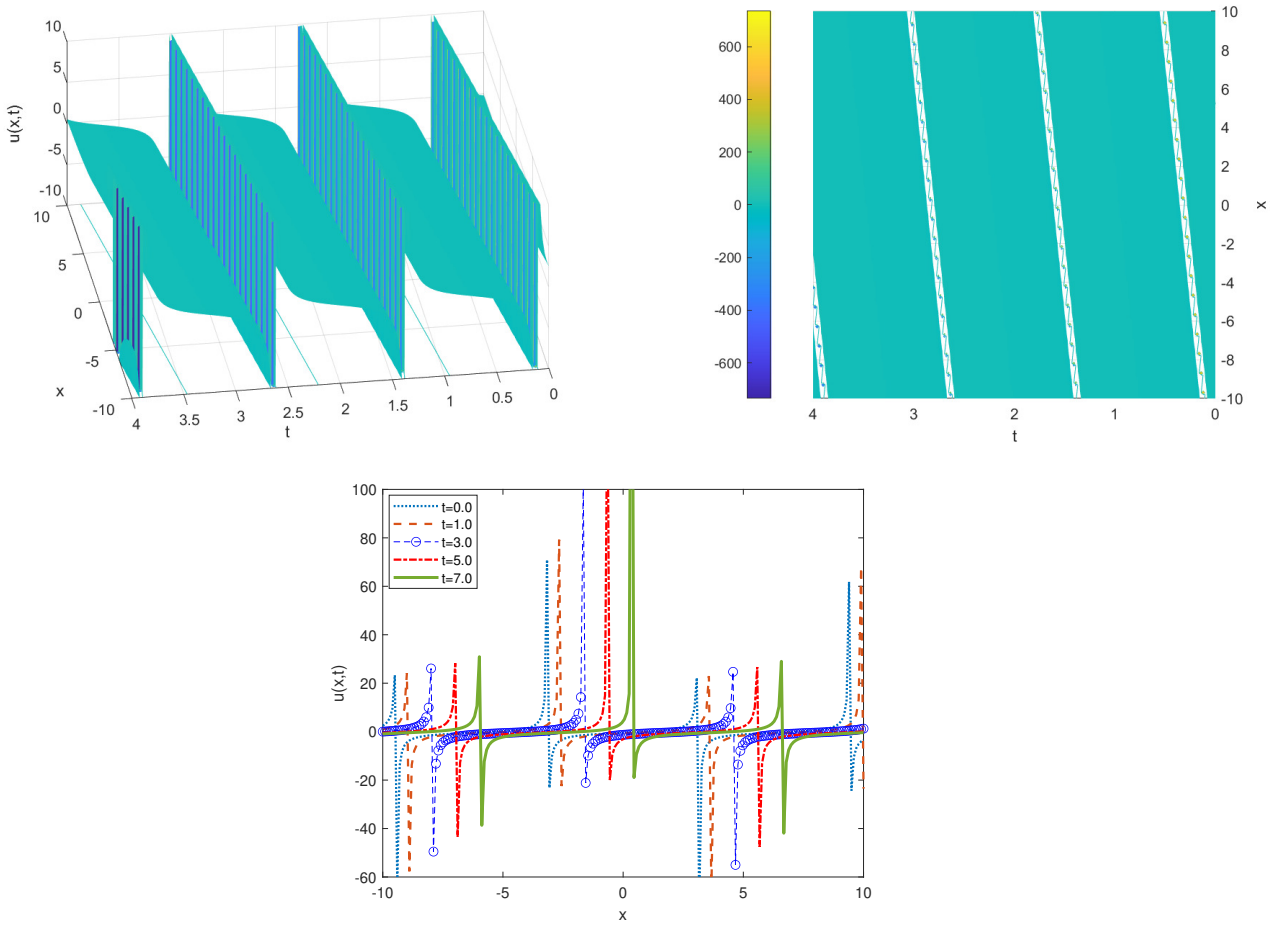

Figure 8: 2D, 3D and contour plots of (39).

4 Results and Discussions

The Results section presents the findings obtained from the application of the VCAEM to the study of exact solutions for the GP equation. Through rigorous mathematical analysis and computational techniques, this study explores the behavior and characteristics of the GP equation under various conditions and parameters. In this paper, all computations have been carried out using Maple 2022. The section begins by detailing the exact solutions derived using the proposed technique, showcasing their forms and properties. Subsequently, these solutions are analyzed and discussed in depth, shedding light on the implications and significance of the results within the context of the GP equation. Insights into the behavior of the equation, its solutions, and their relevance to theoretical and applied research are thoroughly examined, providing a comprehensive understanding of the findings presented in this manuscript.

Fig. 1 illustrates the Kink soliton solution of equation (18) under the conditions $c = k = \omega = \alpha = \beta = C_1 = 1$, presented in three dimensional, contour, and two dimensional formats.

Figure 2 depicts the solitary wave solution of equation (21) with the parameters set as $c = k = \omega = \beta = C_1 = 1$, and $\alpha = -1$, showcased through three dimensional, contour, and two dimensional visualizations.

Figure 3 illustrates an alternative solitary wave solution of equation (24), where the parameters are specified as $c = 0.1$, $k = \omega = 2$, $\beta = -2$, $C_1 = 0.5$, and $\alpha = 1$, presented across three dimensional, contour, and two dimensional representations.

In Figure 4, we depict a periodic wave solution corresponding to equation (27). Here, the parameters take on specific values: $c = k = \omega = 2$, while

$\alpha = \beta = C_1 = C_2 = C_3 = 1$. The illustration showcases the solution through three dimensional, contour, and two dimensional representations.

In Figure 5, we illustrate a periodic wave solution associated with equation (30). The parameters are assigned specific values, with $\alpha = \beta = \varpi = C_1 = C_3 = 1$, and $c = 2$. The visual representation showcases the solution across three dimensional, contour, and two dimensional depictions.

In Figure 6, we depict a solitary wave solution corresponding to equation (33). Specific parameter values are assigned, with $\alpha = \beta = \varpi = C_1 = 1$, and $c = k = 2$. The visual presentation exhibits the solution through three dimensional, contour, and two dimensional renderings.

In Figure 7, we illustrate a dark soliton associated with equation (36). Specific parameter values are assigned, with $C_1 = C_2 = 1$, and $C_3 = 2$. The visual representation displays the solution through three dimensional, contour, and two dimensional depictions.

In Figure 8, we depict a periodic singular solution corresponding to equation (39). Assigning specific parameter values, with $C_1 = 1$ and $c = -0.5$. The visual representation showcases the solution across three dimensional, contour, and two dimensional depictions.

5 Conclusion

This study introduces a novel approach, namely the VCAEM, to investigate the GP equation. Through this method, various types of solutions including Kink solitons, dark solitons, periodic wave solutions, periodic singular solutions, and solitary wave solutions have been derived. These findings significantly contribute to the understanding of the dynamics governed by the GP equation. The versatility of the proposed method enables the exploration of a wide range of phenomena and opens avenues for further research in nonlinear dynamics and related fields. The derived solutions offer valuable insights into the behavior and characteristics of the system under consideration, providing a foundation for future theoretical and experimental studies. Overall, the VCAEM proves to be a powerful tool for analyzing complex nonlinear systems, offering new perspectives and opportunities for advancing our understanding of nonlinear phenomena.

Declarations

Ethical Approval:

Not applicable.

Competing interests:

The authors declare that they have no known competing financial interests or personal relationships that could have appeared to influence the work reported in this paper.

Funding:

No funding received for this paper.

Availability of data and materials:

No applicable.

References

[1] X. Wang, J. Li, J. Li, A deep learning based numerical pde method for option pricing, Computational economics 62 (1) (2023) 149–164.

[2] J. M. Taylor, D. Pardo, I. Muga, A deep fourier residual method for solving pdes using neural networks, Computer Methods in Applied Mechanics and Engineering 405 (2023) 115850.

[3] M. S. Hashemi, E. Darvishi, D. Baleanu, A geometric approach for solving the density-dependent diffusion nagumo equation, Advances in Difference Equations 2016 (2016) 1–13.

[4] S. Abbasbandy, M. S. Hashemi, Group preserving scheme for the cauchy problem of the laplace equation, Engineering analysis with boundary elements 35 (8) (2011) 1003–1009.

[5] M. S. Hashemi, Numerical study of the one-dimensional coupled nonlinear sine-gordon equations by a novel geometric meshless method, Engineering with Computers 37 (4) (2021) 3397–3407.

[6] S. A. Durmus, N. Ozdemir, A. Secer, M. Ozisik, M. Bayram, Bright soliton of the third-order nonlinear schrödinger equation with power law of self-phase modulation in the absence of chromatic dispersion, Optical and Quantum Electronics 56 (5) (2024) 1–17.

[7] W. B. Rabie, H. M. Ahmed, M. S. Hashemi, M. Mirzazadeh, M. Bayram, Generating optical solitons in the extended (3+ 1)-dimensional nonlinear kudryashov's equation using the extended f-expansion method, Optical and Quantum Electronics 56 (5) (2024) 894.

[8] K. Hosseini, E. Hincal, O. Obi, M. Mirzazadeh, Solitary waves of coupled nonlinear schrödinger equations: a generalized method, Optical and Quantum Electronics 55 (7) (2023) 599.

[9] K. Hosseini, K. Sadri, M. Mirzazadeh, A. Ahmadian, Y.-M. Chu, S. Salahshour, Reliable methods to look for analytical and numerical solutions of a nonlinear differential equation arising in heat transfer with the conformable derivative, Mathematical Methods in the Applied Sciences 46 (10) (2023) 11342–11354.

[10] M. Soliman, H. M. Ahmed, N. Badra, I. Samir, Effects of fractional derivative on fiber optical solitons of (2+ 1) perturbed nonlinear schrödinger equation using improved modified extended tanh-function method, Optical and Quantum Electronics 56 (5) (2024) 1–15.

[11] I. Samir, H. M. Ahmed, Extracting stochastic solutions for complex ginzburg–landau model with chromatic dispersion and kerr law nonlinearity using improved modified extended tanh technique, Optical and Quantum Electronics 56 (5) (2024) 824.

[12] C. Gilson, A. Pickering, Factorization and painlevé analysis of a class of nonlinear third-order partial differential equations, Journal of Physics A: Mathematical and General 28 (10) (1995) 2871.

[13] Y. Kai, Y. Li, L. Huang, Topological properties and wave structures of Gilson–Pickering equation, Chaos, Solitons & Fractals 157 (2022) 111899.

[14] A. A. Elmandouh, M. E. Elbrolosy, New traveling wave solutions for Gilson–Pickering equation in plasma via bifurcation analysis and direct method, Mathematical Methods in the Applied Sciences (2022).

[15] F. Zabihi, M. Saffarian, A not-a-knot meshless method with radial basis functions for numerical solutions of Gilson–Pickering equation, Engineering with Computers 34 (2018) 37–44.

[16] K. Ali, R. Yilmazer, H. Baskonus, H. Bulut, New wave behaviors and stability analysis of the Gilson–Pickering equation in plasma physics, Indian Journal of Physics 95 (2021) 1003–1008.

[17] B. Fornberg, G. B. Whitham, A numerical and theoretical study of certain nonlinear wave phenomena, Philosophical Transactions of the Royal Society of London. Series A, Mathematical and Physical Sciences 289 (1361) (1978) 373–404.

[18] J. Zhou, L. Tian, Solitons, peakons and periodic cusp wave solutions for the fornberg–whitham equation, Nonlinear Analysis: Real World Applications 11 (1) (2010) 356–363.

[19] P. Rosenau, J. M. Hyman, Compactons: solitons with finite wavelength, Physical Review Letters 70 (5) (1993) 564.

[20] F. Rus, F. R. Villatoro, Padé numerical method for the rosenau–hyman compacton equation, Mathematics and Computers in Simulation 76 (1-3) (2007) 188–192.

[21] R. Camassa, D. D. Holm, An integrable shallow water equation with peaked solitons, Physical review letters 71 (11) (1993) 1661.

[22] A. Hone, The associated camassa-holm equation and the kdv equation, Journal of Physics A: Mathematical and General 32 (27) (1999) L307.

[23] M. S. Hashemi, A variable coefficient third degree generalized abel equation method for solving stochastic schrödinger–hirota model, Chaos, Solitons & Fractals 180 (2024) 114606.

[24] M. S. Hashemi, M. Bayram, M. B. Riaz, D. Baleanu, Bifurcation analysis, and exact solutions of the two-mode cahn–allen equation by a novel variable coefficient auxiliary equation method, Results in Physics 64 (2024) 107882.

Volume 14, Issue 3, Page 30-39, 2025 https://doi.org/10.46810/tdfd.1691320 Research Article

BİNGÖL UNIVERSITY

Türk Doğa ve Fen Dergisi
Turkish Journal of Nature and Science
www.dergipark.gov.tr/tdfd

Protective Effects of Morin Against Paracetamol-Induced Nephrotoxicity via Modulation of Oxidative Stress, Inflammation, and Apoptosis Pathways

Özge KANDEMİR[1*], Fatih Mehmet KANDEMİR[2], Nurhan AKARAS[3], Hasan ŞİMŞEK[4]

[1] Aksaray University, Aksaray Technical Sciences Vocational School, Department of Food Processing, Aksaray, Türkiye
[2] Aksaray University, Faculty of Medicine, Department of Medical Biochemistry, Aksaray, Türkiye
[3] Aksaray University, Faculty of Medicine, Department of Histology and Embryology, Aksaray, Türkiye
[4] Aksaray University, Faculty of Medicine, Department of Physiology, Aksaray, Türkiye
Özge KANDEMİR ORCID No: 0000-0001-8884-4168
Fatih Mehmet KANDEMİR ORCID No: 0000-0002-8490-2479
Nurhan AKARAS ORCID No: 0000-0002-8457-9448
Hasan ŞİMŞEK ORCID No: 0000-0001-5573-4923

**Corresponding author: ozgekandemir@aksaray.edu.tr*

(Received: 04.05.2025, Accepted: 23.06.2025, Online Publication: 26.09.2025)

Keywords
Apoptosis, Inflammation, Morin, Nephrotoxicity, Oxidative stress, Paracetamol

Abstract: Paracetamol (PCM), although a widely used and non-prescription effective analgesic and antipyretic, can cause nephrotoxicity by causing kidney damage at high doses. Morin (MRN) is a flavonoid found in white mulberry and cranberry, with low toxicity and prominent antioxidant, anti-inflammatory, and antiapoptotic properties. This study aimed to investigate the effects of MRN on PCM-induced kidney toxicity by biochemical, molecular, and histopathological methods.Thirty-five Wistar rats were divided into Control, MRN (100 mg/kg), PCM (1000 mg/kg), PCM+MRN50 (50 mg/kg), and PCM+MRN100 (100 mg/kg) groups (n=7); the substances were administered orally for 6 days. The blood and kidney tissues were evaluated with biochemical (urea, creatinine, MDA, GSH, SOD, CAT, GPx), genetic (NF-κB, TNF-α, Caspase-3, Bax, Bcl-2, KIM-1, AQP2) and histopathological methods. While PCM negatively affected kidney function tests, oxidative stress levels, inflammation, and apoptosis markers and caused kidney damage, MRN suppressed these negative effects at both doses, improved kidney function, antioxidant defense, inflammation, and apoptosis parameters, and reduced histopathological damage. The study found that MRN effectively protected kidney tissue from PCM-induced damage by reversing oxidative stress, inflammation, and apoptosis.

Morin'in Oksidatif Stres, İnflamasyon ve Apoptozis Yollarının Modülasyonu Yoluyla Parasetamol Kaynaklı Nefrotoksisiteye Karşı Koruyucu Etkileri

Anahtar Kelimeler
Apoptozis, İnflamasyon, Morin, Nefrotoksisite, Oksidatif stres, Parasetamol

Öz: Paracetamol (PCM), yaygın ve reçetesiz kullanılan etkili bir analjezik ve antipiretik olsa da, yüksek dozlarda böbrek hasarına neden olarak nefrotoksisiteye yol açabilir. Morin (MRN), beyaz dut ve kızılcıkta bulunan, düşük toksisiteye sahip, antioksidan, antiinflamatuvar ve antiapoptotik özellikleriyle öne çıkan bir flavonoiddir. Bu çalışmada, PCM'nin neden olduğu böbrek toksisitesi üzerine MRN'nin etkileri biyokimyasal, moleküler ve histopatolojik yöntemlerle araştırılması amaçlanmıştır. Otuz beş Wistar sıçan, Kontrol, MRN (100 mg/kg), PCM (1000mg/kg), PCM+MRN50 (50mg/kg) ve PCM+MRN100 (100mg/kg) gruplarına ayrılmış (n=7); maddeler 6 gün boyunca oral uygulanmıştır. Alınan kan ve böbrek dokuları biyokimyasal (üre, kreatinin, MDA, GSH, SOD, KAT, GPx), genetik (NF-κB, TNF-α, Caspase-3, Bax, Bcl-2, KIM-1, AQP2) ve histopatolojik yöntemlerle değerlendirilmiştir. PCM böbrek fonksiyon testlerini, oksidatif stres düzeylerini, inflamasyon ve apoptoz belirteçlerini olumsuz etkileyip böbrek hasarı oluştururken; MRN her iki dozda bu olumsuz etkileri baskılayarak böbrek fonksiyonu, antioksidan savunma, inflamasyon ve apoptoz parametrelerini iyileştirmiş, histopatolojik hasarı azaltmıştır. Çalışmada MRN'nin oksidatif stresi, inflamasyonu ve apoptozu tersine çevirerek böbrek dokusunu PCM kaynaklı hasardan etkili bir şekilde koruduğu bulunmuştur.

1. INTRODUCTION

The deterioration of the kidney's main function, detoxification and elimination, is defined as nephrotoxicity due to exogenous and endogenous toxic substances. Drugs used in clinical settings can damage the kidneys due to their role in elimination and can be the cause of drug-induced nephrotoxicity [1]. Although paracetamol (PCM) is an easily available, effective, and convenient drug that is sold without a prescription in most countries, it has serious side effects at high doses. PCM, which is widely used as a pain reliever and antipyretic, causes liver and kidney failure at excessive doses [2]. The use of 200 mg/kg and above is the main cause of liver toxicity and also causes nephrotoxicity. Excessive PCM use causes liver necrosis in 10-40% of patients, while kidney failure is observed in 2% [3]. Once PCM is taken, a small fraction—around 2–4%—is metabolized in the liver by cytochrome P450 enzymes into a highly electrophilic and toxic compound known as N-acetyl-p-benzoquinone imine (NAPQI). Normally, this metabolite is rendered harmless by conjugation with glutathione and is eliminated through the urine. However, if NAPQI levels exceed the available glutathione stores, the excess compound builds up and can result in damage to both liver and kidney tissues [4]. Morin (MRN), which is commonly found in white mulberry and cornelian cherry, is a flavonoid with antioxidant, anti-inflammatory, antiautophagic, and antiapoptotic properties [5]. The most important feature of MRN is that it reduces oxidative stress by inhibiting ROS production [6]. MRN shows a tissue protective effect against oxidative stress by regulating cytochrome P450 activity, inhibiting ROS production, increasing antioxidant genes and Bcl-2 expression, and reducing apoptotic factor release, even at high concentrations without toxic effects [7]. Additionally, MRN exhibits anti-inflammatory effects by inhibiting the Nuclear factor kappa B (NF-κB) signaling pathway [8]. Also, having minimum toxicity even at high doses provides an important advantage to MRN [9]. It has been reported by Çomaklı et al. [10] that MRN has a protective effect against oxidative stress-induced damage in glomerular mesenchymal cells in the kidney.

The presented study aimed to investigate the effects of MRN on PCM-induced kidney toxicity, which is widely used as an analgesic and antipyretic, by biochemical, molecular, and histopathological methods.

2. MATERIAL AND METHOD

2.1. Chemicals

PCM (Parol, 500 mg/tablet) was obtained from Atabay Chemical Company (Istanbul, Türkiye), and MRN (Cas No: 654055-01-3) was obtained from Sigma Chemical Company (USA).

2.2. Experimental Animals

The study involved 35 Wistar albino rats, each weighing between 220–250 grams and aged 10 to 12 weeks. The animals were housed in cages within a temperature-controlled environment (24–25 °C) under a 12-hour light/dark cycle. They had free access to standard feed and water throughout the study. All experimental procedures were conducted at the KONUDAM Experimental Medicine Practice and Research Center.

2.3. Ethics Committee Approval

Ethics committee approval for the study was obtained from the Necmettin Erbakan University KONÜDAM Experimental Medicine Application and Research Center Directorate with the decision number 2024-62 dated 11.07.2024.

2.4. Experimental Design

Wistar albino rats were randomly divided into 5 groups, each containing 7 rats (Table 1). MRN [11] and PCM [12] doses were determined from previous studies.

Table 1. Groups and experimental design

Group	Substance(s) Administered	Dose	Duration of Administration
Control (C)	Saline	1 ml	Once daily for 6 days (oral)
Morin (MRN)	Morin	100 mg/kg	Once daily for 6 days (oral)
Paracetamol (PCM)	Saline + Paracetamol	Saline: 6 days, PCM: 1000 mg/kg	PCM on day 6, 30 min after saline (oral)
PCM +MRN50	Paracetamol + Morin	PCM: 1000 mg/kg; MRN: 50 mg/kg	MRN: once daily for 6 days; PCM on day 6, 30 min later
PCM+MRN100	Paracetamol + Morin	PCM: 1000 mg/kg; MRN: 100 mg/kg	MRN: once daily for 6 days; PCM on day 6, 30 min later

On the seventh day, 24 hours after the final treatment, the animals were euthanized via decapitation under mild sevoflurane anesthesia. Blood samples were collected into anticoagulant-free vacuum tubes for biochemical evaluations. These samples were centrifuged at 3000 rpm for 10 minutes at +4 °C, and the resulting sera were separated. Portions of the kidney tissue were frozen at –20 °C for biochemical investigations, while other portions were fixed in 10% formaldehyde solution for subsequent histopathological examination.

2.5. Serum Renal Function Markers

Serum urea and creatinine concentrations were determined using commercially available assay kits (Diasis Diagnostic Systems, Istanbul, Turkey) following the protocols provided by the manufacturer.

2.6. Oxidative Stress Parameters

Kidney tissue was homogenized with 1.15% potassium chloride in a tissue homogenizer (IKA T18 digital ultra-

turrax, Germany). Glutathione peroxidase (GPx) was determined by Matkovics [13], glutathione (GSH) by Sedlak and Lindsay [14], malondialdehyde (MDA) by Placer et al. [15], superoxide dismutase (SOD) by Sun et al. [16], catalase (CAT) by Aebi [17] and protein determination by Lowry et al. [18] methods.

2.7. Real Time PCR (RT-PCR)

At the end of the experiment, mRNA transcription levels of genes listed in Table 2 were analyzed by the RT-PCR method in kidney tissues obtained. RNA isolation was performed using commercially available QIAzol Lysis Reagent (Qiagen, 79306). Isolated total RNA was converted to cDNA with OneScript Plus cDNA Synthesis Kit (ABM, G236, Richmond, Canada). Then, the PCR mixture was prepared by adding BlasTaq™ 2X qPCR MasterMix (ABM, G891, Richmond, Canada) with primer sequences, and the reaction started. Primers based on the Rattus norvegicus sequence were designed in the Oligo 6.0 primer design program. The procedures were carried out in appropriate temperature cycles in the Rotor-Gene Q (Qiagen) device according to the protocol specified by the manufacturer. Gene expressions obtained from the analysis were normalized with the β-Actin reference gene and evaluated using the 2-ΔΔCT method [19].

Table 2. Primer sequences

Gene	Sequences (5'-3')
NF-κB	F: AGTCCCGCCCCTTCTAAAAC R: CAATGGCCTCTGTGTAGCCC
TNF-α	F: CTCGAGTGACAAGCCCGTAG R: ATCTGCTGGTACCACCAGTT
Caspase-3	F: ACTGGAATGTCAGCTCGCAA R: GCAGTAGTCGCCTCTGAAGA
Bax	F: TTTCATCCAGGATCGAGCAG R: AATCATCCTCTGCAGCTCCA
Bcl-2	F: GACTTTGCAGAGATGTCCAG R: TCAGGTACTCAGTCATCCAC
KIM1	F:TGGCACTGTGACATCCTCAGA R: GCAACGGACATGCCAACATA
AQP2	F: AGCTGCCTTCTATGTGGCT R: GCGTTGTTGTGGAGAGCATT
β-Actin	F: CAGCCTTCCTTCTTGGGTATG R: AGCTCAGTAACAGTCCGCCT

2.8. Histological Analysis

Kidney tissues obtained from experimental groups were first kept in 10% neutral formalin solution for 24 hours as a fixative to be examined under a light microscope. According to routine paraffin follow-up procedures [20], tissues were dehydrated by passing through increasing grades of alcohol and cleared in xylene. Then, paraffin blocks were obtained from tissues treated with liquid paraffin. 5-micron sections were taken from paraffin blocks with a microtome and stained with hematoxylin-eosin (H&E). A binocular Olympus Cx43 light microscope (Olympus Inc., Tokyo, Japan) and an EP50 camera (Olympus Inc., Tokyo, Japan) were used to obtain images from stained preparations, and evaluation was performed using a blind method.

2.9. Statistical Analysis:

Group comparisons and statistical significance were evaluated using one-way ANOVA followed by Tukey's post hoc test (SPSS version 20.0; Chicago, IL, USA). A p-value of less than 0.05 was considered statistically significant. Data are presented as mean ± standard deviation (SD).

3. RESULTS

3.1. Kidney Function Tests

The effects of PCM and MRN applications on serum urea (Figure 1A) and creatinine (Figure 1B) levels were examined. According to the obtained data, it was determined that there was no difference between the Control and MRN groups ($p>0.05$), PCM application increased serum urea and creatinine levels compared to the Control and MRN groups ($p<0.001$), and MRN applied together with PCM was effective at doses of 50 and 100 and brought these increased values closer to the control group levels ($p<0.001$).

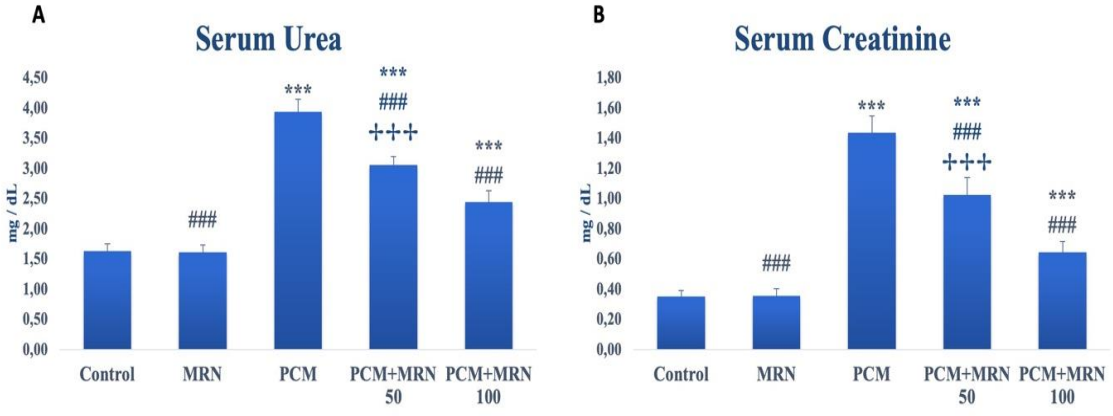

Figure 1. Effects of PCM and MRN on serum urea (A) and serum creatinine (B) levels. Values are given as mean ± SD. Control vs others: *p < 0.05, **p < 0.01, ***p < 0.001, PCM vs others: #p < 0.05, ##p < 0.01, ###p < 0.001, PCM+MRN50 vs PCM+MRN100: + p< 0.05, ++p < 0.01, +++p < 0.001.

3.2. Oxidative Stress Markers

The effects of PCM and MRN applications on kidney tissue oxidative stress markers MDA (Figure 2A), GSH (Figure 2B), SOD (Figure 2C), CAT (Figure 2D) and GPx (Figure 2E) were examined. According to the results, no difference was found in all parameters between the control and MRN groups ($p>0.05$). However, it was determined that PCM application increased MDA levels approximately 2-fold compared to the control group ($p<0.001$) and significantly decreased GSH levels and SOD, CAT and GPx activities ($p<0.001$). It was determined that MRN application, together with PCM, was effective in both doses, reduced PCM-induced increased MDA levels ($p<0.001$), and was effective in reducing oxidative stress by providing an increase in antioxidant parameters ($p<0.001$).

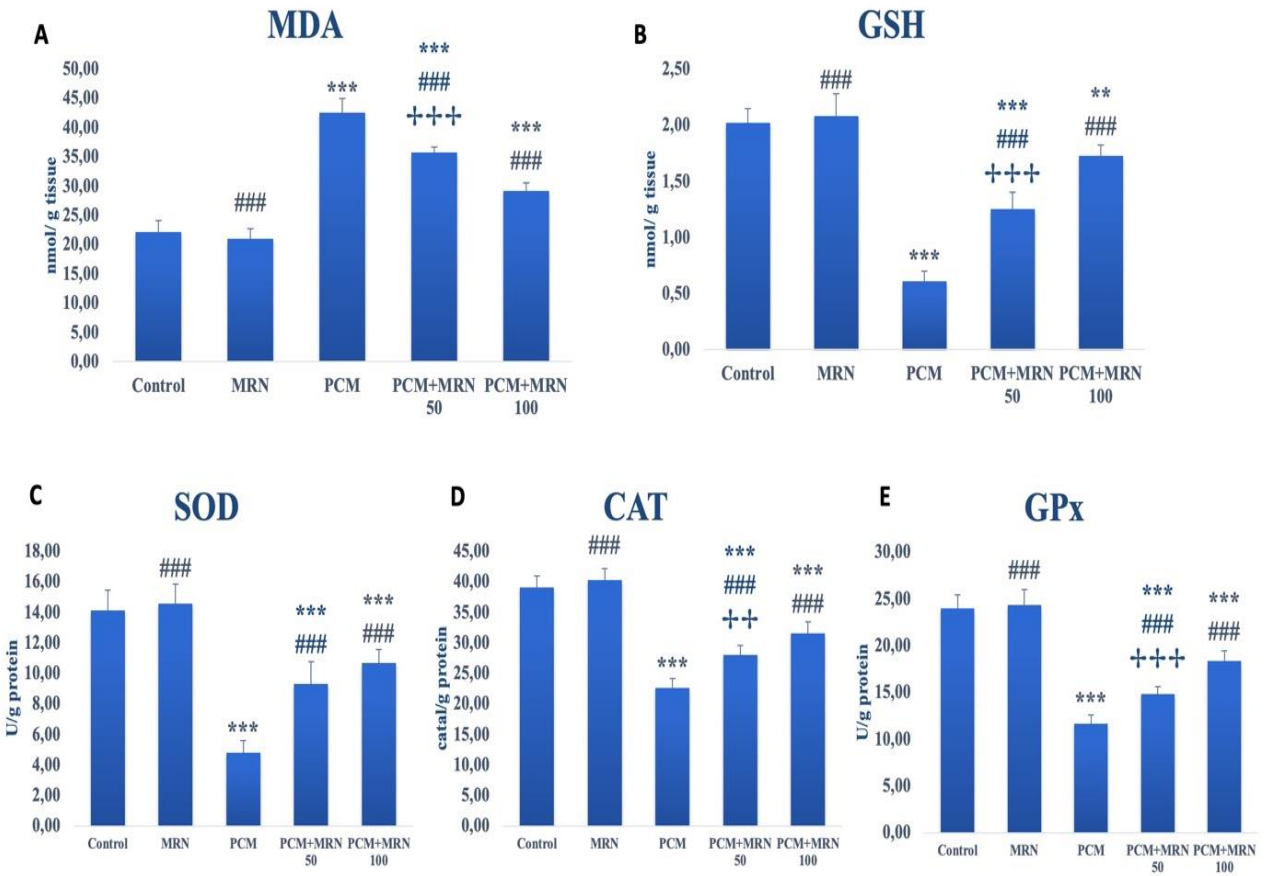

Figure 2. Effects of PCM and MRN on MDA (A) and GSH (B) levels and SOD (C), CAT (D), and GPx (E) activities in rat kidney tissues. Values are given as mean ± SD. Control vs others: *$p < 0.05$, **$p < 0.01$, ***$p < 0.001$, PCM vs others: #$p < 0.05$, ##$p < 0.01$, ###$p < 0.001$, PCM+MRN50 vs PCM+MRN100: ✢ $p< 0.05$, ✢✢$p < 0.01$, ✢✢✢$p < 0.001$.

3.3. Inflammation Results

When the mRNA expression levels of NF-κB (Figure 3A) and TNF-α (Figure 3B) markers of inflammation were examined, it was determined that PCM application caused an increase in both parameters compared to the control and MRN groups and accelerated inflammation ($p<0.001$), and that the application of MRN 50 (NF-κB: $p<0.01$ and TNF-α: $p<0.001$) and MRN 100 ($p<0.001$) doses together with PCM was effective in suppressing PCM-induced increased inflammation by reducing NF-κB and TNF-α expression levels.

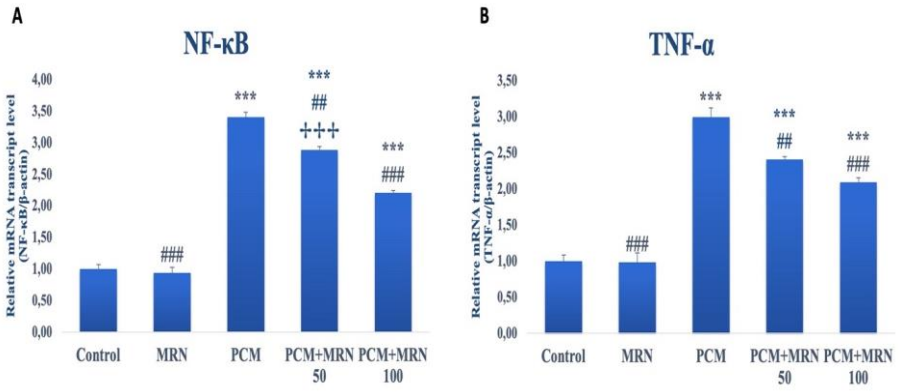

Figure 3. Effects of PCM and MRN on NF-κB (A) and TNF-α (B) mRNA transcription levels in rat kidney tissues. Values are given as mean ± SD. Control vs others: *p < 0.05, **p < 0.01, ***p < 0.001, PCM vs others: #p < 0.05, ##p < 0.01, ###p < 0.001, PCM+MRN50 vs PCM+MRN100: ✢ p< 0.05, ✢✢p < 0.01, ✢✢✢p < 0.001.

3.4. Apoptosis Results

The effects of PCM and MRN applications on the mRNA expression of apoptotic markers Caspase-3 (Figure 4A) and Bax (Figure 4B) and antiapoptotic marker Bcl-2 (Figure 4C) were examined. According to the data obtained, it was determined that PCM application increased the expressions of Caspase-3 and Bax compared to the control and MRN groups, while suppressing the expression of Bcl-2 and triggering the apoptotic process ($p<0.001$). It was determined that the MRN application together with PCM was effective in suppressing apoptosis by decreasing the expressions of Caspase-3 (MRN50: $p<0.01$; MRN100: $p<0.001$) and Bax (MRN50 and MRN100: $p<0.001$) and increasing the expression of Bcl-2 (MRN100: $p<0.01$).

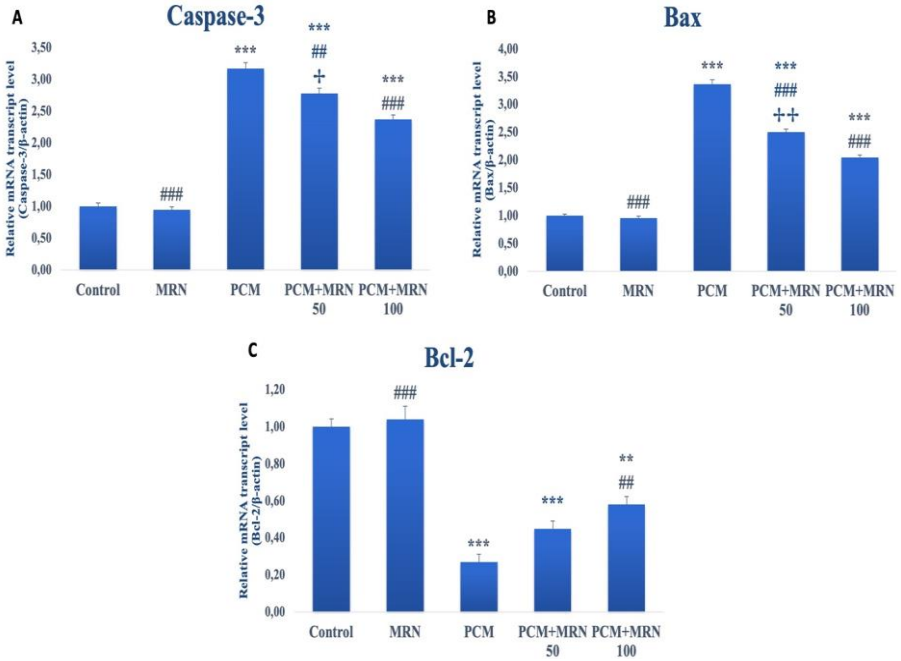

Figure 4. Effects of PCM and MRN on Caspase-3 (A), Bax (B), and Bcl-2 (C) mRNA transcription levels in rat kidney tissues. Values are given as mean ± SD. Control vs others: *p < 0.05, **p < 0.01, ***p < 0.001, PCM vs others: #p < 0.05, ##p < 0.01, ###p < 0.001, PCM+MRN50 vs PCM+MRN100: ✢ p< 0.05, ✢✢p < 0.01, ✢✢✢p < 0.001.

3.5. Kidney Damage Markers

Kidney damage markers Kidney Injury Molecules 1 (KIM1) and Aquaporin 2 (AQP2) mRNA expression levels were examined. Accordingly, it was determined that PCM administration increased kidney KIM1 (Figure 5A) levels and decreased AQP2 (Figure 5B) levels ($p<0.001$) compared to the control group and caused kidney damage. It was determined that the combined administration of PCM and MRN decreased KIM1 levels and increased AQP2 levels (MRN50: $p<0.05$; MRN100: $p<0.001$).

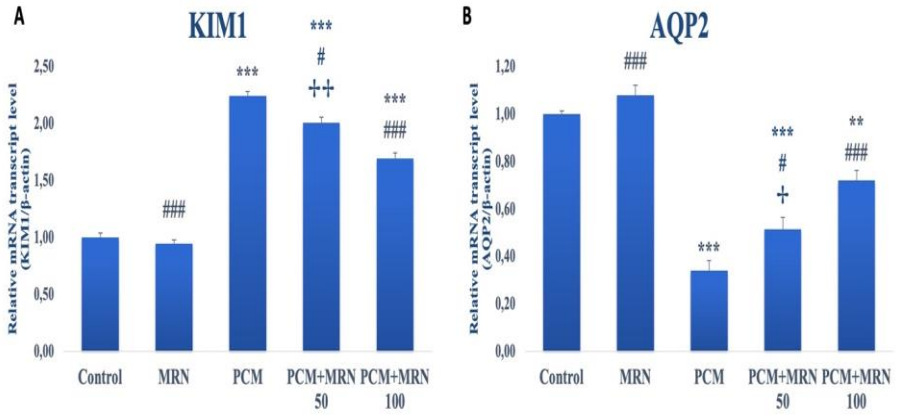

Figure 5. Effects of PCM and MRN on KIM1 (A) and AQP2 (B) mRNA transcription levels in rat kidney tissues. Values are given as mean ± SD. Control vs others: *p < 0.05, **p < 0.01, ***p < 0.001, PCM vs others: #p < 0.05, ##p < 0.01, ###p < 0.001, PCM+MRN50 vs PCM+MRN100: ✢ p< 0.05, ✢✢p < 0.01, ✢✢✢p < 0.001.

3.6. Histopathological Results

Kidney histological images of different groups are presented in Figure 1. When the images of kidney tissues of control and MRN groups were examined, they exhibited well-organized and normal histological features (Figure 6a, 6b). In contrast, atrophic glomerular structures and increased Bowman spaces were noted in the kidneys of rats treated with PCM. In addition, epithelial cells of many cortical tubule structures were shed, and there were degenerative changes and pyknotic nuclei in places. The PCM application caused mononuclear inflammatory cell infiltrates in the interstitial area and vascular congestion (Figure 6c). However, simultaneous PCM+MRN treatments significantly improved PCM-induced pathological changes in kidney tissues. Vascular congestion and tubular degeneration were mild in these groups (Figure 6d, 6e).

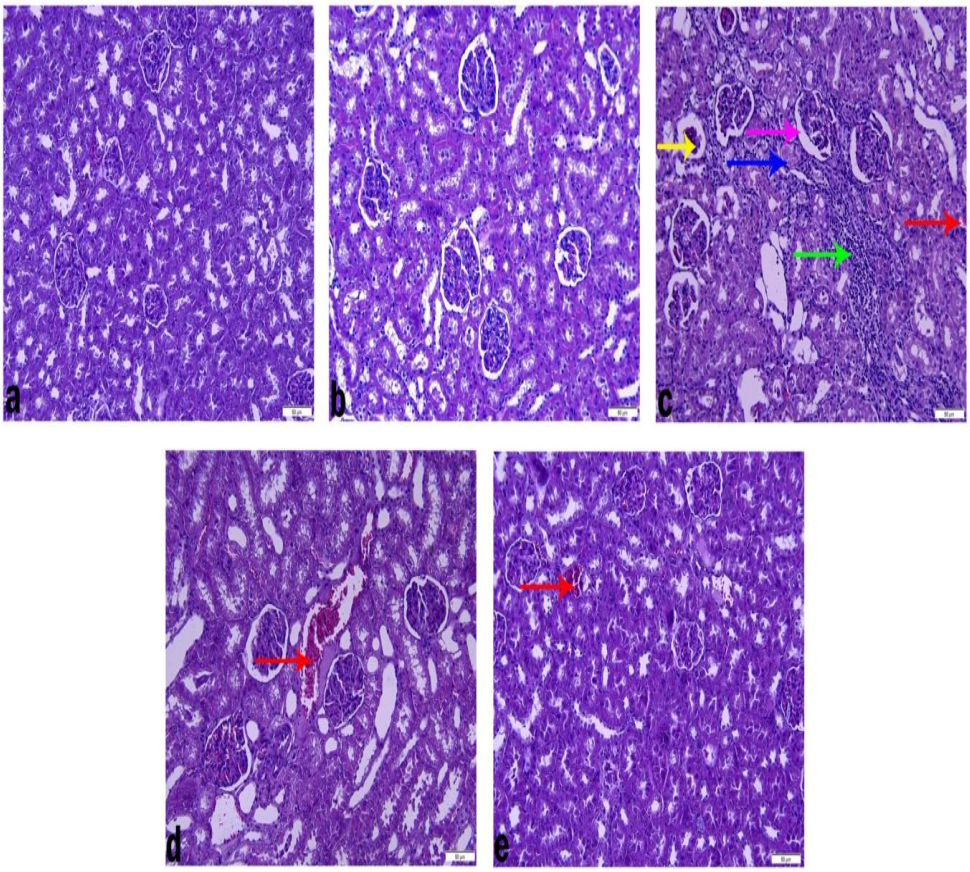

Figure 6. Representative images showing the histopathological effects of PCM and MRN on kidney tissue. a: Normal control group, b: MRN group, c: PCM group, d: PCM+MRN 50, and e: PCM+MRN 100 groups. In the images, yellow arrow: atrophic glomeruli, green arrow: mononuclear inflammatory cell infiltrates, blue arrow: cortical tubule cell degeneration, red arrow: vascular congestion, pink arrow: increased Bowman space. (H&E, x 200).

4. DISCUSSION AND CONCLUSION

PCM is a painkiller and antipyretic drug that can be obtained without a prescription and is safe and effective at normal therapeutic doses, but causes renal toxicity at high doses [21]. High dose PCM administration increases MDA levels by creating oxidative stress in the kidney tissue of rats and weakens antioxidant capacity by decreasing SOD, GSH and GPx levels belonging to the antioxidant defense system. It is also known to impair renal functions by increasing serum creatinine and urea levels [22]. The present study aimed to investigate the effects of MRN, a natural flavonoid, on PCM-induced renal damage.

The most important side effect of PCM is that it causes nephrotic damage by weakening glomerular function. Creatinine is produced from protein metabolism in the muscles, and most of the creatinine is filtered from the blood by the kidneys and excreted in the urine. In kidney disease, the rate of urea production exceeds the clearance rate, which causes an increase in the amount of serum urea [23]. It has been shown in different studies that PCM application causes serious damage to the kidney and impairs its functions [2,24]. In the presented study, it was determined that PCM application caused an increase in serum urea and creatinine levels and that the probable cause of this increase was the decrease in glomerular filtration. It was determined that the MRN application, together with PCM, was effective in reversing these parameters and reducing serum urea and creatinine levels. It has been reported in different studies that MRN regulates glomerular filtration in kidney toxicities caused by different chemical agents and helps to maintain serum urea and creatinine levels at normal levels [10,25,26].

Oxidative stress and free radicals play a role in the pathogenesis of paracetamol-induced renal injury [27]. Free radicals increase lipid peroxidation and trigger the release of inflammatory mediators, leading to renal tissue damage [28]. MDA, a byproduct of lipid peroxidation, serves as an indicator of tissue injury caused by various chain reactions [29,30]. Elevated lipid peroxidation levels and reduced activity of antioxidant enzymes are recognized as key contributors to oxidative stress in renal tissue [31,32]. Yousef et al. [33] reported that PCM increases lipid peroxidation while decreasing antioxidant enzyme activities, thus developing oxidative stress in renal tissue. The body has developed various defense mechanisms against oxidative stress, including antioxidant enzymes such as SOD, CAT, GPx, and the non-enzymatic antioxidant GSH [34]. Cells subjected to oxidative stress are safeguarded by both enzymatic and non-enzymatic antioxidant defense systems, which play a crucial role in maintaining cellular integrity [35,36]. GSH, a non-enzymatic tripeptide, plays a vital role in defending tissues and organs against the harmful impact of ROS. Within the cytochrome P450 pathway, GSH detoxifies NAPQI, a reactive metabolite of paracetamol. However, when GSH reserves are exhausted, excess NAPQI interacts with cellular protein macromolecules, triggering cellular damage that can result in necrosis or apoptosis [37]. While SOD converts superoxide radical to molecular oxygen and hydrogen peroxide, CAT converts hydrogen peroxide to water and molecular oxygen. GPx, similar to CAT, is responsible for the detoxification of hydrogen peroxide [38]. In the presented study, it was determined that PCM increased MDA levels, and in addition, decreased GSH levels and SOD; CAT and GPx activities, causing oxidative stress in the kidney tissue. It was determined that MRN given with PCM was effective in suppressing oxidative stress by regulating these parameters inversely at both doses. It has been demonstrated in different studies that morin is effective in suppressing lipid peroxidation thanks to its antioxidant properties, increases antioxidant enzyme activities, and therefore protects the tissue from oxidative stress [6,7,9].

Growing evidence indicates that oxidative stress plays a crucial role in promoting and sustaining the inflammatory response [39]. Inflammation is one of the adaptive responses to various insults involving biological and chemical agents [40]. The increase in ROS triggers inflammation by elevating NF-κB and TNF-α levels [41,42]. NF-κB, a transcription factor, migrates from the cytosol to the nucleus after dissociating from IκB, where it regulates the expression of up to 500 genes, including those that promote proinflammatory cytokines like TNF-α [43]. Therefore, inhibition of NF-κB is important for the suppression of inflammation [44]. El-Boshy et al. [45] reported that PCM increases oxidative stress by increasing ROS levels in kidney tissue, and that the developing oxidative stress accelerates inflammation by increasing inflammatory cytokines such as NF-κB and TNF-α. In the presented study, it was determined that PCM increased the levels of NF-κB and TNF-α in kidney tissue; this increase developed in parallel with oxidative stress and accelerated the inflammation process in kidney tissue. In addition, it was determined that the MRN application was effective in suppressing PCM-induced inflammation by reducing NF-κB and TNF-α levels. Studies have shown that MRN has anti-inflammatory properties and is effective in suppressing inflammation [6,10,26].

Apoptosis, which eliminates damaged or dangerous cells in the body, also damages healthy cells with the development of oxidative stress [46,47]. Caspase-9 is activated by the combination of cytochrome c and Apaf-1 [48]. The activated caspase-9 activates caspase-3, known as the executioner caspase, and thus the apoptotic process begins. While Bax is an apoptotic factor that opens membrane pores in the mitochondria, Bcl-2 shows an antiapoptotic effect by preventing the opening of mitochondrial membrane pores [49,50]. El-Bakry et al. [51] and Aktaş-Şenocak et al. [52] reported that PCM induces apoptosis through caspase-3 activation. Similarly, Ahmad et al. [27] found that Bcl-2 levels decreased and Bax levels increased in rats to which PCM was applied, thus accelerating the apoptotic process of the cell. In the presented study, it was determined that caspase-3 and bax expression levels increased in the kidney tissue of rats to which PCM was applied, antiapoptotic Bcl-2 expression decreased, and the apoptotic process of the kidney tissue accelerated, and this acceleration in the apoptotic process was parallel to oxidative stress and inflammation. It was

determined that the MRN application together with PCM was effective in suppressing apoptosis by increasing Bcl-2 expression and decreasing caspase-3 and Bax expressions, and MRN showed antiapoptotic properties. In different chemical toxicity models, it has been shown that MRN is effective in suppressing apoptosis, suppressing caspase-3 and bax expressions, and increasing Bcl-2 expression [6,9,11].

When the data obtained in the study were evaluated as a whole, it was determined that PCM application caused damage to the kidney tissue by stimulating oxidative stress, inflammation and apoptosis, and that MRN supportive treatment was effective in protecting the kidney tissue from PCM-induced damage by reversing these pathways, and that MRN application would be beneficial in PCM-induced kidney toxicities.

REFERENCES

[1] Koç A, Erken HA, Koçak FE, Yay A, Güçlü A, Sari E, et al. Nephrotoxic effects of varenicline as the most effective drug used for smoking cessation: a preliminary experimental study. Int Urol Nephrol. 2015;47:823-29.

[2] Topal I, Özdamar MY, Catakli T, Malkoc İ, Hacimuftuoglu A, Mamoulakis C, et al. Renoprotective effect of taxifolin in paracetamol-induced nephrotoxicity: emerging evidence from an animal model. J Clin Med. 2023;12(3):876.

[3] Nazir N, Muhammad J, Ghaffar R, Nisar M, Zahoor M, Uddin F, et al. Phytochemical profiling and antioxidant potential of Daphne mucronata Royle and action against paracetamol-induced hepatotoxicity and nephrotoxicity in rabbits. Saudi J Biol Sci. 2021;28(9):5290-5301.

[4] Çoban FK, İnce S, Demirel HH, İslam İ, Aytuğ H. Acetaminophen-induced nephrotoxicity: suppression of apoptosis and endoplasmic reticulum stress using boric acid. Biol Trace Elem Res. 2023;201(1):242-49.

[5] Şimşek H, Akaras N, Gür C, Küçükler S, İleritürk M, Kandemir FM. Ameliorative effect of morin on diclofenac-induced testicular toxicity in rats: An investigation into different signal pathways. Iran J Basic Med Sci. 2025;28(4):507.

[6] Özdemir S, Kucukler S, Çomaklı S, Kandemir FM. The protective effect of Morin against ifosfamide-induced acute liver injury in rats associated with the inhibition of DNA damage and apoptosis. Drug Chem Toxicol. 2022;45(3):1308-17.

[7] Öztürk, A. B., Şimşek, H., Akaras, N., & Kandemir, F. M. (2025). Effects of Morin on the Wnt, Notch1/Hes1, KI-67/3-Nitrotyrosine and Damage Signaling Pathways in Rats Subjected to Experimental Testicular Ischemia/Reperfusion. Bratislava Medical Journal, 1-20.

[8] Gur, C., Kandemir, F. M., Darendelioglu, E., Caglayan, C., Kucukler, S., Kandemir, O., & Ileriturk, M. (2021). Morin protects against acrylamide-induced neurotoxicity in rats: an investigation into different signal pathways. Environmental Science and Pollution Research, 28(36), 49808-19.

[9] Aygörmez S, Küçükler S, Akaras N, Maraşlı Ş, Kandemir FM. Investigation of the effects of Morin on potassium bromate-induced brain damage in rats via different pathways with biochemical and histopathological methods. Food Chem Toxicol. 2025;115466.

[10] Çomaklı S, Kandemir FM, Küçükler S, Özdemir S. Morin mitigates ifosfamide induced nephrotoxicity by regulation of NF-kappaB/p53 and Bcl-2 expression. Biotechnic Histochem. 2022;97(6):423-32.

[11] Kandemir FM, Yıldırım S, Kucukler S, Caglayan C, Darendelioğlu E, Dortbudak MB. Protective effects of morin against acrylamide-induced hepatotoxicity and nephrotoxicity: A multi-biomarker approach. Food Chem Toxicol. 2020;138:111190.

[12] Ucar F, Taslipinar MY, Alp BF, Aydin I, Aydin FN, Agilli M, et al. The effects of N-acetylcysteine and ozone therapy on oxidative stress and inflammation in acetaminophen-induced nephrotoxicity model. Ren Fail. 2013;35(5):640-47.

[13] Matkovics B. Determination of enzyme activity in lipid peroxidation and glutathione pathways. Laboratoriumi Diagnosztika. 1988;15:248-50.

[14] Sedlak J, Lindsay RH. Estimation of total, protein-bound, and nonprotein sulfhydryl groups in tissue with Ellman's reagent. Anal Biochem. 1968;25:192-205.

[15] Placer ZA, Cushman LL, Johnson BC. Estimation of product of lipid peroxidation (malonyl dialdehyde) in biochemical systems. Anal Biochem. 1966;16(2):359-64.

[16] Sun YI, Oberley LW, Li Y. A simple method for clinical assay of superoxide dismutase. Clin Chem. 1988;34(3):497-500.

[17] Aebi H. Catalase in vitro. In: Methods in Enzymology. Vol. 105. Academic press; 1984. p. 121-26.

[18] Lowry OH, Rosebrough NJ, Farr AL, Randall RJ. Protein measurement with the Folin phenol reagent. J Biol Chem. 1951;193(1):265-75.

[19] Livak KJ, Schmittgen TD. Analysis of relative gene expression data using real-time quantitative PCR and the 2(-Delta Delta C(T)) Method. Methods. 2001;25(4):402-08.

[20] Kandemir Ö, Akaras N, Şimşek H, Gür C, İleritürk M, Küçükler S, et al. Nephroprotective effects of hesperidin on ifosfamide-induced acute nephrotoxicity in rats: Role of NF-κB/TNF-α/IL-1β, p53/caspase-3/Bax/Bcl-2, and ATF6/IRE1/PERK/GRP78 signaling pathways. Arch Biochem Biophys. 2025;110465.

[21] Ahmad I, Alam W, Pirzada AS, Darwish HW, Zafar R, Daglia M, et al. Oxindole derivatives alleviate paracetamol-induced nephrotoxicity and hepatotoxicity: biochemical, histological, and computational expressions. Naunyn Schmiedebergs Arch Pharmacol. 2024:1-13.

[22] Akaras N, Toktay E, Celep NA, Yüce N, Şimşek H, Özkan Hİ. Antioxidant effects of bromelain on

paracetamol-induced renal injury in rats. Arch Basic Clin Res. 2023;5:364-71.
[23] Chinnappan SM, George A, Thaggikuppe P, Choudhary Y, Choudhary VK, Ramani Y, et al. Nephroprotective effect of herbal extract Eurycoma longifolia on paracetamol-induced nephrotoxicity in rats. Evid Based Complement Alternat Med. 2019;2019(1):4916519.
[24] Divyashree R, Sultanpur CM. Protective effect of Acacia Ferruginea bark extract against paracetamol-induced nephrotoxicity in rats. RGUHS J Pharm Sci. 2025;15(1).
[25] Althagafy HS, Hassanein EH. Morin mitigates 5-Fluorouracil-induced nephrotoxicity by activating Nrf2/HO-1 and FXR, and suppressing ERK/VCAM-1 and NF-κB pathways. Int Immunopharmacol. 2025;148:114092.
[26] Darendelioğlu E, Sağ S, Caglayan C. Assessment of morin hydrate as a renal protective agent in rats subjected to methotrexate-induced nephrotoxicity. Drug Chem Toxicol. 2025;48(1):172-79.
[27] Ahmad MM, Rezk NA, Fawzy A, Sabry M. Protective effects of curcumin and silymarin against paracetamol-induced hepatotoxicity in adult male albino rats. Gene. 2019;712:143966.
[28] KELEŞ O, Can S, Cigsar G, Colak S, Erol H, Akaras N, et al. Hepatoprotective effects of B-1, 3-(D)-glucan on bortezomib-induced liver damage in rats. Kafkas Univ Vet Fak Derg. 2014;20(6).
[29] Ozyigit F, Deger AN, Kocak FE, Ekici MF, Simsek H, Arık O. Protective effects of hesperidin in gastric damage caused by experimental ischemia-reperfusion injury model in rats. Acta Cir Bras. 2024;39:e391124.
[30] Yıldız MO, Çelik H, Caglayan C, Kandemir FM, Gür C, Bayav İ, et al. Neuromodulatory effects of hesperidin against sodium fluoride-induced neurotoxicity in rats: Involvement of neuroinflammation, endoplasmic reticulum stress, apoptosis and autophagy. Neurotoxicol. 2022;90:197-204.
[31] Akaras N, Gur C, Kucukler S, Kandemir FM. Zingerone reduces sodium arsenite-induced nephrotoxicity by regulating oxidative stress, inflammation, apoptosis and histopathological changes. Chem Biol Interact. 2023;374:110410.
[32] Şimşek H, Akaras N, Gür C, Küçükler S, Kandemir FM. Beneficial effects of Chrysin on Cadmium-induced nephrotoxicity in rats: Modulating the levels of Nrf2/HO-1, RAGE/NLRP3, and Caspase-3/Bax/Bcl-2 signaling pathways. Gene. 2023;875:147502.
[33] Yousef MI, Omar SA, El-Guendi MI, Abdelmegid LA. Potential protective effects of quercetin and curcumin on paracetamol-induced histological changes, oxidative stress, impaired liver and kidney functions and haematotoxicity in rat. Food Chem Toxicol. 2010;48(11):3246-61.
[34] Kızıl, H. E., Caglayan, C., Darendelioğlu, E., Ayna, A., Gür, C., Kandemir, F. M., & Küçükler, S. (2023). Morin ameliorates methotrexate-induced hepatotoxicity via targeting Nrf2/HO-1 and Bax/Bcl2/Caspase-3 signaling pathways. Molecular Biology Reports, 50(4), 3479-88.
[35] Aydin M, Cevik A, Kandemir FM, Yuksel M, Apaydin AM. Evaluation of hormonal change, biochemical parameters, and histopathological status of uterus in rats exposed to 50-Hz electromagnetic field. Toxicol Ind Health. 2009;25(3): 153-58.
[36] Aksu EH, Kandemir FM, Yıldırım S, Küçükler S, Dörtbudak MB, Çağlayan C, et al. Palliative effect of curcumin on doxorubicin-induced testicular damage in male rats. J Biochem Mol Toxicol. 2019;33(10):e22384.
[37] Kandemir FM, Kucukler S, Eldutar E, Caglayan C, Gülçin İ. Chrysin protects rat kidney from paracetamol-induced oxidative stress, inflammation, apoptosis, and autophagy: a multi-biomarker approach. Sci Pharm. 2017;85(1):4.
[38] Ileriturk M, Kandemir O, Akaras N, Simsek H, Genc A, Kandemir FM. Hesperidin has a protective effect on paclitaxel-induced testicular toxicity through regulating oxidative stress, apoptosis, inflammation and endoplasmic reticulum stress. Reprod Toxicol. 2023;118:108369.
[39] Kucukler S, Benzer F, Yildirim S, Gur C, Kandemir FM, Bengu AS, et al. Protective effects of chrysin against oxidative stress and inflammation induced by lead acetate in rat kidneys: a biochemical and histopathological approach. Biol Trace Elem Res. 2021;199(4):1501-14.
[40] Çağlayan C, Kandemir FM, Darendelioğlu E, Küçükler S, Ayna A. Hesperidin protects liver and kidney against sodium fluoride-induced toxicity through anti-apoptotic and anti-autophagic mechanisms. Life Sci. 2021;281:119730.
[41] Kankılıç NA, Şimşek H, Akaras N, Gür C, Küçükler S, İleritürk M, et al. The ameliorative effects of chrysin on bortezomib-induced nephrotoxicity in rats: Reduces oxidative stress, endoplasmic reticulum stress, inflammation damage, apoptotic and autophagic death. Food Chem Toxicol. 2024;190:114791.
[42] Akaras N, Kandemir FM, Şimşek H, Gür C, Aygörmez S. Antioxidant, antiinflammatory, and antiapoptotic effects of rutin in spleen toxicity induced by sodium valproate in rats. Turk J Nat Sci. 2023;12(2):138–44.
[43] Yilmaz S, Gur C, Kucukler S, Akaras N, Kandemir FM. Zingerone attenuates sciatic nerve damage caused by sodium arsenite by inhibiting NF-κB, caspase-3, and ATF-6/CHOP pathways and activating the Akt2/FOXO1 pathway. Iran J Basic Med Sci. 2024;27(4):485.
[44] Gencer S, Gür C, İleritürk M, Küçükler S, Akaras N, Şimşek H, et al. The ameliorative effect of carvacrol on sodium arsenite-induced hepatotoxicity in rats: Possible role of Nrf2/HO-1, RAGE/NLRP3, Bax/Bcl-2/Caspase-3, and Beclin-1 pathways. J Biochem Mol Toxicol. 2024;38(10):e23863.
[45] El-Boshy M, BaSalamah MA, Ahmad J, Idris S, Mahbub A, Abdelghany AH, et al. Vitamin D protects against oxidative stress, inflammation and hepatorenal damage induced by acute paracetamol

toxicity in rat. Free Radic Biol Med. 2019;141:310–21.
[46] Akaras N, Gür C, Caglayan C, Kandemir FM. Protective effects of naringin against oxaliplatin-induced testicular damage in rats: Involvement of oxidative stress, inflammation, endoplasmic reticulum stress, apoptosis, and histopathology. Iran J Basic Med Sci. 2024;27(4):466.
[47] Bal TT, Akaras N, Demir Ö, Ugan RA. Protective effect of astaxanthin and metformin in the liver of rats in which the polycystic ovary syndrome model was formed by giving letrozole. Iran J Basic Med Sci. 2023;26(6):688.
[48] Kankılıç NA, Küçükler S, Gür C, Akarsu SA, Akaras N, Şimşek H, et al. Naringin protects against paclitaxel-induced toxicity in rat testicular tissues by regulating genes in pro-inflammatory cytokines, oxidative stress, apoptosis, and JNK/MAPK signaling pathways. J Biochem Mol Toxicol. 2024;38(7):e23751.
[49] Akaras N, Kucukler S, Gur C, Ileriturk M, Kandemir FM. Sinapic acid protects against lead acetate-induced lung toxicity by reducing oxidative stress, apoptosis, inflammation, and endoplasmic reticulum stress damage. Environ Toxicol. 2024;39(7):3820–32.
[50] Küçükler S, Caglayan C, Özdemir S, Çomaklı S, Kandemir FM. Hesperidin counteracts chlorpyrifos-induced neurotoxicity by regulating oxidative stress, inflammation, and apoptosis in rats. Metab Brain Dis. 2024;39(4):509–22.
[51] El-Bakry HA, El-Sherif G, Rostom RM. Therapeutic dose of green tea extract provokes liver damage and exacerbates paracetamol-induced hepatotoxicity in rats through oxidative stress and caspase 3-dependent apoptosis. Biomed Pharmacother. 2017;96:798–811.
[52] Aktas Senocak E, Utlu N, Kurt S, Kucukler S, Kandemir FM. Sodium pentaborate prevents acetaminophen-induced hepatorenal injury by suppressing oxidative stress, lipid peroxidation, apoptosis, and inflammatory cytokines in rats. Biol Trace Elem Res. 2024;202(3):1164–73.

Volume 14, Issue 3, Page 40-45, 2025 https://doi.org/10.46810/tdfd.1636038 Research Article

BİNGÖL UNIVERSITY

Türk Doğa ve Fen Dergisi
Turkish Journal of Nature and Science
www.dergipark.gov.tr/tdfd

Assessment of Real Confectionery Industry Wastewater: Characterisation and Treatability with Coagulation-Flocculation

Inci Karakas[1*]

[1] Uskudar University, Vocational School of Health Services, Department of Environmental Health, İstanbul, Türkiye
Inci KARAKAS ORCID No: 0000-0002-3590-3395

**Corresponding author: inci.karakas@uskudar.edu.tr*

(Received: 10.02.2025, Accepted: 06.07.2025, Online Publication: 26.09.2025)

Keywords
Confectionery industry, Real wastewater, Coagulation-flocculation

Abstract: It is important to treat the confectionery industry wastewater with appropriate methods due to the high organic pollutants it contains. When these wastewaters are discharged without pretreatment, they cause serious environmental problems such as eutrophication. In this study, real confectionery industry wastewater was taken from Gebze Plastics Organized Industrial Zone (Türkiye). Pollutant concentrations were determined by detailed characterisation of the wastewater. Lime, polyaluminium chloride and ammonim persulfate coagulants were added and chemical oxygen demand, total phosphate, orthophosphates, total nitrogen and ammonium nitrogen removal by coagulation-flocculation were investigated. The optimum concentrations of the chemicals used in the study were found to be lime: 0.75 g L^{-1}, polyaluminum chloride: 0.5 g L^{-1} and ammonium persulfate: 0.004 g L^{-1}, respectively; and the optimum pH conditions were found to be lime: 10.9, polyaluminum chloride: 8.1 and ammonium persulfate: 8.1, respectively. In the study, chemical oxygen demand, total phosphate, orthophosphates, and ammonium nitrogen removal efficiencies were ≥86%, and total nitrogen removal efficiency was 43%. Conformity of confectionery industry wastewater, which causes serious environmental problems such as eutrophication in case of direct discharge to the receiving environment, to the sewage discharge criteria after pretreatment was also investigated.

Gerçek Şekerleme Endüstrisi Atıksularının Değerlendirilmesi: Karakterizasyonu ve Koagülasyon-Flokülasyon ile Arıtılabilirliği

Anahtar Kelimeler
Şekerleme endüstrisi, Gerçek atıksu, Koagülasyon-flokülasyon

Öz: Şekerleme endüstrisi atık suyunun içerdiği yüksek organik kirleticiler nedeniyle uygun yöntemlerle arıtılması önemlidir. Bu atık sular ön arıtım yapılmadan deşarj edildiğinde ötrofikasyon gibi ciddi çevresel sorunlara neden olmaktadır. Bu çalışmada, Gebze Plastik Organize Sanayi Bölgesi'nden (Türkiye) gerçek şekerleme endüstrisi atık suyu alınmıştır. Atıksuyun detaylı karakterizasyonu ile kirletici konsantrasyonları belirlenmiştir. Kireç, polialüminyum klorür ve amonyum persülfat koagülantları ilave edilmiş ve koagülasyon-flokülasyon ile kimyasal oksijen ihtiyacı, toplam fosfor, ortafosfat, toplam azot ve amonyak giderimi araştırılmıştır. Çalışmada kullanılan kimyasalların optimum konsantrasyonları sırasıyla, kireç: 0,15 g, polialüminyum klorür: 0,1 g ve amonyum persülfat: 0,0008 g olarak; optimum pH koşulları ise sırasıyla, kireç: 10,9, polialüminyum klorür: 8,1 ve amonyum persülfat: 8,1 olarak bulunmuştur. Çalışmada kimyasal oksijen ihtiyacı, toplam fosfor, ortafosfat ve amonyak giderim verimleri ≥%86, toplam azot giderim verimi ise %43 olarak bulunmuştur. Alıcı ortama direkt deşarjı halinde, ötrofikasyon gibi ciddi çevresel risk oluşturan şekerleme endüstrisi atıksuyunun ön arıtımı sonucunda kanalizasyona deşarj kriterlerine uygunluğu da araştırılmıştır.

1. INTRODUCTION

The confectionery industry (CI) is one of the most widespread and important industries worldwide. Cocoa, sugar, various fats, and emulsifiers are used in the production process, including confectionery and chewing gum products [1–3]. With the development of industrial organisations, pollution sources that cause water pollution have also developed. These industries produce large amounts of wastewater with high levels of pollutants. Confectionery wastewater is considered non-toxic because it does not contain compounds such as heavy

metals. The composition and quantity of small-scale CI wastewater varies daily and seasonally. Therefore, it is emphasised that it is not economically and operationally suitable as a raw material. These wastewaters are suitable substrates for microorganisms as they have biodegradable organic matter containing compounds such as high Chemical oxygen demand (COD), nitrogen, and glucose. However, it is risky to discharge wastewater from these industries without pre-treatment [4–6]. Untreated wastewater has many negative effects on human health, flora, fauna, and agricultural lands. CI wastewaters cause eutrophication by increasing phosphorus and nitrogen concentrations in receiving environments and pollute waters that can be used as drinking water [7,8]. Dissolved oxygen concentration in the aquatic environment decreases with the biochemical breakdown of organic pollutants reaching the receiving environment. Thus, anaerobic microorganisms become dominant in the aquatic environment, reducing the self-cleaning capacity of the receiving environment [9]. In order to control water pollution, it is important to treat wastewater with various pre-treatment processes before discharge. Treatment methods such as physicochemical and biological (aerobic/anaerobic) treatment processes [10], membrane technologies [11], adsorption [12], coagulation [13], and electrochemical treatment [14] have been used for the treatment of CI wastewater.

Coagulation-flocculation process has been proven to be effective in wastewater treatment by various studies [15]. Coagulation-flocculation process is generally used to remove suspended solids (SS) and organic pollutants from wastewater. The efficiency of the process is related to the selection of the appropriate coagulant. With lime, which can be used in the process, higher biochemical oxygen demand (BOD) and COD removal (BOD: 34-66% and COD: 32-59%) are achieved under aerobic conditions [16]. Flocculation process is the most widely used method in water treatment due to its ease of operation and economic advantages [17]. Inorganic polymer flocculants added in the flocculation process have advantages such as easy availability and applicability. However, aluminium salts, which are among the coagulants frequently used in the coagulation stage, are among the most widely used inorganic coagulants due to their good treatment performance, easy availability and use, and low cost [18]. It is also reported that polyaluminium chloride (PAC), which is the hydrolysed form of aluminium salt used in present study, is more effective [19].

Adsorption process using activated carbon was applied for the treatment of CI wastewater. After adsorption, BOD and COD were removed with 90% efficiency [20–22]. It has been emphasised that activated carbon is disadvantageous due to its high cost, regeneration, and disposal problems [9]. Electrocoagulation process using zinc electrodes was used for the treatment of sugar industry wastewater. Significant removal of COD (81%), BOD (89%), and total solids content (90%) was achieved [23]. Electrocoagulation process using aluminium anodes and sand filtration process were used for pretreatment of chocolate industry wastewater. Turbidity removal of 96%, colour removal of 98%, and COD removal of 39% were achieved [1]. Turbidity, COD, and BOD removal from sugar industry wastewater using active sugarcane bagasse by coagulation process was investigated. Turbidity, COD, and BOD removal were found to be 68.9%, 64.8%, and 69.9%, respectively [24]. CI wastewater was treated biologically using a pilot-scale filter. COD, nitrate (NO_3-N), and orthophosphates (PO_4-P) removals were found to be 98.9%, 99.5%, and 99.7%, respectively [6].

In this study, real CI wastewater was characterised and investigated by using Lime ($Ca(OH)_2$), PAC, and Ammonim Persulfate $(NH_4)_2S_2O_8$ coagulants with coagulation-flocculation process, COD, total phosphate (TP), PO_4-P, total nitrogen (TN), ammonium nitrogen (NH_4-N), and NO_3-N removal. In addition, SS concentrations in the influent wastewater were also monitored. Studies investigating the removal of COD, TP, PO_4-P, TN, NH_4-N, and NO_3-N parameters, which are important pollution sources in CI wastewater, are limited. The removal of CI wastewater containing high organic pollutants, which discharge without pre-treatment would pose a serious environmental risk, was investigated by coagulation and flocculation process, and the suitability of effluent pollutant concentrations in terms of sewage discharge criteria was investigated.

2. MATERIAL AND METHOD

2.1. Sample collection

The wastewater used in the experiments was obtained from the CI in Gebze Plastics Organised Industrial Zone (Turkiye). The flow rate of the wastewater treatment plant where chemical treatment is performed is 15 m^3. The plant has a rapid mixing tank where the coagulation process takes place, and then a flocculation tank where the wastewater is conveyed for flocculation process. CI wastewater was taken from the inlet of the plant. Samples were taken twice a week, and a total of 4 litres composite sample was formed. The raw wastewater taken from the plant inlet was stored in the refrigerator (4 $^{\circ}C$) before the experiments.

2.2 Coagulation-flocculation jar test procedure

Coagulation-flocculation study was carried out under laboratory conditions (24 °C) using a jar test device. During the research, 200 mL of wastewater volume was used in each trial set. Each coagulation experiment was started by adding coagulant to the reactor containing wastewater, and then the appropriate initial pH was adjusted using HCl and NaOH. In the coagulation step, the reaction time was limited to 3 minutes (mins), and the process was continued at a stirring speed of 120 rpm [15]. The flocculation process was carried out at a mixing speed of 40 rpm with a contact time of 15 mins [15]. The precipitation step was determined as 45 mins, and at the end of the process, samples were taken from the upper phase and analyzed for SS, COD, TP, PO_4-P, TN, NH_4-N. Optimum pH values and coagulant doses to be used in CI wastewater were determined by Jar test. After the jar test, samples were taken from the upper phase, and outlet COD concentrations were measured. The removal efficiencies

of pollutant parameters in the influent wastewater were determined by using the values in the third jar test, which had the lowest effluent COD concentration and the lowest chemical consumption. For coagulation-flocculation in CI wastewater, 5% $Ca(OH)_2$, 17% PAC, and 0.1% $(NH_4)_2S_2O_8$ were used. The properties of the chemicals used are presented in Tables 1.

Table 1. Properties of the chemicals used

	Coagulants and Chemicals				
	HCl	**NaOH**	**PAC**	**$(NH_4)_2S_2O_8$**	**$Ca(OH)_2$**
Concentration	37%	45%	%17	0.1%	5%
Density (g/cm^3)	1.180	1.32	1.4	0.75	2.21
Mole (g/mole)	36.5	40	97.46	228	74.09

2.3. Characterization

The conductivity and pH were measured using a pH meter and a conductivity device. COD (K-7365), TP and PO_4-P (TR-TP), TN (TR-TN), NH_4-N (LCK303), NO_3-N (LCK339), and nitrite (NO_2-N) (LCK341) were carried out with Hach test kits. Suspended Solids (SS) were determined according to Standard Methods [25].

3. RESULTS AND DISCUSSION

The concentrations and pH values of the chemicals used in the three sets in the study were given in Table 2.

Table 2. Coagulants used in the study, coagulant doses and pH values (in 200 mL volume)

Coagulants	**Doses (g)**			**pH values**		
	Set 1	Set 2	Set 3	Set 1	Set 2	Set 3
$Ca(OH)_2$	0.17	0.18	0.15	11.3	11.1	10.9
PAC	0.18	0.2	0.1	7.9	8.2	8.1
$(NH_4)_2S_2O_8$	0.0011	0.0009	0.0008	7.9	8.2	8.1

The concentration and consumption amount of chemicals used in Set 3 were also presented in Table 3. PAC, one of the aluminum salts, was used in the study at a pH value of 8.1. In the coagulation-flocculation process, neutral pH values are given as the first species that provide the sweeping mechanism for aluminum hydroxide precipitates. When the surface charge of colloids is zero at neutral pH values, the sweeping mechanism or charge neutralization occurs.

The content and pH value of the wastewater directly were affected the coagulation-flocculation process [26]. It has been stated that when aluminum salts are used in an oily wastewater, high pH values increase the negative charge of hydroxide (OH^-) and negatively affect the performance of the process [27]. At the optimum polyaluminum chloride silicate dosage and pH 7, COD and turbidity removals were found to be 94.4% and 94.1%, respectively [28].

Table 3. Consumption of coagulants according to set 3

Coagulants	**Concentration**	**Density(d) (g cm^{-3})**	**Consumption (g L^{-1})**
PAC	%17	1.4	0.5
$(NH_4)_2S_2O_8$	%0.1	0.75	0.004
$Ca(OH)_2$	%5	2.21	0.75

An effective volume of 200 mL was used in the present study. The concentrations of the chemicals used in this volume were $Ca(OH)_2$: 0.15 g, PAC: 0.1 g and $(NH_4)_2S_2O_8$: 0.0008, respectively. CI wastewaters have different characterisations according to the product and process. The wastewater characterisation studies are summarised in Table 4.

Table 4. The characterisation of the real CI wastewater and comparison with literatüre

Wastewater Type	**pH**	**COD (mg L^{-1})**	**SS (mg L^{-1})**	**TP (mg L^{-1})**	**PO_4 (mg L^{-1})**	**TN (mg L^{-1})**	**NH_4-N (mg L^{-1})**	**NO_3-N (mg L^{-1})**	**NO_2-N (mg L^{-1})**	**Literature**
Sugar Industry	5.5	3682	790	-	5.9	-	-	-	-	[29]
Sugar Industry	6.7–8.4	1100.3-2148.9	220.3-790.7	-	1.2-9.6	11.1-40.6	0.0-4.2	0.4-0.9	-	[30]
Sugar Cane Industry	7.1	31735	-	-	11.3	61.8	8.1	7.6	-	[15]
Pudding Dessert Wastewater	6.60-7.70	21000-68000	9000-40000	-	50.0-70.0	-	-	-	-	[6]
Chocolate Manufacturing Industry	7.4	3608	-	-	-	-	-	-	-	[1]
Sweet-snacks and Ice-cream Industries	5.6-7.1	8960-11900	-	-	-	78-157	89-120	-	-	[8]
Confectionery Industry	3.83	20025	900	4.5	-	-	-	78	-	[31]
Confectionery Industry	7.5	448	231	10.5	-	-	-	-	-	[32]
Confectionary Wastewater	6.6	8330	1835	11.5	3.70	37	0.25	3.71	0.30	Present Study

The only study in which all of the parameters related to organic pollutants given in the table were monitored is the present study. The pH value of the wastewater in the present study is within the range specified in the literature. While COD concentration varies between 3608-68000 mg L^{-1} in the studies, COD concentration in the present study was found to be 8330 mg L^{-1}, and it is seen that it is compatible with the studies in the literature. SS concentration was found as 1835 mg L^{-1} and it is in parallel with the literature. Studies monitoring TP concentration in CI wastewater are limited.

In the present study, TP concentration was higher than the value given in the literature and was found as 11.5 mg L^{-1}. PO_4-P was measured at different concentration ranges in the studies and was determined as 3.7 mg L^{-1} in the present study. TN, NH_4-N, and NO_3-N concentrations determined in the study were 37 mg L^{-1}, 0.25 mg L^{-1}, and 3.71 mg L^{-1}, respectively. NO_2-N concentration was found as 0.30 mg L^{-1} in the study.

$$\textbf{Removal rate}\ (\%) = \frac{\boldsymbol{C0 - C}}{\boldsymbol{C0}} * \mathbf{100} \qquad (1)$$

Following the coagulation-flocculation process, pollutant removal was monitored in the samples taken from the upper phase, and the removal efficiencies are given in Figure 1. Removal efficiencies were calculated according to the following Equation (1).

C0: the concentration of pollutants in the influent wastewater sample

C: the concentration of pollutants treated wastewater sample

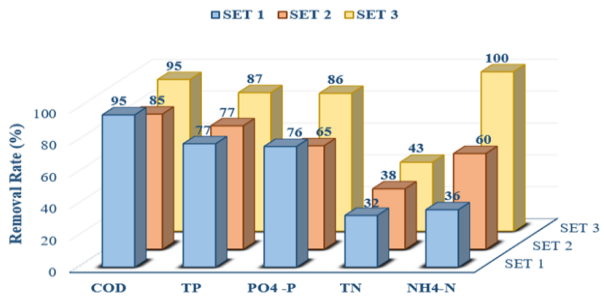

Figure 1. Removal efficiencies of pollutants in all set

When the removal efficiency of pollutants in three sets after the chemicals applied in the Jar test was analysed, the set with the best removal efficiency was Set 3. When the COD removal in Set 3 was analysed, a removal efficiency of 95% was determined. In the literature, it is seen that COD removal efficiencies of CI wastewater by coagulation-flocculation process vary between 56.7% and As seen in Table 5, all of the pollutants detected in this study and included in the Water Pollution Control Regulation supplied the discharge criteria.

96.1% [33]. In the coagulation process using alum, COD removal efficiency was 96.1%, while when polyaluminum chloride was used, the removal efficiency was 95% [34]. In another study investigating the removal of sugar industry wastewater by coagulation, COD removal was found to be 69-80% when $FeCl_3$ was used as coagulant [35], while COD removal was found to be 82% when Alum was used [13].

In a coagulation study using activated sugarcane bagasse coagulant, COD removal was found to be 64.8% [24]. The COD removals in the present study are in parallel with the studies in the literature. In Set 3, TP was removed with high efficiency, and the removal was found to be 87%. There is no study on TP removal using coagulation-flocculation process in CI wastewater in the literature. In the present study, PO_4-P removal was found to be 86%. Coagulation-flocculation process integrated with nanofiltration and reverse osmosis membrane was used for the treatment of sugarcane industry wastewater. In the coagulation-flocculation process with unshelled and shelled moringa seeds, PO_4-P removal was 44% and 23%, respectively.

When moringa seeds were used after degreasing after treatment with ethanol, PO_4-P removal efficiencies reached 59%. When PO_4-P removal was compared with the literature, higher removal efficiencies were obtained with the coagulants used in present study [15]. In the study, TN was removed to a limited extent compared to other compounds and the removal efficiency was found to be 43%, while NH_4-N was completely removed. Unshelled and shelled moringa seeds and moringa seeds formed after ethanol treatment were also used for TN and NH_4-N removal from sugarcane industry wastewater. TN removals were found to be 31%, 27%, and 41%, respectively. NH_4-N removals using unshelled and shelled moringa seeds and moringa seeds formed after ethanol treatment were found to be 20%, 9%, and 25%, respectively [15]. CI wastewater is aimed to supplied the Gebze Plastics Organised Industrial Zone sewerage discharge criteria. Pollutant parameters and sewerage discharge values of the treated wastewater obtained in Set 3 are given in Table 5.

Table 5. Effluent concentrations and discharge criteria

Parameter	Effluent concentrations	Discharge criteria*
COD (mg L^{-1})	416.5	4000
pH	8	6.5-10
SS (mg L^{-1})	<50	500
NH_4-N (mg L^{-1})	<0.005	-
NO_3-N (mg L^{-1})	<0.005	-
NO_2-N (mg L^{-1})	<0.005	-
TN (mg L^{-1})	21.1	80
TP (mg L^{-1})	1.5	2
PO_4-P (mg L^{-1})	0.52	-

* Discharge criteria: GOIZ discharge criteria *(Water Pollution Control Regulation, Table 25)*

4. CONCLUSION

CI wastewater differs according to the type of product produced and the production process and poses a great environmental risk. Wastewater discharged without pre-treatment threatens aquatic life by polluting surface water, groundwater and soil. In the study, detailed characterisation of the wastewater was carried out. The treatability of the wastewater was investigated by coagulation-flocculation process using $Ca(OH)_2$, PAC and $(NH_4)_2S_2O_8$ coagulants and the most effective removal rate was determined in Set 3. There is no study investigating the removal of COD, TP, PO_4-P, TN and NH_4-N using real CI wastewater. The COD removal rate determined in the study coincides with the studies in the literature and it is seen that a higher removal rate is achieved than many studies. No study on TP removal was found in the literature and TP removal in Set 3 was determined with high efficiency. PO_4-P, TN and NH_4-N removal efficiencies were found above the values stated in the literature. Due to the environmental risk of CI wastewater, it is important to increase the studies on pretreatment of wastewater, especially from small-scale establishments. As a result of the study, it was observed that CI wastewater, which poses a serious environmental risk, can be treated by coagulation - flocculation process and using this process discharge criteria are supplied. However, since the disposal of the chemical sludge to be formed after coagulation-flocculation is troubled, the treatability with biodegradable coagulants should be investigated.

REFERENCES

[1] García-Morales MA, Juárez JCG, Martínez-Gallegos S, Roa-Morales G, Peralta E, Del Campo López EM, et al. Pretreatment of Real Wastewater from the Chocolate Manufacturing Industry through an Integrated Process of Electrocoagulation and Sand Filtration. International Journal of Photoenergy 2018;2018:1–7. https://doi.org/10.1155/2018/2146751

[2] Edwards WP. The science of sugar confectionery. Royal Society of Chemistry; 2018.

[3] El-Kalyoubi M, Khallaf MF, Abdelrashid A, Mostafa EM. Quality characteristics of chocolate–Containing some fat replacer. Annals of Agricultural Sciences 2011;56:89–96.

[4] Beal LJ, Raman DR. Sequential two-stage anaerobic treatment of confectionery wastewater. Journal of Agricultural Engineering Research 2000;76:211–7.

[5] Chakraborty B, Kundu P, Mukherjee J, Mukherjee S. Kinetics Study of a Suspended Growth System for Biological Treatment of Bakery and Confectionery Wastewater. In: Ramkrishna D, Sengupta S, Dey Bandyopadhyay S, Ghosh A, editors. Advances in Bioprocess Engineering and Technology, Singapore: Springer Singapore; 2021, p. 339–48. https://doi.org/10.1007/978-981-15-7409-2_34.

[6] Patsialou S, Politou E, Nousis S, Liakopoulou P, Vayenas DV, Tekerlekopoulou AG. Hybrid treatment of confectionery wastewater using a biofilter and a cyanobacteria-based system with simultaneous valuable metabolic compounds production. Algal Research 2024;79:103483.

[7] Demirel B, Yenigun O, Onay TT. Anaerobic treatment of dairy wastewaters: a review. Process Biochemistry 2005;40:2583–95.

[8] Qasim W, Mane AV. Characterization and treatment of selected food industrial effluents by coagulation and adsorption techniques. Water Resources and Industry 2013;4:1–12.

[9] Zajda M, Aleksander-Kwaterczak U. Wastewater treatment methods for effluents from the confectionery industry–an overview. Journal of Ecological Engineering 2019;20:293–304.

[10] Nasr FA, Abdelfattah I, El-Shafai SA. Cost effective management of confectionery industrial wastewater. Egyptian Journal of Chemistry 2022;65:391–9.

[11] Hinkova A, Bubnık Z, Kadlec P, Pridal J. Potentials of separation membranes in the sugar industry. Separation and Purification Technology 2002;26:101–10.

[12] Saxena C, Madan S. Evaluation of adsorbents efficacy for the removal of pollutants from sugar mill effluent. ARPN Journal of Agricultural and Biological Science 2012;7:325–9.

[13] Sahu OP, Chaudhari PK. Physicochemical Treatment of Sugar Industry Wastewater: Coagulation Processes. Environmental Quality Management 2014;23.

[14] Sahu OP, Chaudhari PK. Electrochemical treatment of sugar industry wastewater: COD and color removal. Journal of Electroanalytical Chemistry 2015;739:122–9.

[15] Sawadogo B, Moussa AWN, Konaté Y, Tiendrebeogo C, Sossou S, Sidibé SDS, et al. Integrated coagulation-flocculation with nanofiltration and reverse osmosis membrane for treating sugar cane industry effluent. Heliyon 2024;10.

[16] Vanerkar AP, Satyanarayan S, Satyanarayan S. Treatment of food processing industry wastewater by a coagulation/flocculation process. International Journal of Chemical and Physical Sciences 2013;2:63–72.

[17] Lee CS, Robinson J, Chong MF. A review on application of flocculants in wastewater treatment. Process Safety and Environmental Protection 2014;92:489–508.

[18] Bhatia S, Othman Z, Ahmad AL. Pretreatment of palm oil mill effluent (POME) using Moringa oleifera seeds as natural coagulant. Journal of Hazardous Materials 2007;145:120–6.

[19] Verma AK, Dash RR, Bhunia P. A review on chemical coagulation/flocculation technologies for removal of colour from textile wastewaters. Journal of Environmental Management 2012;93:154–68.

[20] Devi R, Singh V, Kumar A. COD and BOD reduction from coffee processing wastewater using Avacado peel carbon. Bioresource Technology 2008;99:1853–60.

[21] Nayl AEA, Elkhashab RA, El Malah T, Yakout SM, El-Khateeb MA, Ali MM, et al. Adsorption studies on the removal of COD and BOD from treated sewage using activated carbon prepared from date

palm waste. Environmental Science and Pollution Research 2017;24:22284–93.
[22] Sanou Y, Pare S, Baba G, Segbeaya NK, Bonzi-Coulibaly LY. Removal of COD in wastewaters by activated charcoal from rice husk. Revue Des Sciences de l'eau 2016;29:265–77.
[23] Byadgi SA, Sharanappanavar MS, Dhamoji B, Nadaf A, Munennavar S. Treatment of sugar industry waste water using zinc electrodes. International Journal of Engineering Technology Science and Research 2017;4:664–8.
[24] Raziya B, Desai GP. Treatment of industrial wastewater by using sugarcane bagasse. International Research Journal of Engineering and Technology 2019;6:2944–9.
[25] APHA (American Public Health Association). Standard methods for the examination of water and waste water. 19th edition. New York: American Public Health Association Inc.,; 1995.
[26] Zhao C, Zhou J, Yan Y, Yang L, Xing G, Li H, et al. Application of coagulation/flocculation in oily wastewater treatment: A review. Science of The Total Environment 2021;765:142795.
[27] Duan J, Gregory J. Coagulation by hydrolysing metal salts. Advances in Colloid and Interface Science 2003;100:475–502.
[28] Sun Y, Zhu C, Zheng H, Sun W, Xu Y, Xiao X, et al. Characterization and coagulation behavior of polymeric aluminum ferric silicate for high-concentration oily wastewater treatment. Chemical Engineering Research and Design 2017;119:23–32.
[29] Poddar PK, Sahu O. Quality and management of wastewater in sugar industry. Appl Water Sci 2017;7:461–8. https://doi.org/10.1007/s13201-015-0264-4.
[30] Fito J, Tefera N, Van Hulle SWH. Sugarcane biorefineries wastewater: bioremediation technologies for environmental sustainability. Chem Biol Technol Agric 2019;6:6. https://doi.org/10.1186/s40538-019-0144-5.
[31] Ozgun H, Karagul N, Dereli RK, Ersahin ME, Coskuner T, Ciftci DI, et al. Confectionery industry: a case study on treatability-based effluent characterization and treatment system performance. Water Science and Technology 2012;66:15–20.
[32] Kannah Y, Yeom IT, Do K-U. Profitable sludge management via novel combined ozone disperser pretreatment coupled with membrane bioreactor for treating confectionary wastewater. Journal of Cleaner Production 2019;239:118102.
[33] Panhwar A. Chemical Treatment Options of Wastewater from Sugarcane Industry and Its Priority Parameters Comparison as per Smart Rules of Sindh Environmental Protection Agency. Pakistan Journal of Science 2021;73.
[34] Aziz N, Effendy N, Basuki KT. Comparison of poly aluminium chloride (pac) and aluminium sulphate coagulants efficiency in waste water treatment plant. Jurnal Inovasi Teknik Kimia 2017;2.
[35] Sahu OP, Chaudhari PK. Review on chemical treatment of industrial waste water. Journal of Applied Sciences and Environmental Management 2013;17:241–57.
[36] https://www.mevzuat.gov.tr/mevzuat?MevzuatNo=7221&MevzuatTur=7&MevzuatTertip=5 (14.01.2025)

Volume 14, Issue 3, Page 46-56, 2025 https://doi.org/10.46810/tdfd.1629184 Research Article

BİNGÖL UNIVERSITY

Türk Doğa ve Fen Dergisi
Turkish Journal of Nature and Science
www.dergipark.gov.tr/tdfd

Graph-Based Course Scheduling Using the Malatya Vertex Coloring Algorithm for Constraint Optimization

Cezayir KARACA[1*], Selman YAKUT[2]

[1] İnönü University, Faculty of Engineering, Department of Computer Engineering, Malatya, Türkiye
[2] İnönü University, Faculty of Engineering, Department of Software Engineering, Malatya, Türkiye
Cezayir KARACA ORCID No: 0009-0007-9250-2612
Selman YAKUT ORCID No: 0000-0002-0649-1993

**Corresponding author: cezayirkaraca0242@gmail.com*

(Received: 29.01.2025, Accepted: 10.07.2025, Online Publication: 26.09.2025)

Keywords
Course scheduling, Centrality, Malatya coloring, Timetabling

Abstract: The course timetabling problem is a significant combinatorial optimization problem that has attracted the attention of researchers since the second half of the 20th century. Traditionally managed through manual methods, the scheduling process is time-consuming, challenging, and prone to errors. Therefore, with technological advancements, various algorithms have been developed to offer more efficient and faster solutions. In this study, the "MVC Algorithm" is applied to the course timetabling problem. The algorithm operates in two main steps: first, the Malatya Centrality(MC) values of the nodes in the timetable graph are calculated; then, the node with the highest centrality is selected and labeled with an appropriate color. Throughout the process, the main objective is to minimize course conflicts and to generate a valid timetable that complies with defined constraints. The MVC Algorithm stands out with its predictability of procedural steps and its potential to operate in polynomial time, thus offering an effective alternative to classical and heuristic methods proposed in the literature.

Kısıt Optimizasyonu için Malatya Vertex Coloring Algoritması Kullanılarak Graf Tabanlı Ders Çizelgeleme

Anahtar Kelimeler
Ders çizelgeleme, Merkezilik, Malatya coloring, Zaman çizelgesi

Öz: Ders çizelgeleme problemi, 20. yüzyılın ikinci yarısından itibaren araştırmacıların dikkatini çeken önemli bir kombinatoryal optimizasyon problemidir. Geleneksel olarak manuel yöntemlerle yürütülen çizelgeleme süreci, zaman alıcı ve zorlayıcı olmakla birlikte hata yapmaya açık bir yapıdadır. Bu nedenle, teknolojik ilerlemelerle birlikte çeşitli algoritmalar geliştirilerek daha etkili ve hızlı çözümler sunulmaya çalışılmıştır. Bu çalışmada, "Malatya Vertex Coloring(MVC) Algoritması" ders çizelgeleme problemine uygulanmaktadır. Algoritma, iki temel adımda çalışmaktadır: ilk olarak, çizelge grafındaki düğümlerin Malatya Merkezilik değerleri hesaplanmakta; ardından en yüksek merkeziliğe sahip düğüm seçilerek uygun bir renkle etiketlenmektedir. Süreç boyunca temel hedef, ders çakışmalarını en aza indirmek ve tanımlı kısıtlamalara uyumlu, geçerli bir çizelge üretmektir. MVC Algoritması, işlem adımlarının öngörülebilirliği ve polinom zamanda çalışabilme potansiyeliyle dikkat çekmekte, bu yönüyle literatürde önerilen klasik ve sezgisel yöntemlere etkili bir alternatif sunmaktadır.

1. INTRODUCTION

The Course Scheduling Problem (CSP) is a complex optimization problem that has been extensively studied in the fields of operations research and artificial intelligence since the 1960s. This problem aims to assign courses to specific time slots, classrooms, and instructors without conflicts. Particularly in educational institutions, due to the necessity of managing limited resources (classrooms, instructors, time slots) along with numerous constraints, the scheduling process becomes highly time-consuming and error-prone when handled manually[1].

Technological advancements have enabled the development of various algorithms to automate and improve this process. Among the solution methods proposed in the literature, heuristic algorithms, metaheuristic approaches (e.g., genetic algorithms, tabu search)[2], and graph-based algorithms (e.g., bipartite edge coloring, vertex coloring)[3] are particularly

prominent. However, the high computational power required by existing algorithms when applied to large datasets poses a significant challenge, especially in university settings where course repetitions and student enrollments are dense.

Course scheduling is not merely a matter of assigning courses to time slots. It also involves ensuring compliance with various strict constraints, such as preventing conflicts and adhering to class capacities and lecture hours. Some fundamental challenges frequently encountered in universities include:

- Lecture durations not being uniform,
- Courses sharing common students or instructors not being scheduled simultaneously,
- The necessity for certain courses to be repeated more than once a week.

In this context, there is a growing need for more flexible and computationally efficient algorithms that can reduce course conflicts and generate optimal timetables under defined constraints.

In response to these needs, this study proposes a novel approach called the MVC Algorithm. The algorithm consists of two fundamental phases. In the first phase, the Malatya Centrality (MC) values of the nodes representing the courses are calculated. In the second phase, the node with the highest MC value is selected, assigned a color, and removed from the graph. This process continues iteratively, ensuring that adjacent nodes are assigned different colors. The main advantage of the proposed algorithm lies in the predictability of all procedural steps and its ability to produce solutions in polynomial time.

The remainder of this article is organized as follows: Section 2 reviews the related literature and graph-coloring-based approaches. Section 3 presents the method and proposed approach. Experimental results are provided in Section 4. Finally, Section 5 offers interpretations of the findings and discusses recommendations for future work.

2. LITERATURE REVIEW

CSP is a classical combinatorial optimization problem that aims to ensure the efficient and conflict-free use of resources in educational institutions. As the number of courses and the constraints to be applied increase, the problem becomes increasingly complex. Therefore, numerous studies based on various algorithms have been conducted. These studies can be categorized according to the methods employed.

Graph-coloring-based algorithms are widely used to prevent conflicts through structures in which nodes and edges correspond to time slots. Rina I. proposed a solution using the Welch-Powell algorithm, treating each course as a node and assigning the same time slot to nodes with the same color. This method yielded effective results for basic scheduling problems due to its simplicity[4]. A resource scheduling algorithm proposed by Egwuneche successfully scheduled tasks without resource conflicts based on graph coloring[5]. Bania and Duarah developed an examination scheduling model using graph coloring with institutional data and achieved satisfactory results under both hard and soft constraints[6]. Mursyidah (2019) discussed the application of graph coloring to schedule courses effectively and efficiently based on student needs and available spaces at the Department of Mathematics Education, University of Muhammadiyah Surabaya[7]. In their study, the authors used graph coloring to solve the CSP by dividing the data into three sets: time slots, classrooms, and the courses assigned to lecturers[8]. Mishkhal I. and colleagues attempted to solve CSP using a graph coloring approach implemented in the JEdit programming language[9].

These methods aim to scan the solution space more rapidly and manage complex constraints more effectively. Han and Wang developed a hybrid method, POGA-DP, which combines genetic algorithms and dynamic programming for university course timetabling. This method significantly improves scheduling quality, especially in cases where multiple classes attend a single course, and ensures more efficient classroom usage. Tests on real datasets demonstrated substantial performance improvements compared to traditional methods[10]. Budiarto applied genetic algorithms (GA) to school-level CSP. In a study conducted at SMPK Santo Yoseph School in Bali, the difficulties of manual scheduling were highlighted, and a fitness value of 0.0880 was achieved after 100 generations. This method reduced the number of daily classes from seven to four or five, resulting in a more balanced and efficient schedule[11]. Rahardjo and Zulkifli successfully created conflict-free course schedules by integrating dynamic matching with Vertex Graph Coloring, one of the most effective methods for CSP[12]. Burke and his colleagues applied heuristic variants of graph coloring methods in curriculum-based course scheduling problems, modeling constraint sets in the classroom-time-teacher triangle[13].

Mathematical programming-based approaches are often preferred in scheduling problems where precision and optimality are required. E. Rappos and colleagues developed a Mixed Integer Programming (MIP) model to solve the university timetabling problem. The model simultaneously optimizes student, classroom, and time assignments, addressing both student conflicts and classroom usage constraints. Due to the large size of the model, a two-phase solution was proposed: first, a feasible initial solution is obtained, followed by refinement using a local search algorithm. The model yielded strong results when tested on ITC 2019 competition datasets[14]. Steiner and his team used a three-stage modeling process and integer programming to reduce conflicts caused by complex structures such as double major selections at the University of Graz[15]. Subulan argued that timetables should not only balance scheduling but also aim for skill development. The model developed for this purpose was solved using multi-objective mathematical programming and produced promising results[16]. In another study, the authors successfully applied linear programming—an effective method for addressing CSP—to prepare class

schedules at the Sirindhorn International Institute of Technology[17].

Due to the increasing volume and complexity of data, hybrid solutions combining multiple methods have become more prevalent. Gunawan A. developed a hybrid algorithm to solve faculty assignment and course scheduling problems simultaneously. By combining integer programming, greedy heuristics, and a modified simulated annealing method, this approach delivered effective results even on large datasets. The method was tested on data from a university in Indonesia[18]. The authors proposed a two-phase hybrid algorithm combining exact and heuristic methods for university course scheduling. In the first phase, courses were clustered using graph coloring; in the second phase, a tabu search algorithm assigned these clusters to time slots. The model also incorporated additional constraints based on teacher and student preferences to generate realistic schedules[1].

In another study, the authors utilized a hybrid method combining graph coloring methodology and heuristic techniques to solve curriculum-based CSP[19]. Fizzano and Swanson developed an algorithm that assigns only one student group per class at a specific time and day, optimizing the allocation of student groups to classrooms based on this constraint[20].

In this study, a novel algorithm based on the graph coloring approach—Malatya Vertex Coloring (MVC) Algorithm—is proposed to solve the CSP. Unlike many widely used methods in the literature, this algorithm prioritizes the most critical nodes by calculating their Malatya Centrality (MC) values. As a result, course conflicts are minimized, and more efficient timetables are produced using fewer time slots. Furthermore, the algorithm enables the easy integration of additional constraints such as instructor availability, increasing its applicability in highly constrained environments. Test results on real-world datasets demonstrate that the algorithm provides an effective solution in terms of both accuracy and scheduling quality.

3. PROPOSED METHOD

3.1. Problem Definition and Approach

The Course Scheduling Problem (CSP) is a classical and computationally complex scheduling problem commonly encountered in universities and educational institutions. The CSP requires the allocation of courses, instructors, classrooms, and students to appropriate time slots while satisfying a variety of constraints. Due to its broad applicability across different academic domains, the CSP has led to the development of numerous algorithms and solution strategies in the literature. With the advancement of computer science and optimization techniques, increasingly effective and efficient algorithms have been proposed to solve CSPs. Notably, the CSP shares considerable similarities with the Examination Timetabling Problem (ETP). Although some constraints differ between the two, many of the solution approaches are similar, which has led several academic studies to treat them within a unified framework.

In this study, the Malatya Vertex Coloring (MVC) algorithm is applied to address the CSP. The MVC algorithm aims to achieve an optimal or near-optimal coloring of graph vertices, representing courses, in such a way that the number of required time slots is minimized. By efficiently assigning colors (i.e., time slots) to conflicting courses, the algorithm ensures a feasible and conflict-free timetable, ultimately enhancing the utilization of limited temporal resources.

3.2. Application of the MVC Algorithm to the Course Scheduling Problem

In this study, the Malatya Vertex Coloring (MVC) algorithm was employed to develop a solution for the university-level Course Scheduling Problem (CSP). MVC is a graph-theoretic approach that focuses on identifying the most influential vertex during the coloring process. For this purpose, a Malatya Centrality (MC) value is calculated for each vertex, and the vertex with the highest MC value is selected as the next candidate to be colored[21].

The MVC algorithm relies on the centrality values of vertices to determine their relative influence within the graph. The MC value of a vertex is defined as the sum of the ratios between the vertex's degree (i.e., the number of neighbors) and the degrees of its neighboring vertices[22]. This formulation prioritizes vertices that are highly connected but surrounded by relatively less connected neighbors. Consequently, such vertices are selected earlier in the coloring sequence.

The functioning of the MVC algorithm is illustrated through an example graph consisting of six vertices, each representing a course: "Programming," "Mathematics," "Data Structures," "Physics," "Database Systems," and "Discrete Mathematics." Edges between vertices indicate that the corresponding courses are taken by at least one common student, implying a scheduling conflict if assigned to the same time slot. In other words, the existence of an edge between two courses signifies a hard constraint that they must not be scheduled simultaneously.

The resulting graph structure, as shown in Figure 1, models the CSP as a graph coloring problem, where the goal is to assign time slots (colors) to each course (vertex) such that no adjacent courses share the same slot.

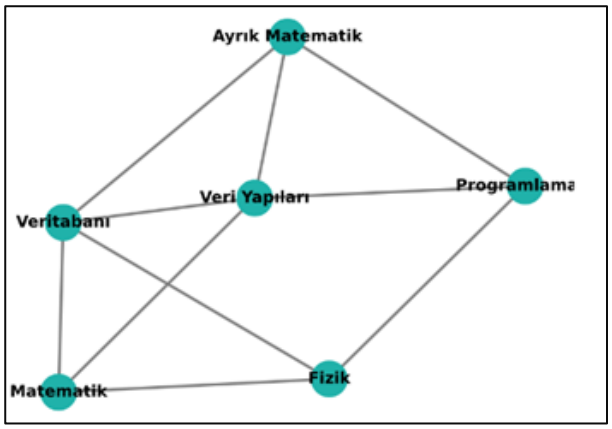

Figure 1. Graph model of a sample course schedule

In order to illustrate how the MC value, which lies at the core of the MVC algorithm, is calculated, the Data Structures course from the sample course graph has been selected. The degree of each node represents the number of edges (i.e., neighbors) it possesses. The degree values of the relevant nodes in the graph are as follows:

Deg(Discrete Mathematics) = 3
Deg(Database) = 4
Deg(Mathematics) = 3
Deg(Physics) = 3
Deg(Programming) = 4
Deg(Data Structures) = 4

$$MC(v_i) = \sum_{v_j \in N(v_i)} \frac{\text{degree}(v_i)}{\text{degree}(v_j)}$$

- v_i: The node for which the MC value is calculated
- $N(v_i)$: The set of neighbors of node v_i
- deg(v): The degree of node v (i.e., the number of edges)

When examining the neighbors of the Data Structures course, it is observed that it is directly connected to the courses Programming, Discrete Mathematics, Mathematics, and Database. Therefore, the MC value of the Data Structures node is calculated by taking the sum of the ratios of its degree (i.e., number of edges) to the degree values of its neighboring nodes.

$$MC(\text{Data Structures}) = \sum (\frac{4}{3} + \frac{4}{3} + \frac{4}{3} + \frac{4}{4})$$
$$MC(\text{Data Structures}) = 1,\overline{3} + 1,\overline{3} + 1,\overline{3} + 1$$
$$MC(\text{Data Structures}) = 5$$

This calculation indicates that the Data Structures node is highly connected, while some of its neighbors exhibit relatively lower connectivity. As a result, within the MVC algorithm, the Data Structures node is prioritized among those to be colored first.

To implement the MVC algorithm, a duplicate of the original graph is initially created. This duplicate graph serves to retain the information of the removed nodes and facilitates comparison with the colors of adjacent nodes during the coloring process. In contrast, the original graph is used for computing MC values and removing nodes as the algorithm progresses.

The procedure begins with the computation of MC values for all nodes in the graph. After these values are calculated, the node with the highest MC value, representing the most influential node, is identified. The colors already assigned to its adjacent nodes are then examined. Starting from the beginning of the color list, the first color that has not been used by any neighboring node is selected and assigned to the current node[23]. If the selected color is already present in a neighboring node, the next color in the list is considered and the same verification is performed. Once a color distinct from all neighboring nodes is found, it is assigned to the selected node. Following the color assignment, the node is removed from the original graph.

Subsequently, the MC values of the remaining nodes are recalculated. The node with the newly highest MC value is then identified and the same color assignment process is repeated. This node is also removed from the graph and the algorithm continues iteratively. This cycle is repeated until all nodes have been colored. By the end of the process, all nodes in the duplicate graph will have been successfully colored with valid assignments.

Algorithm 1. Pseudocode of the MVC Algorithm

```
MVC Algorithm
Input: Graph g = (V, E)
Output: Colored graph f
f ← Copy(g)
Function CentralityCalculate(g):
 // Calculates MC value for each node and finds the one with the
//highest centrality.
    MaxCentrality ← 0
    For each vertex i in V(g):
        Centrality ← 0
        For each neighbor j in Neighbors(i):
            Centrality ← Centrality + Degree(i) / Degree(j)
        If Centrality > MaxCentrality:
            MaxCentrality ← Centrality
            MaxVertex ← i
    Return MaxVertex
// Return the vertex with the highest MC value.

While VertexCount(g) > 0:
 // Repeat until all vertices are removed (colored).
    vertex ← CentralityCalculate(g)
    For each color c in ColorList:   // Iterate over the list of colors.
        If c not in Colors of Neighbors(vertex) in f:
            Assign color c to vertex in f
            Break
    Delete vertex from // Remove the colored vertex from the graph.

Show(f)
```

The detailed steps and control structure of the MVC algorithm are presented with the help of the pseudocode shown in Algorithm 1. The algorithm consists of two fundamental components: the CentralityCalculate function and the main body. The CentralityCalculate function is responsible for calculating the MC values of all nodes in the graph and for selecting the most influential node. In the main body, a copy of the original graph is first created. In each iteration, the most influential node is determined and assigned a color. During the coloring process, it is checked whether there is any conflict with the colors of adjacent nodes. These control operations are

carried out using the copy graph. Once the color is assigned, the node is removed from the original graph. The original graph plays an active role in the removal of nodes and the recalculation of MC values, whereas the copy graph is used solely for tracking color assignments. The coloring process continues until there is only one start to finish, including MC computation, color comparison, color assignment, and node removal from the graph. Additionally, a small sample graph with calculated MC values and step-by-step illustrations of the coloring process will support the reader in better understanding how the algorithm functions.

The primary constraints encountered in solving course timetabling problems are that a student cannot attend multiple classes at the same time and that each course must be offered only once per week. These constraints

node left in the original graph. Once all nodes have been colored, the process ends, and the nodes in the copy graph are left with valid color assignments. To visualize the effectiveness and procedural operation of the MVC algorithm, it is recommended to include a flowchart. This diagram should clearly represent the entire process from

significantly increase the complexity of the timetabling problem.

In this study, the MVC algorithm was employed to address these challenges. During the implementation of the algorithm, each course was modeled as a node, and edges were established between courses taken by the same student, thereby forming a graph structure as illustrated in Figure 2. Through the coloring process applied to this graph structure, time conflicts between courses were effectively avoided[24].

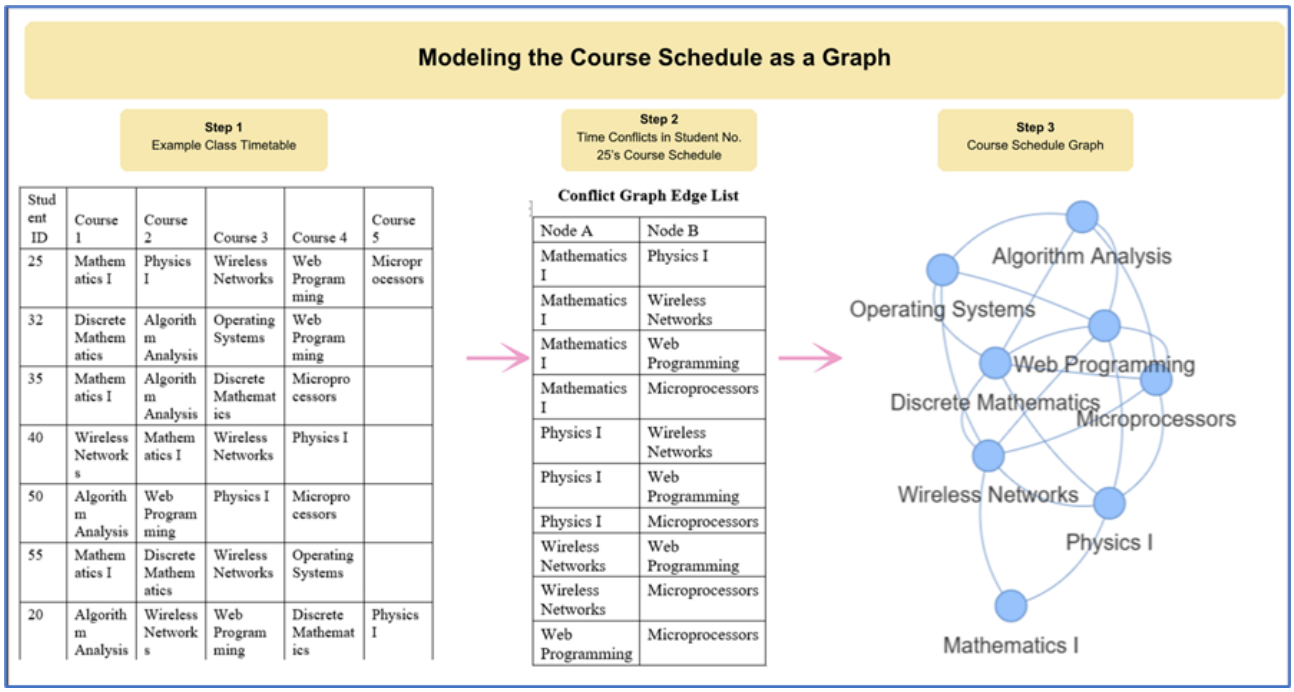

Student ID	Course 1	Course 2	Course 3	Course 4	Course 5
25	Mathematics I	Physics I	Wireless Networks	Web Programming	Microprocessors
32	Discrete Mathematics	Algorithm Analysis	Operating Systems	Web Programming	
35	Mathematics I	Algorithm Analysis	Discrete Mathematics	Microprocessors	
40	Wireless Networks	Mathematics I	Wireless Networks	Physics I	
50	Algorithm Analysis	Web Programming	Physics I	Microprocessors	
55	Mathematics I	Discrete Mathematics	Wireless Networks	Operating Systems	
20	Algorithm Analysis	Wireless Networks	Web Programming	Discrete Mathematics	Physics I

Node A	Node B
Mathematics I	Physics I
Mathematics I	Wireless Networks
Mathematics I	Web Programming
Mathematics I	Microprocessors
Physics I	Wireless Networks
Physics I	Web Programming
Physics I	Microprocessors
Wireless Networks	Web Programming
Wireless Networks	Microprocessors
Web Programming	Microprocessors

Figure 2. Graph-Based Modeling Process of the Course Timetabling Problem

The course timetable datasets used in this study were obtained from the UNITIME.org platform, specifically the Computer Science Department Spring: [pu-spr07-cs] and Fall: [pu-fal07-cs] datasets[25]. In these datasets,

each course is represented as a node, and edges are created between courses taken by the same student, resulting in a relational graph-based structure.

Table 1. Courses Taken by Students

Student No	Lesson 1	Lesson 2	Lesson 3	Lesson 4	Lesson 5
25	Mathematics 1	Physics 1	Wireless Networks	Web Programming	Microprocessors
32	Discrete Mathematics	Algorithm Analysis	Operating Systems	Web Programming	
35	Mathematics 1	Algorithm Analysis	Discrete Mathematics	Microprocessors	
40	Wireless Networks	Mathematics 1	Wireless Networks	Physics 1	
50	Algorithm Analysis	Web Programming	Physics 1	Microprocessors	
55	Mathematics 1	Discrete Mathematics	Wireless Networks	Operating Systems	
20	Algorithm Analysis	Wireless Networks	Web Programming	Discrete Mathematics	Physics 1

The MVC algorithm was applied to a graph structure representing student-course relationships, assigning different colors to potentially conflicting courses. This approach prevented students from being scheduled for multiple classes at the same time. Moreover, by employing a node selection strategy based on MC values, the algorithm effectively grouped interconnected courses into a minimal number of sets. As a result, the timetabling process was optimized by utilizing fewer time slots[21].

Table 2. List Made for the Graph Structure of the Courses Taken by Student No. 25

Edges	
Node	**Node**
Mathematics 1	Physics 1
Mathematics 1	Wireless Networks
Mathematics 1	Web Programming
Mathematics 1	Microprocessors
Physics 1	Wireless Networks
Physics 1	Web
Physics 1	Microprocessors
Wireless Networks	Web Programming
Wireless Networks	Microprocessors
Web Programming	Microprocessors

The primary constraints to be considered in the Course Scheduling Problem (CSP) are as follows:

- Courses taken by the same student must not be scheduled in the same time slot.
- Each course must be offered only once per week.

In accordance with these constraints, the MVC algorithm was implemented by modeling each course as a node (vertex), and establishing edges between courses taken by the same student so that these courses are treated as adjacent nodes. Table 2 illustrates the transformation of the course list of Student 25 into a graph structure. All possible pairwise combinations among this student's courses were generated to form the edge list. This process was repeated for all students to create a comprehensive list of course relationships, which was then used to construct a graph model. The MVC algorithm was applied to this graph. In the graph structure, nodes (courses) sharing the same color do not have a direct connection (edge), meaning that these courses can be scheduled in the same time slot. Conversely, differently colored courses are directly connected, indicating that they are taken by the same student and therefore must be scheduled in separate time slots to avoid conflicts. As such, minimizing the number of required time slots depends on reducing the number of colors used. The MVC algorithm provides efficient results in this context. The student-course data presented in Table 1 was converted into pairwise relationships as shown in Table 2 and then imported into the system. The data was first transformed into a graph structure, and subsequently, the MVC algorithm was applied to this graph. In each step of the algorithm, the MC values of all nodes were calculated as shown in Table 3. Based on these calculations, the iteration process proceeded as follows:

In the first iteration, the course "Wireless Networks", having the highest MC value, was assigned the first color in the list (e.g., green) and then removed from the graph. In the second iteration, the course with the highest updated MC value was "Physics 1" (MC = 6.6). Since its neighbor "Wireless Networks" had been assigned green, the next available color, purple, was assigned to "Physics 1." In the third iteration, three nodes shared the highest MC value, so the one that appeared earlier in the system, "Web Programming", was selected. Its neighbors had green (Wireless Networks) and purple (Physics 1) colors, so the next available color, blue, was assigned. In the fourth iteration, since green had not been used among the neighbors of "Algorithm Analysis", this course was assigned green. In the fifth iteration, "Discrete Mathematics" had neighbors with green, purple, and blue, thus the next suitable color, turquoise, was assigned. In the sixth iteration, the neighbors of "Microprocessors" had green, purple, blue, and turquoise, so the next available color, light green, was chosen. In the seventh iteration, "Operating Systems" had neighbors colored green, blue, and turquoise. Since purple had not been used among its neighbors, it was assigned purple. Finally, in the eighth iteration, "Mathematics 1" had neighbors with green and purple; thus, blue was assigned as the next available color. With this step, the coloring process was completed, and all nodes were removed from the graph. As a result of executing the MVC algorithm, a total of five distinct colors were used, indicating that at least five time slots are needed for scheduling. Once these time slots are created, courses with the same color are scheduled in the same slot, while courses with different colors are assigned to different time periods.

Table 3. MC Values in Each Iteration

.	Mathematics 1	Discrete Mathematics	Algorithm Analysis	Web Programming	Physics 1	Wireless Networks	Micro processors	Operating Systems
1st Iteration	0.73	7.4	3.13	7.4	6.0	8.9	4.75	2.9
2nd Iteration	0.25	6.4	3.9	6.4	6.6		3.59	1.95
3rd Iteration	0	4.6	4.6	4.6			2.25	2.25
4th Iteration	0	4.0	4.0				1.3	1.3
5th Iteration	0	4.0					0.5	0.5
6th Iteration	0						0	0
7th Iteration	0							0
8th Iteration	0							

In solving the CSP, the MVC algorithm prioritizes the coloring of the region with the highest MC value at each step. The coloring process of the map following each execution step is visualized through the stages presented in Figure 3.

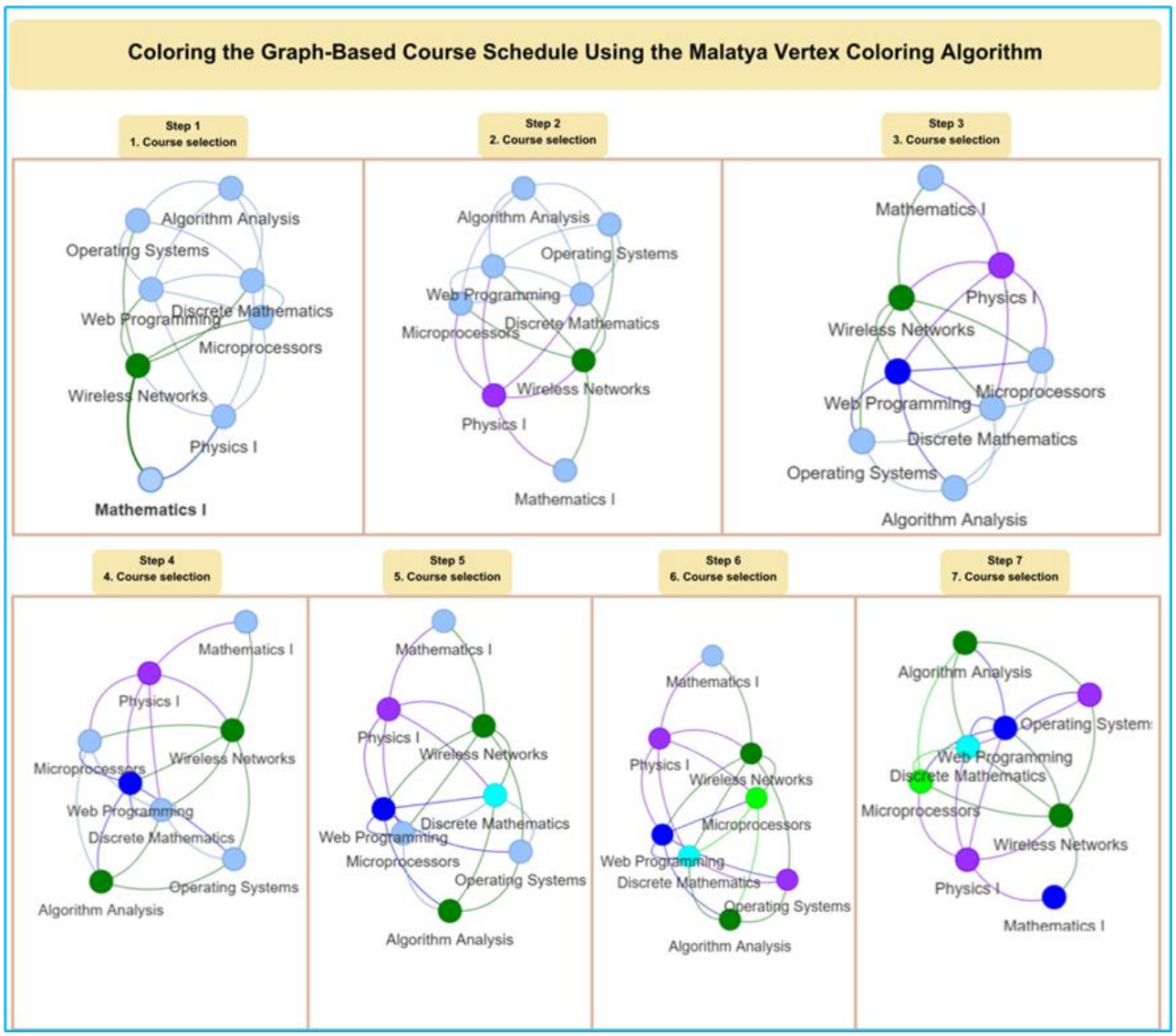

Figure 3. Color Assignment Process According to the Steps of the MVC Algorithm

This figure illustrates, step by step, which node is selected and which color is assigned in each iteration of the MVC algorithm. Starting from the top-left and proceeding to the bottom-right, the sequential stages clearly demonstrate the node selection logic based on centrality (MC) values and the corresponding color assignment process. This procedure effectively avoids color conflicts and ensures minimal color usage.

4. EXPERİMENTAL RESULTS

In this study, the "[pu-fal07-cs]" dataset, which belongs to the Computer Science Department of the University of Purdue and is publicly available on the Unitime.org platform, was utilized. Based on this dataset, a graph structure representing student conflicts between courses was constructed. The resulting graph consists of 466 nodes (courses) and 3,819 edges (student overlaps between courses). The MVC algorithm was applied to this large-scale graph structure, resulting in a coloring with 12 distinct colors. Since nodes with the same color are not adjacent to each other, these courses can be scheduled in the same time slot but in different classrooms. Conversely, courses with different colors are directly connected, indicating that they must be scheduled in separate time slots. As shown in Figure 4, the MVC algorithm enabled the scheduling of all 466 courses using only 12 time slots for this dataset. Additionally, four other commonly used graph coloring algorithms from the literature—DSATUR, Welsh–Powell, RLF, and Greedy—were also applied to the same dataset. As presented in Table 4, the MVC, DSATUR, Welsh–Powell, and Greedy algorithms all produced solutions using 12 colors, whereas only the RLF algorithm required 13 colors.

Table 4. Comparison of the Number of Colors Used by Different Algorithms in the Fall Semester Course Schedule of the Computer Science Department

Algorithm	Number of Colors Used
MVC (Malatya Vertex Coloring)	12
DSATUR (Degree of Saturation Order)	12
Welsh–Powell	12
RLF (Recursive Largest First)	13
Greedy (Rastgele sıra ile)	12

These results demonstrate that the MVC algorithm performs comparably to, or even better than, traditional algorithms, offering an effective approach to the timetabling process.

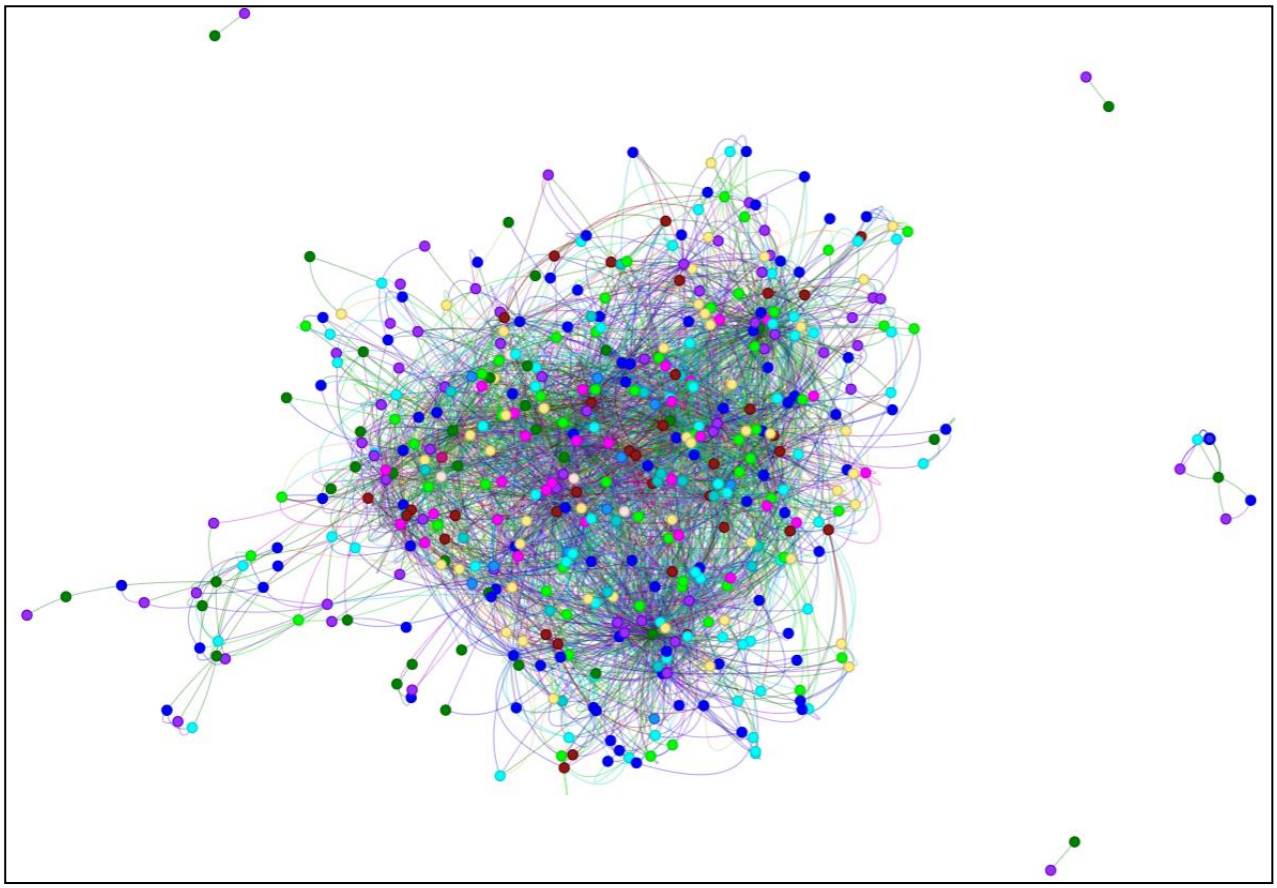

Figure 4. Computer science department fall term coloring

In the second phase of the study, the spring semester course scheduling dataset, labeled "[pu-spr07-cs]" and obtained from the Unitime.org platform, was utilized. In this dataset, each course is modeled as a vertex, and an edge is established between courses that are taken by the same student. As a result, a graph structure consisting of 884 vertices and 9,190 edges was constructed, based on 884 courses and 725 students. The MVC algorithm was applied to this large-scale graph, and a successful coloring was achieved using 14 distinct colors. Each color represents a separate time slot. Since there are no direct connections between vertices with the same color, these courses can be scheduled within the same time period. As illustrated in Figure 5, the MVC algorithm enabled a conflict-free scheduling of all courses in this dataset using only 14 time slots. The aforementioned dataset was also tested with other algorithms, and the corresponding results are presented in Table 5.

Table 5. Comparison of the Number of Colors Used by Different Algorithms in the Spring Semester Course Schedule of the Computer Science Department

Algorithm	Number of Colors Used
MVC (Malatya Vertex Coloring)	14
DSATUR (Degree of Saturation Order)	14
Welsh–Powell	13
RLF (Recursive Largest First)	16
Greedy (Rastgele sıra ile)	13

These comparisons demonstrate that the MVC algorithm yields results equivalent to those of traditional algorithms and can be effectively applied, particularly to large-scale datasets.

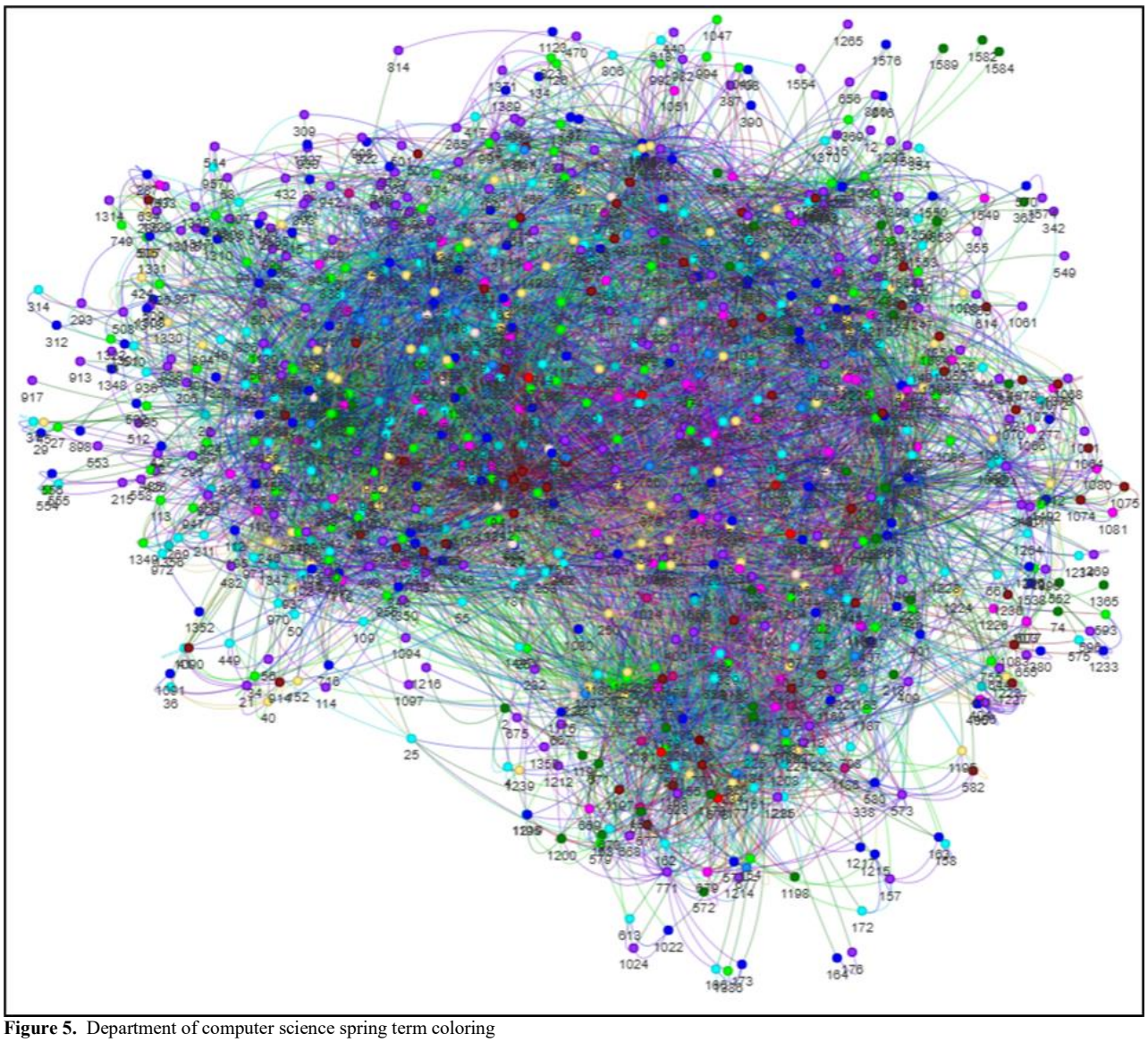

Figure 5. Department of computer science spring term coloring

4. CONCLUSION

This study addresses the complex and frequently encountered Course Scheduling Problem (CSP) in universities by employing a novel graph-based approach, the Malatya Vertex Coloring (MVC) algorithm. The MVC algorithm is designed to minimize conflicts between courses based on their centrality (MC) values. Its core principle is to prioritize the coloring of the most influential (central) nodes, thereby aiming to solve the scheduling problem using the minimum number of colors (i.e., time slots). Experimental applications on real-world datasets demonstrate the effectiveness of the MVC algorithm. Using two distinct semester datasets (Fall and Spring) from the Computer Science Department of Purdue University, the algorithm successfully generated conflict-free schedules with only 12 and 14 colors, respectively. These results indicate that even in large-scale systems involving hundreds of courses and thousands of students, conflict-free scheduling can be achieved with as few as 12–14 time slots. Furthermore, comparative analyses reveal that the MVC algorithm performs comparably to, or better than, traditional algorithms such as DSATUR, Welsh–Powell, Greedy, and RLF. The success of the MVC algorithm lies in its node selection strategy based on MC values. These values measure a node's relative impact within the graph, allowing for the prioritization of the most critical courses during the scheduling process. This mechanism not only optimizes time slot usage but also facilitates the integration of other scheduling actors, such as instructors, into the same framework. In fact, instructors' courses can be modeled in a similar way to students within the graph structure, enabling conflict-free scheduling within a unified algorithmic framework.

In addition, the operational steps of the algorithm were illustrated in detail through examples and visualizations. The clear definition of stages such as MC value calculation, usage of a duplicate graph, and color control mechanisms contributes to both the theoretical strength and practical applicability of the algorithm.

The advantages offered by the MVC algorithm can be summarized as follows:

- Ability to function under complex constraints,

- Conflict-free scheduling with a minimal number of time slots,
- Flexibility to model both student and instructor data within a single structure,
- Applicability to large datasets due to its polynomial-time execution.

In conclusion, the MVC algorithm offers a robust alternative to conventional and heuristic methods for solving CSPs. Its simplicity, predictability, and efficiency in practice suggest that this approach has strong potential for widespread application in educational institutions' scheduling systems.

Future research may focus on extending the algorithm to incorporate additional constraints (e.g., classroom capacities, course priorities, student preferences), performing multi-objective optimization with data from various departments, and testing the algorithm in real-time scheduling environments. Moreover, combining the algorithm with parallel computing techniques could significantly improve its performance on larger-scale problems.

REFERENCES

[1] Xiang, K., Hu, X., Yu, M., & Wang, X. (2024). Exact and heuristic methods for a university course scheduling problem. Expert Systems with Applications, 248. https://doi.org/10.1016/j.eswa.2024.123383.

[2] Zhaohui, F., 2000, A. L.-T. with A. Intelligence. I., & 2000, undefined. (n.d.). Heuristics for the exam scheduling problem. Ieeexplore.Ieee.OrgF Zhaohui, A LimProceedings 12th IEEE Internationals Conference on Tools with, 2000•ieeexplore.Ieee.Org. Retrieved October 21, 2024, from https://ieeexplore.ieee.org/abstract/document/889864/

[3] Pillay, N., & Banzhaf, W. (2007). A genetic programming approach to the generation of hyper-heuristics for the uncapacitated examination timetabling problem. Lecture Notes in Computer Science (Including Subseries Lecture Notes in Artificial Intelligence and Lecture Notes in Bioinformatics), 4874 LNAI, 223–234. https://doi.org/10.1007/978-3-540-77002-2_19.

[4] Rina, I., Sulistiowati, D., & Raudhatuloktavi, D. (2022). Graph Coloring Applications in Scheduling Courses using Welch-Powell Algorithm - A Case Study. Proceeding - 2022 International Symposium on Information Technology and Digital Innovation: Technology Innovation During Pandemic, ISITDI 2022, 131–135. https://doi.org/10.1109/ISITDI55734.2022.9944511

[5] Egwuche, O. S. (2020, March 1). Examination Timetabling with Graph Coloring for Emerging Institutions. 2020 International Conference in Mathematics, Computer Engineering and Computer Science, ICMCECS 2020. https://doi.org/10.1109/ICMCECS47690.2020.246988

[6] Bania, R. K., & Duarah, P. (2018). Exam Time Table Scheduling using Graph Coloring Approach. International Journal of Computer Sciences and Engineering, 6(5), 84–93. https://doi.org/10.26438/ijcse/v6i5.8493

[7] Mursyidah, H. (2019). Graph edges coloring to determine lecture classroom of mathematics education department at muhammadiyah university of surabaya. Journal of Physics: Conference Series, 1188(1). https://doi.org/10.1088/1742-6596/1188/1/012096

[8] Lampung, U. B., Kesuma, R., #2, W., & Yusman, M. (n.d.). The Use of Edge Coloring Concept for Solving The Time Schedule Problem at Senior High School (Case Study at SMAN 9 Bandarlampung).

[9] 2019 1st AL-Noor International Conference for Science and Technology (NICST). (2019). IEEE.

[10] Han, X., & Wang, D. (2025). Gradual Optimization of University Course Scheduling Problem Using Genetic Algorithm and Dynamic Programming. Algorithms, 18(3). https://doi.org/10.3390/a18030158

[11] Budiarto, A. S., Satvika Iswari, N. M., & Dharma, E. M. (2024). Application of Genetic Algorithm for School Timetable Scheduling. 2024 International Conference on Informatics Electrical and Electronics, ICIEE 2024 - Proceedings. https://doi.org/10.1109/ICIEE63403.2024.10920446

[12] Rahardjo, E. Tjipto., & Zulkifli, F. Yuli. (2013). 2013 International Conference on QiR (Quality in Research). Faculty of Engineering, Universitas Indonesia.

[13] Burke, E. K., McCollum, B., Meisels, A., Petrovic, S., & Qu, R. (2007). A graph-based hyper-heuristic for educational timetabling problems. European Journal of Operational Research, 176(1), 177–192. https://doi.org/10.1016/j.ejor.2005.08.012

[14] Rappos, E., Thiémard, E., Robert, S., & Hêche, J. F. (2022). A mixed-integer programming approach for solving university course timetabling problems. Journal of Scheduling, 25(4), 391–404. https://doi.org/10.1007/s10951-021-00715-5

[15] Steiner, E., Pferschy, U., & Schaerf, A. (2024). Curriculum-based university course timetabling considering individual course of studies. Central European Journal of Operations Research. https://doi.org/10.1007/s10100-024-00923-2

[16] Subulan, K. (2024). A multi-objective mathematical programming model for a novel capability-based university course timetabling problem. Journal of the Faculty of Engineering and Architecture of Gazi University, 40(1), 365–379. https://doi.org/10.17341/gazimmfd.1391236

[17] Nakasuwan, J., Asia, P. S.-S. & T., & 1999, undefined. (n.d.). Class scheduling optimization. Thaiscience.Info. Retrieved January 28, 2025, from https://www.thaiscience.info/Journals/Article/TSTJ/10480612.pdf

[18] Gunawan, A., Leng, K., Gunawan, A. ;, Ng, M. ;, & Poh, K. L. (2007). Solving the teacher assignment-

course scheduling problem by a Solving the teacher assignment-course scheduling problem by a hybrid Algorithm hybrid Algorithm Kien Ming NG Citation Citation Solving the teacher assignment-course scheduling problem by a hybrid Algorithm. In International Journal of Computer, Information, and Systems Science, and Engineering (Vol. 1, Issue 2). https://ink.library.smu.edu.sg/sis_research

[19] Computers & Informatics (ISCI), 2013 IEEE Symposium on. (2013). Institute of Electrical and Electronics Engineers.

[20] Fizzano, P., & Swanson, S. (2000). Scheduling Classes on a College Campus. In Computational Optimization and Applications (Vol. 16).

[21] Özavci, A., & Yakut1, S. (n.d.). Based on Malatya Centrality Algorithm Development of Suggestion System in Social Platforms and Commercial Applications.

[22] Karci, A., Yakut, S., & Öztemiz, F. (2022). A New Approach Based on Centrality Value in Solving the Minimum Vertex Cover Problem: Malatya Centrality Algorithm. Computer Science. https://doi.org/10.53070/bbd.1195501

[23] Yakut, S., Öztemiz, F., & Karci, A. (2023). A new robust approach to solve minimum vertex cover problem: Malatya vertex-cover algorithm. Journal of Supercomputing, 79(17), 19746–19769. https://doi.org/10.1007/s11227-023-05397-8

[24] YAKUT, S., & BAKAN, C. T. (2023). Development of Text Summarization Method based on Graph Theory and Malatya Centrality Algorithm. Computer Science. https://doi.org/10.53070/bbd.1350971

[25] UniTime | University Course Timetabling Benchmark Benchmark Datasets. (n.d.). Retrieved January 28, 2025, from https://www.unitime.org/uct_datasets.php

Volume 14, Issue 3, Page 57-66, 2025 https://doi.org/10.46810/tdfd.1711814 Research Article

BİNGÖL UNIVERSITY

Türk Doğa ve Fen Dergisi
Turkish Journal of Nature and Science
www.dergipark.gov.tr/tdfd

Performance Evaluation of a Nature-Inspired Three-Particle Swarm Optimization Algorithm in PV Systems with a Modified SEPIC Converter

Muhammed MAHHO[1], Mehmet YILMAZ[1], M. Fatih ÇORAPSIZ[1*]

[1] Ataturk University, Engineering Faculty, Electrical-Electronics Engineering, Erzurum, Türkiye
Muhammed MAHHO ORCID No: 0009-0005-0938-7031
Mehmet YILMAZ ORCID No: 0000-0001-7624-4245
M. Fatih ÇORAPSIZ ORCID No: 0000-0001-5692-8367

**Corresponding author: corapsiz@atauni.edu.tr*

(Received: 11.06.2025, Accepted: 14.07.2025, Online Publication: 26.09.2025)

Keywords
Maximum power point tracking,
Modified SEPIC converter,
Deterministic particle swarm optimization,
Enhance autonomous group particle swarm optimization

Abstract: The increase in world population, the development of industrialization and people's use of more advanced technologies increase energy demands day by day. People have started to turn to alternative energy sources to avoid the energy crisis that will occur when existing energy sources are exhausted. Photovoltaic (PV) systems are an advantageous option among sustainable energy sources. PV systems are affected by irradiance intensity and temperature. To overcome this problem, Maximum power point tracking (MPPT) algorithms are used. In this study, in order to maximize the efficiency of PV systems, the performance of Particle swarm optimization (PSO), Deterministic Particle swarm optimization (DPSO), Enhance Autonomous Group Particle swarm optimization (EAGPSO) algorithms were evaluated by using a high gain modified SEPIC converter. PSO, DPSO and EAGPSO algorithms were evaluated for three different scenarios under normal irradiance and partial shading conditions. When the results of the first scenario are compared, the EAGPSO algorithm performed MPPT in 0.27s. In the second scenario, the EAGPSO algorithm provided the highest power value with 553.86W. For the third partial shading scenario, the EAGPSO algorithm became the optimization algorithm with the highest efficiency with an efficiency value of 98.91%. It was observed that the EAGPSO algorithm had the fastest convergence time and the highest MPPT efficiency compared to the PSO and DPSO algorithms in all time periods under dynamically changing conditions. When all scenarios are considered, it has been observed that the EAGPSO algorithm has the highest MPPT efficiency of 98.9% and a convergence time of 0.31s for different scenarios. In addition, it has been found that the power oscillation of the EAGPSO algorithm is reduced by approximately half compared to DPSO and by approximately two thirds compared to PSO.

Doğadan Esinlenen Üç Parçacıklı Sürü Optimizasyon Algoritmasının Değiştirilmiş SEPIC Dönüştürücülü PV Sistemlerindeki Performans Değerlendirmesi

Anahtar Kelimeler
Maksimum güç noktasi takibi,
Değiştirilmiş SEPIC dönüştürücü,
Deterministik parçacik sürüsü optimizasyonu,
Geliştirilmiş otonom grup parçacik sürüsü optimizasyonu

Öz: Dünya nüfusunun artması, sanayileşmenin gelişmesi ve insanların daha ileri teknolojileri kullanması enerji taleplerini her geçen gün artırmaktadır. İnsanlar mevcut enerji kaynakları tükendiğinde ortaya çıkacak enerji krizinden kaçınmak için alternatif enerji kaynaklarına yönelmeye başlamıştır. Fotovoltaik (PV) sistemler sürdürülebilir enerji kaynakları arasında avantajlı bir seçenektir. PV sistemler ışınım şiddetinden ve sıcaklıktan etkilenmektedir. Bu sorunu aşmak için Maksimum güç noktası izleme (MPPT) tabanlı algoritmalar kullanılır. Bu çalışmada PV sistemlerin verimliliğini en üst düzeye çıkarmak için, yüksek kazançlı modifiye edilmiş SEPIC dönüştürücü kullanılarak Parçacık sürü optimizasyon (PSO), Deterministik Parçacık sürü optimizasyon (DPSO), Geliştirilmiş Otonom Grup Parçacık Sürü Optimizasyonu (EAGPSO) algoritmalarının performansı değerlendirilmiştir. PSO, DPSO ve EAGPSO algoritmaları normal ışınım ve kısmi gölgelenme koşulları altında üç farklı senaryo için değerlendirilmiştir. Birinci senaryonun

sonuçları karşılaştırıldığında EAGPSO algoritması 0.27s'de MPPT gerçekleştirmiştir. İkinci senaryoda en yüksek güç değerini 553.86W ile EAGPSO algoritması sağlamıştır. Üçüncü kısmi gölgelenme senaryosu için EAGPSO algoritması %98,91 verim değeri ile en yüksek verimliliğe sahip optimizasyon algoritması olmuştur. Dinamik değişen koşullarda tüm zaman dilimlerinde EAGPSO algoritması PSO ve DPSO algoritmalarına göre en hızlı yakınsama süresi ve en yüksek MPPT verimliliğine sahip olduğu gözlemlenmiştir. Tüm senaryolar göz önünde bulundurulduğunda, EAGPSO algoritması farklı durumlar için en yüksek %98,9 MPPT verimliliğine ve 0.37s yakınsama süresine sahip olduğu gözlemlenmiştir. Ayrıca EAGPSO algoritmasının güç salınımının DPSO'ya göre yaklaşık yarı yarıya, PSO'ya göre ise yaklaşık üçte iki oranında azaldığı elde edilmiştir.

1. INTRODUCTION

The increase in the world population increases the need for energy in parallel with the needs in various fields such as technology, production, lighting and transportation. In recent years, there has been a rapid increase in the use of renewable energy sources to meet energy needs [1]. Considering today's technologies, solar energy is one of the lowest-cost sources of electricity production. Photovoltaic (PV) systems, which produce electricity as long as there is light, have become more competitive than traditional energy sources in many geographies, especially with the significant decrease in panel costs in recent years. PV energy systems are an environmentally friendly energy source. PV systems stand out as an important source of sustainable energy production due to their lack of moving parts, low maintenance and operating costs, and easy installation [2, 3]. The main reasons that reduce the efficiency of PV systems are non-linear Power-Voltage (P-V) characteristics and partial shading conditions (PSC). PSC situations prevent the widespread use of PV systems [4]. PV systems consisting of more than one PV panel can have a serial, parallel or series-parallel connection structure according to the needs of the system to which they will be connected [5]. In changing weather conditions, panels receive different irradiance values and PSC occurs [6]. In the case of PSC, PV panels connected in series cause current mismatch, and PV panels connected in parallel cause voltage mismatch [7]. For these reasons, maximum power point tracking (MPPT) algorithms have been used in recent years to increase the efficiency of systems and reduce energy loss. The purpose of these algorithms is to follow the Maximum Power Point (MPP) of PV systems and reduce the energy loss of the system. In existing systems, traditional techniques such as hill climbing (HC) [8], Model predictive control (MPC) [9], incremental conductivity (IC) [10] are used. The MPPT efficiencies of these algorithms are quite high under equal irradiance conditions. However, these classical methods are insufficient in PSC situations and cause large power loss. Metaheuristic-based MPPT algorithms follow GMPP with higher efficiency without getting stuck at local maximum power points (LMPP) in the case of PSC [11]. Some metaheuristic optimization algorithms used for PV systems in the literature; Salp Swarm Optimization Algorithm (SSOA) [12], Arithmetic optimization (AO)[13], artificial bee colony (ABC) [14], Gray Wolf Optimization (GWO) [15], Antlion Optimization Algorithm (ALOA) [16], antlion optimizer (ALO) [17], Henry gas solubility optimization (HGSO) [18], Whale Optimization (WO) [19], Ant Colony Optimization (ACO) [20], Nelder-Mead Simplex Algorithm (NMSA) [21], Moth-Flame Optimization Algorithm(MFOA) [22], Grasshopper Optimization Algorithm (GHOA) [23], Flower Pollination Algorithm (FPA) [24]. The MPPT efficiency and convergence time of these methods, which have been shown to be quite successful in monitoring GMPP under PSC conditions, are affected by many various factors. Metaheuristic-based studies suggested in the literature in this field are given below;

Ref [25] proposed the Improved Gray Wolf BAT Optimization (IGWBO) algorithm to improve MPPT performance in floating photovoltaic (FPV) systems. IGWBO, a combination of GWO and BAT, provides fast and efficient results even in variable weather conditions. The proposed IGWBO algorithm provides more energy production (up to 27.28% increase), lower electricity cost (0.052 $/kWh) and environmental benefit (42.83 tons of CO_2 savings per year) compared to other algorithms. In the future, it is recommended to test the algorithm in real systems and improve it to require less computation [25].

Kumar et al. (2025) examined the integration of different MPPT algorithms (P&O, FLC, ANN) with bidirectional DC-DC converters and compared their performance. They emphasized that although the P&O algorithm has a simple calculation load, it is low efficient, FLC performs MPPT by managing uncertainties well, and ANN requires complex calculations although it offers high accuracy. FLC and ANN have achieved higher efficiency with bidirectional converters. In addition, according to experimental results, ANN followed MPP with the highest efficiency of 91.52%. The study provides recommendations for the development of MPPT algorithms and energy systems integration [26].

Yılmaz et al. proposed a new method for MPPT method in solar PV panels. The proposed method estimates the reference voltage in the MPP using the Gaussian process regression (GPR) method. Then, the PV system voltage was optimized using super twisting sliding mode controller (STSMC) controller. Performance tests were conducted in three different scenarios, including PSC situations. They observed that the proposed method is faster and more efficient than the traditional algorithms P&O algorithm and the metaheuristic algorithms CSA. They also stated that the proposed method provides low oscillation and high tracking performance [27].

In [28], a new MPPT algorithm based on a modified version of heterogeneous multi-swarm PSO algorithm using adaptive factor selection strategy (FMSPSO) is proposed to track MPP in PV systems faster and more stable. FMSPSO solves the instability, oscillation and slow convergence problems of classical PSO with multi-swarm structure and adaptive factor selection strategy. The developed FMSPSO provides high robustness and stability in rapidly changing weather conditions. In the simulations carried out in MATLAB/Simulink environment, the authors obtained the shortest settling time and efficiency from FMSPSO. It showed lower error rate, less oscillation and higher success rate compared to classical P&O, ANFIS and PSO algorithms. The results showed that FMSPSO algorithm is suitable for low cost and high efficiency MPPT applications [28].

Among metaheuristic-based MPPT algorithms, PSO algorithms are the ones that are easy to implement and have high convergence speed. These methods are widely used in MPPT. In this study, the performance of PSO, DPSO and EAGPSO algorithms was evaluated for PV systems using a modified SEPIC converter.

The main contributions of this article are as follows:

- Application of modified SEPIC converter in PV systems
- Novel Implementation of Different PSO Algorithms on a Modified SEPIC Converter for Photovoltaic Systems
- The use of the EAGPSO algorithm with a modified SEPIC converter improves MPPT efficiency in PV systems

Further sections of the paper are organized as follows: Section 2 in Materials and Methods contains a comprehensive overview of the modified SEPIC converter and PSO algorithms. Section 3 Results and Discussions contains simulation results for three different cases of MPPT algorithms under equal irradiance conditions and partial shading conditions. The conclusions of the study are presented in Chapter 4.

2. MATERIAL AND METHOD

2.1. Single diode PV cell model

PV cells are materials that convert solar energy into electrical energy. In order to model the electrical behavior of these cells, the single diode PV cell model is most frequently used in the literature. The single diode PV cell model is shown in Figure 1.

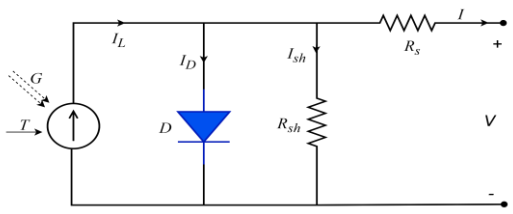

Figure 1. Single diode PV cell model

The mathematical expressions for the single diode PV cell model are given in Equation 1 [29].

$$\left.\begin{aligned} I &= I_L - I_D - I_{sh} \\ I_D &= I_0\left[exp\left(\frac{qV_d}{nkT_c}\right) - 1\right] \\ I_{sh} &= \frac{V + I\,R_s}{R_{sh}} \\ I &= I_L - I_0\left[exp\left(\frac{qV_d}{nkT_c}\right) - 1\right] - \frac{V + I\,R_s}{R_{sh}} \end{aligned}\right\} \quad (1)$$

In the Equation 1, "I" is the output current of the PV model, "I_0" is the leakage current, "q" is the electron charge, "k" is the Boltzmann constant, V_d is the voltage drop of the diode, "n" is the diode ideality factor, R_s is the series resistance, R_{sh} is the parallel resistance and T is the cell temperature.

2.2. DC-DC Modified SEPIC Converter (MSC) Topology

DC-DC converter topology is used to increase/decrease the voltage produced from PV systems depending on the load condition. In PV systems, boost converter topologies are often used to increase the voltage value to ensure efficient energy conversion. The duty cycles of these converter topologies are generally high. The modified SEPIC (MSC) converter generally has twice as much static gain as the boost converter. The modified SEPIC converter is obtained by reversing the polarity of capacitor C_1 in the classical SEPIC converter topology and adding a diode D_1 and an additional capacitor C_2. These converters play an important role in PV energy systems and high-efficiency power conversion applications. Figure 2 shows the modified SEPIC converter topology [30].

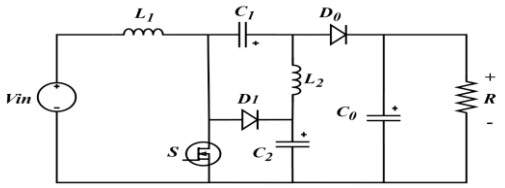

Figure 2. Modified SEPIC converter

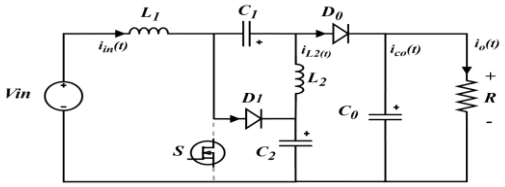

Figure 3. First operating mode of modified SEPIC Converters

The modified SEPIC converter has two different operating states. The operating mode of the converter is determined by the semiconductor switching element S= . When triggered with S=0, the switch is in cut-off state. In this case, the semiconductor switching element shows an open circuit feature. In the cut-off state of the semiconductor switching element D_1 ve D_2 diodes are in conduction. L_1 ve L_2 the energy they store D_1 ve D_2 sequentially through diodes C_2 ve C_0 transmits it to the

capacitors[31]. The state-space equations for this situation are given in Equation 2. The electrical equivalent circuit of the MSC converter for mode I is given in Figure 3.

$$\left.\begin{array}{c} \boldsymbol{V_{L1}(t) = V_{in} - V_{C2}} \\ \mathbf{V_{L2}(t) = -V_{c1}} \\ \mathbf{C_0 \dfrac{dV_0}{dt} = i_{C0} = i_{L2} - {V_o}/{R}} \end{array}\right\} \quad (2)$$

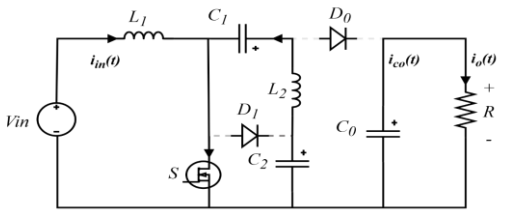

Figure 4. Second operating mode of modified SEPIC Converters.

When triggered with S=1, the switch is in on state. In this situation D_1 ve D_2 diodes are in cut-off state. In this mode, the inductor L_1 is energized from the source, while the capacitor C_2 transfers this energy to L_2. The state-space equations of the switching element's cut-off state are given in Equation 3. The electrical equivalent circuit of the MSC converter for mode II is given in Figure 4 [9].

$$\left.\begin{array}{c} \mathrm{V_{L1}(t) = V_{in}} \\ \mathrm{V_{L2}(t) = V_{c2} - V_{c1}} \\ \mathrm{C_0 \dfrac{dV_0}{dt} = i_{C0} = i_{L2} - {V_o}/{R}} \end{array}\right\} \quad (3)$$

Mathematical expressions of the electrical circuit parameters of the converter used in the study are given in Table 1.

Table 1. Modified SEPIC converter formulas

Parameters	Formulas
Switch Duty Cycle	$D=\frac{V_{out}-V_{in}}{V_{out}+V_{in}}$
Inductance	$L_1 = L_2 = \dfrac{V_{out}}{\Delta i_L f}$
Capacitors	$C_1 = C_2 = \dfrac{I_{out}}{\Delta V_c f}$
	$C_0 = \dfrac{D}{R\left(\frac{\Delta V_{out}}{V_{out}}\right) f}$ $\Delta V_c = \left(\frac{V_{in}}{1-D}\right) 0.1$
Load	R
Switching Frequency	f

2.3. An overview of PSO techniques

2.3.1. Particle Swarm Optimization (PSO)

The PSO algorithm was proposed by Kennedy and Eberhart in 1995, inspired by the behavior of swarming creatures in nature. It is a metaheuristic-based optimization method based on bird flock intelligence. In the PSO algorithm, there are two variables that define the particle position in continuous motion. These x_i position variable and v_i is the rate of change of the particle. With its simple structure and fast convergence, it is quite suitable for nonlinear discrete problems. For the PSO algorithm, the particle's rate of change and position update are calculated according to Equation 4 and Equation 5, respectively [32].

$$\mathrm{v_i^{k+1} = \omega \cdot v_i^k + a_1 * r_1 \cdot \left(P_{best} - x_i^k\right) + a_2 * r_2 \cdot \left(G_{best} - x_i^k\right)} \quad (4)$$

$$\mathrm{x_i^{k+1} = x_i^k + v_i^{k+1}} \quad (5)$$

In Equation 4 ω, coefficient of inertia, a_1 Cognitive coefficient P_{best} The best solution the particle has found so far is a_2 Social coefficient, r_1 ve r_2 random numbers are numbers in the range [0,1], G_{best} The best solution found among all particles. Particle position using PSO algorithm as MPPT controller x_i^k duty cycle D_i^k ve v_i particle's speed change D_i is replaced with. Thus, the new mathematical expression of the PSO algorithm as the MPPT algorithm can be rewritten according to Equation 6 and Equation 7 [32].

$$\mathrm{\Delta D_i^{k+1} = \omega \cdot \Delta D_i^k + a_1 * r_1 \cdot \left(D_{Pbest} - D_i^k\right) + a_2 * r_2 \cdot \left(D_{gbest} - D_i^k\right)} \quad (6)$$

$$\mathrm{D_i^{k+1} = D_i^k + \Delta D_i^{k+1}} \quad (7)$$

2.3.2. Deterministic Particle Swarm Optimization (DPSO)

The most important disadvantage of the PSO algorithm in MPPT applications is the adjustment of constant coefficients (ω, a_1 ve a_2). In order to eliminate this disadvantage, Deterministic Particle Swarm Optimization Algorithm (DPSO) has been proposed. In order for the power oscillation to be low during the update, the change in duty cycle must be low. The task cycle must be updated at a high rate to reach the final solution. However, high-speed updating may cause power oscillations around GMPP. This leads to LMPP instead of GMPP. The novelty of the DPSO algorithm, especially in the case of PSC, is that it eliminates random oscillation by limiting the velocity factor according to the distance between local and global peaks and removing acceleration coefficients. The speed and position update of the DPSO algorithm is given in Equation 8 and Equation 9 [33].

$$\boldsymbol{\Delta D_i^{k+1} = \omega \cdot \Delta D_i^k + \left[D_{Pbest} + D_{gbest} - 2D_i^k\right]} \quad (8)$$

$$\boldsymbol{D_i^{k+1} = D_i^k + \Delta D_i^{k+1}} \quad (9)$$

2.3.3. Enhance Autonomous Group Particle Swarm Optimization (EAGPSO)

The PSO algorithm is preferred for various applications due to its ease of use. Limitations of the PSO algorithm for different conditions in MPPT include the adjustment of acceleration coefficients to reduce power oscillations and convergence time, and the lack of ability to react quickly for different irradiance values. In PSO algorithm a_1 ve a_2 Coefficients play an important role in tuning particle behavior and speed. a_1 coefficient a_2 coefficient is relatively larger. Particles show high performance for local exploration within the search space. During global

search, usually a_2 coefficient a_1 becomes greater than the coefficient. When these coefficients are the same, particles search with the same behavior both within the search area and in the general search [11, 34]. EAGPSO performs velocity and position updates using Equation 10 and Equation 11 as the MPPT algorithm.

$$\Delta D_i^{k+1} = \frac{\pi}{2} arctan\left(\omega \cdot \Delta D_i^k + a_1 * r_1 \cdot (D_{Pbest} - D_i^k) + a_2 * r_2 \cdot (D_{gbest} - D_i^k)\right) \quad (10)$$

$$D_i^{k+1} = D_i^k + \Delta D_i^{k+1} \quad (11)$$

In the EAGPSO algorithm a_1 ve a_2 The values of the acceleration coefficients are limited to the [0, 2] range according to the equations in Table 2. For updates in the study, see Table 2. $K_{max} = 50, \alpha_{max} = 2, \alpha_{min} = 1$ was determined as. According to these determined values, the values of the acceleration coefficients throughout the iteration are shown in Figure 5. Figure 6 shows the flow diagram of the Enhance Autonomous Group PSO-based MPPT algorithm [11, 34].

Table 2. Update equations of acceleration coefficients for the EAGPSO algorithm

a_1 Updating values	a_2 Updating values
$\alpha_1^k = \alpha_{max} - (\alpha_{max} - \alpha_{min})\left(\frac{k^3}{k_{max}^3}\right)$	$\alpha_1^k = (\alpha_{max} - \alpha_{min}) + \alpha_{min}\left(\frac{k^3}{k_{max}^3}\right)$

Table 3 gives the parameters and values of the PSO, DPSO and EAGPSO algorithms used in simulation studies.

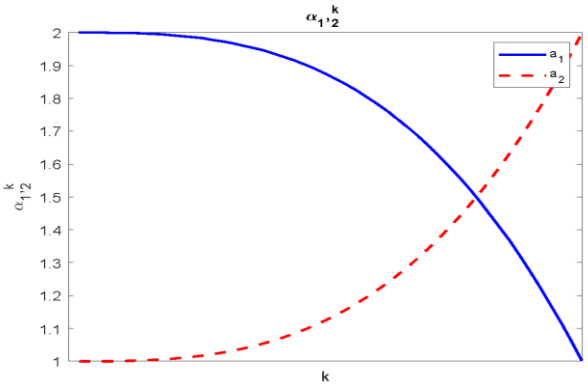

Figure 5. Acceleration coefficients show the values throughout the iteration.

Table 3. Parameters of the algorithms used

Parameters	PSO	DPSO	EAGPSO
ω	0.4	0.4	0.4
a_1	1	1	a_1, a_2 coefficients updated according to Table 2
a_2	1	1	

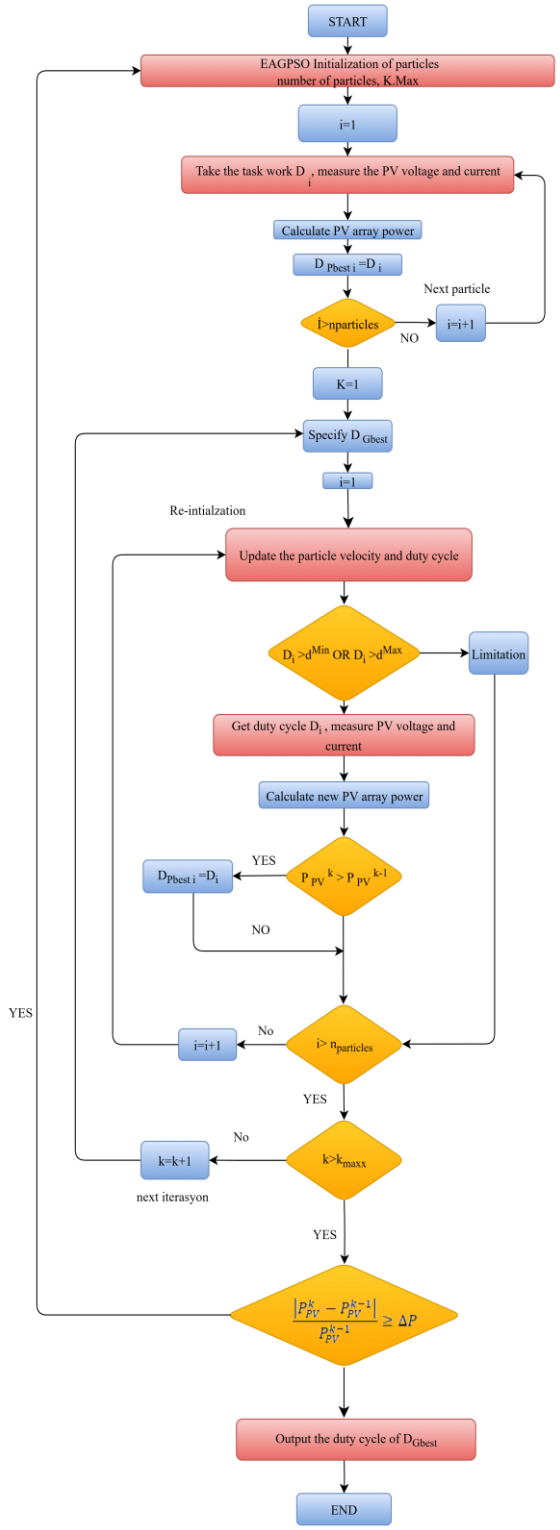

Figure 6. Enhance Autonomous Group PSO based MPPT algorithm flow diagram

3. DISCUSSION AND CONCLUSION

Figure 7 shows the MATLAB/Simulink model of the PV system used for simulation studies. In order to evaluate the performance of MPPT algorithms used with the modified SEPIC converter. 2SX2P PV array architecture consisting of series-parallel connected modules was used. Aavid solar Amas-165 W PV module was used in the study. The technical specifications of the PV Module are given in Table 4. The modified SEPIC converter design

parameters used are given as follows. Input voltage 70.4 V, output voltage 199.5 V, Inductances $L_1, L_2 = 506.4\,\mu H$, Capacitors $C_1, C_2 = 4.93\,\mu F$ If the output capacitor is $C_0 = 79.72\,\mu F$, switching frequency 50 kHz and load resistance $R_{load} = 60\Omega$. In Figure 8 2SX2P P-V characteristics, LMPP and GMPPs for the PV panel connection array are shown.

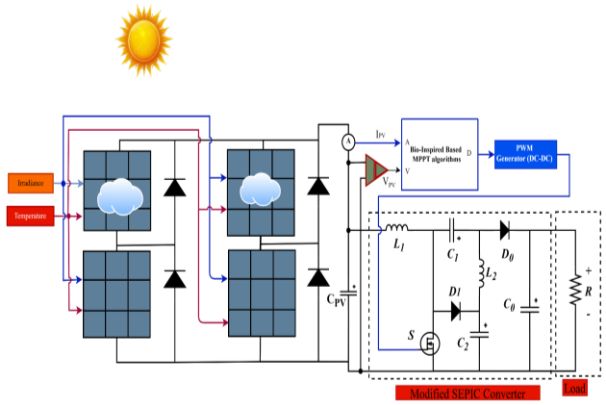

Figure 7. Off-grid PV system designed using MATLAB/Simulink

Table 4. PV Module Specifications

Parameter	Value
P_{mpp}	164.85 W
V_{mpp}	35 V
I_{mpp}	4.71 A
V_{OC}	43.5 V
I_{sc}	5.25 A
$Ncell$	72
R_{sh}	125.0069
R_s	0.62818

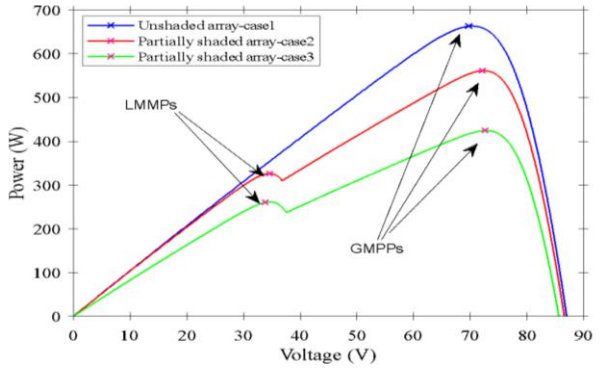

Figure 8. 2SX2P P-V characteristic, LMPP and GMPP for PV panel connection array

In order to evaluate the performances of PSO, DPSO and EAGPSO algorithms, three different scenarios including equal irradiance and partial shading conditions were implemented. In the first scenario, the performances of the algorithms were evaluated under equal irradiance conditions. In the second and third scenarios, the performance of the algorithms in partial shadowing situations was evaluated separately. Table 4 shows the radiation values determined for different situations and the GMPP values according to these values. In order to make a fair comparison of the algorithms for all scenarios, the initial values are taken equal. While making the comparison, the mathematical expression in Equation 12 was used.

Table 4. Irradiance values determined for different situations and GMPP according to these values

Scenarios	Solar Irradiance (W/m²)	Condition	GMPP (W)
PSC1	*1000 – 1000* *1000 – 1000*	*Unshaded array – Case 1*	*663.3 W*
PSC2	*1000 – 1000* *800 – 800*	*Partially shaded array – Case 2*	*561.6 W*
PSC3	*800 – 800* *600 – 600*	*Partially shaded array – Case 3*	*424.7 W*
SRL 1 (0–1 s) *SRL 2 (1–2 s)* *SRL 3 (2–3 s)*	*1000* *500* *750*	*Unshaded array*	*663.3 W* *333 W* *500 W*

$$P_{load} = \sqrt{\left(\frac{1}{n}\right)\sum_{i=0}^{n}(P_i)^2} \qquad (12)$$

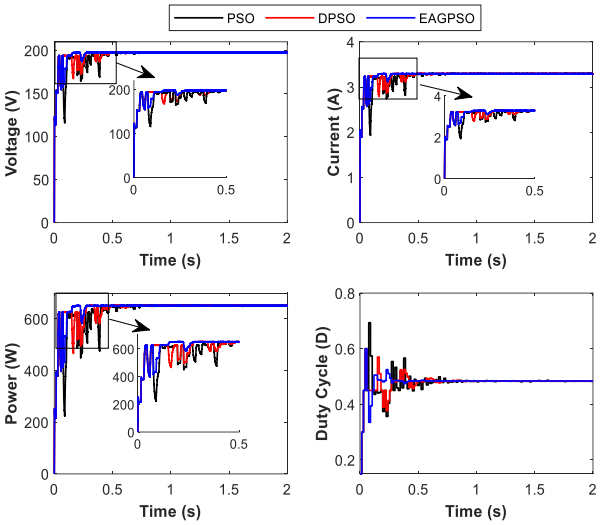

Figure 9. First scenario a) voltage b) current c) power d) duty time changes

In Figure 9, voltage, current, power and duty cycle changes of all PSO programs for standard radiation conditions are shown in detail. The GMPP value for the standard radiation value of the panels specified in Table 4 is 663.3 Watt. In case of application of the PSO, DPSO and EAGPSO algorithms used, the output power obtained was observed as 647.75 W, 649.40 W and 650.32 W, respectively. In terms of efficiency, PSO achieved 97.66% MPPT efficiency, DPSO 97.90% MPPT efficiency and EAGPSO 98.04% MPPT efficiency. In terms of convergence times, in the first scenario, the EAGPSO algorithm has the fastest convergence time at 0.27s. The EAGPSO algorithm is followed by the DPSO algorithm with 0.49s and the PSO algorithm with 0.75s. It has also been observed that the EAGPSO algorithm has 64% less oscillation compared to the PSO algorithm and 44.9% less oscillation compared to DPSO.

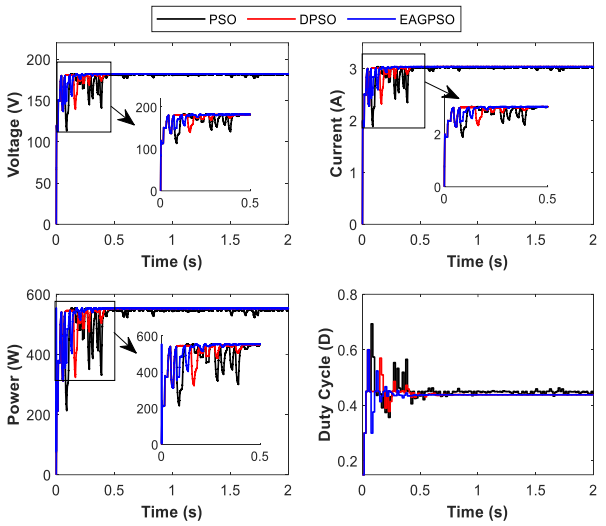

Figure 10. Second scenario a) voltage b) current c) power d) duty time changes

For the second case, GMPP is 561.6 W according to the determined irradiance values. The results of the second scenario are shown in Figure 10. The output power obtained with the PSO, DPSO and EAGPSO used is 542.56 W, 552.86 W, 553.10 W, respectively. Voltage values are 180.34 V, 182.13 V and 182.17 V, respectively. In terms of MPPT efficiency, PSO has 96.61% efficiency, DPSO has 98.44% efficiency and EAGPSO has 98.49% efficiency. In the second scenario, the EAGPSO algorithm shows the fastest convergence performance, reaching GMPP in 0.32 seconds, while the DPSO algorithm reaches steady state in 0.43 seconds and PSO in 0.7 seconds. It has been observed that the EAGPSO algorithm has 54% less oscillation than the PSO algorithm and 31% less oscillation than the DPSO algorithm. Since the PSO algorithm has a larger power swing than the other algorithm by adjusting the randomness and acceleration coefficients, it takes longer to converge to GMPP. In addition, for the second scenario, the DPSO algorithm showed less oscillation than PSO.

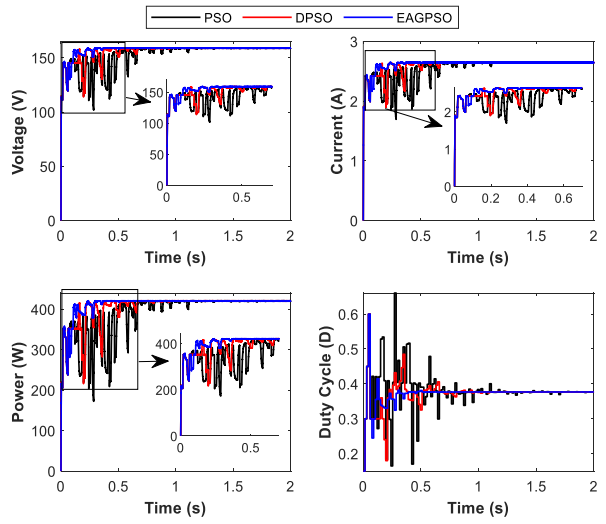

Figure 11. Third scenario a) voltage b) current c) power d) duty time changes

For the third scenario, if the algorithms are applied to the PV system, the changes in voltage, current, power and duty duration over time are shown in Figure 11. According to the radiation value specified for Scenario 3, the maximum voltage and current values that the PV system will produce are 159.6308V and 2.6605A, respectively. If PSO, DPSO and EAGPSO algorithms are used, voltage and current values are 156.47V-2.61A, 158.45V-2.64A and 158.75V-2.65A, respectively. The power values produced by PSO, DPSO and EAGPSO algorithms are 409.53W, 418.45W and 420.05 W, respectively. As seen in Figure 10, the EAGPSO algorithm used reaches GMPP in a shorter time than other algorithms. When the convergence times are compared, the EAGPSO algorithm followed MPP in 0.37s, the DPSO algorithm in 0.96s, and the PSO algorithm in 1.12s. It has been found that the convergence time of EAGPSO is 61% shorter than DPSO and 66% shorter than PSO.

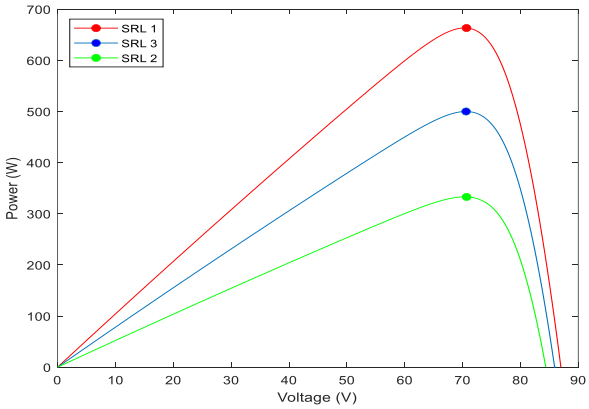

Figure 12. P-V characteristics with FCSR

To evaluate the performance of the EAGPSO algorithm and other MPPT-based algorithms in the dynamic irradiance changing scenario, the robustness and stability of the MPPT algorithm to guarantee the restart after two different fast solar irradiance change (FCSR) cycles when the entire PV array is equally shaded by a passing cloud are evaluated. The P–V characteristics of the PV array obtained for three different solar irradiance levels under the constant temperature condition of 25°C are presented in Figure 12. In this scenario, the PV array output power for solar radiation values of $1\,kW/m^2, 0.75\,kW/m^2$ *and* $0.5\,kW/m^2$ is $663.3W, 500\,W, 333\,W$, respectively. Uniform shading with FCSR, standard test conditions (i.e., no clouds, STCs: $1\,kW/m^2$ and $25\,°C$) were applied for the $0-1s$ time interval. In the $1-2s$ time interval, there was a sudden decrease in solar radiation, and the irradiance values of all panels were determined as $0.5\,kW/m^2$. In the $2-3s$ time interval, the irradiance values of the panels were increased again and determined as $0.75\,kW/m^2$.

The voltage, current, output power and duty cycle obtained for all MPPT algorithms are given comparatively in Figure 13. For this scenario, all metaheuristic based MPPT algorithms successfully demonstrated the reset and restart conditions. The algorithms reached MPP with different convergence times. Despite the rapid change of the radiation value, the EAGPSO algorithm reached MPP in a short monitoring time. The numerical results for this scenario are given in detail in Table 5.

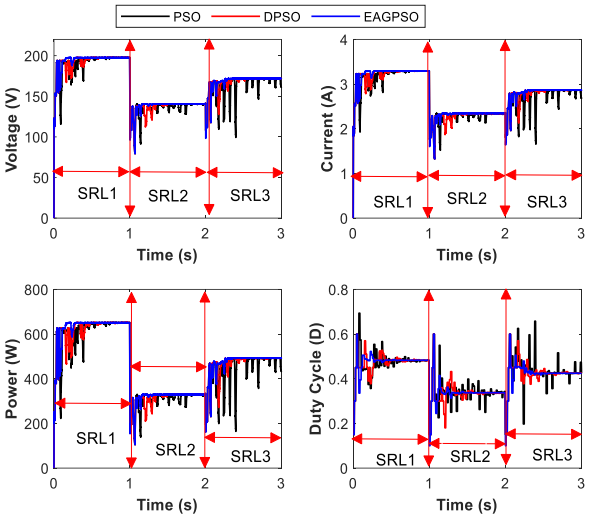

Figure 13. Current, voltage, output power and duty time results of the algorithms under different equal irradiance values

MPPT efficiency values of the scenarios are shown in Figure 14 and tracking times are shown in Figure 15.

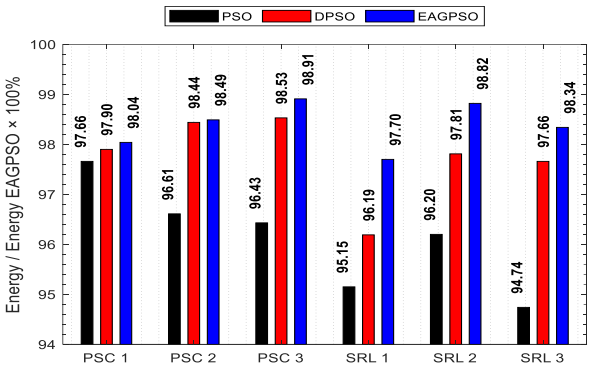

Figure 14. Energy Efficiency of All PSO Based MPPT Algorithms under Used Solar Radiation Patterns

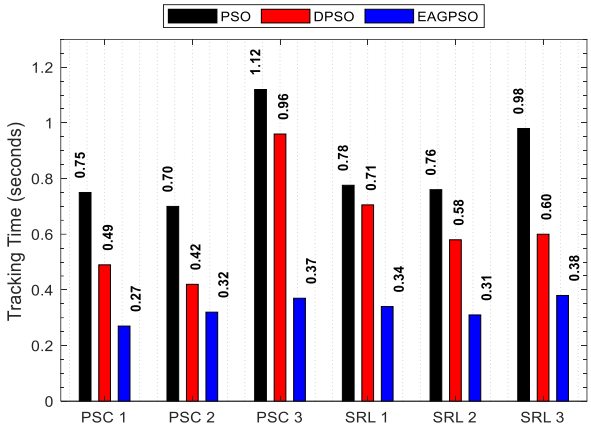

Figure 15. Tracking times of all PSO Based MPPT Algorithms under used solar irradiance patterns

Table 5. Simulation results for different scenarios

Solar Irradiance Patterns	Algorithms	Obtained Power (W)	GMPP (W)	Tracking Time (s)	MPPT Efficiency (%)
PSC 1	PSO DPSO EAGPSO	647.75 649.40 650.32	663.3	0.75 0.49 0.27	97.66% 97.90% 98.04%
PSC 2	PSO DPSO EAGPSO	542.56 552.86 553.86	561.6	0.70 0.42 0.32	96.61% 98.44% 98.49%
PSC 3	PSO DPSO EAGPSO	409.53 418.45 420,05	424.7	1.12 0.96 0.37	96.43% 98.53% 98.91%
SRL1 0-1 s	PSO DPSO EAGPSO	631.10 638.02 648.04	663.3	0.7759 0.7054 0.340	95.15% 96.19% 97.70%
SRL2 1-2 s	PSO DPSO EAGPSO	320.43 325.71 329.06	333	0.76 0.58 0.31	96.20% 97.81% 98.82%
SRL3 2-3 s	PSO DPSO EAGPSO	473.72 488.29 491.67	500	0.98 0.6 0.38	94.74% 97.66% 98.34%

The comparison of EAGPSO with the algorithms frequently used in the literature is given in Table 6.

Table 6. Comparison of the proposed EAGPSO with the studies in the literature

Algorithm	Conditions	Converter	Efficiency (%)
PSO [33]	Partial shading conditions	Buck-boost converter	High
CSA [35]	Partial shading conditions	Boost converter	High
FOCV [36]	Variable Conditions	Boost converter	Medium
EAGPSO	Partial shading conditions & Dynamic weather conditions	Modified SEPIC converter	High

4. CONCLUSION

In this study, the MPPT performance of PSO, DPSO and EAGPSO algorithms was evaluated using a modified SEPIC converter. In the equal irradiance conditions simulation study, the EAGPSO algorithm achieved MPP at an efficiency value of 98.04% with less power voltage swing in the modified SEPIC converter. The EAGPSO algorithm reduced the power fluctuation by 1/2 compared to the DPSO algorithm and by 2/3 compared to the PSO algorithm. For the second scenario, if EAGPSO, DPSO and PSO algorithms were used, power values of 553.10W, 552.86W, 542.56W were obtained, respectively. Additionally, the MPPT efficiencies of EAGPSO, DPSO and PSO algorithms were obtained as 98.49%, 98.44% and 96.61%, respectively. In the third scenario, the EAGPSO algorithm reached 420.05 W, the DPOS algorithm reached 418.45W and the PSO algorithm reached 409.53W. When all scenarios are evaluated, the EAGPSO algorithm stands out as the most stable and efficient algorithm. As the next study, it is planned to implement the real-time application of the EAGPSO algorithm with the modified SEPIC converter, which has shown successful performance in simulation studies.

Acknowledgement

This work was supported by the Atatürk University Coordination Unit of Scientific Research Projects (Project No: FBA-2025-15043)

REFERENCES

[1] Bozkurt A. U., "Yenilenebilir enerji kaynaklarının enerji verimliliği açısından değerlendirilmesi," Dokuz Eylul Universitesi (Turkey), 2008.

[2] Polat A., "Piezoelektrik sistemli suya dayalı enerji sistemlerinin analizi ve uygulaması," Yüksek Lisans Tezi, Bilecik Şeyh Edebali Üniversitesi, 56-70, 2016.

[3] Aboagye B., Gyamfi S., Ofosu E. A., and Djordjevic S., "Investigation into the impacts of design, installation, operation and maintenance issues on performance and degradation of installed solar photovoltaic (PV) systems," Energy for Sustainable Development, vol. 66, pp. 165-176, 2022.

[4] Yılmaz M. and Corapsiz M., "PSO training neural network MPPT with CUK converter topology for stand-alone PV systems under varying load and climatic conditions," Türk Doğa ve Fen Dergisi, vol. 13, no. 1, pp. 88-97, 2024.

[5] Hassaine L., OLias E., Quintero J., and Salas V., "Overview of power inverter topologies and control structures for grid connected photovoltaic systems," Renewable and Sustainable Energy Reviews, vol. 30, pp. 796-807, 2014.

[6] Ram J. P. and Rajasekar N., "A new global maximum power point tracking technique for solar photovoltaic (PV) system under partial shading conditions (PSC)," Energy, vol. 118, pp. 512-525, 2017.

[7] Peled A. and Appelbaum J., "Minimizing the current mismatch resulting from different locations of solar cells within a PV module by proposing new interconnections," Solar Energy, vol. 135, pp. 840-847, 2016.

[8] Bradai R. et al., "Experimental assessment of new fast MPPT algorithm for PV systems under non-uniform irradiance conditions," Applied energy, vol. 199, pp. 416-429, 2017.

[9] Abdel-Rahim O., M. Alghaythi L., Alshammari M. S., and Osheba D. S., "Enhancing photovoltaic conversion efficiency with model predictive control-based sensor-reduced maximum power point tracking in modified sepic converters," Ieee Access, vol. 11, pp. 100769-100780, 2023.

[10] Assiya L., Aziz D., and Ahmed H., "Comparative study of P&O and INC MPPT algorithms for DC-DC converter based PV system on MATLAB/SIMULINK," in 2020 IEEE 2nd international conference on electronics, control, optimization and computer science (ICECOCS), 2020: IEEE, pp. 1-5.

[11] Refaat A., Khalifa A.-E., Elsakka M. M., Elhenawy Y., Kalas A., and Elfar M. H., "A novel metaheuristic MPPT technique based on enhanced autonomous group Particle Swarm Optimization Algorithm to track the GMPP under partial shading conditions-Experimental validation," Energy Conversion and Management, vol. 287, p. 117124, 2023.

[12] Yang B. et al., "Salp swarm optimization algorithm based MPPT design for PV-TEG hybrid system under partial shading conditions," Energy Conversion and Management, vol. 292, p. 117410, 2023.

[13] Zhang R., Yang B., and Chen N., "Arithmetic optimization algorithm based MPPT technique for centralized TEG systems under different temperature gradients," Energy Reports, vol. 8, pp. 2424-2433, 2022.

[14] González-Castaño C., Restrepo C., Kouro S., and Rodriguez J., "MPPT algorithm based on artificial bee colony for PV system," Ieee Access, vol. 9, pp. 43121-43133, 2021.

[15] Mohanty S., Subudhi B., and Ray P. K., "A new MPPT design using grey wolf optimization technique for photovoltaic system under partial shading conditions," IEEE transactions on sustainable energy, vol. 7, no. 1, pp. 181-188, 2015.

[16] Abbass M. J., Lis R., and Saleem F., "The maximum power point tracking (MPPT) of a partially shaded PV array for optimization using the antlion algorithm," Energies, vol. 16, no. 5, p. 2380, 2023.

[17] Kumar S. and Shaw B., "Design of off-grid fuel cell by implementing ALO optimized PID-based MPPT controller," in Soft Computing in Data Analytics: Proceedings of International Conference on SCDA 2018, 2018: Springer, pp. 83-93.

[18] Mirza A. F., Mansoor M., and Ling Q., "A novel MPPT technique based on Henry gas solubility optimization," Energy Conversion and Management, vol. 225, p. 113409, 2020.

[19] Percin H. B. and Caliskan A., "Whale optimization algorithm based MPPT control of a fuel cell system,"

International journal of hydrogen energy, vol. 48, no. 60, pp. 23230-23241, 2023.
[20] Titri S., Larbes C., Toumi K. Y., and Benatchba K., "A new MPPT controller based on the Ant colony optimization algorithm for Photovoltaic systems under partial shading conditions," Applied Soft Computing, vol. 58, pp. 465-479, 2017.
[21] Ye S. P., Liu Y. H., Wang S. C., and Pai H. Y., "A novel global maximum power point tracking algorithm based on Nelder-Mead simplex technique for complex partial shading conditions," Applied Energy, vol. 321, p. 119380, 2022.
[22] Rezk H., Zaky M. M., Alhaider M., and Tolba M. A., "Robust fractional MPPT-based moth-flame optimization algorithm for thermoelectric generation applications," Energies, vol. 15, no. 23, p. 8836, 2022.
[23] Subramanian A. and Raman J., "Grasshopper optimization algorithm tuned maximum power point tracking for solar photovoltaic systems," Journal of Ambient Intelligence and Humanized Computing, vol. 12, no. 9, pp. 8637-8645, 2021.
[24] Ram J. P., Pillai D. S., Ghias A. M., and Rajasekar N., "Performance enhancement of solar PV systems applying P&O assisted Flower Pollination Algorithm (FPA)," Solar Energy, vol. 199, pp. 214-229, 2020.
[25] Elbaksawi O., Elminshawy N. A., Diab S., Eltamaly A. M., Mahmoud A., and Elhadidy H., "Innovative metaheuristic algorithm with comparative analysis of MPPT for 5.5 kW floating photovoltaic system," Process Safety and Environmental Protection, vol. 185, pp. 1072-1088, 2024.
[26] Kumar B. H. and Ghosh A., "Different MPPT Algorithms for DC-DC Converter," in 2025 IEEE International Students' Conference on Electrical, Electronics and Computer Science (SCEECS), 2025: IEEE, pp. 1-6.
[27] Yılmaz M., Kaleli A., and Çorapsız M. F., "Machine learning based dynamic super twisting sliding mode controller for increase speed and accuracy of MPPT using real-time data under PSCs," Renewable Energy, vol. 219, p. 119470, 2023.
[28] Regaya C. B., Hamdi H., Farhani F., Marai A., Zaafouri A., and Chaari A., "Real-time implementation of a novel MPPT control based on the improved PSO algorithm using an adaptive factor selection strategy for photovoltaic systems," ISA transactions, vol. 146, pp. 496-510, 2024.
[29] Çorapsiz M. R., "PV-fed multi-output buck converter-based renewable energy storage system with extended current control for lifetime extension of Li-ion batteries," Computers and Electrical Engineering, vol. 120, p. 109757, 2024.
[30] Saravanan S. and Babu N. R., "RBFN based MPPT algorithm for PV system with high step up converter," Energy conversion and Management, vol. 122, pp. 239-251, 2016.
[31] Mahho M., Yilmaz M., and Çorapsiz M. F., "The performance of modified SEPIC converter for dynamic conditions with PI controller," in 2025 7th International Congress on Human-Computer Interaction, Optimization and Robotic Applications (ICHORA), 2025: IEEE, pp. 1-4.
[32] Sundareswaran K. and Palani S., "Application of a combined particle swarm optimization and perturb and observe method for MPPT in PV systems under partial shading conditions," Renewable Energy, vol. 75, pp. 308-317, 2015.
[33] Ishaque K. and Salam Z., "A deterministic particle swarm optimization maximum power point tracker for photovoltaic system under partial shading condition," IEEE transactions on industrial electronics, vol. 60, no. 8, pp. 3195-3206, 2012.
[34] Refaat A., Elbaz A., Khalifa A. E., Elsakka M. M., Kalas A., and Elfar M. H., "Performance evaluation of a novel self-tuning particle swarm optimization algorithm-based maximum power point tracker for porton exchange membrane fuel cells under different operating conditions," Energy Conversion and Management, vol. 301, p. 118014, 2024.
[35] Abo-Elyousr F. K., Abdelshafy A. M., and Abdelaziz A. Y., "MPPT-based particle swarm and cuckoo search algorithms for PV systems," in Modern maximum power point tracking techniques for photovoltaic energy systems: Springer, 2019, pp. 379-400.
[36] Kota V. R. and Bhukya M. N., "A novel linear tangents based P&O scheme for MPPT of a PV system," Renewable and Sustainable Energy Reviews, vol. 71, pp. 257-267, 2017.

APPENDİX

Nomenclature	Abbreviation
PV	Photovoltaic
MPPT	Maximum power point tracking
P&O	Perturb and observe
FL	Fuzzy logic
EAGPSO	Enhance Autonomous Group Particle swarm optimization
INC	Incremental Conductance
GWO	Grey Wolf Optimization
SSOA	Salp Swarm Optimization Algorithm
ABC	Artificial bee colony
SRA	Search and Rescue Algorithm
ALOA	Ant Lion Optimization Algorithm
WOA	Whale optimization algorithm
SSA	Squirrel search algorithm
ACO	Ant Colony Optimization
HHO	Harris hawk optimization
AO	Antlion Optimizer
PSO	Particle swarm optimization
GPR	Gaussian process regression
STSMC	Super twist sliding mode controller
MSC	Modified SEPIC Converter

Volume 14, Issue 3, Page 67-72, 2025 https://doi.org/10.46810/tdfd.1706519 Research Article

BİNGÖL UNIVERSITY

Türk Doğa ve Fen Dergisi
Turkish Journal of Nature and Science
www.dergipark.gov.tr/tdfd

Determination of Turkey Meat Adulteration in Cooked Ground Beef Using Fluorescence Spectroscopy with Machine Learning

Ali SOYUÇOK[1], Samet UÇAK[2*]

[1]Burdur Mehmet Akif Ersoy University, Department of Food Processing, Burdur Food Agriculture and Livestock Vocational School, Burdur, Türkiye
[2*]Istanbul Aydin University, School of Medicine, Department of Medical Biology, Istanbul, Türkiye
Ali SOYUÇOK ORCID No: 0000-0003-2626-5827
Samet UÇAK ORCID No: 0000-0002-3461-2481

**Corresponding author: sametucak@aydin.edu.tr*

(Received: 26.05.2025, Accepted: 14.07.2025, Online Publication: 26.09.2025)

Keywords
Beef, Fluorescence spectroscopy, Machine learning, Meat adulteration, Turkey

Abstract: Beef adulteration with turkey meat is typically driven by financial motives. Since turkey meat is less expensive than beef, producers aiming to cut costs and boost profits blend turkey meat into beef products in certain ratios. This study aimed to investigate the use of fluorescence spectroscopy as a fast, non-destructive, and comprehensive method, combined with multivariate analysis, to predict meat adulteration. Raw turkey ground was combined with raw beef ground in concentrations from 0-100% (w/w) in 10% increments and then cooked. Fluorescence measurements of the cooked samples were taken (Ex 200-500 nm, Em 525 nm). The resulting spectral data were analyzed using chemometric tools, such as principal component analysis and partial least squares regression, and error metrics (Table 1 and 2) were calculated. For the training, validation, and test datasets, R^2 values of 0.941, 0.922, and 0.916, and RMSE values of 8.124, 10.856, and 8.456 were identified, respectively. This research demonstrated that fluorescence spectroscopy and multivariate analyses can serve as rapid, non-destructive, and effective methods for detecting a 20% turkey meat adulteration in meat products.

Makine Öğrenmesi Destekli Floresans Spektroskopisi ile Pişmiş Kıyma Sığır Etinde Hindi Eti Tağşişinin Belirlenmesi

Anahtar Kelimeler
Sığır eti, Floresans spektroskopisi, Makine öğrenmesi, Et tağşişi, Hindi eti

Öz: Sığır etine hindi eti karıştırılması genellikle finansal nedenlerle gerçekleştirilmektedir. Hindi eti, sığır etine kıyasla daha ucuz olduğundan, maliyetleri düşürmek ve kâr oranlarını artırmak isteyen üreticiler, belirli oranlarda hindi etini sığır eti ürünlerine karıştırmaktadır. Bu çalışma, et hilelerinin tespiti için hızlı, tahribatsız ve kapsamlı bir yöntem olarak floresans spektroskopisinin çok değişkenli analizlerle birlikte kullanımını araştırmayı amaçlamıştır. Çiğ hindi kıyması, %0–100 (a/a) aralığında ve %10'luk artışlarla çiğ sığır kıyması ile karıştırılmış, ardından pişirme işlemi uygulanmıştır. Pişmiş örneklerin floresans ölçümleri (Ex: 200–500 nm, Em: 525 nm) alınmıştır. Elde edilen spektral veriler, temel bileşen analizi (PCA) ve kısmi en küçük kareler regresyonu (PLSR) gibi kemometrik araçlar kullanılarak analiz edilmiş, hata metrikleri (Tablo 1 ve 2) hesaplanmıştır. Eğitim, doğrulama ve test veri kümeleri için sırasıyla 0.941, 0.922 ve 0.916 R^2 değerleri ve 8.124, 10.856 ve 8.456 RMSE değerleri elde edilmiştir. Bu araştırma, floresans spektroskopisi ve çok değişkenli analizlerin, et ürünlerinde %20 oranındaki hindi eti taklitçiliğini tespit etmek için hızlı, tahribatsız ve etkili yöntemler olarak kullanılabileceğini ortaya koymuştur.

1. INTRODUCTION

The adulteration of meat products is not only an economic problem but also a serious concern in terms of public health, religious sensitivities, and consumer rights. The addition of low-cost meat types to beef, which has high economic value, is a common example of food adulteration [1].

Grounded and cooked meat products are adulterated more easily than fresh meat. This is because size reduction, cooking, and use of spices may reduce the effects of

adulteration. Detecting adulteration in minced beef usually becomes more difficult after cooking because thermal process causes denaturation of the protein and loss of the chemical bonds of the meat [2], which makes the detection method more difficult. Therefore, prevention of meat adulteration, proper labelling of food, and prevention of unfair competition in the meat sector have become important issues for the competent authorities of the meat sector [3]. The detection of adulteration in meat products is of great importance for ensuring consumer safety and determining compliance with legal regulations [4].

Different analytical techniques have been used to determine adulteration. Polymerase chain reaction (PCR) is a well-known molecular method involving the chemical amplification of specific DNA sequences [5]. This technique is useful for the identification of different species in a mixed meat sample or for the determination of meat origin based on specific DNA sequences that are unique to different meat species [6]. Chromatographic, immunological, and electrophoresis methods are commonly used for detecting foreign compounds [7,8]. Hoffmann et al. [9] investigated the ability of HPLC-MS/MS scanning to simultaneously detect plant proteins (soya, pea, and lutein) in meat products.

Although the methods described above provide high accuracy and demonstrate robustness, they still have numerous shortcomings; for example, they are more expensive, labourious, and time-consuming, experts are required to perform the experiment, and a considerable amount of time is required to prepare the sample and perform the analysis. Therefore, there is a need to develop fast and accurate techniques suitable for online authentication that are easy to implement by government agencies and quality assurance engineers to monitor counterfeiting in processed meat products. Increasing efforts have been made to introduce fast, innovative, and reliable detection techniques to ensure the authenticity, quality, and safety of meat and meat products [10,11].

Fluorescence spectroscopy has attracted attention as a noninvasive, rapid, and economical method for food analysis. The characteristic fluorescence properties of biomolecules found in meat products are considered potential tools for distinguishing different species [12]. However, the high-dimensional and complex nature of fluorescence data makes it difficult to effectively analyse this information. Machine learning algorithms are powerful tools for pattern extraction, classification, and prediction processes from large datasets [13,14]. This study aimed to develop a new, fast, practical, and low-cost analytical method as an alternative to traditional analysis methods for the determination of adulteration of turkey meat mixed with beef at different ratios.

2. MATERIAL AND METHOD

2.1. Material

Postmortem beef (Longissimus thoracis et lumborum) and turkey breast meat (Musculus superficiolis) were obtained from a local meat supplier, transferred to the laboratory under aceptic conditions, and stored in a freezer (−20 °C) until use.

2.2. Sample Preparation

Water 10% (w/w) and NaCl 2% (w/w) were added to the beef/turkey minced meat mixture, in 50 mL centrifuge tubes (Isolab, Turkey). The tubes were placed in a water bath set at 60°C and the temperature of the water bath was increased to 85°C. The centre temperatures of the experimental groups were monitored using a thermometer (ISOLAB, Turkey). The cooking process was terminated when the centre temperature of the samples reached 74°C (Fig. 1). The cooked samples were kept at room temperature for 30 min after the cooking liquid was removed [15].

Figure 1. A representative sample preparation study (The photograph was taken by A. Soyuçok for this study).

2.3. Fluorescence Spectral Analysis

A fluorescence spectrophotometer (Varioscan Lux, Thermo Fisher. Inc, USA) was used for spectral measurement. To determine the wavelength at which the highest emission occurred, the fluorescence emission spectra of the meat samples were recorded at a constant excitation wavelength (460 nm) and emission values in the range of 480-840 nm and the highest emission value was determined. All spectra were recorded at room temperature and each treatment was performed in triplicate. The excitation spectra were acquired at a fixed emission wavelength of 525 nm over an excitation range of 200-500 nm.

2.4. Chemometric Analysis

The Unscrambler X 10.5 software was employed to preprocess the fluorescence spectra, thereby correcting the initial values. Initially, the raw spectral data were smoothed using a Savitzky-Golay derivative filter (second-order polynomial, 11-point window) to mitigate the signal noise and eliminate variations attributable to light scattering. Subsequently, the data were normalised using a Standard Normal Variate (SNV) transformation. The data were then structured in a mean-centred format by averaging, rendering them suitable for Partial Least

Squares (PLS) modelling. The Partial Least Squares Regression (PLSR) method was utilized in the modeling process, with a kernel-based approach selected as the algorithm. Model accuracy was assessed through the cross-validation method, and the performance evaluation criteria included R^2, RMSE, slope, and offset values.

3. RESULTS AND DISCUSSION

The present study leveraged fluorescence spectroscopy as a rapid, non-destructive means to detect turkey adulteration in cooked ground beef. The highest emission of cooked beef mince containing turkey meat adulteration was observed at 525 nm (Fig. 2A). The spectrum was scanned at 525 nm excitations (Fig. 2B). As the percentage of adulteration of turkey meat varied, the changes in the spectrum increased, indicating that the wavelengths were suitable for the determination of adulteration (Fig. 3) and were also due to the tryptophan content in the myofibril protein and the free amino acids in the meat [16]. The wavelengths at which this change occurs serve as fingerprints for the identification of turkey meat [17].

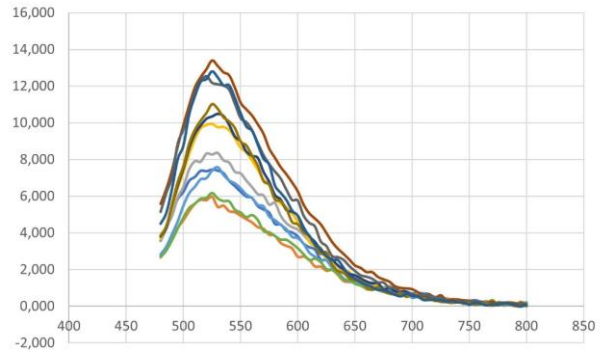

Figure 2A. Emission spectrum (Ex. 460nm).

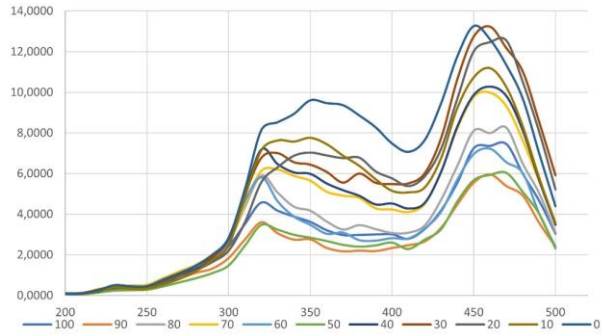

Figure 2B. Fluorescence spectrum (Ex 200-500 nm, Em 525 nm).

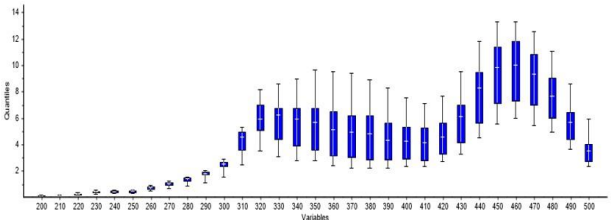

Figure 3. Effect of turkey adulteration at different wavelengths.

Various analytical methods exist for meat fraud detection, each with trade-offs. DNA-based methods (PCR) are gold-standard for species identification and can detect adulterants down to very low levels (often <1%) [18]. Real-time PCR or multiplex PCR reliably confirm species in raw or lightly processed meats. However, PCR requires DNA extraction and thermal cycling instrumentation, and the target DNA can be degraded by intensive processing. For example, Aprilia et al. [19] found that conventional PCR failed to detect pork in heavily heated beef-floss products, whereas an ELISA immunoassay succeeded. Thus, PCR may miss adulterants in highly processed foods, necessitating complementary methods.

Near-Infrared (NIR) spectroscopy is a rapid alternative. NIR (and Vis-NIR) spectroscopy measures overtone vibrations of O–H, C–H, and N–H bonds; it is non-destructive and can be implemented in portable probes. In adulteration studies, NIR (often with PLSR) technique has quantified turkey or other meats in beef with good success. For example, Alamprese et al. [20] used FT-NIR (1000–2500 nm) and PLSR to predict turkey in minced beef, achieving R2>0.884 and RMSE <10.8%. Similarly, Weng et al. [21] applied Vis/NIR (300–2500 nm) plus chemometrics and reported ~99% accuracy in classifying pork or organ adulteration in ground beef. NIR spectroscopy's advantages include fast scanning and minimal sample prep, but its broad overlapping bands can limit specificity. Preprocessing (e.g. SNV, derivatives) is crucial in NIR spectroscopy just as in fluorescence. Notably, studies show NIR spectroscopy often outperforms UV-Vis spectroscopy for meat fraud: Alamprese et al. [20] reported that NIR/MIR spectra gave better turkey detection than UV-Vis spectra.

Liquid Chromatography–Mass Spectrometry (LC-MS) techniques (including proteomics and metabolomics) are highly sensitive and specific. LC-MS can identify species-specific peptide or lipid markers even in processed meat. State-of-the-art targeted proteomics methods achieve detection limits on the order of 0.2–1% in cooked products [18]. For example, Prandi et al. [22] developed an LC-MS/MS assay with LOD ≈0.2–0.8% for eight species (including turkey and chicken) in complex meat matrices. High-resolution LC-MS has also mapped adulteration in multi-component meat meals. These approaches yield definitive results and can handle very low adulteration levels, but they are costly, require skilled operation and heavy sample preparation, and are not suited for on-site or rapid screening. LC-MS is best viewed as a confirmatory or research tool rather than a routine field test.

Immunoassays (ELISA, lateral-flow "dipstick" tests) target specific proteins and can offer rapid, user-friendly detection of particular species (e.g. antibodies against pork myoglobin). ELISAs for meat species are available and can detect ~1% adulteration under ideal conditions [19]. They require no complex optics or chemometrics. However, immunoassays depend on intact antigen epitopes, which may be denatured by cooking. As observed by Aprilia et al. [19], an ELISA detected pork in heat-processed beef where PCR failed, implying ELISA can sometimes outperform DNA methods on cooked products. On the other hand, if proteins are heavily modified, ELISA may give false negatives. Immunoassays are also limited to pre-chosen targets; each

assay detects one species (or one allergen), so screening for multiple adulterants requires multiple tests.

Fluorescence-PLSR occupies a middle ground between these techniques. It is quicker and cheaper than LC-MS and PCR, yet more general (and often more quantitative) than single-target ELISAs. Our approach achieved comparable accuracy to published NIR models [20,23], confirming its viability. However, unlike targeted assays, it does not identify species by unique markers; it instead uses statistical patterns. This means it works well for known adulterations (beef vs turkey), but its generalizability to unknown adulterants must be validated separately. Complementary use (e.g. following up a positive fluorescence screen with PCR or MS for confirmation) would combine the strengths of these methods.

Despite the encouraging performance, several limitations must be acknowledged. First, the detection limit of ~20% turkey content means that very low-level adulteration (below 10–20%) was not reliably quantified. This is evident from the test-set bias (Table 2): the regression slope was well below unity (0.789) and the offset high (≈16%), indicating substantial underestimation at low adulteration levels. One cause is spectral masking: at small percentages, turkey's fluorescent signature is weak relative to the dominant beef background, making it hard to distinguish. The fixed-emission setup (Em = 525 nm) captures only one slice of the fluorescence landscape, possibly missing other differentiating peaks. It's known that overlapping fluorophores (e.g. tryptophan, NADH, collagen crosslinks) can yield broad, featureless spectra in mixed meats [14]. Our preprocessing (SG smoothing, SNV) improves precision but cannot recover information lost in broad overlap.

Table 1. Error metrics for calibration and validation data set.

	Slope	Offset	RMSE	R^2
Calibration	0,941	2,633	8,124	0,941
Validation	0,901	4,573	10,856	0,922

Table 2. Error metrics for test data set.

	SEP	Bias	Slope	Offset	RMSE	R^2
Test	8.96	5.98	0.789	16,544	8,456	0,916

Processing effects also complicate the task. All samples were cooked, which generates Maillard products and denatures proteins. These chemical changes may reduce species-specific contrast. For example, Aprilia et al. [19] noted that intensive heat can degrade DNA, affecting PCR, but also it could alter protein fluorescence. By removing cooking juices, we reduced variability due to moisture and soluble compounds, but this also eliminated any adulterant signals in the liquid fraction. In some cases, juices might carry pigment or vitamin differences (though that fraction was deliberately excluded here to mimic a typical solid-recipe analysis).

Another limitation stems from the PLSR model itself. Partial Least Squares assumes a linear relationship (albeit in latent-space) between spectra and concentration. We used a kernel-PLSR to allow nonlinearity, but extreme concentrations still exhibited bias. The high calibration/validation R2 and low RMSE suggest the model fits the training data well, but some overfitting or calibration transfer issues are possible. In particular, the steep drop in test slope hints at calibration–prediction differences, perhaps due to sample-to-sample variation not captured in the calibration set (Table 1). For example, heterogeneity in fat content or the microdistribution of turkey meat could lead to spectral inconsistencies. Ensuring sample homogeneity and averaging multiple scans per sample can help mitigate this issue.

Fluorescence intensity can be affected by instrument factors (lamp stability, detector sensitivity) and by matrix scattering. We attempted to minimize these by using front-face optics and SNV normalization [24], in addition, our study focused only on turkey in beef; detecting other adulterants (e.g. pork, chicken, lamb) would require retraining the model with corresponding mixtures and possibly different spectral features. While our method shows strong accuracy for moderate to high adulteration levels, its sensitivity limit (~20%) and potential biases mean it is not a definitive single solution. Instead, it is best viewed as a rapid screening tool: samples flagged by fluorescence should be further analyzed by confirmatory methods (PCR, LC-MS). Understanding these limitations guides realistic interpretation of the results and directs improvements.

Food adulteration in Türkiye has been a significant public health and regulatory concern. Turkish law (the Turkish Food Codex) explicitly prohibits mislabeling and mixing of meats. For example, Regulation Notification 2012/74 forbids producing "prepared meat mixtures" by mixing beef with poultry or pork without declaration [25]. Violating this rule not only deceives consumers (especially on religious grounds) but also can endanger health if allergens or unsanitary meats are involved. Studies have documented non-compliance: one nationwide survey of processed beef products found that 34% of samples were adulterated, predominantly with cheaper poultry (32.9%) and occasionally horsemeat (1.3%) [25]. No pork was found in that study, reflecting consumer sensitivities to pork; indeed, while pork is legal, it must be explicitly labeled (due to the majority-Muslim population). Earlier work also found adulteration rates on the order of 15–50% in various regions of Türkiye, underscoring its pervasiveness.

In the past year Turkish authorities have intensified enforcement. In late 2024, Türkiye Ministry of Agriculture and Forestry, publicly released lists of hundreds of food products failing standards. These included cases of beef products containing undeclared pork, equine meat sold as beef, and processed foods with unauthorized additives. For instance, a popular pizzeria was found to serve "beef" pizza laced with pork, causing a social outcry. In one high-profile campaign, over 500 companies and nearly 1,000 product batches were flagged for mislabeling or adulteration. Notable fraud examples included kebabs with hidden pork and cheeses "filled" with margarine. These revelations have prompted calls for stronger routine screening and transparency. Our findings

have direct relevance in this context. A rapid spectroscopy-based test like ours could be incorporated into official monitoring protocols or quality control by food companies. Because it is non-destructive and quick, inspectors could screen batches of ground meat or finished products en masse, identifying suspicious samples in need of further testing. Early detection of fraudulent meat substitution not only protects consumers (from allergen risk or religious violations) but also helps maintain fair markets. In Türkiye, where the economy of meat products is closely tied to cultural norms, ensuring authenticity is doubly important. Moreover, the introduction of portable, fluorescence-based analyzers (as future work) could empower even small processors or market inspectors to perform on-the-spot checks. For example, a hand-held fluorescence sensor could be used at slaughterhouses or meat processing plants to audit mixtures continuously. Even now, our bench-top results support the feasibility of such approaches. Implementing fluorescence-ML screening would complement Türkiye's regulatory framework (e.g. Law No. 5996 and related communiqués [26]) by providing a technical backbone to the "real-time" adulteration alerts announced by the Ministry [27]. In essence, improved analytical tools would enable the promise of these policies – ensuring that all beef-labeled products truly contain only beef, as mandated by the Codex.

Building on this work, several avenues could enhance detection capability and practical utility. First, expanded spectral techniques are promising. Multispectral or hyperspectral imaging could capture both spectral and spatial information of the meat. For example, Yu et al. [28] developed a portable hyperspectral imager (400–1000 nm) with on-board processing that achieved ≈95% accuracy in classifying meat species and even produced spatial "adulteration maps" of samples. Extending fluorescence to three-dimensional excitation–emission matrices (EEMs) rather than a single emission wavelength might likewise extract more features. Similarly, combining UV–Vis, NIR, and fluorescence measurements could provide complementary fingerprints: Alamprese found that MIR/NIR technique together outperformed UV-Vis technique alone for turkey detection [23], suggesting multi-modal fusion could improve sensitivity. Second, miniaturization and portability are key. Developing handheld fluorescence devices (e.g. LED-based fluorimeters) would allow in-field use. Coupling fiber-optic probes with portable spectrometers could enable direct scanning of meat on-site. The Raspberry Pi-controlled HSI system of Yu et al. (2025) demonstrates the feasibility of low-cost portable platforms. Future work should assess such devices in real-world conditions (varying light, temperature, sample presentation) and calibrate them accordingly. Integration with smartphone technology (e.g. smartphone spectrometer add-ons) could also democratize testing. Third, real-time monitoring could transform processing lines. For example, an assembly-line fluorescence scanner could continuously check ground meat moving on a conveyor, flagging adulteration instantly. Coupled with cloud-based machine-learning, this would yield a live dashboard of authenticity. Such "smart factory" integration would greatly aid quality assurance. Research is needed on non-contact or inline sampling approaches (e.g. fluorescence excitation via laser diode, detection through camera-based sensors) to enable non-invasive scanning at speed. Fourth, larger and more diverse datasets will strengthen models. Expanding the sample set to include meats from different breeds, ages, or diet regimens would improve robustness. Including other adulterants (pork, chicken, lamb, offal) either singly or in multi-component mixtures is essential to generalize the method. Multi-species models or variable-selection algorithms could then differentiate among several possible adulterants. Additionally, more replicates at low adulteration levels (5–15% turkey) are needed to push the detection limit lower. Fifth, advanced chemometrics and AI could boost performance. We used kernel-PLSR, but emerging machine-learning techniques (e.g. Random Forests, Support Vector Regression, deep neural networks) may capture complex spectral patterns even better. Deep learning, in particular, has shown promise in spectroscopy: convolutional neural networks can learn features from spectra or images without explicit preprocessing. Future studies might compare PLSR to such methods for quantitation. Data fusion approaches (combining fluorescence with orthogonal sensors) could also be pursued.

4. CONCLUSION

While our fluorescence-PLSR method demonstrates strong potential, its ultimate impact will grow when integrated with these advancements. By extending the spectral range, deploying portable instrumentation, gathering wider datasets, and harnessing modern AI, it should be possible to create real-time, on-site authentication systems. Such tools would not only improve the detection of turkey in beef but could be adapted to a broad array of food fraud challenges, thereby supporting food safety and integrity both in Türkiye and globally.

REFERENCES

[1] Nakyinsige K, Man YBC, Sazili AQ. Halal authenticity issues in meat and meat products. Meat Sci. 2012;91(3):207-214.

[2] Iqbal Z, Afseth NK, Postelmans A, Wold JP, Andersen PV., Kusnadi J, et al. Detection and quantification of pork adulteration in beef meatballs with Raman spectroscopy and near infrared spectroscopy. Spectrochim Acta A Mol Biomol Spectrosc. 2025;337:126069.

[3] Anagaw YK, Ayenew W, Limenh LW, Geremew DT, Worku MC, Tessema TA, et al. Food adulteration: Causes, risks, and detection techniques. SAGE Open Med. 2024;12:20503121241250184.

[4] Borovikov SN, Mukantayev KN, Bulashev AK, Tursunov K, Syzdykova AS. Meat Product Adulteration: Modern Detection Methods and Food Safety Assurance. Herald of science of S. Seifullin KazATU: Vet sci. 2025;1(009);48-62.

[5] Chang L, Fu C, Huang P, Li Y, Liu Y, Lu F. Reliable multiplex real-time PCR method for detecting adulteration in processed beef products. J Food Compos Anal. 2025;143:107595.
[6] Adenuga BM, Biltes R, Villa C, Costa J, Spychaj A, Montowska M, et al. Unravelling red deer (Cervus elaphus) meat adulteration in gourmet foods by quantitative real-time PCR. Food Control. 2025;168:110872.
[7] Alkhalidi AA, Althwani AN. Detecting adulteration in processed meat products from various sources using a multiplex PCR assay targeting cytochrome B genes from cattle, sheep, goat, and chicken. Heath biotechnol biopharma. 2025;8(3):80-94.
[8] Zhao Y, Du X, Liu S, Sun M, Man L, Zhu M, et al. Characterization and Discrimination of Volatile Compounds of Donkey and Horse Meat Based on Gas Chromatography–Ion Mobility Spectrometry. Foods. 2025;14(7):1203.
[9] Hoffmann B, Münch S, Schwägele F, Neusüß C, Jira W. A sensitive HPLC-MS/MS screening method for the simultaneous detection of lupine, pea, and soy proteins in meat products. Food Control. 2017;71:200-209.
[10] Alexandrakis D, Downey G, Scannell AG. Detection and identification of bacteria in an isolated system with near-infrared spectroscopy and multivariate analysis. J Agric Food Chem. 2008;56(10):3431-3437.
[11] Cawthorn DM, Steinman HA, Hoffman LC. A high incidence of species substitution and mislabelling detected in meat products sold in South Africa. Food control. 2013;32(2):440-449.
[12] Aït-Kaddour A, Loudiyi M, Ferlay A, Gruffat, D. Performance of fluorescence spectroscopy for beef meat authentication: Effect of excitation mode and discriminant algorithms Meat Sci. 2018;137:58-66.
[13] Deniz E, Güneş Altuntaş E, Ayhan B, İğci N, Özel Demiralp D, Candoğan, K. Differentiation of beef mixtures adulterated with chicken or turkey meat using FTIR spectroscopy. J Food Process Preserv. 2018;42(10):e13767.
[14] Saleem A, Sahar A, Pasha I, Shahid M. Determination of adulteration of chicken meat into minced beef mixtures using front face fluorescence spectroscopy coupled with chemometric. Food Sci Anim Resour. 2022;42(4):672.
[15] Soyuçok A, Kılıç B, Kılıç GB, Yalçın H. In vitro antimicrobial activity of ginseng extract against Staphylococcus aureus, Salmonella Typhimurium and Listeria monocytogenes and its inhibitory effects on these pathogens in cooked ground beef. Meat Sci. 2024;216: 109559.
[16] Lawrie RA, Ledward DA. Lawrie's meat science, 7th ed. Woodhead Publishing: Abington; 2006.
[17] Sahar A, Boubellouta T, Dufour É. Synchronous front-face fluorescence spectroscopy as a promising tool for the rapid determination of spoilage bacteria on chicken breast fillet. Food Res. Int. 2011;44(1):471-480.
[18] Sidira M, Smaoui S, Varzakas T. Recent proteomics, metabolomics and lipidomics approaches in meat safety, processing and quality analysis. Appl Sci. 2024;14(12):5147.
[19] Aprilia P, Ummami R, Airin CM, Aziz F, Astuti P. Comparison of ELISA and PCR assays for detection of pork adulteration in Halal-labelled beef products. J Food Qual Hazards Control. 2022;9:112-117.
[20] Alamprese C, Amigo JM, Casiraghi E, Engelsen SB. Identification and quantification of turkey meat adulteration in fresh, frozen-thawed and cooked minced beef by FT-NIR spectroscopy and chemometrics. Meat Sci. 2016;121:175-181.
[21] Weng S, Guo B, Tang P, Yin X, Pan F, Zhao J, et al. Rapid detection of adulteration of minced beef using Vis/NIR reflectance spectroscopy with multivariate methods. Spectrochim Acta A Mol Biomol Spectrosc. 2020;230:118005.
[22] Prandi B, Varani M, Faccini A, Lambertini F, Suman M, Leporati A, et al. Species specific marker peptides for meat authenticity assessment: A multispecies quantitative approach applied to Bolognese sauce. Food Control. 2019;97:15-24.
[23] Zuo X, Li Y, Chen X, Chen L, Liu C. Rapid Detection of Adulteration in Minced Lamb Meat Using Vis-NIR Reflectance Spectroscopy. Processes. 2024;12(10):2307.
[24] Chaudhary V, Kajla P, Dewan A, Pandiselvam R, Socol CT, Maerescu CM. Spectroscopic techniques for authentication of animal origin foods. Front Nutr. 2022;9:979205.
[25] Kök S, Atalay S. Determination of the fraud of processed meat products by ELISA. Lahaed. 2018;58(2):95-98.
[26] T.C. Tarım ve Orman Bakanlığı [Internet]. Veteriner Hizmetleri, Bitki Sağlığı, Gıda ve Yem Kanunu (Kanun No: 5996). Resmî Gazete, 27610. 2010 [cited 2025 May 20]. Available from: https://istanbul.tarimorman.gov.tr/Belgeler/SolMenu/RESMIGAZETE2018/5996SAYILIKANUN.pdf
[27] T.C. Tarım ve Orman Bakanlığı [Internet]. Taklit veya tağşiş yapan firmalar listesi. Güvenilir Gıda Bilgi Sistemi. 2025 [cited 2025 May 20]. Available from: https://guvenilirgida.tarimorman.gov.tr/GuvenilirGida/GKD/TaklitVeyaTagsis
[28] Yu Y, Chen W, Zhao D, Zhang H, Chen W, Liu R, et al. Meat species authentication using portable hyperspectral imaging. Front nutr. 2025;12:1577642.

Volume 14, Issue 3, Page 73-89, 2025 https://doi.org/10.46810/tdfd.1610740 Research Article

BİNGÖL UNIVERSITY

Türk Doğa ve Fen Dergisi
Turkish Journal of Nature and Science
www.dergipark.gov.tr/tdfd

Performance Analysis of Four Metaheuristic Algorithms on Benchmark Functions

Sibel ARSLAN[1*], Muhammed Furkan GÜL[2]

[1] Sivas Cumhuriyet University, Faculty of Engineering, Department of Software Engineering, Sivas, Türkiye
[2]Sivas University of Science and Technology, Faculty of Engineering and Natural Sciences, Department of Computer Engineering, Sivas, Türkiye
Sibel ARSLAN ORCID No: 0000-0003-3626-553X
Muhammed Furkan GÜL ORCID No: 0009-0007-0486-0525

**Corresponding author: sibelarslan@cumhuriyet.edu.tr*

(Received: 31.12.2024, Accepted: 15.07.2025, Online Publication: 26.09.2025)

Keywords
Metaheuristics, Artificial rabbit optimization algorithm, African vulture optimization algorithm, Prairie dog optimization algorithm, Genetic algorithm

Abstract: Various metaheuristic algorithms inspired by nature are used to solve optimization problems. With the increasing number of metaheuristics, their performance on problems is gradually improving. In this paper, the performance analysis of the newly proposed metaheuristics Artificial Rabbit Optimization Algorithm (ARO), African Vulture Optimization Algorithm (AVOA), Prairie Dog Optimization Algorithm (PDO) and the well-known Genetic Algorithm (GA) were performed for the first time. ARO is modeled after rabbits' behavioral patterns, such as detour foraging and random hiding. AVOA is developed based on the navigation and competitive behaviors of African vultures. The newly proposed final metaheuristic PDO is inspired by the survival struggle of prairie dogs. As for the popular GA, it is based on survival of the fittest. Unimodal and multimodal test functions were used during the analysis. According to the simulation results, AVOA performed better and generated more successful results compared to the others 22 times in the mean and best values. AVOA was followed by PDO and ARO, proving that the newly proposed metaheuristics will be successful on different problems.

Dört Metasezgisel Algoritmanın Kıyaslama Fonksiyonları Üzerindeki Performans Analizi

Anahtar Kelimeler
Metasezgiseller, Yapay tavşan optimizasyon algoritması, Afrika akbabası optimizasyon algoritması, Çayır köpeği optimizasyon algoritması, Genetik algoritma

Öz: Doğadan ilham alan çeşitli metasezgisel algoritmalar, optimizasyon problemlerini çözmek için kullanılmaktadır. Metasezgisel algoritmaların sayısındaki artışla birlikte, bu algoritmaların problemlerdeki performansları da giderek iyileşmektedir. Bu makalede, yeni önerilen metasezgisel algoritmalar olan Yapay Tavşan Optimizasyon Algoritması (ARO), Afrika Akbaba Optimizasyon Algoritması (AVOA), Çayır Köpeği Optimizasyon Algoritması (PDO) ve iyi bilinen Genetik Algoritma'nın (GA) performans analizleri ilk kez gerçekleştirilmiştir. ARO, tavşanların dolambaçlı beslenme ve rastgele saklanma gibi davranış kalıplarını model alarak geliştirilmiştir. AVOA, Afrika akbabalarının navigasyon ve rekabetçi davranışlarına dayanmaktadır. Yeni önerilen son metasezgisel algoritma PDO ise çayır köpeklerinin hayatta kalma mücadelesinden esinlenilerek geliştirilmiştir. Popüler GA ise en uygun olanın hayatta kalması prensibine dayanır. Analiz sırasında tek modlu (unimodal) ve çok modlu (multimodal) test fonksiyonları kullanılmıştır. Simülasyon sonuçlarına göre, AVOA diğerlerine kıyasla 22 kez ortalama ve en iyi değerlerde daha iyi performans göstermiş ve daha başarılı sonuçlar üretmiştir. AVOA'yı PDO ve ARO takip ederek, yeni önerilen metasezgisel algoritmaların farklı problemlerde başarılı olacağını kanıtlamıştır.

1. INTRODUCTION

Nowadays, the number of metaheuristic algorithms developed inspired by nature is increasing. This increase is due to the fact that metaheuristics are less costly and more effective than traditional approaches. For this reason, they are used in many different fields, especially engineering [1,2]. Metaheuristics used in these areas contribute to the analysis of large data sets, efficient use of resources, improvement of decision-making processes and the solution of many other complex problems. Many popular metaheuristics that contribute to the solution of these complex problems such as Particle Swarm Optimization Algorithm [3], Genetic Algorithm (GA) [4], Artificial Bee Colony Algorithm [5] and Ant Colony Optimization Algorithm [6] are among them. However, newly developed metaheuristics perform better in less time compared to these popular ones [7]. With the increase in performances, determining the best metaheuristic provides important contributions to optimization problems.

The aim of this paper is to compare the performances of the newly proposed metaheuristics, namely Artificial Rabbit Optimization Algorithm (ARO), African Vultures Optimization Algorithm (AVOA), Prairie Dog Optimization Algorithm (PDO), along with the popular metaheuristic GA, using various performance criteria. The motivation for selecting ARO, AVOA, and PDO lies in their novelty and increasing presence in recent metaheuristic research. These algorithms, developed between 2021 and 2023, are inspired by diverse biological systems—rabbits, vultures, and prairie dogs—which offer a wide behavioral spectrum for optimization modeling. Despite promising initial findings in their original proposals, no comprehensive and independent comparison has been conducted under identical test environments. This study aims to address that gap and to evaluate their performance against a well-known algorithm, GA. Other contributions of the paper are as follows:

- To the best of our knowledge, although ARO, AVOA, and PDO have been individually tested in their original studies, this is the first independent work to analyze all three under identical experimental conditions and compare them directly with a common reference algorithm (GA). This provides a more objective assessment of their relative performance.
- The performances of metaheuristics are analyzed with different test functions.
- According to the information obtained from the experiments, AVOA produces the best performance.

In the remainder of the paper is as follows. Section 2 explains information about metaheuristics and their pseudocodes. Section 3 presents the test functions used to analyze the performance of metaheuristics. Additionally, in this section, the parameters of the metaheuristics are given. Section 4 provides simulation results, convergence curves, and t-test results. Finally, Section 5 gives information about the conclusion and future work.

2. MATERIAL AND METHOD

In this section, detailed information about metaheuristic algorithms is given. In order to present the algorithms in a more comprehensive and diverse manner, this study includes pseudocode representations for ARO and AVOA, and flowcharts for GA and PDO. This mixed presentation aims to enhance understanding by offering both algorithmic logic and visual summaries.

2.1. Artificial Rabbit Optimization Algorithm (ARO)

ARO is a metaheuristic based on behavioral models of rabbits [8]. In ARO, the two behaviors that rabbits have are determined according to the energy of the rabbits, and the transition between the behavior is made depending on energy shrink. Initially, the energy levels of the rabbits are high and in order to expand the search space, the rabbits exhibit detour foraging behavior. They do this by selecting grasses in remote areas to prevent predators from finding their nests. Energy shrink occurs when foraging becomes repetitive. When there is enough energy shrink, they switch to random hiding behavior. In order to update their recent position, they build many nests in their territory and aim to hide from predators. They randomly select one of the burrows and complete the random hiding. Energy shrink between detour foraging and random hiding then these two behavioral strategies are described in detail below.

Energy shrink

In the early phases of the iterations, rabbits consistently exhibit detour foraging behavior [8]. However, in the later phases of the iterations they perform random hiding. This intermediate transition is caused by energy shrink and its mathematical model is presented in Equation 1.

$$A(t) = 4\left(1 - \frac{t}{T}\right)\ln\frac{1}{r} \quad (1)$$

where r represents a randomly generated number within the range of 0 to 1. t is the recent number of iterations, while T depicts the total number of iterations.

Detour foraging

Rabbits have a wide field of vision. For this reason, they do not eat food in their habitat to avoid predators detecting their nests [9]. They randomly feed on grasses in remote areas. This behavior is termed detour foraging (exploration). In detour foraging, the ARO helps to avoid local extremes and search globally, as described in Equation 2.

$$\begin{aligned} \vec{v}_i(t+1) &= \vec{x}_j(t) + R \cdot \left(\vec{x}_i(t) - \vec{x}_j(t)\right) + round\left(0.5 \cdot (0.05 + r_1)\right) \cdot n_1, \\ i,j &= 1, \dots, n \text{ and } j \neq i \end{aligned} \quad (2)$$

where $\vec{v}_i$ (t+1) represents the ith rabbit's likely position at time t+1. $\vec{x}_i$ (t) is the ith rabbit's position at time t. n is the rabbit population size. round is rounding to the nearest integer. n_1 depends on the standard normal distribution and is shown in Equation 3. r_1 is a random number from 0 to 1. R is the running operator and is expressed as in Equation 4.

$$n_1 \sim N(0,1) \quad (3)$$

$$R = L \cdot c \quad (4)$$

Equation 5 defines the run length, denoted as L, which signifies the movement speed during detour foraging. c is a mapping vector that can randomly assist the algorithm and is mathematically modeled as in Equations 6-7.

$$L = \left(e - e^{\left(\frac{t-1}{T}\right)^2}\right) \cdot \sin(2\pi r_2) \quad (5)$$

where t and T denote the recent and total number of iterations respectively. r_2 is a random number ranging between 0 and 1.

$$c(k) = \begin{cases} 1 & \text{if } k == g(l) \\ 0 & \text{else} \end{cases} \quad k = 1, \dots, d \text{ and } l = 1, \dots, \lceil r_3 \cdot d \rceil \quad (6)$$

$$g = \text{randperm}(d) \quad (7)$$

where $\lceil \cdot \rceil$ represents the ceiling function, randperm is an integer permutation from 1 to d at random. r_3 is a random number between 0 and 1.

Random hiding

Rabbits can dig different tunnels around their burrows to escape predators [10]. In each iteration, a rabbit digs d tunnels in the search space in each dimension. They also randomly choose one of the tunnels in each dimension to reduce the probability of predation. Mathematical models of random hiding are given in Equations 8-10.

$$\vec{v}_i(t+1) = \vec{x}_i(t) + R \cdot \left(r_4 \cdot \vec{b}_{i,r}(t) - \vec{x}_i(t)\right), i = 1, \dots, n \quad (8)$$

$$g_r(k) = \begin{cases} 1 & \text{if } k == \lceil r_5 \cdot d \rceil \\ 0 & \text{else} \end{cases} \quad k = 1, \dots, d \quad (9)$$

$$\vec{b}_{i,r}(t) = \vec{x}_i(t) + H \cdot g_r \cdot \vec{x}_i(t) \quad (10)$$

where $\vec{b}_{i,r}(t)$ is the randomly chosen hiding place. r_4 and r_5 are random numbers from 0 to 1. $\vec{x}_i(t)$ is the ith rabbit's position at time t. R is the running operator, H is the hiding parameter and d is the problem size. The location update after performing detour foraging or random hiding is given in Equation 11.

$$\vec{x}_i(t+1) = \begin{cases} \vec{x}_i(t) & f(\vec{x}_i(t)) \leq f(\vec{v}_i(t+1)) \\ \vec{v}_i(t+1) & f(\vec{x}_i(t)) > f(\vec{v}_i(t+1)) \end{cases} \quad (11)$$

In cases where the fitness value of the candidate position of the ith rabbit exceeds its recent position, The rabbit will move from where it was and stay at the candidate place that either (Equation 2) or (Equation 8) determines. The ARO pseudocode is presented in Algorithm 1.

Algorithm 1: ARO

```
Generate the initial population randomly and evaluate their fitness
repeat
    for each (rabbit) do
        Calculate the energy shrink using (Equation 1)
        if (energy shrink > 1) then
            Choose a random rabbit
            Calculate the running operator using (Equations 3-7)
            Perform detour foraging using (Equation 2)
            Calculate fitness value
            Update recent individual's position using (Equation 11)
        else
            Generate the nests using (Equation 10)
            Perform random hiding using (Equation 8)
            Calculate fitness value
            Update recent individual's position using (Equation 11)
        end if
        Update the best solution so far
    end for
until (stopping criterion is satisfied)
return the best solution
```

2.2. African Vultures Optimization Algorithm (AVOA)

AVOA is a metaheuristic inspired from the navigation and competition behavior of African vultures [11]. The vultures are divided into two basic groups, each representing a solution. In the algorithm, the fitness value of all solutions is calculated to divide the vultures into groups. The best vulture in the initial group is the first vulture with the highest value. Likewise, the second vulture in the second group is the best vulture in terms of value. Other vultures in the population are used to move or replace these two best vultures.

Vultures are divided into two groups to find food and live in groups. Each group has different foraging and eating abilities. Vultures are prevented from overeating by their tendency to forage and eat for hours. In the metaheuristic, the worst solution is the hungriest and weakest vulture. The other vultures try to get closer to the best vulture by avoiding the worst solution. There are four basic phases in AVOA: Identifying the best vulture in a random group, calculation of hunger rates, exploration and exploitation.

Identifying the best vulture in a random group

The initial population is created, and the solutions' fitness values are calculated. In this phase, the best vulture of the first and second group is selected from the two best solutions, respectively. The other solutions aim to reach the best solutions by moving towards the best two groups.

During each iteration, the population's positioning is adjusted according to their fitness values.

Calculation of the hunger rates

Vultures can fly longer distances when they have high energy after eating their fill [12]. If they're hungry, it means they lack sufficient energy and cannot fly next to a stronger vulture. The hunger rate, which tends to decrease, is given in Equations 12-13.

$$t = h \times \left(\sin^{w}\left(\frac{\pi}{2} \times \frac{iter}{max_{iter}}\right) + \cos\left(\frac{\pi}{2} \times \frac{iter}{max_{iter}}\right) - 1\right) \quad (12)$$

$$F = (2rand_1 + 1) \times z \times \left(1 - \frac{iter}{max_{iter}}\right) + t \quad (13)$$

where, iter and max_{iter} are the recent and total number of iterations respectively. w is a fixed number and decreasing this parameter reduces the probability of starting the exploration. The parameter h is a randomly selected number that can assume values ranging from -2 to 2. Similarly, $rand_1$ is a random number from 0 to 1. F is the hunger rate of vultures. According to the value of z, it is determined whether vultures are hunger or not. If this value is below 0, it indicates the vulture's hunger. If it is above 0, it means that the vulture is fed. In addition, if the hunger rate of the vultures is greater than 1, they start searching for food in different regions and perform the exploration. Otherwise, they move to the exploitation by searching for food near neighboring solutions.

Exploration

Vultures choose two different strategies by searching random areas. They choose strategies based on the parameter p_1 . This parameter should have a value between 0 and 1 and should be evaluated before exploration. The mathematical model of strategy selection is described in Equation 14.

$$P(i+1) = \begin{cases} R(i) - |X \times R(i) - P(i)| \times F & p_1 \geq rand_{P_1} \\ R(i) - F + rand_2 \times \left((u_b - l_b) \times rand_3 + l_b\right) & p_1 < rand_{P_1} \end{cases} \quad (14)$$

where, $R(i)$ is the best vultures and X is the distance the vultures move to protect the food. The rand symbols in the equation are numbers between 0 and 1. u_b and l_b are the boundaries of the search space. The convergence of $rand_3$ to 1 increases the ability to explore different spaces.

Exploitation

If the hunger rate is less than 1, it starts the stage of metaheuristic exploitation. Depending on whether this rate is less than 0.5 or not, this phase is divided into two. If the value is small, vultures compete for food. Two different strategies are selected for each choice with randomly generated values. The selection of strategies is determined by the parameters p_2 and p_3. Vultures have enough energy to search for food during the competition phase and may conflict over food sources. Weaker vultures fly in a spiral pattern and try to take food from stronger ones. This behaviour is given in Equation 15, depending on the parameter p_2.

$$P(i+1) = \begin{cases} |X \times R(i) - P(i)| \times (F + rand_4) - \left(R(i) - P(i)\right) \; if \; p_2 \geq rand_{P_2} \\ R(i) - R(i) \times \left(\frac{P(i)}{2\pi}\right)\left(rand_5 \times \cos\left(P(i)\right) + rand_6 \times \sin\left(P(i)\right)\right) \; if \; p_2 < rand_{P_2} \end{cases} \quad (15)$$

where $P(i)$ represents the recent vector position from which the vulture's distance from the best vultures in two groups is calculated. $R(i)$ denotes one of the two best vultures' position vectors in the last iteration. $rand$ values are numbers between 0 and 1.

In the two stages of the exploration, there are aggressive competitions over the food source. If the hunger rate is less than 0.5, this stage of the phase is started. At the beginning of the stage, a parameter $rand_{P_3}$ is generated between 0 and 1. If this parameter p_3 is greater than or equal, several species of vultures gather on the food source. Otherwise, there is a siege strife among the vultures. The mathematical model for this stage is given in Equation 16. Additionally, the gathering of vultures over the food source is expressed based on Equations 17-18.

$$P(i+1) = \begin{cases} Eq.18 \; if \; p_3 \geq rand_{P_3} \\ Eq.19 \; if \; p_3 < rand_{P_3} \end{cases} \quad (16)$$

$$A_1 = -F \times \frac{\text{BestVulture}_1(i) \times P(i)}{\text{BestVulture}_1(i) - P(i)^2} + \text{BestVulture}_1(\text{i}) \quad (17)$$

$$A_2 = -F \times \frac{\text{BestVulture}_2(i) \times P(i)}{\text{BestVulture}_2(i) - P(i)^2} + \text{BestVulture}_2(\text{i})$$

$$P(i+1) = \frac{A_1 + A_2}{2} \quad (18)$$

where, $\text{BestVulture}_1(\text{i})$ and $\text{BestVulture}_2(\text{i})$ represent the best vultures. F is the hunger rate, P(i) is the recent vulture's position and $\text{P(i} + 1)$ is the position of the vulture in the next iteration.

When the hunger rate is less than 0.5, the leader vultures of the groups remain hungry. Therefore, they lack the

necessary energy to handle the other vultures within the group. However, the remaining vultures also grow more aggressive in their search for food. The leader vultures move in the right different directions. Equation 19 is used to model this movement.

$$P(i+1) = R(i) - F \times LF\ (d) \times |R(i) - P(i)| \tag{19}$$

where d is the problem size and $|R(i) - P(i)|$ is the vulture's distance from among the best vultures in the two groups. To improve the efficiency of AVOA, a Lévy flight [13, 14] is included. The modeling of this flight is given in Equation 20.

$$LF(x) = 0.01 \times \frac{u \times \sigma}{|v|^{\frac{1}{\beta}}}, \sigma = \left(\frac{\Gamma(1+\beta) \times \sin\left(\frac{\pi\rho}{2}\right)}{\Gamma(1+\beta 2) \times \beta \times 2\left(\frac{\beta-1}{2}\right)} \right)^{\frac{1}{\beta}} \tag{20}$$

where u and v are randomly chosen numbers within the range of 0 to 1. The default number value of β is 1.5 and is constant. The AVOA pseudocode algorithm is given in Algorithm 2.

Algorithm 2: AVOA

```
Randomly generate the initial population
repeat
    Calculate fitness values of vultures
    Set the best first position of vulture
    Set the second best position of vulture
    for each (vulture) do
        Choose the best vulture position
        Update hunger rate
        if (hunger rate ≥ 1) then
            if (P1 ≥ rand_P1) then
                Update the position using Equation 14
            else
                Update the position using Equation 14 (part two)
            end if
        end if
        if (hunger rate < 1) then
            if (hunger rate ≥ 0.5) then
                if (P1 ≥ rand_P2) then
                    Update the position using Equation 15
                else
                    Update the position using Equation 15 (part two)
                end if
            else
                if (P1 ≥ rand_P2) then
                    Update the position using Equation 16
                else
                    Update the position using Equation 16 (part two)
                end if
            end if
until (stopping criterion is satisfied)
return the position of the best vulture
```

2.3. Genetic Algorithm (GA)

GA is a metaheuristic algorithm inspired by natural selection and based on survival of the fittest [4]. The algorithm generates the next generation by starting genetic variations and selection processes from a randomly selected initial population. Crossover, mutation and selection operators are used to find the best solution. Problem-specific solutions are customized and encoded as fixed bit strings. Solutions are represented by chromosomes. The first mechanism used in solution improvement, crossover is the replacement of a chromosome or chromosomes passed from generation to generation [15], as shown in Figure 1.

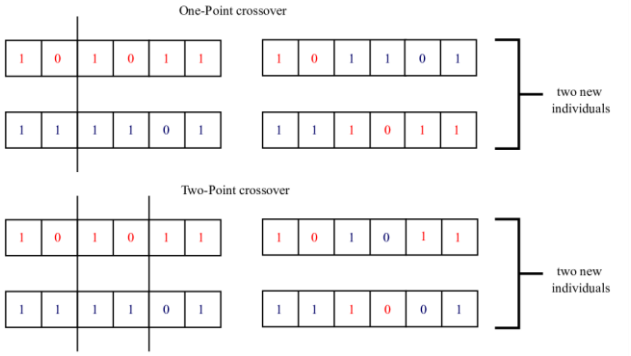

Figure 1. Crossover

In crossover, as seen in Figure 1, there are two different methods. In one-point crossover, a segment is taken from one individual at a one point, and the remaining segment is exchanged with the corresponding segment from the other individual. In two-point crossover, two segments are taken from two different points, and the chromosomes in between are swapped with those of the other individual. Another improvement mechanism, mutation is the replacement of chromosomes that give rise to a gene [16], as shown in Figure 2.

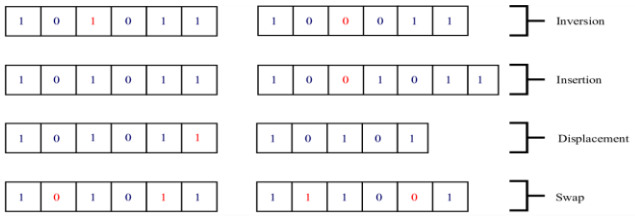

Figure 2. Mutation

Mutation can occur in four different ways: inversion, insertion, displacement, and swap. In inversion, a chromosome's value is reversed. In insertion, a new chromosome is added. Displacement occurs by removing a selected chromosome from its gene sequence. In swap, the positions of two randomly selected chromosomes are exchanged. In GA, the best individual solution is obtained when the termination criterion is met. Additionally, the GA flowchart is given in Figure 3.

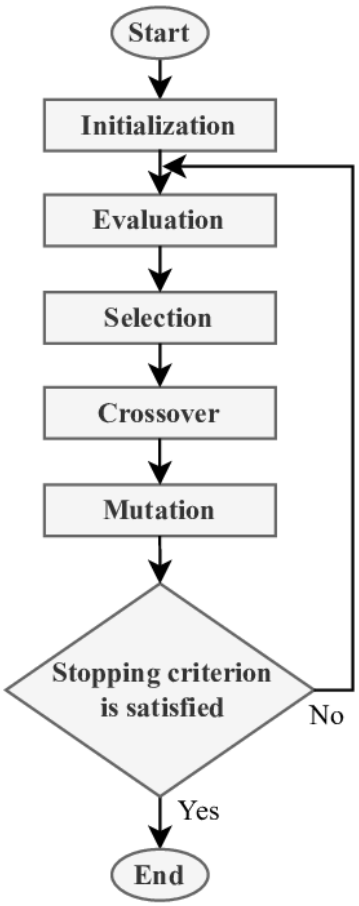

Figure 3. GA flowchart [4]

2.4. Prairie Dog Optimization Algorithm (PDO)

PDO is developed by the survival of prairie dogs and modeling their behavior [17]. In the modeling, their feeding patterns are first used to expand the problem search space. They then look for strategic positions when searching for food. These positions should serve a certain purpose that improves the general functioning of the coterie, the prairie dog community. This purpose enhances exploration, which is the search for new solutions in different regions. After the exploration, the communication skills of prairie dogs against environmental threats play an important role in their ability to prevent predation. The skills enable predators to react differently to different hunting strategies. Reactions carry out the exploitation, which aims to increase fitness to make improvements to existing solutions. The exploration and exploitation are given below.

Exploration

The first strategy for members of the coterie during the exploration is to search for new food sources in the coterie. Prairie dogs are best at catching food sources using Lévy flight movement. They communicate the precise position of food sources to other members by making distinct sounds. Once the food source quality is reached, the best one is selected for food search, and new nests are built based on the food source quality. The position update for the search in the exploration of the metaheuristic is represented in Equation 21. In addition, the Lévy flight movement is as in Equation 20.

$$\begin{aligned} \mathrm{PD}_{i+1,j+1} = {} & \mathrm{GBest}_{i,j} - e\,\mathrm{CBest}_{i,j} * \rho \\ & - \mathrm{CPD}_{i,j} * \\ & * \mathrm{LF}(n) \forall\ \mathrm{iter} < \frac{\mathrm{Max}_{iter}}{4} \end{aligned} \tag{21}$$

where $PD_{i+1,j+1}$ represents the (j + 1)th dimension of the (i + 1)th prairie dog in a coterie. For this experiment, the particular food source alarm, denoted by ρ, is set at 0.1 kHz. Likewise, the second strategy involves evaluating the availability and quality of food sources and assessing the digging strength. New nests are constructed according to the digging strength, a parameter intentionally reduced with each successive iteration. This helps to limit the number of nests that can be constructed. The position update for nest building is given in Equation 22.

$$\begin{aligned} \mathrm{PD}_{i+1,j+1} = {} & \mathrm{GBest}_{i,j} * \mathrm{rPD} * \mathrm{DS} \\ & * \mathrm{LF(n)} \forall \frac{\mathrm{Max}_{\mathrm{iter}}}{4} \\ & \leq \mathrm{iter} < \frac{\mathrm{Max}_{\mathrm{iter}}}{2} \end{aligned} \tag{22}$$

where rPD is a random solution's position. When $\mathrm{GBest}_{i,j}$ represents the globally best solution obtained so far, $e\mathrm{CBest}_{i,j}$ evaluates the impact of the recent best solution as shown in Equation 23. DS represents the digging strength of a random value range group determined by Equation 25, which relies on food source quality.

$$\begin{aligned} & eCBest_{i,j} \\ & = Best_{i,j} * \Delta + \frac{PD_{i,j} * mean\left(PD_{n,m}\right)}{\mathrm{GBest}_{i,j} * \left(UB_j - LB_j\right) + \Delta} \end{aligned} \tag{23}$$

where UB_j and LB_j represent the boundaries for the jth dimension in the optimization problem., respectively. $CPD_{i,j}$ is the random cumulative effect of the whole prairie dogs in the population and is defined in Equation 24.

$$CPD_{i,j} = \frac{\mathrm{GBest}_{i,j} - rPD_{i,j}}{\mathrm{GBest}_{i,j} + \Delta} \tag{24}$$

$$DS = 1.5 \times r \times \left(1 - \frac{iter}{Max_{iter}}\right)^{\left(2\frac{\mathrm{iter}}{Max_{iter}}\right)} \tag{25}$$

where r is a parameter that takes the value -1 or 1. Δ represents a small number explaining existing differences. $iter$ and Max_{iter} represent the recent and total iteration numbers, respectively.

Exploitation

Prairie dogs use vocalizations or signals for various situations, ranging from predator dangers to availability of food [18]. Communication plays an essential part in prairie dogs' ability to meet their nutritional needs and protect against predation. They can also convey

distinctions in the quality of food sources, predator presence, and hunting behaviors. Various communication skills in prairie dogs facilitate the discovery of improved or nearly ideal solutions. These solutions result in approaching a certain position or a promising position in the case of the PDO application, where more searches are conducted. The aim of the exploitation mechanisms used in PDO is to intensively explore promising areas identified during the exploration. The two strategies for this phase are Equations 26-27.

$$PD_{i+1,j+1} = \text{GBest}_{i,j} - e\,\text{CBest}_{i,j} * \varepsilon - CPD_{i,j} * \text{rand}\ \forall \frac{\text{Max}_{\text{iter}}}{2} \leq \text{iter} < 3\frac{\text{Max}_{\text{iter}}}{4} \quad (26)$$

$$PD_{i+1,j+1} = \text{GBest}_{i,j} * PE * \text{rand}\ \forall 3\frac{\text{Max}_{\text{iter}}}{4} \leq \text{iter} < \text{Max}_{\text{iter}} \quad (27)$$

where $PD_{i+1,j+1}$ represents the (j + 1)th dimension of the (i + 1)th prairie dog. ε is a little number representing food source quality. PE denotes the predator effect modeled by Equation 28 and rand indicates a number between 0 and 1, which is random.

$$PE = 1.5 \times \left(1 - \frac{iter}{Max_{\text{iter}}}\right)^{\left(2\frac{iter}{Max_{iter}}\right)} \quad (28)$$

where iter and Max_{iter} are the recent and total number of iterations, respectively. The flowchart of the PDO is given in Figure 4.

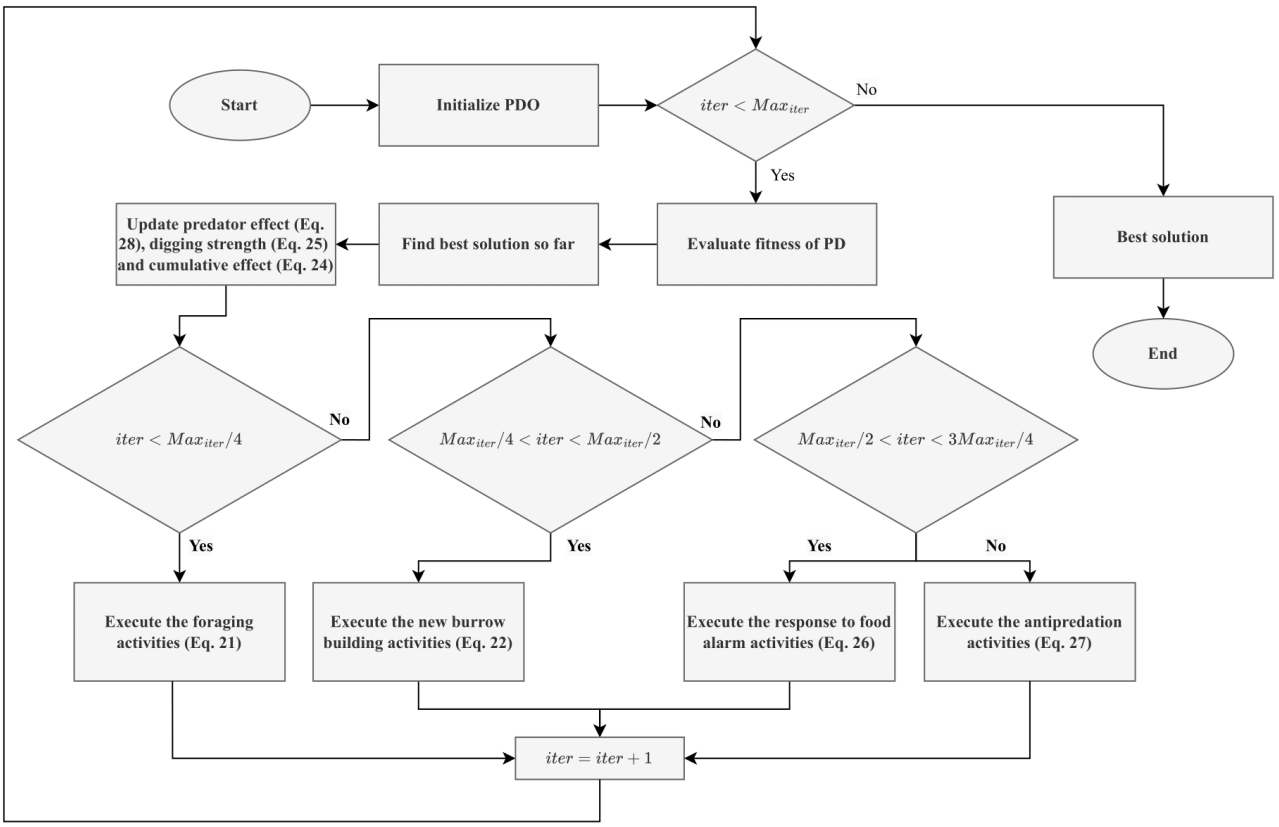

Figure 4. PDO flowchart [17]

3. EXPERIMENTAL DESIGN

In this section, the parameters of the metaheuristics and the test functions to be used in comparisons are given.

3.1. Parameters

Each metaheuristic has its own parameter and is given in Table 1. ARO does not require any algorithm-specific control parameters, as stated by Wang et al. [8]. Therefore, it is not listed in this table. p_1, p_2, p_3 are the parameters for selecting strategies in the exploration and exploitation. The parameters L represents the probabilities associated with the selection of the best vulture. w is the parameter whether the exploration and exploitation will be terminated. p_c gives the crossover probability and P_m represents the probability of mutation. ρ is the food source alarm parameter. ε is the food source quality parameter. Additionally, Δ is individual prairie dog difference.

3.2. Test functions

In this paper, 8 different test functions were used to compare metaheuristics. Among the functions presented in Table 2, F_1, F_2, F_3 and F_4 are unimodal, F_5, F_6, F_7 and F_8 are multimodal. In addition, F_{min} represents the optimum value and the range represents the boundaries of the search space of the functions. The dimension value for all functions is taken as 10, 30, 50 respectively. Furthermore, the plots of the functions are given in Figure 5.

Table 1. Parameters of metaheuristics

Metaheuristic	Parameter	Value
AVOA	p_1	0.6
	p_2	0.4
	p_3	0.6
	L_1	0.8
	L_2	0.2
	w	2.5
GA	p_c	0.80
	P_m	0.20
PDO	ρ	0.1
	ε	2.2204E-16
	Δ	0.005
All metaheuristics	Population size	50
	Max. iterations	1000

A total of 8 benchmark functions were selected to ensure a balanced and representative evaluation of the algorithms' capabilities. Four unimodal functions were included to assess the exploitation performance, i.e., the algorithms' ability to converge quickly to a single global optimum. Four multimodal functions were chosen to evaluate exploration performance, reflecting the ability to escape local optima and explore the solution space broadly. Selecting 4 functions from each category also helps maintain computational efficiency while allowing statistically meaningful analysis across different dimensions.

Table 2. Test functions

Function	Dimension	Range	F_{min}
$F_1(x) = \sum_{i=1}^{n} x_i^2$	10,30,50	[-100,100]	0
$F_2(x) = \sum_{i=0}^{n} \lvert x_i \rvert + \prod_{i=0}^{n} \lvert x_i \rvert$	10,30,50	[-10,10]	0
$F_3(x) = \sum_{i=1}^{n-1} [100(x_i - x_{i+1})^2 + (1 - x_i)^2]$	10,30,50	[-30,30]	0
$F_4(x) = \sum_{i=1}^{n-1} = \sum_{i=1}^{n} ([x_i - 0.5])^2$	10,30,50	[-100,100]	0
$F_5(x) = 10 + \sum_{i=1}^{n} \left(x_i^2 - 10\cos(2\pi x_i)\right)$	10,30,50	[-5.12,5,12]	0
$F_6(x) = -a\exp\left(-0.02\sqrt{n^{-1}\sum_{i=1}^{n} x_i^2}\right) - \exp\left(n^{-1}\sum_{i=1}^{n}\cos(2\pi x_i)\right) + a + e, a = 20$	10,30,50	[-32,32]	0
$F_7(x) = 1 + \frac{1}{4000}\sum_{i=1}^{n} x_i^2 - \prod_{i=1}^{n}\cos\left(\frac{x_i}{\sqrt{i}}\right)$	10,30,50	[-600,600]	0
$F_8(x) = 0.1(\sin^2(3\pi x_1) + \sum_{i=1}^{n}(x_i - 1)^2[1 + \sin^2(3\pi x_i + 1)] + (x_n - 1)^2 1 + \sin^2(2\pi x_n)) + \sum_{i=1}^{n} u(x_i, 5,100,4)$	10,30,50	[-50,50]	0

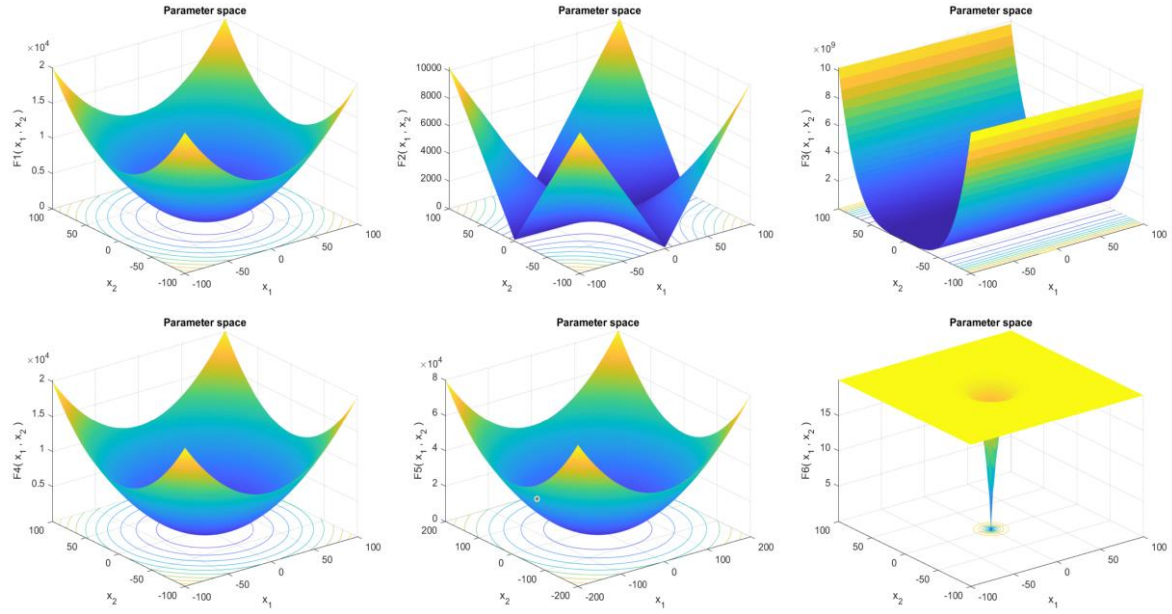

Figure 5. Test functions (F_1- F_8)

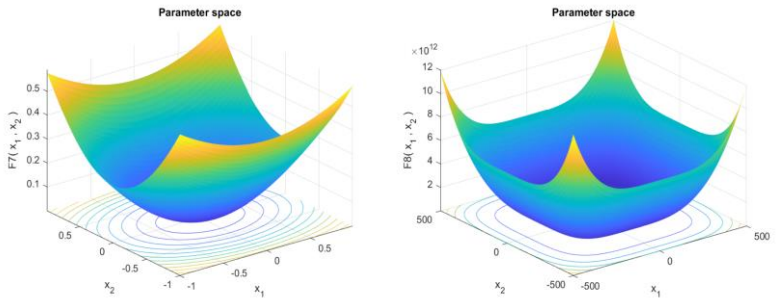

Figure 5. Test functions (F_1- F_8) (continued)

3.3. Engineering problems

In this study, three well-known engineering design problems are investigated: pressure vessel design, tension/compression spring design, and three-bar truss design. This section presents the mathematical formulation of each problem in detail.

3.3.1. Pressure Vessel Design

In this engineering design problem, the goal is to minimize the total cost associated with constructing a cylindrical pressure vessel. The design involves four decision variables: the shell thickness ($z_1 = T_s$), the head thickness ($z_2 = T_h$), the inner radius of the vessel ($z_3 = r$), and the length of the cylindrical section without the head ($z_4 = L$).

The objective function, which represents the cost, is subject to four nonlinear constraints related to structural and volume requirements. The mathematical representation of the problem is given below:

Design vector: $\vec{z} = [z_1, z_2, z_3, z_4] = [T_s, T_h, r, L]$
Objective function:

$$f(\vec{z}) = 1.7781 z_2 z_3^3 + 3.1661 z_1^2 z_4 + 19.84 z_1^2 z_3 + 0.6224 z_1 z_3 z_4$$

Constraints:

$$g_1(\vec{z}) = -z_1 + 0.0193 z_3 \le 0$$

$$g_2(\vec{z}) = -z_3 + 0.00954 z_3 \le 0$$

$$g_3(\vec{z}) = -\pi z_3^2 z_4 - \frac{4}{3}\pi z_3^3 + 1{,}296{,}000 \le 0$$

$$g_4(\vec{z}) = z_4 - 240 \le 0$$

Variable bounds:

$$0 \le z_1, z_2 \le 99, 10 \le z_3, z_4 \le 200$$

This formulation ensures that the structural integrity and volume constraints are met while minimizing material and manufacturing costs.

3.3.2. Tension/Compression Spring Design

This optimization problem focuses on minimizing the weight of a tension or compression spring. The design involves three key variables: the wire diameter ($z_1 = d$), the mean coil diameter ($z_2 = D$), and the number of active coils ($z_3 = N$). These parameters determine the physical structure of the spring.

The objective is to reduce the spring's weight while ensuring it satisfies several mechanical constraints, including limits on deflection, shear stress, and surge frequency. The mathematical formulation of the problem is as follows:

Design vector: $\vec{z} = [z_1, z_2, z_3] = [d, D, N]$
Objective function:

$$f(\vec{z}) = (z_3 + 2) z_2 z_1^2$$

Constraints:

$$g_1(\vec{z}) = 1 - \frac{z_2^3 z_3}{71785 z_1^4} \le 0$$

$$g_2(\vec{z}) = \frac{1}{5108 z_1^2} + \frac{4z_2^2 - z_1 z_2}{12566(z_2 z_1^3 - z_1^4)} \le 0$$

$$g_3(\vec{z}) = 1 - \frac{140.45 z_1}{z_2^2 z_3} \le 0$$

$$g_4(\vec{z}) = \frac{z_1 + z_2}{1.5} - 1 \le 0$$

This formulation ensures that the spring design is both lightweight and structurally feasible under mechanical and dynamic load conditions.

3.3.3. The Three-Bar Truss Design Problem

This structural optimization problem aims to minimize the total weight of a simple planar truss system subjected to external loading. The design involves two decision variables: the cross-sectional areas of two different truss elements, denoted as $x_1 = A_1$ and $x_2 = A_2$. These parameters directly affect the truss's weight and its mechanical behavior under stress. The objective function is defined as a function of the material length and the cross-sectional areas, while the design is subject to multiple nonlinear constraints, including limits on deflection, buckling, and maximum allowable stress. These constraints ensure the structural integrity of the truss under given loading conditions. The mathematical formulation is expressed as follows:

Design vector: $\vec{X} = [x_1, x_2] = [A_1, A_2]$
Objective function:

$$f(\vec{X}) = \left(2\sqrt{2}x_1 + x_2\right) \times L$$

Constraints:

$$g_1(\vec{X}) = \frac{\sqrt{2}x_1 + x_2}{\sqrt{2}x_1^2 + 2x_1 x_2} P - \sigma \le 0$$

$$g_2(\vec{X}) = \frac{x_2}{\sqrt{2}x_1^2 + 2x_1 x_2} P - \sigma \le 0$$

$$g_3(\vec{X}) = \frac{1}{\sqrt{2}x_2 + x_1} P - \sigma \le 0$$

Variable bounds: $0 < x_1, x_2 \le 1$

where: $L = 100$ cm (length of each truss member), $P = 2\text{kN/cm}^2$ (applied load), $\sigma = 2\text{kN/cm}^2$ (maximum allowable stress).

This problem is widely used in the literature to test the effectiveness of optimization algorithms under multi-constraint structural design scenarios, as it combines weight minimization with critical mechanical limitations.

4. Result and Discussion

In order to provide a more comprehensive and structured evaluation of the metaheuristic algorithms, this section is divided into four subsections. First, the simulation results of the test functions are analyzed in terms of mean, best, and worst values. Then, the convergence behaviors of the algorithms are investigated by plotting convergence curves for different dimensions. In the third subsection, a statistical evaluation is conducted using a one-tailed t-test to determine whether the observed performance differences are significant. Finally, a new subsection is introduced to analyze the computational time and complexity of the algorithms. This addition directly addresses reviewer comments regarding the importance of computational cost in real-world applications.

4.1. Benchmark Function Results

In this paper, metaheuristics were run independently 30 times. MATLAB R2022b platform was used for performance analysis of metaheuristics. Simulations were implemented on a machine with AMD Ryzen 5 3500X CPU, 3.6 GHz speed and 16 GB RAM. Simulation results of the test functions are given in Tables 3, 4 and 5, respectively. The mean, standard deviation, best and worst results of all functions are presented in these tables. Additionally, the metaheuristics with the lowest mean and best value are bolded.

Table 3. Simulation results of test functions for dim = 10

Functions	Algorithms	ARO	AVOA	GA	PDO
F_1	**Mean**	2.99E-141	**0.00E+00**	2.04E+03	**0.00E+00**
	Std	1.44E-140	0.00E+00	5.17E+02	0.00E+00
	Best	2.56E-152	**0.00E+00**	8.01E+02	**0.00E+00**
	Worst	8.03E-140	0.00E+00	2.83E+03	0.00E+00
F_2	**Mean**	5.71E-74	**0.00E+00**	1.07E+01	**0.00E+00**
	Std	2.41E-73	0.00E+00	1.85E+00	0.00E+00
	Best	3.36E-82	**0.00E+00**	6.44E+00	**0.00E+00**
	Worst	1.33E-72	0.00E+00	1.38E+01	0.00E+00
F_3	**Mean**	1.36E+00	**4.81E-06**	1.78E+04	4.28E+00
	Std	1.80E+00	6.22E-06	3.76E+03	3.65E+00
	Best	5.94E-06	**4.81E-10**	1.03E+04	6.35E-02
	Worst	4.34E+00	2.03E-05	2.57E+04	9.00E+00
F_4	**Mean**	1.71E-20	1.53E-16	2.24E+03	**2.97E-30**
	Std	3.60E-20	2.02E-16	5.87E+02	1.18E-29
	Best	4.33E-24	5.01E-18	9.15E+02	**3.08E-33**
	Worst	1.8E-19	8.67E-16	3.20E+03	6.43E-29
F_5	**Mean**	**0.00E+00**	**0.00E+00**	4.99E+02	**0.00E+00**
	Std	0.00E+00	0.00E+00	6.29E+00	0.00E+00
	Best	**0.00E+00**	**0.00E+00**	4.80E+02	**0.00E+00**
	Worst	0.00E+00	0.00E+00	5.08E+02	0.00E+00
F_6	**Mean**	**4.44E-16**	**4.44E-16**	1.35E+01	**4.44E-16**
	Std	0.00E+00	0.00E+00	1.27E+00	0.00E+00
	Best	**4.44E-16**	**4.44E-16**	1.05E+01	**4.44E-16**
	Worst	4.44E-16	4.44E-16	1.53E+01	4.44E-16
F_7	**Mean**	**0.00E+00**	**0.00E+00**	2.09E+01	**0.00E+00**
	Std	0.00E+00	0.00E+00	5.58E+00	0.00E+00
	Best	**0.00E+00**	**0.00E+00**	1.25E+01	**0.00E+00**
	Worst	0.00E+00	0.00E+00	3.07E+01	0.00E+00
F_8	**Mean**	**2.43E-18**	1.83E-14	1.12E+06	7.48E-01
	Std	1.22E-17	2.53E-14	7.49E+05	3.70E-01
	Best	**8.52E-25**	5.77E-16	1.07E+05	1.97E-02
	Worst	6.82E-17	1.16E-13	2.85E+06	1.00E+00

When all simulation results are evaluated, AVOA and PDO reach the optimum value in F_1, F_2, F_5 and F_7, while ARO reaches the optimum value in F_5 ve F_7. ARO follows AVOA and PDO with very small differences in F_1 ve F_2 where it does not reach an optimum value. GA, on the other hand, did not achieve the optimum value in any function and was the worst performing metaheuristic. In F_6 function, the newly proposed metaheuristics performed the same. In the simulation results of dimension 10, AVOA has the best and lowest mean values in F_3, PDO in F_4 and ARO in F_8. In the other dimensions, AVOA performs better in these functions. In dimension 10, the new metaheuristics have the largest difference in F_8, with an approximate value of 1.97E-02. For dimension 30, the biggest difference in the best values that the GA has is in F_8 and is about 7.37E+07. In dimension 50, the GA has the largest difference of 1.14E+11 (F_2) and 6.53E+08 (F_8) in the means and best values for all functions.

Table 4. Simulation results of test functions for dim = 30

Functions	Algorithms	ARO	AVOA	GA	PDO
F_1	**Mean**	9.07E-124	**0.00E+00**	3.24E+04	**0.00E+00**
	Std	4.96E-123	0.00E+00	2.85E+03	0.00E+00
	Best	1.05E-143	**0.00E+00**	2.64E+04	**0.00E+00**
	Worst	2.72E-122	0.00E+00	3.69E+04	0.00E+00
F_2	**Mean**	2.74E-70	**0.00E+00**	1.01E+03	**0.00E+00**
	Std	6.50E-70	0.00E+00	1.66E+03	0.00E+00
	Best	6.75E-76	**0.00E+00**	8.76E+01	**0.00E+00**
	Worst	3.04E-69	0.00E+00	6.34E+03	0.00E+00
F_3	**Mean**	1.67E+00	**1.83E-06**	3.63E+05	6.80E+00
	Std	6.33E+00	1.98E-06	3.81E+04	1.05E+01
	Best	1.75E-04	**4.94E-08**	2.91E+05	3.24E-01
	Worst	2.52E+01	7.63E-06	4.39E+05	2.90E+01
F_4	**Mean**	1.86E-06	**1.64E-10**	3.36E+04	3.46E+00
	Std	1.63E-06	1.21E-10	2.68E+03	2.08E+00
	Best	4.46E-08	**2.85E-11**	2.71E+04	1.60E-01
	Worst	5.60E-06	5.35E-10	3.95E+04	7.25E+00
F_5	**Mean**	**0.00E+00**	**0.00E+00**	4.65E+03	**0.00E+00**
	Std	0.00E+00	0.00E+00	1.42E+01	0.00E+00
	Best	**0.00E+00**	**0.00E+00**	4.62E+03	**0.00E+00**
	Worst	0.00E+00	0.00E+00	4.68E+03	0.00E+00
F_6	**Mean**	**4.44E-16**	**4.44E-16**	1.93E+01	**4.44E-16**
	Std	0.00E+00	0.00E+00	2.07E-01	0.00E+00
	Best	**4.44E-16**	**4.44E-16**	1.89E+01	**4.44E-16**
	Worst	4.44E-16	4.44E-16	1.96E+01	4.44E-16
F_7	**Mean**	**0.00E+00**	**0.00E+00**	3.00E+02	**0.00E+00**
	Std	0.00E+00	0.00E+00	2.58E+01	0.00E+00
	Best	**0.00E+00**	**0.00E+00**	2.44E+02	**0.00E+00**
	Worst	0.00E+00	0.00E+00	3.40E+02	0.00E+00
F_8	**Mean**	7.39E-04	**4.80E-10**	2.38E+08	2.93E+00
	Std	2.79E-03	3.05E-10	5.42E+07	1.44E-01
	Best	5.88E-08	**1.47E-10**	7.37E+07	2.44E+00
	Worst	1.10E-02	1.39E-09	3.23E+08	3.00E+00

Table 5. Simulation results of test functions for dim = 50

Functions	Algorithms	ARO	AVOA	GA	PDO
F_1	**Mean**	8.80E-122	**0.00E+00**	7.70E+04	**0.00E+00**
	Std	3.21E-121	0.00E+00	4.59E+03	0.00E+00
	Best	2.21E-137	**0.00E+00**	6.71E+04	**0.00E+00**
	Worst	1.56E-120	0.00E+00	8.48E+04	0.00E+00
F_2	**Mean**	2.10E-66	**0.00E+00**	1.14E+11	**0.00E+00**
	Std	8.24E-66	0.00E+00	3.03E+11	0.00E+00
	Best	8.95E-75	**0.00E+00**	2.11E+06	**0.00E+00**
	Worst	4.14E-65	0.00E+00	1.40E+12	0.00E+00
F_3	**Mean**	2.18E-02	**4.28E-06**	9.71E+05	1.81E+01
	Std	2.05E-02	3.63E-06	6.27E+04	2.01E+01
	Best	3.19E-03	**2.06E-07**	8.13E+05	1.14E+00
	Worst	9.02E-02	1.85E-05	1.08E+06	4.90E+01
F_4	**Mean**	2.28E-04	**1.83E-08**	7.75E+04	7.52E+00
	Std	1.03E-04	1.26E-08	3.44E+03	2.52E+00
	Best	7.22E-05	**4.59E-09**	6.91E+04	2.83E+00
	Worst	4.12E-04	6.22E-08	8.30E+04	1.23E+01
F_5	**Mean**	**0.00E+00**	**0.00E+00**	1.28E+04	**0.00E+00**
	Std	0.00E+00	0.00E+00	1.54E+01	0.00E+00
	Best	**0.00E+00**	**0.00E+00**	1.28E+04	**0.00E+00**
	Worst	0.00E+00	0.00E+00	1.29E+04	0.00E+00
F_6	**Mean**	**4.44E-16**	**4.44E-16**	2.00E+01	**4.44E-16**
	Std	0.00E+00	0.00E+00	9.99E-02	0.00E+00
	Best	**4.44E-16**	**4.44E-16**	1.98E+01	**4.44E-16**
	Worst	4.44E-16	4.44E-16	2.02E+01	4.44E-16
F_7	**Mean**	**0.00E+00**	**0.00E+00**	6.69E+02	**0.00E+00**
	Std	0.00E+00	0.00E+00	5.36E+01	0.00E+00
	Best	**0.00E+00**	**0.00E+00**	5.25E+02	**0.00E+00**
	Worst	0.00E+00	0.00E+00	7.43E+02	0.00E+00
F_8	**Mean**	6.28E-03	**2.11E-09**	8.65E+08	4.85E+00
	Std	1.93E-02	1.98E-09	9.42E+07	7.08E-01
	Best	1.32E-05	**1.07E-10**	6.53E+08	1.13E+00
	Worst	9.74E-02	8.32E-09	1.00E+09	5.00E+00

Table 6. Metaheuristics total rank

Metaheuristic	Best	Mean
ARO	10	10
AVOA	**22**	**22**
GA	0	0
PDO	16	16

The numbers of providing the best and mean result in terms of metaheuristics in all simulation results are given in Table 6. According to the table, in terms of overall success, the best metaheuristic is AVOA, followed by PDO, ARO, and GA, respectively. The most successful values are bolded in the table. AVOA achieved 6 more best results than the closest PDO. Among the new proposed ones, ARO seems to be the most unsuccessful, but it produced very close values compared to the others.

4.2. Convergence curves of functions

The convergence curve is a graph that shows how quickly or accurately a mathematical or computational process progresses towards a specific goal or outcome [19]. The convergence plots of metaheuristics on test functions for dimensions 10, 30, and 50 are provided in Figures 6-7.

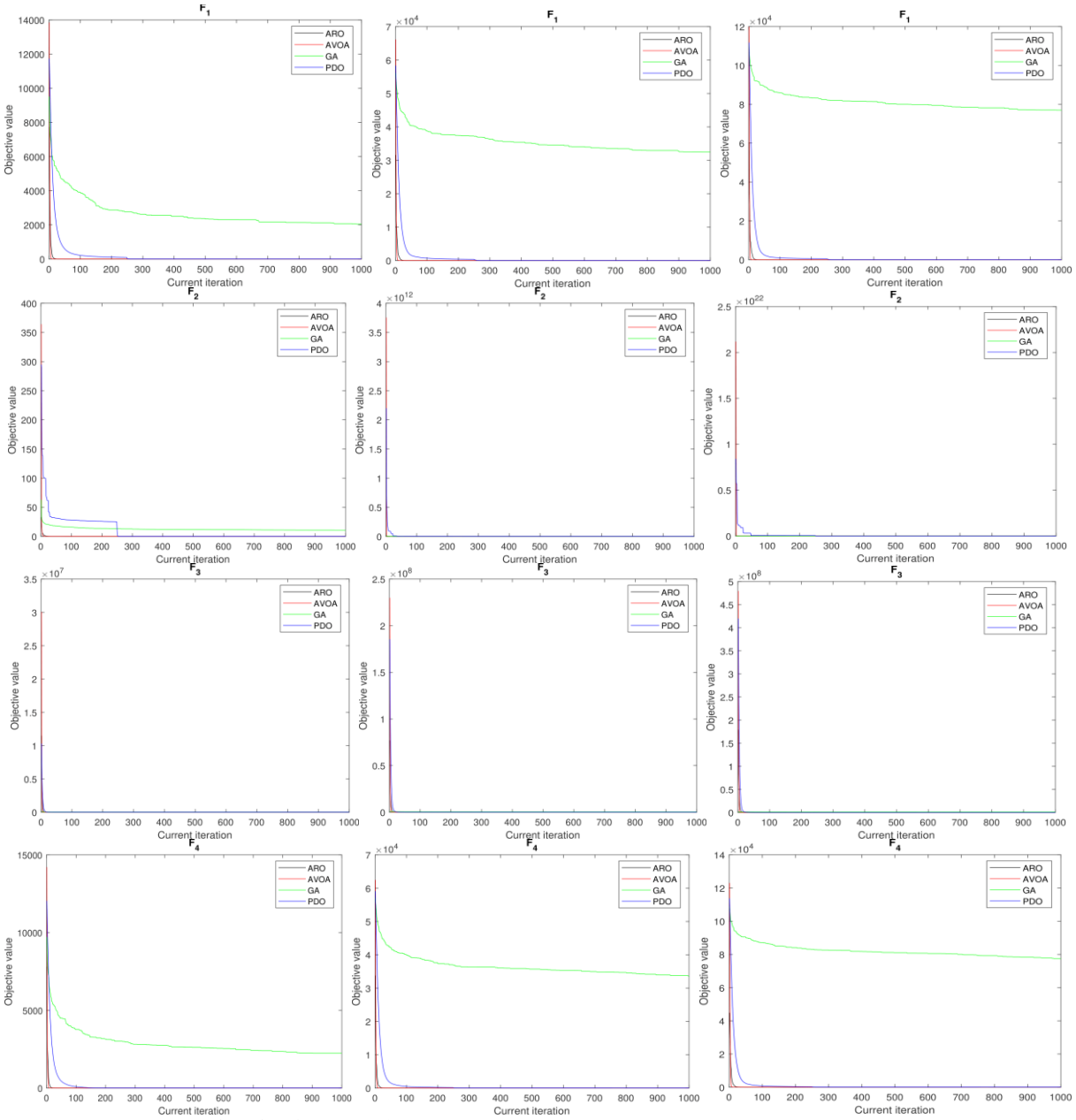

Figure 6. Convergence curves of test functions (F_1 - F_4)

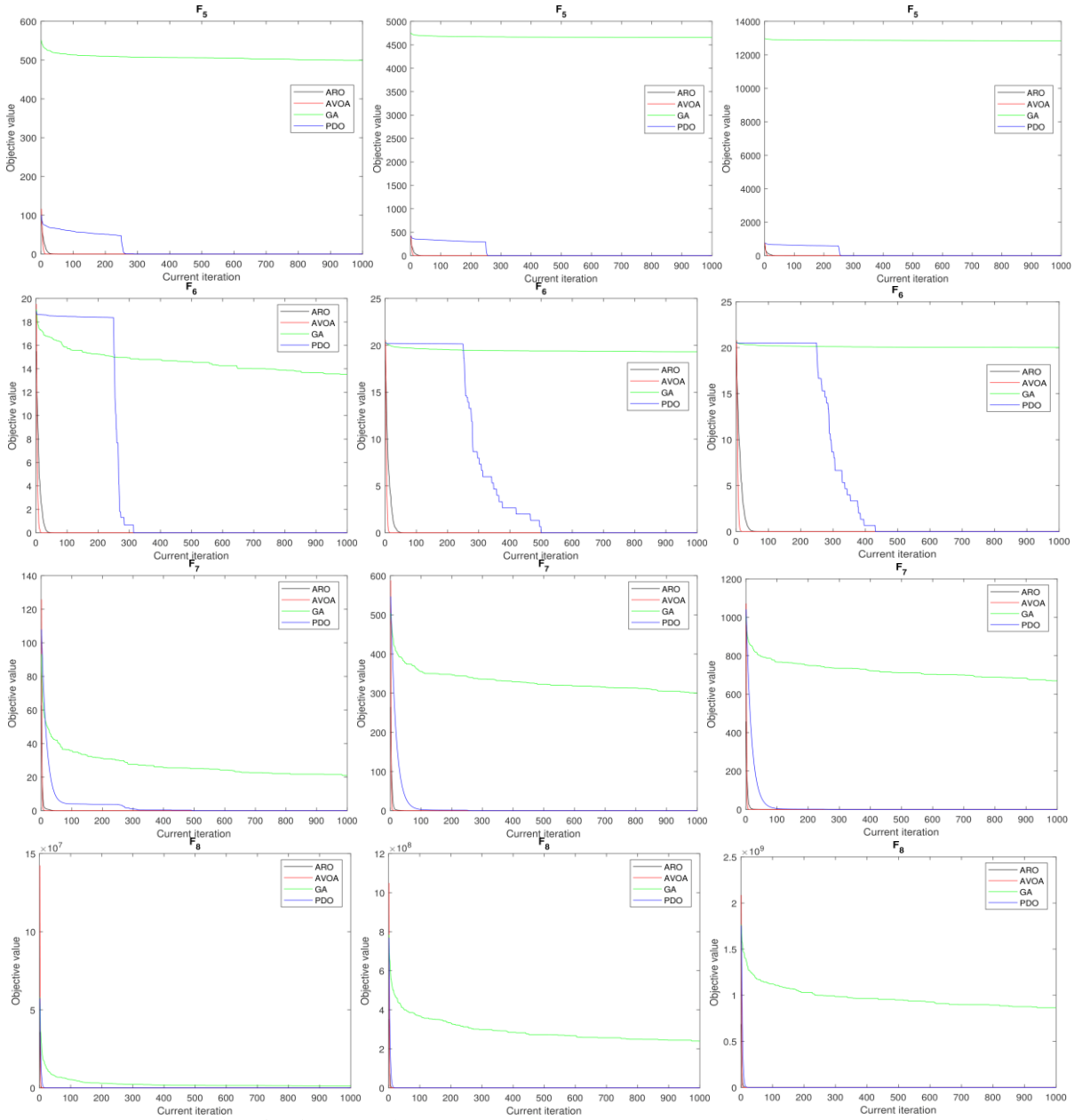

Figure 7. Convergence curves of test functions (F_5 - F_8)

AVOA showed faster convergence for each dimension in all functions. AVOA is followed by ARO. Even though PDO shows slower convergence than ARO, it has better performance in simulation results as seen in Table 6. AVOA and PDO produced the same values after a certain iteration for all dimensions in F_1, F_2, F_5, F_6, and F_7. Similarly, ARO terminated by producing the same values after a certain iteration for all dimensions in F_5, F_6, and F_7. Additionally, the convergence speed of the metaheuristics became slower as the dimension increased. In contrast to the newly proposed metaheuristics, GA performed worse and showed less convergence.

4.3. t-test result

The t-test is a statistical method used to determine whether there is a significant difference between the means of two groups [20, 21]. In this study, a one-tailed t-test was performed on the results of the metaheuristic simulations with a 5% significance level ($\alpha = 0.05$). A result where $h = 1$ and $p < 0.05$ indicates that the metaheuristic algorithm on the right side of the pairwise comparison outperformed the other with statistical significance.

The detailed p-values and h-values for each function and dimension are provided in Tables 7, 8, and 9. However, it is also crucial to interpret the practical implications of these statistical differences in terms of algorithm performance.

Table 7. t-test results (dim=10)

Functions	GA-ARO		GA-AVOA		GA-PDO		ARO-AVOA		ARO-PDO		PDO-AVOA	
	p	h	p	h	p	h	p	h	p	h	p	h
F_1	9.29E-20	**1**	9.29E-20	**1**	9.29E-20	**1**	1.40E-01	0	1.40E-01	0	-	-
F_2	2.13E-24	**1**	2.13E-24	**1**	2.13E-24	**1**	1.10E-01	0	1.10E-01	0	-	-
F_3	6.03E-22	**1**	6.02E-22	**1**	6.01E-22	**1**	1.64E-04	**1**	1.00E+00	**1**	2.58E-07	**1**
F_4	2.42E-19	**1**	2.42E-19	**1**	2.42E-19	**1**	1.00E+00	0	7.90E-03	**1**	1.00E+00	0
F_5	3.65E-57	**1**	3.65E-57	**1**	3.65E-57	**1**	-	-	-	-	-	-
F_6	5.92E-32	**1**	5.92E-32	**1**	5.92E-32	**1**	-	-	-	-	-	-
F_7	4.06E-19	**1**	4.06E-19	**1**	4.06E-19	**1**	-	-	-	-	-	-
F_8	2.33E-09	**1**	2.33E-09	**1**	2.33E-09	**1**	1.00E+00	0	1.00E+00	0	3.12E-12	**1**

Table 8. t-test results (dim=30)

Functions	GA-ARO		GA-AVOA		GA-PDO		ARO-AVOA		ARO-PDO		PDO-AVOA	
	p	h	p	h	p	h	p	h	p	h	p	h
F_1	1.00E-32	**1**	1.00E-32	**1**	1.00E-32	**1**	1.60E-01	0	1.60E-01	0	-	-
F_2	1.20E-03	**1**	1.20E-03	**1**	1.20E-03	**1**	1.00E-02	**1**	1.00E-02	**1**	-	-
F_3	1.63E-30	**1**	1.63E-30	**1**	1.63E-30	**1**	7.97E-02	0	9.99E-01	0	6.51E-04	**1**
F_4	5.65E-34	**1**	5.65E-34	**1**	5.65E-34	**1**	4.06E-07	**1**	1	0	2.46E-10	**1**
F_5	2.17E-74	**1**	2.17E-74	**1**	2.17E-74	**1**	-	-	-	-	-	-
F_6	9.44E-59	**1**	9.44E-59	**1**	9.44E-59	**1**	-	-	-	-	-	-
F_7	4.83E-33	**1**	4.83E-33	**1**	4.83E-33	**1**	-	-	-	-	-	-
F_8	5.24E-21	**1**	5.24E-21	**1**	5.24E-21	**1**	7.85E-02	0	1	0	4.70E-40	**1**

Table 9. t-test results (dim=50)

Functions	GA-ARO		GA-AVOA		GA-PDO		ARO-AVOA		ARO-PDO		PDO-AVOA	
	p	h	p	h	p	h	p	h	p	h	p	h
F_1	1.31E-37	**1**	1.31E-37	**1**	1.31E-37	**1**	7.18E-02	0	7.18E-02	0	-	-
F_2	2.42E-02	**1**	2.42E-02	**1**	2.42E-02	**1**	9.00E-02	0	9.00E-02	0	-	-
F_3	1.80E-36	**1**	1.80E-36	**1**	1.80E-36	**1**	1.31E-06	**1**	1	0	1.55E-05	**1**
F_4	2.55E-41	**1**	2.55E-41	**1**	2.56E-41	**1**	3.85E-13	**1**	1	0	2.00E-16	**1**
F_5	3.36E-72	**1**	3.36E-72	**1**	3.36E-72	**1**	-	-	-	-	-	-
F_6	6.55E-68	**1**	6.55E-68	**1**	6.55E-68	**1**	-	-	-	-	-	-
F_7	6.50E-34	**1**	6.50E-34	**1**	6.50E-34	**1**	-	-	-	-	-	-
F_8	4.53E-30	**1**	4.53E-30	**1**	4.53E-30	**1**	4.22E-02	**1**	1	0	1.91E-26	**1**

According to Tables 7,8 and 9, the evaluations are as follows:

- In all dimensions (10, 30, 50), GA performed significantly worse than the newly proposed metaheuristics (ARO, AVOA, PDO), both statistically and practically. The mean values for GA were multiple orders of magnitude higher, showing weak convergence and poor optimization capacity across all test functions.
- While AVOA consistently outperformed ARO and PDO in most cases, especially in multimodal functions, the differences between AVOA and the other new algorithms were generally small in practical terms, even when statistically significant (e.g., differences on the order of 10^{-4} to 10^{-6}).
- PDO showed strong robustness, occasionally outperforming ARO in certain functions, such as those involving higher dimensions and complex landscapes. Although t-tests confirmed some of these differences as statistically significant, in real-world usage, the differences would yield very similar results from a practical optimization perspective.
- The statistically significant superiority of AVOA in several functions (e.g., F_3, F_4, F_8) highlights its strong exploration and exploitation balance, leading to better convergence. However, in functions where no significant difference was observed between AVOA and PDO or ARO, it is inferred that all three algorithms can be safely considered high-performing alternatives for benchmark problems.

In conclusion, while t-tests reveal which differences are statistically significant, the practical value lies in the consistency, speed of convergence, and robustness of the algorithms. AVOA leads in most metrics, but PDO and ARO offer competitive results, especially when computational cost or algorithm simplicity is considered.

4.4. Engineering problem results

The optimization results for the engineering design problems are evaluated across three benchmark cases: Pressure Vessel Design, Tension/Compression Spring Design, and Three-Bar Truss Design. The best run results obtained for each problem, along with the corresponding parameter values, are presented in Tables 10–12.

Table 10. Best results for the pressure vessel design problem

Algorithm	T_s	T_h	r	L	Optimal value
ARO	0.7782	0.3847	40.3217	199.9712	5.8854e+03
AVOA	0.7790	0.3851	40.3639	10.0010	5.8868e+03
GA	1.2918	0.5706	42.2641	12.7864	1.1017e+04
PDO	0.8156	0.3975	40.8373	10.0000	6.0308e+03

According to Table 10, ARO achieved the best result with the lowest cost (5.8854e+03), followed closely by AVOA (5.8868e+03). GA performed the worst with a significantly higher cost (1.1017e+04), while PDO showed moderate performance (6.0308e+03). The longer cylinder length in ARO's design may have contributed to its better outcome.

Table 11. Best results for the tension/compression spring design

Algorithm	d	D	N	Optimal value
ARO	0.0516	0.3537	10.4114	0.0127
AVOA	0.0500	0.3174	4.2926	0.0127
GA	0.0534	0.3572	2.2595	0.0139
PDO	0.0500	0.3116	8.1058	0.0127

According to Table 11, ARO, AVOA, and PDO all achieved the same optimal value (0.0127), indicating equal performance. GA performed worse with a higher cost (0.0139). Although the optimal values are the same for the three algorithms, the design parameters differ, especially in the number of active coils (N).

Table 12. Best results for the three bar truss design

Algorithm	A_1	A_2	Optimal value
ARO	0.7887	0.4082	263.8958
AVOA	0.7835	0.3640	263.8958
GA	0.7624	0.2454	263.9174
PDO	0.7356	0.4074	263.8958

According to Table 12, ARO, AVOA, and PDO achieved the same optimal value (263.8958), indicating equally successful performance. GA resulted in a slightly higher value (263.9174), making it the least effective among the four. Despite identical outcomes for three algorithms, their parameter values differ slightly, showing that multiple configurations can lead to the same objective value. To provide further insight into the optimization behavior, convergence curves for all three engineering design problems are presented in Figure 8.

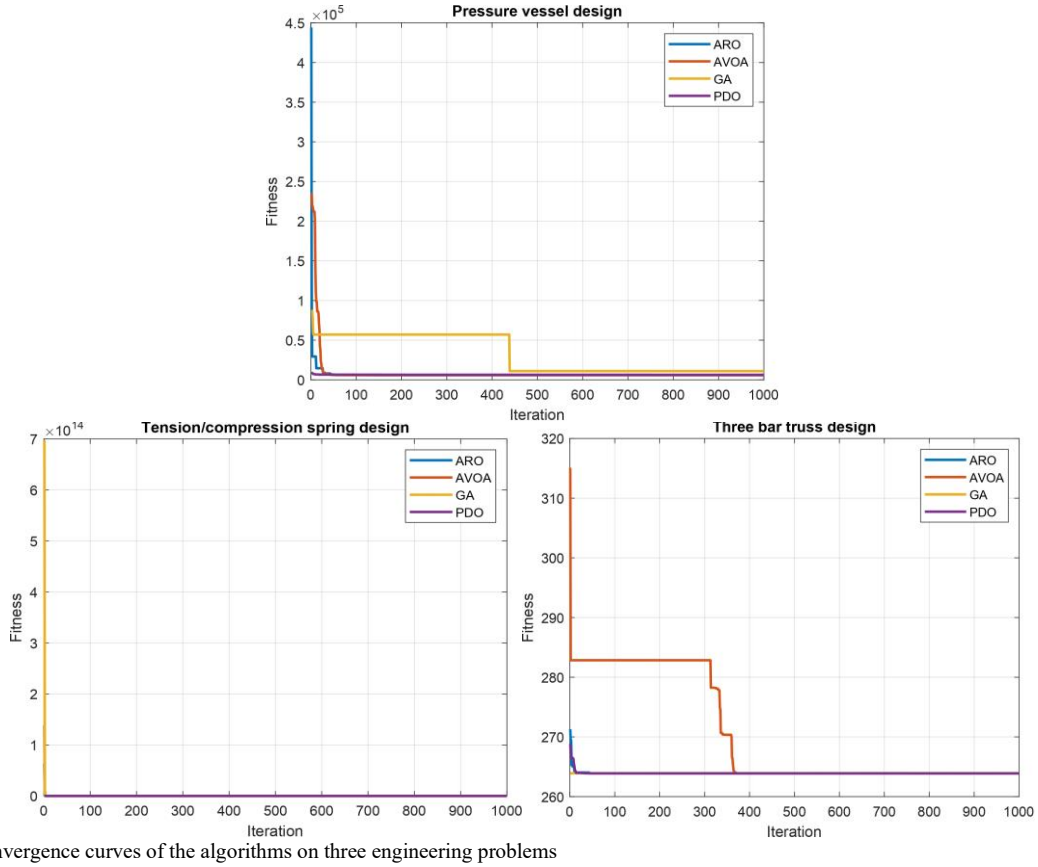

Figure 8. Convergence curves of the algorithms on three engineering problems

The convergence plots reveal that ARO generally demonstrates the fastest and most stable convergence across the problems. In the spring design, ARO, AVOA, and PDO exhibit nearly identical and immediate convergence behavior, indicating comparable effectiveness. In the truss design, ARO and PDO reach the optimum quickly, while AVOA converges more slowly and GA performs moderately. For the pressure vessel problem, ARO achieves the fastest convergence, closely followed by PDO, both clearly outperforming AVOA and GA.

4.4. Computational Complexity Analysis

In addition to the performance outcomes, the algorithms were analyzed in terms of their computational characteristics. While all algorithms were run under identical conditions (population size = 50, iterations = 1000), they differ in the internal number of operations per iteration. Table 13 summarizes the estimated per-iteration computational complexity for each algorithm.

Table 13. Approximate computational complexity per iteration

Algorithm	Complexity	Structural Notes
GA	$O(n)$	Basic evolutionary operators
PDO	$O(n)$	Simple interaction-based updates
AVOA	$O(n \times d)$	Phase switching and adaptive terms
ARO	$O(n \times d + n \log n)$	Behavioral modeling and sorting operations

$n = population\ size, d = problem\ dimension.$

It can be inferred from Table 10 that GA and PDO involve relatively simple operations, while AVOA and ARO include more complex mechanisms such as phase switching, adaptive behaviors, and sorting processes. These internal differences may influence total processing time, especially in high-dimensional problems, although all algorithms remain feasible for standard benchmark testing.

5. CONCLUSION

In this paper, the performance analysis of ARO, AVOA, PDO and GA metaheuristics is conducted for the first time using 8 different test functions. The analyses revealed that the newly proposed metaheuristics outperformed the popular GA. AVOA was observed to be the most successful, producing better results as referenced in Table 6. Other newly proposed is performed slightly worse than AVOA. The obtained simulation results were evaluated for statistical significance using t-tests. The tests indicated that there were minimal significant differences among the newly proposed methods, but these differences were more expressed when compared to the popular GA. In future studies, the performance of ARO, AVOA, and PDO will be compared with other modern metaheuristics such as Particle Swarm Optimization (PSO), Differential Evolution (DE), and Artificial Bee Colony (ABC) under similar conditions to expand the scope of the evaluation. It is also aimed to solve different optimization problems with these metaheuristics.

REFERENCES

[1] Yang XS. Nature-inspired metaheuristic algorithms. 2nd ed. Frome (UK): Luniver Press; 2008.

[2] Jia H, Rao H, Wen C, Mirjalili S. Crayfish optimization algorithm. Artif Intell Rev. 2023;1–61.

[3] Kennedy J, Eberhart R. Particle swarm optimization. In: Proceedings of ICNN'95 - International Conference on Neural Networks. Vol. 4. IEEE; 1995. p. 1942–8.

[4] Mirjalili S. Genetic algorithm. In: Mirjalili S, editor. Evolutionary algorithms and neural networks: theory and applications. Cham: Springer; 2019. p. 43–55.

[5] Karaboga D. Artificial bee colony algorithm. Scholarpedia. 2010;5(3):6915.

[6] Dorigo M, Birattari M, Stützle T. Ant colony optimization. IEEE Comput Intell Mag. 2006;1(4):28–39.

[7] Dehghani M, Montazeri Z, Trojovská E, Trojovský P. Coati optimization algorithm: A new bio-inspired metaheuristic algorithm for solving optimization problems. Knowl Based Syst. 2023;259:110011.

[8] Wang L, Cao Q, Zhang Z, Mirjalili S, Zhao W. Artificial rabbits optimization: A new bio-inspired meta-heuristic algorithm for solving engineering optimization problems. Eng Appl Artif Intell. 2022;114:105082.

[9] Tynes VV, editor. Behavior of exotic pets. Hoboken: John Wiley & Sons; 2010.

[10] Camp MJ, Rachlow JL, Shipley LA, Johnson TR, Bockting KD. Grazing in sagebrush rangelands in western North America: implications for habitat quality for a sagebrush specialist, the pygmy rabbit. Rangel J. 2014;36(2):151–9.

[11] Abdollahzadeh B, Gharehchopogh FS, Mirjalili S. African vultures optimization algorithm: A new nature-inspired metaheuristic algorithm for global optimization problems. Comput Ind Eng. 2021;158:107408.

[12] Xue Y, Jia W, Zhao X, Pang W. An evolutionary computation based feature selection method for intrusion detection. Secur Commun Netw. 2018;2018:1–15.

[13] Yang XS, Deb S. Cuckoo search via Lévy flights. In: Proceedings of the 2009 World Congress on Nature & Biologically Inspired Computing (NaBIC). IEEE; 2009. p. 210–4.

[14] Yang XS. A new metaheuristic bat-inspired algorithm. In: González JR, Pelta DA, Cruz C, Terrazas G, Krasnogor N, editors. Nature inspired cooperative strategies for optimization (NICSO 2010). Berlin: Springer; 2010. p. 65–74.

[15] Gwiazda TD. Crossover for single-objective numerical optimization problems. Vol. 1. Wroclaw: Wroclaw University of Technology Press; 2006.

[16] Vasconcelos JA, Ramirez JA, Takahashi RHC, Saldanha RR. Improvements in genetic algorithms. IEEE Trans Magn. 2001;37(5):3414–7.

[17] Ezugwu AE, Agushaka JO, Abualigah L, Mirjalili S, Gandomi AH. Prairie dog optimization algorithm. Neural Comput Appl. 2022;34(22):20017–65.

[18] Hoogland JL. The black-tailed prairie dog: social life of a burrowing mammal. Chicago: University of Chicago Press; 1995.
[19] Yiğit H, Ürgün S, Mirjalili S. Comparison of recent metaheuristic optimization algorithms to solve the SHE optimization problem in MLI. Neural Comput Appl. 2023;35(10):7369–88.
[20] Kim TK. T test as a parametric statistic. Korean J Anesthesiol. 2015;68(6):540–6.
[21] Mishra P, Singh U, Pandey CM, Mishra P, Pandey G. Application of student's t-test, analysis of variance, and covariance. Ann Card Anaesth. 2019;22(4):407–11.

Volume 14, Issue 3, Page 90-100, 2025 https://doi.org/10.46810/tdfd.1642050 Research Article

BİNGÖL UNIVERSITY

Türk Doğa ve Fen Dergisi
Turkish Journal of Nature and Science
www.dergipark.gov.tr/tdfd

Determination of Earthquake Performance of Existing RC Buildings According to FEMA-356 and TBEC-2018

Mohamed Omar HIRABE[1*], Elif BORU[2]

[1] Sakarya University of Applied Science, Faculty of Engineering, Department of Civil Engineering, Sakarya, Türkiye
[2] Sakarya University of Applied Science, Faculty of Engineering, Department of Civil Engineering, Sakarya, Türkiye
Mohamed Omar Hirabe ORCID No: 0000-0003-1605-732X
Elif Boru ORCID No: 0000-0003-1661-7673

**Corresponding author: hiraabe171@gmail.com*

(Received: 18.02.2025, Accepted: 22.07.2025, Online Publication: 26.09.2025)

Keywords
Existing RC, Pushover analysis, FEMA-356, TBEC-2018,

Abstract: Türkiye, located in a seismically active region with a high concentration of active fault lines, has experienced numerous devastating earthquakes, underscoring the critical need for seismic safety. Over the past 30 years, the country has been struck by several major earthquakes, resulting in significant loss of life and extensive property damage. The 06.02.2023 Kahramanmaraş earthquakes highlighted the severity of seismic activity, emphasizing the need for earthquake-resistant building design and retrofitting of buildings that do not meet modern standards. This ensures resilience and reduces economic losses in the face of earthquakes. This paper assesses the seismic performance of an existing G+2 reinforced concrete (RC) building. A static pushover analysis was performed in accordance with FEMA-356 and TBEC-2018 guidelines. The building was modeled in SAP2000 using the original cross-section and reinforcement details. Target displacements and damage distributions were compared to evaluate structural performance under both codes.

Mevcut Betonarme Binanın Deprem Performansının FEMA-356 ve TBDY-2018'e Göre Belirlenmesi

Anahtar Kelimeler
Mevcut betornarme Bina, itme analizi, Sismik performans, FEMA-356, TBEC-2018

Öz: Türkiye, aktif fay hatlarının yoğun olduğu sismik açıdan aktif bir bölgede yer almakta olup, birçok yıkıcı depreme maruz kalmıştır. Bu durum, deprem güvenliğinin önemini açıkça ortaya koymaktadır. Son 30 yıl içinde ülke, ciddi can ve mal kaybına neden olan birçok büyük depremle sarsılmıştır. 06.02.2023 Kahramanmaraş depremleri, sismik aktivitelerin ciddiyetini gözler önüne sermiş ve depreme dayanıklı bina tasarımı ile modern standartlara uymayan binaların güçlendirilmesi gerekliliğini vurgulamıştır. Bu, depremlere karşı dayanıklılığı sağlar ve ekonomik kayıpları azaltır. Bu çalışmada; mevcut bir Z+2 betonarme binanın sismik performansı değerlendirilmiştir. Statik itme analizi, FEMA-356 ve TBEC-2018 yönetmeliklerine göre gerçekleştirilmiştir. Bina, orijinal kesit ve donatı detaylarına göre SAP2000 programında modellenmiştir. Hedef yer değiştirmeler ve hasar dağılımları karşılaştırılarak, her iki yönetmeliğe göre yapısal performans değerlendirilmiştir.

1. INTRODUCTION

Türkiye is one of the most seismically active countries in the world. It is intersected by two major active fault lines: the North Anatolian Fault (NAF) and the East Anatolian Fault (AEF) [1]. The Anatolian Plate is located between the Arabian Plate and the Eurasian Plate, and is among the fastest-moving tectonic plates globally, exhibiting high seismic activity due to its rapid compressive movement [2]. According to the Disaster and Emergency Management Presidency (DEMP) map, the Seismic hazard map, these fault systems pass through 24 cities in Türkiye. The EAF is a left-lateral strike-slip fault located in the southern part of the country, serving as a tectonic boundary between the Eurasian and Arabian Plates [3]. Extending from the Arabian Plate in the east to the Aegean Sea in the west, these fault lines have caused numerous destructive earthquakes throughout history, as

shown on the DEMP map [2], [3], [4]. The locations of these Earthquake faults are shown in Figure 1.

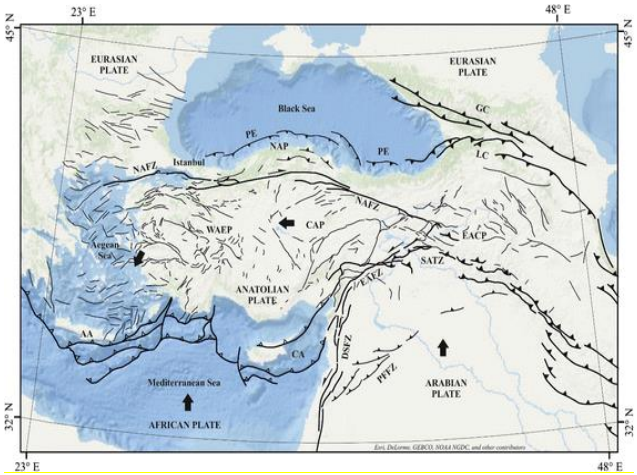

Figure 1. The Earthquake Map faults of Türkiye [5].

Performance-based design is based on designing a structure by choosing a performance target under design criteria to increase the structure's resistance against earthquakes [6]. This concept is crucial for designing important buildings like hospitals, schools, fire stations, and residential buildings, ensuring performance-designed qualities [7]. In recent years, the concept of structural evaluation and design based on displacement and deformation performance criteria has been introduced and developed, particularly in efforts to more accurately assess the seismic safety of existing structures in earthquake-prone areas [8]. The aim of performance-based design for existing buildings under earthquake conditions is to ensure the structure performs well during seismic events, minimizing damage and ensuring occupant safety. Performance is determined by the extent of damage a building sustains during an earthquake, and it is essential to fulfill and manage these requirements effectively [9]. The United States has been developing performance-based seismic design since the 1970s, starting with the 1976 Uniform Building Code (UBC) [10]. The ICBO introduced Occupancy Importance factors to calculate seismic forces, aiming to enhance robustness and performance. However, Civil engineers realized that strength alone wasn't enough. Over time, additional features were developed. In Türkiye it was added the performance-based design was added to the code of TBEC-2007 and TBEC-2018. While the United States of America developed different codes in different years, the Performance-based design, which includes: 1997 FEMA-273, 2000 FEMA-356, and 2007 ASCI/41-13-17.

Different researchers investigated different buildings based on FEMA-356 and TBEC-2018, Such as Tolunay and Hakkan (2021). The performance level of a reinforced concrete building designed by the Turkish building earthquake code, Seismic Code (TBEC-2018), was assessed through static single-mode pushover analysis. The analysis was compared to the target performance level set in the Turkish Seismic [11]. Metin and Besian (2019) investigated the performance evaluation of existing reinforced structures, using the static pushover analysis method, and evaluated their performance and damage levels, comparing them to the Turkish Building Earthquake Code (TBEC-2007) and Eurocode standards [12]. Rey and Geffren (2024), A Four-Story Professional School Building in the University of Mindanao, was assessed using ASCE/SEI 41. They were evaluated using various seismic design principles, including ATC 40, FEMA 356, and FEMA 440. Linear and nonlinear analyses were used, with a pushover curve drawn for plastic hinge behavior, deformation-controlled, and force-controlled actions [13]. Ashwini and his friends (2024) investigated an eight-story structure to evaluate its structural performance using pushover analysis. The assessment was based on parameters such as moment-curvature, ductility, overstrength, inter-story drift, and a detailed computation of base shear [14]. Rohullah (2024) investigated the scope of reinforced concrete buildings, using TBECC-2018 and ASCI-41-17 methods. It discussed the incremental equivalent earthquake load calculation and simplified nonlinear static analysis methods, and performed performance analysis comparing results [15]. Recent earthquakes, particularly the 2023 Kahramanmaraş earthquakes, have demonstrated the vulnerability of reinforced concrete buildings in Türkiye, with widespread collapses attributed to soft-story mechanisms, poor detailing, and inadequate seismic design [16], [17], [18], [19].

Previous studies have focused primarily on evaluating seismic performance using either international guidelines like FEMA-356 or earlier versions of the Turkish seismic code. However, few comparative studies have examined the differences between TBEC-2018 and FEMA-356 in evaluating the same structure. This study fills that gap by applying both regulations to a real, existing building and comparing the outcomes. The findings highlight how the evolution in Turkish seismic code provisions influences performance expectations and design decisions. Thus, the study provides a unique comparative analysis that can inform both national and international retrofitting strategies.

Previous studies have primarily focused on assessing the seismic performance of structures using either previous revisions of the Turkish seismic code or international guidelines like FEMA-356. Comparing FEMA-356 to TBEC-2018, the current national code in Türkiye, when applied to the same structure, hasn't been done much, though. In order to close that gap, this study compares the performance of a real, existing building using both standards. The results show how recent changes to the Turkish seismic code affect design choices and performance expectations, providing insightful information that can guide national and international retrofit and assessment plans.

In this study, the seismic behavior of a three-story (G+2) reinforced concrete residential building in Sakarya Province, Türkiye, was examined through nonlinear static pushover analysis. The structure that was designed as per TBEC-2018 was analyzed and modeled by using SAP2000. Target displacements were determined as per TBEC-2018 and FEMA-356 provisions, and the damage

distributions of the structural elements obtained were compared. The results are compared in this dual-code approach to understand the performance differences between the two regulations.

2. METHOD AND ANALYSIS PROCEDURE

The structure examined in this study is a mid-rise reinforced concrete building designed in accordance with TBEC-2018 guidelines. it was selected because it reflects the latest seismic provisions currently used in Türkiye, allowing for direct comparison of how modern code-compliant structures perform under different assessment standards.

To determine how international standards and national regulations compare when assessing the seismic performance of newly designed structures, the study will evaluate a building that was designed using both TBEC-2018 and FEMA-356.

This influences code development as well as engineering practice by pointing out possible inconsistencies or conservatism in performance evaluation techniques

2.1. Turkish Building Earthquake Code(TBEC-2018)

The Turkish Building Earthquake Code (TBDY-2018) is a set of guidelines and regulations developed by Türkiye's Ministry of Environment and Urbanization to ensure the safety and structural integrity of buildings during earthquakes. Updated in 2018, it aligns with modern seismic research and engineering practices. The code provides detailed standards for the design, construction, and retrofitting of buildings to withstand earthquake forces. It defines seismic hazard zones across Türkiye, considers regional earthquake risks, specifies guidelines for structural systems and materials such as reinforced concrete and steel, and establishes requirements for earthquake-resistant design to absorb seismic forces. It also includes performance criteria to ensure life safety and minimize damage during an earthquake, along with retrofitting guidelines to strengthen existing buildings for better earthquake resistance.

2.1.1. Determination of performance analysis method according to tbec-2018

In order to assess the seismic performance of existing concrete structures following TBEC-2018, the target displacements should be calculated, plastic hinge properties should be defined, and plastic limits should be determined. Chapter 15 of TBEC-2018 outlines the principles for determining the performance levels of existing buildings. To calculate the maximum displacement of the modal single-degree-of-freedom system in the earthquake direction under analysis, the nonlinear spectral displacement (in meters) corresponding to the first natural vibration period (T_1) must be determined. This value can then be used in Equation 1 to find the maximum displacement of the system.

$$d^{X}_{x,max}=S_{di}(T_1) \quad (1)$$

Where S_{di} is the nonlinear spectral displacement, the corresponding S_{di} can be found by using Equation 2.

$$S_{di}(T_1)=C_r S_{de}(T_1) \quad (2)$$

Where C_r= the spectral displacement ratio and T_1 first natural vibration period. To calculate the spectral displacement ratio (CR), the ductility demand $\mu(RyT_1)$, calculated based on the yield strength reduction coefficient and the first natural vibration period, is divided by the yield strength (R_y).

$$C_r=1 \quad when \quad T_1>T_B \quad (3)$$

$$C_r=\frac{1+(R_y-1)\frac{T_B}{T_1}}{R_y}, when\ T_1<T_B \quad (4)$$

In Figure 2, corresponding to the case where Equation 3 is used together, it is necessary to demonstrate that the natural vibration time occurs at the initial thrust phase. period at the first thrust step ($T_1>T_B$) or the first (dominant) mode natural angular frequency values ($\omega_1 \leq \omega_B$) found in the free vibration calculation, renewed at each thrust step.

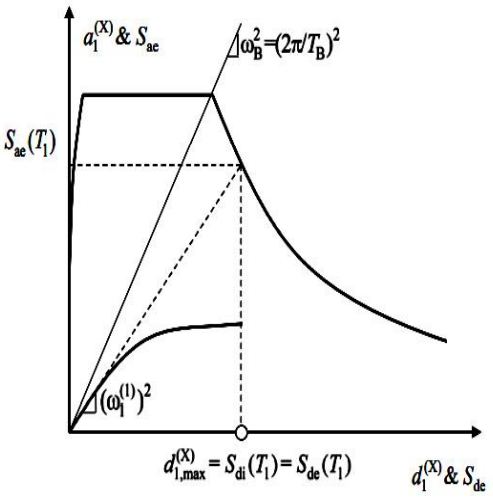

Figure 2. Modal Displacement Demand [20].

In another case given in Figure 3a, the spectral displacement ratio (C_R) is obtained by the successive approximation method. First, the spectral displacement ratio (C_R=1) is assumed. Thus, initially, the modal capacity diagram is transformed into a two-line elasto-plastic diagram. In this process, the areas under the diagrams must be equal. Based on these values, the elasto-plastic diagram is reconstructed as shown in Figure 3a. These graphs were fully explained in TBEC-2018 in section 5B.3.

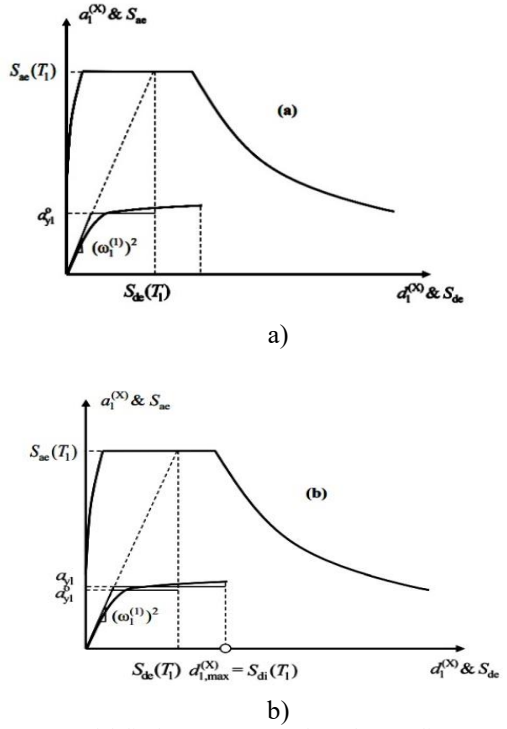

a)

b)

Figure 3. Modal displacement Demand graph according to TBEC-2018

2.1.2. Determination of performance damage levels by TBEC-2018

The moment rotations in Beams, columns, and Shear walls for definitions in SAP2000 can be calculated according to TBEC-2018 in Equation 5.

$$\theta^{p}=(\phi_u-\phi_y)L_p \quad (5)$$

The Axial forces of Column sections in the definition of Plastic hinges can be calculated in Equation 6.

$$N_d=0, \quad N_d=0.2A_cF_{ck} \quad , \quad N_d=0.4A_cF_{ck} \quad (6)$$

The Collapse Prevention Performance Level for inelastic behavior, Plastic Behavior, according to TBEC-2018, can be found in Equations 7-9.

$$\theta_p^{(CP)}=\frac{2}{3}\left[\left(\phi_u-\phi_y\right)L_p\left(1-0.5\frac{L_p}{L_s}\right)+4.5\phi_u d_p\right] \quad (7)$$

$$\theta^{(CD)}=0.75\times\theta^{(Gö)} \quad (8)$$

$$\theta^{(LD)}=0 \quad (9)$$

$\theta^{(CP)}$= Allowable roatation for Collapse Prevention, $\theta^{(CD)}$= Allowable roatation for Controlled Damage, $\theta^{(LD)}$= Allowable roatation for Limited Damage and N_d= is the axial force of the section. The definition of plastic rotation limits and unit deformations for TBEC-2018 is provided in Chapter 5.8 of the code. TBEC-2018 defines seismic performance levels for structures, which are categorized as Limited Damage (LD), Controlled Damage (CD), and Collapse Prevention (CP). The Limited Damage level corresponds to minimal structural damage, where the building remains fully functional. The Controlled Damage level allows for minor structural damage that is repairable. The Collapse Damage level indicates extensive structural damage that may compromise the building's safety during an earthquake. The performance damage levels according to TBEC-2018 are illustrated in Figure 4.

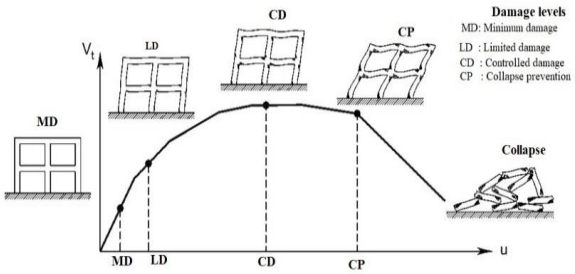

Figure 4. The Performance damage levels of TBEC-2018 [20]

2.2. Determination of Performance Analysis Method According to FEMA-356

FEMA-356 outlines performance-based evaluation procedures, providing detailed guidelines on modeling parameters, acceptance criteria, and methods for performing pushover analysis [21]. FEMA-356 classified two main criteria for determining the yielding behavior of frame members during pushover analysis, as shown in Figure 5. These criteria are categorized as either deformation-controlled (ductile behavior) or force-controlled (brittle behavior) plastic hinges [22]. The displacement-controlled action under flexure is idealized using performance levels A, B, C, D, and E, which represent strain, curvature, rotation, or elongation, allowing engineers to evaluate structural response and predict seismic behavior. Figure 5b illustrates the inelastic force-deformation relationship for displacement-controlled actions under flexural loading [23].

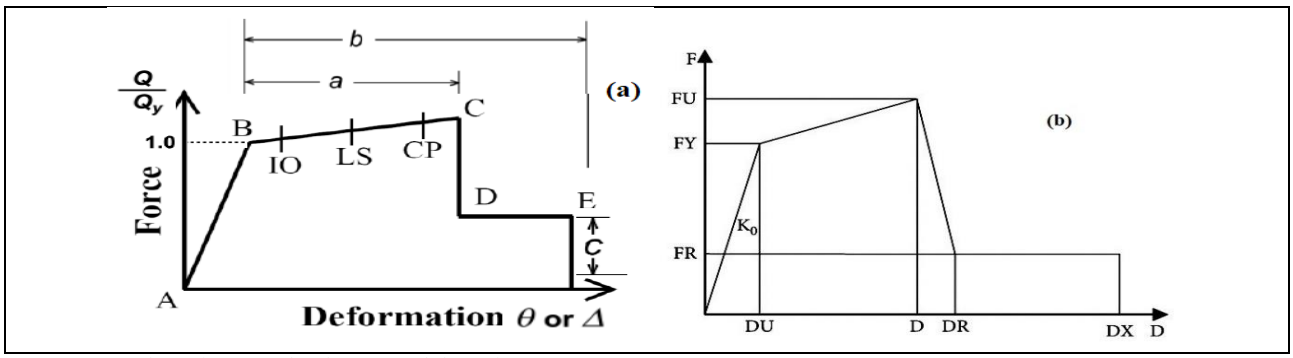

Figure 5. A) Deformation control and B) Force-deformation [24], [25].

According to FEMA-356, the designations IO (Immediate Occupancy), LS (Life Safety), and CP (Collapse Prevention) represent acceptance requirements or performance levels for the plastic hinge that develops near the ends of columns and beams. The P-M interaction curve (ACI code 2000), the stress-strain curve for concrete (Kent Park) [26], and the M-θ relationship, which indicates acceptance criteria corresponding to performance levels, are all represented by default values provided in the software SAP 2000 v24 [27]. The performance damage levels of FEMA-356 can be determined as shown in Figure 6.

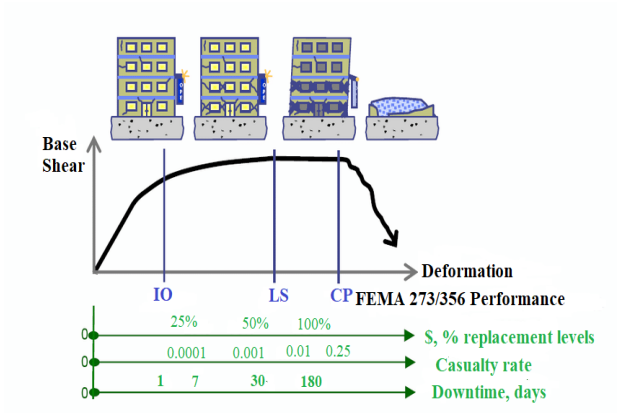

Figure 6. The Performance damage levels of FEMA 273/356 [25], [28].

In the analysis phase, FEMA-356 offers four methods: Linear Static, Linear Dynamic, Nonlinear Static (Pushover), and Nonlinear Dynamic (Time-History). The choice of method depends on the complexity of the structure and the desired accuracy. After analysis, engineers compare results to acceptance criteria for deformation- and force-controlled actions. If elements exceed thresholds, retrofitting strategies like adding shear walls, column jacketing, or base isolators are implemented. Visual outputs such as 3D models, deformed shapes, and pushover curves support decision-making throughout the process.

2.2.1 Target displacement by FEMA-356

According to FEMA 356, the target displacement, δt, at each floor level shall be computed according to Equation (10) and as specified in Section 3.3.3.3.1;

$$\delta_t = C_0 C_1 C_2 C_{C3} S_a \frac{T_e^2}{4\pi^2} g \qquad (10)$$

C_o, C_1, C_2, and C_3 are modification factors used to adjust the displacement response of a building under seismic loading. Co relates the spectral displacement of an equivalent SDOF system to the building's roof displacement. C_1 accounts for expected maximum inelastic displacements, C_2 adjusts for the effects of pinched hysteretic behavior, stiffness degradation, and strength deterioration, and C_3 represents increased displacements due to dynamic P-Δ-effects. Sa refers to the response spectrum acceleration.

Figure 7-8 demonstrates the displacement coefficient method used to determine the target displacement (δ_T). This process begins by establishing the effective fundamental period, which takes into account the inelastic behavior of the structure. The effective fundamental period represents the linear stiffness of an equivalent Single Degree of Freedom (SDOF) system and is associated with the maximum spectral acceleration (S_d) of the system. Once the effective fundamental period is determined, the target displacement can be calculated.

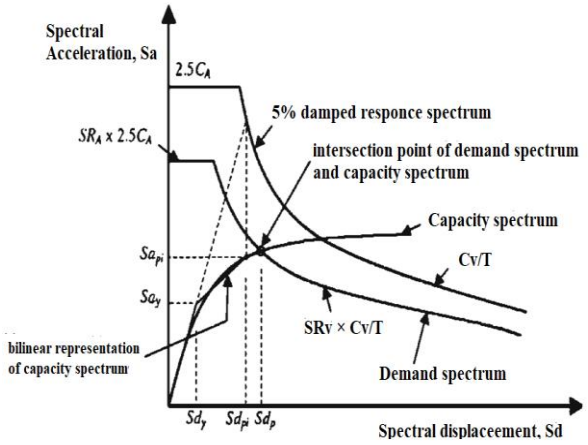

Figure 7. Target displacement method according to FEMA-356 [25].

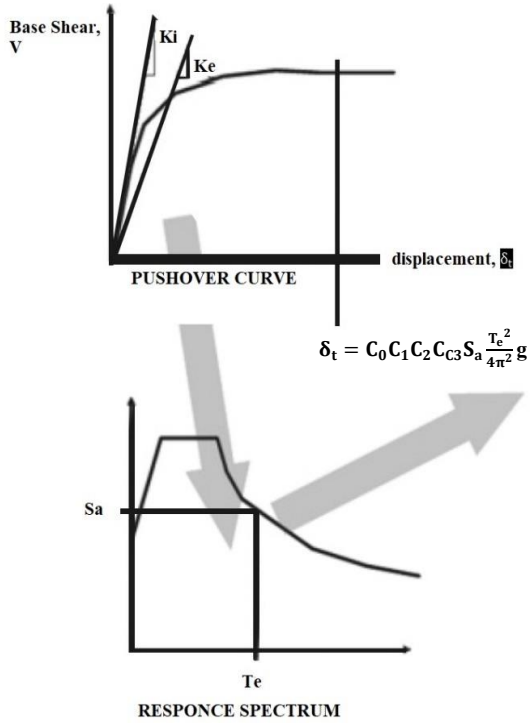

Figure 8. Target displacement method according to FEMA-356 [25]

2.2.2 Determination of performance damage levels by FEMA-356

To determine the performance levels of concrete structures according to FEMA-356, the section rotations of structural elements can be assessed. Section rotations are expressed in radians, and factors such as axial load, section area and properties, concrete weight, and transverse reinforcement distribution are considered. The performance criteria, as outlined in FEMA-356, can be determined for both beams and columns, as shown in Tables 1 and 2.

Table 1. Section rotation limits for reinforced concrete columns

Cross-Section Properties				Damage Limits (plastic rotation angle, radians)			
				Type of building element			
				Primary		Secondary	
$P/(A_g \times f_c)$	Winding feature	$V/(b_w \times d \times f_c)$	IO	LS	CP	LS	CP
≤0.1	C	≤ 3	0.005	0.015	0.020	0.020	0.030
≤0.1	C	≥ 6	0.005	0.012	0.016	0.016	0.024
≤0.4	NC	≤ 3	0.003	0.012	0.015	0.018	0.025
≤0.4	NC	≥ 6	0.003	0.010	0.012	0.013	0.020
≤0.1	NC	≤ 3	0.005	0.005	0.010	0.010	0.015
≤0.1	NC	≥ 6	0.005	0.004	0.005	0.008	0.012
≤0.4	NC	≤ 3	0.002	0.002	0.003	0.006	0.010
≤0.4	NC	≥ 6	0.002	0.002	0.003	0.005	0.008

Table 2. Section rotation limits for reinforced concrete beams

Cross-Section Properties				Damage Limits (plastic rotation angle, radians)			
				Type of building element			
				Primary		Secondary	
$P/(A_g \times f_c)$	Winding feature	$V/(b_w \times d \times f_c)$	IO	LS	CP	LS	CP
≤0	C	≤ 3	0.010	0.02	0.02	0.02	0.05
≤0	C	≥ 6	0.005	0.01	0.025	0.02	0.04
≥0.5	NC	≤ 3	0.005	0.01	0.02	0.02	0.03
≥0.5	NC	≥ 6	0.005	0.005	0.015	0.015	0.02
≤0	NC	≤ 3	0.005	0.01	0.02	0.02	0.03
≤0	NC	≥ 6	0.0015	0.005	0.01	0.01	0.015
≥0.5	NC	≤ 3	0.005	0.01	0.01	0.01	0.015
≥0.5	NC	≥ 6	0.0015	0.005	0.001	0.005	0.01

2.3. Building Details

The seismic performance of a G+2 reinforced concrete building located in the Sakarya province of Türkiye was evaluated in this study. The building consists of a 3.4-meter-high ground floor and two upper stories, each with a uniform height of 2.4 meters. It is designed for residential use (Figure 9). The structural system includes C30-grade concrete and B420C-grade reinforcing steel. The slab thickness is 12 cm. Detailed reinforcement information for columns and beams is provided in Figures 10–11 and Table 3. The site soil classification for the building location is type ZE, according to TBEC-2018. SAP2000 v24 was chosen to simulate the seismic performance of the building because it has strong capabilities in structural modeling and nonlinear analysis [27]. The software provided a precise representation of the building's geometry, material properties, and loading conditions. This made it possible to conduct a detailed pushover analysis following FEMA-356 and TBEC-2018 guidelines.

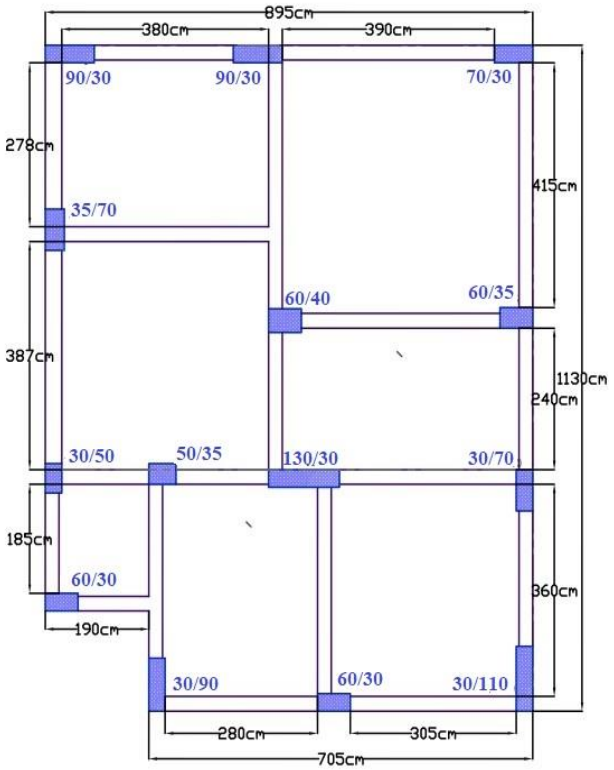

Figure 9. The building Plan layout

Table 3. The reinforcement details of columns

Column dimensions (cm)	Reinforcement details
90×30, 70×35	14Φ16
70×30, 60×40, 60×35	12Φ16
50×35, 50×30, 60×30	10Φ16
110×30	18Φ16
130×30	22Φ16

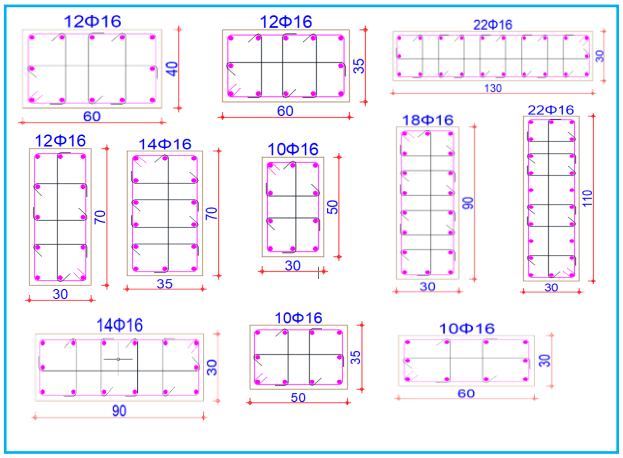

Figure 10. Column reinforcement details

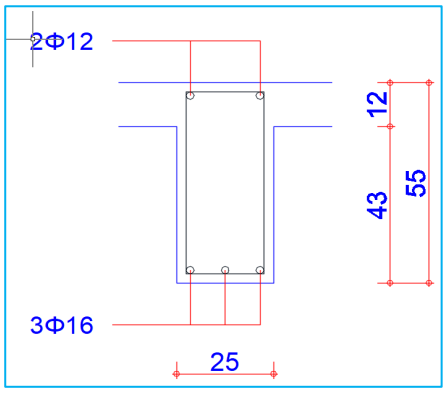

Figure 11. Beam reinforcement detail

3. RESULTS AND DISCUSSIONS

In SAP2000, the target displacement of the model is calculated by default according to FEMA-356 guidelines. For this analysis, the target displacement was found to be 0.08 meters. The relationship between displacement and base shear is shown in Figure 12, which illustrates how the structure's displacement increases with the applied lateral forces. It is important to note that the structural target displacement of the building did not reach the maximum value, indicating that the building's seismic capacity was not fully used during the analysis.

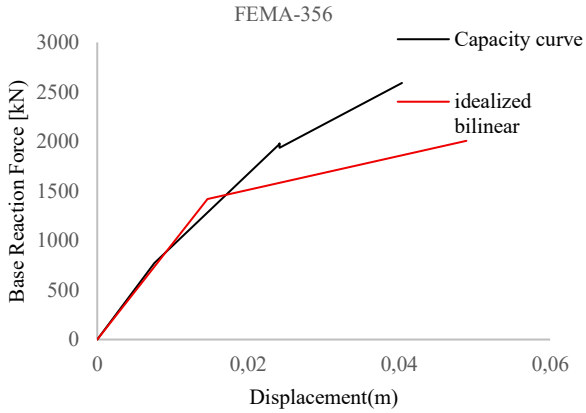

Figure 12. Base shear force-displacement by pushover curve

FEMA 356 3.3.3.3.2, The target displacement, δt, for each floor level must be calculated by Equation (3-15) and as outlined in Section 3.3.3.3.1. The program established defaults and provided the coefficients listed in Table 4, which were determined by SAP2000, while the target displacements were calculated manually.

Table 4. Target displacement coefficient according to FEMA 356

C0	1.3505	Te	0.461
C1	1.1253	Ti	0.4537
C2	1	Ki	101682.7
C3	1	Ke	98481.49
Sa	1.1	Alpha	0.1616

$$\delta_t = C_0 C_1 C_2 C_{C3} S_a \frac{T_e^2}{4\pi^2} g$$

$$\delta_t = 1.3505 \times 1.1253 \times 1 \times 1 \times 1.1 \times \frac{(0.461)^2}{4\times\pi^2} 9.81 = 0.08m$$

3.2 According to FEMA-356 Performance Evaluation Results

According to the analysis results, the building was investigated, and its status is controlled according to FEMA-356. The damage distribution of structural elements is presented in Figures 12-13, and the status of the building is summarized in Table 5, where the column damage levels in the X and Y directions are 31% and 18%, respectively, for the significant damage zones. The column conditions in both the X and Y dimensions were determined under the limited damage (LD) conditions, as per the results and regulations of FEMA-356. Additionally, the beams' relative damage levels are 60% and 78% in the X and Y dimensions, respectively. Based on the FEMA-356 guidelines, the performance status of the beams is also under Controlled Damage. Additionally, the shear damage levels are within the limited Damage according to FEMA-356, as indicated by the results obtained. According to Figure 13-14, the LD is the Limited damage, SD is the significant Damage, and AD is the advanced damage.

Table 5. Building performance evaluation

Earthquake level	Performance target	Directions	Most critical floor	Status of building
DD-2	Controlled damage	X and Y	1	Controlled

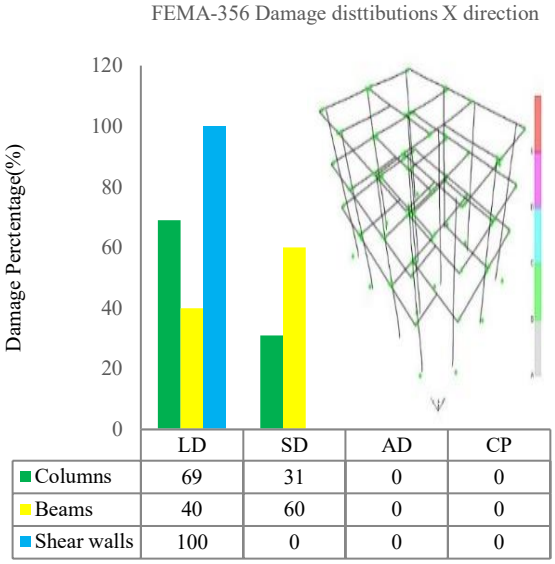

	LD	SD	AD	CP
Columns	69	31	0	0
Beams	40	60	0	0
Shear walls	100	0	0	0

Figure 13. Damage distributions of structural elements in the X direction

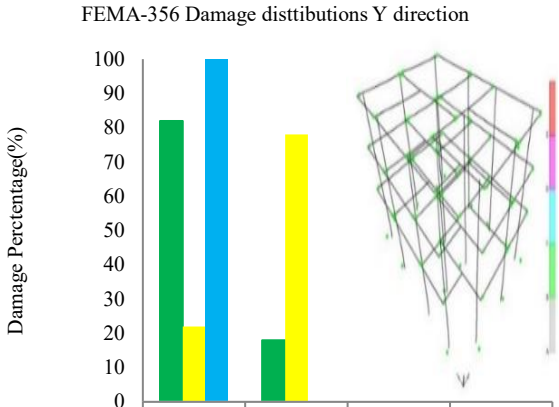

	LD	SD	AD	CP
Columns	82	18	0	0
Beams	22	78	0	0
Shear walls	100	0	0	0

Figure 14. Damage distributions of structural elements in the Y direction

3.3 Target Displacement Results According to TBEC-2018

In order to calculate and find the target displacement of the building, the TBEC-2018 building's spectral demand is determined from the pushover curve and is presented in Figure 15.

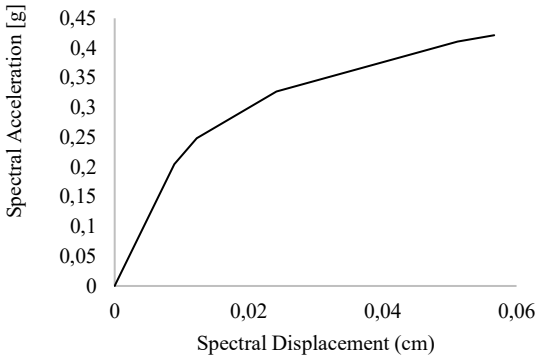

a)

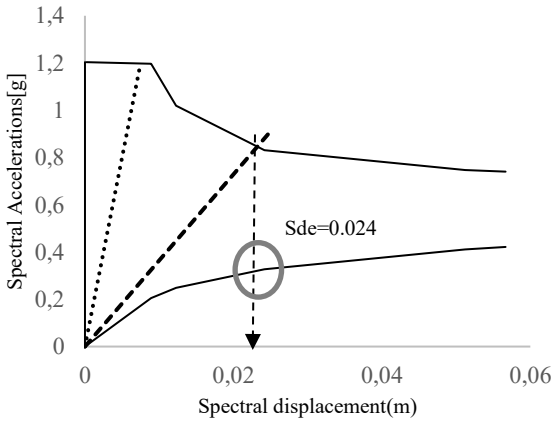

b)

Figure 14. a) Capacity and b) Demand spectrum of the building according to TBEC- 2018

After obtaining the capacity spectrum, the demand spectrum and demand spectrum, converted to spectral acceleration-spectral displacement format, is plotted on the same graph, and an estimated point is selected as the performance point using the equal displacement approach. Displaying the capacity spectrum and demand spectrum together and determining the estimated performance point are given in Figure 14.

As per TBEC-2018 Section 5B.3, the Modal maximum displacement in a single degree of freedom system is defined as nonlinear spectral displacement in Equation 10.

$$d_{1\,max}^{(1)} = S_{di}(T_1) \quad (11)$$

$$d_{1\,max}^{(1)} = 0.024m$$

$d_{1\,max}^{(1)} = CrS_{di}(T_1)$ where Cr depends on the First natural period of building.

$d_{1\,max}^{(1)} = CrS_{di}(T_1)$, 2.548×0.024=0.061m

Therefore, the target displacement of the building according to TBEC-2018 was determined based on Equation 12.

$$u_{xN1}^{(p)} = \emptyset_{di} \times \Gamma \times d_1 \quad (12)$$

Where $\emptyset_{di}$ is the Structure peak mode shape amplitude? Γ =Modal participation factor, d_1 = Peak displacement in a single-degree-of-freedom system.

$u_{xN1}^{(p)} = 0.09m$ The Target displacement of the building according to TBEC-2018 was determined

3.4. Performance Evaluation Results According to TBEC-2018

According to TBEC-2018, the results of the pushover analysis with the incremental equivalent earthquake load method, which is one of the non-linear inelastic methods, the element damage levels of the columns and beams at the critical floor in both directions are determined. As shown in Figures 16-17, the column damage levels in the X and Y directions are 48% and 41%, respectively, for the control damage zones. According to TBEC-2018, the column conditions in both the X and Y directions are classified under the Controlled Damage Zone. The damage levels of the beams in the X and Y directions are 38% and 48%, respectively. Based on the results and TSC-2018 guidelines, the performance status of the beams is also under the Controlled Damage Zone. Additionally, the shear damage levels are within the limited Damage Zone according to TBEC-2018, as indicated by the results obtained.

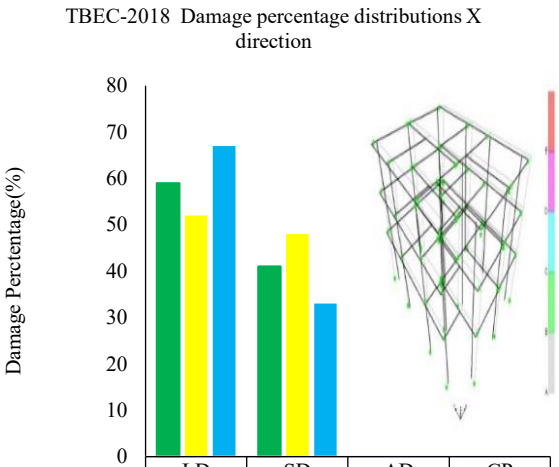

	LD	SD	AD	CP
Columns	59	41	0	0
Beams	52	48	0	0
Shear Walls	67	33	0	0

Figure 16. The Damage distributions of structural elements in the X direction according to TBEC-2018

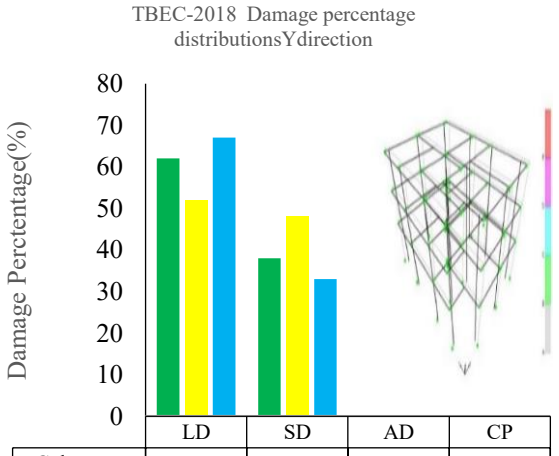

	LD	SD	AD	CP
Columns	62	38	0	0
Beams	52	48	0	0
Shear Walls	67	33	0	0

Figure 17. The Damage distributions of structural elements in the Y direction according to TBEC-2018

3.5. Comparison Of Results From TBEC-2018 And FEMA-356

Based on the results from both the TBEC-2018 and FEMA-356 regulations, it is observed that the structural damage levels for the building elements are similar, with only minor differences in the classification of damage. Both codes use distinct methodologies for evaluating and classifying structural damage, but the overall performance of the building appears to align closely.

Column Damage Analysis:

- FEMA-356: According to the FEMA-356 guidelines, the column damage levels in the X and Y directions are reported as 31% and 18%, respectively, within the Significant damage zones. This indicates that the columns are performing relatively well and are not subjected to a Limited damage level.
- TBEC-2018: reports the column damage levels at 48% and 41% for the X and Y directions, categorizing

them under the Significant Damage zones. While the TBEC-2018 damage levels are higher than those found by FEMA-356, they still fall under the Controlled Damage classification, which implies that the columns are experiencing moderate damage but still within acceptable performance limits.

Beam Damage Analysis:

- FEMA-356: The damage levels for the beams in the X and Y directions are 60% and 78%, respectively. According to the FEMA-356 guidelines, these levels indicate significant damage, but the performance status remains under the Controlled Damage zone.
- TBEC-2018: The beam damage levels in the X and Y directions, as per TBEC-2018, are 38% and 48%, respectively, which are slightly lower compared to the FEMA-356 results. These values fall under the Controlled Damage zone, similar to the FEMA-356 classification, although the damage levels in the Y direction are slightly higher.

Shear Damage Analysis:

- FEMA-356: The shear damage levels in both directions are within the Limited Damage zone, suggesting that the shear capacity of the building elements remains within a safe range.
- TBEC-2018: Similarly, the shear damage levels according to TBEC-2018 also fall within the Limited Damage zone, suggesting consistent performance between the two codes in terms of shear damage classification.

Target Displacement:

- FEMA-356: The target displacement for the building, as determined by FEMA-356, is 0.08 m. This value reflects the expected deformation of the building under seismic loading and aligns with the controlled damage classification for the beams and columns.
- TBEC-2018: While the target displacement for TBEC-2018 were determined 0.09m.

4. CONCLUSIONS

This study thoroughly assessed the seismic performance of a G+2 reinforced concrete building using static pushover analyses, following TBEC-2018 and FEMA-356 guidelines. The results show that the building stays in a Controlled Damage state under design-level seismic loads. There is moderate but acceptable damage to columns, beams, and shear components in both main directions. Although there are slight differences in the predicted damage levels, the overall structural behavior and performance classification closely match, strengthening the trustworthiness of these assessment methods.

Notably, TBEC-2018 consistently predicts more conservative damage levels compared to FEMA-356. This difference arises from TBEC-2018's more detailed damage index calculations, which incorporate cumulative inelastic deformations and stiffness degradation, as well as higher target displacement values reflecting greater ductility demands. Additionally, TBEC-2018 applies stricter force-reduction factors and narrower damage classification thresholds, leading to earlier and higher damage categorization. Understanding these methodological distinctions is essential for accurately interpreting seismic assessment results and making informed retrofit decisions.

The study shows that columns and beams keep their structural integrity within set safety limits. Shear components show little damage, which demonstrates the building's ability to withstand major seismic events. However, some damage, especially in beams, points out the need for ongoing structural health monitoring. Targeted retrofitting can help address potential weaknesses and ensure long-term safety.

Overall, this work shows that code-based pushover analyses are effective for assessing existing RC buildings. It highlights the importance of comparing multiple codes to better understand seismic performance. The insights gained form a strong base for guiding strategies to reduce seismic risk and plan retrofits. This work ultimately improves safety and sustainability in areas prone to earthquakes.

REFERENCES

[1] Naji DM, Akin MK, Cabalar AF. Evaluation of seismic site classification for Kahramanmaras City, Turkey. Environ Earth Sci. 2021;80(3):97. doi:10.1007/s12665-021-09396-x

[2] Tan OM, Tapirdamaz MC, Yörük A. Article 8 1-1-2008 part of the Earth Sciences Commons recommended citation. 2008.

[3] Doğangün A. Performance of reinforced concrete buildings during the May 1, 2003 Bingöl Earthquake in Turkey. Eng Struct. 2004;26(6):841–856.

[4] Book Reviews. Int Stud. 2008;45(3):257–270. doi:10.1177/002088170904500305

[5] Duman TY, et al. Seismotectonic database of Turkey. Bull Earthq Eng. 2018;16(8):3277–3316

[6] Kasimzade A, Nematli E, Kuruoğlu M. The new criterion on performance-based design and application to recent earthquake codes. Earthq Struct. 2023;24(1)

[7] Monti G, Rabi RR, Vailati M. Direct displacement-based design of dissipative bracings for seismic retrofit of reinforced concrete buildings. J Build Eng. 2024;82:108208.

[8] Bakalis AP, Makarios TK. Seismic enforced-displacement pushover procedure on multistorey R/C buildings. Eng Struct. 2021;229:111631.

[9] Dedeoğlu A, Zülfikar AC. Earthquake performance based design and resilience based analysis in high-rise buildings. Disaster Sci Eng. 2020;6(1):12–34.

[10] Hamburger RO, et al. FEMA P58: Next-generation building seismic performance assessment methodology. In: 15th World Conference on Earthquake Engineering; 2012.

[11] İbiş T, Ulutaş H. Yeni yapılacak betonarme bir binanın TBDY 2018'e göre deprem performansının belirlenmesi. Bitlis Eren Univ Fen Bilimleri Derg. 2021;10(3):1104–1124.

[12] Severcan MH, Sinani B. Mevcut betonarme yapıların deprem performansının analizi. Niğde

Ömer Halisdemir Univ Mühendislik Bilimleri Derg. 2019;8(2):936–947.
[13] Cabotaje RAC, Bernardo GR. Performance-based seismic evaluation of a four-story school building by pushover analysis using the Metro Davao Earthquake Model. Key Eng Mater. 2024;987:85–92.
[14] AL K, Keshavamurthy M, Ravikumar CM. Pushover analysis of an eight-story structure: a parametric study. 2024.
[15] Jamal R. A comparison of nonlinear performance evaluation TSC-2018 and ASCE 41-17 methods for reinforced concrete buildings [PhD thesis]. Konya: Selçuk Üniversitesi; 2022.
[16] Isik E, et al. Seismic performance and failure mechanisms of reinforced concrete structures subject to the earthquakes in Türkiye. 2024.
[17] Yön B, et al. Evaluation of the seismic response of reinforced concrete buildings in the light of lessons learned from the February 6, 2023, Kahramanmaraş, Türkiye earthquake sequences. Nat Hazards. 2025;121(1):873–909
[18] Sonmez E, et al. Seismic performance assessment of structural systems in the aftermath of the 2023 Kahramanmaraş earthquakes: Observations and fragility analyses. Earthquake Spectra. 2025;41(1):198–218.
[19] Kazaz I. Evaluation of seismic performance, design and practice of frame-wall buildings in Türkiye after the 6 February 2023 Kahramanmaraş earthquakes. J Build Eng. 2025;99:111557.
[20] TBDY, "Türkiye Bina Deprem Yönetmeliği ," 2018.
[21] Dhannur B, Sushmitha N. Performance assessment of composite steel building considering plan irregularity before and after retrofit: pushover analysis. Mater Today Proc. 2023;88:71–76.
[22] Speicher MS, Harris JL 3rd. Collapse prevention seismic performance assessment of new eccentrically braced frames using ASCE 41. Eng Struct. 2016;117:344–357.
[23] Zameeruddin M, Sangle KK. Seismic performance evaluation of reinforced concrete frames subjected to seismic loads. J Inst Eng (India) Ser A. 2017;98(1):177–183.
[24] Patil VS, Tande SN. Probabilistic versus deterministic method of seismic performance evaluation. Asian J Civ Eng. 2018;19(2):165–176.
[25] Federal Emergency Management Agency, " Prestandard and Commentary for the Seismic Rehabilitation of Buildings," Washington, D.C., 200AD
[26] Kent DC, Park R. Flexural members with confined concrete. J Struct Div. 1971;97(7):1969–1990.
[27] Computers and Structures Inc. SAP2000 v24: Integrated Finite Element Analysis and Design of Structures. Berkeley, CA: Computers and Structures Inc; 2024
[28] Alhaddad MS, et al. Ductility damage indices based on seismic performance of RC frames. Soil Dyn Earthq Eng. 2015;77:226–237.

Volume 14, Issue 3, Page 101-108, 2025 https://doi.org/10.46810/tdfd.1686766 Research Article

BİNGÖL UNIVERSITY

Türk Doğa ve Fen Dergisi
Turkish Journal of Nature and Science
www.dergipark.gov.tr/tdfd

The Campus Flora of Bingöl University (Bingöl/Türkiye)

Mihriban AHISKALI [1*], Deniz CANLI [1,2]

[1] Bingöl University Vocational School of Food, Agriculture and Livestock, Bingöl, Türkiye
[2] Bingol University Bee and Natural Products R&D and P&D Application and Research Center, Bingöl, Türkiye
Mihriban AHISKALI ORCID No: 0000-0003-0580-7594
Deniz CANLI ORCID No: 0000-0001-9794-8911

**Corresponding author:* mahiskali@bingol.edu.tr

(Received: 29.04.2025, Accepted: 05.08.2025, Online Publication: 26.09.2025)

Keywords
Flora, Biodiversity, Bingöl University, Campus area

Abstract: This study was carried out to identify and document the diversity of seed plants in Bingöl University campus area. As a result of the study, a total of 200 taxa, representing 150 genera and 53 families, were identified within the campus. Among these, 103 taxa grow naturally on the campus, while 97 taxa are utilized for landscaping purposes. The identified flora includes 76 taxa of trees and shrubs, 59 annual herbaceous plants, and 65 perennial herbaceous species. The most represented family is Fabaceae, comprising 28 taxa, followed by Rosaceae (22 taxa), Asteraceae (12 taxa), Lamiaceae (9 taxa), and Brassicaceae (9 taxa). A total of four endemic taxa (*Arum rupicola* var. *rupicola, Centaurea fenzlii*, *Iris sari* ve *Verbascum diversifolium*) were identified in the research area, which are naturally distributed or used for landscaping purposes.

Bingöl Üniversitesi Kampüs Florası (Bingöl/Türkiye)

Anahtar Kelimeler
Flora, Bitki Çeşitliliği, Bingöl Üniversitesi, Kampüs Alanı

Öz: Bu çalışma, Bingöl Üniversitesi kampüs alanında bulunan tohumlu bitki çeşitliliğini ortaya koymak ve kayıt altına almak amacıyla yapılmıştır. Çalışma sonucunda kampüs içerisinde 53 familyaya ait 200 takson (150 cins) tespit edilmiştir. Bu taksonlardan 103'ü kampüs alanında doğal olarak yayılış gösterirken, 97'sı peyzaj düzenlemelerinde süs bitkisi olarak kullanılmıştır. Belirlenen bitkilerden 76'sı ağaç veya çalı, 59'u tek yıllık otsu bitki ve geri kalan 65'i çok yıllık otsulardır. Kampüs florasında en fazla taksona sahip familya 28 takson ile Fabaceae olup, onu sırasıyla Rosaceae (22 takson), Asteraceae (12 takson), Lamiaceae (9 takson) ve Brassicaceae (9 takson) takip etmektedir. Alanda doğal olarak yayılış gösteren veya peyzaj amaçlı kullanılan toplam dört adet endemik takson (*Arum rupicola* var. *rupicola*, *Centaurea fenzlii, Iris sari* ve *Verbascum diversifolium*) tespit edilmiştir.

1. INTRODUCTION

Turkey has one of the most advantageous locations in the world in terms of plant diversity. However, urbanization and infrastructural development cause habitat fragmentation, destruction of natural habitats, and loss of biodiversity [1]. Within the habitat fragmentation caused by urbanization, university campuses partially protect the habitat of the region in which they are located, representing the plant diversity of the region and providing an opportunity for the protection of the regional flora by acting as a shelter for these plants [2]. These areas also serve as natural application laboratories for departments in the field of natural sciences [3]. However, especially in newly established universities, factors such as construction, landscaping activities, and the spread of invasive species threaten the plant diversity in these areas [3,4]. Several universities have carried out flora studies to determine the plant biodiversity within their campus and analyse these effects [1,3–15].

Bingöl University campus is situated in the center of Bingöl Province, at $38^0$53' north latitude and $40^0$29' east longitude. The campus is 1,163 meters above sea level. Bingöl University was officially established in 2007 with 3 faculties, 1 school, 2 vocational schools and 2 institutes and has continued to develop and grow since its foundation. It continues to engage in educational, training, and research activities, with a current facilities comprising 10 faculties, 1 school, 5 institutes, 6 vocational schools, 21 research centers, and 1 central research laboratory [16]. As a result of this development, the campus area has been

expanded over the years and construction activities has increased. Concurrent landscaping attempts associated with this growth have the potential to influence and modify the natural flora [2]. Therefore, before the natural flora is further damaged, it is crucial to reveal the floral composition in the campus area. Hence, it will be possible to observe the effects of construction and landscaping activities on natural flora.

The research area is in the Bingöl province, which is in the B8 square of Davis's grid system and is a part of the Irano-Turanian phytogeographic region. According to the recent studies, the number of plant species recorded in the region has exceeded 2,000 [17–26]. In Bingöl province, summers are hot and dry, winters are cold and covered in snow. The average annual temperature is around 12.1 °C. Precipitation in Bingöl is relatively high for the region, averaging 935 mm per year, and is mostly accumulated in the winter months [27]. According to long-term climate data; as is the case throughout Türkiye, there is an increasing trend in temperature and a decreasing trend in precipitation in Bingöl province [28,29]. However, due to its classification as a humid region based on precipitation levels, Bingöl holds an advantage in plant diversity compared to other arid and semi-arid regions of Turkiye. The campus of Bingöl University (Figure 1) is situated in an area rich in plant biodiversity and it is home to a wide variety of cultivated and natural plants, including geophytes. There is also a small-scale natural woodland area dominated by oak species (*Quercus* spp.) in the south-western part of the campus.

This study aimed to identify the flora of Bingöl University campus, which is located in the city center, and contribute to the strategies for the conservation of biodiversity in the campus area based on the findings obtained. In addition to the floristic characteristics, this study highlights the potential use of native plant species in landscape design within the campus area, thereby offering an alternate strategy for the sustainable management of campus green spaces. Furthermore, this study has systematically documented the campus flora of Bingöl University for the first time, establishing a reference for monitoring future floristic changes.

Figure 1. The map of Bingol University campus

2. MATERIAL AND METHOD

The research material consists of all native and landscape plants that were obtained within the Bingöl University Campus between February to November of 2022–2024. Fruits, seeds, flowers, and basal leaves—parts necessary for species identification—were taken and identified wherever possible during specimen collection. To accomplish this, the plant was observed and photographed throughout a three-year period, from spring to fall. The identification of the species was carried out by using the 11-volume Flora of Turkey (Flora of Turkey and the East Aegean Islands) [30–32]). Additionally, the Illustrated Flora of Turkey volumes 2 and 3 [33,34], Trees and Shrubs of Turkey [35] and All Trees and Shrubs of Turkey [36] were used. The latin names and authorship of the taxa were checked from the websites “World Flora Online (WFO)” [37], “The Plant List” [38], “Bizim Bitkiler” [39] and Plant List of Turkey [40]. The local names of plants were provided using the Plant List of Turkey [40] for native or naturalized species to Turkey and Trees and Shrubs of Turkey [35] and All Trees and Shrubs of Turkey [36] for exotic plants.

3. RESULTS AND DISCUSSION

The results of this study indicate that the Bingöl University campus area contains 200 taxa (150 genera) belonging to 53 families. The identified flora includes 76 taxa of trees and shrubs, 59 annual herbaceous plants, and 65 perennial herbaceous species (Table 1). Among these, 103 taxa grow naturally on the campus, while 97 taxa are utilized for landscaping purposes. The geophytes that were determined in the area are shown in Figure 2, the trees and shrubs used for landscape design are presented in Figure 3, and some annual and perennial herbaceous plants are shown in Figure 4. In the landscaping practices implemented within the campus area, in addition to exotic (non-native) species, herbaceous and woody plant species that are found in the natural vegetation of Bingöl and possess aesthetic value have also been used. An arid landscape garden was designed on an area of 2560 m² within the campus territory [41], and the plants in this garden were included within the study.

The most represented family is Fabaceae, comprising 28 taxa, followed by Rosaceae (22 taxa), Asteraceae (12 taxa), Lamiaceae (9 taxa), and Brassicaceae (9 taxa). A total of four endemic taxa (2% endemicity) were identified in the research area, which are naturally distributed or used for landscaping purposes. These are *Arum rupicola* var. *rupicola* Boiss., *Centaurea fenzlii* Reichardt, *Iris sari* Schott ex Baker, and *Verbascum diversifolium* Hochst.

Figure 2. Photographs of natural geophytes for Bingöl taken from the campus area (a: *Ophrys transhyrcana*, b: *Fritillaria imperialis*, c: *Iris persica*, d: *Himantoglossum comperianum* e: *Iris sari,* f: *Crocus pallasii*, g: *Iris reticulata*, h: *Corydalis oppositifolia* subsp. *kurdica*, i: *Tulipa armena*, j: *Ixiolirion tataricum*, k: *Orchis tridentata* l: *Gagea luteoides*)

Table 1. Taxa determined in the research area (*: endemic, □: plants distributed in the native flora of the campus)

Family	Taxa	Local name
Adoxaceae	*Sambucus nigra* L. *'variegata'*	ağaç mürver
Adoxaceae	*Viburnum opulus* L.	gilaburu
Adoxaceae	*Viburnum opulus* L. var. *roseum* Aiton	kartopu
Anacardiaceae	*Cotinus coggygria* Scop.	boyacısumağı
Anacardiaceae	*Rhus coriaria* L.	sumak
Apiaceae	*Lecokia cretica (Lam.) DC.* □	eşekbaldıranı, tırvaş
Apiaceae	*Torilis japonica* (Houtt.) DC. □	uzun dercikotu
Araceae	*Arum rupicola* var. *rupicola* Boiss. * □	dağsorsalı
Asparagaceae	*Muscari neglectum* Guss. ex Ten. □	arapüzümü
Asparagaceae	*Ornithogalum narbonense* L. □	akbaldır
Asparagaceae	*Ornithogalum oligophyllum* E.D.Clarke □	kurtsoğanı
Asparagaceae	*Scilla siberica* Haw.	camışkıran
Asteraceae	*Achillea arabica* Kotschy □	civanperçemi, gorik
Asteraceae	*Centaurea fenzlii* Reichhardt *	sarıbaşdikeni, telu
Asteraceae	*Centaurea iberica* Trev. ex Spreng. □	deligözdikeni, belhok, telı
Asteraceae	*Centaurea solstitialis* L. □	çakırdikeni, telı, belhok
Asteraceae	*Cyanus triumfettii* (All.) Dostál ex Á.Löve & D.Löve	deli kapele, diken
Asteraceae	*Chardinia orientalis* (L.) Kuntze □	çağlaotu
Asteraceae	*Cichorium intybus* L. □	hindiba, tahlık
Asteraceae	*Cnicus benedictus* L. □	topdiken
Asteraceae	*Helichrysum plicatum* subsp. *plicatum* DC.	mantuvar, sesum, altınotu,
Asteraceae	*Onopordum carduchorum* Bornm. & Beauverd □	kavdikeni
Asteraceae	*Senecio vernalis* Waldst. & Kit. □	kanaryaotu
Asteraceae	*Tragopogon dubius* Scop.□	yemlik
Berberidaceae	*Berberis vulgaris* L.	kadın tuzluğu
Betulaceae	*Betula pendula* Roth	huş
Bignoniaceae	*Catalpa bignonioides* Walter	sigara ağacı, katalpa
Boraginaceae	*Anchusa azurea* Mill. □	sığırdili
Boraginaceae	*Cynoglossum officinale* L. □	gözpıtrağı
Boraginaceae	*Echium italicum* L. □	kurtkuyruğu
Boraginaceae	*Heliotropium europaeum* L.	akrepotu
Boraginaceae	*Onosma sericea* Willd. □	kâğıt emcek
Boraginaceae	*Paracaryum cristatum* (Schreb.) Boiss. □	ana çarşakotu
Boraginaceae	*Phyllocara aucheri* (A.DC.) Guşul. □	karadindik, sımsımık
Brassicaceae	*Aethionema arabicum* (L.) Andrz. ex DC.	arap taşçantası
Brassicaceae	*Aethionema grandiflorum* Boiss. & Hohen.	koca kayagülü, gihaye bırına
Brassicaceae	*Alyssum smyrnaeum* C.A.Mey. □	izmir kuduzotu
Brassicaceae	*Capsella rubella* Reut. □	ayşecik
Brassicaceae	*Descurainia sophia* (L.) Webb ex Prantl □	sadırotu
Brassicaceae	*Draba verna* L. □	çırçırotu
Brassicaceae	*Lepidium draba* L. (sin. *Cardaria draba* (L.) Desv.) □	diğnik
Brassicaceae	*Microthlaspi perfoliatum* (L.) F.K.Mey. □	giyle
Brassicaceae	*Sisymbrium altissimum* L. □	ergelenotu
Campanulaceae	*Legousia speculum-veneris* (L.) Durande ex Vill. □	hoş kadınaynası
Caprifoliaceae	*Lonicera tatarica* L.	yalın nevruzotu
Caprifoliaceae	*Pterocephalus plumosus* (L.) Coulter □	gök cücükotu
Caprifoliaceae	*Valeriana officinalis* L. □	kediotu
Caryophyllaceae	*Cerastium perfoliatum* L. □	ekin boynuzotu
Caryophyllaceae	*Dianthus orientalis* Adams, Weber & Mohr	yar karanfili
Caryophyllaceae	*Holosteum umbellatum* var. *umbellatum* L. □	şeytanküpesi
Caryophyllaceae	*Moenchia coerulea* Boiss. □	gökdörtlü
Caryophyllaceae	*Saponaria prostrata* Willd.	ebemterliği, sabunotu
Caryophyllaceae	*Silene vulgaris* (Moench) Garcke	ecibücü
Caryophyllaceae	*Vaccaria hispanica* (Mill.) Rauschert □	ekinebesi
Caryophyllaceae	*Velezia rigida* L.	tığotu
Convolvulaceae	*Convolvulus arvensis* L.	tarla sarmaşığı, leminek
Cupressaceae	*Cupressus arizonica* Greene	Arizona servisi
Cupressaceae	*Juniperus oxycedrus* L.	katran ardıcı
Cupressaceae	*Platycladus orientalis* (L.) Franco	doğu mazısı
Cyperaceae	*Eleocharis quinqueflora* (Hartmann) O. Schwarz	seyreksaz
Elaeagnaceae	*Elaeagnus angustifolia* L.	iğde
Elaeagnaceae	*Elaeagnus rhamnoides* (L.) A.Nelson	çıçıgan
Euphorbiaceae	*Euphorbia denticulata* Lam.	karasütlük

Euphorbiaceae	*Euphorbia esula* subsp. *tommasiniana* (Bertol.) Kuzmanov □	eşek sütleğeni
Fabaceae	*Albizia julibrissin* Durazz.	gül ibrişim
Fabaceae	*Cercis siliquastrum* L.	erguvan
Fabaceae	*Colutea cilicica* Boiss. & Balansa	patlangaç, patpatık
Fabaceae	*Lathyrus inconspicuus* L. □	yılan mürdümüğü
Fabaceae	*Lathyrus setifolius* L. □	büllübaklası
Fabaceae	*Lathyrus sphaericus* Retz. □	çamburçağı
Fabaceae	*Lotus corniculatus* L. □	gazalboynuzu
Fabaceae	*Medicago lupulina* L. □	bitçikotu
Fabaceae	*Medicago sativa* L. □	karayonca
Fabaceae	*Melilotus officinalis* (L.) Desr. □	kokuluyonca
Fabaceae	*Pisum sativum* L. □	bezelye
Fabaceae	*Robinia hispida* L.	pembe çiçekli yalancı akasya
Fabaceae	*Robinia pseudoacacia* L.	beyaz çiçekli yalancı akasya
Fabaceae	*Securigera varia* (L.) Lassen □	körigen
Fabaceae	*Styphnolobium japonicum* (L.) Schott	Japon soforası
Fabaceae	*Trifolium campestre* Schreb. □	üçgül
Fabaceae	*Trifolium pauciflorum* d'Urv. □	sülün üçgülü
Fabaceae	*Trifolium physodes* var. *physodes* Steven & M.Bieb. □	meşe üçgülü
Fabaceae	*Trifolium pratense* L. □	çayır üçgülü
Fabaceae	*Trifolium purpureum* var. *purpureum* Lois. □	mor üçgül
Fabaceae	*Trifolium resupinatum* L. □	anadolu üçgülü, nefil
Fabaceae	*Vicia anatolica* Turrill □	yılan fiği
Fabaceae	*Vicia cracca* subsp. *stenophylla* Vel. □	kuş fiği, mercür, holoz,
Fabaceae	*Vicia hybrida* L. □	melez bakla
Fabaceae	*Vicia pannonica* var. *pannonica* Crantz □	macar fiği
Fabaceae	*Vicia sativa* subsp. *nigra* var. *nigra* (L.) Ehrh □	fiğ
Fabaceae	*Vicia villosa* subsp. *villosa* Roth □	tüylü fiğ
Fabaceae	*Wisteria sinensis* (Sims) DC.	mor salkım
Fagaceae	*Quercus infectoria* Oliv. □	mazı meşesi
Fagaceae	*Quercus libani* Oliv. □	lübnan meşesi
Fagaceae	*Quercus petraea* (Matt.) Liebl. □	sapsız meşe, balu, mazer
Geraniaceae	*Erodium cicutarium* (L.) L Hér. □	iğnelik
Geraniaceae	*Geranium tuberosum* L.	çakmuz, hilok
Hypericaceae	*Hypericum lydium* Boiss. □	cayesancıyan
Hypericaceae	*Hypericum scabrum* L. □	karahasançayı, botav
Iridaceae	*Crocus pallasii* Goldb. □	güzçimi
Iridaceae	*Crocus speciosus* M.Bieb.	çayır çiğdemi
Iridaceae	*Iris persica* L. □	buzala
Iridaceae	*Iris reticulata* M.Bieb. □	karakörpeze
Iridaceae	*Iris sari* Schott ex Baker *	ana kurtkulağı
Ixioliriaceae	*Ixiolirion tataricum* var. *tataricum* (Pall.) Schult. & Schult.f. □	köpekotu
Juglandaceae	*Juglans regia* L.	ceviz
Lamiaceae	*Buddleia davidii* Franch.	kelebek çalısı
Lamiaceae	*Lallemantia iberica* (M.Bieb.) Fisch. & C.A.Mey.	ajdarbaşı
Lamiaceae	*Lamium amplexicaule* L. □	baltutan
Lamiaceae	*Lavandula angustifolia* Mill.	lavanta
Lamiaceae	*Rosmarinus officinalis* L.	biberiye
Lamiaceae	*Salvia multicaulis* Vahl	kürtreyhanı
Lamiaceae	*Salvia sclarea* L.	paskulak, dağ çayı
Lamiaceae	*Salvia verticillata* L.	dadırak, pengi
Lamiaceae	*Ziziphora capitata* L. □	anuk
Liliaceae	*Fritillaria imperialis* L.	ağlayangelin
Liliaceae	*Fritillaria persica* L.	kırklâle
Liliaceae	*Fritillaria pinardii* Boiss.	mahçuplâle
Liliaceae	*Gagea luteoides* Stapf □	altınyıldız
Liliaceae	*Tulipa armena* Boiss. □	hoş lâle
Linaceae	*Linum mucronatum* Bertol.	sarı keten
Lythraceae	*Lythrum salicaria* L. □	hevhulma
Malvaceae	*Hibiscus syriacus* L.	ağaçhatmi
Malvaceae	*Tilia rubra* DC.	kafkas ıhlamuru
Moraceae	*Morus nigra* L.	kara dut,
Oleaceae	*Ailanthus altissima* (Mill.)Swingle. □	kokarağaç
Oleaceae	*Forsytia intermedia* Zabel	altın çanı
Oleaceae	*Ligustrum vulgare* L.	kurtbağrı
Oleaceae	*Spiraea x vanhouttei* (Briot) Carrière	ispirya
Oleaceae	*Syringa vulgaris* L.	leylak
Orchidaceae	*Himantoglossum comperianum* (Steven) P.Delforge □	meşekeşkeşi
Orchidaceae	*Ophrys transhyrcana* Czerniak. □	uslusalep
Orchidaceae	*Orchis tridentata* Scop. □	katranalacası
Orobanchaceae	*Parentucellia viscosa* (L.) Caruel □	salgılı üçdiliotu
Paeoniaceae	*Paeonia arietina* G.Anderson	şakayık
Papaveraceae	*Corydalis oppositifolia* subsp. *kurdica* (Cullen & P.H.Davis) Lidén □	şepirze
Papaveraceae	*Fumaria asepala* Boiss □	ak şahtere
Papaveraceae	*Fumaria officinalis* L. □	şahtere
Papaveraceae	*Fumaria parviflora* Lam. □	tarla şahteresi
Papaveraceae	*Glaucium leiocarpum* Boiss.	gâvurhaşhaşı
Papaveraceae	*Papaver argemone* L. □	kumhaşhaşı
Paulowniaceae	*Paulownia tomentosa* (Thunnb.) Britton.	pavlonya
Pinaceae	*Cedrus libani* A.Rich.	sedir, katranağacı
Pinaceae	*Picea pungens* Engelm.	mavi ladin
Pinaceae	*Pinus nigra* subsp. *pallasiana* var. *pallasiana* □	karaçam
Pinaceae	*Pinus sylvestris* L.	sarı çam
Plantaginaceae	*Globularia trichosantha* Fisch. & C.A.Mey.	köseyayılımı
Plantaginaceae	*Linaria simplex* DC. □	yalın nevruzotu

Plantaginaceae	*Veronica hispidula* Boiss. & A.Huet subsp. *hispidula*	delimaviş
Plantaginaceae	*Veronica orientalis* Mill.	gözmumcuğu
Platanaceae	*Plantago lanceolata* L. □	damarlıca
Platanaceae	*Platanus orientalis* L.	çınar
Poaceae	*Bromus tectorum* L.	kır bromu
Poaceae	*Poa bulbosa* L. □	yumrulusalkım
Ranunculaceae	*Ceratocephala falcata* (L.) Pers. □	yelotu
Ranunculaceae	*Ceratocephala testiculata* (Crantz) Roth □	düğün yelotu
Ranunculaceae	*Ranunculus illyricus* L. □	gümüş düğünçiçeği
Ranunculaceae	*Ranunculus kochii* Ledeb.□	karçiçeği
Rhamnaceae	*Paliurus spina-christi* P. Mill. □	karaçalı
Rosaceae	*Amygdalus communis* L.	badem
Rosaceae	*Cerasus avium* (L.) Moench	kiraz
Rosaceae	*Chaenomeles speciosa* (Sweet) Nakai	bahar dalı
Rosaceae	*Cotoneaster franchetti* Boiss.	Tibet dağ muşmulası
Rosaceae	*Cotoneaster horizontalis* Decne.	bahçe alıcı
Rosaceae	*Crataegus laevigata* (Poir.) DC.	pembe çiçekli süs alıç
Rosaceae	*Crataegus monogyna* Jacq.	yemişen
Rosaceae	*Crataegus orientalis* Pall.	yayılıcı dağ muşmulası
Rosaceae	*Cydonia oblonga* Mill.	ayva
Rosaceae	*Malus floribunda* Siebold ex Van Houtte	Japon elması
Rosaceae	*Malus pumila* Mill.	elma
Rosaceae	*Malus sylvestris* (L.) Mill.	yaban elması
Rosaceae	*Potentilla recta* L. □	suparmakotu
Rosaceae	*Prunus cerasifera* Ehrh.	kırmızı yapraklı erik
Rosaceae	*Prunus serrulata* Lindl.	Japon kirazı
Rosaceae	*Prunus spinosa* L.	çakal eriği
Rosaceae	*Pyracantha coccinea* M.J.Roemer	ateşdikeni
Rosaceae	*Rosa canina* L. □	kuşburnu, sırgul, şilan
Rosaceae	*Sanguisorba minor* L. □	çayırdüğmesi
Rosaceae	*Sorbus aucuparia* L.	kuş üvezi
Rosaceae	*Sorbus torminalis* var. *torminalis* (L.) Crantz	pitlicen
Rosaceae	*Sorbus umbellata* Fritsch	geyikelması
Rubiaceae	*Cruciata taurica* (Pall. ex Willd.) Ehrend. □	kırımgüzeli
Salicaceae	*Populus nigra* L.	kara kavak
Salicaceae	*Populus tremula* L.	titrek kavak
Salicaceae	*Salix babylonica* L.	salkım söğüt
Salicaceae	*Salix matsudana* Koidz.	tirbuşon söğüdü
Salicaceae	*Vitis sylvestris* L. □	yaban asması
Sapindaceae	*Acer negundo* L.	dişbudak yapraklı akçaağaç
Sapindaceae	*Acer pseudoplatanus* L.	dağ akçaağacı
Sapindaceae	*Aesculus hippocastanum* L.	at kestanesi
Sapindaceae	*Hippocastanum aestivum* L.	atkestanesi
Sapindaceae	*Koelreuteria paniculata* Laxm.	güvey kandili
Scrophulariaceae	*Scrophularia canina* L. □	it sıracaotu
Scrophulariaceae	*Verbascum diversifolium* Hochst. * □	nizip sığırkuyruğu
Tamaricaceae	*Tamarix smyrnensis* Bunge □	ılgın
Ulmaceae	*Ulmus glabra* Huds.	dağkaraağacı
Ulmaceae	*Ulmus minor* Mill.	gürgen yapraklı karaağaç
Vitaceae	*Parthenocissus quinquefolia* (L.) Planch.	American sarmaşığı
Vitaceae	*Abelya* x *grandiflora* (Rovelli ex André) Rehder	abelya, Çin güzellik çalısı
Xanthorrhoeaceae	*Eremurus spectabilis* M.Bieb.	çiriş

Similar studies accomplished across varios university campuses in Turkey with the goals of introducing the campus territory, revealing the floral diversity, and laying the groundwork for future studies on biological diversity. Previous studies on the determination of campus floras reported that 161 natural plant taxa belonging to 38 families in Süleyman Demirel University campus [7], 78 families and 452 taxa in Akdeniz University campus [9], 223 taxa belonging to 58 families in Ordu University campus flora [42], 143 species belonging to 53 families in Yıldız Campus historical garden [6], 192 taxa belonging to 50 families in Karadeniz Technical University campus [8], 356 taxa belonging to 56 families in Uludağ University campus [43], 363 taxa belonging to 74 families in Anadolu University campus [5], 510 species belonging to 57 families in Hacettepe University Beytepe Campus [2], 445 species belonging to 79 families in Ankara University Tandoğan Campus [3], 382 taxa belonging to 51 families in Başkent University Bağlıca Campus [1], 371 taxa belonging to 61 families in Kırıkkale University campus [15], 38 tree species in Eskişehir Osmangazi University campus woody plants flora [10], 65 taxa belonging to 27 families in Düzce University Konuralp Campus [44]. Determining the flora of the campus is essential in terms of revealing local biodiversity, establishing scientific databases, and providing a background for landscape planning. The use of plants from Bingöl's natural flora in an arid garden design [41] demonstrated that the native species may be considered both aesthetically and functionally in landscape design. Based on this study, giving endemic and native plant species priority in campus landscaping will help to recognize regional plant diversity and conserve and reproduce local plant genetic resources in a sustainable manner. Furthermore, the use of native plants in landscape design will contribute to increasing the level of ecological awareness of university students and provide a source of living material for practical courses or research activities to be carried out in different departments.

In order to enhance the impact and visibility of landscape design approaches, it is recommended to prepare informative materials (e.g., posters, billboards, brochures, etc.) that introduce the plant species utilized. These types promotional activities will support the awareness of individuals visiting the campus on plant biodiversity and will also contribute to highlighting the natural and cultural heritage of the campus, thereby strengthening its ecotourism potential.

In addition to *Fritillaria* species and *Scilla siberica* obtained from different areas of Bingöl and transplanted to the campus for landscaping purposes, natural geophyte species *Himantoglossum comperianum*, *Ophrys*

transhyrcana, *Orchis tridentata*, *Tulipa armena*, and representatives of the genera *Ornithogalum*, *Crocus, Muscari,* and *Iris* were found to be distributed natively in the campus. The natural presence of these species in the area, their high adaptability to the ecological conditions of the region, and their self-reproducing ability are advantageous for horticultural applications. Specifically, the use of attractive species with high aesthetic value, such as *Paeonia arietina, Fritillaria imperialis*, and *Tulipa armena*, in the campus area will both emphasize the floral diversity of Bingöl and raise awareness about the local flora. These approaches may serve as prototypes for green spaces and garden design in other parts of the province, and the region may be positioned as a prospective ecotourism destination with nature-based landscape design.

Figure 3. Trees and shrubs used for landscaping purposes within the Bingöl University campus
(a: *Chaenomeles speciosa*, b: *Wisteria sinensis*, c: *Abelya x grandiflora*, d: *Syringa vulgaris*, e: *Cercis siliquastrum*, f: *Malus floribunda*, g: *Colutea cilicica*, h: *Lonicera tatarica*, i: *Hibiscus syriacus*, j: *Elaeagnus angustifolia*, k: *Prunus serrulata*, l: *Rosa canina*)

Figure 4. Some perennial and annual plants from Bingöl University campus area
(a: *Achillea arabica, ,* b: *Cynoglossum officinale*, c: *Linum mucronatum,* d: *Cerastium perfoliatum*, e: *Glaucium leiocarpum,* f: *Legousia speculum-veneris,* g: *Trifolium pratense* h: *Lavandula angustifolia,* i: *Centaurea fenzlii*, j: *Convolvulus arvensis*, k: *Hypericum scabrum,*, l: *Chardinia orientalis*)

REFERENCES

[1] Töre D, Erik S. Başkent Üniversitesi Bağlıca Yerleşkesinin Ankara Florası. Hacettepe Journal of Biology and Chemistry 2012;40:267–91.

[2] Mutlu B, Erik S, Tarikahya B. New Contributions to the Flora of Beytepe Campus Ankara and Floristic Comparison with Neighboring Floras and Other Campus Floras. Hacettepe Journal of Biology and Chemistry 2008;36:181–95.

[3] Başköse İ, Körüklü ST, Yapyak AE, Üniversitesi A, Fakültesi F, Bölümü B. Ankara Üniversitesi 10. Yıl (Beşevler) Yerleşkesinin Bitki Biyoçeşitliliği. Biol Divers Conserv 2020;13:217–31. https://doi.org/10.46309/BIODICON.2020.784491.

[4] Parmaksiz A, Atamov V, Aslan M. The flora of Osmanbey Campus of the Harran University. Journal of Biological Sciences 2006;6:793–804. https://doi.org/10.3923/JBS.2006.793.804.

[5] Türe C, Böcük H. The Flora of The Anadolu University Campus (Eskişehir-Turkey). Anadolu Üniversitesi Bilim ve Teknoloji Dergisi 2001;2:83–95.

[6] Erbesler Ayaşlıgil T. Yıldız Teknik Üniversitesi Yıldız Kampüsü Floristik Yapısı. Megaron 2021;16:751–69.

[7] Fakir H, Babalık A, Karatepe Y. Süleyman Demirel Üniversitesi Kampüsünün Dogal Bitki Türleri (Isparta-Türkiye). Süleyman Demirel Üniversitesi Fen Bilimleri Enstitüsü Dergisi 2009;13:33–9. https://doi.org/10.19113/sdufbed.38707.

[8] Çoşkunçelebi K, Beyazoğlu O. Karadeniz Teknik Üniversitesi Kampüsünün Doğal Çiçekli Bitkileri.

Süleyman Demirel Üniv Fen-Ed Fakültesi Fen Dergisi 1996;13:126–39.
[9] Ünal O, Gökçeoğlu M. Akdeniz Üniversitesi Kampus Florası (Antalya-Türkiye). Akdeniz University Journal of the Faculty of Agriculture 2003;16:143–54.
[10] Kadak BN, Ataşlar E. Eskişehir Osmangazi Üniversitesi Kampüsü Odunsu Bitkiler Florası. Düzce Üniversitesi Süs ve Tıbbi Bitkiler Botanik Bahçesi Dergisi 2023;2:1–13. https://doi.org/10.3897/NEOBIOTA.35.12460.
[11] Deveci M, Özbucak T, Demirkol G. Determination of Ordu University campus flora. Akademik Ziraat Dergisi 2012; 1(2): 107-116 .
[12] Abay G, Bal AN. Landscape Plants of Recep Tayyip Erdoğan University, Zihni Derin Campus (Rize-Turkey). Journal of Anatolian Environmental and Animal Sciences 2019;4:11–5. https://doi.org/10.35229/JAES.517526.
[13] Salık V, Güler N. The Flora of Trakya University Balkan Campus. Trak Univ J Nat Sci 2018;19:33–50. https://doi.org/10.23902/trkjnat.350526.
[14] Mutlu B, Karakuş Ş. Floristic List of İnönü University Malatya Main Campus Area. Hacettepe Journal of Biology and Chemistry 2015;43:73–89. https://doi.org/10.15671/HJBC.20154312547.
[15] Nugay ÖZ, Duran A, Doğan B. Kırıkkale Üniversitesi Kampüs Florası. Selçuk Üniversitesi Fen Fakültesi Fen Dergisi 2007;2:79–92.
[16] Anonymous. History. 2025 2025:1–2. https://www.bingol.edu.tr/tr/universitemiz/genel/tarihce (accessed February 23, 2025).
[17] Polat R, Canlı D, Selvi S, Esim N, Çakılcıoğlu U, Ecem Bayram N, et al. Bingöl Arı Florası ve Polen Atlası. Ankara: Akademisyen Kitabevi; 2021. https://doi.org/10.37609/akya.594.
[18] Kılıç Ö, Yıldırımlı Ş, Kıranşan K. Yüzenadalar (Bingöl-Solhan) çevresinin fulorası. OT Sistematik Botanik Dergisi 2017;24:117–55.
[19] Çetin A, Behçet L. Koz Dağı (Genç / Bingöl) ve Çevresinin Florası. Commagene J Biol 2022;6:39–61. https://doi.org/10.31594/COMMAGENE.1086190.
[20] Yapar Y, Behçet L. Hiro Yaylası Adaklı-Bingöl/Türkiye ve çevresinin florası. Biol Divers Conserv 2018;11:126–40.
[21] Sinan A, Behçet L. Altıkardeş Dağı ve çevresinin Genç, Bingöl florası. Biol Divers Conserv 2014;7:98–116.
[22] Cengiz H, Behçet L. Perisuyu Vadisi ve Çevresinin (Yedisu-Karlıova/Bingöl) Florası. Bağbahçe Bilim Dergisi 2024;11:143–74. https://doi.org/10.35163/BAGBAHCE.1436940
[23] Behçet L, Yapar Y. Important plants at the Matan Mountain (Bingöl/Turkey) flora with regard to beekeeping. Biol Divers Conserv 2019;12:149–59.
[24] Demirpolat A, Kılıç Ö, Yildirimli Ş, Bağci E. Genç İlçesi (Bingöl) ve Yakın Çevresinin Florası. Osmaniye Korkut Ata Üniversitesi Fen Bilimleri Enstitüsü Dergisi 2023;6:289–309. https://doi.org/10.47495/OKUFBED.1105935.
[25] Sinan A. Yaylım Sıra Dağları ve Çevresinin (Solhan-Genç /Bingöl) Florası. Doktora Tezi. Bingöl Üniversitesi Fen Bilimleri Enstitüsü, 2024.
[26] Cengiz H. Göynük Nahiyesi ve Çevresinin (Karlıova-Bingöl) Florası. Yüksek Lisans Tezi. Bingöl Üniversitesi, 2016.
[27] Kaya S. The Effect of Global Climate Change on Monthly and Annual Precipitation Amounts in Bingol Province (Turkey). Uluslararası Gıda Tarım ve Hayvan Bilimleri Dergisi 2023;2023:1–12.
[28] Doğan Demir A, Demir Y, Şahin Ü, Meral R. Bingöl ilinde sıcaklık ve yağışların trend analizi ve tarıma etkisi. Türk Tarım ve Doğa Bilimleri Dergisi 2017;4:284–91.
[29] Yükseler U, Dursun ÖF, Alashan S. Yağışların Mevsimsel Değişimlerinin Eğilim Analiz Yöntemleri İle Araştırılması: Bingöl İli Örneği. El-Cezeri 2021;8:45–59. https://doi.org/10.31202/ECJSE.769918.
[30] Davis PH. Flora of Turkey and Aegean Islands. vol. 1–9. Edinburgh: Edinburgh University Press; 1965.
[31] Davis PH, Mill RR, Tan K. Flora of Turkey and The East Aegean Islands. Vol. 10. vol. 10 Supplement 1. Edinburgh: Edinburgh University Press; 1988.
[32] Güner A, Özhatay N, Ekim T, Bafler KHC. Flora of Turkey and the East Aegean Islands, Vol 11 Second Supplement. vol. 11. Edinburgh: Edinburgh: University Press; 2000.
[33] Güner A, Kandemir A, Menemen Y, Yıldırım H, Aslan S, Ekşi G., et al., editors. Resimli Türkiye Florası Cilt 2. vol. 2. İstanbul: NGBB Yayınları Flora Dizisi 2; 2018.
[34] Güner A, Kandemir A, Menemen Y, Yıldırım H, Aslan S, Çimen A.Ö., et al., editors. Resimli Türkiye Florası, Cilt 3a. 2022.
[35] Mamıkoğlu NG. Türkiye'nin Ağaçları ve Çalıları. 3. Baskı. İstanbul: NTV Yayınları; 2010.
[36] Akkemik Ü. Türkiye'nin Bütün Ağaçları ve Çalıları. İstanbul: İş Bankası Kültür Yayınları; 2020.
[37] The WFO Plant List | World Flora Online 2021. https://wfoplantlist.org/ (accessed April 23, 2025).
[38] Home-The Plant List 2010. http://www.theplantlist.org/ (accessed April 23, 2025).
[39] Nezahat Gökyiğit Botanik Bahçesi. Türkiye Bitkileri Listesi 2019. https://bizimbitkiler.org.tr/yeni/demos/technical/ (accessed April 23, 2025).
[40] Güner A, Aslan S, Ekim T, Vural M, Babaç MT. Türkiye Bitkileri Listesi (Damarlı Bitkiler). ANG Nezahat Gökyiğit Botanik Bahçesi Yayınları Flora Dizisi; 2012.
[41] Caf A. Bingöl ili doğal vejetasyonundaki bitkiler ile kurakçıl bahçe oluşturulması üzerine bir araştırma. Doktora Tezi. Atatürk Üniversitesi, Fen Bilimleri Enstitüsü, 2019.
[42] Deveci M, Özbucak TB, Demirkol G. Ordu Üniversitesi kampüs alanı florasının tespiti. Akademik Ziraat Dergisi 2013;1:107–16.
[43] Tarımcılar G. Uludağ Üniversitesi kampüs alanı florası. Yüksek Lisans Tezi. Uludağ Üniversitesi, Fen Bilimleri Enstitüsü, 1992.

[44] Yazlık A, Kavak M, Aşkın E, Külcüoğlu N, Ersoy Ö, Kovankaya F, et al. Kentsel Yaşam Alanında Bitki Çeşitliliği ve Etkileri: Düzce Üniversitesi Konuralp Kampüsü Örneği. Turk Tarim Arast Derg 2020;7:66–77. https://doi.org/10.19159/tutad.665404.

Volume 14, Issue 3, Page 109-119, 2025 https://doi.org/10.46810/tdfd.1694722 Research Article

BİNGÖL UNIVERSITY

Türk Doğa ve Fen Dergisi
Turkish Journal of Nature and Science
www.dergipark.gov.tr/tdfd

Effect of GFRP Anchor on the Performance of Reinforced Concrete Beams to Mitigate The Debonding Failure

Yusuf SÜMER[1*], M. Nawar ZAKOUR[1], Wael ALDHABIR[1]

[1]Sakarya University of Applied Sciences, Faculty of Technology, Department of Civil Eng. Sakarya, Türkiye
Yusuf SÜMER ORCID No: 0000-0002-9314-1640
M.Nawar ZAKOUR ORCID No: 0000-0002-9454-3406
Wael ALDHABİR ORCID No: 0000-0002-5220-7041
**Corresponding author: ysumer@subu.edu.tr*

(Received: 07.05.2025, Accepted: 05.08.2025, Online Publication: 26.09.2025)

Keywords
GFRP anchor, Debonding failure, Strengthening, FRP

Abstract: Strengthening reinforced concrete (RC) beams using fiber-reinforced polymer (FRP) materials has become a widely accepted technique in structural engineering due to its efficiency, light weight, and resistance to corrosion. Among these materials, glass fiber-reinforced polymers (GFRP) are commonly used for flexural strengthening by bonding fabric sheets to the tension side of beams using epoxy adhesives. In this study, an experimental program was carried out to investigate the flexural behavior of an RC beam strengthened with a GFRP fabric sheet bonded to its bottom surface using epoxy. Standard three-point bending was applied to the beam. During loading, premature debonding between the GFRP sheet and the concrete surface was observed at advanced stages, leading to slip and reduction in strengthening efficiency. To mitigate this issue, GFRP anchors, made from the same material as the strengthening sheet were introduced to improve the bond. These anchors had varying dimensions in width and height to assess their influence on the overall performance of the beam. The results revealed that both the load-carrying capacity and displacement capacity of the beam increased significantly with the addition of the anchors. The highest level of performance enhancement was achieved when the anchor width was maximized and the height remained lower than the width, suggesting that wider and flatter anchors enhance bond performance more effectively. A clear proportional relationship was found between anchor width and the beam's structural performance, while increased anchor height showed a diminishing effect. These findings highlight the critical role of anchor geometry in optimizing the performance of GFRP-strengthened RC beams.

GFRP Ankraj Boyutlarının GFRP Levhalar ile Güçlendirilmiş Betonarme Kirişlerin Performansına Etkisi

Anahtar Kelimeler
GFRP ankraj, FRP uç sıyrılması, Güçlendirme, FRP

Öz: Fiber takviyeli polimer (FRP) malzemeler kullanılarak betonarme kirişlerin güçlendirilmesi, verimliliği, hafifliği ve korozyona karşı direnci nedeniyle yapı mühendisliğinde yaygın olarak kabul edilen bir teknik haline gelmiştir. Bu malzemeler arasında, cam elyaf takviyeli polimerler (GFRP), epoksi yapıştırıcılar kullanılarak kirişlerin eğilme güçlendirmesinde yaygın olarak kullanılmaktadır. Bu çalışmada, epoksi kullanılarak alt yüzeyinden GFRP levha ile güçlendirilmiş bir betonarme kirişin eğilme davranışını incelemek için deneysel bir program gerçekleştirilmiştir. Betonarme kirişler, standart bir eğilme yükleme senaryosunu simüle etmek için basit mesnetli ve tek nokta yükü altında test edilmiştir. Deneysel çalışmalarda yükleme sırasında, GFRP levha ile beton yüzey arasında erken ayrılma bilinen bir sorundur ve bu sorun güçlendirme verimliliğinde azalmaya yol açmaktadır. Bu çalışmada erken kopma sorununu gidermek için GFRP levhaların uç noktalarına farklı genişlik ve yükseklikte GFRP kumaşlardan ankrajlar uygulanmıştır. Sonuçlar hem kirişin yük taşıma kapasitesinin hem de yer değiştirme kapasitesinin ankrajların etkisiyle önemli ölçüde arttığını ortaya koymuştur. En etkili iyileştirme, ankraj genişliği maksimuma çıkarıldığında ve yüksekliği ise orta seviyelerde iken meydana gelmiştir. Ankraj genişliği ile kirişin yapısal performansı arasında net bir ilişki bulunurken, artan ankraj yüksekliğinin azaltıcı bir etki gösterdiği görülmüştür. Bu bulgular, ankraj geometrisinin GFRP ile güçlendirilmiş betonarme kirişlerin performansını optimize etmedeki kritik rolünü olduğunu ortaya koymuştur.

1. INTRODUCTION

With the rapid advancement of technology and construction practices, conventional strengthening techniques such as concrete jacketing and steel plate reinforcement are gradually losing favor among construction professionals. These traditional methods often present practical and economic challenges, including complex installation procedures, increased labor demand, and long-term maintenance concerns. In recent years, fiber reinforced polymers (FRPs) have emerged as a promising alternative for the strengthening and rehabilitation of both concrete and steel structures. These composite materials offer a combination of desirable properties, including exceptionally high tensile strength, resistance to corrosion, and lightweight, which contribute to reduced installation time and lower lifecycle costs compared to conventional solutions. As a result, the use of FRP materials in structural retrofitting has gained significant attention for providing efficient, durable, and cost-effective reinforcement strategies [1–9]. Numerous experimental and analytical studies have confirmed that externally bonding fiber-reinforced polymer (FRP) systems to reinforced concrete (RC) elements is an effective method to significantly enhance their flexural strength and load-carrying capacity [10–12]. However, despite these advantages, this strengthening technique still encounters some limitations, especially under failure conditions. Several investigations have revealed the emergence of novel failure mechanisms that may adversely impact the overall performance of FRP systems when applied in structural rehabilitation [13].

According to [10], typical failure modes observed in RC beams strengthened in flexure with externally bonded FRP plates include the following: a) FRP rupture; b) Compressive concrete crushing; c) Shear failure; d) Concrete cover separation (CCS); e) Plate-end interfacial debonding; f) Intermediate flexural crack (IC)-induced debonding; g) Intermediate flexural-shear crack (IC)-induced debonding. Among all debonding-related failure types, IC-induced debonding and concrete cover separation (CCS) near the plate ends have been reported as the most frequently observed and critical failure modes. These are illustrated in Figure 1 as follows: (a) ideal bond between FRP and RC beam, (b) interfacial debonding due to flexural cracking, (c) interfacial debonding due to flexural-shear cracking, and (d) concrete cover separation [14–15]. Several parameters influence the likelihood and type of debonding failure, including the thickness of the concrete cover, number and diameter of tensile steel bars, the distance between the FRP plate end and the beam support, and FRP properties such as length, width, thickness, and modulus of elasticity. Additional contributing factors include the shear span-to-depth ratio, the interaction between shear and bending moments, cross-sectional geometry, and compressive strength of the concrete [14–18].

One of the most concerning forms of failure is plate-end (PE) debonding, which is particularly brittle and tends to occur before the tensile reinforcement yields. This premature failure leads to underutilization of the FRP's tensile strength, making it essential to provide a suitable anchorage at the plate ends to ensure a more ductile response and maximize the effectiveness of externally bonded FRP strengthening systems [14].

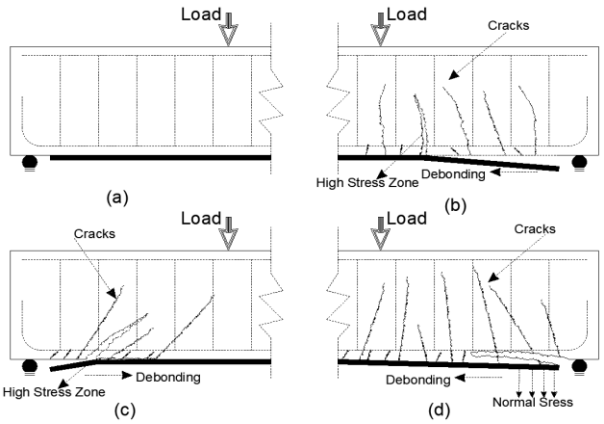

Figure 1. Typical failure modes observed in RC beams strengthened in flexure with externally bonded FRP plates

To mitigate the risk of such brittle debonding failures, several anchorage techniques have been proposed in the literature [14,16,19]. Among these, the use of U-Wrap anchors applied along the beam's sides has gained prominence due to its practicality, quick installation, ease of execution without the need for pre-drilling, and superior resistance to corrosion—an essential factor for long-term durability [14,20].

Consequently, various design standards have begun to incorporate detailed recommendations and guidelines concerning the use of externally bonded FRP for concrete strengthening, specifically aimed at minimizing debonding risks and ensuring system reliability [20–24]. Nevertheless, while several studies have explored the effectiveness of U-Wrap anchors in reducing or eliminating debonding failures [16,20,25,26], there remains a lack of focused research addressing specific design optimization aspects. Furthermore, most existing studies do not comprehensively quantify the enhancement achieved through these anchorage systems, do not determine the effect of changing the anchor dimensions, and reliable design formulas for predicting their contribution are still lacking [7,9,13,14,16,17,19,25– 33].

A recent analytical study using Abacus software examined the effect of anchor geometry on bending behavior and demonstrated that increasing anchor width is more effective in increasing load capacity than increasing anchor height [34]. This experimental study aims to investigate the influence of anchor geometry on the flexural performance of reinforced concrete beams strengthened with a single layer of unidirectional glass fiber-reinforced polymer (GFRP) sheets applied to the tension face. A total of six beams were tested under four point loading: two reference beams, one unstrengthened and one strengthened with GFRP only to assess the baseline effect of external reinforcement, and four beams strengthened with GFRP sheets and end anchors of varying dimensions to evaluate the impact of anchor width and height on structural behavior.

2. EXPERIMENTAL STUDY

A series of flexural tests were conducted on six reinforced concrete beams, all cast and prepared under the same conditions. Each beam had a concrete compressive strength of 10 MPa, and identical reinforcement detailing: two 12 mm diameter steel bars in both the top and bottom longitudinal layers, and 8 mm diameter stirrups spaced at 75 mm intervals, serving as transverse reinforcement. The cross-sectional dimensions of each beam were 150 mm in width and 250 mm in height, with a concrete cover of 25 mm to the reinforcement. Each beam was designated with a specific name corresponding to the type and configuration of the applied strengthening system as follows:

- Control Beam: CB
- Control Beam strengthened with single layer GFRP on the bottom face: L1C
- Beam with 10cm width and 10cm height, GFRP end anchor and single layer GFRP strengthened: L1W10H10
- Beam with 10cm width and 25cm height, GFRP end anchor and single layer GFRP strengthened: L1W10H25
- Beam with 20cm width and 25cm height, GFRP end anchor and single layer GFRP strengthened: L1W20H25
- Beam with 25cm width and 10cm height, GFRP end anchor and single layer GFRP strengthened: L1W25H10

In this study, the experimental design matrix was developed based on a combination of previous finite element analyses, available literature, and practical considerations. The selected anchor dimensions (i.e., 10×10, 10×25, 20×25, 25×10 cm) allowed for isolating the influence of anchor width and height on the flexural behavior of RC beams strengthened with GFRP. These dimensions were chosen to examine the effect of increasing anchor width while keeping height constant, and vice versa, ensuring a controlled parametric evaluation. This methodology ensures the findings are applicable to practical strengthening scenarios. Table 1 shows the variables of experimental study.

Tablo 1. Parametric study matrix

Sample name	Strirrup spacing (mm)	Upper reinforcement	Bottom reinforcement	FRP type	Epoxy Layer	Achor height (mm)	Anchor width (mm)
B	Ø8/75	2T12	2T12	GFRP	NA	NA	NA
L1C	Ø8/75			GFRP	One Layer Bottom	NA	NA
L1W10H10	Ø8/75			GFRP		100	100
L1W10H25	Ø8/75			GFRP		250	100
L1W20H25	Ø8/75			GFRP		250	200
L1W25H10	Ø8/75			GFRP		100	250

Dimensions and schematic views of the designed beams are shown in Figure 2.

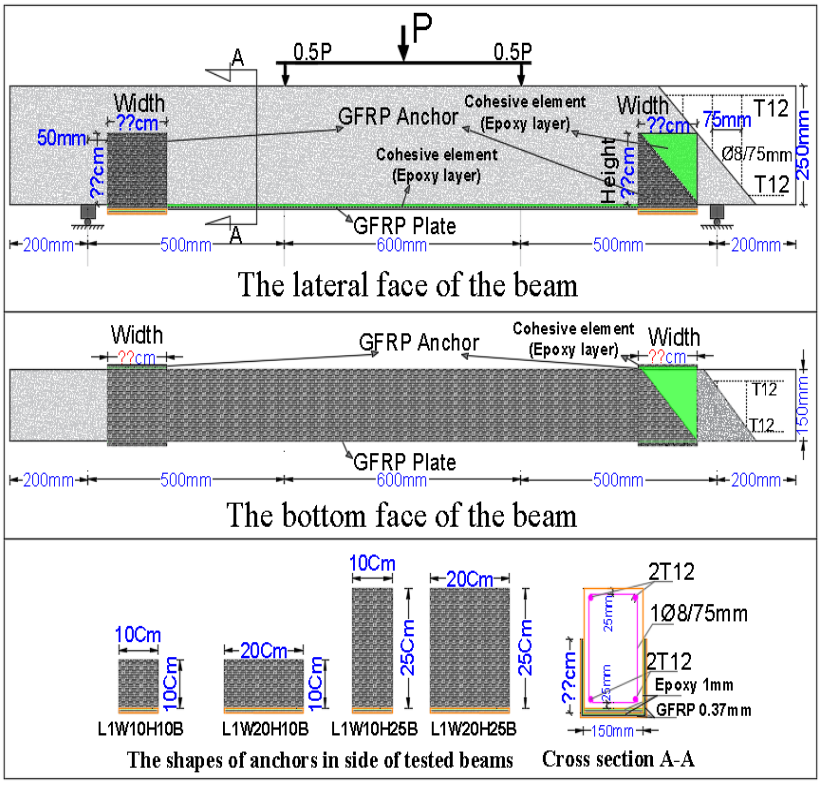

Figure 2. Schematic diagram of anchor placement and dimension changes

2.1. Properties of Materials

2.1.1. Concrete density test

The density of the concrete used in this study was determined by measuring the mass and volume of standard cylindrical specimens in accordance with relevant testing procedures (e.g., ASTM C642). A cylindrical sample with dimensions of 150 mm in diameter and 300 mm in height was used for this purpose (Figure 3).

The average mass of the specimen was recorded as 12.5 kg, and based on its geometric volume (calculated as $\pi \times r^2 \times h$), the resulting unit weight (density) of the concrete was computed to be approximately 23.59 kN/m³. This value is within the typical range for normal-weight concrete, indicating that the mix design used provides a good balance between strength and density, suitable for structural applications.

Figure 3. Concrete density test

The measured density also confirms the homogeneity and proper compaction of the concrete mix, which is essential for the effective bonding with both internal reinforcement and externally bonded GFRP sheets used in the strengthening system.

2.1.2. Slump test

To evaluate the workability of the concrete mix used in this study, a slump test was conducted according to standard procedures (ASTM C143/C143M). The test aimed to assess the consistency and fluidity of the fresh concrete before casting the beam specimens. The measured slump value was 12 cm, indicating a concrete mix with medium to high workability (Figure 4).

Figure 4. Slump test of cast in place concrete

This level of slump is considered appropriate for structural elements such as reinforced concrete beams, as it facilitates adequate compaction and bonding with embedded reinforcement without leading to segregation or excessive bleeding. The achieved slump value also ensured proper surface contact with the bonded GFRP sheet and minimized the presence of voids at the interface, which is critical for the effectiveness of the strengthening system.

2.1.3. Compressive strength test

To evaluate the compressive strength of the concrete used in this study, standard compression tests were conducted on both cylindrical and cubical specimens in accordance with ASTM standards (Figure 5). Concrete cylinders measuring 150 mm in diameter and 300 mm in height (15×30 cm) were cast and tested after 28 days of curing, yielding an average characteristic compressive strength of 10 MPa. In parallel, cubical specimens measuring 200 mm on each side (20×20×20 cm) were tested under the same conditions and exhibited an average compressive strength of 13 MPa at 28 days.

Figure 5. Compressive strength test of concrete samples

The difference in strength values between the cylindrical and cubical specimens is consistent with expected conversion factors, as cube tests typically produce higher results due to differences in specimen geometry and stress distribution during testing. These strength levels indicate that the concrete used was of low to moderate strength, which aligns with the purpose of the experimental program aiming to investigate the performance of externally strengthened RC beams under realistic conditions.

These values serve as a reference for analyzing the flexural behavior and failure mechanisms observed in the beam tests, and for assessing the effectiveness of the GFRP strengthening system under practical material limitations.

2.1.4. Tensile strength of steel reinforcement

To determine the mechanical properties of the steel reinforcement used in the concrete beams, tensile tests were conducted on steel bars of two different diameters: 8 mm and 12 mm, following standard testing procedures

ASTM A370 (Figure 6). The results provided essential data regarding the yield and ultimate strengths of the reinforcement, which are critical for evaluating the flexural performance of the strengthened beams.

For the 8 mm diameter bars, the average yield stress was measured at 365 MPa, while the ultimate tensile strength reached 525 MPa. In contrast, the 12 mm diameter bars showed a higher average yield stress of 425 MPa and an ultimate tensile strength of 585 MPa.

Figure 6. Tensile strength test of steel reinforcement

The variation in strength between bar diameters reflects the manufacturing and mechanical differences associated with size, and provides a reliable basis for the flexural design and analysis of the tested RC beams. These steel properties were taken into account when interpreting the results of the beam tests and assessing the contribution of both internal steel reinforcement and external GFRP strengthening.

2.1.5. Tensile test of CFRP fabric sheets

To determine the tensile properties of the externally bonded GFRP fabric sheets used for strengthening, a series of uniaxial tensile tests were carried out (Figure 9). The GFRP fabric had a nominal areal weight of 330 gr/m².

Figure 7. One-way oriented polymer reinforced fiberglass textile plates

Test specimens were prepared with average dimensions of 17.5 cm in length, 4 cm in width, and a thickness of 0.37 mm (Figure 7).

Figure 8. Tensile tested of GFRP samples

To ensure uniform stress distribution and prevent localized failure at the gripping points, two metal plates were adhesively bonded to both ends of each specimen using Sikadur-330 epoxy resin, forming effective end-tabs for load transfer during testing as shown in Figure 8. The specimens were then loaded using a universal testing machine until failure.

The results showed an average tensile strength of 300 MPa, with an elongation of approximately 3 mm prior to rupture. These values confirm the high tensile capacity of the GFRP fabric, making it suitable for flexural strengthening of reinforced concrete elements. The bonding technique with epoxy and metal end-tabs proved effective in reducing stress concentrations and allowing for accurate measurement of tensile behavior.

Figure 9. Tensile test of GFRP samples

The obtained tensile characteristics were essential in evaluating the contribution of the GFRP sheets to the overall performance of the strengthened beams, particularly in terms of load redistribution and crack control under flexural loading.

2.1.6. Epoxy adhesive properties

The bonding between the GFRP fabric sheets and the bottom surface of the reinforced concrete beam was achieved using Sikadur-330, a high-performance two-component thixotropic epoxy-based adhesive, specifically formulated for structural bonding applications in FRP strengthening systems (Figure 10). This adhesive is widely used due to its excellent mechanical and physical properties, including strong adhesion, ease of application, and compatibility with both

concrete and FRP surfaces. The key mechanical and physical properties of Sikadur-330, as provided by the manufacturer, are summarized in Table 2.

Table 2. The properties of Sikadur-330 [34]

Tensile Strength	Compressive Strength	Flexural Strength	Shear Strength
~30 MPa	~70 MPa	~45 MPa	~18 MPa
Young's Modulus (Tensile)		Elongation at Break	Density
~4500 MPa		~0.9 %	~1.31 kg/L

Application Temperature: +10°C to +35°C
Curing Time: Initial cure in 12 hours; full cure in 7 days

Figure 10. Sikadur-330

These properties ensured efficient stress transfer between the GFRP and concrete, playing a crucial role in the effectiveness and durability of the strengthening system used in this experimental study.

2.2. Experimental Procedure

Five beams were externally strengthened on the bottom tension face using Single layer of textile glass fiber reinforced polymer (GFRP) sheets, which were bonded to the concrete surface using Sikadur-330 epoxy adhesive. To enhance the bond performance and delay premature debonding, GFRP anchors of varying geometries were installed on selected beams, and the flexural behavior was evaluated using a three-point bending test setup, as shown in Figure 11.

Figure 11. Examples of RC retrofitted beams with GFRP plates and anchors

This setup enabled a comparative analysis of load capacity and displacement behavior across all beam specimens, particularly focusing on the role of anchor geometry in enhancing the efficiency of GFRP-strengthened concrete members.

3. CONCLUSIONS AND DISCUSSION

3.1. Load–Deflection Response From Three-Point Bending Tests Of GFRP-Strengthened Beams With Side Anchors

A series of three-point bending tests as Figure 12 in were conducted to examine the flexural behavior of reinforced concrete RC beams strengthened with externally bonded glass fiber reinforced polymer (GFRP) plates.

To address premature debonding of the GFRP plates, mechanical anchors were applied along the sides of the beam webs. The anchors were fabricated in various dimensions, with variations in both height and width, to assess their influence on the load capacity and deflection characteristics of the strengthened beams.

Figure 12. The machine of applied load on the tested beams

Figure 13. Appearance of C collapsed sample after three-point bending test

RC Beams equipped with GFRP anchors exhibited higher peak loads and greater deflection capacities, confirming the contribution of optimized anchorage to delaying or preventing debonding failures, which can be noticed in Figures from 13 even 18.

Figure 14. Appearance of L1C collapsed sample after three-point bending test

Figure 15. Appearance of L1W10H10 collapsed sample after three-point bending test

Figure 16. Appearance of L1W10H25 collapsed sample after three-point bending test

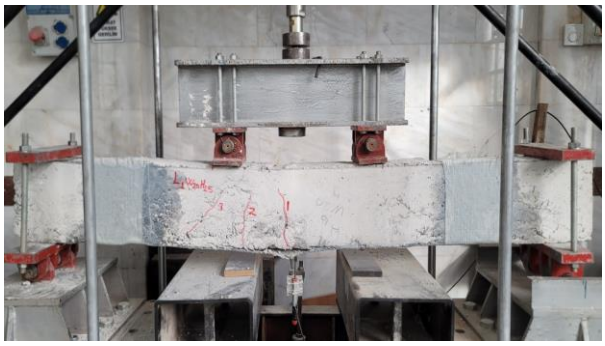

Figure 17. Appearance of L1W20H25 collapsed sample after three-point bending test

The experimental results are illustrated in the load–deflection curves shown in Figure 19. Furthermore, the beams were loaded until collapse occurred due to flexural cracks as a result of debonding failure. These curves reflect the effectiveness of the side anchors in enhancing flexural performance and demonstrate the role of anchor geometry in improving load resistance and ductility.

Figure 18. Appearance of L1W25H10 collapsed sample after three-point bending test

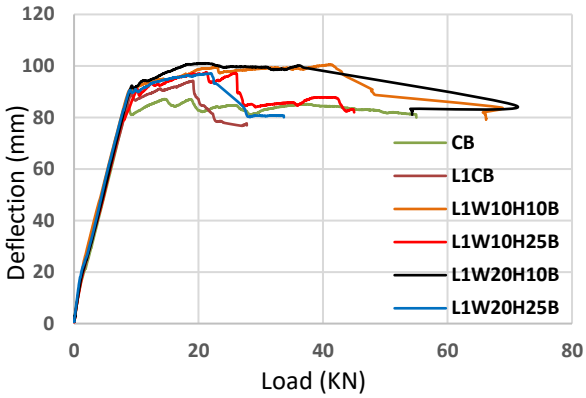

Figure 19. Diagram of three-point bending tests of GFRP-strengthened beams with side anchors and control beam

It is noted that the addition of the anchor led to an increase in the load capacity and ductility of RC beams retrofitted with GFRP plate.

3.2. The Max Capacity Load Of RRC Beams With GFRP Plate

To know the amount of improvement of the load capacity and the effectiveness of the U-Wrap anchor in reducing the problem of debonding failure, the ultimate moment that the beam can be loaded was calculated by information in Table 3, Eq (1), and Eq (2) which is illustrated in Figure 20, according to the ACI 440.2R [35] and in Figure 21, according to the Canadian code ISIS [36] considers a linear strain variation over the depth of sections, and uses the value of 0.003 for the maximum concrete compressive strain. Then the ultimate force was calculated after reducing the arm (500 mm) shown according to the Figure 10 and that is for RRC beam with GFRP plate.

$$M_u = \varphi_s A_s \sigma_s \left(d - \frac{\beta c}{2}\right) + \varphi_{frp} A_f \sigma_f \left(d_f - \frac{\beta c}{2}\right) + \varphi_s A'_s \sigma'_s \left(\frac{\beta c}{2} - d'\right) \quad (1)$$

$$M_u = \text{ØMn} = \text{Ø}\left[A_s \sigma_s \left(d - \frac{\beta_1 c}{2}\right) + \varphi_{frp} A_f \sigma_{fe} \left(h - \frac{\beta_1 c}{2}\right) + A'_s \sigma'_s \left(\frac{\beta_1 c}{2} - d'\right)\right] \quad (2)$$

Mu: Ultimate moment, Nmm, Mn: Nominal moment, Nmm. α, β: Stress-block factors for concrete, Ø: The reduction factors, c: Depth of neutral axis, mm. As, Af and A's are the areas of the tensile reinforcing bars, GFRP sheets and compressive reinforcing bars, respectively, mm^2. φ: The reduction factors' of 0.6, 0.85 and 0.75 for concrete, steel and FRP plate, respectively. σs, σ's, σf Tensile, compressive strength of steel and tensile strength of GFRP Plate, respectively.

According to the use of the previous equations, the load capacity for Eq (1) is 84.3 kN and the load capacity for Eq (2) is 100 kN.

Table 3. Mechanical properties of used materials

Steel	Elastic modulus	Es	210E+3	MPa
	Yielding stress	fy	425	MPa
	Poisson ratio	ν	0.3	-
Concrete	Compression stress	f'c	10	MPa
GFRP	Elastic modulus	E_{GFRP}	65E+3	MPa
	Yielding stress	f_{CFRP}	300	MPa

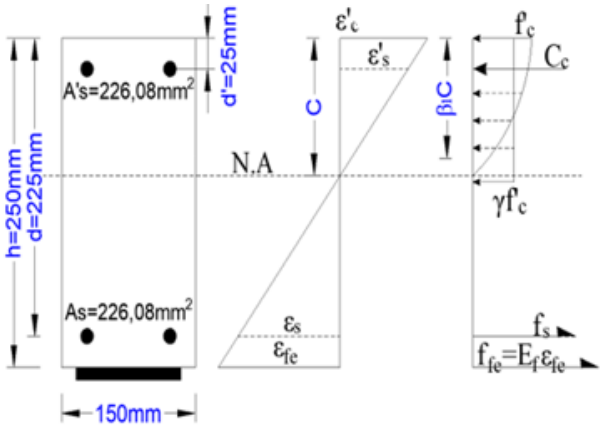

Figure 20. Ultimate moment according to ACI 440.2R [34]

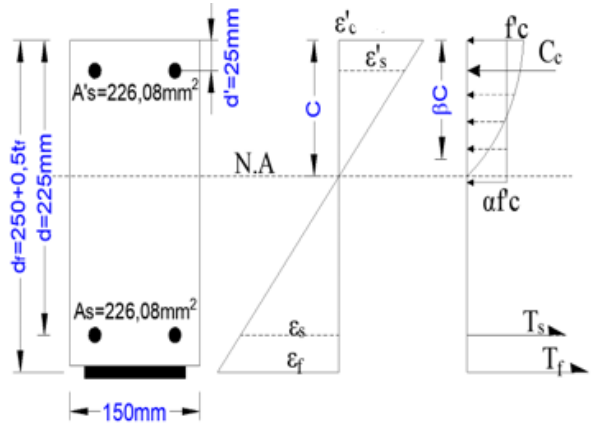

Figure 21. Ultimate moment according to ISIS [35]

3.3. The Improvement Of Capacity Load Of RRC Beams With GFRP Plate And Anchorage:

To observe the amount of improvement in the load capacity, the values of the maximum load carried by each beam during experiment and its corresponding deflection are listed in Table 4.

The obtained results generally align with previous research findings that emphasized the beneficial role of anchors in enhancing bond performance and flexural strength of RC beams (14, 25, 27, 30, 31). However, unlike some prior studies that suggested anchor height plays a significant role, our results showed diminishing improvement with increasing height. This divergence may be attributed to stress concentration patterns and the bond behavior at the tension face. Furthermore, differences in concrete strength and anchorage installation techniques across studies may account for discrepancies. This highlights the necessity of optimizing anchor geometry specifically for each application scenario.

Table 4. Maximum load-deflection values for the tested beams

Tested sample	Max load (P_{kN})	Deflection (Δ_{mm})
C	87.15	14.51
L1C	94.20	19.12
L1W10H10	100.51	40.97
L1W10H25	97.35	21.24
L1W20H25	97.08	21.98
L1W25H10	101.06	20.99

The previous values are also represented graphically in Figure 22.

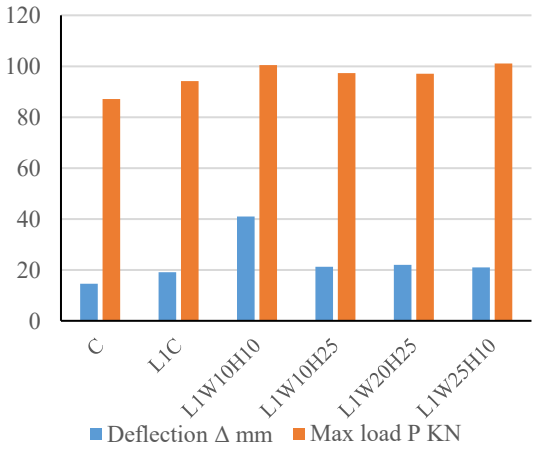

Figure 22. Chart of maximum load values and corresponding deflection for the tested beams

It is clear that increasing the height of the anchor gives a lower load capacity, while increasing the width of the anchor increases the load capacity. The effect that each anchor adds to prevent the sliding of the GFRP plate retrofitting to RC beam is studied as a percentage of the maximum load value provided only by the GFRP plate retrofitting to RC beam, and this is shown in Figure 23.

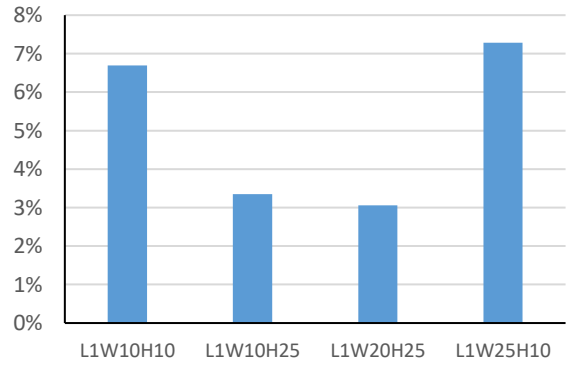

Figure 23. The relative increase in the load capacity after adding different dimensional models of GFRP anchors

Figure 23 shows that adding an anchor improves the load capacity, with the best result being an anchor width of 25 cm and a height of 10 cm, resulting in a 7.28% increase in load capacity.

Table 5. Relative comparison between the load capacity from the code and the experiment

Code	P_{kN}	Comparing with L1C	Comparing with L1W25H10
ACI 440.2R	84.3	-10.5%	19.9%
ISIS	100	6.2%	1.1%

Comparing the theoretical load capacity values from the codes with the laboratory values, it can be noted that when the GFRP plate was added to the beam (L1C), the theoretical load capacity values were 10.5% lower in the American code (ACI 440.2R), in contrast to the Canadian code (ISIS), which gave results 6.2% higher than the laboratory values. Comparing the code values with the maximum values for the L1W25H10 anchor, we find that adding the anchor produced load capacity results that were 19.9% higher than the code results for the American code and 1.1% higher than the Canadian code. This means that adding the anchors mitigated the slippage problem between the GFRP plate and the tensioned RC beam surface, bringing it closer to the theoretical values provided by the code's theoretical calculations.

4. CONCLUSION

This experimental study investigated the flexural performance of RC beams strengthened with externally bonded GFRP sheets and equipped with U-wrap GFRP anchors of varying dimensions. The results confirm that anchorage systems significantly enhance the structural performance of GFRP-strengthened beams by mitigating premature debonding failure and increasing both load capacity and ductility.

Key findings from this research are summarized as follows:

- Effectiveness of GFRP Strengthening:
  The use of externally bonded GFRP sheets alone improved the flexural capacity of RC beams compared to the unstrengthened control beam, demonstrating the fundamental benefit of composite reinforcement.
- Critical Role of Anchors:
  Beams retrofitted with both GFRP sheets and U-wrap anchors showed a significant increase in ultimate load capacity compared to beams strengthened with GFRP sheets alone. This indicates that proper anchorage can significantly delay the onset of debonding and allows better utilization of the GFRP's tensile strength.
- Influence of Anchor Geometry:
  The width of the U-wrap anchor had a more pronounced effect on load capacity enhancement than the anchor height. Wider anchors led to higher peak loads and improved flexural performance, whereas increasing anchor height showed diminishing or negative returns.
- Load-Deflection Behavior:
  Anchored beams displayed greater ductility and higher deflection at peak load compared to non-anchored specimens. This implies improved energy absorption and structural resilience under loading.
- Theoretical Validation:
  The experimental results were found to be in reasonable agreement with predictions made using ACI 440.2R and the Canadian ISIS code, supporting the validity of current design models and the relevance of accounting for anchorage effects in flexural capacity calculations.
- Design Implications:
  The study highlights the necessity of optimizing anchor dimensions for maximizing the benefits of FRP retrofitting systems. In particular, anchor width should be considered a key parameter in design guidelines aimed at enhancing the effectiveness of FRP strengthening.

This study contributes to the ongoing development of efficient, durable, and cost-effective strengthening methods for RC structures. Future research should explore long-term durability, fatigue behavior, and the performance of hybrid anchorage systems under dynamic or seismic loading conditions.

Acknowledgments
The authors would like to thank Dr. Ali SARIBIYIK for his contributions.

Funding
This work was supported by Sakarya University of Applied Science Scientific Research Projects Coordination Unit (SUBU BAPK, Project Number: 166-2023)

REFERENCES

[1] TBDY 2018, Türkiye Bina Deprem Yönetmeliği, Afet ve Acil Durum Yönetimi Başkanlığı, Ankara, Türkiye, 2018.P15.
[2] Kachlakev D, Mccurry DD. Behavior of full-scale reinforced concrete beams retrofitted for shear and flexural with FRP laminates. Compos J 2000;31:445–52.
[3] Valivonis J, Skuturna T. Cracking and strength of reinforced concrete structures in flexure strengthened with carbon fibre laminates. Civ Eng Manage J 2006;13(4):317–33.
[4] Xian, G.; Guo, R.; Li, C. Combined effects of sustained bending loading, water immersion and fiber hybrid mode on the mechanical properties of carbon/glass fiber reinforced polymer composite. Compos. Struct. 2022, 281, 115060.
[5] Yeong-soo S, Chadon L. Flexural behavior of reinforced concrete beams strengthened with carbon fiber-reinforced polymer laminates at different levels of sustaining load. ACI Struct J 2003;100:231–40.
[6] Hollaway LC. A review of the present and future utilisation of FRP composites in the civil infrastructure with reference to their important in-service properties. Constr Build Mater 2010;24(12):2419–45.
[7] Ammar MA. Bond durability of basalt fibre-reinforced polymers (BFRP) bars under freeze-and-

thaw conditions Ph.D thesis Dept. of Civil Engineering, Université Laval; 2014.p. 125.
[8] Banibayat P, Patnaik A. Creep rupture performance of basalt fiber-reinforced polymer bars. J Aerosp Eng 2013;28(3):04014074.
[9] Aram MR, Gzaderski C, Motavalli M. Debonding failure modes of flexural FRP strengthened RC beam. Compos Part B 2008;39:826–41.
[10] Teng, J.G.; Smith, S.T.; Yao, J.; Chen, J.F. Intermediate crack-induced debonding in RC beams and slabs. Constr. Build. Mater. 2003, 17, 447–462.
[11] Al-Negheimish, A.I.; El-Sayed, A.K.; Al-Saawani, M.A.; Alhozaimy, A.M. Effect of Stirrups on Plate End Debonding in Reinforced Concrete Beams Strengthened with Fiber Reinforced Polymers. Polymers 2021, 13, 3322.
[12] Szewczak, A. Influence of Epoxy Glue Modification on the Adhesion of CFRP Tapes to Concrete Surface. Materials 2021, 14, 6339.
[13] Esfahani M, Kianoush M, Tajari A. Flexural behaviour of reinforced concrete beams strengthened by CFRP sheets. Eng Struct 2007; 29:2428–44.
[14] Kalfat R, Al-Mahaidi R and Smith S T 2013 Anchorage devices used to improve the performance of reinforced concrete beams retrofitted with FRP composites: State-of-the-art review J. Compos. Constr. 17(1) 14-33.
[15] Al-Saawani, M.A.; El-Sayed, A.K.; Al-Negheimish, A.I. Effect of shear-span/depth ratio on debonding failures of FRPstrengthened RC beams. J. Build. Eng. 2020, 32, 101771.
[16] Smith, S.T.; Teng, J.G. Shear-bending interaction in debonding failures of FRP-plated RC beams. Adv. Struct. Eng. 2003, 6, 183–199.
[17] Teng, J.G.; Yao, J. Plate end debonding in FRP-plated RC beams I: Experiments. Eng. Struct. 2007, 29, 2457–2471
[18] El-Sayed, A.K.; Al-Saawani, M.A.; Al-Negheimish, A.I. Empirical shear based model for predicting plate end debonding in FRP strengthened RC beams. J. Civ. Eng. Manag. 2021, 27, 117–138
[19] Khalifa E S and Al-Tersawy S H 2013 Experimental and analytical investigation for enhancement of flexural beams using multilayer wraps Compos. B. Eng. 45(1) 1432–40.
[20] Pham H B and Al-Mahaidi R 2006 Prediction models for debonding failure loads of carbon fiber reinforced polymer retrofitted reinforced concrete beams J. Compos. Constr. 10(1) 48–59.
[21] ACI 440.2R-17 2017 Guide for the design and construction of externally bonded FRP systems for strengthening concrete structures ACI Committee 440, American Concrete Institute, Farmington Hills, MI, USA.
[22] GB-50608 2010 Technical code for infrastructure application of FRP composites, China Planning Press, Beijing, China.
[23] Concrete Society Design guidance for strengthening concrete structures using fibre composite materials 2012 Concrete Society Technical Report No. 55, Crowthorne, UK.
[24] CNR-DT 200 2013 Guide for the design and construction of externally bonded FRP systems for strengthening existing structures Advisory Committee on Technical Regulations for Constructions, National Research Council, Rome, Italy.
[25] Khan A A R and Ayub T 2010 Effectiveness of U-shaped CFRP wraps as end anchorages in predominant flexure and shear region 5th Int. Conf. FRP Compos. Civil Eng. Beijing China.
[26] Fu B, Teng J G, Chen J F and Guo Y C 2017 Concrete cover separation in FRP-plated RC beams: Mitigation using FRP U-jackets J. Compos. Constr. 21(2) 1–13.
[27] Khan A. R. and Ayub T., (2015). Performance of RC beams strengthened for shear and flexure using different schemes of U-Shaped CFRP anchorages and/or stripss. *IJST, Transactions of Civil Engineering*, Volume 39, Number C1.
[28] Sharaky I.A., Baena M. et al, (2018). Effect of axial stiffness of NSM FRP reinforcement and concrete cover confinement on flexural behaviour of strengthened RC beams: Experimental and numerical study. Engineering Structures 173, 987–1001. https://doi.org/10.1016/j.engstruct.2018.07.062
[29] Yazdani, N.; Aljaafreh, T.; Beneberu, E, (2020). Concrete beam flexural strengthening with anchored pre-saturated CFRP laminates. *Compos. Struct.*, 235, 111733. https://doi.org/10.1016/j.compstruct.2019.111733
[30] Zhang, S. S., Y. Ke, S. T. Smith, H. P. Zhu, and Z. L. Wang, (2021). Effect of FRP U-Jackets on the behavior of RC beams strengthened in flexure with NSM CFRP strips.*Compos. Struct.*256:113095. https://doi.org/10.1016/j.compstruct.2020.113095
[31] Muslum Murat Maras, Fatih Kantarci et all, (2022). Structural behavior of RC beams strengthened using fiber-reinforced polymer U-Jackets.*fib wiley*, 1-18. https://doi.org/ 10.1002/suco.202200932
[32] Aditya Kumar Tiwary, Sandeep Singh et all, (2022). Comparative Study on the Behavior of Reinforced Concrete Beam Retrofitted with CFRP Strengthening Techniques. *Polymers*, 14, 4024. https://doi.org/10.3390/polym14194024
[33] Mohammed A Al-Saawani, Ahmed K El-Sayed et al, (2022). Mitigation of Concrete Cover Separation in Concrete Beams Strengthened with Fiberreinforced Polymer Composites, IOP Conf. Series: *Earth and Environmental Science*, 1-11. https://doi.org/10.1088/17551315/1026/1/012008
[34] Sikadur-330, in: Product data sheet, 2006.
[35] Yusuf Sümer, M. Nawar Zakour et all, (2024). Finite elements investigations of the effect of different parameters on the retrofitted RC beams with anchored FRP plate. *Structural Engineering and Mechanics,* Vol. 93, No.3, 165-179. https://doi.org/10.12989/sem.2025.93.3.165
[36] ACI 440.2R-17 2017 Guide for the design and construction of externally bonded FRP systems for strengthening concrete structures ACI Committee 440, American Concrete Institute, Farmington Hills, MI, USA.

[37] ISIS Canada Educational Module No. 4. "An Introduction to FRP- Strengthening of Concrete Structures", Principal Contributor: L.A. Bisby, Ph.D., P.Eng., Department of Civil Engineering, Queen's University Contributor: B.K. Williams, February 2004.

Volume 14, Issue 3, Page 120-129, 2025 https://doi.org/10.46810/tdfd.1615276 Research Article

BİNGÖL UNIVERSITY

Türk Doğa ve Fen Dergisi
Turkish Journal of Nature and Science
www.dergipark.gov.tr/tdfd

A New Model for Transmission Line Modelling Method to Investigate Frequency-Dependent Bioelectromagnetic Interactions

Burak ARICIOĞLU[1*], Abdullah FERİKOĞLU (Retired)[1]

[1] Sakarya University of Applied Sciences, Faculty of Technology, Electrical & Electronics Engineering Department, Sakarya, Türkiye
Burak ARICIOĞLU ORCID No: 0000-0001-9526-7629
Abdullah FERİKOĞLU ORCID No: 0000-0002-5907-1845

**Corresponding author: baricioglu@subu.edu.tr*

(Received: 08.01.2025, Accepted: 09.08.2025, Online Publication: 26.09.2025)

Keywords
TLM,
Skin depth,
SAR

Abstract: In this article, a new transmission line model is presented for the frequency-dependent analysis of bioelectromagnetic interactions. For the frequency-dependent analysis, the transmission line is modelled with dependent voltage sources in PSpice, allowing the transmission line lumped parameters to be defined as functions of frequency. This approach enables frequency-dependent analysis with a single simulation. As an example, the frequency-dependent electric field distribution in a multilayer human tissue model over the frequency range of 1 GHz to 100 GHz is investigated. The multilayer tissue model consists of skin, fat, and muscle layers. A finite element method (FEM)-based analysis of the electric field distribution in the multilayer tissue model is also conducted at the resonant frequency of the model, determined in this study to be 10.44 GHz. The transmission line modelling (TLM) and FEM-based results are in good agreement. Additionally, the skin depth of the multilayer tissue model is calculated. The results from both the electric field distribution analysis and the skin depth calculation confirm the accuracy of the proposed frequency-dependent transmission line model. Finally, the study examines the frequency-dependent electromagnetic energy absorption in the multilayer tissue model over the 1 GHz to 100 GHz frequency range.

İletim hattı modelleme yöntemi ile frekansa bağlı biyoelektromanyetik etkileşim için yeni bir model tasarımı

Anahtar Kelimeler
İHM,
Deri kalınlığı,
ÖSO

Öz: Bu makalede biyoelektromanyetik etkileşimlerin frekansa bağlı analizi için yeni bir iletim hattı modeli sunulmaktadır. Frekansa bağlı analiz için iletim hattı, PSpice programında bağımlı voltaj kaynaklarıyla modellenerek iletim hattı toplu parametrelerinin frekansa bağlı fonksiyonlar olarak tanımlanmıştır. Bu yaklaşım ile tek bir simülasyonla frekansa bağlı analiz gerçekleştirilebilir. Örnek olarak çok katmanlı bir insan doku modelinde 1 GHz ile 100 GHz frekans aralığı için frekansa bağlı elektrik alan dağılımı incelenmiştir. Çok katmanlı doku modeli deri, yağ ve kas katmanlarından oluşmaktadır. Yapılan analizde modelin rezonans frekansı 10,44 GHz olarak belirlenmiştir. Bu frekans için sonlu elemanlar yöntemi ile analiz gerçekleştirilmiştir. İletim hattı modelleme (İHM) ve sonlu eleman yöntemleri ile elde edilen sonuçlar oldukça uyumlu olduğu gözlemlenmiştir. Ayrıca çok katmanlı doku modelinde deri kalınlığı hesaplanmıştır. Simülasyondan ve hesaplamadan elde edilen deri kalınlığı değerleri birbiriyle uyumlu olduğu gözlemlenmiştir. Bu da önerilen iletim hattı modelinin başarımını göstermektedir. Son olarak çalışma, 1 GHz ila 100 GHz frekans aralığında çok katmanlı doku modelinde frekansa bağlı elektromanyetik enerji emilimini incelenmiştir.

1. INTRODUCTION

The study of electromagnetic (EM) wave interactions with biological systems is a critical and evolving field, driven by the pervasive use of wireless technologies, advancements in medical diagnostics, and therapeutic applications. Understanding these interactions, particularly at high frequencies, is essential for both safety assessment and the development of novel biomedical technologies. The fundamental description of all electromagnetic phenomena is encapsulated in Maxwell's equations. However, obtaining of an analytic solution to Maxwell's equations is not easy in most cases. Numerous numerical techniques have been developed to solve these equations. The most widely used methods include the finite element method (FEM) [1], the method of moments (MoM) [2], the finite-difference time-domain technique (FDTD) [3], the finite integration technique (FIT) [4], the method of lines (MoL) [5], and the transmission line modelling (TLM) method [6]. These numerical methods differ in several aspects, such as their applicable domains (some are suited only for time or frequency domains, while others can handle both), their discretization approaches, their model boundaries, and their capability to be applied to nonlinear complex media [7].

Table 1. Comparative overview of some numerical methods in computational electromagnetics

Method	Primary Domain	Discretization Approach	Key Strengths	Key Limitations
FEM	Frequency	Volume-based	Handles complex geometries, multi-physics coupling, no numerical dispersion (FD), guaranteed convergence [8]	Computationally expensive (volumetric meshing), complex meshing, steeper learning curve [8]
MoM	Frequency	Surface-based	Efficient for open regions/scattering, surface meshing, no numerical dispersion [9]	Computationally intensive (dense matrices), limited to linear/homogeneous media, convergence not guaranteed, harder to parallelize [9]
FDTD	Time	Volume-based	Conceptual simplicity, broadband analysis from single run (with FFT), handles nonlinearity, guaranteed convergence [10]	Global grid issues for complex geometries, numerical dispersion error (accumulates), CFL condition constraint [10]
TLM	Time (adaptable to Frequency)	Network/ Circuit-based	Unconditional stability, intuitive visualization, material/mesh flexibility, computational efficiency (parallelizable), complex/nonlinear/dispersive material handling, better boundary geometry modeling [11]	Higher memory per node, early 3D complexity [11]
FIT	Time/ Frequency	Volume-based	Stability and discretization of Maxwell's equations in their integral form. [12]	Poor performance in transverse scaling, complex implementation [12]
MoL	Time/ Frequency	Line-based	Suitable for longitudinally repeating objects and resonant structures. [13]	The scaling performance in the transverse direction is very poor, it is somewhat difficult to visualize. [13]

TLM is, firstly, used by G. Kron [14,15] as an equivalent circuit representation of Maxwell's equations. P. B. Johns and R. L. Beurle introduce a numerical method based on Kron's equivalent circuit representation with impulse excitation of the circuit [16]. Some features of TLM, which explain why it is preferred in computational electromagnetics [11] can be listed as:

- It is unconditionally stable.
- It allows easy visualization of the problem being simulated.
- It supports variable mesh size and material.
- Its numerical solution is simple and can be easily parallelized.

PSpice is a general-purpose circuit simulator. It is capable of handling analog, logical, and mixed-signal components, circuits, and systems. There are studies in the literature where electromagnetic problem solved in PSpice environment based on TLM method. For instance, in [17], the transmission line model of PSpice is employed to simulate wave propagation in a lossless medium. Similarly, in [18], the same model is used to compute the voltage standing wave ratio (VSWR) for various types of terminations. In [19], a one-dimensional multilayered planar tissue model is used to investigate electromagnetic energy absorption when the model is exposed to radiation from a base-station antenna for two different frequencies. However, as seen in the aforementioned studies, traditional implementations often assume frequency-independent parameters or rely on repeated simulations across discrete frequencies, limiting their applicability in broadband scenarios within PSpice environment.

This study addresses that gap by developing a frequency-dependent TLM framework implemented in PSpice using dependent voltage sources (ELaplace devices). This approach allows the lumped parameters of the transmission line—resistance, inductance, capacitance, and conductance—to be explicitly defined as functions of frequency.

In this study, a one-dimensional (1D) multilayer planar tissue model was employed to investigate electromagnetic energy absorption using the TLM method. Previous studies have analysed electromagnetic energy absorption in tissues using various models [20–23]. In this work, the stratification model of tissues was selected as skin, fat, and muscle, as described in [24–27]. A simulation was performed for frequencies ranging from 1 GHz to 100

GHz, assuming far-field radiation conditions, and its performance is validated through comparison with FEM-based analysis and theoretical skin depth calculations
The structure of the paper is as follows: Section 2 describes the materials and methods, Section 3 presents the simulations and results, and Section 4 offers a conclusion.

2. MATERIAL AND METHOD

2.1. Material and Method Subheading

In this study, a one-dimensional (1D) multilayer human tissue model is used for simulations. The solution of the field equations for a plane wave traveling through a medium is analogous to the solution of a voltage wave on a transmission line.

Consider a plane wave propagating in the z-direction within a lossy medium. The field equation for a transverse electromagnetic (TEM) wave can be expressed as:

$$\nabla^2 E - \gamma^2 E = 0 \tag{1}$$

where

$$\gamma^2 = j\omega\mu(\sigma + j\omega\varepsilon) \tag{2}$$

In Equation 2, ω represents angular frequency, and μ, σ, and ε represent field parameters permeability, conductivity, and permittivity, respectively.

The solution of Equation 1 can be written as:

$$E_x(z) = E_0 e^{-\gamma z} + E_0' e^{\gamma z} \tag{3}$$

where E_0 and E_0' represent the magnitude of the incident and reflected electric field, respectively.

Similarly, the equation of a voltage wave on a transmission line can be written as:

$$\nabla^2 V - \gamma^2 V = 0 \tag{4}$$

where

$$\gamma^2 = (j\omega L + R)(j\omega C + G) \tag{5}$$

In Equation 5, ω represents angular frequency, and L,R,C and G represent transmission line parameters inductance, resistance, capacitance, and conductance per meter, respectively.

The solution of Equation 4 can be written as:

$$V_x(z) = V_0 e^{-\gamma z} + V_0' e^{\gamma z} \tag{6}$$

Where V_0 and V_0' represent the magnitude of the incident and reflected voltage wave, respectively.

Finally, the intrinsic impedance of a lossy medium is,

$$\eta = \sqrt{\frac{j\omega\mu}{\sigma + j\omega\epsilon}} \tag{7}$$

and, the corresponding characteristic impedance of a lossy line is,

$$Z_0 = \sqrt{\frac{R + j\omega L}{G + j\omega C}} \tag{8}$$

As evident from the equations above, the solution for an electromagnetic wave traveling through a medium is mathematically equivalent to that of a voltage wave traveling through a transmission line. For this equivalence to hold, the medium's parameters μ (permeability), σ (conductivity), and ε (permittivity) must correspond to the transmission line's parameters L (inductance meter $^{-1}$), G (conductance meter $^{-1}$), and C (capacitance meter $^{-1}$), respectively. Additionally, the value of R (resistance meter $^{-1}$) in the transmission line must be set to zero, as there is no analogous parameter for R in the medium.

2.2. Frequency-Dependent Transmission Line Model

In this section, the transmission line model for frequency-dependent parameters is described. The currents at both ends of a transmission line, shown in Figure 1a, can be expressed as below [28]:

$$\begin{aligned} i_a &= \frac{V_a}{Z_0} - i_b' \\ i_b &= -\frac{V_b}{Z_0} + i_a' \end{aligned} \tag{9}$$

where Z_0 is the characteristic impedance of the transmission line discussed in the previous section, and i_a' and i_b' are described as:

$$\begin{aligned} i_a' &= i_a e^{-\gamma l} + \frac{V_a}{Z_0} e^{-\gamma l} \\ i_b' &= i_b e^{-\gamma l} + \frac{V_b}{Z_0} e^{-\gamma l} \end{aligned} \tag{10}$$

where γ is the propagation constant of the line, as described in Equation 5.

Using Equation 9, the Thevenin model of a transmission line link can be implemented as shown in Figure 1b.

The Thevenin model given in Figure 1b can be implemented in PSpice with an 'ELaplace' device for frequency-dependent simulations. The impedances in Figure 1b can also be modelled with the 'ELaplace' device.

In Figure 2, the PSpice implementation of the Thevenin model is given. All the sources in the figure are dependent voltage sources. Among the sources, V_{a1},V_{a3},V_{b1}, and V_{b3} are current controlled voltage sources with gain Z_0, $Z_0 e^{-\gamma l}$,Z_0, and $Z_0 e^{-\gamma l}$, respectively, while V_{a2} and V_{b2} are voltage controlled voltage sources with gain $e^{-\gamma l}$.

These dependent voltage sources are implemented in PSpice with 'ELaplace' devices, in which the gains of these sources can be defined in terms of frequency, and the 'ELaplace' device can be either a current or voltage-controlled voltage source. The PSpice expression of Figure 2 is given in Appendix B. An example of a PSpice expression of a frequency-dependent transmission line cell for tissue is provided in Appendix C.

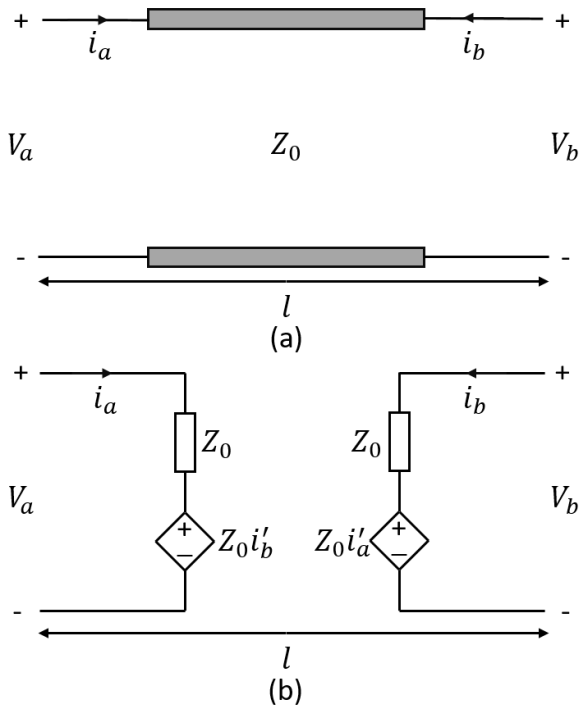

Figure 1. (a) Transmission line and **(b)** its Thevenin model

.

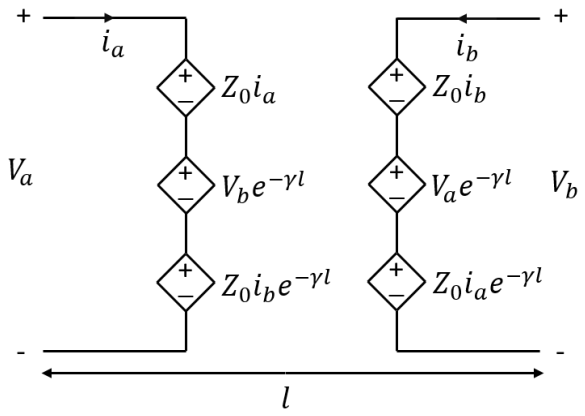

Figure 2. PSpice implementation of transmission line Thevenin model

2.3. The Multilayer Human Tissue Model Used in Simulations

The multilayer human tissue model used in this study is depicted in Figure 3. The model consists of three layers: skin, fat, and muscle tissues. For the simulations, the thicknesses of the skin, fat, and muscle layers were set to 1 mm, 4 mm, and 10 mm, respectively, as specified in [29].

The TLM method is used to analyse electric field distribution in multilayer tissue. A transmission line model is generated for each tissue layer since the medium parameters are different for each tissue. Each layer is further subdivided into 100 identical transmission line cells, as illustrated in Figure 4. The frequency-dependent parameters, namely C and G of the transmission line, were defined as a function of frequency.

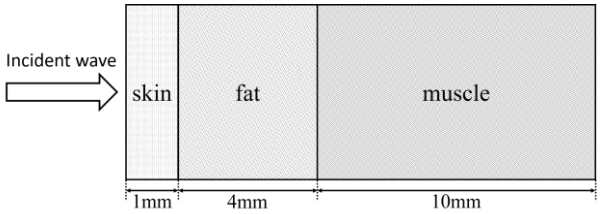

Figure 3. Multilayer tissue model used in the study

The lengths of the transmission line cells are 10^{-2} mm for skin, 4 x 10^{-2} mm for fat, and 10^{-1} mm for muscle tissue. In Figure 4, the transmission line cells depicted as TSi, TFi, and TMi represent skin, fat, and muscle tissues, respectively, Z_{air} is intrinsic impedance of air (377Ω), independent of frequency, and Z_L is the intrinsic impedance of muscle tissue, which is frequency-dependent

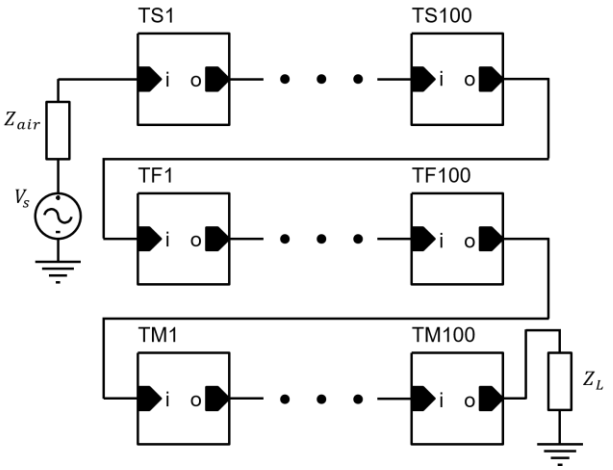

Figure 4. PSpice schematic for the simulation of electric field distribution in the multilayer tissue model, TSi, TFi, and TMi represent skin, fat, and muscle tissues respectively

Z_L is selected as the intrinsic impedance of muscle tissue to prevent waves from being reflected back at the end of the muscle tissue. Since Z_L is frequency-dependent, an 'ELaplace' device is used to emulate a frequency-dependent impedance. The general expression of 'ELaplace' is:

"E{name} {+node} {-node} LAPLACE {expression} {s expression} "

An example PSpice expression for frequency-dependent impedance is given in Appendix A.

As mentioned in the previous section, L, G, and C parameters of the line are equivalent to μ, σ, and ε parameters of the medium, respectively. Among the medium parameters, σ and ε parameters vary with frequency, while μ parameter does not, since human tissues are a non-magnetic material that their magnetic

permeability (μ) is the same as or very close to that of vacuum [30–33]. In Figure 5, relative permittivity (ε_R) and conductivity (σ) of tissues are given for a frequency range of 1 GHz-100 GHz.

In order to perform an AC analysis of the multilayer tissue, some of the transmission line parameters, namely C and G, should be defined as a function of frequency. As a first step, for each curve in Figure 5, a frequency-dependent polynomial is constructed using the curve fitting method.

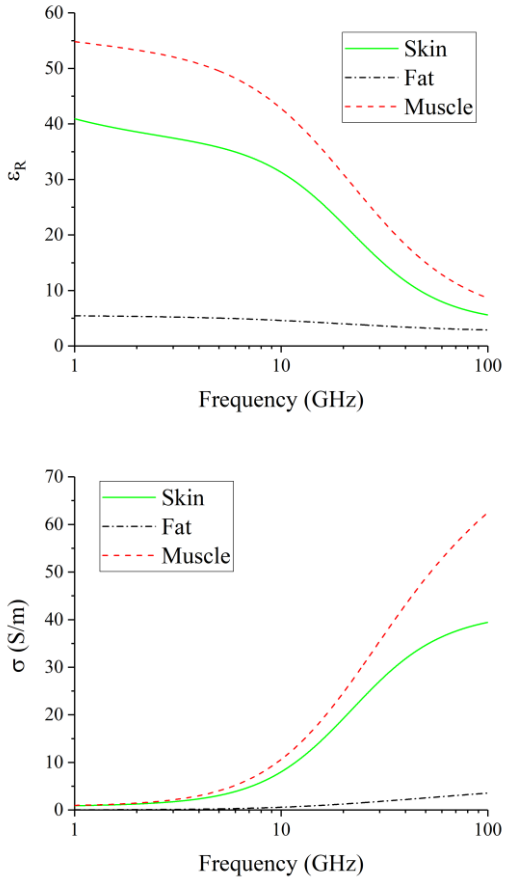

Figure 5. Relative permittivity (above) Conductivity of the tissues (bottom) used in the study with respect to frequency

The process for defining frequency-dependent parameters in PSpice involves modelling a frequency-dependent transmission line, which was detailed in the previous section.

3. SIMULATIONS AND RESULTS

In the analysis of electric field intensity distribution in the multilayer tissue model for the frequency range of 1 GHz-100 GHz, the root mean square (RMS) value of the incoming electric field is set as 1 V m^{-1}. The normalized electric field distribution is given in Figure 6.

As shown in Figure 6, at certain frequencies, the electric field magnitude exceeds that of the incoming electric field. The maximum occurs at approximately 10.44 GHz, where the electric field magnitude nearly doubles that of the incoming field. In this study, the human tissue modelled as a multilayer with each layer having different electrical properties. Because of this, there will be multiple reflections. Other than reflections, there will be phase changes and standing wave effects. The electric field strength, shown in Figure 6, takes into account the aforementioned effects. Because of these effects, the magnitude of the electric field may increase as it travels through the multilayer medium [34]. Similar results were found in [34-39] where the magnitude of the electric field increased as it travelled through multilayer tissue model. However, in all these studies, the frequency at which this phenomenon occurs is different since the number of layers in the multilayer tissue model and the thickness of each tissue are different from the model employed in this study.

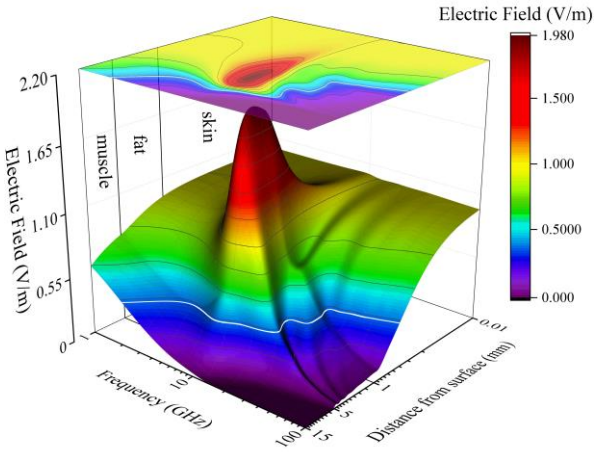

Figure 6. The normalized electric field distribution in the multilayer tissue model for the frequency range 1GHz – 100 GHz

To further investigate this phenomenon, the equivalent characteristic impedance of the multilayer tissue is analysed, as it can be related to the resonant frequency. The input impedance of a transmission line can be written as:

$$Z_{in} = Z_0 \frac{Z_L + Z_0 \tanh(\gamma l)}{Z_0 + Z_L \tanh(\gamma l)} \quad (11)$$

where Z_0 is the characteristic impedance of the line, as described in Equation 8. Z_L is the load impedance of the line, γ is the propagation constant, as described in Equation 5, and l is the length of the line.

Accordingly, the equivalent characteristic impedance of the multilayer tissue can be written as:

$$Z_{eq} = Z_{0_s} \frac{Z_{L_s} + Z_{0_s} \tanh(\gamma_s l_s)}{Z_{0_s} + Z_{L_s} \tanh(\gamma_s l_s)} \quad (12)$$

where Z_{0_s}, γ_s, and l_s are the characteristic impedance, propagation constant, and the length of skin tissue, respectively. Z_{L_s} is the load seen by the skin tissue, which is equal to the input impedance of the fat tissue and can be written as:

$$Z_{L_s} = Z_{0_f} \frac{Z_{0_m} + Z_{0_f} \tanh(\gamma_f l_f)}{Z_{0_f} + Z_{0_m} \tanh(\gamma_f l_f)} \quad (13)$$

where Z_{0_f}, γ_f, and l_f are the characteristic impedance, propagation constant, and the length of the fat tissue, respectively, and Z_{0_m} is the characteristic impedance of the muscle tissue. The load seen by the fat tissue is equivalent to the characteristic impedance of the muscle tissue, as the muscle tissue is terminated with a perfectly matched layer (PML).

The magnitude, real, and imaginary parts of the equivalent impedance of the multilayer tissue are given in Figure 7 with respect to frequency.

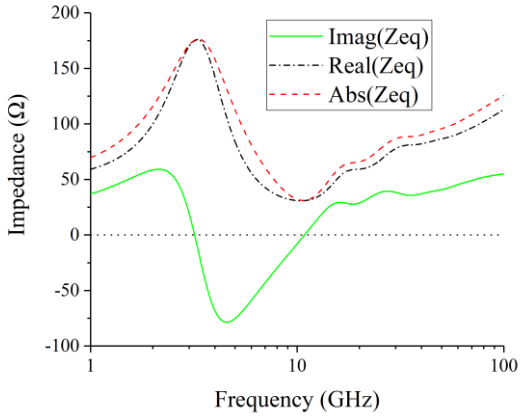

Figure 7. The magnitudes of absolute, real part, and imaginary part of the multilayer tissue model equivalent impedance with respect to frequency

If Figure 7 is examined, the imaginary part of the equivalent impedance is zero at two frequencies, 3.83 GHz and 10.44 GHz. In other words, at these two frequencies the equivalent impedance is purely resistive. The resonant frequency can be described as the frequency at which the equivalent impedance of a circuit has no imaginary part. Hence, 3.83 GHz and 10.44 GHz are the two resonant frequencies of the multilayer tissue model used in this study. As can be seen in Figure 7, the real part is minimum at 10.44 GHz while it has a maximum at 3.83 GHz. Since the real part of the equivalent impedance at 10.44 GHz has a minimum, a maximum peak electric field occurs at this frequency.

Finite element method (FEM)-based analysis of electric field distribution in the multilayer human tissue at 10.44 GHz is conducted to compare the result of transmission line modelling (TLM) method analysis at this frequency. The results of both methods at 10.44 GHz are given in Figure 8. As can be seen in the figure, the results of both methods are very close to each other. This shows the successful performance of the proposed transmission line.

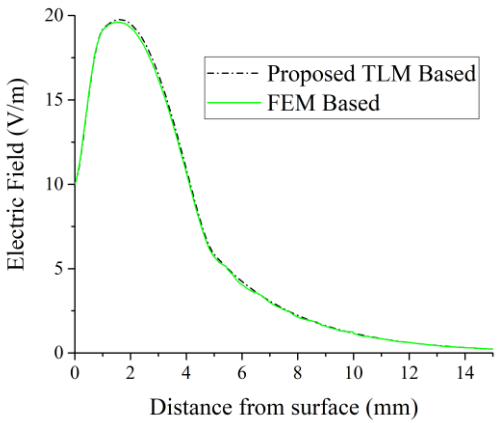

Figure 8. FEM and TLM-based analysis of electric field distribution in the multilayer tissue model at the resonant frequency of 10.44 GHz

To evaluate the results of TLM-based analysis, the skin depth of the multilayer tissue is also calculated over the frequency range 1 GHz – 100 GHz, and both results are compared.

For an N-layer medium, effective skin depth can be calculated as [40]:

$$\delta_{eff} = \sum_{i=1}^{N+1} d_i$$

$$d_i = \int_{\sum_{j=1}^{i-1} l_j}^{\sum_{j=1}^{i} l_j} \left| \frac{\prod_{j=1}^{i-1}(1+\Gamma_j)}{\prod_{j=1}^{i}(e^{\gamma_j}+\Gamma_j e^{-\gamma_j})} \left(e^{-\gamma_i (z-\sum_{j=0}^{i-1} l_j)} + \Gamma_i e^{\gamma_i (z-\sum_{j=0}^{i} l_j)} \right) \right| dz \qquad (14)$$

$$d_{N+1} = \int_{\sum_{j=1}^{N} l_j}^{\infty} \left| \frac{\prod_{j=1}^{N}(1+\Gamma_j)}{\prod_{j=1}^{N}(e^{\gamma_j}+\Gamma_j e^{-\gamma_j})} (e^{-\gamma_i (z-\sum_{j=0}^{N+1} l_j)}) \right| dz$$

where δ_{eff} is the effective skin depth, d_i contribution of each layer to the effective skin depth, and Γ_i, γ_i and l_i are the reflection coefficient, the propagation constant and the length of the i^{th} layer, respectively. The calculated effective skin depth of the multilayer tissue is given in Figure 9.

Skin depth can be simply defined as the depth at which the current density has fallen to 1/e (about 0.37) of surface current density. Since

$$J = \sigma E \qquad (15)$$

where J is the current density, σ is conductivity, and E is the electric field, skin depth can be redefined as the depth at which the electric field magnitude has fallen to e^{-1} (about 0.37) of the electric field magnitude at the surface of the medium.

In Figure 9, skin depth in the TLM-based analysis is obtained from Figure 6 by plotting distance at which the electric field magnitude has fallen to e^{-1} of the incoming electric field against frequency. In Figure 6, the white line shows the skin depth.

If Figure 9 is examined, it can be said that the calculated skin depth result confirms that of TLM-based analysis. However, the two results are not very close to each other because, in TLM-based analysis, the field parameters are constructed with curve fitting.

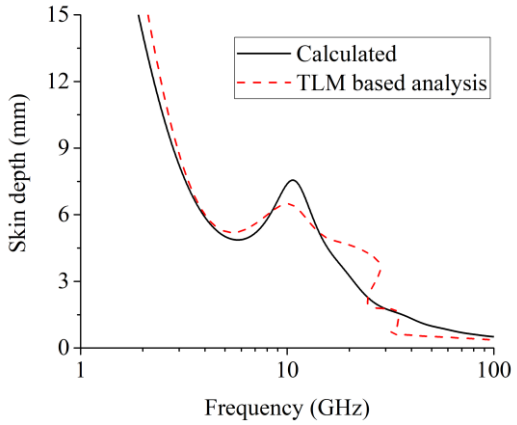

Figure 9. Calculated effective skin depth and skin depth obtained from TLM-based analysis with respect to frequency

It is stated that in [34, 37, 41-43], at higher frequencies (above 30 GHz), the electromagnetic waves have a smaller penetration depth typically on the millimetre (mm) order. This is also observed in this study, as shown in Figure 9, where the skin depth above 30 GHz is less than 1 mm. It is also found that the skin depth is less than 1 mm above 30 GHz in [34, 37]

Finally, specific absorption rate (SAR) of the multilayer tissue is calculated for the frequency range 1GHz-10GHz. SAR can be expressed as:

$$SAR = \frac{\sigma}{\rho} E_{rms}^2 \tag{16}$$

where σ and ρ represent conductivity and density of tissue, and E_{rms} is the RMS value of the electric field.

The average SAR of the multilayer tissue for the frequency range 1 GHZ-100 GHz is given in Figure 10. For the SAR value calculation, the magnitude of the incident electric field at the surface of the tissue model is 1 V m^{-1} (RMS). If the magnitude of the incident fields is doubled, then the SAR value is quadrupled since SAR is squarely proportional to the magnitude of the electric field.

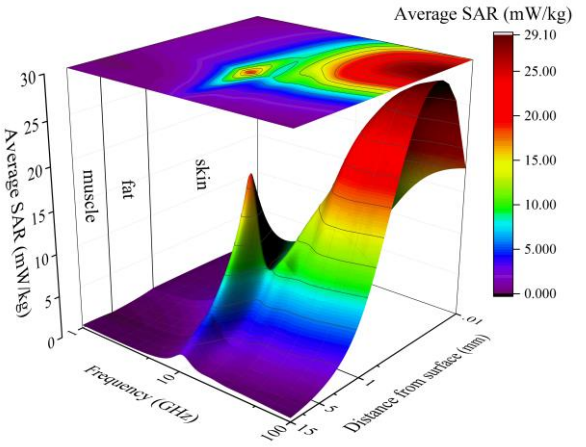

Figure 10. The average SAR of the multilayer tissues model with respect to both distance and frequency for the normalized electric field

If Figure 10 is examined, the local maximum SAR is observed at the largest frequency in the skin tissue since SAR is proportional to conductivity and squarely proportional to the electric field. However, the maximum average SAR is observed at the resonant frequency of the multilayer tissue model, since the magnitude of the electric field at that frequency is the highest. Also, at all the frequencies the maximum local SAR is observed near the surface of the skin tissue at the incident wave side except for the frequencies in the neighbourhood of the resonant frequency 10.44 GHz. In the latter frequencies, the maximum local SAR is observed at the other end of the skin tissue, near the fat tissue.

4. CONCLUSION

The accurate modelling of electromagnetic wave interactions with biological tissues is a cornerstone of modern bioelectromagnetic, driven by the complexities of human anatomy and the pervasive nature of electromagnetic fields in daily life and medical applications. The inherent heterogeneity, anisotropy, and frequency-dependent dielectric properties of biological media fundamentally limit the utility of analytical solutions to Maxwell's Equations, necessitating the adoption of sophisticated numerical techniques.

The present work contributes to the literature by introducing a novel TLM implementation that leverages the capabilities of the circuit simulation software, PSpice, to perform frequency-dependent analysis. The employment of dependent voltage sources (ELaplace devices, which can be defined as a function of frequency) allows for the direct definition of frequency-dependent lumped parameters, enabling a comprehensive broadband analysis in a single simulation run. This approach offers significant computational efficiency compared to traditional frequency sweeps.

A TLM-based frequency-domain analysis of a multilayer tissue model is conducted. To validate the proposed approach, several additional analyses are performed. The resonant frequencies of the multilayer tissue model are identified by examining the imaginary part of the characteristic impedance. It is found that, at one of the resonant frequencies (10.44 GHz), the electric field

distribution is maximized. Subsequently, a FEM-based electric field distribution analysis is carried out at this frequency, yielding results that closely match those of the TLM-based analysis. In a final analysis, the skin depth of the multilayer tissue is calculated, and the skin depth obtained from the TLM-based analysis is found to be in agreement with the theoretical calculation.

Following these analyses, the average SAR values for the frequency range 1 GHz to 100 GHz are calculated using the electric field distributions from the TLM-based analysis. As the frequency increases, the maximum local SAR value rises, primarily near the surface of the skin tissue. However, the highest average SAR is observed at the resonant frequency of the multilayer tissue model. At this resonant frequency (10.44 GHz), the maximum local SAR is observed at the far end of the skin tissue. Future studies will focus on frequency analysis of other human tissues, such as ocular tissue, and will explore temperature distribution in tissues induced by the electric field.

REFERENCES

[1] Zhang J, Jin J, Li X, Feng F, Liu W, Zhang W, et. al. A Novel Design Space Decomposition Technique to Accelerate FEM-Based Electromagnetic Topology Optimization for Waveguide Structures. IEEE Transactions on Microwave Theory and Techniques. 2024.

[2] Chai SR, Meng LH, Zou YF, Dai PK. Fast Computation of EM Scattering from Moving PEC Target Based on MT-ACA-MoM Algorithm. IEEE Antennas and Wireless Propagation Letters. 2024.

[3] Ball JM, Li W. Using high-resolution microscopy data to generate realistic structures for electromagnetic FDTD simulations from complex biological models. Nature Protocols. 2024; 1-33.

[4] Lin G, Huang T, Cai W, Gong D, Jin X. An Efficient Scheme of Waveguide Port Modeling Based on Conformal and Nonuniform Mesh for Time Domain Finite Integration Technique. IEEE Transactions on Antennas and Propagation. 2024.

[5] Wang X, Huang B. Analysis of conductor losses of planar transmission lines with surface roughness by the method of lines. Applied Computational Electromagnetics Society Symposium (ACES), 2017; p.1-2.

[6] Johns PB, Beurle RL. Numerical solutions of 2-dimentional scattering problems using a transmission-line matrix. Proc IEEE. 1971; 118(9): 1203-1208.

[7] Park S, Kotzev M, Brüns HD, Kam DG, Schuster C. Lessons from applying IEEE standard 1597 for validation of computational electromagnetics computer modeling and simulations. IEEE Electromagnetic Compatibility Magazine. 2017; 6(2): p.55-67.

[8] Sheng XQ, Song W. Essentials of computational electromagnetics. John Wiley & Sons. 2011.

[9] Ayari M, Gharbi A, El Touati Y, Klai Z, Elsayed MS. Advanced numerical methods in electromagnetics: techniques and applications. Letters in High Energy Physics. 2024; 791–803.

[10] Rylander T, Ingelström P, Bondeson A. Computational electromagnetics. Springer Science & Business Media. 2012.

[11] Duffy AP. The application of transmission-line modelling to EMC design. Does Electromagnetic Modelling Have A Place in EMC Design IEE Colloquium on IET. 1993.

[12] Weiland T. Finite integration method and discrete electromagnetism. In: Monk P, Carstensen C, Funken S, Hackbusch W, Hoppe RHW, editors. Computational Electromagnetics. Lecture Notes in Computational Science and Engineering, vol. 28. Springer, Berlin, Heidelberg. 2003.

[13] Schiesser WE. Method of lines PDE analysis in biomedical science and engineering. John Wiley & Sons. 2016.

[14] Kron G. Equivalent circuits to represent the electromagnetic field equations. Physical Review. 1943; (643)-4: 126.

[15] Kron G. Equivalent circuit of the field equations of Maxwell-I. Proceedings of the IRE 325. 1944; p.289-299.

[16] Peter JB, Beurle RL. Numerical solution of 2-dimensional scattering problems using a transmission-line matrix. Proceedings of the Institution of Electrical Engineers.1971; 118(9).

[17] Portnoy WM. PSPICE as a simulation tool in teaching electrodynamics. In: Technology-Based Re-Engineering Engineering Education, Proceedings of Frontiers in Education (FIE'96) 26th Annual Conference. IEEE. 1996; 1: 238–241.

[18] Tobin P. The role of PSpice in the engineering teaching environment. In: International Conference on Engineering Education – ICEE. 2007.

[19] Ferikoğlu A, Çerezci O, Kahriman M, Yener ŞÇ. Electromagnetic absorption rate in a multilayer human tissue model exposed to base-station radiation using transmission line analysis. IEEE Antennas and Wireless Propagation Letters. 2014; 13: 903–906.

[20] Curto S, Ammann MJ. Electromagnetic interaction between resonant loop antenna and simulated biological tissue. Microw Opt Techn Let. 2006; 48(12): 2418–2421.

[21] Zhang HH, Lin ZC, Wei EI, Choi WW, Tam KW, Donoro DG, et. al. Electromagnetic-thermal analysis of human head exposed to cell phones with the consideration of radiative cooling. IEEE Antennas and Wireless Propagation Letters.2018; 17(9): 1584-1587.

[22] Lee AK, Choi HD. Environmental EMF Evaluation for Mobile Communication Base Stations. 2021 XXXIVth General Assembly and Scientific Symposium of the International Union of Radio Science (URSI GASS) IEEE;2021. p. 1-2

[23] Karipidis K, Baaken D, Loney T, Blettner M, Brzozek C, Elwood M et.al. The effect of exposure to radiofrequency fields on cancer risk in the general and working population: A systematic review of human observational studies–Part I: Most researched outcomes. Environment International. 2024;108983.

[24] Wang H. Analysis of electromagnetic energy absorption in the human body for mobile terminals. IEEE Open Journal of Antennas and Propagation. 2020; 1: p. 113-117.
[25] Melia G. Electromagnetic absorption by the human body from 1-15 GHz (Doctoral dissertation) University of York, 2013.
[26] Maiorana E, Ramaccia D, Stefanini L, Toscano A, Bilotti F, Campisi P. Biometric Recognition Based on Hand Electromagnetic Scattering at Microwaves. IEEE Transactions on Microwave Theory and Techniques, 2023.
[27] Azzaz-Rahmani S, Zerrouki H, Dekkiche L. Novel Microstrip Patch Antenna for implantable medical telemetry devices. Journal of Applied Science and Engineering. 2021; 24(6): p.853-860.
[28] Moreno P, Ambrosio A, Gómez P. The characteristics approach for modeling single phase transmission lines with frequency dependent electrical parameters. Transmission and Distribution Conference and Exposition: Latin America 2008 IEEE/PES;2008. p. 1-4.
[29] Lin JC. Microwave propagation in biological dielectrics with application to cardiopulmonary interrogation. Medical applications of microwave imaging. 1986; p.47–58.
[30] Hennig A, vom Bogel G. Analysis of power absorption by human tissue in deeply implantable medical sensor transponders. Advanced Microwave Circuits and Systems. 2010.
[31] Schwan HP, Foster KR. RF-field interactions with biological systems: electrical properties and biophysical mechanisms. Proceedings of the IEEE. 1980; 68(1): p.104–113.
[32] Barchanski A. Simulations of low-frequency electromagnetic fields in the human body. (Phd thesis) Berlin: Technische Universitt; 2007
[33] Stuchly MA. Biological Effects of Electromagnetic Fields. International Journal of Bioelectromagnetism. 2002; 14(2): p.157–160
[34] Ziskin MC, Alekseev SI, Foster KR, Balzano Q. Tissue models for RF exposure evaluation at frequencies above 6 GHz. Bioelectromagnetics. 2018; 39(3): 173–189.
[35] Gustrau F, Bahr A. W-band investigation of material parameters, SAR distribution, and thermal response in human tissue. IEEE Transactions on Microwave Theory and Techniques. 2002; 50(10): 2393–2400.
[36] Sabbah AI, Dib NI, Al-Nimr MA. Evaluation of specific absorption rate and temperature elevation in a multi-layered human head model exposed to radio frequency radiation using the finite-difference time domain method. IET Microwaves, Antennas & Propagation. 2011; 5(9): 1073–1080.
[37] Kaburcuk F, Elsherbeni AZ, Lumnitzer R, Tanner A. Electromagnetic waves interaction with a human head model for frequencies up to 100 GHz. Applied Computational Electromagnetics Society Journal (ACES). 2020; 613–621.
[38] Grund J, Rathjen KU, Rädel C, Stiemer M, Dickmann S. Planar multilayer model of human tissue exposed to a plane electromagnetic wave. IEEE Journal of Electromagnetics, RF and Microwaves in Medicine and Biology. 2020; 5(4): 305–312.
[39] Laganà F, Bibbò L, Calcagno S, De Carlo D, Pullano SA, Pratticò D, Angiulli G. Smart electronic device-based monitoring of SAR and temperature variations in indoor human tissue interaction. Applied Sciences. 2025; 15(5): 2439.
[40] Hong-Wei D. et. al. Effective skin depth for multilayer coated conductor. Progress In Electromagnetics Research. 2009; p.1-8.
[41] Kanezaki A, Hirata A, Watanabe S, Shirai H. Effects of dielectric permittivities on skin heating due to millimeter wave exposure. BioMedical Engineering OnLine. 2009; 8(1): 20.
[42] Christ A, Samaras T, Neufeld E, Kuster N. RF-induced temperature increase in a stratified model of the skin for plane-wave exposure at 6–100 GHz. Radiation Protection Dosimetry. 2020; 188(3): 350–360.
[43] Kaburcuk F. Effect of skin thickness on electromagnetic dosimetry analysis of a human body model up to 100 GHz. International Journal of Microwave and Wireless Technologies. 2024; 16(8): 1373–1380.

Appendices

Appendix A. An exemplary PSpice expression for frequency-dependent impedance

```
 E_IMP n+ n- LAPLACE {i(vL)} {
*real part of the impedance
++pre1*(abs(s) + pre0
*imaginary part of the impedance
++(s*(pl1*abs(s) + pl0))}
```

where i(vL) is the current flown through the impedance, pre1, pre0, pl1, and pl0 are the parameters are obtained from curve fitting. s is the complex angular frequency $s = j\omega$ and abs(.) is the absolute value function.

Appendix B. The PSpice expression of the frequency-dependent transmission line model

```
.subckt tlossyline_thevenin_model A1 A2 B1 B2 params:
len=1 R=1 L=1 G=1 C=1
EA1 A1 1 laplace {i(EA1)} = {sqrt((L*s+R)/(C*s+G))}
EA2 1 2 laplace {v(B1,B2)} =
+{exp(-len*sqrt((L*s+R)*(C*s+G)))}
EA3 2 3 laplace {i(EB1)} =
+{exp(-len*sqrt((L*s+R)*(C*s+G)))
+*sqrt((L*s+R)/(C*s+G))}
R1 3 A2 50n

EB1 B1 4 laplace {i(EB1)} = {sqrt((L*s+R)/(C*s+G))}
EB2 4 5 laplace {v(A1,A2)} =
+{exp(-len*sqrt((L*s+R)*(C*s+G)))}
EB3 5 B2 laplace {i(EA1)} =
+ {exp(-len*sqrt((L*s+R)*(C*s+G)))
+*sqrt((L*s+R)/(C*s+G))}
.ends
```

There is an extra resistor element 'R1' to break the voltage source loop in the simulation. If the value of 'R1' is selected R1$\ll Z_0$, then the effects of resistor 'R1' can be omitted.

Appendix C. An example PSpice expression of frequency-dependent transmission line cell for skin tissue

```
.subckt Tskin  A1  A2  B1  B2 params: len=0.1e-4
****conductivity curve*****
.param pc0 {4.5546e-09}
.param pc1 {3.2281e-09}
****relative permittivity curve****
.param pr0 {0.0008023}
.param pr1 {0.0057397}
.param eps0 {8.854e-12}
xlossydskin A1 A2 B1 B2 tlossyline_thevenin_model params: len={len}
****here the lumped elements can be defined as a function of angular frequency abs(s)=ω=2πf)
+          r={0}
+          l={1.257u}
+          g={ pc1*abs(s) + pc0}
+          c={eps0*(pr1*abs(s) + pr0)}
.ends.
```

Volume 14, Issue 3, Page 130-138, 2025 https://doi.org/10.46810/tdfd.1666413 Research Article

BİNGÖL UNIVERSITY

Türk Doğa ve Fen Dergisi
Turkish Journal of Nature and Science
www.dergipark.gov.tr/tdfd

Synthesis and Characterization of (Sn, Al) Co-doped ZnO Semiconductors

Özlem BİLGİLİ[1*]

[1]Dokuz Eylul University, Science Faculty, Physics Department, Izmir, Turkey
Özlem BİLGİLİ ORCID No: 0000-0002-6334-2513

**Corresponding author: ozlem.bilgili@deu.edu.tr*

(Received: 26.03.2025, Accepted: 10.08.2025, Online Publication: 26.09.2025)

Keywords
Sn and Al co-doped, ZnO, XRD, SEM, EDX, UV-Vis spectroscopy

Abstract: This study presents the effects of tin and aluminium doping and tin/aluminium co-doping on structural, optical, morphological properties of ZnO. Solid state reaction method was used to prepare the samples $Zn_{1-x-y}Sn_xAl_yO$ ((x:y) = (0.00: 0.00), (0.00: 0.03), (0.03: 0.00), (0.03: 0.03)). The properties of the samples were examined by XRD, SEM, EDX spectroscopy and UV–vis spectroscopy. XRD results demonstrated that the lattice parameters a and c, unit cell volume, bond length L decreases while dislocation density increases with doping. The average crystallite size decreased compared to undoped ZnO. SEM images indicated that all samples show presence of hexagonal like grains and grain size decreases with doping. The optical band gaps were estimated from Tauc plots and found as 3.27, 3.26, 3.23, 3.25 eV for undoped and doped $Zn_{0.97}Sn_{0.03}O$, $Zn_{0.97}Al_{0.03}O$ and $Zn_{0.94}Sn_{0.03}Al_{0.03}O$ samples, respectively. The structural and optical calculations showed that characteristic properties of ZnO changed with Al and Sn doping.

(Sn, Al) Eş-katkılı ZnO Yarıiletkenlerinin Sentezi ve Karakterizasyonu

Anahtar Kelimeler
Sn ve Al eş-katkılama, ZnO, XRD, SEM, EDX, UV-Vis spektroskopi

Öz: Bu çalışma, kalay ve alüminyum katkılamasının ve kalay/alüminyum eş katkılamasının ZnO'nun yapısal, optik ve morfolojik özellikleri üzerindeki etkilerini sunmaktadır. Katı hal reaksiyon yöntemi, $Zn_{1-x-y}Sn_xAl_yO$ ((x:y) = (0.00: 0.00), (0.00: 0.03), (0.03: 0.00), (0.03: 0.03)) örneklerini hazırlamak için kullanılmıştır. Örneklerin özellikleri XRD, SEM, EDX spektroskopisi ve UV-vis spektroskopisi ile incelenmiştir. XRD sonuçları, örgü parametreleri a ve c, birim hücre hacmi, bağ uzunluğu L'nin azalırken, dislokasyon yoğunluğunun katkılama ile arttığını göstermiştir. Ortalama kristalit boyutu, katkılanmamış ZnO ile karşılaştırıldığında azalmıştır. SEM görüntüleri, tüm örneklerde hekzagonal benzeri tanelerin varlığını ve tane boyutunun katkılama ile azaldığını göstermiştir. Optik bant aralıkları Tauc grafiklerinden hesaplanmıştır ve sırasıyla katkısız ve katkılı $Zn_{0.97}Sn_{0.03}O$, $Zn_{0.97}Al_{0.03}O$ ve $Zn_{0.94}Sn_{0.03}Al_{0.03}O$ numuneleri için 3.27, 3.26, 3.23, 3.25 eV olarak bulunmuştur. Yapısal ve optik hesaplamalar, ZnO'nun karakteristik özelliklerinin Al ve Sn katkısıyla değiştiğini göstermiştir.

1. INTRODUCTION

Zinc oxide (ZnO) is an II–VI semiconductor with wide direct band gap (3.37 eV) and large exciton binding energy (60 meV) coupled with excellent chemical stability. ZnO is known as an important semiconductor which can be utilized in various areas because of its properties like non-toxicity, being plenty in nature, having low cost, and suitability to doping [1-6].

ZnO doping with transition elements, rare-earth elements, alkaline earth elements, and other elements is extensively worked to reach the desirable optical, electrical, and structural properties [7-20]. The impact of doping by single element on ZnO properties drew significant interest among researchers, and in many studies Al, In, Si, B and Sn were proposed as a good dopant for various metal oxides [21-32]. In addition, numerous studies were deployed to investigate the effects of co-dopant on the optical and structural properties of ZnO [33-44].

The objective of this work is to explore the effects of Al and Sn doping and (Sn–Al) co-doping on the structural and optical properties of ZnO prepared by solid state

reaction method. In this study, the solid-state reaction method was selected due to its advantages, including rapid synthesis, simple synthesis process, high efficiency, low preparation cost, reduced risk of contamination, and effective control over the resulting material's morphology. The structural characteristics were studied by X-ray diffractometer (XRD), the morphological features were monitored by Scanning Electron Microscopy (SEM), Energy Dispersive X-ray (EDX) spectroscopy and optical properties were examined by Ultraviolet–Visible (UV–vis) spectroscopy.

2. MATERIAL AND METHOD

Solid state reaction method was used to prepare the undoped ZnO and Sn-Al co-doped ZnO ($Zn_{1-x-y}Sn_xAl_yO$ ((x:y) = (0.00:0.00), (0.03:0.00), (0.00:0.03), (0.03:0.03)) samples. The stoichiometric amounts of starting powders ZnO, SnO_2 and Al_2O_3 were mixed and ground which is followed by calcination at 450 °C for 8 h. The resulting material was reground and pelletized upon cooling. Eventually, pellets of 10 mm diameter were prepared using press and these pellets were sintered at 900 °C for 12 h. The samples are referred as undoped ZnO (for x= 0, y= 0), Sn-ZnO (for x= 0.03, y= 0.00), Al-ZnO (for x= 0.00, y= 0.03) and (Sn, Al)-ZnO (for x= 0.03, y= 0.03).

For structural characterization, X-ray diffraction (XRD) using CuKα radiation (λ=1.5406 Å) accelerated in a 2θ range of 20–70° with a scan speed of 2° min^{-1} was performed. The surface morphology and grain structure of the samples were observed by scanning electron microscope (SEM) at magnification of 30 kx, and the elemental analysis of the samples was performed by energy-dispersive X-ray spectroscopy (EDX). The optical properties of all samples were characterized by using a UV–Vis spectrophotometer in the wavelength range of 300–800 nm.

3. RESULTS

3.1. XRD Analysis

Figure 1(a) demonstrates XRD patterns of undoped ZnO, $Zn_{0.97}Sn_{0.03}O$, $Zn_{0.97}Al_{0.03}O$ and $Zn_{0.94}Sn_{0.03}Al_{0.03}O$ samples. The diffraction patterns indexed with the 'hkl' values (100), (002), (101), (102), (110), (103), (200), (112) and (201) are the characteristic peaks of the hexagonal wurtzite crystal structure of ZnO (space group $P6_3mc$), which agrees with the standard data (JCPDS card No 36-1451).

An enlarged version of XRD pattern between 2θ= 31° and 37° to facilitate monitoring effect of doping on the structure is shown in Figure 1(b). The peaks (100), (002) and (101) of doped ZnO were slightly shifted to higher angles compared to undoped ZnO, which might have resulted from the compression of the lattice parameters due to the size difference between Sn, Al, and Zn atoms. The intensity of the peaks of doped ZnO decreased and the full width at half maximum (FWHM) became wider with doping. The lattice distortion produced around Sn and Al atoms increasing the tensile stress, may be held accountable for the decline in diffraction peak intensity and the increase of FWHM (Table 1).

Table 1. The peak position (2θ) values of undoped, Sn-doped, Al-doped and (Sn, Al) co-doped ZnO samples

Sample	(hkl)					
	(100)		(002)		(101)	
	2θ (°)	Intensity	2θ (°)	Intensity	2θ (°)	Intensity
ZnO	31.74	747	34.42	534	36.24	1376
Sn-ZnO	31.77	384	34.42	353	36.27	674
Al-ZnO	31.75	417	34.43	331	36.25	684
(Sn, Al)-ZnO	31.85	328	34.51	323	36.35	523

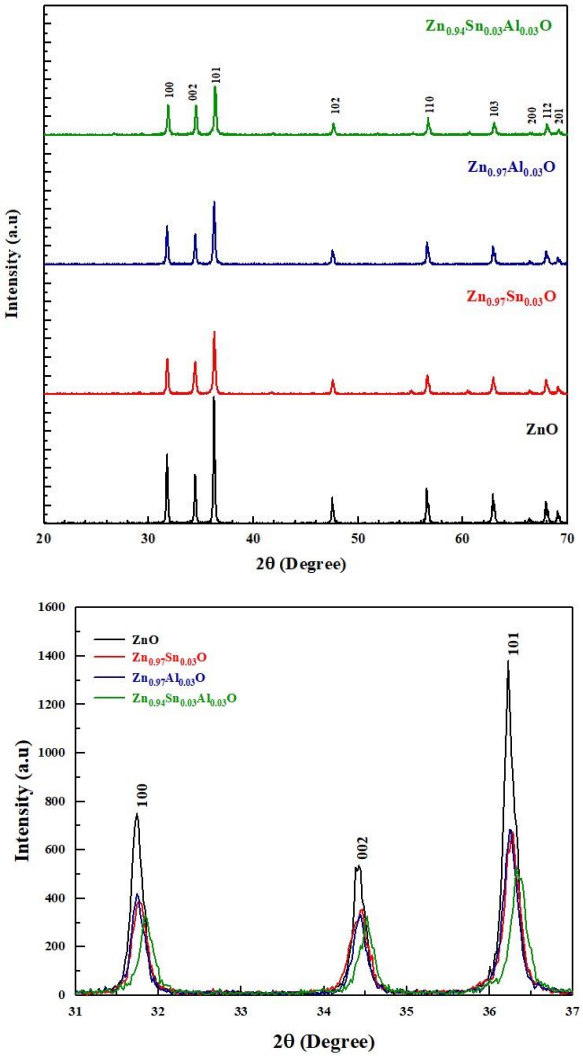

Figure 1. (a) XRD patterns of undoped ZnO, $Zn_{0.97}Sn_{0.03}O$, $Zn_{0.97}Al_{0.03}O$ and $Zn_{0.94}Sn_{0.03}Al_{0.03}O$ samples (b) enlarged view of (100), (002) and (101) peaks

Following relation was used to calculate the lattice constants (a, c) of the samples [45, 46]:

$$\frac{1}{d_{hkl}^2} = \frac{4}{3}\left(\frac{h^2 + hk + k^2}{a^2}\right) + \frac{l^2}{c^2} \quad (1)$$

where d_{hkl} is interplanar distance, determined from the Bragg's law ($2d_{hkl}\sin\theta = n\lambda$). From the lattice constants (a, c), the volume of the unit cell (V) for each sample was computed as follows [47, 48]:

$$V = \frac{\sqrt{3}}{2} a^2 c \quad (2)$$

The calculated values for the samples are given in table 2. The lattice parameters for undoped ZnO are a= 3.2523 Å, c= 5.2065 Å with unit cell volume V= 47.6920 Å^3. A small change was monitored in the lattice parameters a and c for Sn-ZnO compared to undoped ZnO which were prepared under same conditions. The lattice parameter a and c values decreased slightly after Al doping and Al, Sn co-doping. The radius of Al^{3+} (0.053 nm) and Sn^{4+} (0.069 nm) are smaller than the radius of Zn^{2+} (0.074 nm). In general, it is expected that the lattice constant gets smaller by Sn, Al atoms substituting Zn atoms in ZnO lattice. The lattice distortion c/a ratio is approximately 1.633 in a stoichiometric wurtzite structure. The calculated c/a of the samples are also given in table 2, and it was noticed that the values are slightly deviated from the ideal ratio indicating the presence of extended defects.

For hexagonal structure of ZnO, Zn–O bond length (L) was calculated via following equation [49, 50]:

$$L = \sqrt{\frac{a^2}{3} + \left(\frac{1}{2} - u\right)^2 c^2} \quad (3)$$

where u is a positional parameter of the wurtzite structure. The parameter u was calculated using below:

$$u = \frac{a^2}{3c^2} + 0.25 \quad (4)$$

The calculated value of Zn-O bond length (L) was found as 1.9788 Å for undoped ZnO, slightly higher than Zn-O bond length in the unit cell and decreased for doped ZnO. The bond length (L) and position parameter (u) values for the samples are listed in table 2.

Table 2. Lattice constants (a and c), unit cell volume (V), lattice distortion (c/a), displacement parameter (u) and bond length (L) of undoped, Sn-doped, Al-doped and (Sn, Al) co-doped ZnO samples

Sample	a(Å)	c(Å)	c/a	V (Å)^3	u	L (Å)
ZnO	3.2523	5.2065	1.6009	47.6920	0.3801	1.9788
Sn-ZnO	3.2493	5.2066	1.6024	47.6058	0.3798	1.8798
Al-ZnO	3.2514	5.2055	1.6010	47.6549	0.3800	1.8810
(Sn, Al)-ZnO	3.2412	5.1933	1.6023	47.2471	0.3798	1.8751

The crystallite size (D) and lattice strain (ε) were calculated using Scherrer's and Williamson–Hall method. The average crystallite size (D) was calculated below using Scherrer's equation [51, 52]:

$$D = \frac{K\lambda}{\beta cos\theta} \quad (5)$$

where K is the shape factor (is approximately given as 0.9), λ is the wavelength of Cu-K_α radiation (λ= 0.15406 nm), and β is full width at half maximum (FWHM). For undoped, Sn-doped, Al-doped and (Sn, Al) co-doped ZnO samples, average crystallite size was calculated as 35.69, 32.63, 33.06 and 30.10 nm, respectively. The average crystallite size of the samples was smaller than that of undoped ZnO as shown in table 3. The decrease in the crystallite size might be due to the distortion in the host ZnO lattice.

The lattice strain (ε) values were calculated using the following formula [53]:

$$\varepsilon = \frac{\beta cot\theta}{4} \quad (6)$$

The calculated lattice strain (ε) values are given in table 3. It was clearly seen that in doped samples average crystallite size (D) decreases while lattice strain values (ε) increases compared to undoped ZnO. To approximate structural flaws in the samples, dislocation density (δ) is an important parameter. Following equation gives the dislocation density (δ) [54, 55]:

$$\delta = \frac{1}{D^2} \quad (7)$$

The dislocation density variation trend is like that of lattice strain, which is the expected behavior. It was observed that diffraction broadening causes a decrease in crystallite size (D) and an increase in lattice strain (ε). This may be attributed to the growth in the overall defect concentration in the structure.

W-H method yields a more accurate crystallite size than that of obtained using Scherrer's method, as W–H method considers the contribution of intrinsic strain due to i.e. the presence of point defect, stacking faults, grain boundaries. The average crystallite size (D) and strain (ε) were determined below using Williamson-Hall method [56, 57]:

$$\beta cos\theta = \frac{K\lambda}{D} + 4\varepsilon sin\theta \quad (8)$$

The plots of βcosθ as a function of 4sinθ for all samples are shown in figure 2. The y-intercept of the corresponding linear fit extrapolation is used to determine D values, while the slope of this fit gives ε values. The strain and crystallite size values obtained from W-H plot is given in table 3.

The calculated value of D and ε for undoped ZnO by Scherrer's method is 35.69 nm and 2.42x10^{-3}, respectively. By Williamson–Hall's method, D is found as 118.50 nm which is larger than that obtained by Scherrer's method, while ε is smaller, which is 1.68x10^{-3}. The reduction in the ε may explain the strain contribution in crystal size using Williamson–Hall's method that leads to obtaining large size compared to Scherrer's method. In both method, D decreased with doping Sn and Al into ZnO, which may be attributed to the slight decrease in the lattice parameters.

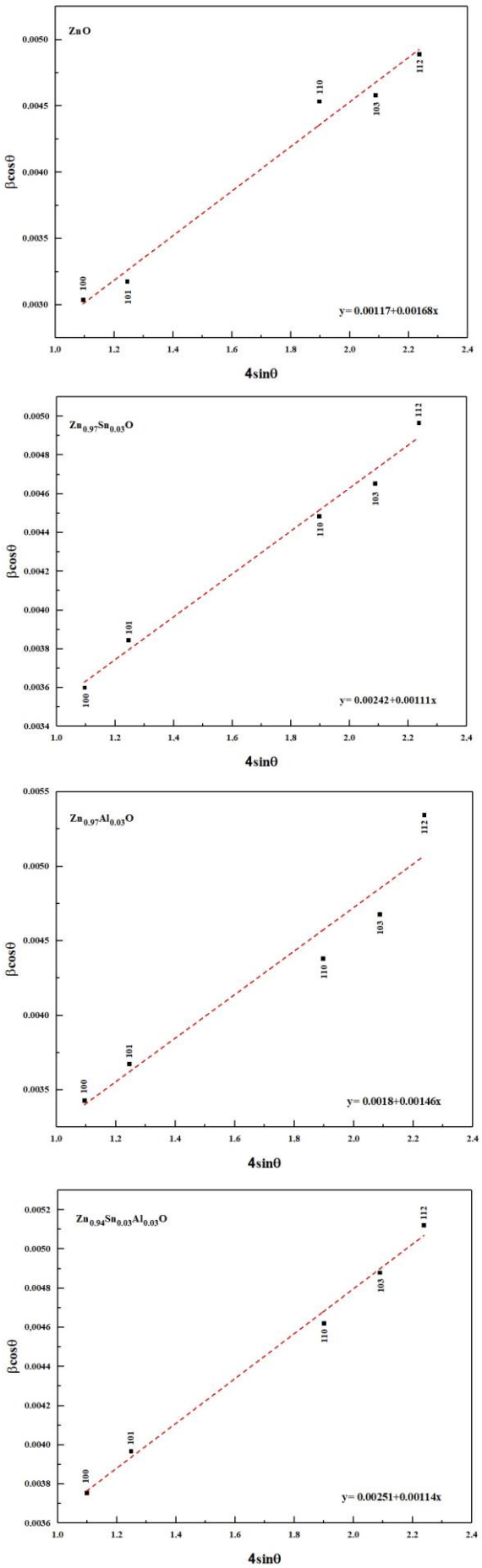

Figure 2. βcosθ versus 4sinθ of undoped ZnO, $Zn_{0.97}Sn_{0.03}O$, $Zn_{0.97}Al_{0.03}O$ and $Zn_{0.94}Sn_{0.03}Al_{0.03}O$ samples

Table 3. The calculated crystallite size (D), dislocation density (δ) and the lattice strain (ε) for undoped, Sn-doped, Al-doped and (Sn, Al) co-doped ZnO samples

Sample	Scherrer's D (nm)	ε (10^{-3})	δ $(nm)^{-2}$	W-H	
				D (nm)	ε (10^{-3})
ZnO	35.69	2.42	0.00078	118.50	1.68
Sn-ZnO	32.63	2.64	0.00094	57.29	1.11
Al-ZnO	33.06	2.61	0.00091	77.03	1.46
(Sn, Al)-ZnO	30.10	2.56	0.00110	55.24	1.14

3.2. SEM and EDX Analysis

SEM images of undoped ZnO and co-doped ZnO are displayed in figure 3. In all samples, it was monitored that the grains were homogeneously distributed and there were hexagonal like grains. Grains were more closely packed in undoped sample, whereas the voids between the grains increased with doping which may be linked to the existence of defects. SEM images also showed that the grain size was smaller in doped samples when compared to the undoped ZnO. In accordance with the crystallite size obtained from XRD measurements, it was observed from SEM images that the grain sizes decreased with doping.

Figure 4 presents the EDX spectra of all samples. Each image includes an inset showing the atomic and molecular weights of the elements involved in the synthesis process. It was observed that all the samples contain Zn, Sn, Al, and O elements according to their respective stoichiometric amounts. EDX spectrum and elemental mapping confirmed the presence of the host and substituted elements without any other element. The dopant concentration and reduction in host element content indicated that materials retain their stoichiometric compositions.

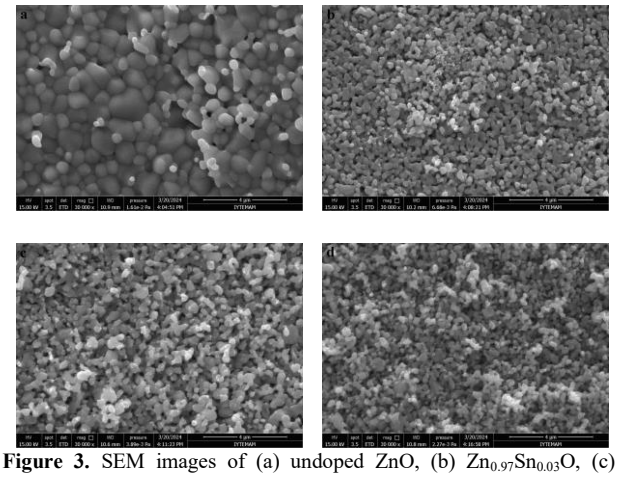

Figure 3. SEM images of (a) undoped ZnO, (b) $Zn_{0.97}Sn_{0.03}O$, (c) $Zn_{0.97}Al_{0.03}O$ and (d) $Zn_{0.94}Sn_{0.03}Al_{0.03}O$ samples at 30000×magnifcation

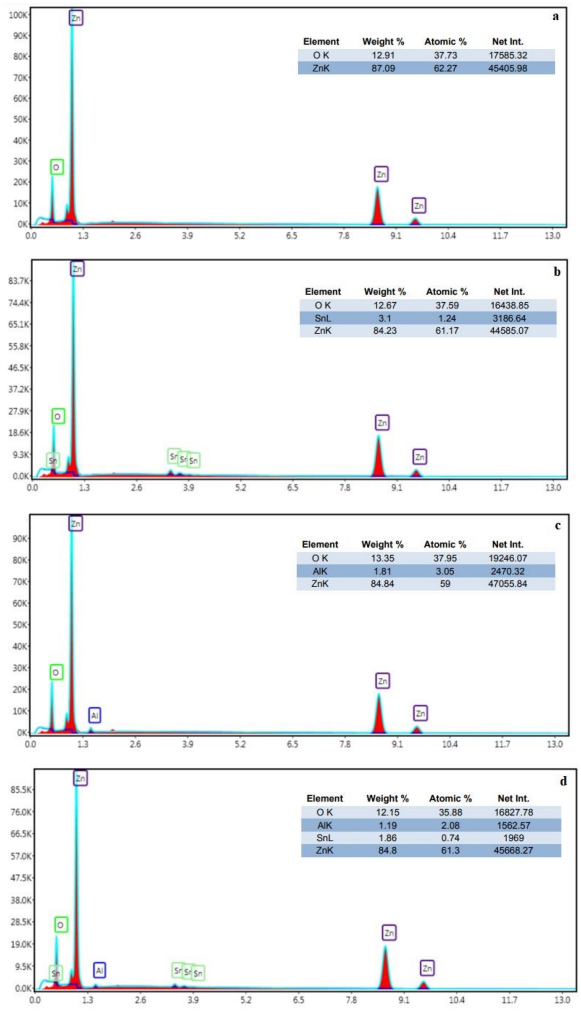

Figure 4. EDX spectra of (a) undoped ZnO, (b) $Zn_{0.97}Sn_{0.03}O$, (c) $Zn_{0.97}Al_{0.03}O$ and (d) $Zn_{0.94}S_{n0.03}Al_{0.03}O$ samples

3.3. UV–Vis Spectroscopy Analysis

The impact of doping on the optical properties of ZnO was investigated via reflectance UV–vis spectroscopy measurement in the wavelength range of 300−800 nm. Reflectance spectra of undoped and doped ZnO are displayed in figure 5. From the reflectance spectra, the absorption edge spectra for each sample were determined. The reflectance data was converted to absorption spectra through Kubelka-Munk equation. The optical absorption spectra of all samples are displayed in figure 6. The absorption edge spectra of doped samples were shifted towards higher wavelength as compared to undoped ZnO sample.

Tauc equation was used to calculate the optical band gap energy (E_g) [58, 59]:

$$\alpha h\upsilon = A\left(h\upsilon - E_g\right)^n \quad (9)$$

where α is the absorption coefficient ($\alpha = 2.303A/t$) and n is a constant depending on optical transition type and equal to 1/2 for direct gap transitions. Figure 7 denotes the plotting of $(\alpha h\upsilon)^2$ as a function of photon energy hυ. Plotting a line tangent to the linear part of the $(\alpha h\upsilon)^2$ versus hν curve and taking its intersection point with the x-axis (hν) gives the energy bandgap, E_g. The obtained results are also listed in table 4.

The energy band gap value of the prepared undoped ZnO was estimated as 3.27 eV which is less than that the reported for ZnO (3.37 eV). This deviation might be driven by the structural defects that encompass the sample during the synthesis process and thermal treatment. A slight decrease compared to undoped ZnO was observed with doping and co-doping. The samples' estimated band gap values were retrieved as 3.26, 3.23 and 3.25 eV for $Zn_{0.97}Sn_{0.03}O$, $Zn_{0.97}Al_{0.03}O$ and $Zn_{0.94}Sn_{0.03}Al_{0.03}O$, respectively. Compared with that of Sn doping, it was seen that Al doping makes the band gap narrowing more apparent. The values being close to each other may be attributed to low doping concentration.

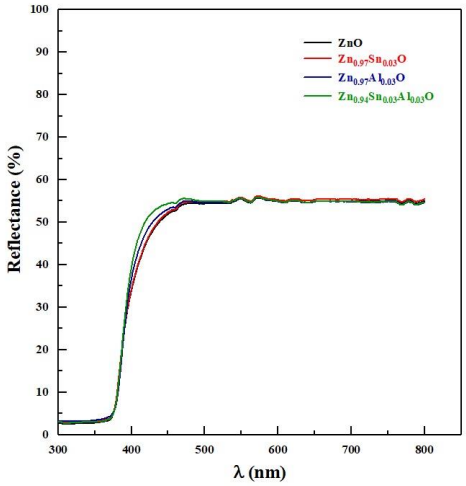

Figure 5. Reflectance spectra of undoped ZnO, $Zn_{0.97}Sn_{0.03}O$, $Zn_{0.97}Al_{0.03}O$ and $Zn_{0.94}Sn_{0.03}Al_{0.03}O$ samples

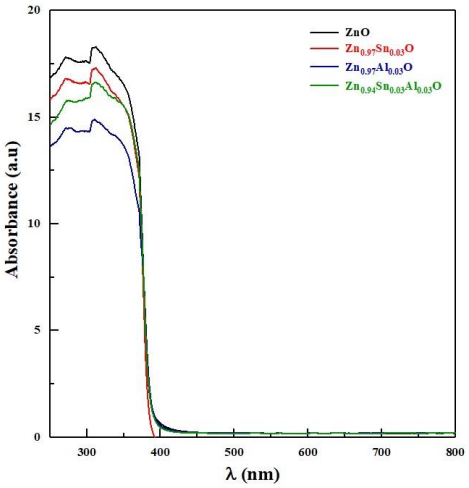

Figure 6. Absorbance spectra of undoped ZnO, $Zn_{0.97}Sn_{0.03}O$, $Zn_{0.97}Al_{0.03}O$ and $Zn_{0.94}Sn_{0.03}Al_{0.03}O$ samples

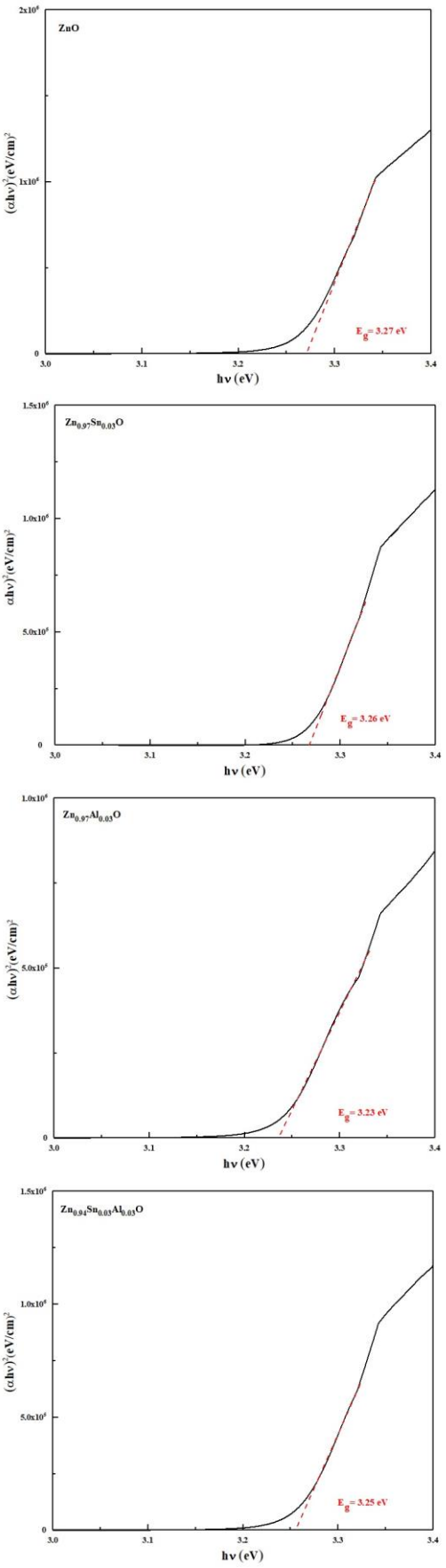

Figure 7. Tauc plots of undoped ZnO, $Zn_{0.97}Sn_{0.03}O$, $Zn_{0.97}Al_{0.03}O$ and $Zn_{0.94}Sn_{0.03}Al_{0.03}O$ samples

The band gap of ZnO exhibits a slight reduction upon doping with Al and Sn, which is attributed to the presence of defect bands in the band gap. Interactions between ZnO lattice and dopant ions leads to the creation of localized states within ZnO band gap. An urbach tail is produced by these defect states which extends deep into the forbidden gap and the energy associated with this tail is referred as Urbach energy [60].

The Urbach energy (E_u), which correlates the band tails of the localized states with the crystal defects and microstructural lattice disorders, and is determined from the following relation [61-63]:

$$\alpha = \alpha_0 \exp\left(h\nu/E_u\right) \quad (10)$$

where α_0 is a constant, α is the absorption coefficient, and hν is the photon energy. E_u is determined by plotting ln(α) versus (hν). The value of E_u was obtained by taking the reciprocal of the slope of the linear fit. The obtained values of E_u are given in table 4.

The values of Urbach energy evaluated from the slopes of the fitted curves were found as 0.491, 0.554, 0.577 and 0.660 eV for undoped ZnO, $Zn_{0.97}Sn_{0.03}O$, $Zn_{0.97}Al_{0.03}O$ and $Zn_{0.94}Sn_{0.03}Al_{0.03}O$, respectively. An opposite trend in the variations of E_u and E_g with doping concentration was observed. The E_u value is relatively high for doped samples, and this might be associated with structural defects or disorder presents in the samples.

The Urbach energy of doped ZnO was found to be higher than that of undoped ZnO. Previous studies have reported that increasing Urbach energy results in an increase in dislocation density. Consistent with the XRD and UV–vis spectroscopy results, the observed increase in Urbach energy in doped ZnO was accompanied by an increase in dislocation density [64-65].

Table 4. The optical band gap (E_g) and Urbach (E_u) energy for undoped, Sn-doped, Al-doped and (Sn, Al) co-doped ZnO samples

Sample	E_g (eV)	E_u (eV)
ZnO	3.27	0.491
Sn-ZnO	3.26	0.554
Al-ZnO	3.23	0.577
(Sn, Al)-ZnO	3.25	0.660

4. DISCUSSION AND CONCLUSION

The effects of Al, Sn doping and co-doping on the structural, optical, and morphological properties of ZnO samples prepared by solid-state reaction method were reported in this study. XRD, SEM, EDX, and U-Vis measurements were deployed to investigate the main characteristic features of the samples. From XRD, it was concluded that the doping resulted with no change in the hexagonal wurtzite structure of ZnO. With doping, there was a slight decrease in the cell parameters and bond length which results in the shrink of the cell volume. The crystallite size (D) estimated both by Scherrer's and Williamson–Hall methods decreased with Sn, Al doping and with (Sn-Al) co-doping compared to undoped ZnO. SEM indicated the presence of hexagonal like grains in all samples and showed that the grain size decreases with doping. The band gap values were determined to be 3.26 eV and 3.23 eV for Sn and Al-doped ZnO, respectively,

and 3.25 eV for Sn, Al co-doped ZnO, compared to 3.27 eV for undoped ZnO. According to the UV–Vis spectroscopy data, both doping and co-doping of ZnO led to a slight narrowing of the band gap and an increase in Urbach energy compared to undoped ZnO. The increase in Urbach energy may be attributed to a higher degree of structural disorder and a reduction in crystallite size resulting from the incorporation of Al and Sn dopants into the ZnO lattice. Overall, the obtained results suggested that the structural and optical properties of ZnO can be altered by doping.

Acknowledgement

Samples were prepared at Physics Laboratory Dokuz Eylul University, Faculty of Science, Physics Department, in Izmir, Turkey. XRD and U-Vis measurements were performed at Electronic Materials Production and Application Center (EMUM) Dokuz Eylul University. SEM and EDX were performed at İzmir Institute of Technology Integrated Research Centers.

REFERENCES

[1] Boshra Ghanbari Shohany, Ali Khorsand Zak. Doped ZnO nanostructures with selected elements - Structural, morphology and optical properties: A review, Ceramics International 2020; 46: 5507-5520.

[2] Dhirendra Kumar Sharma, Sweta Shukla, Kapil Kumar Sharma, Vipin Kumar. A review on ZnO: Fundamental properties and applications, Materials Today: Proceedings. 2022; 49: 3028-3035.

[3] Dongwoon Jung. Syntheses and characterizations of transition metal-doped ZnO, Solid State Sciences 2010; 12: 466-470.

[4] Asikuzun Tokeser E., Ozturk O. . Estimation of microstructural parameters by Williamson–Hall, Halder–Wagner, and size–strain plot methods and magnetic properties of (Cu/Mn) co-doped ZnO nanoparticles, J Mater Sci: Mater Electron. 2023; 34: 2075

[5] Geetha Devi P., Sakthi Velu A.. Synthesis, structural and optical properties of pure ZnO and Co doped ZnO nanoparticles prepared by the co-precipitation method. J Theor Appl Phys. 2016; 10: 233–240.

[6] Xiurong Qu, Shuchen Lu, Dechang Jia, Sheng Zhou, Qingyu Meng. First-principles study of the electronic structure of Al and Sn co-doping ZnO system, Materials Science in Semiconductor Processing 2013; 16: 1057-1062.

[7] Huaming Yang, Sha Nie. Preparation and characterization of Co-doped ZnO nanomaterials. Materials Chemistry and Physics 2009; 114: 279–282.

[8] Amalia M., Cristina D. G, Mihaela P., Raluca M, Adriana Popa, Traian Petrisor Jr., Mihai Gabor, Adrian Ionut Cadis, Bogdan S. Vasile. Synthesis, structural and morphological characteristics, magnetic and optical properties of Co doped ZnO nanoparticles, Ceramics International 2014; 40: 2835-2846.

[9] Chao Xu, Lixin Cao, Ge Su, Wei Liu, Xiaofei Qu, Yaqin Yu, Preparation, characterization and photocatalytic activity of Co-doped ZnO powders, Journal of Alloys and Compounds 2010; 497: 373–376.

[10] N.H. Erdogan, T. Kutlu, N. Sedefoglu, H. Kavak Effect of Na doping on microstructures, optical and electrical properties of ZnO thin films grown by sol-gel method. Journal of Alloys and Compounds 2021; 881: 160554.

[11] Imen Massoudi, Taher Ghrıb, Amal L. Al-Otaıbı, Kawther Al-Hamadah, Shadıa Al-Malky, Maha Al-Otaıbı, and Marıam Al-Yatımı Effect of Yttrium Substitution on Microstructural, Optical, and Photocatalytic Properties of ZnO Nanostructures, Journal of Electronic Materials 2020; 49: 5353-5362.

[12] G. Murtaza, R. Ahmad, M.S. Rashid, M. Hassan, A. Hussnain, Muhammad Azhar Khan, M. Ehsan ul Haq, M.A. Shafique, S. Riaz Structural and magnetic studies on Zr doped ZnO diluted magnetic semiconductor, Current Applied Physics 2014; 14: 176-181.

[13] R. Elilarassi, G. Chandrasekaran Structural, optical and magnetic characterization of Cu-doped ZnO nanoparticles synthesized using solid state reaction method, J Mater Sci: Mater Electron. 2010; 21: 1168–1173.

[14] Zafer Gultekin, Mursel Alper1, M. Cuneyt Hacıismailoglu, and Cengiz Akay Effect of Mn doping on structural, optical and magnetic properties of ZnO films fabricated by sol–gel spin coating method, J Mater Sci: Mater Electron. 2023; 34: 2-14.

[15] G. Bulun, A. Ekicibil, S. K. Cetin, S. Demirdis, A. Coskun, K. Kıymac Elaboration of the structural and physical characteristics: Ni-doped ZnO bulk samples prepared by solid state reactions, Journal of Optoelectronics and Advanced Materials 2011; 13: 231-236.

[16] Sujit Anil Kadam, Susmi Anna Thomas, Yuan-Ron Ma, Lolly Maria Jose, D. Sajan, Arun Aravind Investigation of adsorption and photocatalytic behavior of manganese doped zinc oxide nanostructures, Inorganic Chemistry Communications 2021; 134: 108981.

[17] T. Akilan, N. Srinivasan, R. Saravanan Magnetic and optical properties of Ti doped ZnO prepared by solid state reaction method, Materials Science in Semiconductor Processing 2015; 30: 381-387.

[18] Jing Xie, Yali Cao, Dianzeng Jia, Yizhao Li, Yang Wang Solid-state synthesis of Y-doped ZnO nanoparticles with selective-detection gas-sensing performance Ceramics International 2016; 42: 90-96.

[19] Hakan Colak, Orhan Turkoglu Structural and electrical properties of V-doped ZnO prepared by the solid-state reaction, J Mater Sci: Mater Electron. 2012; 23: 1750–1758.

[20] N. K. Divya, P.P. Pradyumnan, Solid state synthesis of erbium doped ZnO with excellent photocatalytic activity and enhanced visible light emission, Materials Science in Semiconductor Processing 2016; 41: 428-435.

[21] Chaeseon Hong, Kyung-Mun Kang, Minjae Kim, Yue Wang, Taehee Kim, Chan Lee, Hyung-Ho Park Structural, electrical, and optical properties of Si-doped ZnO thin films prepared via supercycled atomic layer deposition, Materials Science and Engineering: B 2021; 273: 115401.

[22] Caiying Mao, Liang Fang, Hong Zhang, Wanjun Li, Fang Wu, Guoping Qin, Haibo Ruan, Chunyang Kong Effect of B doping on optical, electrical properties and defects of ZnO films, Journal of Alloys and Compounds 2016; 676: 135-141.

[23] Bircan Dindara, Ali Can Güler Comparison of facile synthesized N doped, B doped and undoped ZnO for the photocatalytic removal of Rhodamine B. Environmental Nanotechnology, Monitoring & Management 2018; 10: 457-466

[24] J. Mayandi, R.K. Madathil, C. Abinaya, K. Bethke, V. Venkatachalapathy, K. Rademann, T. Norby, T.G. Finstad Al-doped ZnO prepared by co-precipitation method and its thermoelectric characteristics, Materials Letters 2021; 288: 129352.

[25] Chien-Yie Tsay, Hua-Chi Cheng, Yen-Ting Tung, Wei-Hsing Tuan, Chung-Kwei Lin Effect of Sn-doped on microstructural and optical properties of ZnO thin films deposited by sol–gel method Thin Solid Films 2008; 517: 1032–1036.

[26] Rajwali Khan, Vineet Tirth, Amjad Ali Kashif Irshad, Nasir Rahman, Ali Algahtani, Mohammad Sohail, Saiful Isalm Effect of Sn-doping on the structural, optical, dielectric and magnetic properties of ZnO nanoparticles for spintronics applications, J Mater Sci: Mater Electron. 2021; 32: 21631–2164.

[27] A.D. Acharya, Shweta Moghe, Richa Panda, S.B. Shrivastava, Mohan Gangrade, T. Shripathi, D.M. Phase, V. Ganesan Growth and characterization of nano-structured Sn doped ZnO, Journal of Molecular Structure 2012; 1022 8-15.

[28] Manjeet Kumar, Vishwa Bhatt, A.C. Abhyankar, Joondong Kim, Akshay Kumar, Ju-Hyung Yun Modulation of structural properties of Sn doped ZnO for UV photoconductors, Sensors and Actuators A: Physical 2018; 270: 118-126.

[29] Mustafa Ozgür, Suat Pat, Reza Mohammadigharehbagh, Caner Musaoglu, Ugur Demirkol, Saliha Elmas, Soner Ozen, Sadan Korkmaz Sn doped ZnO thin film deposition using thermionic vacuum arc technique, Journal of Alloys and Compounds 2019; 774: 1017-1023.

[30] Mejda Ajili, Michel Castagné, Najoua Kamoun Turki Study on the doping effect of Sn-doped ZnO thin films, Superlattices and Microstructures 2013; 53: 213-222.

[31] H. Aydin, H.M. El-Nasser, C. Aydin, Ahmed. A. Al-Ghamdi, F. Yakuphanoglu Synthesis and characterization of nanostructured undoped and Sn-doped ZnO thin films via sol–gel approach, Applied Surface Science 2015; 350: 109-114.

[32] Weibao Guan, Liying Zhang, Chao Wang, Yuanxu Wang Theoretical and experimental investigations of the thermoelectric properties of Al-, Bi- and Sn-doped ZnO, Materials Science in Semiconductor Processing 2017; 66: 247-252.

[33] Jin Zhaoa, Qiao Liping, Guo Chen, He Zhili, Liu Lidong, Rong Mei First-priniciple study of electrical and optical properties of (Al,Sn) co-doped ZnO, Optik 2016; 127: 1988-1992.

[34] Susanta Kumar Sahoo, Chandan Ashis Gupta, Udai P. Singh Impact of Al and Ga co-doping with different proportion in ZnO thin film by DC magnetron sputtering, J Mater Sci: Mater Electron. 2016; 27: 7161–7166.

[35] M. K. Alqadi, A. B. Migdadi, F. Y. Alzoubi, H. M. Al-Khateeb, Ahmad A. Almasri, Influence of (Ag–Cu) co-doping on the optical, structural, electrical, and morphological properties of ZnO thin films, Journal of Sol-Gel Science and Technology 2022; 103: 319–334.

[36] G. Vijayaprasath, R. Murugan, S. Asaithambi, P. Sakthivel, T. Mahalingam, Y. Hayakawa, G. Ravi Structural and magnetic behavior of Ni/Mn co-doped ZnO nanoparticles prepared by co-precipitation method, Ceramics International 2016; 42: 2836–2845.

[37] Rajwali Khan, Simbarashe Fashu, Zia-Ur-Rehman Structural, dielectric and magnetic properties of (Al, Ni) co-doped ZnO nanoparticles, J Mater Sci: Mater Electron. 2017; 28: 4333–4339.

[38] B. Poornaprakash, U. Chalapathi, S. Babu, Si-Hyun Parka Structural, morphological, optical, and magnetic properties of Gd-doped and (Gd, Mn) co-doped ZnO nanoparticles, Physica E: Low-dimensional Systems and Nanostructures 2017; 93: 111-115.

[39] Wubishet Kejela Tolossa, Paulos Taddesse Shibeshi Structural, optical and enhanced antibacterial activities of ZnO and (Co, Fe) co-doped ZnO nanoparticles by sol-gel combustion method, Chemical Physics Letters 2022; 795: 139519.

[40] Fazal Kabir, Adil Murtaza, Azhar Saeed, Awais Ghani, Anwar Ali, Saleh Khan, Kaili Li, Qizhong Zhao, Kang Kang Yao, Yin Zhang, Sen Yang Structural, optical and magnetic behavior of (Pr, Fe) co-doped ZnO based dilute magnetic semiconducting nanocrystals, Ceramics International 2022; 48: 19606-19617.

[41] Rajwali Khan, Zulfiqar, Simbarashe Fashu, Zia Ur Rehman, Aurangzeb Khan, Muneeb Ur Rahman Structure and magnetic properties of (Co, Mn) co-doped ZnO diluted magnetic semiconductor nanoparticles, J Mater Sci: Mater Electron. 2018; 29: 32–37.

[42] Sudipta Mondal, Moniruzzaman Jamal, Sikder Ashikuzzaman Ayon, Md Jannatul Ferdous Anik, Md Muktadir Billah Synergistic enhancement of photocatalytic and antimicrobial efficacy of nitrogen and erbium co-doped ZnO nanoparticles, Journal of Rare Earths 2024; 42: 859-868.

[43] S.D. Senol, E. Ozugurlu, L. Arda Synthesis, structure and optical properties of (Mn/Cu) co-doped ZnO nanoparticles, Journal of Alloys and Compounds 2020; 822: 153514.

[44] Darshan Sharma, Ranjana Jha Transition metal (Co, Mn) co-doped ZnO nanoparticles: Effect on

structural and optical properties, Journal of Alloys and Compounds 2017; 698: 532-538
[45] Anu Katiyar, Nishant Kumar, Priyanka Srivastava, R.K. Shukla, Anchal Srivastava Structural and physical parameters of sol-gel spin coated ZnO thin films: Effect of sol concentration, Materials Today: Proceeding 2020; 29: 1098-1103.
[46] Esra Aslan, Maharram Zarbali Tuning of photosensitivity and optical parameters of ZnO based photodetectors by co-Sn and Ti doping, Optical Materials 2022; 125: 112030.
[47] Mona A. Mohaseb Effect of Co doping onto physical properties of ZnO films and its UV detection performance, J Mater Sci: Mater Electron. 2023; 34: 1219.
[48] A. Khorsand Zak, W.H. Abd. Majid, M.E. Abrishami, Ramin Yousefi X-ray analysis of ZnO nanoparticles by Williamson-Hall and size estrain plot methods, Solid State Sciences 2011; 13: 251-256.
[49] H. Saadia, F.I.H. Rhouma, Z. Benzarti, Z. Bougrioua, S. Guermazi, K. Khirouni Electrical conductivity improvement of Fe doped ZnO nanopowders, Materials Research Bulletin 2020; 129: 110884.
[50] A. A. Ahmad, A. B. Migdadi, A. M. Alsaad, Qais M. Al-Bataineh, Ahmad Telfah Optical, structural, and morphological characterizations of synthesized (Cd–Ni) co-doped ZnO thin flms, Applied Physics A 2021; 127: 922.
[51] Noubeil Guermat, Warda Daranfed, Idris Bouchama, Nadir Bouarissa Investigation of structural, morphological, optical and electrical properties of Co/Ni co-doped ZnO thin films, Journal of Molecular Structure 2021; 1225: 129134
[52] N. Siva, D. Sakthi, S. Ragupathy, V. Arun, N. Kannadasan Synthesis, structural, optical and photocatalytic behavior of Sn doped ZnO nanoparticles, Materials Science and Engineering: B 2020; 253: 114497.
[53] Aradhana Tiwari, P.P. Sahay Highly c-axis oriented (Mg, Sn) co-doped ZnO thin films for optoelectronic applications, Optical Materials 2022; 134: 113098.
[54] Safa Hamdi, Hichem Smaoui, Samir Guermazi, Gerard Leroy, Benoit Duponchel Enhancing the structural, optical and electrical conductivity properties of ZnO nanopowders through Dy doping, Inorganic Chemistry Communications 2022; 144: 109819.
[55] V. Ganesh, I.S. Yahia, S. AlFaify, Mohd. Shkir Sn-doped ZnO nanocrystalline thin films with enhanced linear and nonlinear optical properties for optoelectronic applications, Journal of Physics and Chemistry of Solids 2017; 100: 115-125.
[56] P. Norouzzadeh, Kh. Mabhouti, M. M. Golzan, R. Naderali Consequence of Mn and Ni doping on structural, optical and magnetic characteristics of ZnO nanopowders: the Williamson–Hall method, the Kramers–Kronig approach and magnetic interactions, Applied Physics A 2020; 126: 154
[57] Shradha Roy, Mritunjoy Prasad Ghosh, Samrat Mukherjee Introducing magnetic properties in Fe-doped ZnO nanoparticles, Applied Physics A 2021; 127: 451
[58] T. Ates, C. Tatar, F. Yakuphanoglu Preparation of semiconductor ZnO powders by sol–gel method: Humidity sensors, Sensors and Actuators A: Physical 2013; 190: 153-160.
[59] Yongmei Zhu, Guoyue Xu, Tengchao Guo, Haili Hou, Shujuan Tan Preparation, infrared emissivity and thermochromic properties of Co doped ZnO by solid state reaction, Journal of Alloys and Compounds 2017; 720: 105-115.
[60] Cosmas Muiva, Dineo P. Sebuso, Edigar Muchuweni, Microstructural and optical properties of nanostructured Al/Ag co-doped ZnO thin films (AgxAl0.03ZnO0.97-x) by spray pyrolysis for optoelectronic applications, Physica B 2024; 690: 416206.
[61] S. Rajasekar, Jafar Ali Ibrahim Syed Masood, N.S. Kalyan Chakravarthi, P. Shunmuga Sundaram, M. Karunakaran, Gaurav Jayaswal, L. Bruno Chandrasekarf, Abdullah N. Alodhayb, George Z. Kyzas, Synthesis and characterization of cobalt-strontium co-doped zinc oxide nanoparticles by chemical precipitation, Inorganic Chemistry Communications 2023; 158: 111607.
[62] Mehmet Ozkan, Sercan Sadık Erdem, Reza Mohammadigharehbagh, Sema Kurtaran, Suat Pat Investigation of substrate effect on Co-doped ZnO thin films prepared by thermionic vacuum arc technique, Inorganic Chemistry Communications 2022; 146: 110095.
[63] M. Thobega, K. Maabong-Tau, K. Lefatshe, C. Muiva, Study of structural, optical and electrical properties of Nickel doped ZnO (Ni–ZnO) nanorods grown by chemical bath deposition, Physica B 2024; 673: 415500.
[64] K. Salima, M. Medles, A. Nakrela, R. Miloua, A. Bouzidi, R. Desfeux, Enhancement of optical and electrical properties of spray pyrolysed ZnO thin films obtained from nitrate chemical by Al-Sn co-doping, Optik 2020; 210: 164504.
[65] Imadeddine Bellili, Mohamed Mahtali, Warda Darenfad, Noubeil Guermat, The figure of merit improvement of (Sn, Co)–ZnO sprayed thin films for optoelectronic applications, Optical Materials 2024;154: 115785.

Volume 14, Issue 3, Page 139-144, 2025 https://doi.org/10.46810/tdfd.1734194 Research Article

BİNGÖL UNIVERSITY

Türk Doğa ve Fen Dergisi
Turkish Journal of Nature and Science
www.dergipark.gov.tr/tdfd

Fabrication and Characterisation of TiO_2 Thin Film Methanol Vapor Sensor

Ömer ÇOBAN[1*]

[1]Atatürk University, Engineering Faculty, Electrical and Electronic Engineering Department, Erzurum, Türkiye
Ömer ÇOBAN ORCID No: 0000-0003-4312-9026

Corresponding author: omercoban@atauni.edu.tr

(Received: 03.07.2025, Accepted: 10.08.2025, Online Publication: 26.09.2025)

Keywords
TiO_2 thin film, Sensor, Chemical vapor, Methanol

Abstract: In this study, a titanium dioxide (TiO_2) thin film with a thickness of approximately 250 nm was deposited on silicon dioxide (SiO_2) substrate using the pulsed DC sputtering technique to investigate the gas sensing performance for methanol vapor detection. The structural, morphological, and vibrational characteristics of the film were analyzed using X-ray diffraction (XRD), scanning electron microscopy (SEM), and micro-Raman spectroscopy, respectively. UV–Vis spectrophotometry was used to analyze the optical properties, including light absorption behavior, and to determine the band gap of the sensing material. For sensor measurements under methanol vapor ambient conditions, aluminum interdigitated electrodes (IDEs) with ohmic contacts were fabricated on the surface of the TiO_2 film using DC sputtering. The sensor was subsequently exposed to various concentrations of methanol vapor (up to 1900 ppm) at three different operating temperatures: 150 °C, 200 °C, and 250 °C. The dynamic gas sensing performance, including response and recovery times, was systematically monitored under each condition. The highest sensor response was recorded at 200 °C, with a Ra/Rg value of 6.5 under exposure to 1900 ppm methanol, while the shortest response and recovery times were obtained at 250 °C. In contrast, at other operating temperatures (150 °C and 200 °C), the sensor response decreased, and both the response and recovery times were significantly prolonged.

TiO_2 İnce Film Metanol Buharı Sensörünün Üretimi ve Karakterizasyonu

Anahtar Kelimeler
TiO_2 ince film, Sensör, Kimyasal buhar, Metanol

Öz: Bu çalışmada, yaklaşık 250 nm kalınlığındaki titanyum dioksit (TiO_2) ince film, metanol buharının algılanmasına yönelik gaz algılama performansını araştırmak amacıyla pulse DC saçtırma tekniği kullanılarak silisyum dioksit (SiO_2) alttaş üzerine kaplanmıştır. Filmin yapısal, morfolojik ve titreşimsel özellikleri sırasıyla X-ışını kırınımı (XRD), taramalı elektron mikroskobu (SEM) ve mikro-Raman spektroskopisi kullanılarak analiz edilmiştir. Optik özellikler, ışık soğurma davranışı dahil olmak üzere, UV–Vis spektrofotometresi ile incelenmiş ve algılayıcı malzemenin bant aralığı belirlenmiştir. Metanol buharı ortamında sensör ölçümleri gerçekleştirebilmek için, TiO_2 film yüzeyine DC saçtırma yöntemiyle ohmik temas sağlayan alüminyum iç içe geçmiş elektrotlar (IDE) üretilmiştir. Sensör daha sonra üç farklı çalışma sıcaklığında (150 °C, 200 °C ve 250 °C) 1900 ppm'e kadar çeşitli metanol buharı konsantrasyonlarına maruz bırakılmıştır. Her bir koşul altında, yanıt ve iyileşme süreleri dahil olmak üzere dinamik gaz algılama performansı sistematik olarak izlenmiştir. En yüksek sensör tepkisi, 1900 ppm metanol maruziyeti altında 6.5 Ra/Rg değeri ile 200 °C'de kaydedilmiş olup, en kısa tepki ve iyileşme süreleri ise 250 °C'de elde edilmiştir. Buna karşılık, diğer çalışma sıcaklıklarında (150 °C ve 200 °C) sensör tepkisi azalmış, yanıt ve iyileşme süreleri ise belirgin şekilde uzamıştır.

1. INTRODUCTION

Volatile organic compounds (VOCs) are carbon-based chemicals that readily evaporate at room temperature [1,2]. They are commonly found in indoor and outdoor environments, originating from sources such as industrial solvents, fuels, cleaning agents, and paints. Among these compounds, methanol is particularly notable due to its widespread use in pharmaceuticals, food processing, disinfectants, and chemical manufacturing. While useful, methanol vapors can pose serious health risks—such as respiratory irritation and central nervous system effects—

when inhaled over extended periods [3,4]. Therefore, monitoring methanol concentrations is essential in settings such as laboratories, production facilities, and medical environments to ensure occupational and public safety [5–7].

Conventional analytical techniques such as gas chromatography (GC) [8] and mass spectrometry (MS) offer high precision and sensitivity for methanol detection [9]. However, these methods are inherently limited by their operational complexity, cost, and the requirement for bulky instrumentation and skilled personnel. This restricts their application in scenarios demanding portable, low-power, and real-time sensing capabilities. To address this gap, solid-state gas sensors based on metal oxide semiconductors (MOS) materials have become highly attractive due to their low cost, stability, high sensitivity, and compatibility with microelectronic integration [10–18]. Titanium dioxide (TiO_2) is considered one of the most promising MOS materials for methanol sensing due to its excellent chemical stability, high surface reactivity, and ease of synthesis in various nanostructured forms [11,19]. When synthesized into nanostructures such as nanowires, nanoparticles, or nanotubes, the surface area of TiO_2 increases significantly, allowing for greater interaction with target gas molecules. This situation leads to enhanced gas adsorption and improved sensitivity and response time.

TiO_2 naturally exists in three polymorphs: anatase, rutile, and brookite. Among them, anatase is considered the most suitable for gas-sensing applications due to its higher surface area and enhanced chemical activity [20]. It has a band gap of approximately 3.2 eV, whereas rutile, the thermodynamically stable phase, has a slightly smaller band gap of about 3.0 eV but lower reactivity [21–23]. The wide band gap of TiO_2 facilitates strong UV absorption, which can be harnessed in photoactivated gas sensing to generate electron-hole pairs and enhance surface redox reactions.

Furthermore, the electronic and structural characteristics of TiO_2 can be tailored through doping or surface functionalization, enabling selective interaction with specific gas molecules such as methanol. The high surface-to-volume ratio of TiO_2 nanomaterials improves adsorption dynamics [24], making them ideal for developing fast-response, low-power gas sensors. Thanks to these attributes, TiO_2 has gained significant attention for next-generation methanol sensing platforms aimed at smart and wearable electronics.

In this study, a TiO_2 thin film was deposited onto a SiO_2 substrate using the pulsed DC sputtering technique to investigate its response to methanol vapor. After forming the TiO_2/SiO_2 sensor structure, the sample was annealed at 350 °C in ambient air for 1 hour. Following the structural and optical characterizations, aluminum contacts were implemented to finalize the sensor construction. The device was then exposed to methanol vapor at various concentrations, and it demonstrated a high sensitivity to methanol at 250 °C.

2. MATERIAL AND METHOD

TiO_2 thin film was deposited onto silicon oxide substrates using a pulsed DC magnetron sputtering system. Before deposition, silicon substrates were cut into 15 mm x15 mm and cleaned with RCA 1 (NH_4OH: H_2O_2: H_2O = 1: 1: 5) and RAC 2 (HCl: H_2O_2: H_2O = 1: 1: 6) each process. After the cleaning process, substrates were annealed for 1 hour at 1000 °C at 100 sccm oxygen ambient. A 99.9% pure Ti target was used for deposition under a mixed atmosphere of argon and oxygen gases. The argon gas flow was set to 22 sccm, while the oxygen gas flow was maintained at 0.8 sccm. The deposition was carried out at a base pressure of 9×10^{-6} torr and a working pressure of 3.6×10^{-3} torr. The bias voltage was maintained at 540 V with a pulse frequency of 100 Hz and duty cycle of 2 ms. The deposition time was combined with film thickness. After the film thickness reached 2500 Angstroms, film deposition was stopped. The annealing process was performed at 350 °C for 1 hour in ambient air to improve crystallinity and surface adhesion.

The TiO_2 sensor was analyzed to examine its structural and morphological characteristics. XRD analyses were conducted using a PANalytical Empyrean system with Cu Kα radiation (λ = 1.5406 Å), scanning over a 2θ range from 10° to 80°. SEM imaging and surface morphology analysis was performed with a TESCAN VEGA 3 LMU brand scanning electron microscope. Raman spectroscopy analysis was performed using a Renishaw inVia Reflex Raman Microscope. The optical absorption measurement was performed with a Shimadzu UV-2600 model UV-VIS spectrophotometer in the wavelength range of 200–800 nm. Aluminum interdigitated electrode (IDE) contacts were fabricated via DC sputtering using a 99.9 % pure Al target. A shadow mask was employed to define the IDE pattern on the TiO_2 sensor surface. During the deposition, the argon gas flow was maintained at 15 sccm. The deposition was performed under a base pressure of 5×10^{-6} Torr and a working pressure of 3.6×10^{-3} Torr, with a total deposition time of 10 minutes.

The sensing characteristics of the sensor were investigated using a gas-sensing system. Resistance measurements were performed under both methanol vapor and dry air environments. A gas sensing chamber with an internal volume of 0.1 L was employed. The chamber was specifically designed to facilitate both conductometric and optical measurements while allowing precise temperature control from room temperature up to 350 °C.

Methanol vapor was generated using a bubbler system and accurately controlled using two Alicat mass flow controllers (MFCs) that diluted the vapor with dry air to achieve the desired ppm-level concentrations. Throughout all measurements, the total gas flow was maintained at 500 sccm, and the methanol bubbler was kept at a constant temperature of 25 °C. An integrated heater was employed to regulate the temperature, and gas sensing measurements were conducted at various operating temperatures ranging from 150 °C to 250 °C. A Keithley 487 voltage source/picoammeter was used to measure the

resistance of the sensor. All measurement components were automated, enabling real-time monitoring, and the acquired data were transferred to a computer via LabVIEW software for further analysis. The experimental setup used for gas sensing measurements is shown in Figure 1.

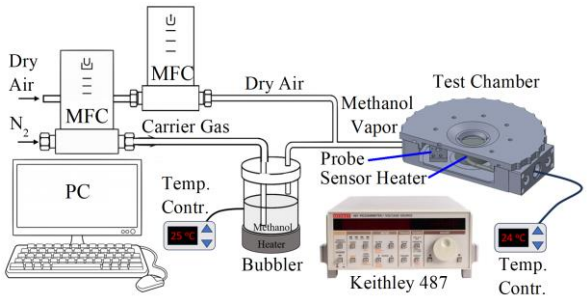

Figure 1. Experimental setup for gas sensing measurements.

Sensor resistance was measured at 150 °C, 200 °C, and 250 °C in dry air and desired methanol vapor concentration environments, respectively.

3. RESULTS AND DISCUSSION

The surface morphologies of the synthesized TiO_2/SiO_2 chemical vapor sensor deposited by pulsed DC sputtering were investigated using SEM, as shown in Figure 2(a). The image confirms that the sensor surface is uniform and composed of nanoislands, which provide a large surface area a critical feature for gas sensing applications. Figure 2(b) shows the cross-sectional SEM image, verifying that the film thickness is approximately 250 nm, in good agreement with the thickness monitor of the pulsed DC sputtering system. The thickness of the oxide layer on Si is approximately 300nm.

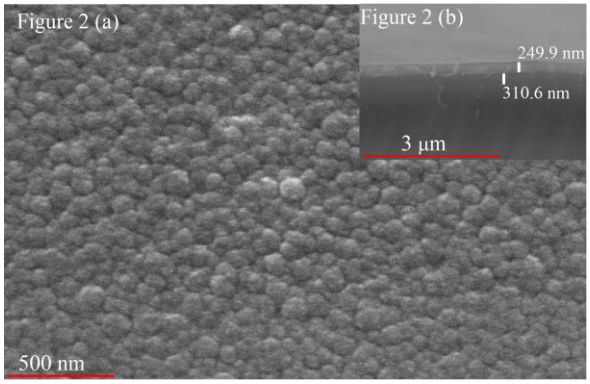

Figure 2. (a) SEM image of TiO_2/SiO_2 sensor surface and (b) Cross-section of sensor structure.

Figure 3 presents the particle size distribution obtained using a MATLAB-based image processing algorithm applied to a single SEM image captured at 150,000× magnification. The workflow began with converting the image to grayscale, followed by Gaussian filtering to reduce high-frequency noise. Sharpening was applied to enhance edge definition, and histogram equalization was used to improve contrast. The enhanced image was then binarized using adaptive thresholding, which adjusts to local intensity variations.

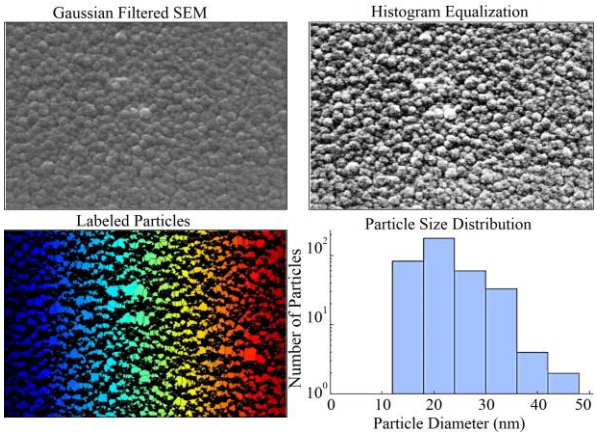

Figure 3. Particle size distribution analysis using MATLAB-based image processing.

To further refine particle boundaries and remove residual artifacts, a series of morphological operations—namely opening, closing, and hole-filling—was performed. Overlapping or closely spaced particles were separated using watershed segmentation based on the negative distance transform. Each segmented particle was labeled and analyzed to extract morphological features with equivalent diameter, eccentricity, major and minor axis lengths, and area. Objects with areas below a specified threshold were excluded to minimize the influence of noise. Particle diameters were converted from pixels to nanometers using a predefined scale factor, and the average particle diameter was computed. The results were visualized through a colored label map and a particle size distribution histogram plotted on a logarithmic scale, providing both spatial and statistical insight into the sample's morphology. As a result of the analysis, the average particle size was calculated to be approximately 22.37 nm ± 0.2 nm. This technique has also been employed in our previous studies [25].

The XRD patterns of the sensor material, are shown in Figure 3. The observed diffraction peaks at 25.3°, 36.9°, 37.8°, 38.5°, 48.01°, 53.8°, 55.05°, 62.6°, 68.7°, 70.2°, and 75.01° are assigned to the anatase phase of TiO_2 nanoparticles which are indexed to (101), (103), (004), (112), (200), (105), (211), (204), (116), (220) and (215) crystal planes, respectively (JCPDS No. 21-1272) [26–28]. The crystallite size was estimated to be around 22 nm using Scherrer's equation, calculated from the FWHM of seven Bragg peaks.

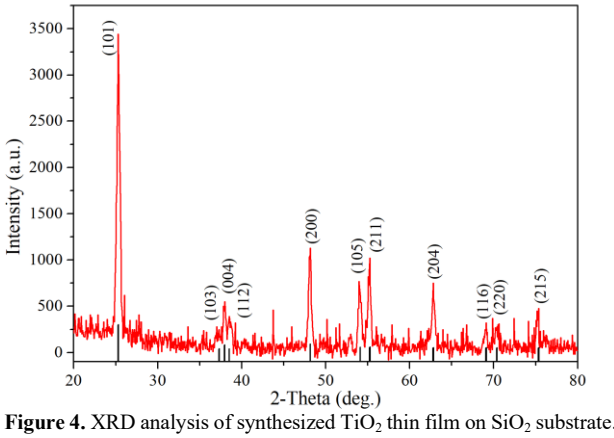

Figure 4. XRD analysis of synthesized TiO_2 thin film on SiO_2 substrate.

Optical absorption measurements were carried out using a PerkinElmer Lambda 2S UV/VIS spectrometer. The absorption characteristics of TiO_2 are presented in Figure 5. The optical band gap value was determined to be 3.24 eV. This is in good agreement with the values reported in the literature [21–23,29].

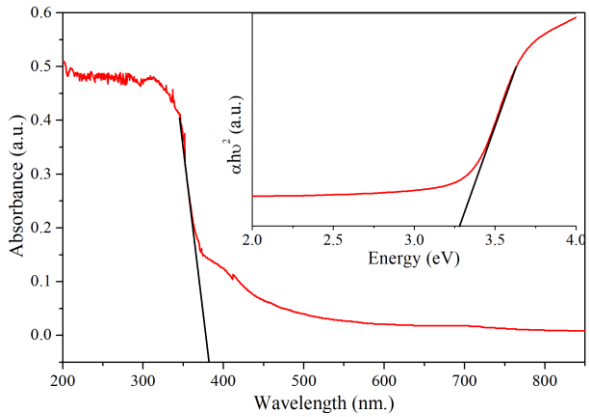

Figure 5. Absorbance measurement of TiO_2 sensor material.

The Raman spectrum of the TiO_2/SiO_2 sensor, shown in Figure 6, indicates characteristic anatase phase bands at 144, 197, 397, 517, and 638 cm^{-1}, with no peaks corresponding to the rutile or brookite phases. The peak at 638 cm^{-1} (Eg) is attributed to Ti–O stretching vibrations, while the peak at 517 cm^{-1} (A_{1g}/B_{1g}) also corresponds to Ti–O stretching modes. The band at 397 cm^{-1} (B_{1g}) is assigned to O–Ti–O bending vibrations [30–34].

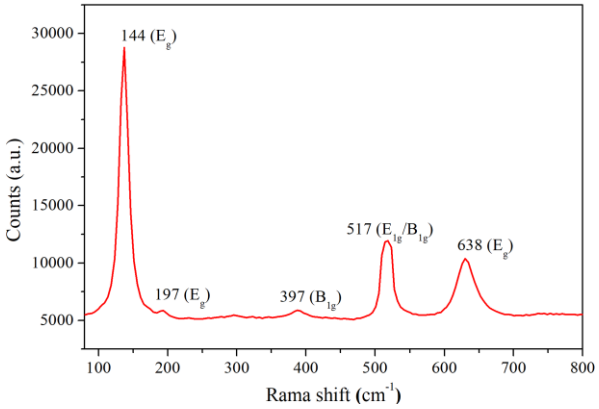

Figure 6. Raman spectrum of the as-prepared anatase TiO_2 recorded with the 514.5-nm excitation wavelength.

The gas sensing performance of the TiO_2/SiO_2 sensor was evaluated at various operating temperatures (150 °C, 200 °C, and 250 °C). Each test began with the introduction of dry air into the test chamber, followed by methanol vapor at the desired concentration. During all measurements, the methanol source was maintained at 25 °C, and the total gas flow rate was kept constant at 500 sccm.

Figure 7 shows the methanol sensing response of the TiO_2/SiO_2 sensor at operating temperatures of 150 °C, 200 °C, and 250 °C. Even at a relatively low temperature of 150 °C, the sensor exhibited a measurable response to 455 ppm methanol vapor, with a response value calculated as 1.8 ± 0.08. As the temperature increased, the sensor response improved significantly, reaching 6.5 ± 0.02 at 200 °C. This temperature at which the sensor exhibited its highest response is consistent with the findings reported in the literature [35]. Moreover, it was observed that the sensor approached saturation more rapidly at 250 °C. The sensor's response to the lowest methanol vapor concentration reached its maximum at 200 °C (~3.75 ± 0.02), in agreement with the literature. At lower temperatures (150 °C), the response decreased significantly to approximately 1.75 ± 0.08, whereas at higher temperatures (250 °C), the response was around 2.75 ± 0.1, with the sensor reaching saturation more rapidly. The measurement duration of 600 seconds was insufficient for the sensor to reach saturation at 150 °C and 200 °C, while it was adequate for full saturation at 250 °C.

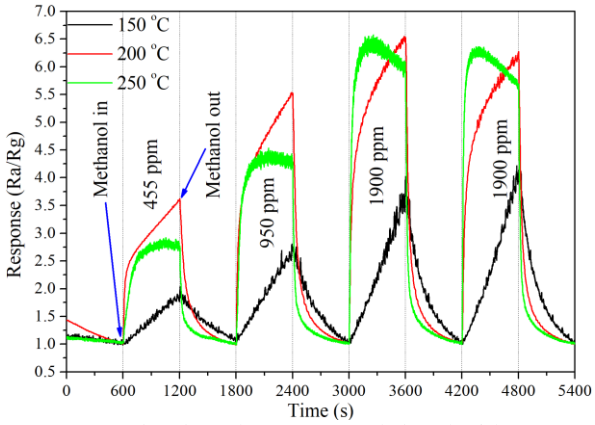

Figure 7. Methanol sensing response of the TiO_2/SiO_2 sensor at operating temperatures of 150 °C, 200 °C, and 250 °C.

For gas sensors based on n-type semiconducting metal oxides such as TiO_2, the sensing response to reducing gases (e.g., methanol) is typically defined by the ratio of the sensor's resistance in dry air to its resistance in the presence of the target gas [36,37]:

Response (S)=Ra / Rg

Where: Ra is the sensor resistance in dry air, and Rg is the sensor resistance when exposed to methanol vapor. This formulation reflects the fact that reducing gases donate electrons to the sensing layer, which decreases the resistance in n-type materials [36].

When the sensor is exposed to dry air, oxygen molecules are adsorbed onto the TiO_2 surface and extract electrons from the material, forming reactive oxygen ions (O_2^-, O^-, O^{2-}). The type of oxygen ion formed depends on the operating temperature: molecular ions (O_2^-) dominate at lower temperatures (T < ~100 °C), while atomic species ($2O^-$ and O^{2-}) become more prevalent as temperature increases ((150–300 °C), (T > 300 °C)) [22]. The removal of electrons leads to the formation of a depletion layer, which increases the material's electrical resistance [37]. Upon the introduction of methanol vapor, surface reactions occur between methanol and the adsorbed oxygen ions. These reactions result in the oxidation of methanol into carbon dioxide and water, releasing previously trapped electrons back into the conduction band. This process reduces the thickness of the depletion

region, thereby lowering the electrical resistance of the sensing layer [38].

$$CH3OH\ (gas) + 3O^{-}_{(ads)} \rightarrow CO_2 + 2H_2O + 3e^{-} \quad (1)$$

This change in resistance is monitored as the sensing response. When methanol is removed and dry air is reintroduced, the adsorbed oxygen species are regenerated, and the resistance returns to its original value, demonstrating a reversible sensing mechanism.

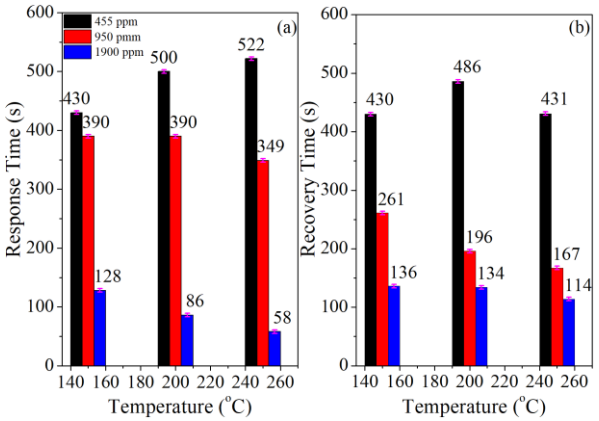

Figure 8. Response and Recovery time of sensor at different sensor temperature.

Figure 8 presents the response time of the sensor to methanol vapor at various concentrations and operating temperatures. As illustrated in the Figure 8, at 150 °C, the response time increased with increasing methanol concentration, which contrasts with the behavior observed at higher concentrations and elevated temperatures. This trend can be attributed to the fact that the sensor did not reach saturation at 150 °C, causing a longer duration to be required for the response to reach the target level at higher concentrations. At 250 °C, the sensor demonstrated rapid dynamics, with a response time of 58 s ± 3 s and a recovery time of 114 s ± 3s. Additionally, the recovery time was observed to be longer than the response time under all conditions.

4. CONCLUSION

TiO_2 thin film was fabricated on SiO_2 substrates with a thickness of 250 nm using pulsed DC sputtering. Following structural, optical characterizations, MATLAB image processing carry out and particle size determined (22.37 nm ± 0.2 nm). Aluminum IDE (interdigitated electrode) contacts were deposited for electrical measurements under methanol vapor ambient. The sensor was exposed to methanol vapor at sensor operating temperatures of 150 °C, 200 °C, and 250 °C. According to the sensing results, the highest response (6.5 ± 0.02) was observed at 200 °C and lowest response time and recovery time observed at 250 °C. It was also noted that the recovery time was shorter than the response time at 150 °C and 200 °C sensor temperature.

Acknowledgement

This work is supported by the Atatürk University BAP Program (Project No: FYL-2024-14322)

I would like to thank Prof. Dr. Hasan Efeoğlu and Prof. Dr. Tevhit Karacalı for providing the laboratory infrastructure and technical support for this study.

REFERENCES

[1] Hendricks AJ, Thompson AM, Shi VY. 9- Oxidative Stress, Environmental Factors, and Pollutants. In: Chan LS, Shi VY, editors. Atopic Dermatitis: Inside Out Or Outside in. Elsevier; 2023. p. 79–84.

[2] Pandey P, Yadav R. A Review on Volatile Organic Compounds (VOCs) as Environmental Pollutants: Fate and Distribution. International Journal Of Plant And Environment. 2018; 4:14–26.

[3] Nekoukar Z, Zakariaei Z, Taghizadeh F, Musavi F, Banimostafavi ES, Sharifpour A, et al. Methanol poisoning as a new world challenge: A review. Ann Med Surg (Lond). 2021; 66:102445.

[4] Alrashed M, Aldeghaither NS, Almutairi SY, Almutairi M, Alghamdi A, Alqahtani T, et al. The Perils of Methanol Exposure: Insights into Toxicity and Clinical Management. Toxics. 2024; 12:924.

[5] Wallace LA. Human exposure to volatile organic pollutants: Implications for Indoor Air Studies. Annual Review of Environment and Resources. 2001; 26:269–301.

[6] Organization WH, Safety IP on C, Programme UNE, Organization IL. Methanol: health and safety guide. World Health Organization; 1997.

[7] Occupational Safety and Health Administration (OSHA). Methanol [Internet]. [Cited 2025 July 29]. Available from: https://www.osha.gov/chemicaldata/474

[8] Dorman FL, Overton EB, Whiting JJ, Cochran JW, Gardea-Torresdey J. Gas Chromatography. Anal Chem. 2008; 80:4487–97.

[9] Pontes H, Guedes de Pinho P, Casal S, Carmo H, Santos A, Magalhães T, et al. GC Determination of Acetone, Acetaldehyde, Ethanol, and Methanol in Biological Matrices and Cell Culture. Journal of Chromatographic Science. 2009; 47:272–8.

[10] Liu X, Cheng S, Liu H, Hu S, Zhang D, Ning H. A Survey on Gas Sensing Technology. Sensors. 2012; 12:9635–65.

[11] Korotcenkov G. Metal oxides for solid-state gas sensors: What determines our choice? Materials Science and Engineering: B. 2007; 139:1–23.

[12] Dey A. Semiconductor metal oxide gas sensors: A review. Materials Science and Engineering: B. 2018; 229:206–17.

[13] Penza M, Rossi R, Alvisi M, Serra E. Metal-modified and vertically aligned carbon nanotube sensors array for landfill gas monitoring applications. Nanotechnology. 2010; 21:105501.

[14] Göpel W, Schierbaum KD. SnO_2 sensors: current status and future prospects. Sensors and Actuators B: Chemical. 1995; 26:1–12.

[15] Amiri V, Roshan H, Mirzaei A, Neri G, Ayesh AI. Nanostructured Metal Oxide-Based Acetone Gas Sensors: A Review. Sensors. 2020; 20:3096.
[16] Mohd Chachuli SA, Hamidon MN, Ertugurl M, Mamat MdS, Coban O, Shamsudin NH, et al. Effects of silver diffusement on TiO_2-B_2O_3 nanocomposite sensor towards hydrogen sensing. Materials Research Innovations. 2024; 28:365–78.
[17] Chachuli SAM, Hamidon MN, Ertugrul M, Mamat MS, Coban O, Tuzluca FN, et al. Effects of MWCNTs/graphene nanoflakes/MXene addition to TiO_2 thick film on hydrogen gas sensing. Journal of Alloys and Compounds. 2021; 882:160671.
[18] Mohd Chachuli SA, Hamidon MN, Ertugrul M, Mamat MdS, Coban O, Shamsudin NH. Comparative analysis of hydrogen sensing based on treated-TiO_2 in thick film gas sensor. Appl Phys A. 2022; 128:596.
[19] Comini E, Faglia G, Sberveglieri G. UV light activation of tin oxide thin films for NO_2 sensing at low temperatures. Sensors and Actuators B: Chemical. 2001; 78:73–7.
[20] Zhang J, Liu X, Neri G, Pinna N. Nanostructured Materials for Room-Temperature Gas Sensors. Advanced Materials. 2016; 28:795–831.
[21] Diebold U. The surface science of titanium dioxide. Surface Science Reports. 2003; 48:53–229.
[22] Tang H, Prasad K, Sanjinès R, Schmid PE, Lévy F. Electrical and optical properties of TiO_2 anatase thin films. Journal of Applied Physics. 1994; 75:2042–7.
[23] Grätzel M. Photoelectrochemical cells. Nature. 2001; 414:338–44.
[24] Yi Q, Hao X, Li X, Dong H, Sun L. Effect of TiO_2 nanoparticles on the mass transfer process of absorption of toluene: Experimental investigation and molecular dynamics simulation. Journal of Environmental Chemical Engineering. 2023; 11:109474.
[25] Ozden M, Coban O, Karacali T. Fabrication and Characterization of a PZT-Based Touch Sensor Using Combined Spin-Coating and Sputtering Methods. Sensors. 2025; 25:3938.
[26] Zhang J-Y, Boyd IW, O'Sullivan BJ, Hurley PK, Kelly PV, Sénateur J-P. Nanocrystalline TiO_2 films studied by optical, XRD and FTIR spectroscopy. Journal of Non-Crystalline Solids. 2002; 303:134–8.
[27] Srinivasu P, Singh SP, Islam A, Han L. Novel Approach for the Synthesis of Nanocrystalline Anatase Titania and Their Photovoltaic Application. Advances in OptoElectronics. 2011; 2011:539382.
[28] Chu L, Qin Z, Yang J, Li X. Anatase TiO_2 Nanoparticles with Exposed {001} Facets for Efficient Dye-Sensitized Solar Cells. Sci Rep. 2015; 5:12143.
[29] Kuriechen SK, Murugesan S, Paul Raj S. Mineralization of Azo Dye Using Combined Photo-Fenton and Photocatalytic Processes under Visible Light. Journal of Catalysts. 2013; 2013:104019.
[30] Challagulla S, Tarafder K, Ganesan R, Roy S. Structure sensitive photocatalytic reduction of nitroarenes over TiO_2. Sci Rep. 2017; 7:8783.
[31] Vetrivel V, Rajendran DK, Kalaiselvi V. Synthesis and characterization of Pure Titanium dioxide nanoparticles by Sol- gel method.
[32] Ekoi EJ, Gowen A, Dorrepaal R, Dowling DP. Characterisation of titanium oxide layers using Raman spectroscopy and optical profilometry: Influence of oxide properties. Results in Physics. 2019; 12:1574–85.
[33] Balachandran U, Eror NG. Raman spectra of titanium dioxide. Journal of Solid State Chemistry. 1982; 42:276–82.
[34] Ivanda M, Musić S, Popović S, Gotić M. XRD, Raman and FT-IR spectroscopic observations of nanosized TiO_2 synthesized by the sol–gel method based on an esterification reaction. Journal of Molecular Structure. 1999;480–481:645–9.
[35] Shooshtari M, Salehi A, Vollebregt S. Effect of temperature and humidity on the sensing performance of TiO_2 nanowire-based ethanol vapor sensors. Nanotechnology. 2021; 32:325501.
[36] Shimizu Y, Egashira M. Basic Aspects and Challenges of Semiconductor Gas Sensors. MRS Bulletin. 1999; 24:18–24.
[37] Yamazoe N. New approaches for improving semiconductor gas sensors. Sensors and Actuators B: Chemical. 1991; 5:7–19.
[38] Korotcenkov G. The role of morphology and crystallographic structure of metal oxides in response of conductometric-type gas sensors. Materials Science and Engineering: R: Reports. 2008; 61:1–39.

Volume 14, Issue 3, Page 145-150, 2025 https://doi.org/10.46810/tdfd.1691969 Research Article

BİNGÖL UNIVERSITY

Türk Doğa ve Fen Dergisi
Turkish Journal of Nature and Science
www.dergipark.gov.tr/tdfd

Strength Performance of 304 Series Steels Welded by Plasma Arc Method

Tanju TEKER[1*], Sinan AYDIN[2]

[1] Sivas Cumhuriyet University, Technology Faculty, Manufacturing Engineering Department, Sivas, Türkiye
[2] Sivas Cumhuriyet University, Technology Faculty, Mechatronics Engineering Department, Sivas, Türkiye
Tanju TEKER ORCID No: 0000-0001-7293-0723
Sinan AYDIN ORCID No: 0000-0003-2285-0906

**Corresponding author: tanjuteker@cumhuriyet.edu.tr*

(Received: 05.05.2025, Accepted: 12.08.2025, Online Publication: 26.09.2025)

Keywords
Plasma arc welding, AISI 304, Microstructure, Strength test

Abstract: Austenitic stainless steel has superior mechanical and corrosion performance and is used in many sectors. Welding is a commonly used method in the production of stainless-steel structures. Plasma transfer arc welding is a technique performed by an electric arc between tungsten electrodes. In this research, AISI 304 plates were welded using plasma welding. The joint interface was analyzed through scanning electron microscopy, optical microscopy, energy dispersive spectroscopy, X-Ray diffraction. The strength performance of the samples were assessed via tensile testing. The fracture surfaces of samples were studied by SEM. The PTA method achieved complete penetration in AISI 304 plate joint. The recorded seam widths were 6 mm for S1, 6.5 mm for S2, and 7 mm for S3. The samples exhibited strengths of 336 MPa at 70 A, 360 MPa at 80 A, and 374 MPa at 90A. All joints showed good strength.

Plazma Ark Yöntemiyle Kaynaklanan 304 Serisi Çeliklerin Dayanım Performansı

Anahtar Kelimeler
Plazma ark kaynağı, AISI 304, Mikroyapı, Mukavemet testi

Öz: Östenitik paslanmaz çelik, üstün mekanik ve korozyon performansına sahiptir ve birçok sektörde kullanılır. Kaynak, paslanmaz çelik yapıların üretiminde yaygın olarak kullanılan bir yöntemdir. Plazma transfer ark kaynağı, tungsten elektrotlar arasındaki elektrik arkı ile yapılan bir tekniktir. Bu araştırmada, AISI 304 plakalar plazma kaynağı kullanılarak kaynaklanmıştır. Birleşme arayüzeyi, taramalı elektron mikroskobu, optik mikroskop, enerji dağılımlı spektroskopi ve X-Ray diffraction ile analiz edilmiştir. Numunelerin mukavemet özellikleri, çekme testi ile değerlendirilmiştir. Numunelerin kırılma yüzeyleri SEM ile incelenmiştir. PTA yöntemi, AISI 304 plaka birleşme arayüzeyinde tam penetrasyon sağlamıştır. Kaydedilen dikiş genişlikleri S1 için 6 mm, S2 için 6,5 mm ve S3 için 7 mm'dir. Numuneler düşük ısı girdisi altında 336 MPa, orta ısı girdisi altında 360 MPa ve yüksek ısı girdisi altında 374 MPa mukavemet sergilemiştir. Tüm birleşimler iyi dayanım göstermiştir.

1. INTRODUCTION

Stainless steels are key materials in engineering. Austenitic stainless steels (ASS) are recognized for their excellent resistance to corrosion, high flexibility, and strong weldability [1]. In these steels, austenite is the primary phase at room temperature. AISI 304 is a stainless-steel grade commonly utilized in aerospace, chemical machinery, nuclear applications, and pressure vessels. ASS is more commonly chosen than other stainless-steel types because of its ease of welding [2,3]. Welding is indispensable in many fields such as chemical, oil and gas industries. Because various combinations of materials can be combined. However, the welding process can notably influence the mechanical properties of welded joints by altering the microstructure, leading to issues such as micro segregation, phase precipitation, pores, and cracks [4,5]. Plasma transferred arc welding (PTAW) has high efficiency and cleanliness quality. PTAW is the most reliable welding method for stainless steel with its ability to weld complex shapes. It is also recognized for being cost-effective and widely adopted [6,7]. PTAW has gained significant popularity in the manufacturing industry for metal joining in recent years. It is preferred over other arc methods due to its high speed, quality weld production and stable performance. Recently, numerous advancements have been made to enhance the stability of the PTAW process, as well as to improve penetration depth and weld quality [8-10]. Bodkhe et al. [11] reported the optimization of TIG welding of 304L materials.

Penetration depth was influenced by current, torch speed, and arc gap. In single pass conventional TIG, penetration is limited to 3 mm. Ramakrishnan et al. [12] investigated the strength performances and microstructure of TIG welded AISI 304 and AISI 316. The highest tensile strength was attained through welding with the peak current. AISI 308L welding wire provided the best results and enhanced mechanical properties.

This study aims to achieve the joining of AISI 304 plates in a single pass using plasma welding, without employing filler wire or a weld groove. Analyses of macrostructure, microstructure, phase composition, mechanical properties, and fracture surfaces of welded samples were conducted.

2. MATERIAL AND METHOD

For the present study, 304 austenitic stainless-steel plates with dimensions of 100x100x6 mm were utilized. The chemical values of AISI 304 is shown in Table 1. The plasma welding schematic is illustrated in Figure 1. Argon was utilized as both the plasma and the shielding gas. The welding conditions for the samples are listed in Table 2.

Table 1. Chemical values of AISI 304 alloy.

Materials	Fe	Cr	C	Ni	Si	Mo	Mn
AISI 304	Bal.	19.2	0.042	8.25	0.46	0.25	1.75

Table 2. Welding conditions.

Sample no	S1	S2	S3
Current intensity (A)	70	80	90
Plazma gas flow speed (l/min)	0.5	0.5	0.5
Shielding gas flow speed (l/min.)	13	13	13
Travel speed (mm/min.)	0.01	0.01	0.01
Nozzle size (mm)	2.4	2.4	2.4

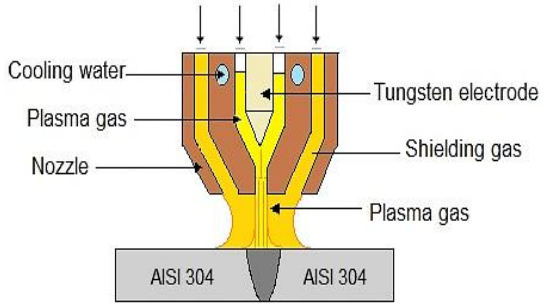

Figure 1. The plasma welding schematic.

The samples were welded in one pass using a Thermal Dynamics PS 3000 welding machine. Following the welding process, the samples were sanded with 220-1200 grit SiC sandpaper and subsequently polished with 3 µm diamond paste. The surfaces were electrolytically etched using 50% HNO_3 + 50% H_2O solution at 12 V for 10 s. The microstructure of the joint interface was analyzed using scanning electron microscopy (SEM: TESCAN MIRA3) and optical microscopy (OM: LEICA DM750). The chemical composition was identified through energy dispersive spectroscopy (EDS). The phases in the samples were identified using a Bruker D8 X-ray diffractometer. To detect the tensile strength of the joints, tensile samples were fabricated following ASTM E8 guidelines [13]. Dimensions of the tensile test samples are presented in Figure 2. These samples were tested on an Instron 8500 tensile machine at a tensile speed of 0.5 $mm{\cdot}min^{-1}$. The fracture surfaces of samples were studied by SEM.

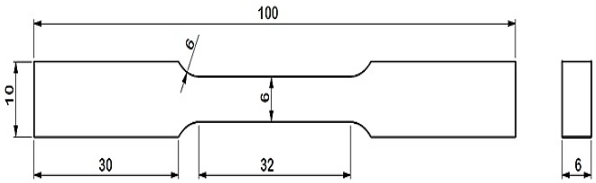

Figure 2. Dimensions of the tensile test samples.

3. RESULTS

3.1. Macro and microstructure

Macro visuals of the S1-S3 joints are presented in Figure 3. A smooth and clean surface in stainless steel joints was achieved using the PTA method. Heat input significantly influences the weld quality and visual appearance. Higher heat input results in the melting of a larger amount of material during the welding process [14]. The seam widths were measured as S1 = 6 mm at 70 A, S2 = 6.5 mm at 80 A, and S3= 7 mm at 90 A. A minimal extent was observed in both the HAZ and FZ. The PTA method achieved complete penetration in a 6 mm-thick 304 plate joint. The weld shape was thin and smooth. The level of heat input led to the development of a coarse microstructure. With increased heat input, the cooling rate diminished. The closed-loop current was directly related to the heat flux density. Consequently, raising the current intensity enhanced the heat input and temperature gradient, thereby enhancing thermo-capillary convection [15]. However, higher currents also intensified the electromagnetic and aerodynamic resistance forces. The electromagnetic force caused the weld pool to deepen. The aerodynamic friction force reduced the weld penetration and created a wider pool. At higher currents, the electromagnetic forces induced considerable mixing within weld material. This led to vortex formation that enhanced weld penetration and reduced bead width [16].

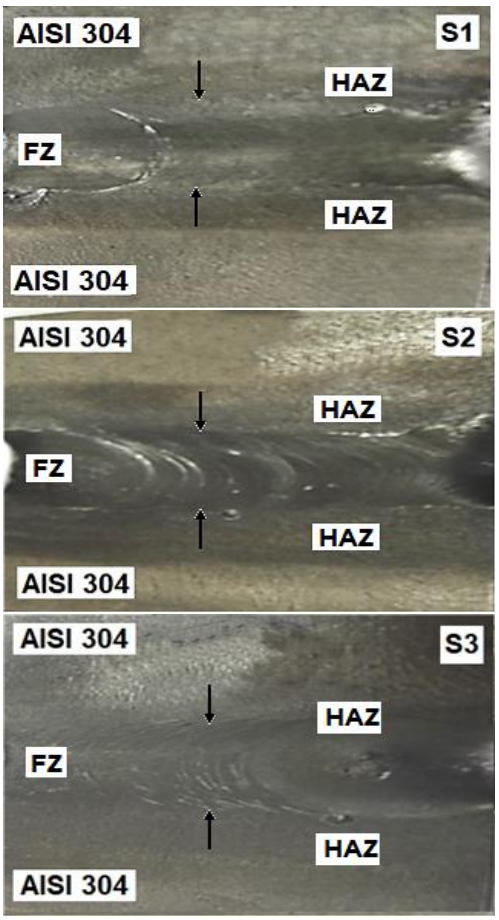

Figure 3. Macro view of S1-S3 joints.

Optical micrographs of the S1-S3 joints are presented in Figure 4. The welded zone, transition zone and HAZ are shown. At the interface, a columnar dendritic microstructure formed along the solidification direction as a result of the fast solidification of the stainless steel. SEM micrographs of S3 joint is given in Figure 5. Figure 5 exhibited the change of δ-ferrite morphology in the FZ. Lathy and skeletal δ-ferrite species were detected in the austenite matrix. With rising thermal input, the weld metal exhibited larger dendrites and wider interdendritic gaps. The alteration in dendrite shape resulted from sharp thermal gradients and rapid cooling caused by low heat input. This allowed less time for dendrite growth. Reduced cooling rates under high heat input provided adequate time for dendrite development in the fusion zone [17,18]. As heat intensity raised, the FZ and HAZ area also expanded. Significant grain growing is observed in the HAZ of all welds. Additionally, it was noted that the degree of grain growing incremented with higher heat intensity.

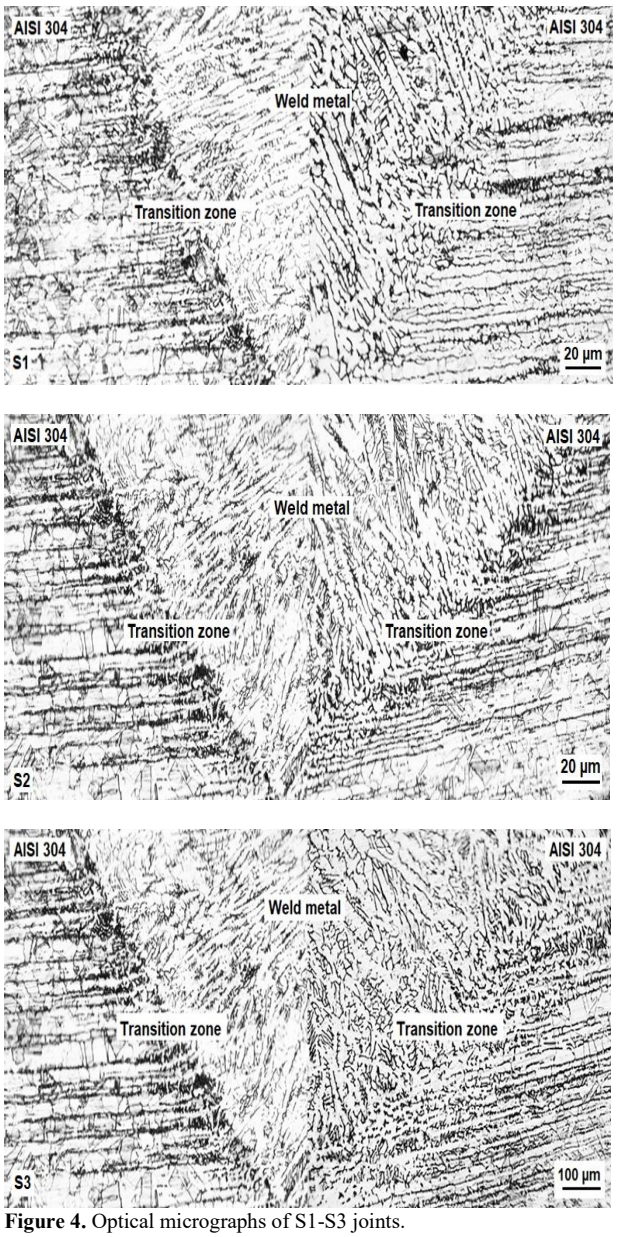

Figure 4. Optical micrographs of S1-S3 joints.

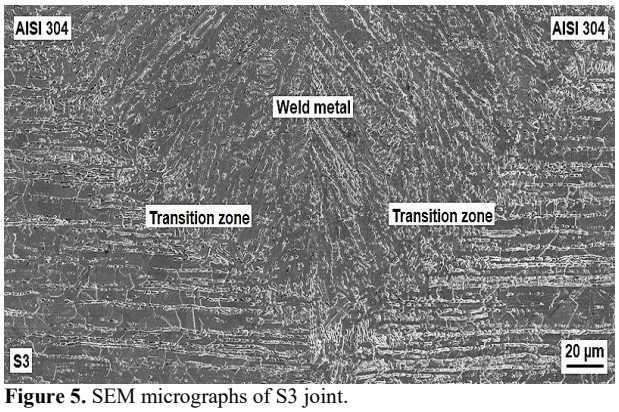

Figure 5. SEM micrographs of S3 joint.

EDS analysis points and results of S1 joint is shown in Figure 6. The presence of C, Fe, Cr, Ni, and Mn was verified by EDS. In the AISI 304 sample, the main elements that affected the phase compositions were Cr and Ni. Ni was depleted in the regions where Cr was enriched. In PTAW samples, the low thickness resulted in a high cooling rate and FA solidification mode. Solidification began with the formation of delta ferrite,

followed by peritectic-eutectic transformation and austenite nuclei. An intensified transformation took place with the increased cooling rate. This led to the formation of thinner austenite. The delta ferrite between the austenite layers also became thinner [19]. XRD graph of S3 joint is shown in Figure 7. The analysis revealed the presence of δ-Fe and γ-Fe.

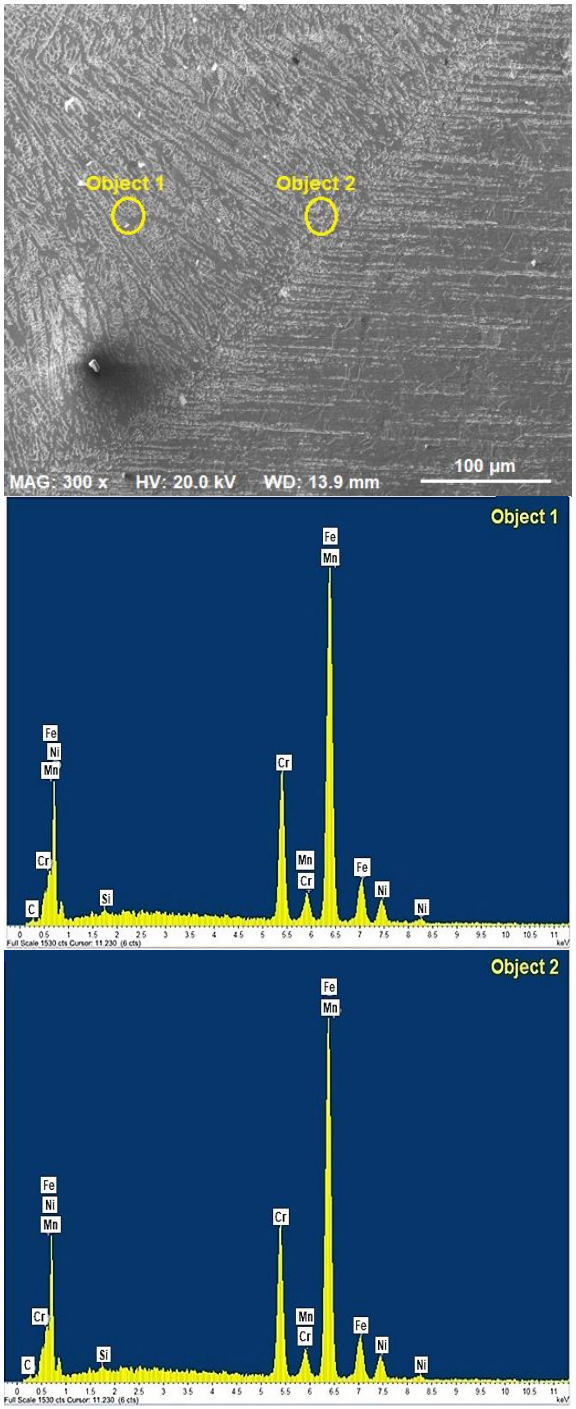

Figure 6. EDS analysis of S1 joint.

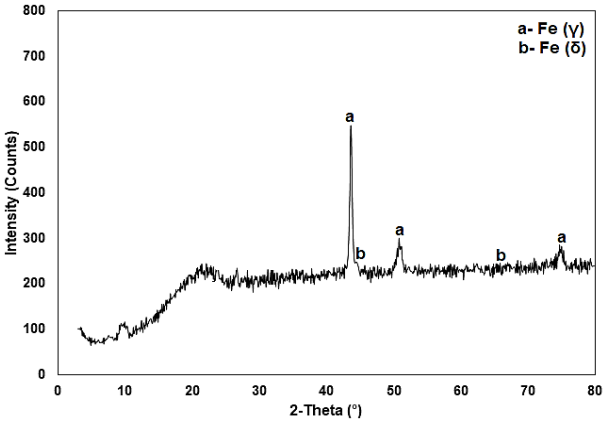

Figure 7. XRD graph of S3 joint.

3.2. Tensile behaviour

Macro images of samples are shown in Figure 8. The fracture of the welded 304 SS material took place in the HAZ. Stress-strain graph of samples is shown in Figure 9. The sample strength made with low heat intensity had 336 MPa, followed by 360 MPa for medium heat intensity, and 374 MPa for high heat intensity. Due to low current intensity, full penetration could not be achieved. This caused the disconnected sections at the interface to create a notch effect and weakened the strength. Increased welding current altered the intensity of forces during welding. Thus, affecting the flow of molten metal and the shape of the weld alloy. Higher heat input altered the weld metal microstructure and mechanical characteristics [19,20]. The weld strength was influenced by the HAZ of the weld alloy. In PTAW, the volume of melt alloy was comparatively low at any moment, resulting in quicker cooling of the weld metal and a smaller weld zone size [21]. During PTAW, fluid movement in the molten area intensified, leading to a reduction in grain size within the weld metal. The increased heat input advanced the occur of more δ-ferrite in PTAW. Ferrite formation may take place at low temperatures with restricted diffusion due to the enrichment of ferrite stabilizers like Cr and the depletion of austenite stabilizers such as Ni. During rapid solidification, δ-ferrite can stay in a metastable state, failing to fully transform into the γ phase. The Cr-enriched interdendritic δ-ferrite in the microstructure can significantly hinder the dislocation motion [2,21]. The advanced δ-ferrite structure alleviates localized stress in surrounding phases, promoting a more uniform austenite transformation. As a result, the retained austenite exhibits enhanced mechanical stability and improved ductility [23]. The δ-ferrite in the weld material minimized microcracks, refined the particle shape, improved ductility, and helped prevent susceptibility to hot cracking in the weld.

Figure 8. Macro image of samples.

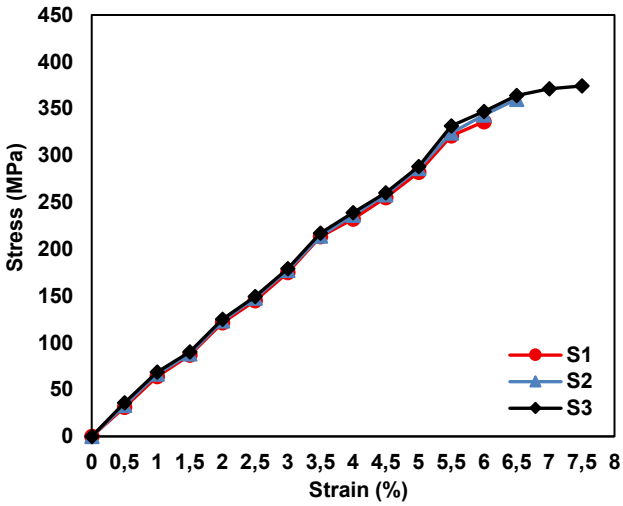

Figure 9. Stress-strain graph of samples.

3.4. Fracture characteristics

Figure 10 displays the fracture characteristics of the S1 joint. The fracture surfaces exhibited dimples of different sizes and shapes, suggesting that the primary fracture mechanism was ductile in nature [24]. With the increase in crack growth rate near the fracture zone, the merging of voids along with pits and lines became evident. Distinct pit formations were present in the rapid fracture area. Voids originating from inclusions or larger precipitates expanded and developed a fibrous texture as yielding progressed [25-27].

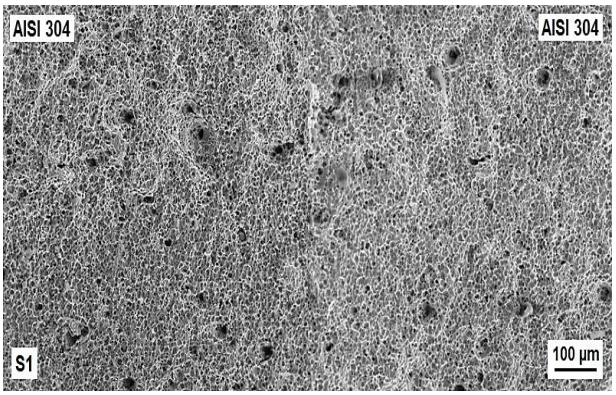

Figure 10. Fracture characteristics of S1 joint.

4. CONCLUSION

AISI 304 plates were joined using the PTAW. The following insights can be gathered from this study.

1. The 304 stainless plates with full penetration were obtained by using PTAW.
2. A smooth and clean surface in stainless steel joints was achieved using the PTAW.
3. The samples exhibited strengths of 336 MPa at 70 A, 360 MPa at 80 A, and 374 MPa at 90A.
4. For 6 mm thick AISI 304, the PTA process offered a wide range of parameters.
5. Ductile pits of different sizes and shapes were detected on the fracture surfaces.

Acknowledgement

The authors declare no conflict of interest.

REFERENCES

[1] Yan J, Gao M, Zeng X. Study on microstructure and mechanical properties of 304 stainless steel joints by TIG, laser and laser-TIG hybrid weldings. Opt Lasers Eng. 201048(4):512-7.

[2] Lippold JC, Kotecki DJ. Welding metallurgy and weldability of stainless steel. 5nd ed. New York, USA: John Willey & Sons; 2005.

[3] Zumelzu E, Sepulveda J, Ibarra M. Influence of microstructure on the mechanical behaviour of welded 316 L SS joints. J Mater Process Technol. 1999;94(1):36-40.

[4] Korinko PS, Malene SH. Considerations for the weldability of types 304L and 316L stainless steel. Pract Fail Anal. 2001;1:61-8.

[5] Shyu SW, Huang HY, Tseng KH, Chou CP. Study of the performance of stainless steel A-TIG welds. J Mater Eng Perform. 2008;17:193-201.

[6] Kumar S, Shahi AS. Effect of heat input on the microstructure and mechanical properties of gas tungsten arc welded AISI 304 stainless steel joints. Mater Des. 2011;32(6):3617-23.

[7] Mirshekari GR, Tavakoli E, Atapour M, Sadeghian B. Microstructure and corrosion behavior of multipass gas tungsten arc welded 304L stainless steel. Mater Des. 2014;55:905-11.

[8] Teker T. Effect of melt-in and key-hole modes on the structure and mechanical properties of AISI 430 steel welded using plasma transfer arc welding. Phys Metals Metallogr. 2018;119(7): 669-77.

[9] Singh NK. Performance of activated TIG welding in 304 austenitic stainless steel welds. Mater Today. 2017;4(9):9914-18.

[10] Ogundimu EO, Akinlabi ET, Erinosho MF. Study on microstructure and mechanical properties of 304 stainless steel joints by TIG–MIG hybrid welding. Surf Rev Lett. 2018;25(01):1850042.

[11] Bodkhe SC, Dolas DR. Optimization of activated tungsten inert gas welding of 304L austenitic stainless steel. Procedia Manuf. 2018;20:277-82.

[12] Ramakrishnan A, Rameshkumar T, Rajamurugan G, Sundarraju G, Selvamuthukumaran D. Experimental investigation on mechanical properties of TIG welded dissimilar AISI 304 and AISI 316 stainless

steel using 308 filler rod. Mater Today. 2021;45(9):8207-11.
[13] ASTM E8M-04, Standard test methods for tension testing of metallic materials. West Conshohocken, PA, USA, ASTM International; 2004.
[14] Taufiqurrahman I, Ahmad A, Mustapha M, Ginta TL, Haryoko LAF, Shozib, IA. The effect of welding current and electrode force on the heat input, weld diameter, and physical and mechanical properties of SS316l/Ti6Al4V dissimilar resistance spot welding with aluminum interlayer. Mater. 2021;14(5):1129.
[15] Somani CA, Lalwani DI. Experimental investigation of TIG-MIG hybrid welding process on austenitic stainless steel. Mater Today. 2019;18(7):4826-34.
[16] Prasad KS, Rao CS, Rao DN. Study on weld quality characteristics of micro plasma arc welded austenitic stainless steels. Procedia Eng. 2014;97:752-57.
[17] Zhang L, Lu ZJ, Luo KY, Feng AX, Dai FZ, Zhong JS, Luo M, Zhang YK. Residual stress, micro-hardness and tensile properties of ANSI 304 stainless steel thick sheet by fiber laser weldings. Mater Sci Eng: A. 2013;56:136-44.
[18] Cui S, Liu Z, Fang Y, Luo Z, Manladan S M, Yi S. Keyhole process in K-TIG welding on 4 mm thick 304 stainless steel. J Mater Process Technol. 2017:243;217-28.
[19] Feng Y, Luo Z, Liu Z, Li Y, Luo Y, Huang Y. Keyhole gas tungsten arc welding of AISI 316L stainless steel. Mater Des. 2015;85:24-31.
[20] Lee WS, Lin CF. Impact properties and microstructure evolution of 304L stainless steel. Mater Sci Eng: A. 2001;308(1-2):124-35.
[21] Saha S, Mukherjee M, Pal TK. Microstructure, texture, and mechanical property analysis of gas metal arc welded AISI 304 austenitic stainless steel. J Mater Eng Perform. 2015;24:1125-39.
[22] Ramkumar KD, Singh S, George JC, Anirudh S, Brahadees G, Goyal S, Gupta SK, Vishnu C, Sharan NR, Kalainathan S. Effect of pulse density and the number of shots on hardness and tensile strength of laser shock peened, activated flux TIG welds of AISI 347. J Manuf Proces. 2017;28(1):295-308.
[23] Liu M, Li Y, Cui Z, Yang Q. High ductility of spray formed low density TRIP steel with the improvement of δ-ferrite matrix. Mater Charact. 2019;156:109828.
[24] Abioye TE, Gbadeyan OO, Adebiyi DI. Analysis of the mechanical properties and penetration depth of gas metal arc welding on AISI 304 stainless steel. Int J Microstruct Mater Prop. 2019;14(1):47-9.
[25] Puchi-Cabrera ES, Saya-Gamboa RA, La Barbera-Sosa JG, Staia MH. Ignoto-Cardinale V, Berríos-Ortiz JA, Mesmacque G. Fatigue life of AISI 316L stainless steel welded joints, obtained by GMAW. Weld Int. 2009;23(10):778-88.
[26] Sabzi M, Dezfuli SM. Post weld heat treatment of hypereutectoid hadfield steel: characterization and control of microstructure, phase equilibrium, mechanical properties and fracture mode of welding joint. J Manuf Process. 2018;34:313-28.
[27] Haldar V, Biswal SK, Pal S. Formability study of micro-plasma arc-welded AISI 316L stainless steel thin sheet joint. J Braz. Soc Mech Sci Eng. 2022;44:564.

Volume 14, Issue 3, Page 151-155, 2025 https://doi.org/10.46810/tdfd.1695605 Research Article

BİNGÖL UNIVERSITY

Türk Doğa ve Fen Dergisi
Turkish Journal of Nature and Science
www.dergipark.gov.tr/tdfd

Investigation of the Joining of SiC-Reinforced Copper Matrix Composites via Friction Welding

İhsan KIRIK[1], Ömer BARAÇ[2], Anıl İMAK[2*], Serhat ŞAP[3]

[1]Bingol University, Technical Sciences Vocational School, Department of Machinery, Bingöl, Türkiye
[2]Bingol University, Faculty of Engineering and Architecture, Department of Mechanical Engineering, Bingöl, Türkiye
[3]Bingol University, Technical Sciences Vocational School, Department of Electricity and Energy, Bingöl, Türkiye
İhsan KIRIK ORCID No: 0000-0002-8361-319X
Ömer BARAÇ ORCID No: 0000-0003-2624-0224
Anıl İMAK ORCID No: 0000-0001-6091-1584
Serhat ŞAP ORCID No: 0000-0001-5177-4952

**Corresponding author: aimak@bingol.edu.tr*

(Received: 09.05.2025, Accepted: 02.09.2025, Online Publication: 26.09.2025)

Keywords
Friction welding, SiC, Copper matrix composite, Microstructure

Abstract: Considering that it is inevitable to use dissimilar materials together with the rapidly developing industry, this makes it necessary to join materials with different properties with each other. From this point of view, friction welding method gives good results among solid state welding methods. In the study, the joining of Cu matrix composite material with SiC reinforcement at different rates, produced by using powder metallurgy method, among themselves and with pure copper (Cu) rods via friction welding method was investigated. Optical, SEM, hardness and strength tests were performed after the joining process. As a result of the analysis, it was concluded that it was difficult and problematic to join SiC-reinforced Cu matrix composites via friction welding.

Sürtünme Kaynağı ile SiC Takviyeli Bakır Matrisli Kompozitlerin Birleştirilmesinin Araştırılması

Anahtar Kelimeler
Sürtünme kaynağı, SiC, Bakır matrisli kompozit, Mikroyapı

Öz: Günümüzde hızla gelişen sanayi ile birlikte farklı özelliklere sahip malzemelerin birlikte kullanımı kaçınılmaz hâle gelmiştir. Bu durum farklı fiziksel ve mekanik özelliklere sahip malzemelerin birleştirilmesini zorunlu kılmaktadır. Bu bağlamda katı hâl kaynak yöntemleri arasında yer alan sürtünme kaynağı yöntemi başarılı sonuçlar vermektedir. Bu çalışmada toz metalurjisi yöntemiyle üretilen farklı oranlarda SiC takviyeli Cu matrisli kompozit malzemelerin hem kendi aralarında hem de saf bakır (Cu) çubuklarla sürtünme kaynağı yöntemiyle birleştirilmesi incelenmiştir. Kaynak işlemi sonrasında optik mikroskop, SEM, sertlik ve mekanik dayanım testleri uygulanmıştır. Yapılan analizler sonucunda SiC takviyeli Cu matrisli kompozitlerin sürtünme kaynağı ile birleştirilmesinin zor ve çeşitli problemler içerdiği sonucuna varılmıştır.

1. INTRODUCTION

Advances in technology have led to the need to improve many of the properties of materials and have made a major contribution to the development of materials science [1-9]. Thus, serious efforts are made to improve materials [10-13]. The desired properties have led to the combined use of dissimilar materials [14-18]. Composites are called as material groups consisting of two or more components that do not visibly dissolved in each other and have the desired properties of the materials used [19, 26]. Ersoy [20, 26] defined composite materials as a group of materials formed by combining at least two different materials for a specific purpose. It typically consists of a composite material, a low-strength resin or matrix, and a small number of reinforcing elements. The components of composite materials are combined at the macro level to maintain their boundaries. When composite materials are examined, it is seen that the components are selected and at a distinguishable level. Even though these materials

have homogeneous properties, they actually have heterogeneous structures. In this regard, materials combined at the molecular and atomic level do not belong to the class of composites, even though they appear homogeneous [20, 26]. Powder metallurgy is one of the common methods used in the manufacture of metal matrix composites (MMC). Sintering, hot isostatic pressing, hot pressing, nano particle techniques, powder metal injection and mechanical alloying methods are the advanced technologies addressing an ever-growing market in powder metallurgy [22]. This method allows us to obtain durable objects with the help of pressure and temperature below the molten temperature of metals and alloys [23]. Friction welding is a solid-state joining method. Friction welding is a welding method in which the parts to be welded rotate at a certain speed and are joined by pressure. Friction welding is one of solid-state methods that can be used to join metals with different thermal and mechanical properties. The fact that the temperature in the friction welding process is below the melting temperature and the joining time is short allows the joining of materials that are difficult and problematic to join with other methods [24, 26].

The joining problem in the application area of composite materials has been the cause of an increase in studies on this subject. The present study was conducted to investigate the hardness, strength, and microstructures of the welding interface formed upon joining of SiC-reinforced copper matrix via friction welding, one of the joining methods.

2. MATERIAL AND METHOD

Before the welding process, standard copper material and SiC-reinforced Cu matrix composite materials obtained by powder metallurgy method were cut in Ø12x40 mm size. These parts were cleaned from rust, foreign matter and oxide layer on the front surfaces on CNC lathe and made suitable for friction welding.To apply the friction welding method, a continuous drive friction welding machine was used, which is schematically shown in Figure 1. The setup of this welding machine consists of five parts including movable chucks, fixed chucks, drive motor, reciprocating bearing and directional control valves.

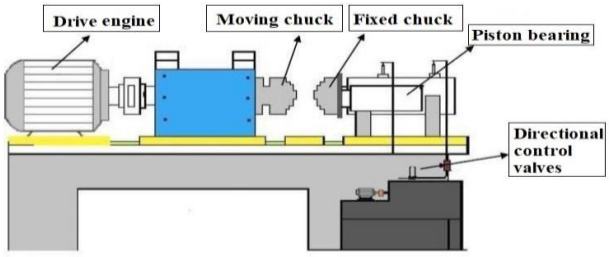

Figure 1. Schematic view of a continuous drive friction welding machine [25]

The parameters that have a significant effect on the mechanical and microstructure of the friction welded joints obtained parameters are temperature, rotation speed, friction pressure, rates of reinforcing element, and upsetting pressure. In the present study, temperature, rotation speed and friction pressure were taken as constant and the rate of reinforcing element in the specimen was considered as a parameter.

Table 1. Parameters used in friction welding

Sample no	SiC (%)	Rotation speed (rpm)	Temperature (^{0}C)	Friction pressure (MPa)
S1	0	1700	1000	30
S2	5			
S3	10			
S4	15			

As shown in Table 1, 5%, 10% and 15% silicon carbide-reinforced copper composite specimens were friction welded at 1700 rpm and 10000C with a friction pressure of 30 MPa. Pure copper specimens were connected to the rotational mirror connected to the engine of the machine and Cu-SiC specimens were connected to the axially moving hydraulic mechanism. The produced specimens were cut from the welding joint area for microstructure analysis, then the welded area was sanded with 80-1200 mesh sandpaper and polished with 3% diamond paste. After sanding and polishing, they were etched with Nital etchant.

As a result of friction welding, it was observed that the deposit formed on the surface of the weld zone varied. Figure 2 shows the bonding of pure copper and SiC-reinforced copper matrix composites paired for the bench. Figure 3 shows the composites produced by powder metallurgy method and the composites joined via friction welding.

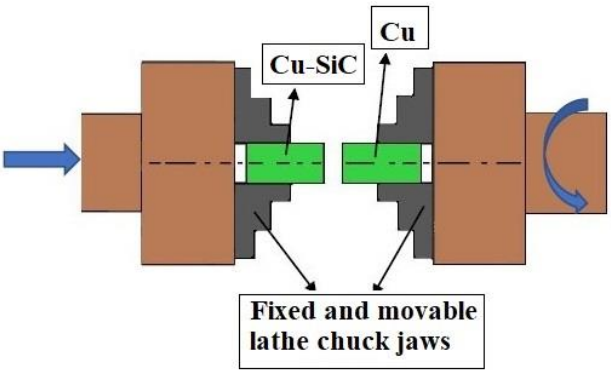

Figure 2. Joining way of the parts [25]

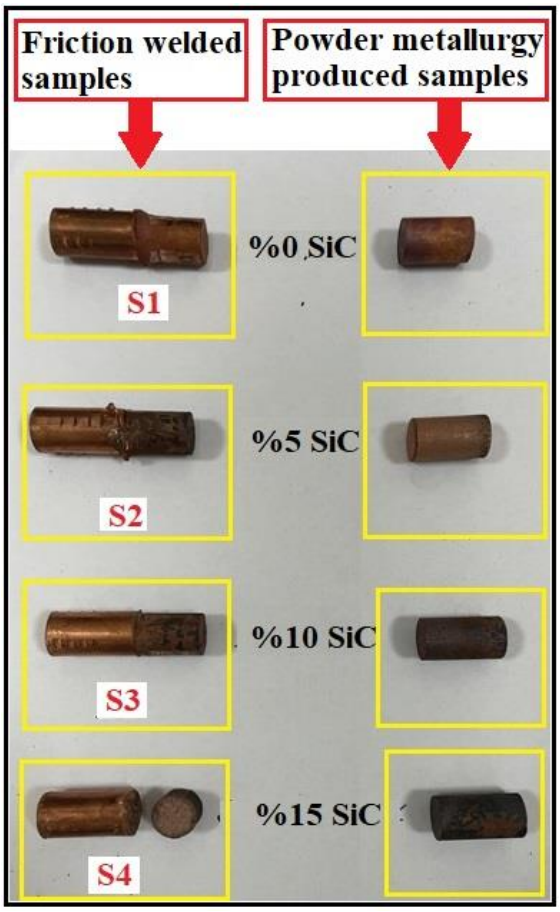

Figure 3. Images of the composites produced and friction welded specimens of these composites [26]

3. RESULTS

3.1. Optical Analysis

The specimens were sanded, polished, and then etched with a Nital solution in order to see the microstructural properties. Optical microscope and SEM images were taken to get an idea of the different structures in this microstructure. The optical images taken from specimen S3, which contained standard 10% SiC, were observed to have five different regions and they are shown in Figure 4. These regions were defined as the intermediate zone (A), the heat affected zones (D-B), and the base materials (E-C). As can be seen from the optical image, it is clear that the SiC grains in the copper have a density under heat and pressure toward the intermediate zone. From this point of view, it was observed that the SiC rate had a negative effect on the joint quality and the joint was achieved in all specimens other than the specimen containing 15% SiC. In their study, Meral et al., observed a good bond between the coating and the substrate in the SiC-reinforced specimens. However, they noted that the coating quality was negatively affected in the 16% SiC-reinforced specimen and there was a lot of uncoated area in the coating area. They also mentioned that increasing rate of the SiC reinforcement increased the number and size of fire channels, which impaired the quality of the coating [27].

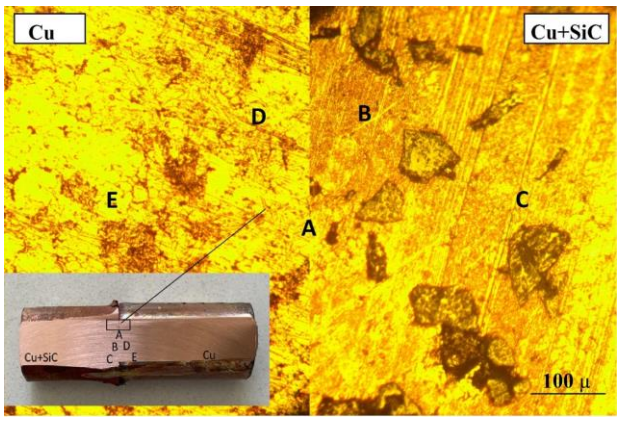

Figure 4. Optical image of the specimen S3

3.2. SEM Analysis

Figure 5 shows the SEM images taken from the specimens with different SiC rates. When these specimens are examined, it was observed that an complex porous structure dominated in specimen S1, and the grain boundaries were clear. However, with SiC reinforcement, the grain boundaries in the composite material become more pitted and bonding quality of grains impaired. Increasing SiC reinforcement caused a negative effect on the friction welded joint of the composite materials and did not show a homogeneous structure. It is clear that both the production of composite material and its joining with Cu via friction welding were negatively affected by this irregularity. Buytoz et al., mentioned in their study that the presence of SiC reinforcement affected the formation of the microstructure, low powder content produced softer dendritic structures, while high powder content produced harder and more durable structures [28].

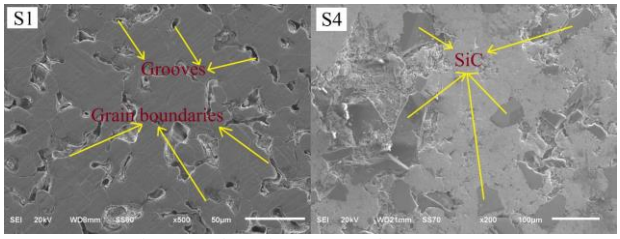

Figure 5. SEM images of specimens S1 and S4

3.3. Microhardness Analysis

Figure 6 shows the results of microhardness measurements of SiC-reinforced Cu matrix composites joined via friction welding. While the average hardness values both on the composite side and Cu side were around 50 HV in specimen S1, an increase of 16-18% was observed in specimen S2 with 5% reinforcement. In specimen S3 with 10% reinforcement and S4 with 15% reinforcement, the hardness values increased by 60-64%. This average increase in hardness is thought to be caused by the presence of carbide formations and intermetallic compounds in the microstructure with increasing SiC reinforcement. Kılıç et al., mentioned in their study that SiC reinforced specimens were approximately twice as hard as unreinforced specimens [29].

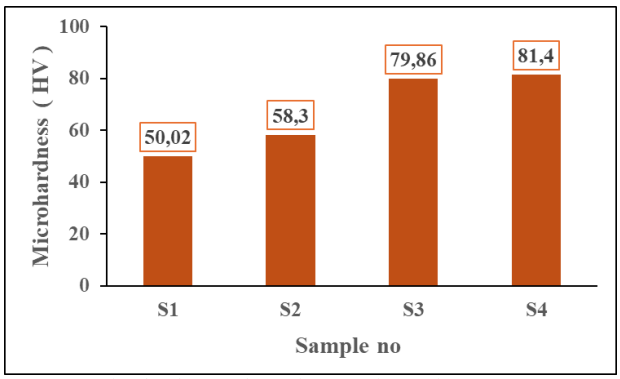

Figure 6. Microhardness values of Cu matrix specimens

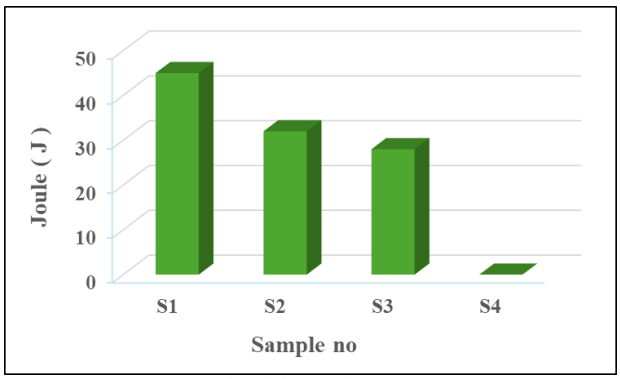

Figure 8. Impact test results of the specimens

3.4. EDS Analysis

Figure 7 and Table 2 show the EDS images and results obtained from specimens with different SiC rates. While the Cu content in the unreinforced specimen was around 95.755%, it was 89.382% in the 5% SiC-reinforced specimen, 69.346% in the 10%-reinforced specimen, and 54.702% in the 15%-reinforced specimen. From the EDS results, there was also presence of oxygen due to some oxidation in all specimens. Kılıç et al., stated that SiC increased the solid phase formation in the coating, changed the chemical distribution and made the microstructure more homogeneous based on EDS analysis [29].

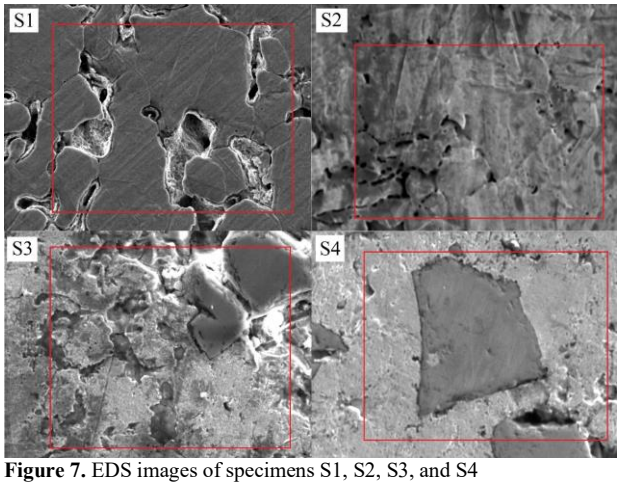

Figure 7. EDS images of specimens S1, S2, S3, and S4

Table 2. EDS results of specimens S1, S2, S3, and S4

Elements (wt.%)	Sample no			
	S1	S2	S3	S4
C	1.976	9.622	9.581	7.524
O	1.270	0.772	12.406	5.812
Si	-	0.223	20.667	31.962
Cu	95.755	89.382	57.346	54.702
Total	100.000	100.000	100.000	100.000

3.5. Impact Analysis

Charpy impact tests were carried out using TERCO MT 3016 impact tester at room temperature with a maximum energy of 150 Nm. Figure 8 shows results of the notch impact test as a bar graph. Increasing SiC rate caused a decrease in impact energy. Forty-five J was obtained in specimen S1, 32 J in specimen S2 and 28 J in specimen S3. Specimen S4 was unsuccessful.

4. DISCUSSION AND CONCLUSION

It was observed that the results varied in friction welding of Cu matrix composites containing different rates of SiC depending on the SiC reinforcement rate. As a result, it is clear that friction welded joint of Cu matrix SiC-reinforced composites produced via powder metallurgy method with Cu material is difficult and problematic. No joining process could be achieved above 15% reinforcement rate.

It was observed that the hardness-value of the specimens increased as the carbide content increased. Although SiC particles decreased the density of the composite material, they improved its mechanical properties. However, they also reduced the friction welding capability.

In the present study, it was thought that the reason for the lack of joint due to the increase in SiC reinforcement rate was the atomic structure, melting temperatures, different welding capabilities, and the pressure applied in friction welding.

REFERENCES

[1] Şap S, Usca ÜA, Uzun M, Giasin K, Pimenov DY. Development of the hardness, three-point bending, and wear behavior of self-lubricating Cu-5Gr/Al2O3-Cr3C2 hybrid composites. J. Comp. Mater. 2023;57(8):1395-1409.

[2] Usca Ü.A., Şap S., Uzun M., Giasin K., Pimenov DY. Evaluation of Mechanical and Tribological Aspect of Self-Lubricating Cu-6Gr Composites Reinforced with SiC–WC Hybrid Particles. Nanomater. 2022:12(13): 2154.

[3] Şap S, Uzun M, Usca UA, Pimenov DY, Giasin K, Wojciechowski S. Investigation of machinability of Ti–B-SiCp reinforced Cu hybrid composites in dry turning, J. Mater. Res. Technol. 2022;18: 1474-1487.

[4] Şap S., Usca ÜA, Uzun M, Kuntoğlu M, Salu E, Pimenov DY. Investigation of the Effects of Cooling and Lubricating Strategies on Tribological Characteristics in Machining of Hybrid Composites. Lubricants, 2022;10(4):63.

[5] Şap S, Uzun M, Usca UA, Pimenov DY, Giasin K, Wojciechowski S. Investigation on microstructure, mechanical, and tribological performance of Cu base

hybrid composite materials, J. Mater. Res. Technol. 2021;15: 6990-7003.
[6] Şap S, Turgut A, Uzun M. Investigation of microstructure and mechanical properties of Cu/Ti–B–SiCp hybrid composites, Ceramics Int., 2021;47(21): 29919-29929.
[7] Bayrak KG, Umutlu ON, Koroglu L, Demir B. Mechanical characteristics of dual-phase medium-mntropy Boride/Carbide ceramics synthesized through SPS, J. American Cer. Soci. 2025;108(3): e20282.
[8] Demir B, Duden EI, Ayas E. Characterization of MoAlB ceramics synthesized via spark plasma sintering with Si addition and SiC reinforcement, J. Alloy. Comp. 2023; 953: 170115.
[9] Sreenivasan KS, Satish Kumar S, Katiravan J. Genetic algorithm based optimization of friction welding process parameters on AA7075-SiC composite, Eng. Sci. Technol., Int. J. 2019; 22(4):1136-48.
[10] Midling OT, Grong Ø. A process model for friction welding of Al Mg Si alloys and Al SiC metal matrix composites-I. haz temperature and strain rate distribution, Act. Metall. Materia. 1994;42(5): 1595-1609.
[11] Rotundo F, Marconi A, Morri A, Ceschini A. Dissimilar linear friction welding between a SiC particle reinforced aluminum composite and a monolithic aluminum alloy: microstructural, tensile and fatigue properties, Mater. Sci. Eng.: A. 2013;559:852-60.
[12] Maity D, Racherla V. Effect of SiC interlayer on microstructure and joint strength of Cu-Al welds obtained using a new friction processing method CIRP, J. Manuf. Sci. Technol. 2024;52: 73-85.
[13] Imak A. Overview of friction welding processes for different metallic materials, Mater.Test. 2022; 64(9): 1372-82.
[14] Imak A. NiTi-SiC composite coating on Ti6Al4V alloy produced by SHS using induction heating. Mater. Test. 2022; 64(12): 1851-59.
[15] Bati S, Kilic M, Kirik I. Friction welding of dissimilar AISI 304 and AISI 8640 steels. Europ. J. Techn. 2016; 6(2): 79-86.
[16] Buytoz S. Effect on high temperature oxidation behavior of vanadium and titanium element in FeCrC coating, Trans. Indian. Inst. Met. 2022; 75: 3149-57.
[17] Buytoz S, Kilic M, Carboga C. Microstructure and wear behaviour of Ni-Based/TiC composite coating, Int. J. Surf. Sci. Eng. 2022; 16(1): 71-90.
[18] Somunkiran I, Buytoz S, Dagdelen F. Determination of curie temperatures and thermal oxidation behavior of fe-cr matrix composites produced by hot pressing, J. Alloy. Comp. 2019;777: 302-308.
[19] Kaw AK. Composite material mechanics, Efil Publications, Ankara, 2014. p 10- 84.
[20] Ersoy HY. Composite materials, Literature Publications, İstanbul, 2001. p 44-62.
[21] Sahin Y. Introduction to composite materials, Gazi University, Gazi Bookstore, Ankara, 2020. p 300-327.
[22] Toptan F. Production of aluminum matrix B4C reinforced composites by casting method. Master Thesis, Department of Metallurgical Engineering. Istanbul: Yıldız Technical University; 2006.
[23] Yilmaz N. Machinability of iron based powder metal materials. PhD Thesis, Department of Mechanical Engineering. Isparta: Süleyman Demirel University; 2006.
[24] Sahin AZ, Yilbaş BS, Ahmed M, Nickel J. Analysis of the friction welding process in relation to the welding of copper and steel bars, J. Mater. Process. Technol. 1998;82: 127-36.
[25] Omer B. Investigation of weldability of copper with SiC reinforced copper matrix composites produced by powder metallurgy method, Master Thesis, Department of Mechanical Engineering. Bingol: Bingol University; 2022.
[26] Kirik I, Imak A, Barac O. Friction welding of Cu matrix SiC reinforced composite, Global Summit on Adv. Mater. & Sustain. Energy (G-AMSE22). 208-215, Van, Türkiye.
[27] Beltir MY, Imak A, Kirik I, Turgut A, Koc V. Microstructure and wear properties of NiTi–XSiC coating of AISI 1020 by SHS. Mater. Test. 2025; 67(2): 386-96.
[28] Buytoz S, Ulutan M. In situ synthesis of SiC reinforced MMC surface on AISI 304 stainless steel by TIG surface alloyin., Surf. & Coat. Technol. 2006; 200(12-13): 3698-3704.
[29] Kilic M, Imak A, Kirik I. Surface modification of AISI 304 stainless steel with NiBSi-SiC composite by TIG method, J. of Materi Eng and Perform. 2021; 30: 1411–19.

Volume 14, Issue 3, Page 156-164, 2025 https://doi.org/10.46810/tdfd.1624013 Research Article

BİNGÖL UNIVERSITY

Türk Doğa ve Fen Dergisi
Turkish Journal of Nature and Science
www.dergipark.gov.tr/tdfd

Formulation and Evaluation of a Peel-off Gel Mask Containing Macerate St. John's Wort Oil and Activated Carbon Derived from Pine Cones

Hatice KARAER YAĞMUR[1*], Hatice Kübra ÖZER [2]

[1]Dicle University, Faculty of Science, Chemistry Department, Diyarbakır, Türkiye
[2]Dicle University, Science and Technology Application and Research Center, Diyarbakır, Türkiye
Hatice KARAER YAĞMUR ORCID No: 0000-0002-3728-1825
Hatice Kübra ÖZER ORCID No: 0009-0003-5666-5538

**Corresponding author: profhatice23@hotmail.com*

(Received: 21.01.2025, Accepted: 02.09.2025, Online Publication: 26.09.2025)

Keywords
Peel-off mask, Active carbon, St. John's wort oil, Hypericum perforatum

Abstract: Skin needs care to protect against environmental pollution. The facial skin can be protected such as cream, peel off mask and lotion facemask. The aim of this study was to obtain an antibacterial peelable gel mask containing macerated St. John's wort oil (*Hypericum perforatum* oil). This peel-off gel mask consists of ascorbic acid, polyvinyl alcohol (PVA, as preservative), polyethylene glycol (PEG), glycerine (as plasticizer), polysorbate (tween 20, as stabilizer), ethanol, distilled water, macerate St. John's Wort oil and active carbon. The physical properties (homogeneity, spreadability, viscosity, film drying time) and chemical properties (pH value, stability and antibacterial activity properties) of the peelable gel mask were examined. Using of an active ingredient in peel off mask, it strengthens the role of peel off mask by opening the clogged pores. Activated carbon (AC) was added to this formulation as an active ingredient due to its adsorbent activity. In this present study, activated carbon was obtained from pine cone (PC). The specific surface area (SBET) and pore diameter of activated carbon were found to be 536.998 m^2/g and 1.8 nm. Microporous activated carbon was obtained. The antimicrobial activity of the St. John's Wort oil was tested against Gram-negative bacteria (*Pseudomonas aeruginosa*) and Gram-positive bacteria (*Staphylococcus aureus*) as well as one pathogenic fungus (*Candida albicans*, ATCC 10231). Disc diffusion method was used to study antimicrobial activity. The resulting peel off mask is a black mask that smells of bergamot essential oil and can be easily spread on the skin. The drying time of the mask was determined as 17 minutes. The prepared peel of mask that can be easily peeled off in one piece is obtained.

Sarı Kantaron Yağı ve Çam Kozalaklarından Elde Edilen Aktif Karbon İçeren Soyulabilir Jel Maskenin Formülasyonu ve Değerlendirilmesi

Anahtar Kelimeler
Soyulabilir maske, Aktif karbon, Sarı kantaron yağı, Sarı kantaron

Öz: Cildin çevre kirliliğinden korunması için bakıma ihtiyacı vardır. Yüz cildi krem, soyulabilir maske ve losyon yüz maskesi gibi ürünlerle korunabilir. Bu çalışmanın amacı, macerat sarı kantaron yağı (*Hypericum perforatum* yağı) içeren antibakteriyel soyulabilir jel maske elde etmektir. Bu soyulabilir jel maske; askorbik asit, polivinil alkol (PVA, koruyucu olarak), polietilen glikol (PEG), gliserin (plastikleştirici olarak), polisorbat (tween 20, stabilizatör olarak), etanol, damıtılmış su, macerat, sarı kantaron yağı ve aktif karbondan oluşur. Soyulabilir jel maskenin fiziksel özellikleri (homojenlik, yayılabilirlik, viskozite, film kuruma süresi) ve kimyasal özellikleri (pH değeri, kararlılık ve antibakteriyel aktivite özellikleri) incelendi. Soyulabilir maskede aktif bir bileşen kullanılması, tıkalı gözenekleri açarak soyulabilir maskenin etkisini güçlendirir. Adsorban aktivitesi nedeniyle bu formülasyona aktif bileşen olarak aktif karbon (AC) eklendi. Bu çalışmada, aktif karbon çam kozalağından (PC) elde edilmiştir. Aktif karbonun özgül yüzey alanı (SBET) ve gözenek çapı 536,998 m^2/g ve 1,8 nm olarak bulunmuştur. Mikrogözenekli aktif karbon elde edildi. Sarı kantaron yağının antimikrobiyal aktivitesi Gram negatif bakterilere (*Pseudomonas aeruginosa*) ve Gram pozitif bakterilere (*Staphylococcus aureus*) karşı ve ayrıca bir patojen mantara (*Candida albicans*, ATCC 10231) karşı test edildi. Antimikrobiyal aktiviteyi incelemek için disk difüzyon yöntemi kullanıldı. Elde edilen soyulabilir maske, bergamot esansiyel yağı kokulu ve cilde kolayca uygulanabilen siyah bir maskedir. Maskenin kuruma süresi 17 dakika olarak belirlendi. Tek parça halinde kolayca soyulabilen hazırlanmış bir maske elde edildi.

1. INTRODUCTION

The skin is a covering layer of the body against the external environment and microorganisms. For women, the face is the most important part of the body in terms of beauty. For this reason, many women try to beautify themselves by using cosmetic products [1]. Cosmetic products are used to improve the appearance of the skin by action of cleansing, beautifying and promoting attractiveness [2]. Facemask is one of the cosmetic products for skin care that are generally often used by women so that the appearance of facial skin becomes healthier and more beautiful [3]. Peel off masks may be used for cleansing and moisturizing the skin [4]. Peel off masks use film-forming polymers so they can be easily peeled off without leaving any residue after complete drying [5]. The peel-off mask is available in gel and dry form. It can be applied onto the face, neck and hands. It is useful in removing blackheads and dead skin [4].

The peel-off mask gel is one of the popular forms of applications used to improve the quality of the face. The face masks in gel form have the advantage of being easily peeled off, is helpful for recovering facial skin, and can be used to minimize pores. In addition, it is also useful for relaxing facial muscles [6]. The gel mask can stay on the face for 15-20 minutes; the drying time may vary depending on its content. Polyvinyl alcohol (PVA) or polyvinyl acetate is usually used as a film former in peel-off facemasks [7]. It can be obtained with synthetic ingredients such as activated charcoal, polyvinyl alcohol, polyethylene glycol, glycerin, tween 20, ascorbic acid and water [4]. Industrial, agricultural and domestic wastes are discharged to the environment due to the rapid development of technology [8]. Agricultural waste materials are economical and environmentally friendly thanks to their chemical composition. Pine seeds are borne in cones. The large quantities of pine cones are produced each year in pine fields cultivated for the paper industry [9]. Activated charcoal is a black powder produced by high temperature pyrolysis of carbonaceous materials [10]. Activated carbon is a material with a high surface area and porous structure. It is widely used in various industrial processes as an adsorbent [8]. The production of commercial activated carbon is quite expensive, and therefore, efforts are being made to develop low-cost and efficient activated carbon by using various alternative sources [11]. In the recent past, researchers have been studying on the preparation of activated carbons from low-cost and ecofriendly biomass/bio-waste. Peanut shells, coffee beans, sunflower seed shells, coconut shells, almond shells, bamboo, waste paper, rice husk, dead leaves, seaweed, etc. resources that can be used for the production of activated carbon [12]. *Hypericum perforatum L*. (*Hypericaceae*) (HPL), known as St. John's Wort (SJW), is one of the most studied medicinal plants. *H. Perforatum* has been used in alternative medicine since ancient times against wounds, depression, burns, internal and external diseases. The last studies have revealed anticancer, antimicrobial, antifungal, anti-inflammatory, antioxidant, wound healing, antidiabetic and antidepressant activity of *H. perforatum* extracts. Several methods have been used for extraction of *H. perforatum* include; methanol maceration, boiling water extraction, ethanol/water maceration, olive oil maceration, aqueous glycerol extraction, ethanol extraction with soxhlet apparatus and ultrasonic-assisted extraction with methanol/HCl [13]. The traditional way of preparing the St. John's Wort oil is obtained by maceration of fresh flowers of Hypericumn perforatum in sunlight for several weeks. The oil prepared by this method acquires a bright orange-red color [14,15]. According to the old preparation methods, the effect of sunlight can be seen. According to the studies, yellow oil was obtained from dried St. John's Wort flowers, which were kept in hot olive oil for 3 hours owing to the color of the flower pigments. The red color and fluorescence of a St. John's Wort oil is generally ascribed to hypericin. According to lıterature, St. John's Wort oil contain no hypericin in St. John's Wort oil but only lipophilic compounds with a hypericin-like color and fluorescence. These compounds were considered lipophilic substituted hypericins, which were also present in St. John's Wort flowers [15]. According to studies, with respect to the analysis of traditional Oleum hypericin, the characteristic red color can be attributed to lipophilic components because of the degradation of hypericin by exposure to sunlight [16]. *Hypericum perforatum* plant has therapeutic effect in wound healing because it contains Hypericin and hyperforin. Hypericins consist of hypericin and pseudohypericin (an oxidized derivative of hypericin) and are found in leaf and petal margins, stamens, dark glands [17]. *H. perforatum* contains hypericin, pseudohypericin, hyperforin, adhyperforin, flavonoids such as quercetin, quercitrin, biapigenin, rutin, kaempferol, hyperoside, and amento flavone [18, 19]. Among its components, hyperforin has been found to have antidepressant, anti-biotic and antitumor activities. Hyperforin is used in the treatment of skin problems such as atopic dermatitis. Hypericin has antibacterial, antiviral and anti-inflammatory activity, while hyperforin has antidepressant activity [14, 18, 20, 21]. Atopic dermatitis (AD) is a common inflammatory skin disease caused by the overgrowth of *S. aureus* [22]. This condition was expressed by the term 'eczema' [23]. Researchers have long been aware that bacteria and other microorganisms play a role in atopic dermatitis.

Many authors consider infections important. ‘Secondary contribute infection with *S. aureus* emerges as a cause of atopic dermatitis. Therefore, colonization by *S. aureus* may both be a cause and a consequence of atopic dermatitis [24, 25]. The skin in patients with atopic dermatitis is constantly colonized by *S. aureus*, in part because of a deficit in epidermal antimicrobial peptides [26]. Futhermore, an imbalance between *S. aureus (S. aureus)* and the skin microbiota can create a state of dysbiosis that compromises the skin barrier. The skin dysbiosis that occurs through an increase in the pathogen *S. aureus* and a variation in the composition and number of skin commensal bacteria also contributes to skin barrier defects and can be a trigger for atopic dermatitis [23]. *Hypericum perforatum* oil has been determined to have antimicrobial activity on various Gram-positive and Gram-negative bacterial strains [19]. and is widely used

in pharmacy and medicine because of its antibacterial, antifungal and antiviral properties [21].
For the present study, the bio-waste pinecone was used as the raw precursor for the preparation of activated carbon. The active carbon was characterized with FT-IR, DLS, TGA and BET measurements. The objective of this study was to develop and formulate St. John's Wort oil peel-off mask by using activated carbon obtained from pine cones and evaluate by test methods as an alternative of facial skin care product. The antimicrobial test was performed by disc diffusion method and the growth inhibitory effects of *Hypericum perforatum* oil on *P. aeruginosa* and *S. aureus* and *Candida albicans* were investigated.

2. MATERIAL AND METHOD

2.1. Material and Method

The pine cone (PC) shells used in the preparation of activated carbon were collected from pine trees in the Dicle University campus (Diyarbakır, Turkey). Pine tree cones were collected July 2021. Ascorbic acid, polyvinyl alcohol (PVA), polyethylene glycol (peg), glycine, polysorbate (tween 20), ethanol, distilled water.

2.2. Preparation of the activated carbon (AC)

The pine cones (PC) were washed thoroughly with distilled water to remove impurity; the cone biomass was then dried at 100°C for 24 h in an oven. The dried cones ground in a crusher. The pine cone shells were placed in a tube oven (which was set in a horizontal stainless-steel tubular reactor (7 cm x100 cm) and heated from room temperature to 500 ºC at a heating rate of 5 oC min-1 in an N_2 atmosphere and carbonized at 500 ºC for 1h [11, 27]. The charred sample was mixed with HCl (0.1 M) solution to remove impurities for 5 hours. Then the activated carbon was washed with distilled water and dried at 120 °C for 48 hours. The dried activated carbon was powdered and stored in a desiccator (Fig. 1).

2.3. Preparation methods for St. John's Wort oil by traditional maceration

St. John's Wort upper flowered parts (with flowers and leaves) were collected in the region of Turkey, central İstanbul in July 2022. The plant materials were dried at room temperature for 3 days. The natural olive oil obtained from olives of Manisa region in Turkey was used in the macerate preparation. About 400 grams of the dried plant materials (*Hypericum perforatum*), were mixed with 1.5 L of olive oil in a transparent glass bottle and kept under sunshine for 40 days from the mid- July to beginning September. In this process, the mixture was stirred in the glass every other day. At the end of 40 days the macerate oil, which turned to red color, was filtered and then stored in an amber glass bottle in a dark place at room temperature until use (Fig.2) [13, 28, 29]. Fig. 3 shows biologically active compounds of Hypericum perforatum.

Figure 1. Preparation of activated carbon (AC).

Figure 2. Preparation of St. John's Wort oil.

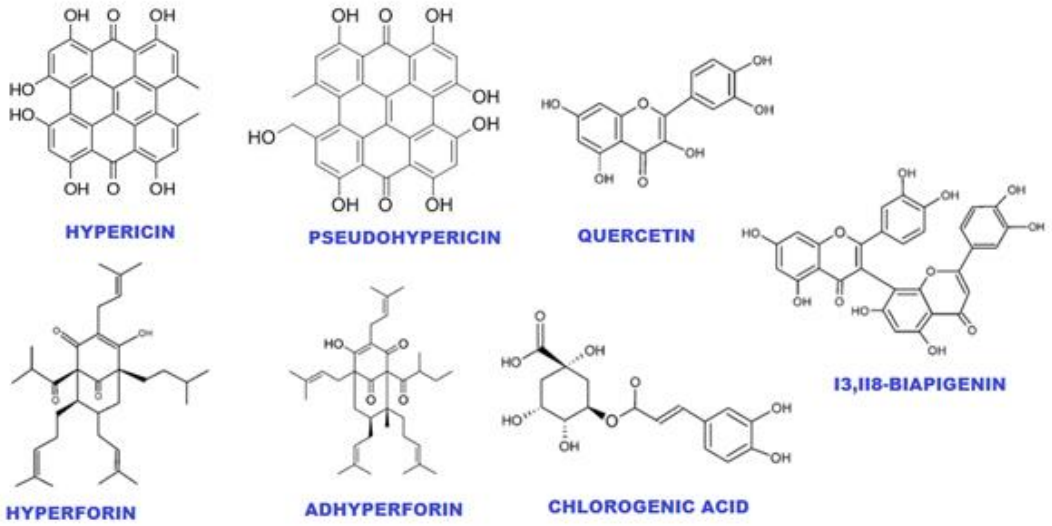

Figure 3. Biologically Active Compounds of *Hypericum perforatum*.

Figure 4. Preparation and application of the gel mask.

2.4. Formulation of Peel off Gel Mask

I. This phase involves the addition of (14%) of polyvinyl alcohol (film former) to distilled water (70%, as base) in the beaker at 80°C temperature with a constant vigorous stirring. Further, this mixture is allowed to cool down at 40°C.

II. In this phase a mixture of St. John's Wort oil (or glycerine, smoothing agent or a humectant) and PEG (as a surfactant) in the ratio of 3:1 is added to phase I at 40°C temperature and mix well.

III. Add (0.5%) polysobate (tween 20) (Polymer and emulsifier)

IV. Add ethanol (solvent) 1ml and add (1%) distilled water with (0.1%) ascorbic acid into the phase III mixture and mixed well. Moreover, distilled water was added until 100% w/w total volume.

V. Add activated charcoal (5%) and stirred well and cooled for few minutes [4, 6, 30]. Bergamot (essential oil) was added to mixture to be 1%. Fig. 4 shows preparation and application of the mask on face and hand.

2.5. Characterization

The active carbon was characterized by Fourier transform infrared spectroscopy (FT-IR Perkin Elmer, ATR sampling in the range of 4000 to 400 cm-1), Brunauer-Emmett-Teller (BET), dynamic light scattering (DLS), particle size of the active carbon was determined Malvern mastersizer 3000 hydro. Thermal analysis of the active carbon was determined by PerkinElmer Diamond Thermal Analysis (between 20-1000 ºC (in N_2, 10 oC min-1). The surface area and pore volume of the active carbon were obtained from Brunauere EmmetteTeller (BET) (NOVA model). Hanna HI 2002-02 Desktop pH meter was used for pH study. Koehler Instrument KV1000 Digital Constant Temperature Kinematic Viscosity Bath was used for viscosity measurements.

2.6. Preparation of Inoculum

The antimicrobial properties of the St John's Wort oil were tested against gram-positive bacteria (*S. aureus* (ATCC 25923)), gram-negative bacteria (*P. aeruginosa* (ATCC 27853)) as well as one pathogenic fungus (Candida albicans (ATCC 10231)) and they are purchased from Kwik-Stick. Bacteria and fungus were pre-cultured in Tryticase Soy Broth (TSB) (Merck) overnight in a rotary shaker at 37°C. Afterward, each bacteria strain was adjusted at a concentration of 108 cells mL^{-1} using 0.5 McFarland standard [31]. The fungal inoculum was prepared from the 48 h culture at a final concentration of 106 cells mL^{-1}.

2.7. Antimicrobial Screening

The antibacterial and antifungal activities of the St. John's Wort oil were determined by using Agar well diffusion method [32]. The suspension was prepared from an overnight culture for each microorganism. Mueller Hinton Agar (MHA) (Biolife) and Sabouraud Dextrose Agar (SDA) (Biokar) were swabbed with the bacterial and fungal suspension and wells were made using a sterile pipet tip (6 mm in diameter) into agar plates containing inoculums. Then, 100 mL of St John's Wort oil in tween 20 extracts were added to respective wells. The plates were placed in the refrigerator for 30 min to let the extracts diffusion well into the agar. Then, the plates were incubated at 37°C for 18-24 h. Antimicrobial activity was detected by measuring the zone of inhibition (including the wells diameter) appeared after the incubation period. Tween 20 was employed as a negative control.

3. RESULTS

3.1. The structure and characterization

PVA, which acts as a gelling agent, is used to form an elastic film layer so that the formed film can be easily removed without cracking. In the prepared mask, Glycerin / Centaury oil acts as a moisturizer to preserve skin moisture. The preservative used in the peel-off gel mask formula is Ascorbic acid. Ascorbic acid (vitamin C) is an ingredient of antiaging cosmetic products used for its collagen synthesis, depigmentation, and antioxidant properties. Because of these properties, it has been used as a stabilizer in various pharmaceutical dosage forms [33, 34]. A combination of preservatives is used to enhance the effect against bacteria and fungi [1, 5, 30]. The preservatives are used in gel masks to increase the effect against bacteria and fungi.

The FT-IR spectrum of active carbon (AC) was given Fig. 5. The peaks at 3283 cm^{-1} and are related to the OH stretching vibration in alcoholic, phenolic and carboxylic functional groups and the CH stretching of aldehyde. The band at ~1700 cm^{-1} is attributed to the C=O stretching vibration. The peaks at 1622, 1517, 1443 and 1372 cm^{-1} are attributed to the C=C stretching vibration, the C-H asymmetrical and symmetrical bending vibrations, respectively. The peaks at 1242, 1027 and 812 cm^{-1} are attributed to stretching vibrations of C-O in volatile species, carboxyl acids and bending vibration of CH aromatic ring, respectively [35]. The band 2681 cm^{-1} is related to C-H vibrational stretching for alkanes and alkyl respectively. The bands at 1572 cm^{-1} account for C=C and C–O stretching vibrations of carboxyl group. The bands around 1159 cm^{-1} are attributed to C–O stretching in alcohol and asymmetric stretching of ester and ether functional group. The bands between (400 and 800) cm^{-1} are due to bending vibration of −OH groups, stretching vibration of C–O and C–H bonds [11].

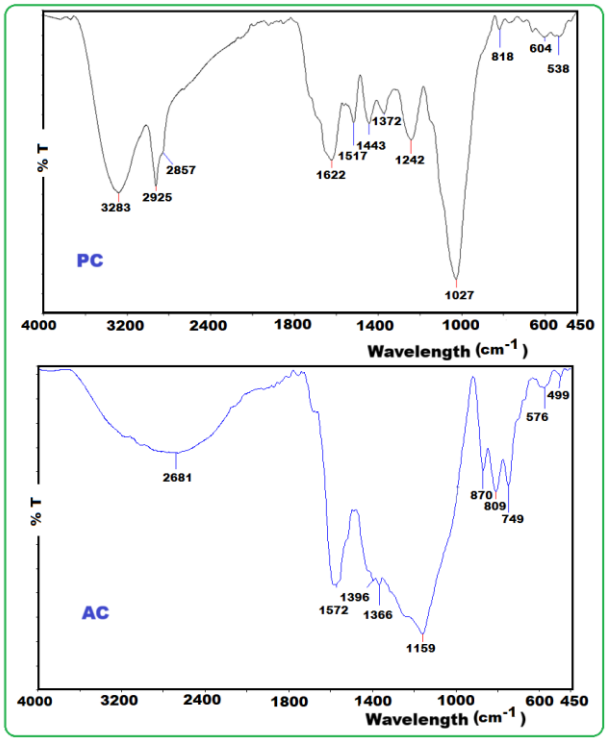

Figure 5. FT-IR spectra of pine cone (PC) and active carbon (AC).

The thermal behaviour of active carbon was determined using thermogravimetric analysis. The TGA-DTGA curves were given in Fig. 6. Thermal decomposition of pine cones has a weight loss % at 120–150 °C due to physically adsorbed water and structured water [35, 36]. The initial degradation temperature (Tonset) of the composite was found 540 ºC. Tmax value is determined from the DTGA curve, was determined 599 ºC. Furthermore, temperature values corresponding to weight

losses of 5% (T5) and 10 % (T10) were determined 489 and 661°C. The event in the range of 160–286 °C, 507–757 °C and of 817–901 °C were owing to the decomposition of hemicellulose and cellulose, decomposition of lignin and the carbon constituent [35].

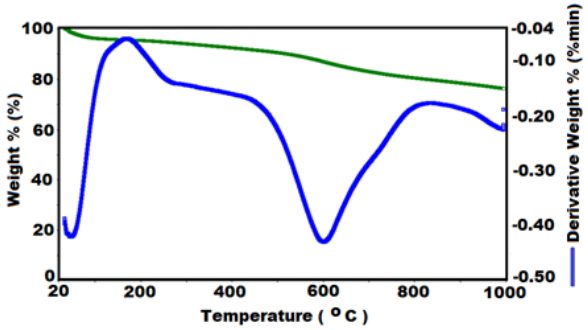

Figure 6. TGA-DTGA curves of active carbon.

The specific surface area (SBET), total pore volume and average pore diameter of AC were found to be 536.998 m^2/g, 4.9x10 $cm3g^{-1}$ and 1.8 nm, respectively. According to literature, the pore size distributions were determined in nitrogen adsorption/desorption isotherms, as micropore (0-2 nm), mesopore (2-50 nm) and macropore (50-300 nm) [37]. According to BET results, diameter pores of activated carbon show micro. These pores on the activated carbon surface absorb chemicals, which enables it to draw bacteria and impurities from the skin, improve acne, minimize pores, treat skin conditions [38]. Activated carbon peel off mask show a very efficient effect on to the skin. The most important characteristic of an activated carbon is its adsorption capacity. Using it as an active ingredient in peel off mask, it adds to its value by enhancing the role of peel off mask by absorbing dust particles and opening the clogged pores [4]. Activated carbon has micro pores, which increase its surface area and therefore its adsorptive properties. Activated carbon is added to cosmetic preparations because of its ability to adsorb oils and clogged pores [38].

The particle size distribution of the sample was evaluated using a light scattering particle size analyzer equipped with an aqueous sample dispersion unit. Results were expressed as the median (d50%) and as the span, which is an index indicative of the particle size dispersity. Span is calculated with equation 1 follow:

$$\text{Span} = (d90\% - d10\%)/ d50\% \quad (1)$$

where dx% (x%=10, 50, or 90%) means that the volume percentage of particles with diameters up to dx % is equal to x%, and the smaller the span, the narrower the particle size distribution [5]. The active carbon was diluted using deionized water. Size distribution of the active carbon was found as < 17 < 68 and < 204 mm for 10, 50 and 90% cumulative mass, respectively. Light scattering particle size analysis was carried out, and it was verified a particle size disparity (span=2.75).

The antimicrobial activities of the St. John wort oil was investigated by using disc diffusion method on Gram-positive bacteria (*S. aureus*), Gram-negative bacteria (*P. aeruginosa*) as well as C.albicans. The antimicrobial activities of St John's Wort oil was studied by the agar well diffusion method. St. John's Wort oil diluted with tween 20 as 0.1 %, 0.2% and 0.4%. Three standard reference antibiotic, amikacin was used as reference controls for the tested bacteria. The antibacterial activity was evaluated by measuring the diameter of inhibitory zones in millimeters using digital calliper. Inhibition zone diameters (mm) were measured and summarized on Table 1. Atopic dermatitis is caused by abnormal overgrowth of *S. aureus*, a common cause of skin infections [22]. The results showed that St. John's Wort oil sample has antimicrobial activity on both test microorganisms (Fig.7). In the case of *C.albicans*, the inhibition of the fungus's development was no observed. The healing rate of chronic wounds is affected by bacterial infections (such as *S. aureus, E. coli,* and *P. aeruginosa*), pain, inflammation, and blood flow, and thus infection and inflammation control can assist in accelerating healing [39]. The effect of antibacterial activity of essential oils depends on the growth of bacteria (bacteriostatic) or destroying bacterial cells (bactericidal). In addition, essential oils extracted from oregano, basil, and coriander plants possess an inhibitory effect against *P. aeruginosa* and *S. aureus* [40]. Moreover, it was reported that essential oils were more effective against Gram-positive bacteria than Gram-negative bacteria, which also supports our findings [41]. These results prove that St John's Wort oil could be a good candidate to inhibit target microorganisms. Experiments were repeated 3 times.

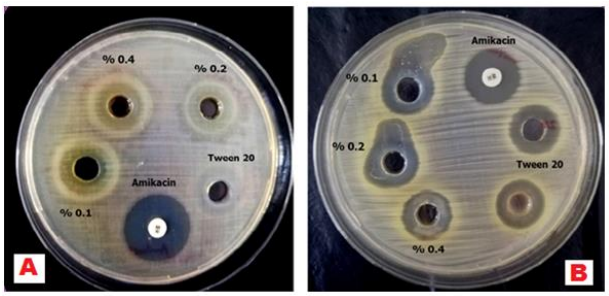

Figure 7. Antibacterial effects of membranes on *P. aeruginosa* (A) & *S. aureus* (B).

Table 1. Inhibition zone diameters of membranes on *S. aureus* and *P. aeruginosa.*

	Inhibition zones (mm)				
	Tween 20 (0)	Amikacin (antibiotic)	St.John's wort oil concentration (%)		
			0.1	0.2	0.4
S. aureus	17	20	21	20	15
P. aeruginosa	14	23	20	20	18

3.2. Evaluation parameters

The mask formula was placed in a plastic container, stored in the refrigerator and measured stability parameters such as odor, color, pH, time of preparation dried, and viscosity evaluated during 4 weeks storage with observations every 2 weeks. Since the prepared peel-off mask was stored in the refrigerator for 4 weeks, the evaluation parameters were repeated at least 3 times during this period.

i. **Color and odour:** The Mask is black in color because of activated carbon. It is bergamot oil smells because of bergamot essential oil.
ii. **The consistency of the gel mask:** Smooth and lightly applied.
iii. **Peel Test:** Peel-off facemask gel is one of the popular forms of topical formulation, which is applied to hand is peeled off after few minutes of its application. According to literature, these masks have many advantages like giving moisturizing effects, cleanness, removing dead cells. They are also used for the skin problems such as acne, wrinkles, atopic dermatitis [42]. Peeling gel was applied evenly to the back of the hand. The peel was allowed to dry. According to the studies, the ideal drying time of the peel able mask gel is 15-30 minutes [43]. The drying time of the gel mask was then determined using a stopwatch. The drying time of the peel-off gel mask is 17 minutes. At the end of the period, the dried mask was removed from the skin surface. It was observed that the mask was easily removed without breaking as shown in Fig. 4.

3.3. Determination of viscosity

The viscosity of the peel-off gel mask was measured using a Koehler viscometer. As the amount of gelling agent increases, the viscosity of the gel mask increases. PVA is a film-forming or gelling agent and has considerable flexibility. This will cause a greater binding and retention of the fluid by the gelling agent, so the viscosity of the mask increases [43]. The viscosity value of the peel off gel mask was determined 111.57 cSt. Temperature-dependent viscosity measurement was not made. Measurements were taken at room conditions.It was observed that the viscosity increased during the 16-week storage period. The pH value should be (4.0 to 7.0) to avoid any skin irritation [44]. In addition, should be lower than 5.0 for better skin condition. The pH of the gel mask was determined using a pH meter. pH measurements were taken at room conditions. pH measurement was made at 1% concentration using distilled water [1]. The pH test results on all peel off gel mask showed a pH of 6.74. According to Hariyad and et.al., pH 4.5–6.5 was safe for use on the skin [45].

3.4. Physicochemical stability

The gel mask stored at low temperature (4± 1°C) did not show signs of instability. When exposed to sunlight, the drying time of the gel mask increases as the ethanol will evaporate in the gel [5]. It was observed that there was no change in the color and odor of the peel-off gel mask during 16 weeks of storage in the refrigerator. The results showed that the longer the storage time, the longer the drying time of peel-off gel masks [1].

4. DISCUSSION AND CONCLUSION

The peel off mask was successfully obtained containing activated carbon added St. John's Wort oil and showed a good spreadability. St. John's Wort oil has been found to be effective on *S. aureus* and *P. aeruginosa*. We found that peel-off mask gel containing St. John's Wort oil had antibacterial activity with an inhibition zone of 20 mm against *S. aureus* and 21mm against *P. aeruginosa*. Due to activated carbon adsorbing properties, it is being used in all sorts of beauty products from face masks to cleansers and even soaps. It is suggested that the prepared peel-off mask gel formulation was physico-chemically stable. Based on the physical evaluation and antibacterial activity of the peel-off mask gel preparations, a formula which has good characteristics was selected.

Research involving human participation and/or animals
None

Ethical approval
None of the studies conducted in this article include any studies conducted on animals or humans. Since the product obtained in this study is not considered a commercial product, no ethics committee certificate has been obtained**.**

Conflict of interests
The authors have no conflict of interest to declare.

Authors contribution statement
Hatice Karaer Yağmur: Conceptualization, Data curation, Investigation, Methodology, Resources, Software, Visualization, Validation, Writing-original draft, Writing - review & editing. Hatice Kübra Özer: Data curation, Methodology, Validation, Writing - review & editing.

REFERENCES

[1] Ridwanto R, Lubis M, Syahputra R, Inriyani H. Utilisation of biopolymer combination as a material for making gel peel off mask. Proceedings of The 5th Annual International Seminar on Trends in Science and Science Education. AISTSSE 18-19 October 2018, Medan, Indonesia.
[2] Somwanshi S, Kudale K, Dolas R, Kotade K. Formulatıon and evaluatıon of cosmetıc herbal face pack for glowıng skın. International Journal of Pharmacy and Biological Sciences. 2018:8 (4):49-52. https://doi.org/ 10.7897/2277-4343.083199.
[3] Rum I, Suherman H. Formulation and evaluation of peel-off gel mask from whole milk yogurt and seaweed (Eucheuma cottonii) as antioxidants sources. Pharmacy & Pharmacology International Journal. 2021;9(4):132–135. https://doi.org/10.15406/ppij.2021.09.00338.
[4] Kulkarnı S, Gupta D, Bhawsar S. Formulatıon and evaluatıon of actıvated charcoal peel off mask. International Journal of Pharmacy Research & Technology. 2019; 9 (2): 44-48. https://doi.org/10.31838/ijprt/09.02.06.

[5] Beringhs A, Rosa J, Stulzer H, Budal R. Sonaglio D. Green clay and aloe vera peel-off facial masks: response surface methodology applied to the formulation design. AAPS Pharm Sci Tech. 2013;14(1):444-455. https://doi.org/10.1208/s12249-013-9930-8.

[6] Budiman A, Aulifa D, Kusuma A, Kurniawan I, Sulastri A. Peel-off gel formulation from black mulberries (Morus nigra) extract as anti-acne mask. January National Journal of Physiology Pharmacy and Pharmacology. 2017; 7(10):987-994. https://doi.org/10.5455/njppp.2017.7.04131230520 17.

[7] Vieira R, Fernandes A, Kaneko T, Consiglieri V, Pinto C, Pereira C, et al. Physical and physicochemical stability evaluation of cosmetic formulations containing soybean extract fermented by Bifidobacterium animalis. Brazilian Journal of Pharmaceutical Science. 2009; 45(3):515-525.https://doi.org/10.1590/S1984-82502009000300018.

[8] Iqbal M, Ashiq M. Adsorption of dyes from aqueous solutions on activated charcoal. Journal of Hazardous Materials B. 2007; 139: 57–66. https://doi.org/10.1016/j.jhazmat.2006.06.007.

[9] Demirak A, Keskin F, Şahin Y, Kalemci V. Removal of ammonium from water by pine cone powder as biosorbent. Mugla Journal of Science and Technology. 2015; 1(1): 5-12. https://doi.org/10.22531/muglajsci.209992.

[10] Gaudreault P. Activated Charcoal Revisited. Clinical Pediatric Emergency Medicine. 2005; 6(2) :76-80. https://doi.org/10.1016/j.cpem.2005.04.005.

[11] Bhomick P, Supong A, Baruah M, Pongener C, Sinha D. Pine Cone biomass as an efficient precursor for the synthesis of activated biocarbon for adsorption of anionic dye from aqueous solution: Isotherm, kinetic, thermodynamic and regeneration studies. Sustainable Chemistry and Pharmacy. 2018; 10:41–49. https://doi.org/10.1016/j.scp.2018.09.001.

[12] Bhat M, Yadav N, Hashmi S. Pinecone-derived porous activated carbon for high performance all-solid-state electrical double layer capacitors fabricated with flexible gel polymer electrolytes. Electrochimica Acta. 2019; 304:94-108. https://doi.org/10.1016/j.electacta.2019.02.092.

[13] Eroglu E. Girgin S. A unique phenolic extraction method from olive oil macerate of *Hypericum perforatum* using DMSO: Assessment of in vitro anticancer activity, LC-MS/MS profile, total phenolic content and antioxidant capacity. South African Journal of Botany. 2021; 139: 6-11. https://doi.org/10.1016/j.sajb.2021.01.015.

[14] Orhan I, Kartal M, Gülpinar A, Cos P, Matheeussen A, Maes L. et al. Assessment of antimicrobial and antiprotozoal activity of the olive oil macerate samples of *Hypericum perforatum* and their LC-DAD-MS analyses. Food Chemistry. 2013;138 (2–3):870-875. https://doi.org/10.1016/j.foodchem.2012.11.053.

[15] Maisenbacher P, Kovar K. Analysis and stability of Hyperici oleum, Planta Med. 1992; 58(4): 351-354. https://doi.org/10.1055/s-2006-961483.

[16] Isacchi B, Bergonzi M, Carnevali F, Esch S, Vincieri F, Bilia A. Analysis and stability of the constituents of St. John's wort oils prepared with different methods. Journal of Pharmaceutical and Biomedical Analysis. 2007; 45: 756–761. https://doi.org/10.1016/j.jpba.2007.08.025.

[17] Gîtea D, Şipoş M, Mırcea T, Paşca B. The analysis of alcoholic extracts of hypericum species by: UVv/Vis spectrophotometry. Analele Universităţii din Oradea-Fascicula Biologie Tom. XVII / 1, 2010: 111-115.

[18] Milosevic T, Solujıc S, Sukdolak S. In vitro study of ethanolic extract of *Hypericum perforatum* L. on growth and sporulation of some bacteria and fungi. Turkish Journal of Biology. 2007: 31: 237-241.

[19] Eğri Ö, Erdemir N. Production of *Hypericum perforatum* oil-loaded membranes for wound dressing material and in vitro tests. Artıfıcıal Cells, Nanomedıcıne, And Bıotechnology. 2019; 47(1) :1404–1415. https://doi.org/10.1080/21691401.2019.1596933.

[20] Zhang J, Feng C, Ge P, Wang Q, Liu Y, Xu H, Zhou X. High purity separation of hypericin from *Hypericum perforatum* L. Extract with macroporous resin column coupling preparative liquid chromatography. Process Biochemistry. 2021; 103: 107–113. https://doi.org/10.1016/j.procbio.2021.02.012.

[21] Jarzębski M, Smułek W, Baranowska H, Masewicz L, Kobus-Cisowska J, Ligaj M, et al. Characterization of St. John's wort (*Hypericum perforatum L.)* and the impact of filtration process on bioactive extracts incorporated into carbohydrate-based hydrogels. Food Hydrocolloids. 2020; 104: 105748. https://doi.org/10.1016/j.foodhyd.2020.105748.

[22] Shimamori Y. Mitsunaka S, Yamashita H, Suzuki T, Kitao T, Kubori T, et al. Staphylococcal Phage in Combination with Staphylococcus epidermidis as a Potential Treatment for *Staphylococcus aureus*-Associated Atopic Dermatitis and Suppressor of Phage-Resistant Mutants. Viruses. 2021; 13 (7). https://dx.doi.org/10.3390/v13010007.

[23] Magnifico I, Petronio G, Venditti N, Cutuli M, Pietrangelo L, Vergalito F, et al. Atopic dermatitis as a multifactorial skin disorder. Can the analysis of pathophysiological targets represent the winning therapeutic strategy. Pharmaceuticals. 2020; 13(411). https://doi.org/10.3390/ph13110411.

[24] Lubbe J. Secondary infections in patients with atopic dermatitis. American Journal of Clinical Dermatology. 2003; 4 (9):641-654. https://doi.org/10.2165/00128071-200304090-00006.

[25] Nowicka D, Chilicka K, Dziendziora-Urbinska I. Host-microbe interaction on the skin and its role in the pathogenesis and treatment of atopic dermatitis. Pathogens. 2022; 11 (71). https://doi.org/10.3390/pathogens11010071.

[26] Lacour J. Skin microbiota and atopic dermatitis: toward new therapeutic options?. Annales de Dermatologie et de Vénéréologie. 2015;142(1):18-22. https://doi.org/10.1016/S0151-9638(15)30003-X.

[27] Li K, Tian S, Jiang J, Wang J, Chen X, Yan F. Pine cone shells-based activated carbon used for CO2 adsorption. Journal of Materials Chemistry A. 2016;4(14):5223–5234. https://doi.org/10.1039/C5TA09908K.

[28] Arsić I. Preparation and characterization of St. John's Wort herb extracts using olive, sunflower and palm oils. Acta Facultatis Medicae Naissensis. 2016;33(2):119-126. https://doi.org/10.1515/afmnai-2016-0013.

[29] Aydın G, Şirin N, Kekeçoğlu M, Türken T, Sipahi N., Göksu H. The use of natural preservative propolis and *hypericum perforatum* oil in herbal cream production. International Journal of Traditional and Complementary Medicine Research. 2021; 2 (1): 27 – 35. https://dergipark.org.tr/tr/pub/ijtcmr/issue/61352/807509.

[30] Tanjung Y, Julıantı A, Isnayantı I, Ricsa A. Formulation and evaluatıon of peel off gel facıal mask from arabica coffee fruıt peel extract (coffea arabica L.). International Journal of Applied Pharmaceutics. 2021;13(4):148-151. https://doi.org/10.22159/ijap.2021.v13s4.43845

[31] Bhalodia R, Shukla J. Antibacterial and antifungal activities from leaf extracts of cassia fistula l.: An ethnomedicinal plant. J. Adv. Pharm. Technol. Res. 2011; 2:104-109. https://doi.org/ 10.4103/2231-4040.82956.

[32] Daoud A, Malika D, Bakari S, Hfaiedh N, Mnafgui K, Kadri A, et al. Assessment of polyphenol composition, antioxidant and antimicrobial properties of various extracts of date palm pollen (DPP) from two Tunisian cultivars. Arab. J. Chem. 2015;12(8) 3075-3086. https://doi.org/10.1016/j.arabjc.2015.07.014.

[33] Ahmad I, Sheraz M, Ahmed S, Shaikh R, Vaid F, Khattak S, et al. Photostability and interaction of ascorbic acid in cream formulations. AAPS PharmSciTech. 2011;12(3):917. https://doi.org/ 10.1208/s12249-011-9659-1.

[34] Sheraz M, Khan M, Ahmed S, Kazi S, Khattak S, Ahmad, I. Factors affecting formulation characteristics and stability of ascorbic acid in water-in-oil creams. International Journal of Cosmetic Science. 2014;36: 494–504. https://doi.org/10.1111/ics.12152.

[35] Sarabandi D, Roudini G, Barahuie F. Activated carbon derived from pine cone as a framework for the preparation of n-heptadecane nanocomposite for thermal energy storage. Journal of Energy Storage. 2019; 24100795. https://doi.org/10.1016/j.est.2019.100795.

[36] Assefi M, Davar F, Hadadzadeh H. Green synthesis of nanosilica by thermal decomposition of pine cones and pine needles. Advanced Powder Technology. 2015; 26: 1583–1589. https://doi.org/10.1016/j.apt.2015.09.004.

[37] Zsirka B, Horvath E, Jarvas Z, Dallos A, Mako E, Kristof J. Structural and energetical characterization of exfoliated kaolinite surfaces. Appl. Clay Sci. 2016;124-125: 54-61. https://doi.org/10.1016/j.clay.2016.01.035.

[38] Sajjad M, Sarwar R, Ali T, Khan L, Mahmood S. Cosmetic uses of activated charcoal. International Journal of Community Medicine and Public Health. 2021; 8: 4572-4574. https://dx.doi.org/10.18203/2394-6040.ijcmph20213569.

[39] Orchard A, Vuuren S. Commercial essential oils as potential antimicrobials to treat skin diseases. Evidence-Based Complementary and Alternative Medicine. 2017;4517971: 92. https://doi.org/10.1155/2017/4517971.

[40] Elgayyar M, Draughon F. A, Golden D. A, Mount J. R. Antimicrobial activity of essential oils from plants against selected pathogenic and saprophytic microorganisms. Journal of Food Protection. 2001; 64:1019–1024. https://doı: 10.4315/0362-028x-64.7.1019.

[41] Burt S. Essential oils: their antibacterial properties and potential applications in foods-a review. Int. J. Food Microbiol. 2004;94: 223–253. https://doı:10.1016/j.ijfoodmicro.2004.03.022.

[42] Badnore A, Sorde K, Datir K, Ananthanarayan L, Pratap A, Pandit A. Preparation of antibacterial peel-off facial mask formulation incorporating biosynthesized silver nanoparticles. Applied Nanoscience. 2019;9: 279–287. https://doi.org/10.1007/s13204-018-0934-2.

[43] Rahmasari D, Ermawati D, Weka Nugraheni R, Ramadhaningtyas Putri D, Nur Pratiwi I. Design and development of peel-off mask gel formulation of citronella oil for acne vulgaris. In Proceedings of the 2nd Health Science International Conference (HSIC 2019), 157-163. ISBN: 978-989-758-462-6. https://doi.org/10.5220/0009126101570163.

[44] Ali S, Yosipovitch G. Skin pH: From Basic Science to Basic Skin Care. Acta Derm Venereol. 2013; 93: 261–267. https://doi.org/10.2340/00015555-1531.

[45] Hariyadi D, Isnaeni I, Sudarma S, Suciati S, Rosita N. Peel-off emulgel mask of *Cocos nucifera* L. extract using gelling agent carbomer 940 as antiacne against Propionibacterium acnes ATCC 11827. Journal of Advanced Pharmaceutical Technology & Research, 2022;11 (4): 220-225. https://doi.org/10.4103/japtr.JAPTR_51_20from: https://www.fhi.no/nettpub/utbruddsveilederen/

Volume 14, Issue 3, Page 165-171, 2025 https://doi.org/10.46810/tdfd.1738630 Research Article

BİNGÖL UNIVERSITY

Türk Doğa ve Fen Dergisi
Turkish Journal of Nature and Science
www.dergipark.gov.tr/tdfd

Investigation of the Effects of CNC Nanoparticle-Added Nanofluids on the Machinability of Cupral 4M Alloy

Üsame Ali USCA[1*]

[1]Selçuk University, Akşehir Faculty of Engineering and Architecture, Mechanical Engineering Department, Konya, Türkiye
Üsame Ali USCA ORCID No: 0000-0001-5160-5526

**Corresponding author: ali.usca@selcuk.edu.tr*

(Received: 09.07.2025, Accepted: 03.09.2025, Online Publication: 26.09.2025)

Keywords
Cupral 4M, Nanofluid, Minimum quantity lubrication, Crystalline nano cellulose

Abstract: The machinability of copper-nickel-based alloys, such as Cupral 4M, is known to be quite challenging in the manufacturing industry due to their high thermal conductivity, sticky chip formation, and susceptibility to tool wear. Conventional cooling and lubrication methods are insufficient for improving the machinability of these materials, resulting in a negative impact on machinability metrics such as production quality and tool life. In this study, the effects of adding 0.5 wt% CNC nanopowder to the MQL fluid on the milling process of Cupral 4M material were investigated. The experiments were conducted under two different cutting speeds (125-150 m/min), two different feed rates (0.04-0.06 mm/rev), and three different cooling/lubrication conditions (dry, pure MQL, and CNC nanoparticle MQL). As a result of the experiment, surface roughness, tool wear, and energy consumption were measured, and the obtained data were compared. The addition of CNC nanopowder to MQL fluid provided significant improvements (up to 66% in surface quality, 39% in tool wear, and 10% in energy consumption) in all three results compared to dry and MQL conditions. These results indicate that the addition of CNC nanoparticles has a friction-reducing and tribofilm-protecting effect in the cutting zone. This study fills one of the essential gaps in the literature on improving the sustainable millability of Cupral 4M material and reveals the effectiveness of nanoparticle-added MQL fluids.

CNC Nanopartikül Katkılı Nanoakışkanların Cupral 4M Alaşımının İşlenebilirliği Üzerine Etkilerinin Araştırılması

Anahtar Kelimeler
Cupral 4M, Nanosıvı, Minimum miktarda yağlama, Kristalin nano selüloz

Öz: Cupral 4M gibi bakır-nikel esaslı alaşımların işlenebilirliği, yüksek termal iletkenlik, yapışkan talaş oluşumu ve takım aşınmasına yatkınlık nedeniyle imalat endüstrisinde oldukça zorlu işlenebilirliğe sahip olarak bilinir. Geleneksel soğutma ve yağlama yöntemleri bu malzemelerin işlenebilirliğinde yetersiz kalmakla birlikte, üretim kalitesi ve takım ömrü gibi işlenebilirlik metrikleri üzerinde olumsuzluğa neden olmaktadır. Bu çalışmada, ağırlıkça %0,5 CNC nanotozu katkılı MQL sıvısının Cupral 4M malzemesinin frezeleme işlemi üzerindeki etkileri incelenmiştir. Deneyler iki farklı kesme hızı (125-150 m/dk), iki farklı ilerleme hızı (0,04-0,06 mm/dev) ve üç farklı soğutma/yağlama koşulu (kuru, saf MQL, CNC nano parçacık MQL) altında gerçekleştirilmiştir. Deney sonucu olarak yüzey pürüzlülüğü, takım aşınması ve enerji tüketimi ölçülmüş, elde edilen veriler karşılaştırmalı olarak irdelenmiştir. CNC nanotoz ilaveli MQL sıvısı, kuru ve MQL ortamına göre her üç sonuçta da anlamlı iyileşmeler (yüzey kalitesinde %66'ya, takım aşınmasında %39'a, enerji tüketiminde ise %10'a kadar) sağlamıştır. Bu sonuçlar, CNC nano partikül ilavesinin kesme bölgesinde sürtünme azaltıcı ve tribo-film koruyucu bir etki oluşturduğunu göstermiştir. Bu çalışma, Cupral 4M malzemesinin sürdürülebilir frezelenebilirliğini artırmaya yönelik literatürdeki önemli boşluklardan birini doldurmakla birlikte ve nano partikül katkılı MQL sıvılarının etkinliğini ortaya çıkarmıştır.

1. INTRODUCTION

Machining is one of the fundamental principles of producing precise, economical, and efficient parts in modern manufacturing. Machining, particularly milling, plays a central role in the production of complex geometries in industries requiring high precision, such as aerospace, automotive, mould, and energy [1]. This method enables the machining of complex geometries, such as slots, precision molds, and complex forms, with high accuracy [2]. One of the most decisive factors in the success of these processes is the adequate cooling and lubrication of the cutting zone.

There are many different cooling/lubrication (C/L) methods used in machining (flood, cryogenic, minimum quantity lubrication, etc.). Minimum quantity lubrication (MQL) is widely used to reduce power consumption, ensure environmental sustainability, improve surface quality, effectively lubricate the cutting zone, and extend tool life. Traditional (flood) cutting and lubrication (C/L) media, commonly used in machining, are achieved by using high volumes of water and solvent-based cutting fluids. This not only wastes fluid but also creates a significant environmental waste burden. [3, 4]. This poses a significant disadvantage in terms of both liquid waste and energy and cost. However, MQL media offer an environmentally friendly and economical alternative to traditional lubrication systems by spraying the liquid in tiny particles [4, 5]. The minimum quantity lubrication (MQL) method is widely used in industry and scientific studies to reduce production costs, extend tool life, improve surface quality, and ensure environmental sustainability [6-9]. MQL fluid provides the necessary amount of lubrication to the cutting area, reducing cutting temperatures and improving friction conditions, thereby enhancing tool wear and surface quality [10-12]. Thanks to these advantages, MQL systems stand out as a solution that increases environmental sustainability and process efficiency in manufacturing processes [13]. However, research was conducted to further enhance the benefits of MQL systems in machining, and as a result, modifying the MQL fluid content has been proposed as an alternative method.

In recent years, researchers have reported that adding nano-sized additives to MQL fluids has improved the tribological and thermal properties of the fluids. [14]. The addition of nanoparticles to MQL fluids significantly reduces friction in the cutting zone and significantly improves lubrication performance. For example, in the milling of Ti-6Al-4V material, MQL fluids containing Al_2O_3 nanoparticles were found to substantially reduce cutting force and surface roughness compared to MQL fluids without additives [15]. Similarly, in hybrid nanopowder-added MQL systems, it was found that a synergistic improvement in wear and thermal transport performance is achieved by combining different ionic and carbon-based nanoparticles [16]. Additionally, positive effects on friction and wear were demonstrated in nanofluid MQL systems utilising MoS_2–CNT mixtures, enhancing the machinability of Ni-based alloys [17]. Positive results of adding nanopowders to MQL liquids have also been mentioned explicitly in the literature [18-20]. As a result, MQL fluids with nanopowder additives offer advantages in thermal conductivity and tribological efficiency compared to pure MQL fluids. They also increase cutting efficiency and productivity in difficult-to-machine materials. These developments demonstrate the potential of nanostructured additives, particularly in cutting operations of difficult-to-machine materials.

Machining copper-nickel-based alloys is challenging due to problems such as high thermal conductivity, chip formation, rapid wear, and surface quality. The selection of appropriate cutting parameters and effective cooling/lubrication environments is critical for the machinability of these materials. Original data on the machinability of these materials is relatively limited in the literature. Furthermore, there is no study investigating the effects of MQL fluids containing CNC (Cellulose Nanocrystal) nanopowder on the machinability of Cupral 4M. This lack highlights the need for more comprehensive investigation of the potential effects of new-generation MQL fluids on this particular alloy. This study aims to investigate the effects of MQL fluid containing 0.5 wt% CNC nanopowder on the surface quality, tool wear, and power consumption on the machinability of Cupral 4M alloy. In this context, different cutting speeds and feed rates, along with three different cooling/lubrication environments, were used in the experiments. This study makes an original contribution to the literature by demonstrating the feasibility of a new, environmentally friendly cooling/lubrication strategy to enhance the machinability of Cupral 4M.

2. MATERIAL AND METHOD

In this study, the CuAl10Ni5Fe4 (commercial name “Cupral 4M”) material, which is frequently used in press moulds, bearing bushes, aircraft landing gear, and welding electrodes, was employed. Two 21 x 50 x 50 mm pieces of this workpiece, used for milling experiments, were supplied by Sağlam Metal. The chemical composition, mechanical properties, and physical properties of the workpiece are listed in Tables 1, 2, and 3, respectively.

Table 1. Chemical composition of Cupral 4M

Chemical Composition (wt.%)					
Al	**Fe**	**Ni**	**Mn**	**Cu**	**Other**
8.5-11.5	3-5	4-6	Max. 1	75-85	difference

Table 2. Mechanical properties of Cupral 4M

Mechanical Properties	
Hardness (HB)	170-220
Tensile Strength (N/mm²)	650-800
Yield Strength (N/mm²)	270-400
Moduls of Elasticity (GPa)	124
Compressive Strenght (N/mm²)	1200

Table 3. Mechanical properties of Cupral 4M

Physical Properties	
Electrical Conductivity (MS/m)	5
*Thermal Expansion Coefficient (1/K * 10^{-6})*	16
Thermal Conductivity (20°C, W/mK))	42
Density (g/cm³)	7.45

A three-axis (x-y-z) Dahlih MCV-860 vertical machining centre (VMC) was used for machinability tests on the Cupral 4M workpiece. The workpiece was clamped in a precision vice and fixed to the VMC. Before the test, a 1 mm pass was removed from the workpieces with a surface scanning tool to ensure the flatness of the workpiece surface and to remove material slag. Two different cutting speeds (125-150 m/min), two different feed rates (0.04-0.06 mm/rev), and three different C/L media (Dry-MQL-Nano) were selected as experimental variables. Parameters were determined from preliminary experiments. To fully explore the relative effects of the variables, a complete experimental design system (22 × 31) was adopted. Both surfaces of the materials were used in the tests. Four experiments were conducted on each workpiece surface, totalling 12 experiments (Figure 1).

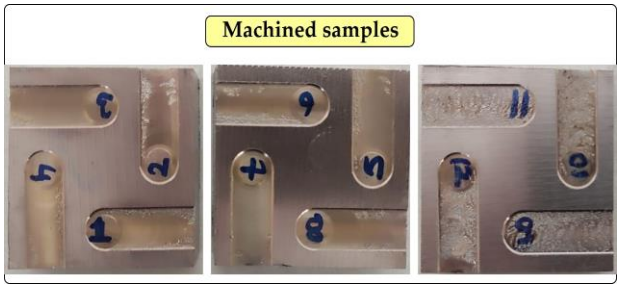

Figure 1. Machined workpiece surface

A collet tool holder was used in the experiments on this machine with a BT-40 taper. A new insert (ISCAR HM 90 APKT 1003PDR IC908) was used for each experiment. The insert was clamped onto a 12 mm diameter indexable milling cutter (SMOXH ST90 AP10D12W12L120Z01). The milling cutter was mounted in a MAS 403 BT 40 tool holder with a clamping length of 50 mm. A "Zig" tool path was generated in the experiments using commercial CAM software. The milling length (L) was kept constant at 30 mm, and the cutting width or step (ae) was kept constant at 12 mm. The cutting depth (ap) was set at 0.5 mm for each experiment.

Dry and MQL media were used in the experiments to investigate the usability of the nano C/L medium produced with CNC nanopowder on the workpiece. A Werte-STN 15 device was used for the MQL and nanofluid media. KT-2000 synthetic oil was chosen for the MQL medium due to its high hydrodynamic lubrication properties [21]. The operating pressure of the device was set at 6 bar. The 3 mm diameter MQL nozzle was kept fixed at a distance of 75 mm from the workpiece during the experiments. The operating flow rate of the MQL device was determined as 50 mL/h. Water-soluble and environmentally friendly Cellulose Nanocrystal (CNC) nanopowder was used for the nanofluid. More details about the preparation of the CNC nanofluid, which was added to pure water at a concentration of 0.5% by volume, can be found in the relevant literature [21]. This synthetic oil, prepared with pure water, was sent to the experimental area with the MQL device without mixing.

After the experiments, the workpiece surface was cleaned with alcohol and air to prepare it for surface roughness measurements. Surface roughness measurements were performed with an Insize ISR-C100 surface roughness measuring device. The device was first calibrated with a calibration sample. Five different measurements were taken from each machined surface, and the average of these measurements was determined as the surface roughness value. The average surface roughness value (Ra) was taken into account when determining the surface roughness value. Another result obtained from the experiments was the maximum flank wear (Vbmax). After the experiments were completed, each cutting edge was cleaned with compressed air, and the maximum wear amounts were measured and recorded under a digital microscope (Insize ISM PM200SB). Finally, the power consumption for each machinability test was performed using a HIOKI PW 3198 device. The device is capable of performing precise measurements for all test parameters according to international measurement standards. The current and voltage values obtained from three phases during the tests were used to obtain energy consumption results using the device software. Figure 1 represents the experimental schematic.

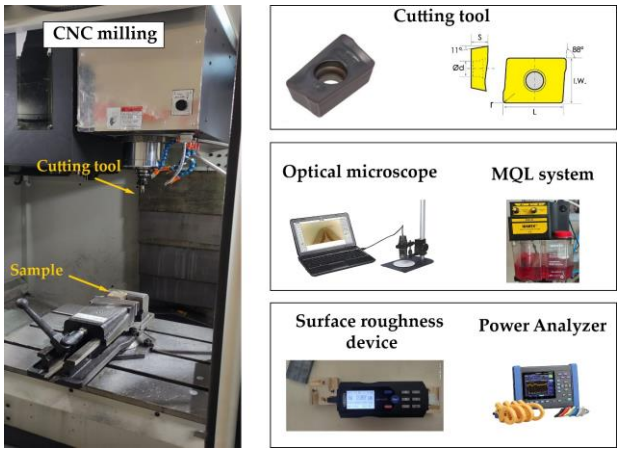

Figure 2. Experimental setup

3. RESULTS

This study examined the differences between CNC nanopowder-added MQL fluid and other C/L methods in the milling of Cupral 4M material. Machinability metrics, including surface roughness, flank wear, and energy consumption, were analysed.

3.1. Analysis of surface roughness results

In terms of machinability, surface roughness (R_a) is a critical parameter in studies evaluating environmentally friendly and high-performance manufacturing methods [22]. Surface roughness is considered one of the most essential indicators of machinability and is a quality criterion that directly affects the functional performance of parts produced by machining [23]. The surface quality

of a part is not only an aesthetic element, but also a determinant of numerous engineering parameters such as fatigue resistance, wear behaviour, lubrication capacity, sealing performance, and assembly fit [24, 25]. Especially in precision components used in the aerospace, automotive, mold and die making, and energy sectors, surface roughness must be kept within specific tolerance ranges. Figure 3 shows the effects of experiments conducted under different cutting parameters and different C/L conditions on the surface roughness value. The best surface quality (R_a = 1.235 µm) was achieved in the C/L condition of CNC nanoparticle-added MQL at a cutting speed of 150 m/min and a feed rate of 0.04 mm/rev. In this cutting parameter group, where the best surface quality was achieved, other surface roughness values were obtained: R_a = 3.679 µm for the dry environment and R_a = 2.57 µm for the MQL fluid. The lowest surface quality (R_a = 4.204 µm), as expected, was achieved in the dry environment, at the lowest cutting speed and highest feed rate. In this cutting parameter group, where the worst surface quality was achieved, other surface roughness values were obtained: R_a = 3.32 µm for the MQL fluid and R_a = 2.42 µm for the CNC nanoparticle-added MQL fluid. In general, experiments conducted with the CNC nanoparticle-added MQL fluid showed improvements in surface roughness values between 42% and 66% compared to the dry environment and between 27% and 52% compared to the MQL fluid alone.

The effect of CNC nanopowder-added MQL fluid on surface quality is essential for demonstrating the potential of nanoadditives to improve lubrication and heat transfer [26]. Thanks to the high specific surface area of CNC nanopowder, it is expected to reduce friction in the cutting zone and improve temperature distribution. This results in a more balanced interaction between the tool and the workpiece. These effects are directly reflected in surface roughness, resulting in smoother, more homogeneous, and functional surfaces. Studies in the literature support these findings [21, 27]. Furthermore, the performance comparisons under different cutting and feed speeds, as shown in Figure 3, indicate that the CNC-added MQL fluid yielded the best results across all parameter combinations. This study not only demonstrates the feasibility of an environmentally friendly and innovative cooling condition but also provides concrete data on how production quality can be sustainably improved by influencing cutting parameters. This analysis of surface roughness quantitatively demonstrates the superiority of nanotechnology-based lubrication systems over conventional MQL and dry conditions, guiding future production strategies.

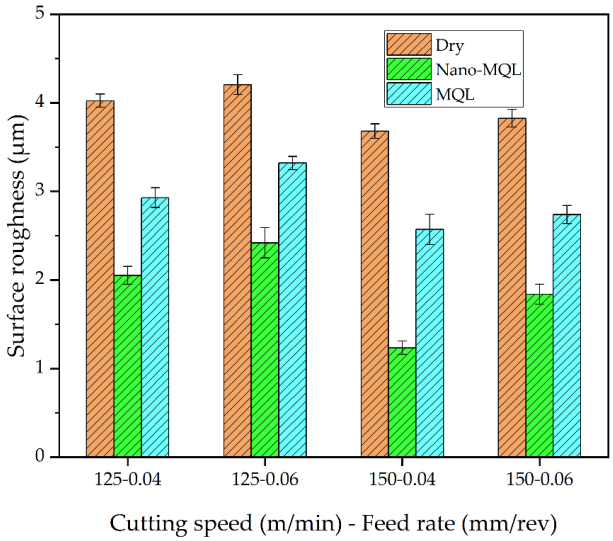

Figure 3. Effect of different C/L conditions and different cutting parameters on surface roughness

3.2. Analysis of flank wear results

Tool wear is one of the most critical determinants of productivity and cost in machining processes. Therefore, flank wear is a fundamental wear factor that directly affects the performance of the cutting tool [28]. Flank wear is a type of wear that occurs on the side surface of the tool in contact with the workpiece and grows over time in parallel with the feed rate. This type of wear generally occurs due to friction, temperature, and plastic deformation during the cutting process [29]. As flank wear increases, tool sharpness decreases, cutting forces increase, surface roughness deteriorates, and cutting temperature increases, creating a feedback loop that accelerates wear [30]. Furthermore, as wear progresses, deviations from dimensional tolerances increase, and the risk of component failure increases. Therefore, flank wear is not only an indicator of tool life but also an important criterion that determines the stability and economic efficiency of the production process. Figure 4, illustrates the effects of different C/L environments and cutting parameters on flank wear. The lowest flank wear value (V_b = 0.280 mm) was obtained in the CNC nanopowder-added MQL C/L condition at a cutting speed of 150 m/min and a feed rate of 0.04 mm/rev. In these cutting parameters, where the lowest flank wear value was obtained, other flank wear values were determined as 0.439 mm and 0.373 mm for dry environment and MQL fluid, respectively. The highest wear value (V_b = 0.480 mm) was achieved in a dry environment, at the highest cutting speed and feed rate. In this cutting parameter group where the highest flank wear value was obtained, other wear values were obtained as V_b = 0.397 mm for MQL fluid and V_b = 0.304 mm for CNC nanoparticle added MQL fluid. In experiments conducted with CNC nanoparticle-added MQL fluid, it was observed that flak wear values improved by 36-39% compared to a dry environment and by 23-31% compared to MQL fluid.

Upon examination of the graph (Fig. 4), it is evident that the CNC nanoparticle additive significantly reduces flank wear values. Carbon-based nanoparticles, such as CNC, have a very high surface-to-area ratio. Thanks to this

property, when dispersed in the cutting zone, they easily penetrate the friction zone between the tool and the workpiece. It is believed that this can reduce flank wear values by reducing the friction coefficient and resulting in less mechanical friction in the cutting zone. Furthermore, CNC particles, especially in the MQL system, pulverise and reach the cutting zone, forming a lubricating film on the tool surface [31]. This directly prevents contact between the tool and the workpiece, eliminating the microscopic causes of wear initiation. Studies in the literature support the obtained results [21, 27, 31].

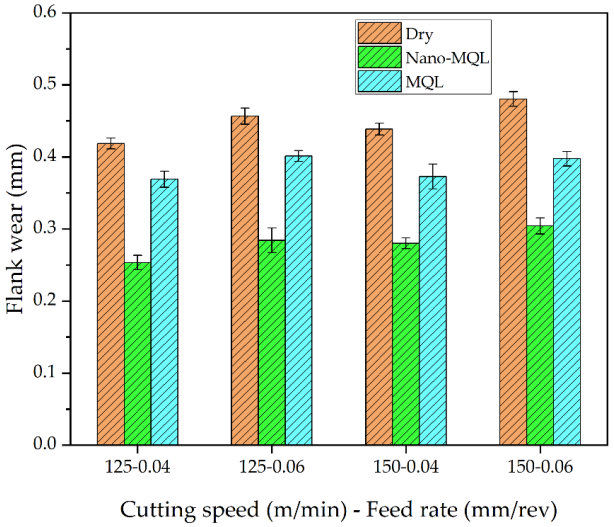

Figure 4. Effect of different C/L conditions and different cutting parameters on flank wear

3.3. Analysis of energy consumption

In the modern manufacturing industry, energy consumption has become one of the fundamental performance criteria encompassing not only technical but also environmental and economic dimensions of machinability [32]. While traditional machinability analyses are often evaluated based on mechanical outputs such as surface roughness, tool wear, and chip formation, energy efficiency has emerged as a key factor that should be assessed in conjunction with these outputs [33]. The total energy consumption of a cutting process directly affects production costs and determines the carbon footprint and environmental impact. Especially in Industry 4.0-focused systems where sustainable production targets are adopted, achieving high-quality outputs with low energy consumption is a primary goal of process optimization. Therefore, examining energy consumption in cutting processes is crucial. Figure 5 shows the effects of different cutting fluids on the machinability of Cupral 4M material with different cutting parameters. The CNC nanopowder-added MQL fluid exhibited the lowest energy consumption across all cutting parameters. The power consumption of the MQL device, which sprays the fluids onto the cutting zone, was neglected in the comparisons. For this type of cutting process, the effect of cutting media on power consumption is evident. The lowest power consumption in the experiments was 19.92 kJ, at a cutting speed of 150 m/min and a feed rate of 0.06 mm/rev. It was determined that lower power consumption would occur because the unit material would be processed in less time at high cutting speeds and feed rates. It can be said that the power consumption values are lower due to the reduction in cutting time at high cutting and feed speeds, the thermal softening of the workpiece, and the reduction of friction between the tool and the material, resulting from the presence of nanoparticles [34-37]. The highest power consumption, 25.65 kJ, occurred at the lowest cutting parameters. In other experiments, CNC nanopowder-added MQL fluid was found to reduce energy consumption by 1.6-9.9% compared to dry media and by 0.8-6.5% compared to MQL fluid.

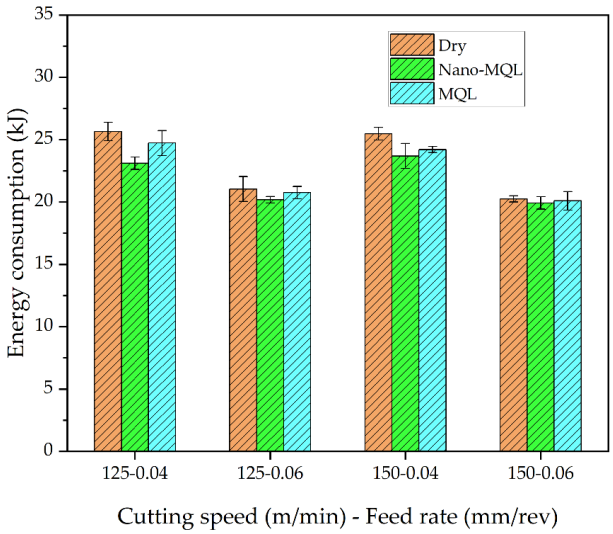

Figure 5. Effect of different C/L conditions and different cutting parameters on energy consumption

4. CONCLUSION

This study examined how the machinability of Cupral 4M material was affected by CNC nanopowder-added MQL fluid under various cutting conditions. In this article, the proposed CNC nanopowder-added MQL fluid was compared with dry media and pure MQL fluid to examine its advantages and disadvantages. The key results obtained from the experiments are listed below:

- Surface roughness results indicate that the MQL fluid containing 0.5% CNC nanopowder significantly improved surface roughness compared to other media. Experiments with the MQL fluid containing CNC nanoparticles demonstrated improvements in surface roughness of 42-66% compared to dry media and 27-52% compared to the MQL fluid. It can be concluded that the CNC nanopowder additive enhances surface quality by reducing friction in the cutting zone and creating a more uniform lubricant film. The results demonstrate that the MQL fluid containing CNC nanoparticles provides an effective solution for precision applications that require high surface quality.

- The effect of 0.5% CNC nanopowder-added MQL fluid on flank wear compared to other conditions has been extensively studied. Experiments with the CNC nanoparticle-added MQL fluid showed

improvements in flank wear values between 36% and 39% compared to dry conditions and between 23% and 31% compared to MQL fluid. The addition of CNC nanoparticles to the MQL fluid resulted in a significant reduction in flank wear. Thus, the study demonstrated that an environmentally friendly cutting fluid can be used to mill difficult-to-machine alloys, such as Cupral 4M.

- The addition of CNC nanopowder to MQL fluid also resulted in improved power consumption. In other experiments, MQL fluid with CNC nanopowder added reduced energy consumption by 1.6-9.9% compared to dry conditions and by 0.8-6.5% compared to MQL fluid alone. The study offers a comprehensive evaluation of key industry issues, including energy efficiency and environmental sustainability. Furthermore, this study presents a compelling case for the widespread adoption of CNC nanopowder in MQL fluids within the manufacturing industry

Future studies can investigate the effects of CNC nanoparticles on machinability by adding them to mineral-based coolants. Furthermore, the wear phenomena affecting cutting temperatures, cutting forces, and tool wear can be examined in more detail. It is also essential to investigate the effects of CNC nanopowder additives on the machinability of steels frequently used in the manufacturing industry. This will enable the expansion of industrial applications for environmentally friendly nanoadditives. While CNC nanopowder additives to MQL fluids have positive effects on machinability, their industrial use is limited by the cost of powder production. As the cost of obtaining nanopowder decreases with the advancement of production technologies, its use in industry is expected to increase.

REFERENCES

[1] Uzun M, Usca ÜA, Kuntoglu M, Gupta MK. Influence of tool path strategies on machining time, tool wear, and surface roughness during milling of AISI X210Cr12 steel. Int J Adv Manuf Tech. 2022;119(3-4):2709-20.

[2] Kar BC, Panda A, Kumar R, Sahoo AK, Mishra RR. Research trends in high speed milling of metal alloys: A short review. Mater Today-Proc. 2020;26:2657-62.

[3] Polo S, Rubio EM, Marín MM, de Pipaón JMS. Evolution and Latest Trends in Cooling and Lubrication Techniques for Sustainable Machining: A Systematic Review. Processes. 2025;13(2).

[4] Sap S. Understanding the Machinability and Energy Consumption of Al-Based Hybrid Composites under Sustainable Conditions. Lubricants. 2023;11(3).

[5] Sap E, Usca ÜA, Degirmenci Ü, Sap S, Uzun M. Evaluation of Machinability and Energy Consumption of CK45 Steel Using Synthetic-Based Nanofluid and Minimum Quantity Lubrication Cutting Fluid. Metals-Basel. 2025;15(1).

[6] Sap E, Usca ÜA, Uzun M. Machining and optimization of reinforced copper composites using different cooling-lubrication conditions. J Braz Soc Mech Sci. 2022;44(9).

[7] Sap E, Usca ÜA, Sap S, Polat H, Giasin K, Kalyoncu M. Understanding the effects of machinability properties of Incoloy 800 superalloy under different machining conditions using artificial intelligence methods. Mater Today Commun. 2024;38.

[8] Sap S, Acar E, Degirmenci U, Usca UA, Memis S, Sener R. Machinability of different Cu-Gr composites in milling: Performance parameters prediction via machine learning models. Expert Syst Appl. 2025;272.

[9] Dogan MA, Yazman S, Gemi L, Yildiz M, Yapici A. A review on drilling of FML stacks with conventional and unconventional processing methods under different conditions. Compos Struct. 2022;297.

[10] Dambatta YS, Li CH, Yang M, Beikai LI, Gao T, Liu MZ, et al. Grinding with minimum quantity lubrication: a comparative assessment. Int J Adv Manuf Tech. 2023;128(3-4):955-1014.

[11] Sap E, Usca ÜA, Sap S. Impacts of Environmentally Friendly Milling of Inconel-800 Superalloy on Machinability Parameters and Energy Consumption. Int J Pr Eng Man-Gt. 2024;11(3):781-97.

[12] Usca UA, Sap S, Uzun M, Degirmenci U. Assessment of the machinability and energy consumption characteristics of Cu-6Gr hybrid composites under sustainable operating. J Braz Soc Mech Sci. 2024;46(4).

[13] Degirmenci Ü, Usca ÜA, Sap S. Machining characterization and optimization under different cooling/lubrication conditions of Al-4Gr hybrid composites fabricated by vacuum sintering. Vacuum. 2023;208.

[14] Chinchanikar S, Kore SS, Hujare P. A review on nanofluids in minimum quantity lubrication machining. J Manuf Process. 2021;68:56-70.

[15] Bai XF, Li CH, Dong L, Yin QA. Experimental evaluation of the lubrication performances of different nanofluids for minimum quantity lubrication (MQL) in milling Ti-6Al-4V. Int J Adv Manuf Tech. 2019;101(9-12):2621-32.

[16] Abellán-Nebot JV, Ameen KH, Khan AM, Mondragón R. Application of Hybrid Nanofluids in MQL Assisted Machining Operations: Exploring Synergies and Establishing Guidelines. Int J Pr Eng Man-Gt. 2025;12(2):657-89.

[17] Zhang YB, Li CH, Jia DZ, Li BK, Wang YG, Yang M, et al. Experimental study on the effect of nanoparticle concentration on the lubricating property of nanofluids for MQL grinding of Ni-based alloy. J Mater Process Tech. 2016;232:100-15.

[18] Günay M, Korkmaz ME. Understanding the Relationship between Surface Quality and Chip Morphology under Sustainable Cutting Environments. Materials. 2024;17(8).

[19] Pal A, Chatha SS, Sidhu HS. Tribological characteristics and drilling performance of nano-MoS-enhanced vegetable oil-based cutting fluid using eco-friendly MQL technique in drilling of

AISI 321 stainless steel. J Braz Soc Mech Sci. 2021;43(4).
[20] Wang Y, Liu CF. State-of-the-art on minimum quantity lubrication in green machining. J Clean Prod. 2023;429.
[21] Usca UA. The Effect of Cellulose Nanocrystal-Based Nanofluid on Milling Performance: An Investigation of Dillimax 690T. Polymers-Basel. 2023;15(23).
[22] Şap S. Effects on Machinability of Minimum Quantity Lubrication Strategy during Milling of ST52 Steel. Türk Doğa ve Fen Dergisi. 2023;12(1):82-90.
[23] Yildirim ÇV. Investigation of hard turning performance of eco-friendly cooling strategies: Cryogenic cooling and nanofluid based MQL. Tribol Int. 2020;144.
[24] Abellán-Nebot JV, Pastor CV, Siller HR. A Review of the Factors Influencing Surface Roughness in Machining and Their Impact on Sustainability. Sustainability-Basel. 2024;16(5).
[25] Liao ZR, la Monaca A, Murray J, Speidel A, Ushmaev D, Clare A, et al. Surface integrity in metal machining - Part I: Fundamentals of surface characteristics and formation mechanisms. Int J Mach Tool Manu. 2021;162.
[26] Zerooglu T, Degirmenci Ü, Sap S. A Study on the Machinability and Environmental Effects of Milling AISI 5140 Steel in Sustainable Cutting Environments. Machines. 2024;12(7).
[27] Sap S, Usca A, Tarih YS, Yar A, Kuntoglu M, Gupta MK. Novel Use of Cellulose Based Biodegradable Nano Crystals in the Machining of PPS Composites: An Approach Towards Green Machining. Int J Pr Eng Man-Gt. 2024;11(1):1-19.
[28] Sap S. Machining and Energy Aspect Assessment with Sustainable Cutting Fluid Strategies of Al-12Si Based Hybrid Composites. Int J Pr Eng Man-Gt. 2024;11(1):33-53.
[29] Salur E. Understandings the tribological mechanism of Inconel 718 alloy machined under different cooling/lubrication conditions. Tribol Int. 2022;174.
[30] Hsu SM, Shen MC, Ruff AW. Wear prediction for metals. Tribol Int. 1997;30(5):377-83.
[31] Mughal K, Mughal MP, Farooq MU, Anwar S, Ammarullah MI. Using Nano-Fluids Minimum Quantity Lubrication (NF-MQL) to Improve Tool Wear Characteristics for Efficient Machining of CFRP/Ti6Al4V Aeronautical Structural Composite. Processes. 2023;11(5).
[32] Dağılgan G. Kayit Dişi Ekonomi Özelinde Diş Ticaret Ve Ekonomik Büyümenin Enerji Tüketimi Üzerindeki Etkisi: G20 Ülkeleri Örneği. Toplum Ekonomi Ve Yönetim Dergisi. 2023;4(2):214-27.
[33] Eren N, Hayat F, Günay M. Sertleştirilmiş 1.2367 Takım Çeliğinin İşlenmesinde Enerji Tüketiminin Analizi ve Modellenmesi. Manufacturing Technologies and Applications. 2020;1(3):41-9.
[34] Li PN, Chen M, Kang XJ, Zhang L, Zhou M. The Optimization of Cutting Parameters for Surface Roughness in High Speed Milling based on Taguchi Method. Mater Sci Forum. 2012;723:196-+.
[35] Liu ZQ, Zhang F, Jiang FL. Investigations of Transient Machined Workpiece Surface Temperature in High Speed Peripheral Milling Using Inverse Method. Mater Sci Forum. 2012;723:14-9.
[36] Yogeswaran M, Kadirgama K, Rahman MM, Devarajan R. Temperature Analysis When Using Ethylene-Glycol-Based Tio as a New Coolant for Milling. Int J Automo Mech E. 2015;11:2272-81.
[37] Storchak M, Hlembotska L, Melnyk O. Generation of Mechanical Characteristics in Workpiece Subsurface Layers through Milling. Materials. 2024;17(7).Carlson BM. Human embryology and developmental biology. 4th ed. St. Louis: Mosby; 2009.

Volume 14, Issue 3, Page 172-182, 2025 https://doi.org/10.46810/tdfd.1708150 Research Article

BİNGÖL UNIVERSITY

Türk Doğa ve Fen Dergisi
Turkish Journal of Nature and Science
www.dergipark.gov.tr/tdfd

Combined Humic Acid and Lichen-Derived Endophytic Bacteria Application Alleviates Salt Stress-Induced Oxidative Damage in Alfalfa (*Medicago sativa* L.)

Aytekın MAMMADOVA[1], Ökkeş ATICI[1*], Özlem GÜLMEZ[1]

[1]Department of Biology, Faculty of Science, Atatürk University, 25240 Erzurum, Türkiye
Aytekın MAMMADOVA ORCID: 0009-0008-6109-1221
Ökkeş ATICI ORCID: 0000-0001-6256-5101
Özlem GÜLMEZ ORCID: 0000-0002-7199-4634

**Corresponding author: oatici@atauni.edu.tr*

(Received: 28.05.2025, Accepted: 03.09.2025, Online Publication: 26.09.2025)

Keywords
Salt stress, Alfalfa, Humic acid, Endophyte, Antioxidant, Lichen,

Abstract: This study investigates the synergistic effects of leonardite-sourced humic acid (HA) and a lichen-derived endophytic bacterium (*Bacillus wiedmannii*) in mitigating salt stress in alfalfa (*Medicago sativa* L., cv. Konya). Alfalfa seeds were grown in a peat-perlite mix with different combinations of 100 mM NaCl, HA (500 or 1000 mg L^{-1}), and *B. wiedmannii*. After 35 days, relative water content (RWC), ROS (H_2O_2, $O_2^{\cdot-}$), MDA, antioxidant enzyme activities, and photosynthetic pigments were measured. The salt stress alone reduced RWC, the photosynthetic pigment amount, and the antioxidant enzyme activities, while elevating H_2O_2 and $O_2^{\cdot-}$, and MDA accumulation. HA or *B. wiedmannii* (Bw) individually partially ameliorated these effects, however, the combined HA+Bw treatment under saline conditions (especially 1000 mg L^{-1} HA+Bw+NaCl) elevated RWC, and reduced ROS and MDA levels close to the control values. In addition, the antioxidant enzyme activities and the photosynthetic pigment contents were enhanced under the combined treatments compared to the salt alone. These results demonstrate a synergistic effect between HA and *B. wiedmannii* in alleviating salt stress in the alfalfa by enhancing water status, reducing oxidative damage, and activating antioxidant defenses, suggesting that the co-application of HA and *B. wiedmannii* is a promising strategy for improving salt tolerance in forage crops.

Humik Asit ve Liken Türevli Endofitik Bakterilerin Kombine Uygulaması, Yoncada (*Medicago sativa* L.) Tuz Stresi Kaynaklı Oksidatif Hasarı Yatıştırır

Anahtar Kelimeler
Tuz stresi, Yonca, Humik asit, Endofit, Antiosidan, Liken,

Öz: Bu çalışma, leonardit kaynaklı humik asit (HA) ile liken kökenli bir endofitik bakteri (*Bacillus wiedmannii*) arasındaki sinerjik etkinin, yonca bitkisinde (*Medicago sativa* L., cv. Konya) tuz stresini hafifletmedeki rolünü araştırdı. Yonca tohumları, 100 mM NaCl, HA (500 veya 1000 mg L^{-1}) ve *B. wiedmannii*'nin farklı kombinasyonlarını içeren turba-perlit karışımında ekildi. 35 gün sonra, bağıl su içeriği (RWC), reaktif oksijen türleri (H_2O_2, $O^{\cdot-}$), MDA (malondialdehit), antioksidan enzim aktiviteleri ve fotosentetik pigment düzeyleri ölçülmüştür. Tuz stresi, tek başına uygulandığında RWC, fotosentetik pigment miktarı ve antioksidan enzim aktivitelerinde azalmaya, H_2O_2, $O^{\cdot-}$, ve MDA birikiminde ise artışa neden olmuştur. HA veya *B. wiedmannii* tek başına bu olumsuz etkileri kısmen hafifletmiştir. Ancak, özellikle 1000 mg L^{-1} HA+*B. wiedmannii*+NaCl kombinasyonu, RWC'yi artırmış ve ROS ile MDA seviyelerini kontrol grubuna yakın düzeylere düşürmüştür. Ayrıca, bu kombine uygulama antioksidan enzim aktiviteleri ile fotosentetik pigment içeriklerini, sadece tuz uygulamasına kıyasla artırmıştır. Bu sonuçlar, HA ile *B. wiedmannii* arasındaki sinerjik etkinin, su dengesini iyileştirerek, oksidatif zararı azaltarak ve antioksidan savunma sistemlerini aktive ederek tuz stresini hafiflettiğini göstermektedir. Bu nedenle HA ve *B. wiedmannii*'nin birlikte uygulanması, yem bitkilerinde tuz toleransını artırmak için umut verici bir strateji olarak değerlendirilebilir.

1. INTRODUCTION

Salt (NaCl) stress is one of the major abiotic stress factors threatening agricultural production worldwide. In particular, in irrigation-based agricultural systems, the accumulation of Na^+ and Cl^- ions in the soil hinders water uptake by plants and disrupts ionic balance by interfering with the absorption of essential nutrients such as potassium (K^+), calcium (Ca^{2+}), and magnesium (Mg^{2+}) [1, 2]. Salt stress also causes excessive accumulation of reactive oxygen species (ROS), leading to oxidative damage to proteins, lipids, DNA, and cellular membranes. ROS components such as superoxide anion ($O_2^{\cdot-}$), hydrogen peroxide (H_2O_2), hydroxyl radical ($^{\cdot}OH$), and singlet oxygen ($^1O_2$) are produced abundantly in energy-related organelles such as chloroplasts, mitochondria, and peroxisomes, thereby threatening cellular integrity. Plants attempt to neutralize these harmful compounds through non-enzymatic antioxidants and enzymatic such as superoxide dismutase (SOD), catalase (CAT), and ascorbate peroxidase (APX). However, under severe stress conditions, these defense mechanisms may prove insufficient [3, 4]. Consequently, cell membrane damage, reduced photosynthetic activity, stunted growth, and disruption of metabolic processes may occur. Soil salinity affects not only plant health but also the microbial structure of the soil. High salt concentrations reduce the activity and populations of beneficial microorganisms, thereby weakening their symbiotic relationships with plants. Combined with physical problems such as soil structure deterioration, reduced water permeability, and hindered aeration, this leads to a further decline in productivity [1, 5].

Humic acid (HA), a natural biostimulant, is gaining attention in environmentally friendly agricultural practices. HA is complex substances formed during the decomposition of organic matter and are found in soil, water, and sediments [6, 7]. Stabilized by hydrophobic interactions and hydrogen bonds, these compounds exert multifaceted effects such as regulating osmotic balance, maintaining ion homeostasis, supporting photosynthesis, and reducing oxidative stress. They also promote the accumulation of osmolytes like proline to reduce water loss and limit Na^+ accumulation while facilitating the uptake of beneficial ions such as K^+, Ca^{2+}, and Mg^{2+} [8, 9, 10]. Additionally, HA enhances chlorophyll synthesis and activate antioxidant defense systems to maintain cellular integrity [7]. Their ability to support microbial viability and facilitate ion exchange makes them valuable components in biofertilizer formulations. By promoting soil aggregation, increasing water retention capacity, regulating pH, and enhancing cation exchange capacity, HA helps create a more favorable microhabitat in the soil [11]. This environment facilitates colonization by microorganisms-especially fungi and bacteria-in the rhizosphere. However, the potential synergistic or carrier role of HA in conjunction with beneficial microorganisms remains underexplored.

Recent limited studies have highlighted the promising role of lichen-derived microorganisms in plant stress responses, drawing growing interest in their use in agricultural biotechnology [12, 13, 14]. Lichens, which are symbiotic organisms composed of algae/cyanobacteria and fungi, offer metabolic flexibility and microbial diversity that can support ion balance, nitrogen fixation, phosphate solubilization, and oxidative stress mitigation [14, 15]. These microorganisms also support plants through mechanisms such as the production of phytohormones like indole-3-acetic acid (IAA), gibberellins, and cytokinins; secretion of ACC deaminase to reduce the stress hormone ethylene; siderophore production to enhance iron uptake; nitrogen fixation; and increased phosphate solubilization [16, 17]. Some endophytic microorganisms isolated from lichens have also demonstrated plant growth-promoting effects similar to those of plant growth-promoting rhizobacteria (PGPR), reducing ion toxicity and effectively mitigating osmotic stress [12]. Nevertheless, studies examining the combined use of HA and lichen-derived microorganisms on forage crops of economic importance are still quite limited.

Alfalfa (*Medicago sativa* L.) is a valuable forage crop due to its high protein, mineral, and vitamin content, and also stands out for its contribution to biological nitrogen fixation and soil fertility. Alfalfa not only serves as a fundamental feed source in livestock production but is also appreciated for its high biomass yield, wide adaptation capacity, natural resistance to diseases, ability to improve soil structure, and ecosystem services [18, 19]. However, environmental stress factors, particularly salt stress, negatively affect key physiological processes in alfalfa, such as germination, photosynthesis, and growth, leading to yield loss. Alfalfa is especially sensitive to salt stress during the germination and early seedling stages. Under saline conditions, physiological responses such as stomatal closure, chlorophyll degradation, ion accumulation, and a decline in turgor pressure significantly restrict alfalfa development and productivity [4, 20].

This study hypothesizes that the HA can alleviate salt-induced damage in plants by modulating the antioxidant system, and that lichen-derived microorganisms may synergistically enhance this effect by reducing oxidative stress through the secretion of antioxidant compounds. In line with this hypothesis, the study investigates the combined application of the leonardite-derived HA and an endophytic bacterium (*Bacillus wiedmannii*) isolated from the lichen *Rhizoplaca melanophthalma*, and evaluates their effects on the physiological and biochemical responses of alfalfa (*Medicago sativa* L., cv. Konya) under salt stress conditions.

2. MATERIALS AND METHODS

2.1. Determination of Salt and Humic Acid Concentrations

In this study, alfalfa (*Medicago sativa* L., cv. Konya) was obtained from the Eastern Anatolia Agricultural Research Institute. To determine the salt stress level, preliminary experiments were conducted to identify the NaCl concentration that inhibited germination and seedling

development by approximately 50%. Germination percentages of the seeds were monitored daily, and by day 5, root-shoot lengths and germination data were evaluated. Based on the results, it was determined that 100 mM NaCl inhibited germination and seedling development by approximately 50% compared to the control, whereas concentrations of 200 mM and above caused 95-100% germination inhibition.

Leonardite-derived humic acid (HA) was used as the humic substance source due to its high humic acid content, low ash content, and natural composition. For this purpose, Agro Elbistan HA product from Tarım 11, sourced from the Maraş-Elbistan region, was used (https://tarim11.com). A preliminary experiment was carried out to determine the most effective HA concentration for promoting plant growth in alfalfa. For this purpose, a stock solution of HA (pH 6-6.5) with a concentration of 5000 mgL^{-1} was first prepared. This stock solution was sterilized in an autoclave and diluted with sterile distilled water to obtain germination media containing HA at concentrations of 0.0, 25, 50, 100, 250, 500, 750, 1000 and 2000 mgL^{-1}. Eight milliliters of these sterile solutions were added to sterile Petri dishes (9 cm) containing two layers of sterile filter paper. Subsequently, 25 seeds were sown into each Petri dish in a sterile cabinet. The Petri dishes were sealed with parafilm. On the 5th day of germination, the root-stem length and germination percentages of the seedlings were recorded. As a result, the concentrations of 500 and 1000 mgL^{-1} HA, which most effectively supported germination and seedling development, were selected for the main experiment. The pot experiments were conducted using one salt concentration (100 mM NaCl) and two humic acid concentrations (500 and 1000 mg L^{-1}) as determined from the preliminary tests.

2.2. Microorganism Isolation

In this study, the microbial material used was an endophytic bacterium, *Bacillus wiedmannii* OG24 (NCBI accession number OQ300504), isolated from a rock lichen (*Rhizoplaca melanophthalma*) collected from Erzurum, Turkey [12]. The bacterial isolation was performed with minor modifications to the method described by Yamamoto et al. (2002) [12, 21]. The endophytic *B. wiedmannii* (Bw) was cultured on Nutrient Agar and incubated for 24 hours at 25 °C. After incubation, bacterial colonies were collected with an inoculation loop and suspended in sterile physiological saline. The suspension was adjusted to an OD600 of 1.00 and applied to the developed plant leaves by spraying until leaf surfaces were visibly wet [12]. The ability of *B. wiedmannii* OG24 (Bw) to degrade HA (use it as a carbon source) was tested, and it was found that 100% degradation occurred after one week of incubation.

2.3. Plant Growth and Incubation Conditions

To ensure plant growth and development, a soil mixture of perlite and peat in a 1:3 (w/w) ratio, previously sterilized by autoclaving, was used in sterilized pots. Prior to sowing, the water-holding capacity of each pot was determined, and salt concentration in the potting medium was maintained constant throughout the experiment. Before sowing, each pot was treated with combinations of distilled water (Control), Salt (100 mM NaCl), HA (500 or 1000 mg L^{-1}), *B. wiedmannii* OG24 (Bw), and all possible combinations to prepare for sowing. The sterilized alfalfa seeds were sown into each pot at a density of 25 seeds. The pots were then transferred to a controlled climate chamber with a 16/8-hour day/night photoperiod and temperature conditions of 25/22 °C. Seedlings (with at least 3-4 leaves) were harvested after a total of 35 days. During harvest, the samples required for further analysis were separated, and the remaining plant material was stored at -80 °C for subsequent analyses.

2.4. Determination of Relative Water Content

After harvesting, the leaves were washed and surface moisture was removed using blotting paper. The fresh weight of the leaves was then measured using a precision balance. Following this, the samples were dried in an oven at 65 °C for 48 hours until a constant weight was achieved, and the dry weight was recorded. Based on these values, the percentage relative water content (RWC%) of the leaves was calculated using the following formula:

RWC (%) = [(Fresh weight - Dry weight) / Fresh weight] x 100

2.5. Determination of Photosynthetic Pigment Content

Chlorophyll a (Chl a), chlorophyll b (Chl b), carotenoid, and total pigment contents were determined according to Witham et al. (1971) [22]. From each sample, 0.25 g of fresh leaf tissue was extracted with 80% acetone. The ground tissue was extracted in 2.5 mL of 80% acetone, filtered, and the volume was adjusted to 5 mL. Absorbance values at 450, 645, and 663 nm were measured, and pigment contents were calculated in mg g^{-1} fresh tissue:

Chl a (mg g^{-1}) = [12.7 (D663) - 2.69 (D645)] x (V/1000 x W)
Chl b (mg g^{-1}) = [22.9 (D645) - 4.68 (D663)] x (V/1000 x W)
Total Chl (mg g^{-1}) = [20.2 (D645) + 8.02 (D663)] x (V/1000 x W)
Total carotenoids (mg g^{-1}) = 4.07 x D450 - (0.0435 x Chl a + 0.367 x Chl b)

Where D is absorbance at the specified wavelength, V is the final volume of 80% acetone, and W is the fresh weight of the tissue extracted.

2.6. Determination of Lipid Peroxidation

Lipid peroxidation (LPO) levels in plant tissues were determined by measuring malondialdehyde (MDA) content. For this, 0.25 g fresh tissue was homogenized in 5% TCA and centrifuged at 12,000 rpm for 15 minutes. To the supernatant, 0.5 mL of 0.5% TBA solution was added, incubated in a boiling water bath for 30 minutes, cooled in an ice bath, and centrifuged at 10,000 rpm for 5 minutes. Absorbance was measured at 532 and 600 nm, and MDA content was calculated [23]:

MDA (μmol mL^{-1}) = [(A532 - A600) - (A450 - A600) x 0.0571] / 157,000 x 10^6

2.7. Determination of H_2O_2 and $O_2^{\cdot-}$ Content

For H_2O_2 quantification, 0.25 g of tissue was homogenized in 2.5 mL cold acetone and centrifuged at 10,000 x g for 10 minutes. Then, 1.5 mL of the supernatant was mixed with 0.15 mL 5% $Ti(SO_4)_2$ and 0.3 mL 19% NH_4OH, centrifuged again, and the precipitate was dissolved in 3 mL 2 M H_2SO_4. Absorbance was measured at 415 nm, and values were calculated in ng g^{-1} using a standard curve [24]. For superoxide anion ($O_2^{\cdot-}$), 0.25 g tissue was homogenized in 2.5 mL 65 mM phosphate buffer (pH 7.8), centrifuged at 5,000 x g for 10 minutes, and 1 mL of the supernatant was mixed with 0.9 mL buffer and 0.1 mL 10 mM hydroxylamine HCl. After 20 minutes at 25 °C, 1 mL of 17 mM aminobenzenesulfonic acid and 1 mL of 17 mM 1-naphthylamine were added and incubated for another 20 minutes. Then, 3 mL of n-butanol was added and absorbance was read at 530 nm. Superoxide levels were determined using a $NaNO_2$ standard curve [23, 25].

2.8. Determination of Antioxidant Enzyme Activities

For antioxidant enzyme activity assays, 0.25 g of plant tissue was ground with liquid nitrogen and homogenized in 0.25 mL of 0.1 M KH_2PO_4 buffer (pH 7.0) containing 1% PVP and 1 mM EDTA. The homogenate was centrifuged at 15,000 x g at 4 °C for 15 minutes. The supernatant was used as the enzyme extract [24, 26].

Superoxide dismutase (SOD; EC 1.15.1.1) activity is based on the inhibition of the reduction of NBT to blue-colored formazan by superoxide radicals in the presence of SOD. The 3 mL reaction mixture prepared for the analysis contained 50 mM KH_2PO_4 (pH 7.8), 13 mM methionine, 63 μM NBT, 13 μM riboflavin, and 0.1 mM EDTA. 2.58 mL of the riboflavin-free mixture was taken into a spectrophotometer cuvette, and 30 μL of enzyme extract was added. The reaction was carried out in front of a white light source for 15 minutes after the addition of 390 μL of 13 μM riboflavin, and absorbance values were taken at 560 nm at the end of this period. The amount of enzyme that provided 50% inhibition of NBT reduction compared to the enzyme-free control group was defined as 1 enzyme unit. The results are presented as EU mg $protein^{-1}$ [26, 27]. Catalase (CAT; EC 1.11.1.6) enzyme activity was determined by measuring the decrease in absorbance at 240 nm during the breakdown of H_2O_2 into water and oxygen. For measurement, a reaction mixture containing H_2O_2 solution and enzyme extract was prepared, and the change in absorbance was monitored at 240 nm for 3 minutes in a spectrophotometer. The values calculated from the minute decrease in absorbance were converted to H_2O_2 amount using the molar absorptivity coefficient (ε = 39.4 mM^{-1} cm^{-1}), and the results were expressed in EU mg $protein^{-1}$ [26]. Guaiacol peroxidase activity (GPX; EC 1.11.1.7) was measured based on the increase in absorbance at 470 nm of the colored compound formed as a result of the reaction of guaiacol with H_2O_2. For the analysis, 10 μL of enzyme extract was added to 3 mL of substrate solution containing 0.1 M KH_2PO_4 (pH 5.5) and 5 mM guaiacol. The increase in absorbance was measured at 470 nm every minute for a total of 5 minutes. The amount of enzyme that caused an increase of 0.01 absorbance per minute was accepted as 1 enzyme unit (EU), and the results were presented in EU mg $protein^{-1}$ [26, 27]. Ascorbate peroxidase (APX; EC 1.11.1.11) activity was determined based on the decrease in absorbance observed at 290 nm during the reaction of ascorbic acid (ASA) with H_2O_2 [28]. The reaction mixture was prepared to contain 50 mM potassium phosphate buffer (pH 7.0), 250 μM ASA, 5 mM H_2O_2, and 100 μL of enzyme extract. The obtained absorbance changes were measured at 290 nm, and the enzyme activity was calculated using the epsilon coefficient (2.8 mM^{-1} cm^{-1}), and the results were expressed as EU mg $protein^{-1}$. Glutathione reductase (GR; EC 1.6.4.2) activity was determined by a spectrophotometric method based on the oxidation of NADPH [29]. The reaction mixture was prepared by dissolving 200 μL of 0.5 mM EDTA, 250 μl of GSSG, and 500 μL of NADPH solutions in 2.95 mL of 50 mM Tris-HCl buffer (pH 7.8). A 50 μL of enzyme extract was added to this mixture. The obtained absorbance changes were measured at 340 nm, and the enzyme activity was calculated using the epsilon coefficient of NADPH (ε = 6.22 mM^{-1} cm^{-1}), and the results were expressed as EU mg $protein^{-1}$.

2.9. Statistical Analysis

Data were presented as mean values from three independent biological replicates (n=3), each with two technical replicates (total of six measurements). Statistical analyses were performed using SPSS 21.0 software. One-Way ANOVA was used to determine significant differences among groups, and Duncan's Multiple Range Test was applied for post-hoc analysis. Differences were considered statistically significant at $p<0.05$.

3. RESULTS

Our preliminary experiments indicated that 100 mM NaCl imposed a moderate level of salt stress on the alfalfa by reducing both seed germination and seedling growth by approximately 50%. The salt dozes of 200 mM NaCl and above caused 95-100% germination inhibition. Based on this, 100 mM NaCl was chosen as the stress-inducing concentration for the main pot experiments. Additionally, HA did not significantly affect seedling development at doses below 500 mg/L compared to the control ($p<0.05$), but the doses above 1000 mg/L significantly inhibited seedling growth. During the same study, the bacterium was applied to a group of the developing alfalfa seedlings, and it was determined that the bacteria did not exhibit any pathogenicity in the developing alfalfa seedlings (As shown in Figure 1, this finding has also been observed in pot experiments.).

With regard to relative water content (RWC) of leaves, neither HA nor the bacterial isolate (*Bacillus wiedmannii*) treatments alone resulted in significant ($p<0.05$) differences compared to the control group (90.54%)

(Figure 1). In contrast, the exposure to salt stress alone led to a substantial decrease in RWC, reducing it to 82.5%.

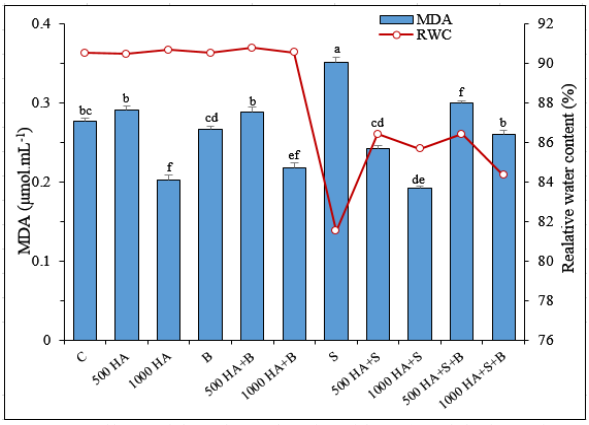

Figure 1. Effects of the salt (S), humic acid (HA) and the bacterium (B) treatments on MDA and RWC contents. Differences between groups with the same letters are insignificant according to Duncan's Multiple Comparison test ($p<0.05$).

However, the combined application of HA and *B. wiedmannii* (Bw) under the saline conditions mitigated this adverse effect. For example, in the treatment group receiving 1000 mg L^{-1} HA and Bw under salt stress, RWC improved to 85.7%, indicating a partial restoration of water status in the leaves.

3.1. Effect of Treatments on ROS and MDA Content

The salt stress significantly ($p<0.05$) increased both H_2O_2 and $O_2^{\cdot-}$ levels in *M. sativa* seedlings compared to the control group (Figure 2). The highest levels of H_2O_2 (6 µM) and $O_2^{\cdot-}$ (10.5 nmol mg $protein^{-1}$) were observed in the group exposed to salt stress alone. While the application of HA (500 and 1000 mg L^{-1}) alone led to a slight increase in H_2O_2 and $O_2^{\cdot-}$ levels, the Bw treatment did not cause a marked change in these parameters and tended to reduce superoxide accumulation in particular. When HA and Bw were applied together, the partial reductions were observed in both ROS levels. Under the salt stress, individual applications of HA and Bw reduced MDA level, but the most notable reductions were recorded in the groups where HA and Bw were applied in combination. Especially 1000 mg L^{-1} HA+Bw+Salt group significantly reduced H_2O_2 and $O_2^{\cdot-}$ levels compared to the salt-stressed group, making it the most effective combination in suppressing oxidative stress. These results indicate that the combined application of HA and *B. wiedmannii* provides a synergistic protective effect against salt stress. Compared to the control group, the HA treatments significantly ($p<0.05$) reduced MDA levels, lowering them to 0.23 and 0.30 µmol mL^{-1}, respectively (Figure 1). When applied alone, the bacterium decreased MDA levels to 0.27 µmol mL^{-1}, showing a moderate reduction compared to the control. However, the HA+Bw combinations did not show a significant effect relative to the control. Under stress conditions induced by the salt treatment, MDA levels rose to 0.36 µmol mL^{-1}, representing the highest value among all groups ($p<0.05$). In the HA+Salt combinations, MDA levels were reduced again to 0.23 and 0.27 µmol mL^{-1}, indicating that high-dose HA effectively mitigated oxidative stress even under salt stress conditions. In combinations involving both salt and HA with Bw, MDA levels were measured at 0.30 µmol mL^{-1} in the 500 HA+Salt+Bw group and 0.27 µmol mL^{-1} in the 1000 HA+Salt+Bw group.

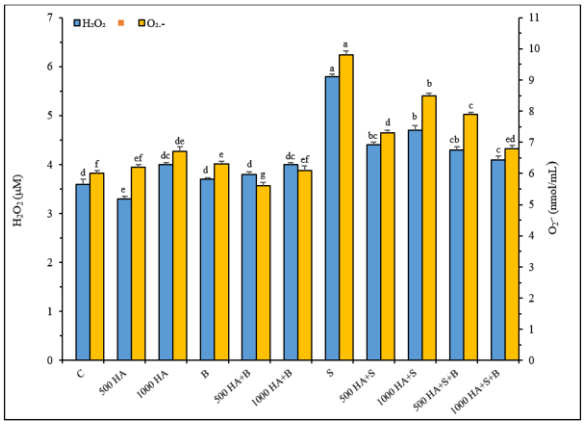

Figure 2. Effects of the salt (S), humic acid (HA) and the bacterium (B) treatments on H_2O_2 and $O_2^{\cdot-}$ MDA and RWC contents. Differences between groups with the same letters are insignificant according to Duncan's Multiple Comparison test ($p<0.05$).

3.2. Effects of Treatments on Antioxidant Enzyme Activities

SOD activity was approximately 1.8 EU mg $protein^{-1}$ in the control group (Figure 3). The HA (500 mg L^{-1}) treatment slightly increased SOD activity, helping to maintain the enzyme activity, while 1000 HA treatment showed a slightly lower activity. The bacterial treatment resulted in a similar level of activity. Combinations of the HA and the bacterium led to the highest levels of SOD activity, reaching around 2.0 EU mg $protein^{-1}$. Under the salt stress, SOD activity significantly ($p<0.05$) decreased to about 1.4 EU mg $protein^{-1}$. The Salt+HA treatments partially restored SOD activity, however, the most notable increases were observed in the 500 HA+Salt+Bw and 1000 HA+Salt+Bw groups, which elevated SOD activity back to approximately 1.8-1.9 EU mg $protein^{-1}$. On the other hand, CAT activity, compared to the control group (1.3 EU mg $protein^{-1}$), was not significantly ($p<0.05$) altered by HA or Bw treatments alone (Figure 3). Similarly, HA+Bw combinations did not cause a meaningful change in CAT activity. The salt treatment significantly reduced CAT activity to about 1.0 EU mg $protein^{-1}$ compared to the control. Salt+HA treatments provided slight increases in CAT activity, with a significant improvement particularly observed in the 1000 HA+Salt group. The most remarkable increases were determined in the 500 HA+Salt+Bw and 1000 HA+Salt+Bw groups.

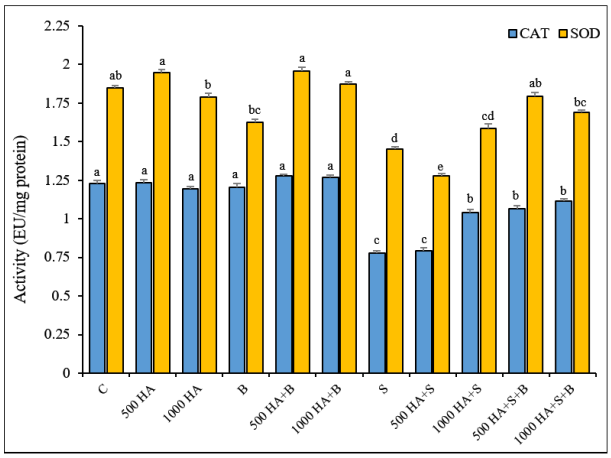

Figure 3. Effects of the salt (S), humic acid (HA) and the bacterium (B) treatments on CAT and SOD activity. Differences between groups with the same letters are insignificant according to Duncan's Multiple Comparison test ($p<0.05$).

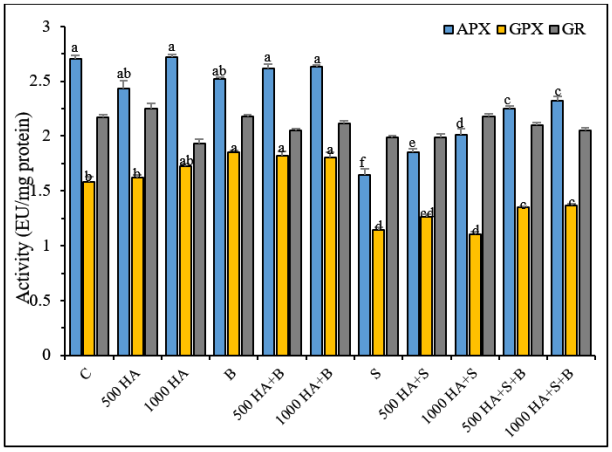

Figure 4. Effects of the salt (S), humic acid (HA) and the bacterium (B) treatments on APX, GPX, and GR activity. Differences between groups with the same letters are insignificant according to Duncan's Multiple Comparison test ($p<0.05$).

APX activity was not significantly affected by HA and Bw applications compared to the control (Figure 4). However, the salt stress significantly reduced APX activity in the seedlings, with activity decreasing to approximately 1.6 EU mg protein^{-1}. When HA+Salt treatment was applied together, APX activity significantly ($p<0.05$) increased compared to the salt alone. More pronounced increases in APX activity were observed in the groups where both HA and Bw were applied under salt stress. As for GPX activity, HA and Bw treatments did not result in a significant increase compared to the control and remained at similar levels (Figure 4). The salt application caused a substantial decrease in GPX activity, reducing it to 1.1 EU mg protein^{-1}. In the groups treated with salt in combination with 500 or 1000 mg L^{-1} HA, slight but significant increases in GPX activity were observed. The most notable increases occurred in the groups treated with both HA and Bw under the salt stress, where GPX activity reached approximately 1.6-1.7 EU mg protein^{-1}. In terms of GR activity, HA and Bw treatments alone caused slight, non-significant increases compared to the control (Figure 4). In the salt-stressed group, GR activity was significantly reduced, dropping to around 1.5 EU mg protein^{-1}. In groups where HA and salt were applied together, significant increases in GR activity were observed, with a more noticeable rise particularly in the 1000 HA+Salt group. The most remarkable recovery was detected in the groups where both HA and Bw were applied under salt stress, with GR activity reaching up to 2.0 EU mg protein^{-1}. These results demonstrate that the combined application of HA and *B. wiedmannii* is effective in restoring the antioxidant enzyme activities to normal levels under the salt stress conditions.

3.3. Effects of Treatments on Photosynthetic Pigment Content

When salt stress was applied alone, all Chl parameters declined significantly ($p<0.05$), and the proportional decrease in Chl a was greater than that of Chl b (Figure 5). HA treatments, especially at the high dose (1000 mg L^{-1}), induced significant increases in Chl a, Chl b, and total Chl relative to the control. Notably, the enhancing effect of 1000 mg L^{-1} HA was more pronounced on Chl a than on Chl b. The Bw inoculation alone also elevated Chl content, with the increase in Chl a slightly exceeding that in Chl b, although this rise was less marked than with HA treatments. Combinations of the salt stress with HA and Bw treatments partially alleviated the adverse effects of the salinity. In particular, the 1000 mg L^{-1} HA+Salt+Bw treatment produced a significant ($p<0.05$) recovery in Chl levels compared to salt alone. Across these combined treatments, improvements in Chl a were generally more pronounced than those in Chl b.

The application of salt alone reduced the carotenoid content compared to the control. However, individual applications of 1000 mg L^{-1} humic acid (HA) and bacteria significantly increased carotenoid levels (Figure 5). Notably, the highest carotenoid content (approximately 0.26) was observed in the group treated solely with bacteria. The 500 mg L^{-1} HA treatment and the combination applications (500 HA+Bw, and 1000 HA+Bw) also showed an increase compared to the control, although the increase in the 1000 HA+Bw group was not considered statistically significant. When the effects of HA+Bw applications under salt stress were examined, it was found that in the 500 HA+Salt and 1000 HA+Salt groups, the negative impact of salt was partially mitigated. However, carotenoid levels in these groups still remained below the control level. In the groups where bacterial treatment was combined with salt (Salt+Bw and 1000 HA+Salt+Bw), carotenoid levels were observed to be higher than in the group treated with salt alone.

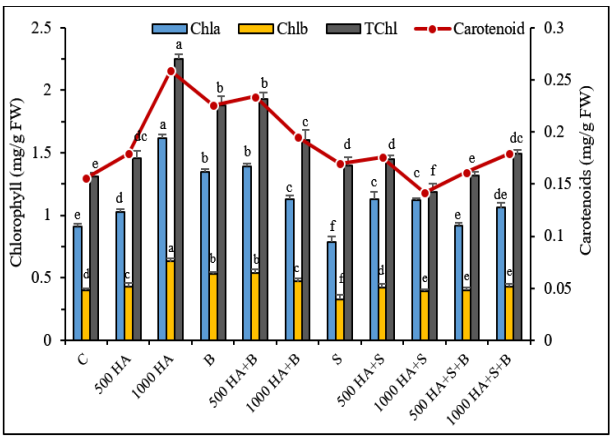

Figure 5. Effects of the salt (S), humic acid (HA) and the bacterium (B) treatments on photosynthetic pigment content. Differences between groups with the same letters are insignificant according to Duncan's Multiple Comparison test ($p<0.05$). FW: Fresh weight.

4. DISCUSSION

In this study, humic acid (HA) derived from leonardite, produced in the Maraş-Elbistan region (Türkiye) was preferred due to its content and natural origin (https://tarim11.com). This HA is a domestically produced humic acid obtained from natural leonardite with a pH range of 2-4, containing 12% total organic matter, 12% total humic acids, 2.5% water-soluble potassium oxide (K_2O), and a final pH range of 7-9 [30]. Leonardite-based HA exerts a strong effect on plants due to its high humic content. Additionally, being a natural and organic source allows for environmentally friendly use. Compared to other HA sources, leonardite has a lower ash content, which means it does not increase soil salinity or inhibit microbial activity [7,31,41]. In contrast, HA derived from lignite and coal generally have lower organic matter content and limited solubility, reducing their effectiveness on plant growth [32, 33]. Synthetic HAs, on the other hand, are not obtained from natural sources, making them unsuitable for use in organic farming and potentially more harmful to the environment [31]. For these reasons, leonardite-based HA offers a more effective and sustainable solution compared to other sources.

Relative water content (RWC) of leaves reveals the impact of stress on the plant's water balance. In the control group, RWC was measured at 90.54%, whereas in the plants exposed only to the salt stress, this value decreased to 82.5% (Figure 1). This decline aligns with literature indicating that salt reduces osmotic potential, thereby limiting water uptake and increasing water loss in plants [34]. However, under the salt stress, significant improvements in RWC values were observed with the application of HA and *B. wiedmannii* (Bw) Notably, in the combination of 1000 mg L^{-1} HA+Bw+Salt, the RWC value increased to 85.7%, indicating the potential of these treatments to enhance water retention capacity. This ameliorative effect is likely due to HA promoting root development, thereby facilitating water uptake, and the bacterial isolate (*B. wiedmannii*) enhancing the plant's response to salt stress [35].

Salt stress is a significant abiotic factor that induces oxidative damage in plants by increasing the accumulation of ROS such as H_2O_2 and $O_2^{\cdot-}$ [5, 34]. In this study, compared to the control, the individual applications of HA, bacteria, or HA+Bw did not have a strong or statistically significant effect on the ROS content in the seedlings leaves (Figure 2). In contrast, salt stress significantly increased H_2O_2 and $O_2^{\cdot-}$ levels compared to the control. High salt concentrations can trigger ROS production by causing ionic imbalances in cells, denaturation of proteins, and reduced photosynthetic activity [5, 34]. However, a synergistic effect in suppressing oxidative stress was observed in the groups where HA and the bacteria were applied together. Specifically, in the 1000 mg L^{-1} HA+Bw+Salt, H_2O_2 and $O_2^{\cdot-}$ levels were significantly lower than in the salt-only group, indicating that this combination is much more effective in protecting plants against salt stress than the individual treatments (Figure 2). This synergistic effect may be attributed to HA improving the plant's physiological state, thereby enhancing the effectiveness of the bacterium's stress-mitigating mechanisms, or to the bacterium facilitating the uptake and utilization of HA's bioactive components by the plant. When examining MDA levels, an indicator of LPO (Figure 1), it was found that both HA and the bacterial treatments alone significantly reduced MDA content compared to the control, supporting their individual potential to mitigate oxidative damage. Salt treatment significantly increased MDA levels, aligning with existing literature indicating membrane damage due to salt stress [5, 32]. Reductions in MDA levels were also observed in HA+Salt and HA+Salt+Bw treatments. Notably, the low MDA level in the 1000 mg L^{-1} HA+Salt+Bw provides further evidence of the synergistic effect of HA and bacteria in reducing salt-induced membrane damage. These findings demonstrate that the combined application of HA and *B. wiedmannii* significantly alleviates oxidative stress and suppresses lipid peroxidation in *M. sativa* under salt stress through a synergistic mechanism.

SOD isoforms the first line of defense in plants against free radicals by converting superoxide anions into H_2O_2 [5]. Salt stress typically elevates intracellular ROS levels and acts as a trigger to stimulate SOD activity. For example, Younesi and Moradi (2014) reported that 200 mM NaCl significantly increased SOD activity in alfalfa seedlings [37]. In contrast, in our study, under 100 mM salt stress, SOD activity decreased compared to control levels (Figure 3). This reduction may be associated with the salt tolerance level of the cultivar used. Indeed, the alfalfa variety (Konya) used in this study exhibited 50% growth inhibition at 100 mM salt and failed to germinate or grow at 200 mM. According to the literature, salt-tolerant cultivars tend to have higher SOD activity, enabling them to better cope with salt-induced stress. For instance, salt-tolerant rice varieties have shown elevated expression of SOD genes and higher SOD activity compared to salt-sensitive varieties [5]. However, this decline in SOD activity was partially mitigated by the application of HA or Bw, and the combination of HA+Bw even restored SOD activity to near control levels. Similarly, HA treatments have been shown to enhance salt

tolerance in wheat by boosting antioxidant system activity, including SOD [8]. In addition, inoculation with Bacillus PGPR strains has been reported to increase SOD activity by 25-50% in salt-stressed rice plants [38]. In our findings as well, inoculation with *B. wiedmannii* led to a noticeable increase in SOD activity, which returned to near-control levels when applied in combination with HA. Similarly, CAT activity significantly decreased under 100 mM NaCl treatment, but substantial increases in CAT activity were observed with the combined application of 500 and 1000 mg L^{-1} HA and the bacterium (Figure 3). In a similar study, applications of *B. subtilis* and *B. aryabhattai* significantly enhanced CAT activity in salt-stressed rice and tomato plants [39, 40]. Likewise, HA has been reported to mitigate oxidative damage in plants and strengthen enzymatic defenses [9]. Additionally, Bacillus consortia with catalase-producing ability have been shown to increase CAT activity by more than 50% [40].

APX is one of the key enzymes responsible for detoxifying H_2O_2 within the ascorbate (AsA)-glutathione (GSH) cycle. Under saline conditions, APX activity typically increases; for instance, Younesi and Moradi (2014) reported that 200 mM NaCl more than doubled APX activity in alfalfa [37]. High APX expression and activity in salt-tolerant genotypes have also been reported in the literature [5]. However, in our study, APX activity decreased under the salt stress in the alfalfa (Figure 4). This decline may be related to the salt sensitivity of the specific cultivar. As noted earlier, the Konya variety of alfalfa showed 50% growth inhibition at 100 mM salt and failed to germinate at 200 mM. On the other hand, while individual applications of HA or bacteria led to a slight recovery, the HA+Bw combination restored APX activity to near-control levels. Some studies have suggested that HA can enhance APX activity. For example, HA application increased APX activity in salt-stressed sorghum plants [38]. Similarly, Bacillus PGPR inoculation has been shown to increase APX activity in rice by 45-58% [39]. Furthermore, co-application of PGR and HA generally enhances antioxidant enzyme activities and reduces peroxidation levels, which indicate cellular damage [43]. These findings demonstrate that the combination of HA and *B. wiedmannii* helped restore APX activity to near baseline levels.

GPX is a type of peroxidase that uses phenolic substrates to break down H_2O_2 and protects cell membranes from oxidative damage [5]. In many plant species, increased peroxidase activities have been observed under salt stress conditions [44]. This suggests that plants activate the GPX pathway to mitigate salt-induced ROS accumulation. In our findings, however, GPX activity was reduced under the salt stress (Figure 4). A study on ryegrass reported that antioxidant enzyme activities, including GPX, initially increased under salt stress but began to decline after the 12th day of exposure. This indicates that antioxidant enzymes may be activated during the early phase of stress as a defense response but can become suppressed as stress persists [45]. The alfalfa seedlings in our study were subjected to 35 days of salt stress, the observed decline in GPX activity is consistent with this pattern. On the other hand, the decline in GPX activity due to the salt stress was partially recovered with the application of either HA or bacteria, and near-control levels were achieved with the combined HA+Bw treatment. Literature supports the role of HA in enhancing GPX activity and protecting plants from oxidative stress [8, 39]. Similarly, Bacillus inoculation has been shown to positively influence GPX activity in crops like wheat and maize [8]. Therefore, these findings indicate that the combined application of HA+*B. wiedmannii* helps restore GPX activity in salt-stressed alfalfa, thereby supporting cellular ROS detoxification mechanisms.

GR is a crucial component of the AsA-GSH cycle in plants. This enzyme regenerates ascorbate (AsA) from dehydroascorbate via DHAR and also converts oxidized glutathione (GSSG) back to its reduced form (GSH), thereby maintaining redox homeostasis [5]. Under salt stress, changes in GR activity are often reported to be more limited. For instance, in alfalfa, salt stress was found to increase SOD and APX activities, while no significant change in GR activity was observed [37]. This suggests that GR tends to remain more stable in order to preserve the integrity of the AsA-GSH cycle. In the study, however, GR activity decreased under salt stress compared to the control, and this reduction was only partially alleviated by either HA or bacterial treatments alone (Figure 4). This response may be closely related to the salt tolerance level of the alfalfa variety used and the duration of salt exposure. Notably, the combined application of HA+Bw restored GR activity to levels close to that of the control group. Overall, it is known that HA and PGPR applications enhance the AsA-GSH cycle by activating GR and other associated enzymes, thereby improving H_2O_2 detoxification [43]. Our findings are consistent with this mechanism, as the HA+*B. wiedmannii* treatment effectively restored GR activity, supporting the antioxidant defense system in the salt-stressed alfalfa.

Salt stress is well known to impair photosynthetic pigment synthesis and accelerate pigment degradation in plants, often leading to lower Chl a, Chl b, and total Chl contents [46]. In this study, 100 mM NaCl alone elicited a marked decline in Chl a and Chl b compared to control plants, with Chl a exhibiting a proportionally larger reduction than Chl b (Figure 5). These results are consistent with previous findings in alfalfa, where salinity reduced Chl content and impaired photosystem II (PSII) efficiency, but did not significantly affect activity at lower salinity levels [46]. The HA treatments, especially at 1000 mg L^{-1}, significantly increased Chl a, Chl b, and total Chl relative to control plants, with a more pronounced effect on Chl a than Chl b. In addition, Sofi et al. (2018) demonstrated that HA improved Chl a, Chl b, and total Chl in alfalfa seedlings exposed to various salinity levels, particularly under 120 mM NaCl [47]. Similarly, studies in maize and cucumber showed that HA application ameliorated salinity effects by elevating pigment contents, and maintaining RWC, and enhancing antioxidant enzyme activities. In this study, *B. wiedmannii* inoculation alone slightly increased Chl a and Chl b (with a slightly higher relative rise in Chl a) compared to controls, although to a lesser extent than HA treatments. These increments align with evidence that PGPR can enhance pigment synthesis

by improving water relations and osmolyte accumulation [48, 49]. Specifically, in alfalfa, inoculation with Bacillus strains under saline conditions prevented Chl loss by lowering chlorophyllase activity and preserving PSII functionality [48, 49]. When HA and Bw were combined under salt stress (100 mM NaCl), partial recovery of Chl contents was evident. The 1000 mg L^{-1} HA+Salt+Bw treatment yielded a significant restoration of Chl a and Chl b relative to the salt alone, with Chl a improvements more pronounced.

Carotenoids play essential roles in photoprotection by scavenging ROS and dissipating excess excitation energy under abiotic stress. It is well documented that salinity decreases carotenoid content, compounding oxidative damage [50, 51]. In this study, the salt alone reduced carotenoid levels below those of controls. Conversely, individual HA (1000 mg L^{-1}) and the bacterial treatments significantly increased carotenoid content, with *B. wiedmannii* alone achieving the highest carotenoid concentration (Figure 5). Similarly, Bacillus-mediated carotenoid enhancement has been observed in rice and tomato under salt stress, where PGPR-induced antioxidant enzyme activation coupled with elevated carotenoid synthesis mitigated oxidative damage [49, 50]. Furthermore, in Salt+Bw and 1000 HA+Salt+Bw, carotenoid concentrations exceeded those in the salt alone, underscoring the superior efficacy of Bw (with or without HA) in bolstering carotenoid defenses under salinity. This suggests that the bacillus-induced modulation of carotenoid biosynthesis may be more potent than HA alone for restoring antioxidant capacity in alfalfa under salt stress [49, 50]. Taken together, this data demonstrates that HA (1000 mg L^{-1}) and *B. wiedmannii* can mitigate salt-induced declines in photosynthetic pigments in alfalfa, with combined applications offering superior recovery.

5. CONCLUSION

This study demonstrated that the application of HA derived from the leonardite and endophytic *Bacillus wiedmannii* OG24 from the lichen reduced the adverse effects of the salt stress (100 mM NaCl) on the *Medicago sativa* seedlings. The combination of HA and the bacterial treatments significantly increased RWC, reduced ROS level and LPO, and restored the activities of key antioxidant enzymes (SOD, CAT, APX, GPX, and GR) that were suppressed under the salt stress. Additionally, both HA and *B. wiedmannii* helped restore the photosynthetic pigment levels, with the combined treatment showing the most pronounced improvements. Overall, these improvements can be attributed to the restoration of mechanisms such as ion balance, osmotic regulation, antioxidant defense, and water-holding capacity in the plant. For example, HA can increase the K^+/Na^+ ratio in the plant by enhancing K^+ uptake and limiting Na^+ accumulation, and it also reduces LPO level and ion leakage by increasing antioxidant enzyme activities [9]. In this case, oxidative stress is suppressed while photosynthesis and water uptake are supported. With the supportive environment effect in the soil, root development is stimulated, and the RWC in the plant increases, thereby enhancing water-holding capacity [41]. We believe that the *B. wiedmannii* OG24 isolate supports plant growth through various PGPR mechanisms. Such strains exhibit characteristics such as high indole-3-acetic acid (IAA) production, phosphate solubility, and nitrogen fixation [17, 43]. Additionally, exopolysaccharide secretion facilitates water retention and bacterial colonization in the rhizosphere [52]. ACC deaminase activities also promote growth by reducing stress ethylene in plants [24]. HA also enriches the root environment with organic acids and nutrients, enhancing the attachment and efficacy of such bacterial isolates to roots [43]. According to our findings, such a synergistic interaction could explain the increased stress response observed in the *M. sativa* under salt stress. In conclusion, the combined application of HA derived from leonardite and *B. wiedmannii* demonstrates a promising, environmentally friendly strategy to enhance salt stress resistance in alfalfa by strengthening physiological, biochemical, and antioxidant defense responses.

Author Contributions

Ö.A. was responsible for the study design, conducting the experiments, literature review, and manuscript writing. A.M. contributed to the experimental work and literature review. Ö.G. was involved in conducting the experiments and performing statistical analyses.

Conflict of Interest Statement

The authors declare that there is no conflict of interest regarding this study.

REFERENCES

[1] Stavi İ, Thevs N, Priori S. Soil salinity and sodicity in drylands: A review of causes, effects, monitoring, and restoration measures. Front Environ Sci. 2021;9:712831.

[2] Parida AK, Das AB. Salt tolerance and salinity effects on plants: a review. Ecotoxicol Environ Saf. 2005;60(3):324-349.

[3] Hernández JA. Salinity tolerance in plants: trends and perspectives. Int J Mol Sci. 2019;20:2408.

[4] Yılmaz E, Tuna AL, Bürün B. Bitkilerin tuz stresi etkilerine karşı geliştirdikleri tolerans stratejileri. Celal Bayar Univ J Sci. 2011;7(1):47-66.

[5] Hasanuzzaman M, Raihan MRH, Masud AAC, Rahman K, Nowroz F, Rahman M, Fujita M. Regulation of reactive oxygen species and antioxidant defense in plants under salinity. Int J Mol Sci. 2021;22(17):9326.

[6] Akıncı Ş. Hümik asitler, bitki büyümesi ve besleyici alımı. Marmara Univ Fen Bilimleri Dergisi. 2011;23(1):46-56.

[7] Canellas LP, Teixeira Junior LRL, Dobbss LB, Silva CA, Medici LO, Zandonadi DB, Façanha AR. Humic acids cross-interactions with root and organic acids. Ann Appl Biol. 2008;153(2):157-166.

[8] Abbas G, Rehman S, Siddiqui MH, Ali HM, Farooq MA, Chen Y. Potassium and humic acid synergistically increase salt tolerance and nutrient uptake in contrasting wheat genotypes through ionic

homeostasis and activation of antioxidant enzymes. Plants. 2022;11(3):263.
[9] Abu-Ria M, Shukry W, Abo-Hamed S, Albaqami M, Almuqadam L, Ibraheem F. Humic acid modulates ionic homeostasis, osmolytes content, and antioxidant defense to improve salt tolerance in rice. Plants. 2023;12(9):1834.
[10] Boydak E, Enes B, Demirkıran AR. Effect of leonardite material doses on the elimination of salt stress in groundnut. Türk Doğa ve Fen Dergisi. 2025;14(1):1-8.
[11] Tiwari J, Ramanathan AL, Bauddh K, Korstad J. Humic substances: Structure, function and benefits for agroecosystems-A review. Pedosphere. 2023;33(2):237-249.
[12] Gülmez O, Tiryaki D, Atıcı Ö, Baris O. Boron-resistant *Alternaria alternata* (OG14) mitigates boron stress by improving physiological and antioxidative response in wheat (*Triticum aestivum* L.). Plant Physiol Biochem. 2023;202:107911.
[13] Li B, Mamuti R, Xiao L, Qian B, Wang Y, Wei X. The adaptation of lichen symbiosis to desert saline-alkali stress depends more on their symbiotic algae. Physiol Plantarum. 2024;176(5):e14510.
[14] Patil PS, Gore NS. Botanical symbiosis unveiled: a review of mycorrhizas, lichen, and plant consorts. Bot Rev. 2025;1-24.
[15] Bianchi E, Benesperi R, Colzi I, Coppi A, Lazzaro L, Paoli L, Gonnelli C. The multi-purpose role of hairiness in the lichens of coastal environments: Insights from *Seirophora villosa* (Ach.) Frödén. Plant Physiol Biochem. 2019;141:398-406.
[16] Ma Y, Freitas H, Dias MC. Strategies and prospects for biostimulants to alleviate abiotic stress in plants. Front Plant Sci. 2022;13:1024243.
[17] Emilia DA, Luisa DA, Stefania DP, Petronia C. Use of Biostimulants to Improve Salinity Tolerance in Agronomic Crops. In: Hasanuzzaman, M. (eds) Agronomic Crops. Springer, Singapore. 2020;423-441.
[18] Wu S, Lu YC, McMurtrey JE, Weesies G, Devine TE, Foster GR. Soil conservation benefits of large biomass soybean (LBS) for increasing crop residue cover. J Sustain Agric. 2004;24(1):107–128.
[19] Brahmbhatt NH, Kalasariya HS. Effect of algae on seedling growth of "Queen of Forages." Int J Eng Res Gen Sci. 2015;3:827-833.
[20] Özkurt M, Saygılı İ, Dirik KÖ. Bazı yonca çeşitlerinin erken gelişme dönemindeki kuraklık toleransının belirlenmesi. KSÜ Tar Doga Derg. 2019;22:557-562.
[21] Yamamoto Y, Kinoshita Y, Thor GR, Hasumi M, Kinoshita K, Koyama K, et al. Isofuranonaphthoquinone derivatives from cultures of the lichen *Arthonia cinnabarina* (DC.) Wallr. Phytochemistry. 2002;60(7):741-745.
[22] Witham FH, Blaydes BF, Devlin RM. Experiments in plant physiology. Van Nostrand Reinhold Company; 1971. p. 167-200.
[23] Hodges DM, DeLong JM, Forney CF, Prange RK. Improving the thiobarbituric acid-reactive-substances assay for estimating lipid peroxidation in plant tissues containing anthocyanin and other interfering compounds. Planta. 1999;207:604-611.
[24] Atıcı Ö, Aydın İ, Karakuş S, Tiryaki D. Inoculating maize (*Zea mays* L.) seeds with halotolerant rhizobacteria from wild halophytes improves physiological and biochemical responses of seedlings to salt stress. Biologia Futura. 2025;1-16.
[25] Elstner EF, Heupel A. Inhibition of nitrite formation from hydroxylammonium chloride: a simple assay for superoxide dismutase. Anal Biochem. 1976;70:616-620.
[26] Esim N, Atıcı Ö. Nitric oxide alleviates boron toxicity by reducing oxidative damage and growth inhibition in maize seedlings (*Zea mays* L.). Aust J Crop Sci. 2013;7(8):1085-1092.
[27] Agarwal S, Pandey V. Antioxidant enzyme responses to NaCl stress in *Cassia angustifolia*. Biologia Plantarum. 2004;48(4):555-560.
[28] Nakano Y, Asada Y. Hydrogen peroxide is scavenged by ascorbate-specific peroxidase in spinach chloroplasts. Plant Cell Physiol. 1981;22:867-880.
[29] Foyer CH, Halliwell B. The presence of glutathione and glutathione reductase in chloroplasts: a proposed role in ascorbic acid metabolism. Planta. 1976;133:21-25.
[30] İlay R, Aktaş M, Aslantekin NB, Özcan H. Farklı kaynaklardan elde edilen organik materyalin kumlu tın bünyeli toprağın bazı özellikleri üzerine etkileri. Toprak Bilimi ve Bitki Besleme Dergisi. 2021;9(1):30-38.
[31] Pekcan T, Esetlili BÇ, Turan HS, Aydoğdu E. Leonardit kökenli organik materyallerin bazı fiziksel ve kimyasal özelliklerinin belirlenmesi. Uludağ Üniversitesi Ziraat Fakültesi Dergisi. 2018;32:31-41.
[32] Tahir MM, Khurshid M, Khan MZ, Abbasi MK, Kazmi M. H. Lignite-derived humic acid effect on growth of wheat plants in different soils. Pedosphere 2011;21;124-131.
[33] Sharif M, Khattak RA, Sarir MS. 2002). Effect of different levels of lignitic coal derived humic acid on growth of maize plants. Commun Soil Sci Plant Anal. 2002;33:3567-3580.
[34] Gupta B, Huang B. Mechanism of salinity tolerance in plants: physiological, biochemical, and molecular characterization. Int J Genom. 2014:701596.
[35] Egamberdieva D, Wirth SJ, Alqarawi AA, Abd_Allah EF, Hashem A. Phytohormones and beneficial microbes: essential components for plants to balance stress and fitness. Front Microbiol. 2017;8:2104.
[36] Gill SS, Tuteja N. Reactive oxygen species and antioxidant machinery in abiotic stress tolerance in crop plants. Plant Physiol Biochem. 2010;48(12):909-930.
[37] Younesi O, Moradi A. Effect of priming of seeds of *Medicago sativa* "Bami" with gibberellic acid on germination, seedling growth and antioxidant enzymes activity under salinity stress. J Hortic Res. 2014:22(2).
[38] Ali AYA, Ibrahim MEH, Zhou G, Nimir NEA, Jiao X, Zhu G, Yue W. Exogenous jasmonic acid and

humic acid increased salinity tolerance of sorghum. Agronomy Journal. 2020;112(2): 871-884.
[39] Ali Q, Ayaz M, Mu G, Hussain A, Yuanyuan Q, Yu C, Gao X. Revealing plant growth-promoting mechanisms of Bacillus strains in elevating rice growth and its interaction with salt stress. Frontiers in Plant Science. 2022;13: 994902.
[40] Patani A, Prajapati D, Ali D, Kalasariya H, Yadav VK, Tank J. Evaluation of the growth-inducing efficacy of various Bacillus species on the salt-stressed tomato (*Lycopersicon esculentum* Mill.). Front Plant Sci. 2023;14:1168155.
[41] Siddika A, Rashid AA, Khan SN, Khatun A, Karim MM, Prasad PV, Hasanuzzaman M. Harnessing plant growth-promoting rhizobacteria, *Bacillus subtilis* and *B. aryabhattai* to combat salt stress in rice: a study on the regulation of antioxidant defense, ion homeostasis, and photosynthetic parameters. Front Plant Sci. 2024;15:1419764.
[42] Saeed SWZ, Naseer I, Zahir ZA, Hilger T, Shahid S, Iqbal Z, Ahmad M. Bacillus strains with catalase enzyme improve the physiology and growth of rice (*Oryza sativa* L.). Stresses. 2023;3(4):736-748.
[43] da Silva MSRDA, dos Santos BDMS, da Silva CSRDA, da Silva CSRDA, Antunes LFDS, dos Santos RM, Rigobelo EC. Humic substances in combination with plant growth-promoting bacteria as an alternative for sustainable agriculture. Front Microbiol. 2021;12:719653.
[44] Yıldız M, Terzi H, Akçalı N. Tuz stresi altındaki bitkilerin metabolik yollarındaki proteom değişimleri. Bitlis Eren Univ Fen Bilimleri Dergisi. 2014;3(1):81-93.
[45] Hu LongXing HL, Li HuiYing LH, Pang HuangCheng PH, Fu JinMin FJ. Responses of antioxidant gene, protein and enzymes to salinity stress in two genotypes of perennial ryegrass (*Lolium perenne*) differing in salt tolerance. J Plant Physiol Biochem. 2012; 146-156.
[46] Jabborova D, Zhang Y, Alhewairini SS, Jabbarov Z, Barasarathi J, Abdrakhmanov T, Saharan BS. Enhancing growth and physiological traits in alfalfa by alleviating salt stress through biochar, hydrogel, and biofertilizer application. Front Microbiol. 2025;16:1560762.
[47] Sofi A, Ebrahimi M, Shirmohammadi E. Effect of humic acid on germination, growth, and photosynthetic pigments of *Medicago sativa* L. under salt stress. Ecopersia, 2018; 6(1):21-30
[48] Han L, Zhang M, Du L, Zhang L, Li B. Effects of *Bacillus amyloliquefaciens* QST713 on photosynthesis and antioxidant characteristics of alfalfa (*Medicago sativa* L.) under drought stress. Agronomy. 2022;12(9):2177.
[49] Ansari M, Shekari F, Mohammadi MH, Juhos K, Végvári G, Biró B. Salt-tolerant plant growth-promoting bacteria enhanced salinity tolerance of salt-tolerant alfalfa (*Medicago sativa* L.) cultivars at high salinity. Acta Physiol Plant. 2019;41:1-13.
[50] Khan MA, Hamayun M, Asaf S, Khan M, Yun BW, Kang SM, Lee IJ. Rhizospheric *Bacillus spp*. rescues plant growth under salinity stress via regulating gene expression, endogenous hormones, and antioxidant system of *Oryza sativa* L. Front Plant Sci. 2021;12:665590.
[51] Seven S, Akinci Ş. Effects of humic acid and salt stress on growth, physiological parameters and mineral substance uptake in *Artemisia dracunculus* L. (Tarragon). Turk J Bot. 2025;49(2), 64-79.
[52] Bhagat N, Raghav M, Dubey S, Bedi N. Bacterial exopolysaccharides: Insight into their role in plant abiotic stress tolerance. J Microbiol Biotech. 2021;31:1045.

Volume 14, Issue 3, Page 183-191, 2025 https://doi.org/10.46810/tdfd.1664372 Research Article

BİNGÖL UNIVERSITY

Türk Doğa ve Fen Dergisi
Turkish Journal of Nature and Science
www.dergipark.gov.tr/tdfd

Phytochemical contents and *in vitro* activities of *Berberis thunbergii* hydroethanolic extract

Elif Ceren KARAKUS[1], Tevfik OZEN[1*], Semiha YENIGUN[1], Yunus BASAR[2], Ibrahim DEMIRTAS[3], Ilyas YILDIZ[4]

[1]Ondokuz Mayis University, Faculty of Science, Chemistry, Samsun, Türkiye
[2]Igdir University, Research Laboratories Application and Research Center (ALUM), Iğdır, Türkiye
[3]Ondokuz Mayis University, Faculty of Pharmacy, Pharmaceutical Chemistry, Samsun, Türkiye
[4]Tokat Gaziosmanpaşa University, Faculty of Arts and Sciences, Molecular Biology and Genetics, Tokat, Türkiye
Elif Ceren KARAKUS ORCID No: 0009-0004-5082-7919
Tevfik OZEN ORCID No: 0000-0003-0133-5630
Semiha YENIGUN ORCID No: 0000-0002-1979-5427
Yunus BASAR ORCID No: 0000-0002-7785-3242
Ibrahim DEMIRTAS ORCID No: 0000-0001-8946-647X
Ilyas YILDIZ ORCID No: 0000-0003-1254-1069

**Corresponding author: tevfikoz@omu.edu.tr*

(Received: 16.04.2025, Accepted: 05.09.2025, Online Publication: 26.09.2025)

Keywords
Berberis thunbergii, Hydroethanolic extract, Phytochemical, *İn vitro* bioactivity,

Abstract: *Berberis thunbergii*, also known as Japanese dogwood, has many medicinal properties due to its rich phytochemical components. Therefore, *B. thunbergii* hydroethanolic extract was investigated for its phytochemical content, antioxidant, anti-inflammatory, and enzyme inhibition activities. In LC-ESI-MS/MS and GC-MS/MS analysis, the main components of the extract were determined as chlorogenic and oleic acid, respectively. Total phenol and flavonoid amounts were found as 259.40±0.96 mg GAE/g extract and 2.60±0.57 mg QE/g extract, respectively. It was recorded that it could reduce iron as 6.38 mg TE/g extract in the FRAP test and had an activity effect of 85.26% in the DPPH˙ scavenging test. The anti-inflammatory property of the extract was found to be 60.80±2.22 µg/mL, while DFS was found to be 45.23±0.68 µg/mL. Additionally, in enzyme inhibition, it was observed that it inhibited urease at a low level of 44.19±0.22 µg/mL and xanthine oxidase (XO) at a high level of 0.91±0.21 µg/mL. It was recorded that it protected DNA with a 57.55% Form I value. Based on these results, it was determined that its high phenolic content also contributes to its high radical scavenging ability. Furthermore, the high XO inhibition of this extract suggests that further detailed studies will be required to demonstrate this property. Further *in vivo* and *in silico* studies may be conducted for this purpose. Furthermore, *B. thunbergii* is thought to have potential applications in the food, cosmetics, and medical fields.

Berberis thunbergii bitkisinin hidroetanolik ekstraktının fitokimyasal içerikleri ve *in vitro* aktiviteleri

Anahtar Kelimeler
Berberis thunbergii, Hidroetanolik ekstrakt, Fitokimyasal, *İn vitro* biyoaktivite

Öz: Japon kan otu olarak bilinen *Berberis thunbergii* çeşitli fitokimyasal bileşenleri nedeniyle birçok tıbbi özelliğe sahiptir. Bu nedenle, *B. thunbergii*'nin hidroetanolik ekstraktının fitokimyasal içeriği, antioksidan, anti-inflamatuar ve enzim inhibisyon aktiviteleri incelenmiştir. LC-ESI-MS/MS ve GC-MS/MS analizinde ekstraktın ana bileşenleri sırasıyla klorojenik ve oleik asit olarak belirlendi. Toplam fenol ve flavonoid miktarları sırasıyla 259.40±0.96 mg GAE/g ekstrakt ve 2.60±0.57 mg QE/g ekstrakt olarak bulunmuştur. FRAP testinde 6.38 mg TE/g ekstrakt düzeyinde demiri indirgediği ve DPPH˙ radikal süpürme testinde %85.26 oranında aktivite etkisine sahip olduğu kaydedilmiştir. Ekstraktın antiinflamatuar özelliği 60.80±2.22 µg/mL düzeyinde iken DFS nin 45.23±0.68 µg/mL bulundu. Enzim inhibisyonu açısından değerlendirildiğinde, üreazı düşük düzeyde (44.19±0.22 µg/mL) ve ksantin oksidazı (KO) yüksek düzeyde (0.91±0.21 µg/mL) inhibe ettiği gözlemlenmiştir. Ayrıca, DNA'yı %57.55 oranında (Form I değeri) koruduğu kaydedilmiştir. Bu sonuçlar doğrultusunda, yüksek fenolik bileşen miktarına sahip olması nedeniyle radikal giderme

yeteneğinin de yüksek olduğu belirlenmiştir. Ayrıca yüksek KO inhibisyonu göstermesi bu ekstraktın daha detaylı çalışmalarla bu özelliğinin ortaya koyulabileceği öngörülmektedir. Bunun için *in vivo* ve *in siliko* çalışmalar daha ileri çalışmalarda gerçekleştirilebilir. Ek olarak, *B. thunbergii*'nin gıda, kozmetik ve tıp alanlarında potansiyel uygulamalara sahip olduğu düşünülmektedir.

1. INTRODUCTION

Antioxidants are organic molecules in low quantities that stop various substances from oxidizing by free radicals. Due to their exceptional effectiveness over extended periods, synthetic antioxidants were employed in the food sector for preservation during the past century. Nonetheless, recent studies have revealed the carcinogenic risks of synthetic antioxidants, and many nations have started to impose regulatory limitations on their usage [1]. The food sector and pharmaceutical treatment have recently increased their need for natural antioxidants found in herbs. Consequently, there is an increasing focus on natural antioxidants, particularly those derived from plants [2]. Some plant phenolics are commercially synthesized and have lately been identified as antioxidants. In this regard, understanding the biological availability and necessary concentrations of these antioxidants that offer dietary protection is essential. Natural antioxidants can be used as reducing agents, free radical scavengers, medicinal herbs, and singlet oxygen suppressors. Bioactive substances, including lignans, flavones, isocatechins, coumarins, isoflavones, catechins, anthocyanins, and flavonoids, are responsible for these plant antioxidant properties. Natural antioxidants with few or no adverse effects are being studied pharmacologically more often these days for application in preventative medicine. Many nations have successfully employed these spices in their local remedies due to their well-known health benefits (diuretic, expectorant, laxative, antibacterial, and antipyretic) [3].

Berberis (Berberidaceae) comprises about 500 species and is widely distributed in many regions, including central and southern Europe, the northeastern United States, southern Asia, and northern Pakistan [4, 5]. *B. thunbergii*, known as Japanese dogwood, is an ornamental plant with bright red leaves that can grow up to 2 m tall and is a deciduous structure known as a woody shrub [6]. *Berberis* species are known for their numerous medicinal properties, including antiviral, antimicrobial, antifungal, antioxidant, anti-inflammatory, antiemetic, antipyretic, sedative, and antihypertensive properties, gallbladder stones, ischemic heart disease (IHDS), cardiac arrhythmias, and cardiomyopathies [4, 5]. *B. thunbergii* is rich in phytochemical constituents such as tannins, steroids, alkaloids, terpenoids, proteins, carbohydrates, flavonoids, phenolic compounds, and essential oils [6, 7]. In previous studies, the MTT antioxidant, lipid peroxidation, and COX-1 and COX-2 enzyme inhibition of the methanol extract of *B. thunbergii* var. *atropurpurea* were investigated [8]. In the study by Villinski et al. (2003) [6], the antibacterial activity of the ethanolic extract of *B. thunbergii* was determined. In the other study, silver nanoparticles of *B. thunbergii* were formed, and DPPH˙ scavenging and pancreatic cancer activity were investigated [9]. In the study by Fernández-Poyatos et al. (2019) [7], the antioxidant, enzyme inhibition, and phytochemical contents of the methanol and water extracts of *B. thunbergii* were determined.

In our study, we aimed to evaluate antioxidant (FRAP and DPPH˙ scavenging), anti-inflammatory, DNA protection, and enzyme inhibition (urease and XO) activities of *B. thunbergii* hydroethanolic extract, which has been investigated in a limited number of studies. Also, the contents of *B. thunbergii* extracts were determined by total phenol, total flavonoid, LC-ESI-MS/MS, and GC-MS/MS analysis. The results obtained in this study will contribute new data to the literature. As a result of the tests performed on the *B. thunbergii* hydroethanolic extract, it is recommended that the molecule be used as a drug precursor in the pharmaceutical industry.

2. MATERIAL AND METHOD

2.1. Plant Material and Extraction

The *B. thunbergii* fruits were collected on February 16, 2024, on the Şehit Bülent Yurtseven Campus of Iğdır University/Turkey at 420851.1286 latitude and 4409496.2388 longitude. It was taken to the Iğdır University Research Laboratory Application Center (ALUM) and dried in a suitable ventilated environment. After drying, it was pulverized using a grinder, and 25 grams of the sample was weighed on a precision balance and transferred to a 250 mL Erlenmeyer. 50 mL of ethanol and 50 mL of pure water were added, and the opening was closed with aluminum foil. The extract-solvent mixture was filtered after seven days, and a rotary evaporator was used to remove the solvent. 2 grams of crude *B. thunbergii* hydroethanolic extract (BTHE) were obtained. It was stored at +4 degrees for more accurate analysis.

2.2. LC-ESI-MS/MS and GC-MS/MS Analysis

We used the Agilent 1260 Infinity II LC-ESI-MS/MS equipment to do the content analysis of the *B. thunbergii* hydroethanolic extract. A 100 mm × 3.0 mm, 2.7 µm Agilent Poroshell120 EC-C18 reversed-phase analytical column was employed for the chromatographic separation [10, 11]. 34 phenolic standards were used in the LC-ESI-MS/MS analysis.

1 mL of methanol was added to 50 mg of BTHE. Then, 1 mL of hexane was added to remove lipophilic components, and liquid-liquid extraction was performed. Centrifugation was performed at 9000 rpm for 10 min to clarify the phase separation. 100 µL of the methanol phase obtained after centrifugation was carefully taken, and 450 µL of ultrapure water and 450 µL of methanol were added to make a total volume of 1 mL. The extract was filtered

through a membrane filter with a 0.25 µm pore diameter to prevent particle interference. The prepared samples were injected into the LC-ESI-MS/MS system in the final stage. The device conditions used during the analysis were: Injection volume: 5.12 µL, Flow rate: 0.400 mL/min, Method time: 30.00 min, Column temperature: 40.0 °C. The mobile phase transition rate during the method time was used as follows: 75% A (water) + 25% B (methanol) at 3 min, 50% A + 50% B at 12 min, 10% A + 90% B at 16 min, 10% A + 90% B at 21 min, 97.5% A + 2.5% B at 24 min.

The analysis of the BTHE extract was performed on a GC-MS/MS device, as our previously published article described. This analysis used the Agilent 7000 A GC/MS Triple Quad with 7693 Autosampler, 7697A Headspace Sampler, and 7890 GC [12, 13]. As a procedure, the initial temperature was determined at 50 °C and maintained for two minutes, then increased at 3 °C/min to 140 °C, 4 °C/min to 220 °C for 10 min, and constant at 4 °C/min to 270 °C, and finally continued at 270 °C for 30 min. The ion temperature of the MS detector is 280 °C. The filtered sample with a 0.22 µm disposable syringe filter was run with a 1 mL He gas flow by injecting a volume of 1 µL at a ratio of 1:10. Agilent HP-5 (5%-phenyl)-methyl polysiloxane) (30m x 0.25 mm x 0.25 µm) was carried out on the GC column. 30 mg of the sample was taken, 2 mL MeOH was dissolved, and 2 mL *n*-hexane was added. Then, 1 ml KOH solution (1M) was added and mixed with a vortex device at 2500 rpm for 30 seconds. It was taken from the upper phase (*n*-hexane phase), which contained fatty acid methyl esters and was filtered with 0.22-micron PVDF and injected.

2.3. Total Phenolic and Flavonoid Content Assays

The total phenolic (TP) and flavonoid (TF) contents of plant extract were obtained by Golmakani, Mohammadi et al. (2014) [14] using the methods applied.

To determine the TP content, 500 µL of Folin-Ciocalteu reagent was mixed with 100 µL of extract (or standard gallic acid) solution (1024 µg/mL). One minute after, 1.5 mL of 20% Na_2CO_3 was added, and the mixture was allowed to sit at room temperature for two hours in the dark. At 760 nm, the absorbance values of the mixed solutions were determined. Based on the gallic acid calibration graph, the TP content values of the samples were converted to mg gallic acid equivalent (GAE) using the formula y = 0.0022x + 0.0408 (R^2 = 0.99).

500 µL extract and standard quercetin (1024 µg/mL) solutions were mixed with 1.5 mL methanol, 100 µL 10% $AlCl_3$, 100 µL 1 M CH_3COOK, and 2.8 mL deionized water to determine the TF concentration. Absorbance measurements were taken at 415 nm after the combination was allowed to sit at room temperature in the dark for half an hour. Using the formula y = 0.0061x + 0.0046 (R2 = 0.99), which was derived from the quercetin calibration graph, the TF content values of the samples were converted to mg quercetin equivalent (QE).

2.4. DPPH• Scavenging Activity

In this study, DPPH˙ scavenging activity was evaluated by measuring the DPPH˙ scavenging activity not quenched in the environment by the interaction of antioxidant species. 10 mL of a 100 µg/mL DPPH solution was mixed with 10 mL of the plant extract (250 ppm) or standard (ascorbic acid, 10 ppm). It waited 30 minutes until the interaction reaction of the antioxidant species in the plant content with DPPH˙ was completed, and the potential values were measured by directly immersing these samples in a DPPH-selective PVC membrane biosensor (DPPH-SPMB). The following formula (1) was used. The results were expressed as percentages [15, 16].

$$\%\text{DPPH}^{\cdot}\ \text{scavenging} = \frac{[(E1-E0)-(E2-E0)]}{E1-E0} x100 \qquad (1)$$

E_0 is the potential value of the plant sample. E1 is the potential value of the DPPH• standard solution, and E_2 is the potential value of the DPPH˙ scavenging activity remaining in the medium after 30 minutes of reaction.

2.5. Ferric Reducing Antioxidant Power Activity

The Ferric Reducing Antioxidant Power (FRAP) activity of Fe (III) ions in a dissolved environment was successfully measured using FRAP-SPMB. In our study, iron (III) reduction activity was evaluated by measuring the activity of Fe (III) ion that remained unreduced in the environment as a result of the reduction of Fe (III) ion to Fe (II) ion by antioxidant species. Fe (III) reduction activity results in spectrometer measurements that are expressed as trolox equivalent (mg/g extract). Therefore, in our study, we reported our results as trolox equivalent. For this purpose, a calibration curve for Fe (III)–equivalent trolox was created. Using this calibration curve, the Fe (III) reduction activity of the plant extract (250 ppm) was calculated potentiometrically [15, 16].

2.6. Anti-inflammatory Activity

The anti-inflammatory activity was assessed *in vitro* using the Kandikattu, Kumar et al. (2013) [17] technique to measure its impact on the denaturation of bovine serum albumin (BSA). The procedure involved adding 500 µL of the BSA solution (0.2% produced in ddH_2O) to 500 µL of extract or Diclofenac sodium (DFS) at several concentrations (1000, 500, 250, and 125 µg/mL) in tubes. Additionally, a control tube containing 500 µL of BSA and 500 µL of hydroethanolic was made. After 15 minutes of incubation at 37°C, the mixture was heated for five minutes at 72°C. In a UV-visible spectrophotometer, the absorbance was measured at 660 nm after cooling. IC_{50} (µg/mL) values were calculated using the absorbance values.

2.7. Xanthine Oxidase Inhibition

The 96-well microplate was filled with 50 µL of sample or allopurinol solution, 100 µL of substrate solution

(0.041 mM xanthine), and 50 µL of newly made enzyme solution (0.1 U/mL xanthine oxidase (XO) in PBS (pH 7.5)). For five minutes, the samples were incubated at 37°C. After that, 100 µL of 1 M HCl was added to halt the reaction. A UV-Vis spectrophotometer set at 292 nm was used to measure the absorbance [18]. The absorbance data were used to generate the IC_{50} (µg/mL) values.

2.8. Urease Inhibition

The indophenol technique was used to measure the materials' urease inhibition activity [19]. In a 96-well plate, 50 µL of 17 mM urea, 25 µL of 1 U urease (in 100 mM pH 8.2 Na-K buffer), and 10 µL of samples or thiourea at various concentrations were combined evenly. For fifteen minutes, the samples were incubated at 30ºC. Forty-five liters of phenol reagent (0.1% (w/v) sodium nitroprusside and 8% (w/v) phenol) and seventy liters of alkaline reagent (4.7% (v/v) NaOCl and 2.5% (w/v) NaOH) solutions are combined into the mixture. The mixture was stored for 50 minutes at 30ºC. Using a BIOTEK (Epoch2) microplate reader, the absorbance values of each combination were determined and displayed at 630 nm. The findings' IC_{50} values (µg/mL) were computed.

2.9. DNA Protection Activity

An induced DNA agarose gel electrophoresis assay was performed to evaluate the DNA protection activity of the extracts. In this test, plasmid DNA and H_2O_2 were made to react with UV radiation. The fragmentation ratio of the plasmid DNA molecules was measured by adding pure compounds to a test mixture using an electrophoresis gel tank and a gel imaging system. Results were calculated using the imaging system as the percentage of fragmentation as a positive control. Quercetin was used and compared to the negative control using only the DNA and H_2O_2 mixture [20, 21].

2.10. Statistical Analysis

Activity or enzyme levels ± standard deviations were used to evaluate *in vitro* enzyme inhibitory and antioxidant activities. All data were subjected to one-way ANOVA analysis as the analytical means recorded using the IBM SPSS 20.0 program had a normal distribution. This procedure subjects the data to the Tukey $HSD^{a,b}$ multiple comparison test. The value $p<0.05$ was used to assess the statistical significance level of the data.

3. RESULTS

2.1. LC-ESI-MS/MS Analysis

The phenolic content of the BTHE was obtained by LC-ESI-MS/MS analysis (Figure 1). A total of 10 compounds were found (Table 1). According to the analysis results, chlorogenic acid (2797.41 µg/g extract), *trans*-ferulic acid (192.50 µg/g extract), isoquercitrin (129.07 µg/g extract), and hesperidin (85.48 µg/g extract) were detected in the highest amounts.

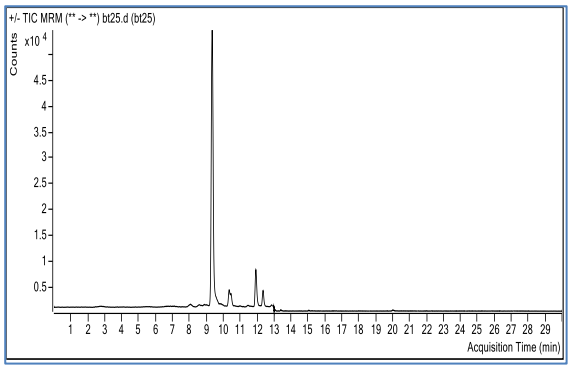

Figure 1. LC-ESI-MS/MS chromatogram of BTHE

Table 1. The LC-ESI-MS/MS analysis results of BTHE

No	RT, min.	Compound name	BTHE, µg/g extract
1	9.35	Chlorogenic acid	2797.41
2	11.44	Vanillic acid	23.11
3	10.35	Caffeic acid	38.37
4	10.48	Hydroxybenzaldehyde	2.10
5	11.90	Rutin	35.41
6	11.45	Polydatin	6.63
7	12.35	*trans*-ferulic acid	192.50
8	11.94	Isoquercitrin	129.07
9	11.90	Hesperidin	85.48
10	13.42	Kaempferol	7.00

RT: Retention time, n:1

2.2. GC-MS/MS Analysis

Fatty acid methyl esters of the hydroethanolic extract of *B. thunbergii* were determined by GC-MS/MS analysis (Figure 2), and it was discovered that it contained six fatty acids (Table 2). According to the analytical result, oleic acid methyl ester (40.91%), palmitic acid methyl ester (22.74%), linoleic acid methyl ester (16.58%), stearic acid, methyl ester (11.01%), oleic acid methyl ester isomer (5.44%) and benzene propanoic acid, 3,5-bis(1,1-dimethyl ethyl)-4-hydroxy- methyl ester (2.07%) were detected.

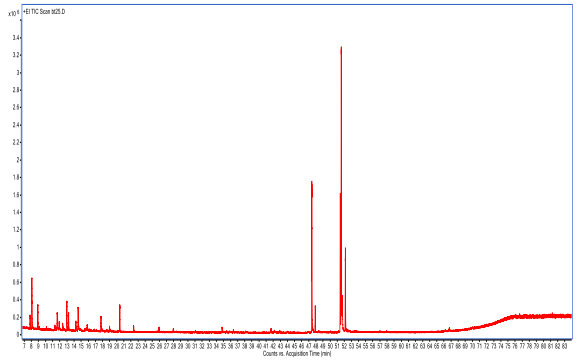

Figure 2. GC-MS/MS chromatogram of BTHE

Table 2. The GC-MS/MS analysis results of BTHE

No	RT, min.	Compound Name	BTHE, %
1	47.43	Palmitic acid, methyl ester	22.74
2	47.90	Benzenepropanoic acid, 3,5-bis(1,1-dimethyl ethyl)-4-hydroxy-, methyl ester	3.32
3	51.43	Linoleic acid, methyl ester	16.58
4	51.56	Oleic acid, methyl ester	40.91
5	51.70	Oleic acid, methyl ester-isomer	5.44
6	52.14	Stearic acid, methyl ester	11.01
Total			100

RT: Retention time, n:1

2.3. Total Phenol (TP) and Flavonoid (TF) Contents

This study shows the TP and TF contents of BTHE. According to this analysis's results, the hydroethanolic extract's total phenol content was found to be 259.40±0.96 mg GAE/g extract. In contrast, the total flavonoid content was 2.61±0.57 mg QE/g extract.

2.4. Antioxidant Activities

Antioxidant activities of BTHE are presented in Table 3. It reduced iron at the rate of 6.38 mg TE/g extract in the FRAP test and scavenged radicals at the rate of 85.26 % (ascorbic acid, 82.35 %) in the DPPH˙ scavenging test.

2.5. Anti-inflammatory Activity

The Inhibition of denaturation of proteins assay is a popular *in vitro* technique for assessing a compound's ability to reduce inflammation, especially phytochemicals. Proteins lose their tertiary structure if they are denatured by external stressors such as heat, pH shifts, or chemicals. As a result, their beneficial qualities are lost. Oxidative stress and inflammation frequently cause protein denaturation, which worsens tissue damage and leads to illnesses [22]. To ascertain if a molecule can prevent protein denaturation, heat or chemical stress is applied to a protein solution, often egg albumin or BSA. When the test substance is added to the protein solution, changes in absorbance, turbidity, or loss of enzyme activity are measured to determine the degree of denaturation [23]. By contrasting the absorbance or activity levels in the presence of the test compound with a control, the protective effects of the chemical are ascertained. By stabilizing proteins and limiting their denaturation, phytochemicals such as flavonoids, polyphenols, and alkaloids demonstrated their anti-inflammatory and protective properties in this test [24]. Bovine serum albumin (BSA) is the most often used protein model. It is heated to 70°C for ten minutes to denaturize the protein solution.

The anti-inflammatory activity of BTHE was seen, and it was observed that BTHE ($IC_{50,}$ 60.80±2.22 µg/mL) had a lower inhibition effect than DFS ($IC_{50,}$ 45.23±0.68 µg/mL) in Table 3. Since no such study on *B. thunbergii* was found in the literature search, this study is the first.

2.6. Urease Inhibition

Numerous eukaryotic and prokaryotic organisms, such as bacteria, plants, fungi, algae, and invertebrates, have nickel-containing amidohydrolase urease. Urea is hydrolyzed by urease to produce carbon dioxide and ammonia [25]. It is well known that *Helicobacter pylori* thrives in the stomach with an increased ammonia level. High ammonia concentrations caused by urease hyperactivity raise the pH of the stomach and can result in peptic and gastric ulcers, kidney stones, pyelonephritis, and hepatic coma [26-28].

Slicing synthetic small molecules to decrease urease activity is the most appealing and successful method of controlling its function. This avoids the gastrointestinal issues brought on by hyperactive urease [29]. Few synthetic urease inhibitors have progressed to the next stage of therapeutic research, such as urease inhibitors, despite a few papers on the topic up to this point [30].

As can be seen in Table 3, the urease inhibition results of BTHE were given, and it was observed that BTHE ($IC_{50,}$ 44.19±0.22 µg/mL) had a lower inhibition effect than thiourea ($IC_{50,}$ 18.79±0.12 µg/mL). Since no such study on *B. thunbergii* was found in the literature search, this study is the first.

2.7. XO Inhibition

Animal hepatic organs are the primary expression site for the molybdenum-containing metalloenzyme XO [31]. It promoted the conversion of hypoxanthine to xanthine, producing uric acid [32, 33]. One significant contributing cause of gout is excessive uric acid. Anti-gout medications have been on the market for a few decades [34], and they fall into several categories, such as uric acid transporter inhibitors [35], urine alkalizing agents [36], XO inhibitors [37], anti-inflammatory analgesics [38], and others. The issue of excessive uric acid generation is not addressed by other pharmacological classes, except for XO inhibitors, which primarily target the inflammatory response triggered by uric acid [39]. XO inhibitors' primary effects are decreasing uric acid generation and inhibiting XO activity. XO activities are intimately linked to the therapeutic effects of XO inhibitors. It has long been challenging for researchers to create a dynamic, real-time process and method to track XO levels *in vivo* and evaluate drug effectiveness. The primary techniques to assess XO activities are radiation, colorimetry, spectrophotometry, and manometry [40].

The XO inhibition findings of BTHE are shown in Table 3, and it was found that BTHE (IC_{50}, 27.07±3.26 µg/mL) had a higher inhibition effect than allopurinol (IC_{50}, 0.91±0.21 µg/mL). This study is the first because the literature search yielded no similar research on *B. thunbergii.*

2.8. DNA Protection Activity

In the agarose gel image of DNA protection activity shown in Figure 3, the brightness of BTHE in Form I is lower than that of the controls. When the percentage form values were calculated, the percentage values of BTHE in Form I and Form II were determined as 57.09 and 51.41, respectively. According to this result, it was observed that in addition to its DNA protection feature, it also has a DNA degradation feature. When compared to C2, it was noted that BTHE's DNA protection activity was low.

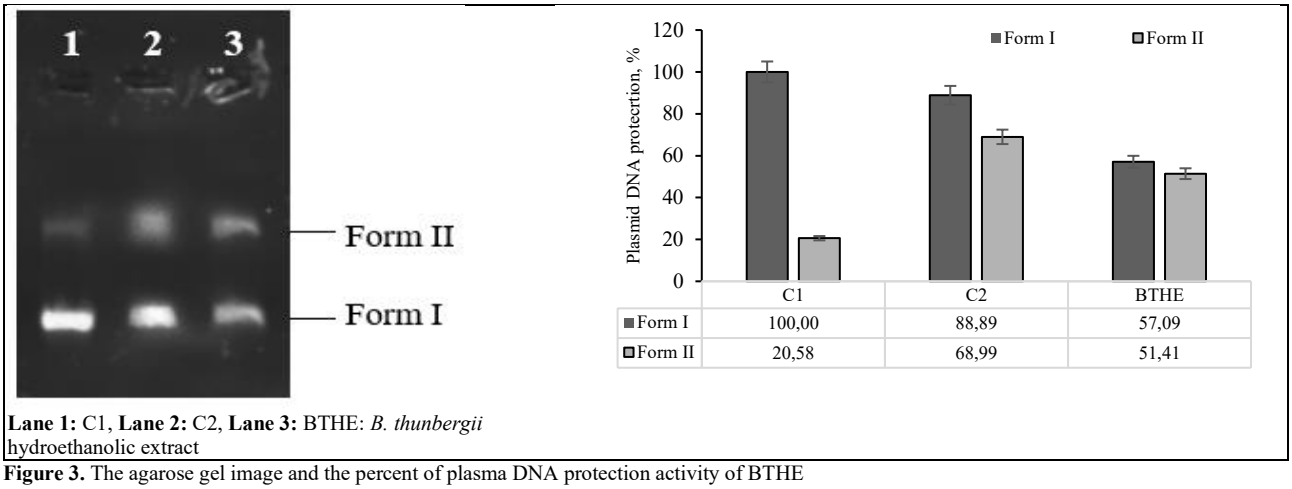

Lane 1: C1, **Lane 2:** C2, **Lane 3:** BTHE: *B. thunbergii* hydroethanolic extract

Figure 3. The agarose gel image and the percent of plasma DNA protection activity of BTHE

Table 3. The antioxidant, anti-inflammatory, urease, and XO inhibition results of BTHE

Sample	FRAP (mg TE/g extract)	DPPH˙ scavenging, %	Anti-inflammatory, IC_{50} (µg/mL)	Urease inhibitory, IC_{50} (µg/mL)	XO inhibitory, IC_{50} (µg/mL)
BTHE	6.37±1.88^{d}	85.26±1.45^{b}	60.80±2.22	44.19±0.22	0.91±0.21
BHT	20.81±1.24^{c}	60.00±1.22^{e}	*nu*	*nu*	*nu*
BHA	23.22±1.20^{b}	47.06±1.50^{f}	*nu*	*nu*	*nu*
Trolox	18.73±1.22^{c}	66.67±1.02^{d}	*nu*	*nu*	*nu*
Gallic acid	27.38±1.21^{a}	75.63±1.22^{c}	*nu*	*nu*	*nu*
Ascorbic acid	22.45±1.20^{b}	89.35±1.23^{a}	*nu*	*nu*	*nu*
DFS	*nu*	*nu*	45.23±0.68	*nu*	*nu*
Thiourea	*nu*	*nu*	*nu*	18.79±0.12	*nu*
Allopurinol	*nu*	*nu*	*nu*	*nu*	27.07±3.26

BHA: Butylated hydroxyanisole, **BTHE:** *B. thunbergii* hydroethanolic extract, **FRAP:** Ferric reducing antioxidant power, **DFS:** Diclofenac sodium, **BHT:** Butylated hydroxytoluene, **XO:** Xanthine oxidase, **nu:** not used **n:**3, $p < 0.05$

4. DISCUSSION AND CONCLUSION

In a similar study, the main constituents in the HPLC-MS analysis of *B. thunbergii* methanol and aqueous extracts were determined to be berberine, rutin, and chlorogenic acid [7]. In a similar study, caffeic acid, rutin hydrate, procyanidin, quinic acid, protocatechuic acid, chlorogenic acid, and narcissin were determined in high amounts in the LC-HRMS analysis of the methanol extract of *B. thunbergii* [41]. A comparison of the literature shows that various extracts of *B. thunbergii* are rich in chlorogenic acid.

In a similar study, analysis of the fatty acid content of the hexane extract of the fruits of *B. crataegina* by GC-MS revealed palmitic acid (9.48%), stearic acid (3.18%), oleic acid (14.07%), linolenic acid (35.25%), α-linolenic acid (37.57%), tricosanoic acid (0.44%) [41].

The total bioactive compounds of many *Berberis* species have been documented in earlier research. Nonetheless, Berberis fruits were the subject of the majority of research [42-44]. In their study, Fernández-Poyatos et al. (2019) [7] found the TPC and TFC results of the *B. thunbergii* methanol extract as 216.00±6.00 mg GAE/g and 46.00±1.00 mg RE/g, respectively. In contrast, the TPC and TFC content of the water extract was found as 194.00±1.00 mg GAE/g and 20.60±0.50 mg RE/g, respectively. When we compared the results of our study with the results in the literature, it was determined that the hydroethanolic extract had a higher phenolic content than the methanol and water extracts.

In a recent study, the TFC and TPC contents were found in methanol (80%, 13.94±0.5 mg CE/g extract for TFC, 53.86±0.40 mg GAE/g extract for TPC), ethanol (80%, 12.2±0.34 mg CE/g extract for TFC, 46.73±1.10 mg GAE/g extract for TPC), and water (10.03±0.47 mg CE/g extract for TFC, 41.76±0.95 mg GAE/g extract for TPC) extracts of *B. orthobotrys* [45]. The literature shows that lower phenolic content was obtained than in our results.
In a recent study, the EC_{50} values of DPPH˙ scavenging activities were found in methanol (80%, 203.15±2.67), ethanol (80%, 270.3±2.16), and water (412.41±6.06) extracts of *B. orthobotrys* and BHA (51.5±2.50), BHT (60.2±2.00) [45]. In the previous study, the FRAP and DPPH˙ scavenging activity results of the *B. thunbergii* methanol and water extracts were found to be

620.00±10.00 mg TE/g for FRAP, 549.00±6.00 mg TE/g for FRAP, 429.00±6.00 mg TE/g for DPPH˙, and 360.00±20.00 mg TE/g for DPPH˙ scavenging [7]. The results of the same plant in the literature are lower than those of the hydroethanolic extract obtained in our study.

In the study conducted by Vignesh, Pradeepa Veerakumari et al. (2021) [46], the anti-inflammatory effects of *B. tinctoria* leaf, stem, and root extracts in methanol, water, ethyl acetate, petroleum ether, and chloroform were investigated, respectively, and the standard used was aspirin. According to this standard, the stem part of the plant showed a lower effect. In contrast, they observed that leaf and fruit parts' ethyl acetate and methanol extracts had higher anti-inflammatory effects. Ethyl acetate and methanol extracts have been reported in the literature to have high anti-inflammatory activity, but in our study, the hydroethanolic extract was found to have

lower activity. This is thought to be due to the different phenolic compounds contained due to the use of different plant species or their different amounts.

This study observed that the *B. thunbergii* hydroethanolic extract examined had a high phenolic content and the highest amount of chlorogenic acid among these phenolic compounds. It was recorded to contain a high amount of oleic acid among fatty acids. In addition, it was determined that its iron-reducing property was lower than the standards, with 6.38 mg TE/g extract value, and its radical scavenging activity was higher than the other standards except for the ascorbic acid standard, with 85.26%. According to this result, it was seen that it had radical scavenging properties. Its anti-inflammatory property was determined by the BSA denaturing method, and it was found that it denatured BSA at a lower rate than the standard DFS used. In enzyme inhibitions, it was observed that the urease inhibition property was weak, but the XO inhibition property was very high. Accordingly, it is thought to lead to further studies as an XO inhibitor. In addition, it was calculated that its DNA protection activity was low. According to all these results, this extract's high xanthine oxidase inhibition suggests that further detailed studies will be needed to demonstrate this property. Future studies may require *in vivo* and *in silico* studies.

Acknowledgement
This work was supported by Ondokuz Mayis University (BAPKOB) with the code BAP04-A-2025-5586.

Conflict of interest
The authors declare that any known financial conflicts or personal relationships did not impact the work presented in this journal.

REFERENCES

[1] Madhavi, D. and D. Salunkhe, Toxicological aspects of food antioxidants, in Food antioxidants. 1995, CRC Press. p. 281-374. https://doi.org/10.1201/9781482273175-12.
[2] Hall, C. and S. Cuppett, Structure-activities of natural antioxidants. Antioxidant methodology in vivo and in vitro concepts, 1997: p. 2-29.
[3] Zainol, M., et al., Antioxidative activity and total phenolic compounds of leaf, root and petiole of four accessions of Centella asiatica (L.) Urban. Food Chemistry, 2003. 81(4): p. 575-581. https://doi.org/10.1016/s0308-8146(02)00498-3.
[4] Rounsaville, T.J. and T.G. Ranney, Ploidy levels and genome sizes of Berberis L. and Mahonia Nutt. species, hybrids, and cultivars. HortScience, 2010. 45(7): p. 1029-1033.
[5] Mokhber-Dezfuli, N., et al., Phytochemistry and pharmacology of berberis species. Pharmacognosy reviews, 2014. 8(15): p. 8.
[6] Villinski, J., et al., Antibacterial activity and alkaloid content of *Berberis thunbergii*, Berberis vulgaris and Hydrastis canadensis. Pharmaceutical Biology, 2003. 41(8): p. 551-557.
[7] Fernández-Poyatos, M.d.P., et al., Phenolic characterization, antioxidant activity, and enzyme inhibitory properties of *Berberis thunbergii* DC. leaves: A valuable source of phenolic acids. Molecules, 2019. 24(22): p. 4171.
[8] Zhang, C.-R., R.E. Schutzki and M.G. Nair, Antioxidant and anti-inflammatory compounds in the popular landscape plant *Berberis thunbergii* var. atropurpurea. Natural Product Communications, 2013. 8(2): p. 1934578X1300800207.
[9] Guo, J., et al., Novel green synthesis and characterization of a chemotherapeutic supplement by silver nanoparticles containing *Berberis thunbergii* leaf for the treatment of human pancreatic cancer. Biotechnology and Applied Biochemistry, 2022. 69(3): p. 887-897.
[10] Yildiz, İ., et al., A phytochemical content analysis, and antioxidant activity evaluation using a novel method on Melilotus officinalis flower. South African Journal of Botany, 2024. 174: p. 686-693.
[11] Erenler, R., et al., Phytochemical analyses of Ebenus haussknechtii flowers: Quantification of phenolics, antioxidants effect, and molecular docking studies. Bütünleyici ve Anadolu Tıbbı Dergisi, 2024. 5(2): p. 1-9. https://doi.org/10.53445/batd.1479874.
[12] Başar, Y., et al., Phytochemical profiling, molecular docking and ADMET prediction of crude extract of Atriplex nitens Schkuhr for the screening of antioxidant and urease inhibitory. International Journal of Chemistry and Technology, 2024. 10.32571/ijct.1389719.
[13] Başar, Y. and R. Erenler, Phytochemical analysis of Silybum marianum flowers: Quantitative analysis of natural compounds and molecular docking application. Turkish Journal of Biodiversity, 2024. 7(1): p. 20-31. https://doi.org/10.38059/biodiversity.1450643.
[14] Golmakani, E., et al., Phenolic and flavonoid content and antioxidants capacity of pressurized liquid extraction and perculation method from roots of Scutellaria pinnatifida A. Hamilt. subsp alpina (Bornm) Rech. f. The Journal of Supercritical Fluids, 2014. 95: p. 318-324. https://doi.org/10.1016/j.supflu.2014.09.020.
[15] Isildak, Ö., I. Yildiz and N. Genc, A new potentiometric PVC membrane sensor for the determination of DPPH radical scavenging activity of plant extracts. Food Chem, 2022. 373(Pt A): p. 131420. 10.1016/j.foodchem.2021.131420.
[16] Isildak, Ö., et al., New potentiometric PVC membrane electrode for Ferric Reduction Antioxidant Power assay. Food Chemistry, 2023. 423: p. 136261. https://doi.org/10.1016/j.foodchem.2023.136261.
[17] Kandikattu, K., et al., Evaluation of anti-inflammatory activity of Canthium parviflorum by in-vitro method. Indian Journal of Research in Pharmacy and Biotechnology, 2013. 1(5): p. 729-731.
[18] Li, Z., et al., İn silico identification and experimental validation of two types of angiotensin-converting enzyme (ACE) and xanthine oxidase (XO) milk inhibitory peptides. Food Chemistry, 2025. 464: p. 141864. https://doi.org/10.1016/j.foodchem.2024.141864.

[19] Zhang, L., et al., Inhibition of urease by bismuth (III): implications for the mechanism of action of bismuth drugs. Biometals, 2006. 19(5): p. 503-511. https://doi.org/10.1007/s10534-005-5449-0.
[20] Yenigun, S., et al., DNA protection, molecular docking, antioxidant, antibacterial, enzyme inhibition, and enzyme kinetic studies for parietin, isolated from Xanthoria parietina (L.) Th. Fr. Journal of Biomolecular Structure and Dynamics, 2024. 42(2): p. 848-862. https://doi.org/10.1080/07391102.2023.2196693
[21] İpek, Y., et al., İn vitro bioactivities and in silico enzyme interactions of abietatrien-3β-ol by bio-guided isolation from Nepeta italica subsp. italica. Journal of Biomolecular Structure and Dynamics, 2024. 42(1): p. 1-24. https://doi.org/10.1080/07391102.2024.2322626.
[22] Hasan, M.M., et al., Unveiling the therapeutic potential: Evaluation of anti-inflammatory and antineoplastic activity of Magnolia champaca Linn's stem bark isolate through molecular docking insights. Heliyon, 2024. 10(1).
[23] Kalaskar, M., et al., Isolation and Characterization of Anti-Inflammatory Compounds from Ficus microcarpa Lf Stem Bark. Plants, 2023. 12(18): p. 3248.
[24] Akbar, A., et al., Investigation of Anti-Inflammatory Properties, Phytochemical Constituents, Antioxidant, and Antimicrobial Potentials of the Whole Plant Ethanolic Extract of Achillea santolinoides subsp. wilhelmsii (K. Koch) Greuter of Balochistan. Oxidative Medicine and Cellular Longevity, 2023. 2023(1): p. 2567333.
[25] Begum, F., et al., Synthesis and urease inhibitory potential of benzophenone sulfonamide hybrid in vitro and in silico. Bioorganic & Medicinal Chemistry, 2019. 27(6): p. 1009-1022.
[26] Yakan, H., et al., Synthesis, structure elucidation, biological activity, enzyme inhibition and molecular docking studies of new Schiff bases based on 5-nitroisatin-thiocarbohydrazone. Journal of Molecular Structure, 2023. 1277: p. 134799.
[27] Yakan, H., et al., Kinetic Studies, Antioxidant Activities, Enzyme Inhibition Properties and Molecular Docking of 1, 3-Dihydro-1, 3-Dioxoisoindole Derivatives. Acta Chimica Slovenica, 2023. 70(1): p. 29-43. https://doi.org/10.17344/acsi.2022.7808.
[28] Çakmak, Ş., Novel diamide derivatives: Synthesis, characterization, urease inhibition, antioxidant, antibacterial, and molecular docking studies. Journal of Molecular Structure, 2022. 1261: p. 132932.
[29] Kosikowska, P. and Ł. Berlicki, Urease inhibitors as potential drugs for gastric and urinary tract infections: a patent review. Expert opinion on therapeutic patents, 2011. 21(6): p. 945-957.
[30] Jiang, X.-Y., et al., Mechanism, kinetics, and antimicrobial activities of 2-hydroxy-1-naphthaldehyde semicarbazone as a new Jack bean urease inhibitor. New Journal of Chemistry, 2016. 40(4): p. 3520-3527.
[31] Cao, H., J. Hall and R. Hille, X-ray crystal structure of arsenite-inhibited xanthine oxidase: μ-sulfido, μ-oxo double bridge between molybdenum and arsenic in the active site. Journal of the American Chemical Society, 2011. 133(32): p. 12414-12417.
[32] Shi, C., et al., Recent advances in gout drugs. European Journal of Medicinal Chemistry, 2023. 245: p. 114890.
[33] Theken, K.N., Variability in analgesic response to non-steroidal anti-inflammatory drugs. Prostaglandins & other lipid mediators, 2018. 139: p. 63-70.
[34] Lomen, P.L., et al., Flurbiprofen in the treatment of acute gout: a comparison with indomethacin. The American journal of medicine, 1986. 80(3): p. 134-139.
[35] Herman, M.K., Differential spectrophotometry of purine compounds by means of specific enzymes. Journal of Biological Chemistry, 1947. 167: p. 429-443.
[36] Grum, C.M., et al., Plasma xanthine oxidase activity in patients with adult respiratory distress syndrome. Journal of critical care, 1987. 2(1): p. 22-26.
[37] Huang, J. and K. Pu, Near-infrared fluorescent molecular probes for imaging and diagnosis of nephro-urological diseases. Chemical Science, 2021. 12(10): p. 3379-3392.
[38] Pillinger, M.H. and B.F. Mandell. Therapeutic approaches in the treatment of gout. in Seminars in Arthritis and Rheumatism. 2020. Elsevier.
[39] Yu, X., et al., Mitochondria-targetable small molecule fluorescent probes for the detection of cancer-associated biomarkers: A review. Analytica chimica acta, 2024. 1289: p. 342060.
[40] Yang, Y., et al., Development of xanthine oxidase activated NIR fluorescence probe in vivo imaging. Sensors and Actuators B: Chemical, 2025. 422: p. 136563.
[41] Ercan, L., Bioactive components, antioxidant capacity, and antimicrobial activity of Berberis crataegina fruit. Pharmacological Research - Natural Products, 2024. 2: p. 100020. https://doi.org/10.1016/j.prenap.2024.100020.
[42] Shan, S., et al., Evaluation of polyphenolics content and antioxidant activity in edible wild fruits. BioMed research international, 2019. 2019(1): p. 1381989.
[43] Bustamante, L., et al., Pharmacokinetics of low molecular weight phenolic compounds in gerbil plasma after the consumption of calafate berry (Berberis microphylla) extract. Food chemistry, 2018. 268: p. 347-354.
[44] Lemoui, R., et al., Isolation of phytoconstituents and evaluation of biological potentials of Berberis hispanica from Algeria. Bangladesh Journal of Pharmacology, 2018. 13(2): p. 179-186.
[45] Karimkhani, M., et al., Effect of extraction solvents on lipid peroxidation, antioxidant, antibacterial and antifungal activities of Berberis orthobotrys Bienerat ex CK Schneider. Journal of Food Measurement and Characterization, 2019. 13: p. 357-367.

[46] Vignesh, A., et al., Nutritional assessment, antioxidant, anti-inflammatory and antidiabetic potential of traditionally used wild plant, Berberis tinctoria Lesch. Trends in Phytochemical Research, 2021. 5(2): p. 71-92.

Volume 14, Issue 3, Page 192-201, 2025 https://doi.org/10.46810/tdfd.1652908 Research Article

BİNGÖL UNIVERSITY

Türk Doğa ve Fen Dergisi
Turkish Journal of Nature and Science
www.dergipark.gov.tr/tdfd

Non-Destructive Prediction of Maturity from the Sound of Hand Hitting a Watermelon Using Machine Learning

Savaş KOÇ[1*], Ferit AKBALIK[2]

[1] Batman University, Faculty of Engineering and Architecture, Department of Mechanical Engineering, Batman, Türkiye
[2] Batman University, Vocational School of Social Sciences, Batman, Türkiye
Savaş KOÇ ORCID No: 0000-0002-5257-3287
Ferit AKBALIK ORCID No: 0000-0002-9791-1809

**Corresponding author: savas.koc @batman.edu.tr*

(Received: 06.03.2025, Accepted: 12.09.2023, Online Publication: 26.09.2025)

Keywords
Acoustic feature extraction,
Agricultural signal processing,
Maturity prediction,
Non-invasive fruit analysis,
Sound classification,
Supervised learning models

Abstract: Traditional methods for assessing the quality, taste, and maturity of fruits and vegetables without cutting rely on external attributes such as color, shape, surface patterns, and acoustic responses. In this study, maturity levels of watermelons were validated through physical inspection after cutting, and the corresponding acoustic data were analyzed using spectrograms, extracting 120 features each sample. Several machine learning algorithms, including Support Vector Classifier, Decision Tree Classifier, Random Forest Classifier (RFC), Multi-Layer Perceptron Classifier, and K-Nearest Neighbors Classifier (KNC), were evaluated. Among them, the KNC model achieved the highest accuracy (96.04%), followed closely by the RFC model (95.47%). Specifically, the RFC model classified mature watermelons with 98.2% accuracy, while the KNC model effectively distinguished overmature and immature samples with accuracies of 96.3% and 96.2%, respectively. Robustness against background noise was also demonstrated despite the naturally recorded dataset. The findings were compared with studies on acoustic pattern recognition in animals, environmental acoustics, and healthcare, highlighting the potential of machine learning-based approaches as a reliable, non-invasive method for maturity and taste assessment with practical applications in agriculture and the food industry.

Makine Öğrenimi Kullanarak Elle Vurulan Karpuzun Sesinden Tahribatsız Olgunluk Tahmini

Anahtar Kelimeler
Akustik özellik çıkarımı,
Gözetimli öğrenme modelleri,
Olgunluk tahmini,
Ses sınıflandırma,
Tahribatsız meyve analizi,
Tarımsal sinyal işleme

Öz: Meyve ve sebzelerin kesilmeden kalite, tat ve olgunluklarının değerlendirilmesinde geleneksel yöntemler genellikle renk, şekil, yüzey desenleri ve akustik tepkiler gibi dış özelliklere dayanır. Bu çalışmada, karpuzların olgunluk seviyeleri kesim sonrası fiziksel inceleme ile doğrulanmış, elde edilen akustik veriler spektrogramlarla analiz edilerek her örnek için 120 öznitelik çıkarılmıştır. Destek Vektör Sınıflandırıcısı (SVC), Karar Ağacı Sınıflandırıcısı, Rastgele Orman Sınıflandırıcısı (RFC), Çok Katmanlı Algılayıcı Sınıflandırıcısı (MLP) ve K-En Yakın Komşu Sınıflandırıcısı (KNC) algoritmaları değerlendirilmiştir. Bunlar arasında en yüksek doğruluğu %96,04 ile KNC modeli elde etmiş, onu %95,47 ile RFC modeli izlemiştir. Özellikle, RFC modeli olgun karpuzları %98,2 doğrulukla sınıflandırırken, KNC modeli aşırı olgun ve az olgun örnekleri sırasıyla %96,3 ve %96,2 doğrulukla ayırt etmiştir. Doğal ortamda kaydedilen veri setine rağmen arka plan gürültüsüne karşı da sağlamlık gösterilmiştir. Bulgular, hayvanlarda akustik desen tanıma, çevresel akustik ve sağlık alanındaki çalışmalarla karşılaştırılmış olup, makine öğrenmesine dayalı yaklaşımların olgunluk ve tat değerlendirmesinde güvenilir ve invazif olmayan bir yöntem sunduğu, tarım ve gıda endüstrisinde pratik uygulama potansiyeline sahip olduğu ortaya konmuştur.

1. INTRODUCTION

Agriculture is a cornerstone of global economic development and serves as a primary source of employment for impoverished populations worldwide [1]. The emergence of Smart Agriculture has introduced a transformative paradigm that utilizes Information and Communication Technologies (ICT) to address critical global challenges such as hunger, malnutrition, and food security. By incorporating advanced technologies, Smart Agriculture seeks to enhance crop yields, optimize cultivation practices, improve productivity, and ensure higher product quality [2]. Increasing consumer expectations for efficiency, reduced physical labor, and rapid outcomes have further accelerated the adoption of digital farming systems [3]. These innovations not only lower the dependency on traditional manual practices but also improve operational efficiency and generate new employment opportunities in the agricultural sector [4].

Watermelon (Citrullus lanatus), prized for its sweetness and high-water content, is among the most widely consumed fruits worldwide, primarily enjoyed fresh [5]. According to the Food and Agriculture Organization of the United Nations (FAO), nearly 70 million tons of watermelon are produced annually across approximately 100 countries and regions [6]. The quality of watermelon is influenced by both external characteristics, such as shape and size, and internal attributes, including maturity, pulp firmness, sugar concentration, water content, and internal defects. Among these, sweetness remains the most decisive factor shaping consumer preference and internal quality [7–8].

1.1. Non-Destructive Assessment of Watermelon Maturity

Traditionally, watermelon maturity has been evaluated using empirical methods such as tapping sounds, rind pattern inspection, and weight measurement. However, these approaches are often subjective and lack precision. Recent advancements in non-destructive technologies have introduced more reliable alternatives, including X-ray Computed Tomography (CT) [9], acoustic analysis [10], machine vision [11], dielectric property measurement [12], Hyperspectral Imaging (HSI) [13], and Surface-Enhanced Raman Spectroscopy (SERS) [14]. These methods support the development of regression and classification models for maturity prediction, leveraging acoustic and image processing for precise evaluation [6,15].

Non-destructive approaches have successfully assessed watermelon hardness and sweetness by integrating data from tapping sounds, rind features, and weights. Acoustic impulse methods, combined with linear models and Artificial Neural Networks (ANN), have achieved promising accuracy in classifying watermelon maturity [16]. Moreover, fusion techniques that combine acoustic and visual information have reported classification accuracies as high as 92% using gradient tree-based models [17]. These findings demonstrate the potential of integrating traditional practices with advanced technologies for improved agricultural outcomes.

The rapid progress of Artificial Intelligence (AI) has further transformed agricultural practices. AI methods such as neural networks, fuzzy logic, genetic algorithms, and machine learning are increasingly applied across domains including agriculture, healthcare, and robotics [18–20]. In sound-based analysis, approaches originally developed for medical applications such as heartbeat and respiratory monitoring are now being adapted to agriculture. These applications include classifying animal sounds, environmental noises, and fruit maturity [21–23]. For audio signal processing, representations such as spectrograms, Mel-Frequency Cepstral Coefficients (MFCC), and Zero-Crossing Rate (ZCR) are commonly employed. Advanced deep learning techniques, particularly Convolutional Neural Networks (CNN), enhance feature extraction from spectrograms and waveforms, significantly improving classification accuracy. Architectures such as VGGish and bottleneck CNN further strengthen feature representation through 1D and 2D convolutional layers, offering robust solutions for sound-based classification tasks [24–26].

Table 1. Non-destructive quality assessment methods

Studies	Technique	Advantages	Disadvantages
[27]	NIR Spectroscopy	Non-destructive, fast, accurate (>88%), can be portable	Expensive, sensitive to lighting/surface, needs calibration
[28]	Image Processing	Simple, low-cost, reasonably accurate (76–89%)	Surface-only info, lighting/angle dependent, rind pattern affects results
[29]	Acoustic Response	Easy, non-destructive, high accuracy (>90%)	Sensitive to tapping, noisy environments, some fruits must be cut
[30]	Microwave Imaging	Visualizes internal structure, high-resolution	Expensive, complex setup, limited field use
[31]	Portable NIR Spectrometer	Field-ready, practical accuracy	Requires per-variety calibration, sunlight may affect results, costly
[32]	Traditional/Visual Methods	Very simple, no equipment needed	Subjective, low accuracy, causes fruit waste

Recent studies have explored a variety of non-destructive techniques for assessing agricultural product quality, each with distinct advantages and limitations, as summarized in Table 1. Near-Infrared (NIR) Spectroscopy has been shown to provide fast, non-destructive, and accurate measurements (>88%), with potential for portable applications, though it remains costly and sensitive to lighting and surface conditions [27]. Image processing methods, including color and texture analysis, offer a simple and low-cost approach with reasonable accuracy (76–89%), yet they provide only surface-level information and are affected by lighting, camera angle, and rind patterns [28]. Acoustic response techniques, such as hand-tapping combined with MFCC analysis, are easy

to implement, non-destructive, and achieve high accuracy (>90%), but their performance is influenced by tapping force, environmental noise, and occasionally requires cutting fruits for labeling [29]. Microwave imaging enables visualization of internal structure with high resolution, but its complexity, high cost, and limited field applicability restrict widespread use [30]. Portable NIR spectrometers offer practical, field-ready solutions, although calibration per variety and sunlight interference remain challenges [31]. Traditional visual methods, such as tapping and rind inspection, are simple and require no equipment, but they are subjective, less accurate, and can lead to fruit waste [32]. Despite these advances, scalable, non-destructive, and cost-effective quality evaluation methods remain a critical need. Combining traditional evaluation practices with modern machine learning algorithms holds promise for developing more accurate and objective assessment systems.

The primary aim of this study is to evaluate watermelon maturity in a non-destructive manner using machine learning. Unlike traditional methods that rely solely on tapping sounds or rind patterns, this study integrates traditional indicators with advanced acoustic signal processing and image analysis. The collected data are used to train classification models, including Multi-Layer Perceptron (MLP), Support Vector Classifier (SVC), Random Forest Classifier (RFC), and K-Nearest Neighbors Classifier (KNC), to identify the most accurate prediction approach.

Feature extraction focuses on acoustic representations such as mel-spectrograms, MFCC, and other sound-based attributes, which are subsequently analyzed using machine learning techniques. By bridging traditional practices with modern data-driven methods, this research aims to provide an efficient, scalable, and objective framework for agricultural quality assessment.

2. MATERIAL AND METHOD

The shape of a watermelon has traditionally been an important criterion for selection, particularly in markets and greengrocers. Experienced farmers often assess quality by tapping the watermelon and interpreting the resulting acoustic signals. To evaluate watermelon taste through these sounds, as illustrated in Figure 1, systematic sound recordings are collected during the data acquisition process. The tapping-generated acoustic signals from the outer surfaces of selected watermelons are recorded, after which the watermelons are cut and categorized into three groups: immature, mature, and overmature.

The recorded signals are then analyzed, and their features are extracted to serve as inputs for classification models. These models are trained on the extracted features to predict watermelon maturity and quality. The results highlight the correlation between tapping sounds and internal taste attributes, confirming the potential of sound-based methods as effective tools for agricultural quality assessment.

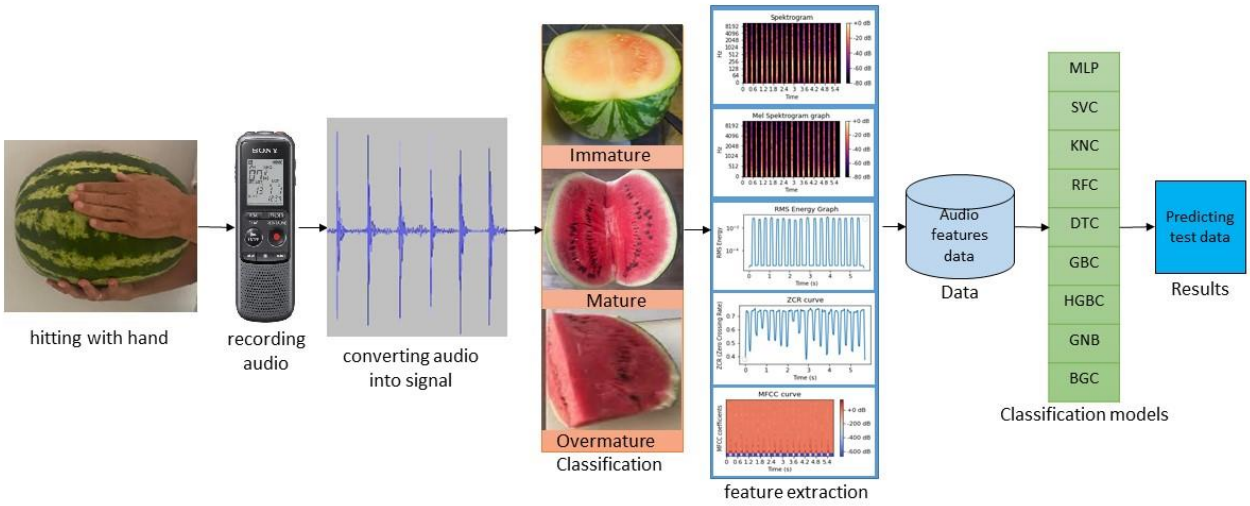

Figure 1. An overview of this study

2.1. Data Acquisition

This study was conducted on watermelons cultivated in the South-Eastern region of Turkey during the summer season, where two primary cultivation practices are common: irrigated and non-irrigated farming. Regional consumers generally prefer non-irrigated watermelons, which are perceived to offer superior taste and quality. Accordingly, for this study, non-irrigated watermelons weighing between 4 and 12 kilograms were selected as the main data source.

The samples were collected both directly from fields and from various points of sale, including local markets and roadside stands. During data acquisition, acoustic signals were recorded by tapping the outer surface of each watermelon with a seller's hand. Before cutting, the watermelons were classified into three maturity groups: immature, mature, and overmature. The recorded signals were then used for feature extraction and classification analyses, allowing a systematic investigation of the relationship between acoustic properties and watermelon maturity.

2.2. Pre-processing Data

The acoustic signals generated by tapping the watermelons were recorded using a high-quality sound device and processed with Audacity software for detailed analysis. To ensure data integrity and clarity, background noise between taps—arising from natural environmental conditions—was carefully removed. The cleaned audio files were then systematically categorized according to watermelon maturity and organized into separate class folders, as shown in Figure 2. This structured procedure ensured accurate labeling and reliable preparation of the dataset for subsequent feature extraction, analysis, and classification.

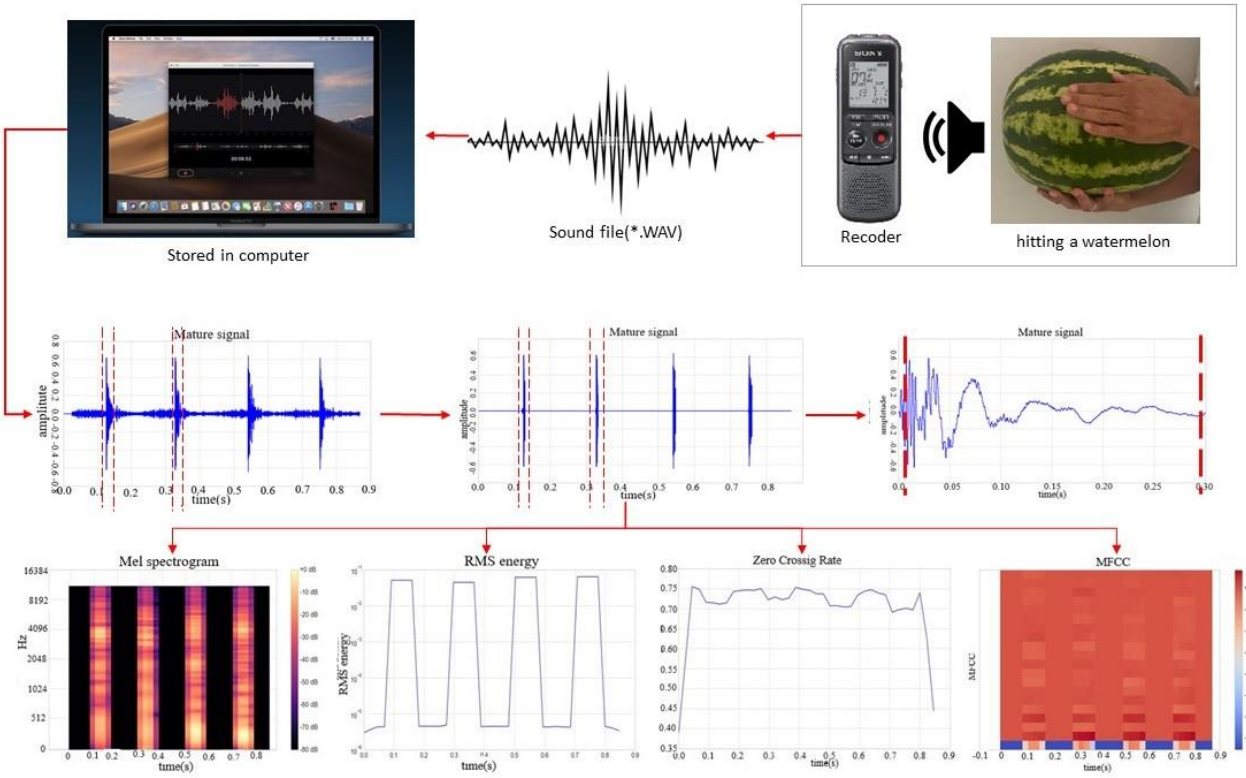

Figure 2. Processing and schematic of sound files

2.3. Sound Analysis and Feature Extraction

The Librosa library is widely used for sound and music analysis, providing essential tools for building audio-focused information systems. It supports various audio formats, including WAV and MP3, and enables spectrogram analysis as well as the extraction of relevant acoustic features. In addition to feature extraction, Librosa offers functionalities for audio manipulation, playback, and visualization. Key methods for generating instantaneous frequency spectrograms include spectral bandwidth, Short-Time Fourier Transform (STFT), and spectral flatness, with outputs presented graphically [33].

In this study, sound feature data were obtained through spectrograms, mel-spectrograms, MFCC images, Root Mean Square (RMS) energy curves, and ZCR curves. Spectrograms visually represent sound characteristics by showing signal intensity across different frequencies. The mel-spectrogram applies a perceptual scale based on human hearing (Eq. 3), while MFCC images capture frequency perception dynamics. ZCR indicates how often the signal crosses the zero amplitude line, reflecting the frequency of signal changes (Eq. 1), and RMS curves represent the overall energy distribution of the signal (Eq. 2). Using these analytical and visual techniques, a total of 120 features were extracted from each sound sample.

$$ZCR = \frac{1}{2N}\sum_{n=1}^{N} |sign(x[n]) - sign(x[n-1])| \quad (1)$$

$$RMS\ Energy = \sqrt{\frac{1}{N}\sum_{n=1}^{N} |x(n)|^2} \quad (2)$$

$$Mel(f) = 2595 \log\left(1 + \frac{f}{700}\right) \quad (3)$$

In this study, several libraries were employed to read sound files from directories and extract relevant features. The os library facilitated folder access and management, while Librosa was used for audio processing. NumPy and Pandas supported data manipulation and organization, and Matplotlib and Seaborn were used for visualization.

The scikit-learn (sklearn) library was applied to split the dataset into training and testing sets, develop classification models, and evaluate their performance. Key audio features were extracted and converted into a structured format suitable for analysis. The resulting feature dataset was then divided into training and testing subsets and applied to various classification techniques, allowing the identification of the most effective prediction models using machine learning methods.

2.4. Machine Learning Classification Models

In this study, various classification models were applied to the dataset, including SVC, Simple Linear Regression (SLR), Polynomial Regression, Decision Tree Classifier (DTC), RFC, MLP, KNC, Gradient Boosting Classifier (GBC), Gaussian Naive Bayes Classifier (GNB), and Bagging Classifier (BGC). The primary models used for classification were MLP, SVC, KNC, GBC, GNB, DTC, RFC, and BGC, as shown in Figure 3. SVC models employ linear and non-linear decision boundaries to maximize the margin between classes by identifying support vectors. Equation 4 defines linear support vectors, while Equation 5 provides the formulation for non-linear support vectors [34]. For the SVC, kernel="poly", degree=2, and gamma="auto" were used.

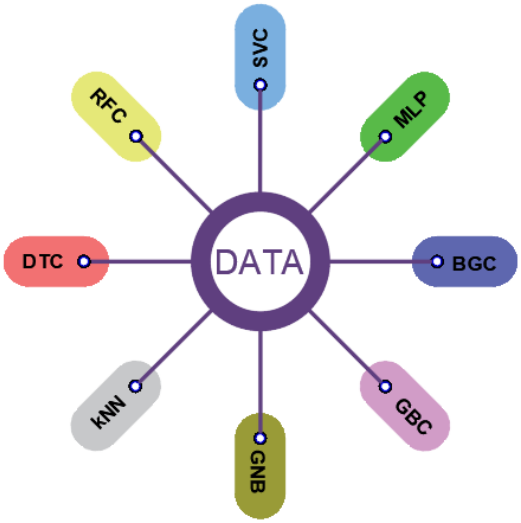

Fig. 3: Machine learning classification models

$$\sum_{i=1}^{N}(\alpha_i - \alpha_1^*).\langle x_i, x\rangle + b \quad (4)$$

$$\sum_{i=1}^{N}(\alpha_i - \alpha_1^*).\langle \varphi(x_i), \varphi(x)\rangle + b \quad (5)$$

The DTC algorithm partitions input data, which may include varying numbers of nodes and branches, into leaves and branches based on a function determined during training. It recursively splits the data space, integrating simple prediction models within each partition to construct a graphical decision tree. The primary goal is to generate an optimal decision tree from the dataset [35]. For the DTC, criterion="entropy" and splitter="best" were used.

The RFC creates multiple decision trees using different subsets of the input data to form an ensemble model for classification. Each tree is built from independently sampled data, and final predictions are obtained by aggregating outputs from all trees. Increasing the number of trees generally reduces generalization error, enhancing predictive accuracy, internal correlation, and error characteristics [36]. The KNC is widely used for its simplicity and robust performance. Selecting the optimal parameter k is critical, as both accuracy and training efficiency depend on it. KNC classifies data points by measuring their distance to the nearest neighbors in the training set, making decisions based on proximity within the feature space [37]. For the KNC, n_neighbors=3 was used.

ANN, inspired by the human nervous system, are applied to tasks such as dynamic system identification, pattern classification, and function approximation. In ANN, input data are processed by multiplying connection weights and applying activation functions across hidden layers. MLP models, a type of ANN, consist of an input layer, one or more hidden layers, and an output layer, and use a non-linear, supervised training algorithm to learn complex patterns [38]. For the MLP, hidden layers = (1024, 1024, 1024, 1024) and max_iter=1000 were used. The performance of the classification models was evaluated using accuracy, precision, recall, and F1 score, calculated according to Equations 6–9.

$$Accuracy = \frac{TP+TN}{TP+TN+FP+FN} \quad (6)$$

$$Precision = \frac{TP}{TP+FP} \quad (7)$$

$$Recall = \frac{TP}{TP+FN} \quad (8)$$

$$F1 = 2\frac{Precision*Recall}{Precision+Recal} \quad (9)$$

Where TP is the number of true positives, TN is the number of true negatives, FP is the number of false positives and FN is the number of false negatives.

3. RESULTS

In this study, watermelons were sourced from grocery stores and directly from fields. After being tapped by hand, the resulting sounds were recorded. Classification was determined post-cut based on internal color and taste: red and sweet watermelons were labeled mature, deteriorated or degraded watermelons as overmature, and white or pink interiors as immature, resulting in three classes. The dataset comprised 1,672 samples: 802 mature, 500 overmature, and 370 immature. Features were extracted using spectrograms, mel-spectrograms, MFCC images, RMS energy, and ZCR curves via Librosa, totaling 120 features each sample.

The dataset was split into 80% training and 20% test data. Training data were applied to classification models including MLP, KNC, SVC, RFC, DTC, GBC, HGBC, GNB, and BGC. Model performance was evaluated using precision, recall, and F1 scores. As shown in Table 2, KNC achieved the highest accuracy at 96.66%, while GNB had the lowest at 51%. KNC attained the highest precision (98.77%) for the mature class, whereas HGBC scored highest for immature (100%) and overmature (96.34%). Regarding recall, MLP scored highest for overmature (98.15%), and KNC performed best for mature (98.78%) and immature (96.15%). These results demonstrate that sound-based classification provides a

reliable, non-destructive method for assessing watermelon maturity.

For F1 scores, the KNC model achieved the highest score of 97.3% for the mature class, while HGBC scored highest for overmature (95.93%) and immature (96.61%). The DTC, GNB, and BGC models showed lower F1 scores. Overall, precision, recall, and F1 analyses indicate that KNC and HGBC outperformed the others, particularly for the mature and overmature classes, whereas GNB and BGC underperformed. Classification training results are presented in Figure 4, highlighting KNC and HGBC as the most effective models for predicting watermelon maturity.

Confusion matrices generated from test data are shown in Figure 5. These matrices compare actual versus predicted classes to determine prediction success. For MLP, 159 of 167 mature samples were correctly classified (95.2%), 96 of 108 overmature samples were correctly predicted (88.9%), and 73 of 78 immature samples were correctly identified (93.6%). Misclassifications occurred among the remaining samples across the classes.

Table 2. Classification metric results

Model	Class	Accuracy (%)	Precision (%)	Recall (%)	f1 (%)
MLP	mature	92.92	97.39	89.22	93.13
	overmature		86.18	**98.15**	91.78
	immature		90.91	89.75	90.33
RFC	mature	95.46	93.72	98.2	95.91
	overmature		96.23	94.45	95.33
	immature		98.61	91.03	94.67
DTC	mature	70.26	78.95	71.86	75.24
	overmature		65.22	69.45	67.27
	immature		62.8	69.23	65.86
HGBC	mature	96.34	94.12	97.56	95.81
	overmature		**96.34**	95.5	**95.93**
	immature		**100**	93.59	**96.61**
GBC	mature	93.21	91.48	96.41	93.88
	overmature		94.34	92.6	93.46
	immature		95.78	87.18	91.28
SVC	mature	91.5	91.13	92.22	91.67
	overmature		94.4	93.52	93.96
	immature		88.32	87.18	87.75
GNB	mature	51	53.61	71.26	61.19
	overmature		55	30.56	39.29
	immature		39.44	35.9	37.59
KNC	mature	**96.66**	**98.77**	**98.78**	**97.3**
	overmature		95.42	93.7	95.86
	immature		91.47	**96.15**	96.16
BGC	mature	87.82	85.03	95.21	89.84
	overmature		90.91	83.34	86.96
	immature		91.05	78.21	84.14

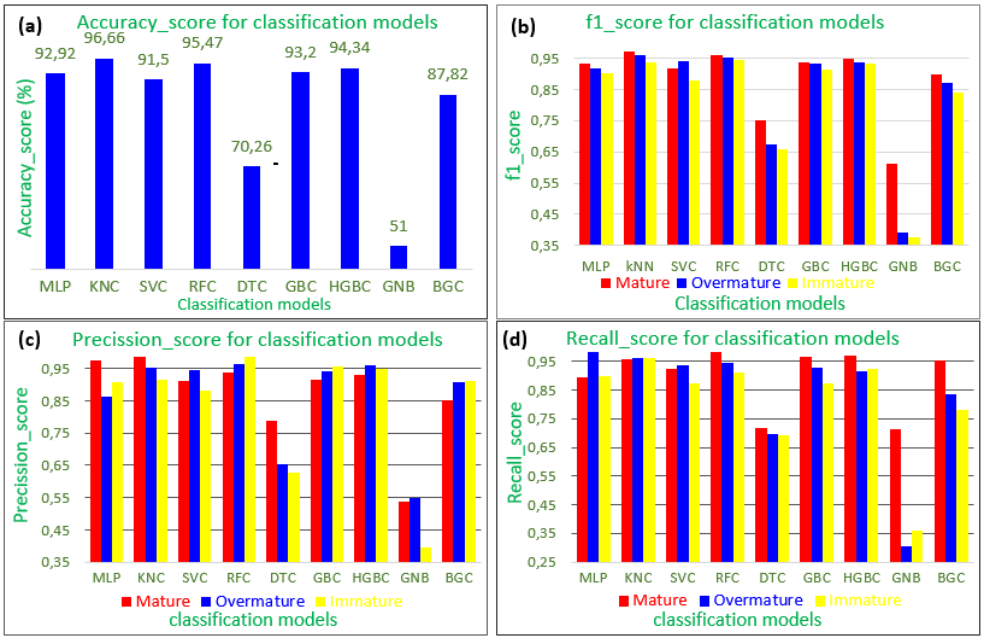

Figure 4. Results of training a) Accuracy_score b) f1_score c) Precission_score d) Recall_score

These confusion matrices illustrate model prediction accuracy across watermelon maturity classes. High success rates demonstrate that the classification models generally perform well, though some variation exists between classes. The RFC model achieved the highest accuracy for the mature class, while KNC performed best for the immature and overmature classes. In contrast, GNB exhibited the lowest accuracy across all classes. For the mature class, the top-performing model correctly predicted 164 of 167 test samples (98.2%), whereas the lowest-performing model correctly predicted only 119 samples (71.3%). For overmature, the best model achieved 104 correct predictions out of 108 (96.3%), while the lowest model predicted 33 correctly (30.6%). Similarly, for immature, the highest-performing model achieved 75 correct predictions out of 78 (96.2%), compared to 28 correct predictions (35.9%) by the lowest-performing model.

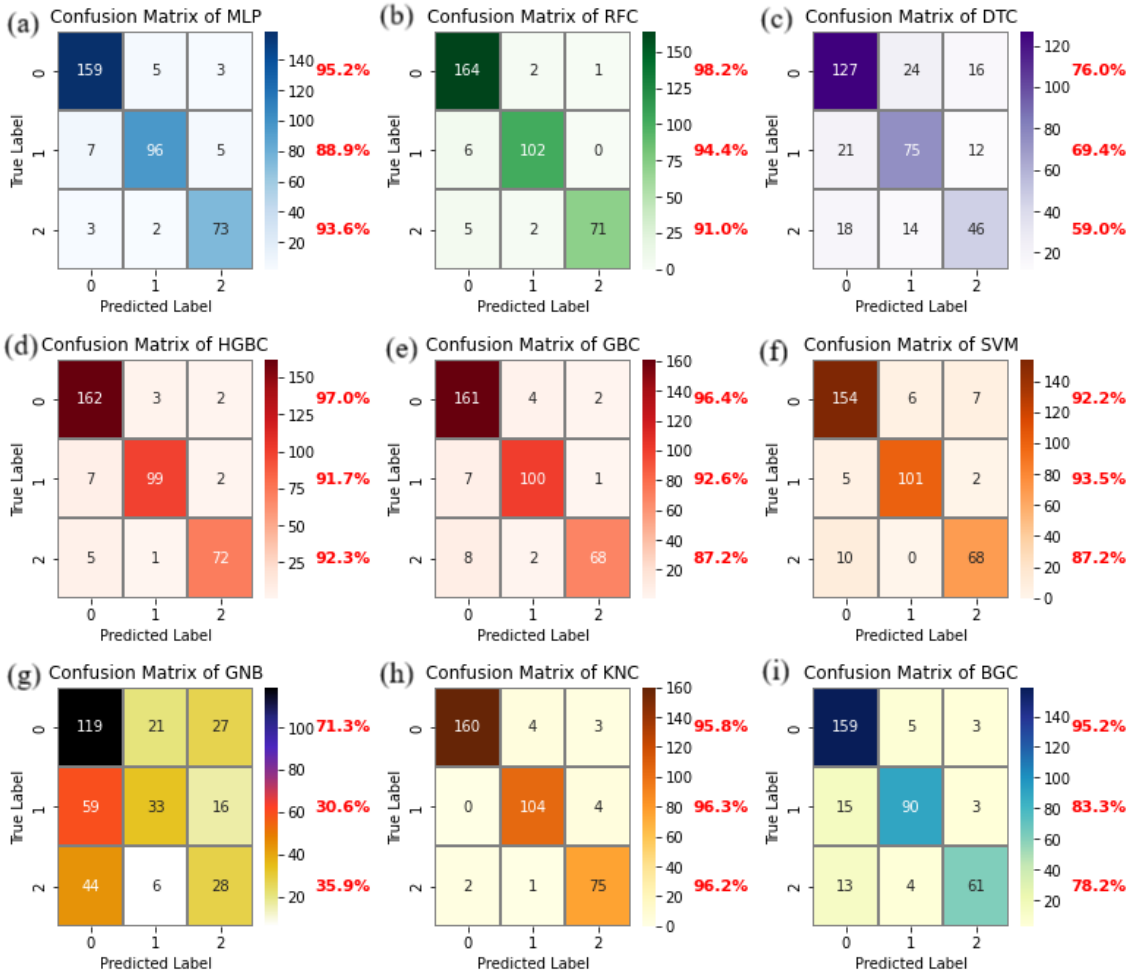

Figure 5. Predicting classification for machine learning models

Success rates, along with visualizations of true and false predictions for each class, are presented in Figure 6. DTC and GNB showed comparatively lower accuracy, whereas RFC and KNC demonstrated strong overall performance.

These findings indicate that machine learning models, particularly RFC and KNC, can effectively predict watermelon maturity based on hand-tapping sounds.

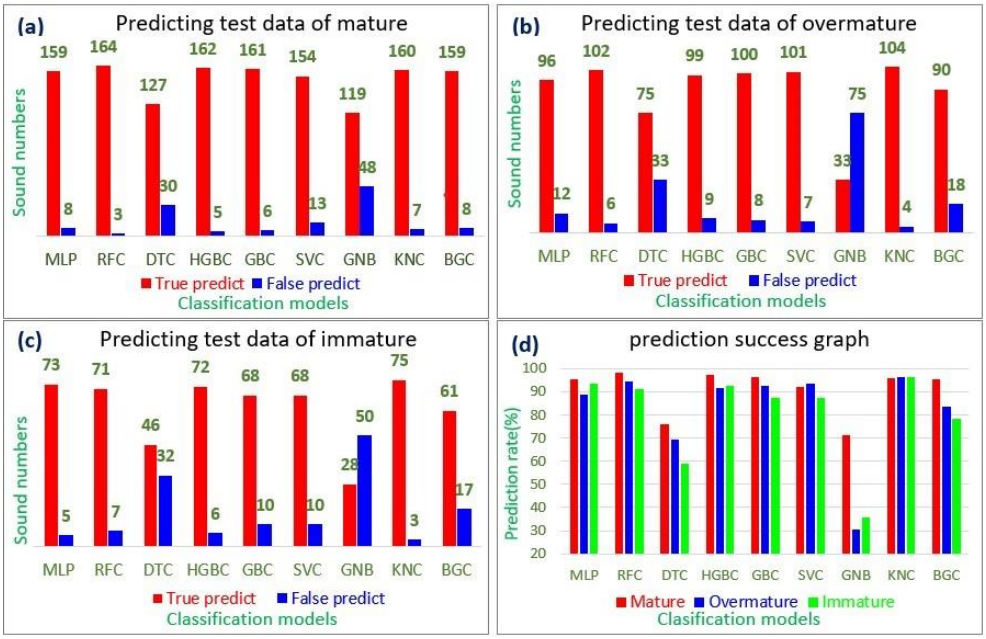

Figure 6. Predicting results for classification model

4. DISCUSSION AND CONCLUSION

This study demonstrates the potential of sound-based classification for assessing watermelon maturity, achieving a high accuracy of 96.66% using the KNC model. These results are comparable to or surpass those reported in similar studies across various domains, including animal sounds, environmental noises, and health-related audio data. The findings highlight the robustness of the proposed method, particularly under real-world conditions with ambient noise, and underscore the effectiveness of machine learning models in processing complex audio signals.

Previous studies have successfully applied sound classification, as shown in the research summarized in Table 3. For example, VGGish-MFCC features combined with KNC achieved 94.79% accuracy for honey bee sound classification [25], transformer CNN achieved 96.05% for domestic pig sounds [39], subspace KNC ensembles reached 96.23% for environmental sounds using spectrograms [40], and RFC-SVC models achieved 96.9% for fish sound classification [23]. Health-related studies, such as heartbeat and respiratory sound analysis, achieved accuracies ranging from 85% to 93% [21,41].

Table 3. Sample studies for sound classification

The studies	Sound dataset	Feature Extraction	Classification method	Accuracy (%)
[25]	Colony honey bee	VGGish-MFCC	KNC	94.79
[39]	Domestic pig sound	LM, MFCC, spectrogram	Transformer CNN	96.05
[22]	Bird sound	Mel-spectrogram, harmonic-component based spectrogram	CNN	86.31
[21]	Heartbeat sound	MFCC	ABC-ANFIS	93
[40]	Enviromental sound	Spectrogram image, CNN	Subspace KNC ensembles	96.23
[41]	Respiratory Sound	Chrome vector, MFCC, ZCR	MLP	85
[23]	Fish sound	time, frequency, and cepstral domains	RFC-SVC	96.9
[42]	Chewing sound	Bottleneck-DNN	Bi-LSTM	97.42
[17]	Watermelon Tapping sound	Image processing	GBC	92
This study	Hand hitting sound	Spectrogram, MFCC, ZCR, RMS energy	KNC	**96.66**

In comparison, the 96.66% accuracy obtained in this study using KNC is competitive with the highest performing methods in the literature. Notably, this performance was achieved despite background noise in recordings, reflecting real-world conditions in grocery stores, fields, and markets, unlike many studies that minimize ambient noise. Feature extraction employed spectrograms, mel-spectrograms, MFCC, ZCR, and RMS energy curves, which are widely recognized as effective for audio analysis. This combination allowed the extraction of 120 distinct features each sound sample, providing a robust dataset for classification and enabling reliable assessment of watermelon maturity.

Among the machine learning models tested, KNC and RFC demonstrated superior performance, achieving the highest accuracy and precision. KNC excelled in classifying immature and overmature watermelons, with success rates of 96.2% and 96.3%, respectively, while RFC achieved 98.2% for the mature class. These results align with previous studies, where KNC and RFC performed well in sound classification tasks [23, 40].

A key innovation of this study is the use of sound data recorded under natural conditions, including ambient noise. This is the first study to employ sound recordings obtained by tapping under natural conditions for watermelon maturity classification. Unlike traditional approaches that minimize background noise, this study reflects real-world scenarios where consumers and producers select watermelons based on tapping sounds. The high prediction accuracy under such conditions demonstrates the robustness of the proposed method and its potential for practical agricultural applications.

This study also builds on research linking watermelon sound characteristics to internal qualities such as sweetness and maturity. By applying machine learning, it provides an objective and scalable alternative to subjective methods like visual inspection or manual tapping, offering a reliable, non-destructive assessment of watermelon quality. However, there are limitations. The dataset was limited to a specific region and recordings were conducted under controlled but natural conditions. Future studies should include watermelons from diverse regions and growing conditions and examine the impact of varying ambient noise levels on classification accuracy. Additionally, while traditional machine learning models were employed, future work could explore deep learning architectures, such as CNN or transformer-based models, which have shown success in other sound classification tasks [33,42]. Integrating these techniques could further enhance the accuracy and robustness of watermelon maturity classification.

Overall, this study demonstrates the effectiveness of sound-based classification for assessing watermelon maturity, achieving high accuracy despite ambient noise. By combining advanced feature extraction with robust machine learning models, particularly KNC and RFC, it provides a practical and innovative solution for non-destructive quality assessment in agriculture. Future research should expand datasets and explore advanced machine learning methods to improve both accuracy and applicability.

Estimating the quality and maturity of fruits without cutting is a critical challenge for both producers and consumers. This study demonstrated the effectiveness of sound-based, non-destructive methods for assessing

watermelon maturity. By recording the sounds produced when watermelons were hand-tapped and extracting features such as MFCC, ZCR, RMS energy, spectrogram, and mel spectrogram, a total of 120 features per sample were obtained. These features were used to train multiple machine learning models, with KNC achieving the highest overall accuracy (96.66%) and RFC showing the highest precision for mature watermelons (98.2%). KNC also performed best for overmature (96.3%) and immature (96.2%) classes.

The study highlights that KNC and RFC models are highly effective for predicting watermelon maturity, even in natural environments with ambient noise, reflecting real-world conditions. Compared to previous studies reporting accuracies between 85% and 99.6%, the results of this work are competitive, underscoring the robustness and practical applicability of the proposed method.
A key contribution of this study is the integration of traditional empirical practices, such as tapping and auditory evaluation, with advanced feature extraction and machine learning techniques. This approach provides a scalable, objective, and non-destructive solution for quality assessment, enabling consumers to make informed decisions and assisting producers in maintaining product standards.

Future work could expand the dataset to include watermelons from diverse regions and cultivation conditions, investigate the impact of varying ambient noise levels, and explore advanced deep learning models, such as CNN or transformer-based architectures, to further improve classification accuracy and robustness. Overall, the findings demonstrate that sound-based machine learning methods offer a practical, innovative, and reliable approach for non-destructive quality evaluation in agriculture.

REFERENCES

[1] Gondchawar N, Kawitkar RS. IoT-based smart agriculture. Int J Adv Res Comput Commun Eng. 2016; 5(6): 838-42.

[2] O'Grady MJ, Langton D, O'Hare GMP. Edge computing: A tractable model for smart agriculture? Artif Intell Agric. 2019; 3: 42-51.

[3] Femling F, Olsson A, Alonso-Fernandez F. Fruit and vegetable identification using machine learning for retail applications. In: 2018 14th International Conference on Signal-Image Technology & Internet-Based Systems (SITIS). IEEE; 2018 Nov. p. 9-15.

[4] Barbole DK, Jadhav PM, Patil SB. A review on fruit detection and segmentation techniques in agricultural field. In: International Conference on Image Processing and Capsule Networks. Springer, Cham; 2021 Sep 10. p. 269-88.

[5] Kyriacou MC, Leskovar DI, Colla G, Rouphael Y. Watermelon and melon fruit quality: The genotypic and agro-environmental factors implicated. Sci Hortic. 2018; 234: 393-408.

[6] Jie D, Wei X. Review on the recent progress of non-destructive detection technology for internal quality of watermelon. Comput Electron Agric. 2018; 151: 156-64.

[7] Kyriacou MC, Soteriou GA, Rouphael Y, Siomos AS, Gerasopoulos D. Configuration of watermelon fruit quality in response to rootstock-mediated harvest maturity and postharvest storage. J Sci Food Agric. 2016; 96(7): 2400-9.

[8] Soteriou GA, Kyriacou MC, Siomos AS, Gerasopoulos D. Evolution of watermelon fruit physicochemical and phytochemical composition during ripening as affected by grafting. Food Chem. 2014; 165: 282-9.

[9] Arendse E, Fawole OA, Magwaza LS, Opara UL. Non-destructive characterization and volume estimation of pomegranate fruit external and internal morphological fractions using X-ray computed tomography. J Food Eng. 2016; 186: 42-9.

[10] Wiktor A, Gondek E, Jakubczyk E, Nowacka M, Dadan M, Fijalkowska A, Witrowa-Rajchert D. Acoustic emission as a tool to assess the changes induced by pulsed electric field in apple tissue. Innov Food Sci Emerg Technol. 2016; 37: 375-83.

[11] Zhang B, Huang W, Li J, Zhao C, Fan S, Wu J, Liu C. Principles, developments and applications of computer vision for external quality inspection of fruits and vegetables: A review. Food Res Int. 2014; 62: 326-43.

[12] Nelson SO, Guo WC, Trabelsi S, Kays SJ. Dielectric spectroscopy of watermelons for quality sensing. Meas Sci Technol. 2007; 18(7): 1887.

[13] Wang L, Sun DW, Pu H, Zhu Z. Application of hyperspectral imaging to discriminate the variety of maize seeds. Food Anal Methods. 2016; 9: 225-34.

[14] Fan Y, Lai K, Rasco BA, Huang Y. Determination of carbaryl pesticide in Fuji apples using surface-enhanced Raman spectroscopy coupled with multivariate analysis. LWT Food Sci Technol. 2015; 60(1): 352-7.

[15] Mohd Ali M, Hashim N, Bejo SK, Shamsudin R. Quality evaluation of watermelon using laser-induced backscattering imaging during storage. Postharvest Biol Technol. 2017; 123: 51-9.

[16] Mao J, Yu Y, Rao X, Wang J. Firmness prediction and modeling by optimizing acoustic device for watermelons. J Food Eng. 2016; 168: 1-6.

[17] Chawgien K, Kiattisin S. Machine learning techniques for classifying the sweetness of watermelon using acoustic signal and image processing. Comput Electron Agric. 2021; 181: 105938.

[18] Chen M, Challita U, Saad W, Yin C, Debbah M. Artificial neural networks-based machine learning for wireless networks: A tutorial. IEEE Commun Surv Tutor. 2019; 21(4): 3039-71.

[19] Probst P, Wright MN, Boulesteix AL. Hyperparameters and tuning strategies for random forest. WIREs Data Min Knowl Discov. 2019; 9(3): e1301.

[20] Rani KV, Jawhar SJ. Lung lesion classification scheme using optimization techniques and hybrid (KNN-SVM) classifier. IETE J Res. 2022; 68(2): 1485-99.

[21] Keikhosrokiani P, Naidu AB, Iryanti Fadilah S, Manickam S, Li Z. Heartbeat sound classification using a hybrid adaptive neuro-fuzzy inference system (ANFIS) and artificial bee colony. Digit Health. 2023; 9: 20552076221150741.
[22] Xie J, Hu K, Zhu M, Yu J, Zhu Q. Investigation of different CNN-based models for improved bird sound classification. IEEE Access. 2019; 7: 175353-61.
[23] Malfante M, Mars JI, Dalla Mura M, Gervaise C. Automatic fish sounds classification. J Acoust Soc Am. 2018;143(5): 2834-46.
[24] Salau AO, Jain S. Feature extraction: A survey of the types, techniques, applications. In: 2019 International Conference on Signal Processing and Communication (ICSC). IEEE; 2019 Dec 23. p. 158-64.
[25] Di N, Sharif MZ, Hu Z, Xue R, Yu B. Applicability of VGGish embedding in bee colony monitoring: Comparison with MFCC in colony sound classification. PeerJ. 2023; 11: e14696.
[26] Sharma G, Umapathy K, Krishnan S. Trends in audio signal feature extraction methods. Appl Acoust. 2020; 158: 107020.
[27] Jie D, Zhou W, Wei X. Nondestructive detection of maturity of watermelon by spectral characteristic using NIR diffuse transmittance technique. Scientia Horticulturae, 2019; 257: 108718.
[28] Gu Q, Li T, Hu Z, Zhu Y, Shi J, Zhang L, Zhang X. Quantitative analysis of watermelon fruit skin phenotypic traits via image processing and their potential in maturity and quality detection. Computers and Electronics in Agriculture, 2025; 230:109960.
[29] Zhang YX, Han JL, Yao W. Non-destructive watermelon maturity detection by acoustic response. In 2010 2nd International Conference on Information Engineering and Computer Science, 2010; 1-4. IEEE.
[30] Garvin J, Abushakra F, Choffin Z, Shiver B, Gan Y, Kong L, Jeong N. Microwave imaging for watermelon maturity determination. Current Research in Food Science, 2023; 6: 100412.
[31] Vega-Castellote M, Sánchez MT, Torres I, De la Haba MJ, Pérez-Marín D. Assessment of watermelon maturity using portable new generation NIR spectrophotometers. Scientia Horticulturae, 2022; 304: 111328.
[32] Pamungkas WA, Bintoro N. Evaluation of watermelon ripeness using self-developed ripening detector. In IOP Conference Series: Earth and Environmental Science, 2021; 653:1, 012020. IOP Publishing.
[33] Babu PA, Nagaraju VS, Vallabhuni RR. Speech emotion recognition system with Librosa. In: 2021 10th IEEE International Conference on Communication Systems and Network Technologies (CSNT). IEEE; 2021 Aug 12. p. 421-4.
[34] Wu CH, Ho JM, Lee DT. Travel-time prediction with support vector regression. IEEE Trans Intell Transp Syst. 2004; 5(4): 276-81.
[35] Pekel E. Estimation of soil moisture using decision tree regression. Theor Appl Climatol. 2020; 139(3-4): 1111-9.
[36] Breiman L. Random forests. Mach Learn. 2001; 45: 5-32.
[37] Soucy P, Mineau GW. A simple KNN algorithm for text categorization. In: Proceedings of the 2001 IEEE International Conference on Data Mining. IEEE; 2001; p. 647-8.
[38] Han HG, Qiao JF. A structure optimisation algorithm for feedforward neural network construction. Neurocomputing. 2013; 99: 347-57.
[39] Liao J, Li H, Feng A, Wu X, Luo Y, Duan X, Li J. Domestic pig sound classification based on TransformerCNN. Appl Intell. 2023; 53(5): 4907-23.
[40] Kim CI, Cho Y, Jung S, Rew J, Hwang E. Animal sounds classification scheme based on multi-feature network with mixed datasets. KSII Trans Internet Inf Syst. 2020; 14(8): 3384-98.
[41] Demir F, Abdullah DA, Sengur A. A new deep CNN model for environmental sound classification. IEEE Access. 2020; 8: 66529-37.
[42] Monaco A, Amoroso N, Bellantuono L, Pantaleo E, Tangaro S, Bellotti R. Multi-time-scale features for accurate respiratory sound classification. Appl Sci. 2020; 10(23): 8606.
[43] Khan MI, Acharya B, Chaurasiya RK. iHearken: Chewing sound signal analysis-based food intake recognition system using Bi-LSTM Softmax network. Comput Methods Programs Biomed. 2022; 221: 106843.
[44] Akbal E, Tuncer T, Dogan S. Vehicle interior sound classification based on local quintet magnitude pattern and iterative neighborhood component analysis. Appl Artif Intell. 2022; 36(1): 2137653.

Volume 14, Issue 3, Page 202-217, 2025 https://doi.org/10.46810/tdfd.1704418 Research Article

BİNGÖL UNIVERSITY

Türk Doğa ve Fen Dergisi
Turkish Journal of Nature and Science
www.dergipark.gov.tr/tdfd

Spatial Evaluation of Urban Green Space-Population Relationship Using Sentinel-2 Satellite Data and Object-Based Image Analysis: A Case Study Antalya

Mesut ÇOŞLU[1*]

[1]Burdur Mehmet Akif Ersoy University, Science and Letters Faculty, Precision Agriculture and Agricultural Robots Department, Burdur, Türkiye
Mesut ÇOŞLU ORCID No: 000-0003-3952-6563

**Corresponding author: mcoslu@mehmetakif.edu.tr*

(Received: 26.05.2025, Accepted: 14.09.2025, Online Publication: 26.09.2025)

Keywords
Landscape, NDVI, OBIA, PCGS, Remote Sensing and GIS

Abstract: The relationship between urban green space (UGS) and population is essential for the quality of life in cities. This study proposes a method to determine the relationship between UGS and population in Antalya, Türkiye, and to assess short-term changes, using Sentinel-2 satellite data and object-based image analysis (OBIA). In the study, two different dated Sentinel-2 data were utilized as the basic data set to analyze the vegetation. The Normalized Difference Vegetation Index (NDVI) was calculated for the threshold value and UGSs were analyzed according to different categories. Then, the Urban Green Space Index (UGSI) was computed to determine the amount of green space and Per Capita Green Space (PCGS) was also computed for this purpose. The OBIA general accuracy values of the proposed method are 93% and 94% for 2017 and 2023, respectively. The results showed that PCGS across the study area decreased by 7.33 m² in a short time. It is evaluated that the method proposed in this study, which reveals the short-term change in UGS and PCGS more quickly and at lower cost, can be used effectively in sustainable city management.

Sentinel-2 Uydu Verileri ve Nesne Tabanlı Görüntü Analizi Kullanarak Kentsel Yeşil Alan-Nüfus İlişkisinin Mekânsal Değerlendirilmesi: Antalya Örneği

Anahtar Kelimeler
Peyzaj, NDVI, OBIA, KBYA, Uzaktan Algılama ve CBS

Öz: Kentsel yeşil alan (KYA) ile nüfus arasındaki ilişki, kentlerdeki yaşam kalitesi için önemlidir. Bu çalışmada, Türkiye, Antalya'da KYA ile nüfus arasındaki ilişkiyi belirlemek ve kısa dönemdeki değişimi ortaya koymak için Sentinel-2 uydu verileri ve nesne tabanlı görüntü analizi (OBIA) kullanılarak bir yöntem önerilmiştir. Çalışmada bitki örtüsünü analiz etmek için iki farklı tarihli Sentinel-2 uydu görüntüsü temel veri seti olarak kullanılmıştır. Eşik değeri için Normalize Edilmiş Fark Bitki Örtüsü İndeksi (NDVI) hesaplanmış ve KYA'lar farklı kategorilere göre analiz edilmiştir. Ardından, yeşil alan miktarını belirlemek için Kentsel Yeşil Alan İndeksi (KYAI) ve aynı zamanda Kişi Başına Yeşil Alan (KBYA) da hesaplanmıştır. Önerilen yöntemin OBIA genel doğruluk değerleri 2017 ve 2023 yılları için sırasıyla %93 ve %94'tür. Sonuçlar, çalışma alanı genelinde KBYA'nın kısa vadede 7.33 m² azaldığını göstermiştir. KYA ve KBYA'da kısa vadeli değişimi daha hızlı ve daha düşük maliyetle ortaya koyan bu çalışmada önerilen yöntemin sürdürülebilir kent yönetiminde etkin bir şekilde kullanılabileceği değerlendirilmektedir.

1. INTRODUCTION

A Remote sensing (RS) technology is an important tool for monitoring the current status and dynamics of vegetation ecosystems [1]. With the developing technology, there have been significant developments both hardware and sensor technologies in satellite systems that provide data for RS. In this context, satellite systems with higher spatial, radiometric, spectral and temporal resolution have increased the use of this technology in Earth observation studies. Temporal resolution, especially expressed as revisit time, is essential to detect change in agriculture, forest and urban areas and to provide a rapid response to this change. Nowadays, many companies offer systems with high-resolution RS data for a fee. However, the European Space Agency (ESA) offers free data access with multispectral (MS) instruments such as

Sentinel-2, which have high spatial (10 m), temporal (5 days) resolution and wide coverage area [2-4].

Urbanization causes changes in surface materials due to reasons such as suppression of vegetation and a decrease in soil permeability. Variations in the energy reflected from the surface in urban areas cause higher temperatures relative to rural areas, contributing to the formation of an urban heat island, which represents an anthropogenic change [5, 6]. In addition, urban growth causes changes in land use and land cover (LULC) in many areas around the world, especially in developing countries [7]. One of the most important effects of urbanization is that it poses a threat to the use of agricultural lands. Depending on the LULC, this may cause agricultural lands to change or even disappear [8].

Urban green space (UGS), an essential element of urban environmental systems, is the structure consisting of various vegetation types that have diverse social functions and are associated with urban land use types [9, 10]. UGS, which plays a crucial role in maintaining ecological balance and supporting human health, is essential for improving air quality for urban residents and encouraging greater physical activity, reducing the negative effects of urbanization and promoting the sustainable growth of urban ecology [11]. Recent studies have revealed that the coronavirus pandemic (COVID-19), which emerged in late 2019, may have significant physical and mental effects on human health. The restrictions imposed during COVID-19 have especially increased people's desire to access UGS [12].

Effective management and planning of UGS are essential to fully realize their advantages for both urban residents and the urban ecosystem in general. Nonetheless, inventorying urban vegetation through traditional methods is expensive and requires a significant amount of time. [17]. In this context, studies such as monitoring and determining temporal changes in LULC in urban areas using RS and geographic information systems (GIS) technologies [18, 19], urban planning and environmental management [20], land cover classification and coastal spatial planning [21] and analysis of the impact of urbanization on urban agriculture [8] can be carried out both at lower cost and with less labor in a shorter time.
One of the most important developments in RS technology, which is closely related to urban science, is object detection using RS data [22]. OBIA, which identifies image objects that are neighboring pixel groups and is used for object detection in RS, is a very useful method for image classification [23]. Studies carried out in urban areas with OBIA include monitoring urban tree cover [24], determining urban tree species and mapping carbon stocks for urban green planning and management [25], evaluating small UGS with OBIA and the vegetation index [26] and analyzing how UGS affect the health of the city's residents [27]. Pouya and Aghlmand [12] used RS and GIS technology to evaluate PCGS according to the population of neighborhoods in the Battalgazi District of Malatya Province and revealed that existing UGSs are not distributed equally across neighborhoods. Ortçeşme et al. [28], who investigated the situation of Antalya's active green areas comprehensively, used zoning plans and the explanation reports for these zoning plans. The findings obtained by the researchers showed that active green areas are insufficient and irregular throughout the city. In another study carried out in Antalya, Manavoğlu and Ortaçeşme [29] developed a proposal for a green space system in the Konyaaltı urban area. In another study, Manavoğlu and Ortaçeşme [30], examined open and green areas with the help of Landsat satellite data and multi-criteria analysis. Researchers have found that active green spaces are unevenly distributed; however, their overall presence is on the rise.

The primary aim of this study is to assess UGS in terms of quantity and quality with RS data, GIS and OBIA method. In the study, Sentinel-2 images were used as RS data to determine LULC. LULC classes in the study area consist of UGSs (landscape, forest and agricultural areas) and impervious surfaces (buildings, roads, etc.). With the findings obtained from the UGSI and PCGS values calculated within the scope of the study, the short-term change in UGS was revealed and thus it is aimed to contributing to urban planning.

2. MATERIAL AND METHOD

2.1. Material and Method

The research was conducted in Antalya Province, located in southern Türkiye, a region known for its significance in both agriculture and tourism. The study was conducted in Muratpaşa District, one of the central districts with the largest population of Antalya (Figure 1). Muratpaşa, the oldest settlement in Antalya, has a 20 km coastal strip. The Mediterranean Sea is in the south of Muratpaşa, Kepez District in the north, Konyaaltı District in the west, and Aksu District in the east [31]. Although the study area, which includes the International Antalya Airport and tourist facilities, has a dense urban area, there are also landscape areas, forest areas and agricultural production areas. The average temperature of the study area, where the Mediterranean climate is observed, in the long-term (1930-2023) was recorded as the lowest in January (10.0 °C) and the highest in July (28.4 °C) [32].

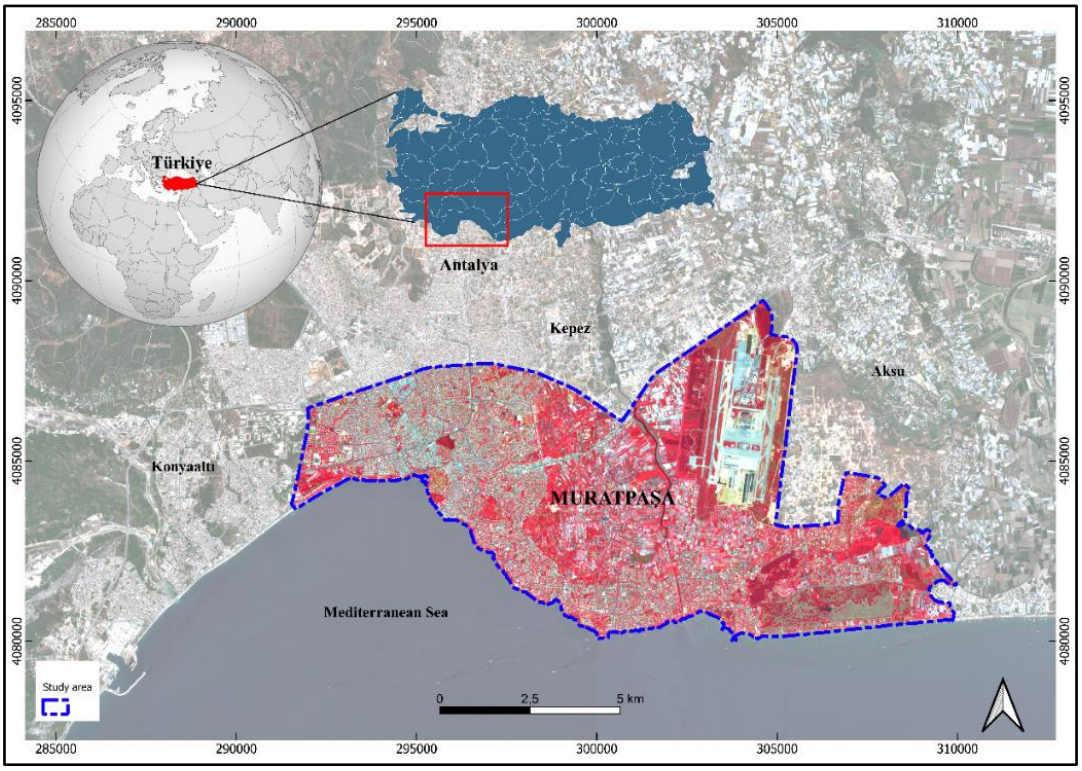

Figure 1. Study area

i) it is one of the central districts with the largest population,
ii) the change in population during the specified dates is the lowest compared to other districts,
iii) it has an old and dense urban area.

2.2. Satellite Data

Sentinel-2 is a wide-coverage, high-resolution, MS imaging mission that is supporting Copernicus land monitoring efforts. Sentinel-2 satellites, which have 13 spectral bands, are used in monitoring vegetation, forest, soil and water surfaces [33] (Table 1).

Table 1. Bands of Sentinel-2 [34]

Band	Band name	Central Wavelength (nm)	Spatial Resolution (m)
1	Coastal aerosol	443	60
2	Blue	490	10
3	Green	560	10
4	Red	665	10
5	Vegetation red edge	705	20
6	Vegetation red edge	740	20
7	Vegetation red edge	783	20
8	NIR	842	10
8A	NIR	865	20
9	Water vapour	940	60
10	SWIR-Cirrus	1375	60
11	SWIR	1610	20
12	SWIR	2190	20

nm: Nanometer, m: Meter, NIR: Near Infrared, SWIR: Shortwave Infrared

In this study, the 10 m spatial resolution Blue, Green, Red and NIR bands of the Sentinel-2 satellite for 2017 and 2023 were used (Figure 2).

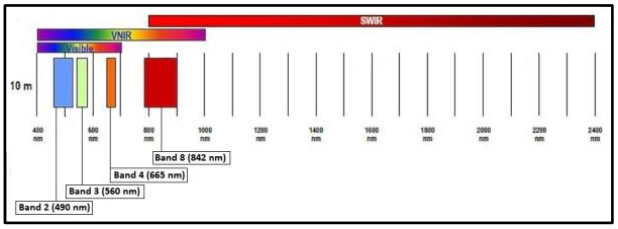

Figure 2. 10 m spatial resolution bands [34]

2.3. Demographic Data

The demographic data utilized in the study are population data and were sourced from the Turkish Statistical Institute (TSI). As part of the study, the population data of all districts of Antalya between 2017 and 2023 were arranged and those of Muratpaşa for 2017 and 2023 were filtered (Appendix A).

2.4. Methodology

This study includes the key steps of acquisition of Sentinel-2A images, demographic data, district and neighborhood boundaries, pre-processing, OBIA and evaluation of analysis results with population data (Figure 3). eCognition (Trimble Inc., Sunnyvale, CA, USA) software was used in the OBIA stage of the study, and ArcGIS (ESRI, California, USA) software was used to transfer and evaluate the analysis results in the GIS environment.

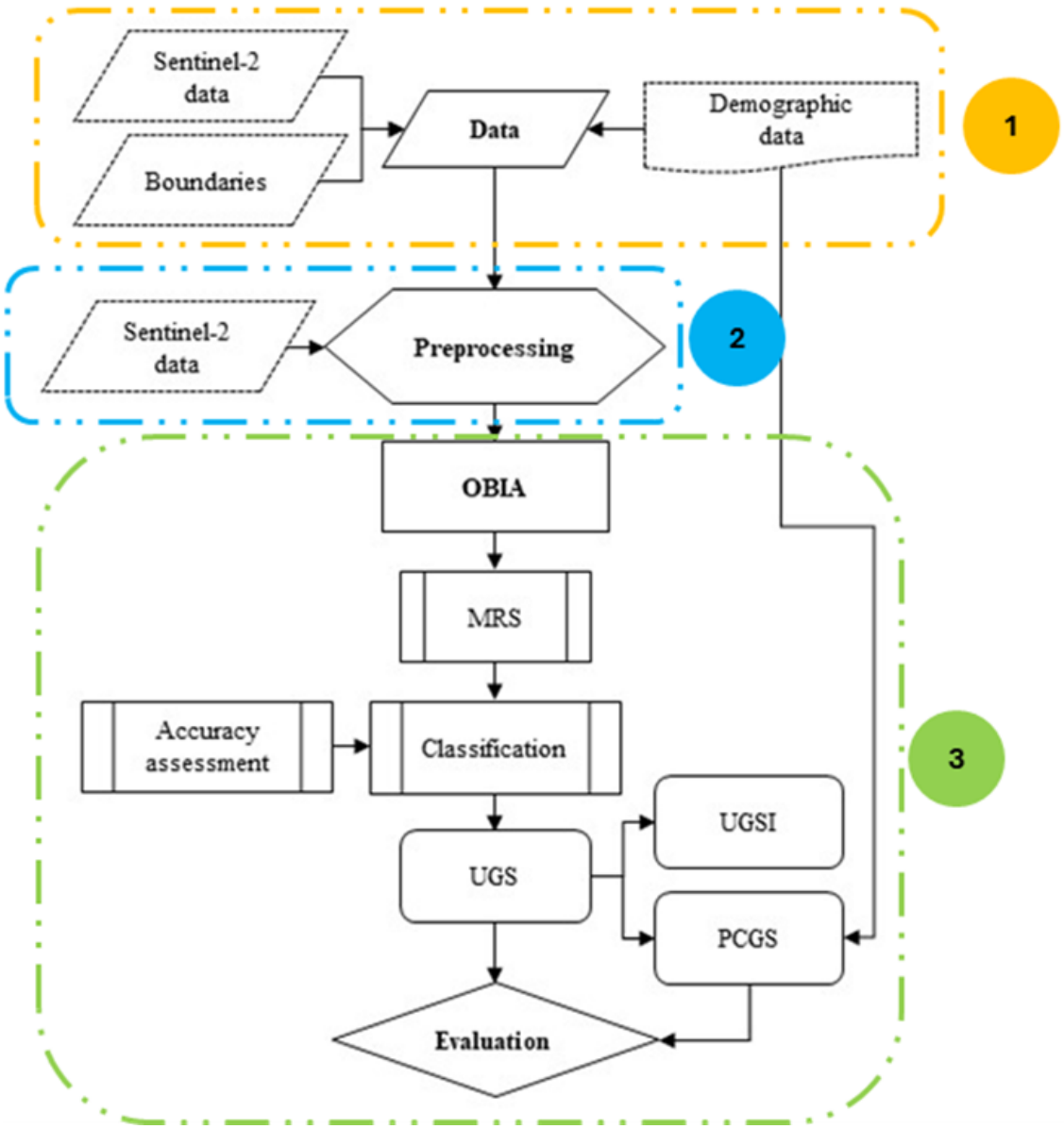

Figure 3. General workflow of the study

During the data acquisition stage, Sentinel-2 data were obtained from the Copernicus Open Access Hub. The study utilized data starting from 2017, as the earliest Sentinel-2 satellite images for the region achieved sufficient quality and temporal consistency from that year onward. The year 2023 was chosen as the endpoint to capture short-term variations and to encompass a complete vegetation cycle within the study period. Considering the cloudness and greenness of the vegetation in the study area, June was determined as the most suitable month for both years. In this context, data dated 26 June 2017 and 15 June 2023 were used in the study. The data provided for these dates are Level-2A data, which are atmospherically corrected surface reflectance data obtained from Level-1C products. Atmospheric correction of Sentinel-2 data involves correcting the scattering of air molecules, atmospheric gases especially such as ozone, oxygen, and water vapor, and absorption-scattering effects caused by aerosols [35]. During the preprocessing stage of Sentinel-2 satellite data, band composition, merging of image frames and clipping according to the boundaries of the study area for 10 m spatial resolution bands were performed. In addition, the projection and datum information of the vector data which contains the study area boundary used at this stage were reprojected according to Sentinel-2 data.

The OBIA method was used to analyze Sentinel-2 data. OBIA consists of two basic stages: segmentation and classification. During the segmentation phase, the multiresolution segmentation (MRS) algorithm was applied, and the threshold value classification method was used in the classification stage. The most important stage of OBIA is segmentation. When sample areas at different dates in the study area were examined, it was determined that scale parameter values below 30 (10 and 20) caused over-segmentation while values above 40 caused under-segmentation. In this context, the most appropriate scale parameter value for both years was determined as 30, and the composition of the homogeneity criterion (shape and compactness) was determined as 0.1 and 0.5, respectively. To determine green spaces, three classes were created during the classification stage: non-vegetation (NV), low vegetation (LV) and high vegetation (HV) Hashim et al. [36]. Among these classes, NV encompasses barren areas,

built-up areas, and road networks; LV comprises shrub and grassland; and HV includes urban forest areas. Additionally, NDVI, which will be used as a threshold value, was calculated at this stage. NDVI is an analysis method that can be used to monitor the density and health status of vegetation in an area [37]. NDVI takes a value between -1 and +1. While NDVI approaching +1 means that the vegetation in the area is dense or healthy, approaching -1 means that the vegetation is relatively sparse, unhealthy, or even indicates lack of vegetation in the area depending on its value. Aryal et al. [38] stated that the use of NDVI was acceptable in the study of mapping green areas in an urban area. In this context, NDVI was calculated using Equation 1 to determine the UGS in the study area [39].

$$NDVI = \frac{R_{NIR} - R_{Red}}{R_{NIR} + R_{Red}} \quad (1)$$

where R_{NIR} refers to the reflection in the NIR region and R_{Red} refers to the reflection in the red region.

In this study, NDVI threshold values recommended in previous studies were used [36, 39]. An error matrix based on the samples was used to evaluate the results of the classification stage in OBIA. In the accuracy evaluation, a total of 100 sample objects were selected for three classes, considering their distribution in the study area.

The Urban Green Space Index (UGSI) given in Equation 2 was used to determine the UGS in the study area [40].

$$UGSI = \frac{G_i}{A_i} \quad (2)$$

where G_i, green space area and A_i, total area.
The average amount of green space per capita was calculated using Per Capita Green Space (PCGS) given in Equation 3 [40].

$$PCGS = \frac{G_i}{PN_i} \quad (3)$$

where G_i, total green space in i and P_{Ni}, total population in i.

3. RESULTS AND DISCUSSION

Based on the address-based population registration system (ABPRS), the total population of the five districts comprising the center of Antalya is 1,489,792. This population corresponds to 55% of the total population of Antalya. This means that one in two people in Antalya lives in one of these districts.

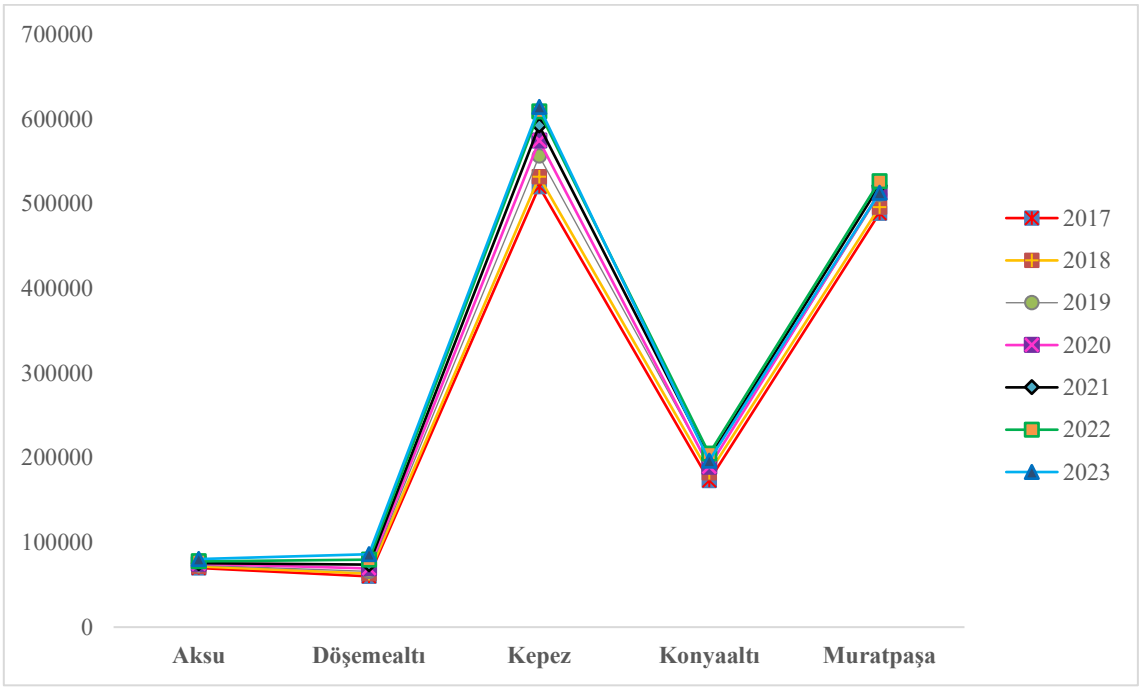

Figure 4. 2017-2023 population data of the five districts

From 2017 to 2023, which includes the study period, the population growth rate was highest in Döşemealtı District (44%) and lowest in Muratpaşa District (5%) (Figure 4). According to the results of the segmentation process performed at four scale levels in OBIA for 2017 (L1: 10, L2: 20, L3: 30, L4: 40), 514958 objects at L1, 135073 objects at L2, 58281 objects at L3 and 33321 objects at L4 were extracted. According to the results of the segmentation process carried out for 2023, 503286 objects at L1, 130635 objects at L2, 56477 objects at L3 and 32320 objects at L4 were extracted. The result of the segmentation process at different levels for a sample area for 2023 is seen in Figure 5. Determining the appropriate parameters and criteria during the segmentation process of the OBIA method, which is very advantageous in extracting information from high spatial resolution data, by trial and error, requires expertise and prolongs the processing time [41, 42, 21].

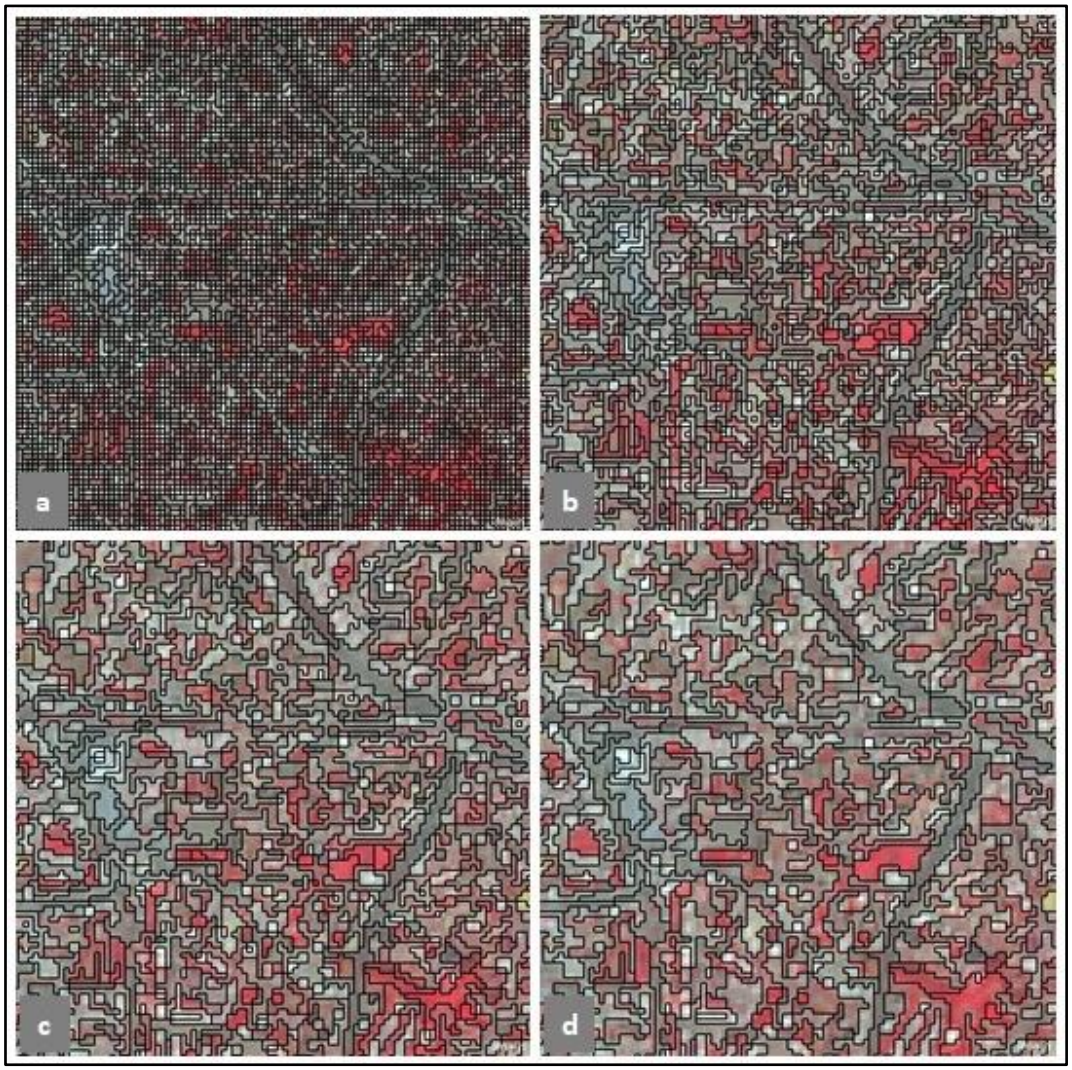

Figure 5. Results of the segmentation process: (a) L1, (b) L2, (c) L3 and (d) L4

According to the accuracy evaluation results of OBIA, high overall accuracy (OA) values and kappa statistics were obtained for both years. For 2017, the OA value is 93% and the kappa statistic is 0.88, and for 2023, the OA value is 0.94 and the kappa statistic is 0.90. The accuracy assessment results demonstrated that the proposed method was effective in identifying UGS. The results were determined to be quite high, similar to the findings in the study by Shekhar and Aryal [40] in which UGS was determined using GeoEye satellite data and OBIA. Zaki et al. [21], used Sentinel-2 data and the OBIA method, and producing similarly high OA values compared to previous studies. The results of the classification process obtained from OBIA were transferred to the GIS environment to map UGS and calculate UGSI and PCGS (Figure 6). According to the OBIA results obtained from the study, in Muratpaşa, one of the most populous and densest urban areas of Antalya, the NV area for 2017 is 45.72 km², LV area is 36.15 km² and HV area is 7.16 km², and the NV area for 2023 is 47.32 km², LV is 38.22 and HV is 3.49 km². These findings showed that NV and LV areas increased slightly from 2017 to 2023 while HV areas decreased.

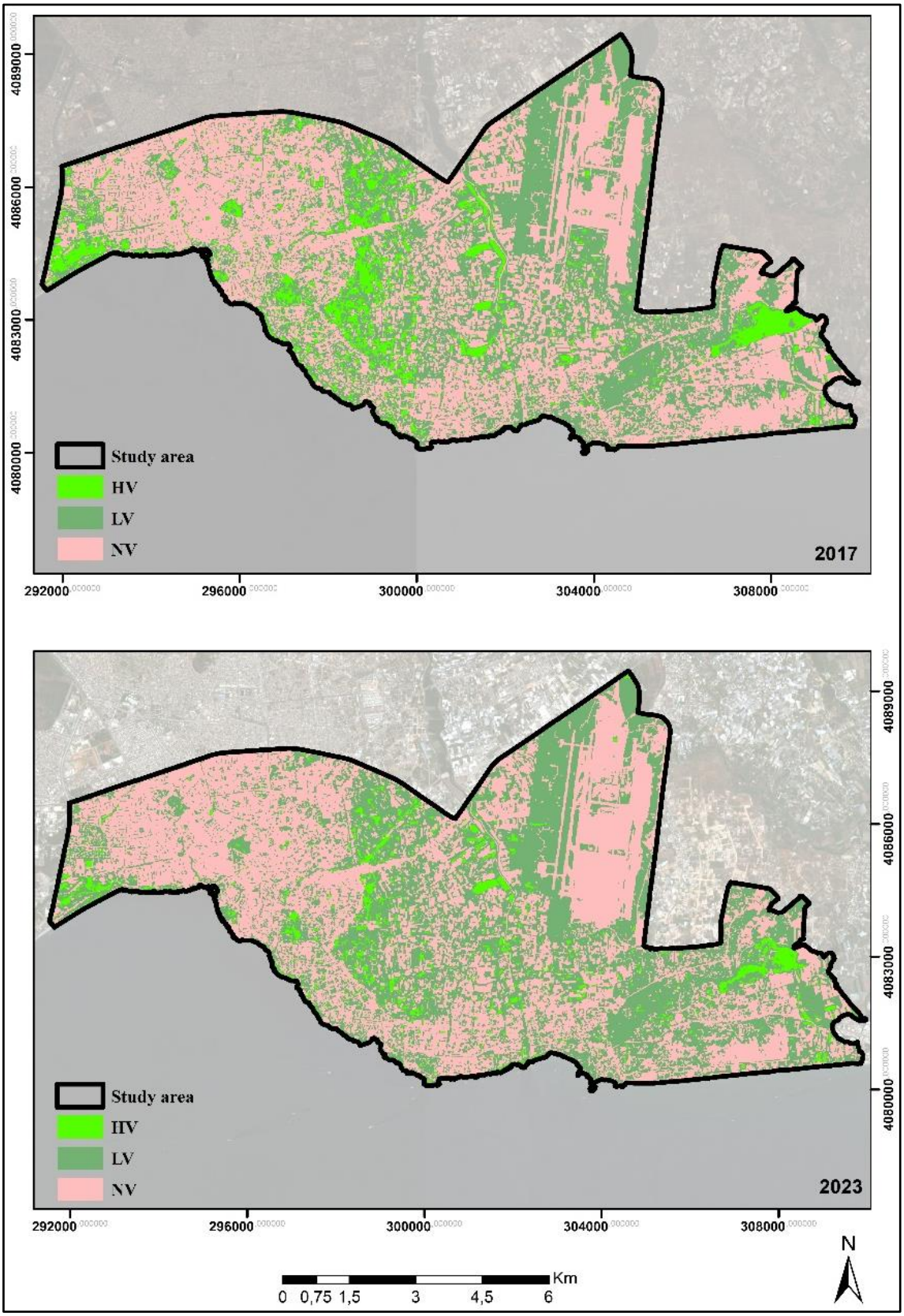

Figure 6. Results of OBIA (UGS)

In Muratpaşa, where the total UGS amount for 2017 is 43.31 km², the UGSI value is 48.65% (40.60% LV and 8.05% HV) and the PCGS value is 88.68 m². The total amount of UGS for 2023 is 41.71 km², the UGSI value is 46.85% (42.93% LV and 3.92% HV), and the PCGS value is 81.35 m² (Table 2). Findings show that PCGS values in Muratpaşa in both years are above Türkiye's minimum (>10 m²), WHO's minimum (>10 m²) and ideal (>50 m²) values. In the study conducted by Manavoğlu and Ortaçeşme [30], when the ratio of active green areas to the total area of the districts throughout Antalya was examined, it was determined that Muratpaşa had a higher ratio than the others. In the study conducted by Pouya and Majid [2022] in another city of Türkiye, PCGS values were found to be above the minimum values specified by

both Türkiye and the WHO. It was determined that the population in Muratpaşa increased by only 2658 people compared to the previous year (2019), especially in 2020, when COVID-19 restrictions began, and it increased by 8144 in 2021 and 5114 in 2022 but decreased by 13564 people in 2023. In this period (2017-2023), it was determined that the population, which fluctuated in the short-term due to both COVID-19 and other factors, increased by 24308 people and the change in UGSI was only 1.8%. The findings obtained from this study showed that PCGS decreased by 7.33 m² in Muratpaşa over the period from 2017 to 2023.

Table 2. UGSI and PCGS on different dates

Year	Area (km²)	Population	Non-Vegetation (km²)	Vegetation(km²)	UGSI (%)			PCGS*
					None	Low	High	
2017	89.03	488392	45.72	43.31	51.35	40.60	8.05	88.68
2023	89.03	512700	47.32	41.71	53.15	42.93	3.92	81.35

m^2 per capita

The method proposed in this study, which involved determining the changes in UGS and PCGS on different dates throughout Muratpaşa, was also evaluated separately in 55 neighborhoods of Muratpaşa (Figure 7). There are different regions in terms of the urban area, green area and demographic structure. For example, the largest neighborhood in terms of area is Yenigöl (17.4 km²), where Antalya Airport is also located, while the most crowded neighborhood in terms of population is Güzeloba (37074). UGSI values for all neighborhoods in the study area for 2017 and 2023, PCGS values are given in Appendix B and, Appendix C.

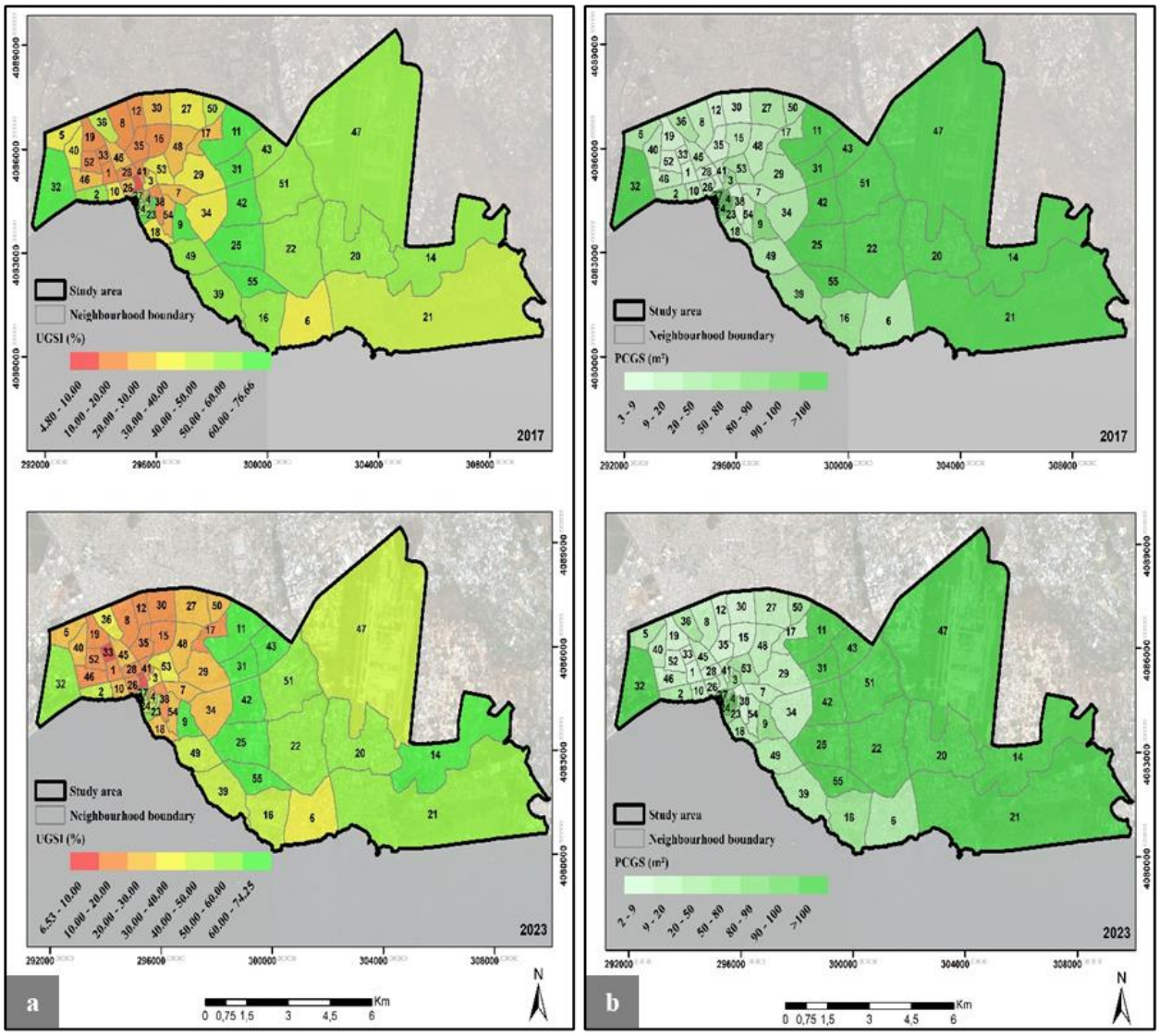

Figure 7. Results of UGSI and PCGS: (a) UGSI and (b) PCGS

The average UGSI values of all neighborhoods in Muratpaşa for 2017 and 2023 are 39.34% and 34.53%, respectively. Accordingly, it was determined that there was a 4.31% decrease in the average UGSI. For 2017 and 2023, the lowest UGSI (4.80% and 6.53%, respectively) was calculated for Elmalı neighborhood (ID: 13), and the highest UGSI (76.66% and 74.25%, respectively) was

calculated for Mehmetçik neighborhood (ID: 31). In the study area, the region where the change in terms of UGSI is seen the most (from 58.17% to 31.81%) is Barbaros neighborhood (ID:04), while the region where the change is seen the lowest (from 12.76% to 12.42%) is Altındağ neighborhood (ID:01) (Figure 8a and Appendix B). It was determined that there were slight increases in UGSI in some regions (10 neighborhoods). Accordingly, it was determined that the regions where the UGSI value increased the most were Ermenek (ID: 14) and Topçular (ID: 43) neighborhoods, and the UGSs in these areas were generally comprised mostly of agricultural areas. In addition, according to the study's findings, it was determined that some areas with an increase in UGS (such as airports and agricultural zones) were either not public spaces or consisted primarily of agricultural regions.

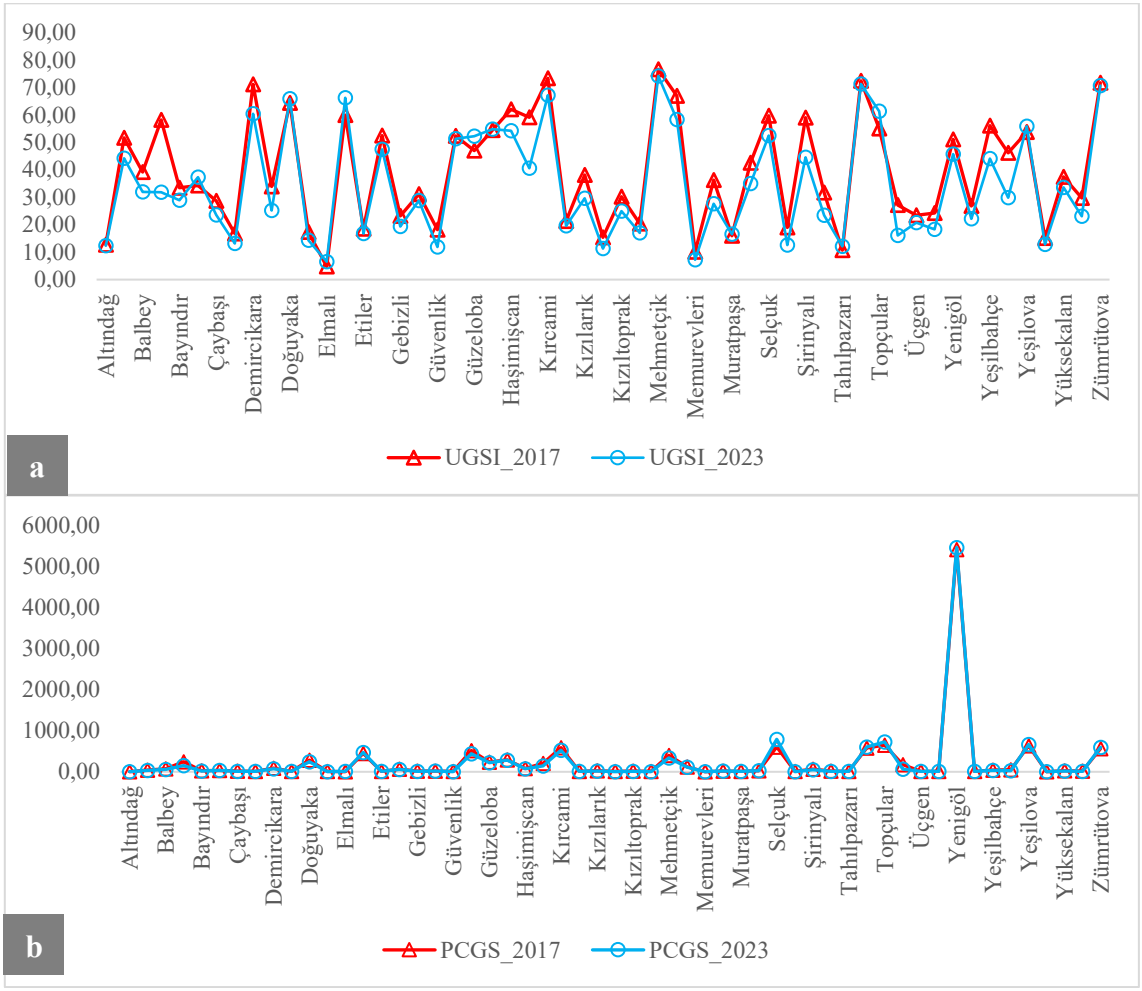

Figure 8. Change of UGSI and PCGS from 2017 to 2023: (a) UGSI and (b) PCGS

The average PCGS values for 2017 and 2023 are 234.32 m² and 229.10 m², respectively. Consequently, it was found that the average PCGS values were both very similar and relatively high. For 2017 and 2023, the lowest PCGS (2.69 m² and 2.06 m², respectively) was calculated for Memurevleri neighborhood (ID: 33), and the highest PCGS (5402.25 m² and 5448.43 m²) was calculated for Yenigöl neighborhood (ID: 47). The reason why the highest PCGS values are in Yenigöl neighborhood and the average PCGS values in Muratpaşa are high is that Antalya Airport is in this neighborhood (low UGS, high population). When Figure 8b, which is showing the change in PCGS and Appendix C are examined, it is seen that 45 out of 55 neighborhoods are above the minimum PCGS value determined by WHO, and 43 are above the minimum value determined by Türkiye for 2017. For 2023, while the number of neighborhoods above the WHO minimum value was 45, the number of neighborhoods above the minimum value determined by Türkiye was 42. In addition, while there were 22 neighborhoods above WHO's ideal PCGS value for 2017, this number decreased to 21 neighborhoods due to the change in Şirinyalı neighborhood (ID: 39) for 2023.

UGS serves as a valuable data source for tracking and evaluating urban environments as well as analyzing ecological services. Satellite RS technology makes significant contributions to long-term and large-scale monitoring of spatiotemporal changes in UGS models [43]. Additionally, as stated by Zhu and Ling [44], spatiotemporal changes have important advantages for landscape and urban planning. Although there has been a slight decrease in UGSI and PCGS both in Muratpaşa and on a neighborhood basis in the short-term, it should not be ignored that the UGS in this area is on decreasing trend, and there may be changes in other UGSs in the long-term. One of the most important issues within the scope of UGS is the rapid and uncontrolled urbanization, which is one of the main reasons for the loss of UGS in urban areas. This situation creates great pressure on the urban environment, and as a result, the quality of urban life gradually

decreases [9]. In this context, one of the most crucial issues is the division of open spaces and UGSs in urban areas into smaller pieces. Zhu and Ling [44] revealed that over 40 years, open spaces in the Shanghai city center were gradually fragmented and their sizes decreased. Fragmentation of the existing holistic vegetation in open areas and UGSs into smaller pieces in urban areas may cause environmental degradation. This situation is an important threat, especially to the ecosystem, and significantly impacts the protection of biodiversity, environmental quality and urban microclimates [45, 46]. The findings of this study are consistent with previous research on the classification and monitoring of UGS; however, they advance current understanding by explicitly revealing the relationship between population dynamics and PCGS in the case of Antalya, thereby offering new perspectives for urban sustainability and planning strategies. Furthermore, as emphasized by Manavoğlu and Ortaçeşme [30], in UGS areas demonstrating minimal or positive change (Figure 9a, Figure 9d, and Figure 9f), restricting urban development can play a significant role in mitigating UGS losses. In this regard, urban planners and policy-makers may develop protective strategies for such areas to promote the equitable distribution and sustainable management of UGS.

Figure 9. Large UGS sample areas in the study area: (a) Agricultural area, (b) Airport, (c) Park, (d) Agricultural area belonging to a public institution, (e) Urban cemetery, (f) Forest area, (g) Park (Image from Google Earth dated June 2023)

One of the important issues is that not all UGSs have sufficient size and function, as revealed by Pouya and Aghlmand [2]. For example, although Figure 9a, Figure 9b, Figure 9d and Figure 9e, which cover a very large area in Muratpaşa, and contain quite large UGS, these are not areas that the public can use daily. In addition, some UGSs are smaller and inadequate in terms of function since they are in densely populated neighborhoods. In short, as the area covered by UGSs shrinks and the population increases, their functions in these areas decrease. Lockdown and population growth, especially those caused by sudden and rapidly spreading pandemics that may occur on a global scale, such as COVID-19, may also negatively affect UGSs and PCGS [47]. Not UGSs located in Muratpaşa have sufficient size and function, as in Figure 9c and Figure 9g, due to the dense urban texture. As stated by researchers, some UGSs are generally used as children's playgrounds, outdoor fitness equipment areas, walking/jogging tracks, or for recreation. In the planning of UGSs, it is necessary to consider not only quantitative values such as PCGS and impact areas but also the socio-economic, socio-cultural and ecological values of UGSs. In the studies to be carried out in this context, as suggested by Olgun [48], multidisciplinary studies involving professions such as planning, design, engineering and those working in the fields of social sciences, RS and GIS will be more useful.

4. CONCLUSION

This study determined the short-term changes in UGS and PCGS in a dense urban area using Sentinel-2 satellite data, demographic data, and the OBIA method. The OBIA method, which has significant advantages over classical pixel-based classification, was used in the study. The findings obtained from this study are quite high (over 90% OA), as in similar LULC or object detection studies. Additionally, the study utilized UGSI and PCGS values to examine the relationship between urban green space and the city's population across various time points. Analysis results show that there were slight changes in UGSI and PCGS over the short-term from 2017 to 2023, but PCGS (88.68 m² for 2017 and 81.35 m² for 2023) is above the minimum values determined by both Türkiye and WHO (>10 m²), even on a neighborhood basis. This indicates that, despite the city's increasing population and densification trends, the availability of urban green space per capita continues to be relatively sufficient. However, the minor decline observed suggests that future urban development and demographic growth could exert pressure on green space distribution. Therefore, it is crucial for city managers and urban planners to monitor this relationship closely, ensuring that green space planning keeps pace with population growth. Integrating such spatially explicit and temporally comparative analyses into urban planning can contribute to maintaining equitable access to green areas across neighborhoods and safeguarding the ecological and social functions of urban green infrastructure. This study suggests that the findings are transferable to urban areas of varying scales, offering valuable support to managers, urban planners, and landscape architects in promoting more effective and equitable planning practices. Additionally, it underscores the potential for integrating the remote sensing–based green space monitoring approach into national and municipal green infrastructure planning frameworks, thereby strengthening data-driven decision-making and fostering sustainable urban development. In the future, research will focus on the potential use of the remote sensing–based green space monitoring approach, not only in urban planning but also in precision agriculture, digital agriculture, and smart farming applications, to support data-driven decision-making and sustainable land management.

Acknowledgement

The author would like to thank ESA and TSI for free data sharing and thank Akdeniz University Remote Sensing and GIS Department for software and hardware support.

REFERENCES

[1] Li L, Xin X, Zhao J, Yang A, Wu S, Zhang H, et al. Remote sensing monitoring and assessment of global vegetation status and changes during 2016–2020. Sensors. 2023;23(20):8452.

[2] Sun Z, Du W, Jiang H, Weng Q, Guo H, Han Y, et al. Global 10-m impervious surface area mapping: A big earth data based extraction and updating approach. International Journal of Applied Earth Observation and Geoinformation. 2022;109:102800.

[3] Chen G, Zhou Y, Voogt JA, Stokes EC. Remote sensing of diverse urban environments: From the single city to multiple cities. Remote Sensing of Environment. 2024;305:114108.

[4] ESA [Internet]; 2024 [cited 2024 april 25]. Revisit and Coverage. Available from: https://sentinels.copernicus.eu/web/sentinel/user-guides/sentinel-2-msi/revisit-coverage

[5] Oke TR. The energetic basis of the urban heat island. Quarterly Journal of the Royal Meteorological Society. 1982;108(455):1–24.

[6] De Almeida CR, Teodoro AC, Gonçalves A. Study of the urban heat island (UHI) using remote sensing data/techniques: A systematic review. Environments. 2021;8(10):105.

[7] Belal AA, Moghanm FS. Detecting urban growth using remote sensing and GIS techniques in Al Gharbiya governorate, Egypt. The Egyptian Journal of Remote Sensing and Space Science. 2011;14(2):73–9.

[8] Nasser IA, Adam E. Urbanisation in Sub-Saharan Cities and the implications for urban agriculture: Evidence-based remote sensing from Niamey, Niger. Urban Science. 2024;8(1):5.

[9] Chen W, Huang H, Dong J, Zhang Y, Tian Y, Yang Z. Social functional mapping of urban green space using remote sensing and social sensing data. ISPRS Journal of Photogrammetry and Remote Sensing. 2018;146:436–52.

[10] Zhang X, Du S, Wang Q. Integrating bottom-up classification and top-down feedback for improving urban land-cover and functional-zone mapping. Remote Sensing of Environment. 2018;212:231–48.

[11] Anteneh MB, Damte DS, Abate SG, Gedefaw AA. Geospatial assessment of urban green space using multi-criteria decision analysis in Debre Markos City, Ethiopia. Environmental Systems Research. 2023;12(1).
[12] Pouya S, Aghlmand M. Evaluation of urban green space per capita with new remote sensing and geographic information system techniques and the importance of urban green space during the COVID-19 pandemic. Environmental Monitoring and Assessment. 2022;194(9).
[13] Badiu DL, Iojă CI, Pătroescu M, Breuste J, Artmann M, Niță MR, et al. Is urban green space per capita a valuable target to achieve cities' sustainability goals? Romania as a case study. Ecological Indicators. 2016;70:53–66.
[14] Gül A, Dinç G, Akin T, Koçak Aİ. Kentsel açık ve yeşil alanların mevcut yasal durumu ve uygulamadaki sorunlar. İdealkent. 2020;11:1281–312.
[15] Doğu G, Kesim Ü, Sivrikaya Ö. Belediyelerin sporla ilgili işlevleri: Düzce belediyesi örneği. Çağdaş Yerel Yönetimler. 2002;11(1):5–14.
[16] Anonymous [Internet]: 2024 [cited 2024 april 25]. Available from: https://csb.gov.tr/turkiyede-kisi-basina-dusen-agaclik-yesil-alan-miktari-12-63-metrekare-oldu-bakanlik-faaliyetleri-39952#:~:text=99%20B%C4%B0N%20485%20HEKTAR%20YE%C5%9E%C4%B0L,bin%20331%20dolar%20olarak%20hesapland%C4%B1
[17] Neyns R, Canters F. Mapping of urban vegetation with high-resolution remote sensing: A review. Remote Sensing. 2022;14(4):1031.
[18] Sönmez NK, Onur I. Monitoring of land use and land cover changes by using fuzzy supervised classification method: A case study of Antalya, Türkiye. Journal of Food Agriculture & Environment. 2012;10(3-4):963–7.
[19] Soyaslan İ. Hepdeniz K. Coğrafi bilgi sistemleri ve uzaktan algılama kullanılarak Burdur İli arazi kullanımının zamansal değişiminin belirlenmesi. Mehmet Akif Ersoy Üniversitesi Fen Bilimleri Enstitüsü Dergisi. 2016;7(2):94-101.
[20] Deliry SI, Avdan ZY, Avdan U. Extracting urban impervious surfaces from Sentinel-2 and Landsat-8 satellite data for urban planning and environmental management. Environmental Science and Pollution Research. 2020;28(6):6572–86.
[21] Zaki A, Buchori I, Sejati AW, Liu Y. An object-based image analysis in QGIS for image classification and assessment of coastal spatial planning. The Egyptian Journal of Remote Sensing and Space Science. 2022;25(2):349–59.
[22] Yu D, Fang C. Urban remote sensing with spatial big data: A review and renewed perspective of urban studies in recent decades. Remote Sensing. 2023;15(5):1307.
[23] Kucharczyk M, Hay GJ, Ghaffarian S, Hugenholtz CH. Geographic object-based image analysis: A Primer and future directions. Remote Sensing. 2020;12(12):2012.
[24] Moskal LM, Styers DM, Halabisky M. Monitoring urban tree cover using object-based image analysis and public domain remotely sensed data. Remote Sensing. 2011;3(10):2243–62.
[25] Choudhury MAM, Marcheggiani E, Despini F, Costanzini S, Rossi P, Galli A, et al. Urban tree species identification and carbon stock mapping for urban green planning and management. Forests. 2020;11(11):1226.
[26] Popa AM, Onose DA, Sandric IC, Dosiadis EA, Petropoulos GP, Gavrilidis AA, et al. Using GEOBIA and vegetation indices to assess small urban green areas in two climatic regions. Remote Sensing. 2022;14(19):4888.
[27] Simović I, Dubljević JT, Tošković O, Trkulja MV, Živojinović I. Underlying mechanisms of urban green areas' influence on residents' health—A case study from Belgrade, Serbia. Forests. 2023;14(4):765.
[28] Ortaçeşme V. Karagüzel O. Atik M. Sayan S. Antalya kentinin aktif yeşil alan varlığı üzerinde bir araştırma. Akdeniz Üniversitesi Ziraat Fakültesi Dergisi. 2000;13(1):11-22.
[29] Manavoğlu E. Ortaçeşme V. Konyaaltı kentsel alanında bir yeşil alan sistem önerisi geliştirilmesi. Konyaaltı kentsel alanında bir yeşil alan sistem önerisi geliştirilmesi. 2007;20(2):261-271.
[30] Manavoğlu E. Ortaçeşme V. Antalya kenti yeşil alanlarının çok ölçütlü analizi ve planlama stratejilerinin geliştirilmesi. Akdeniz Üniversitesi Ziraat Fakültesi Dergisi. 2015;28(1):11-19.
[31] Muratpaşa Belediyesi [Internet]: 2024 [cited 2024 april 20]. Tanıtım. Available from: https://muratpasa-bld.gov.tr/icerik/tanitim
[32] TSMS. [Internet]: 2024 [cited 2024 april 21]. Antalya. Available from: https://www.mgm.gov.tr/veridegerlendirme/il-ve-ilceler-istatistik.aspx?m=ANTALYA)
[33] ESA [Internet]: 2024 [cited 2024 april 20]. Overview. Available from: https://sentinels.copernicus.eu/web/sentinel/user-guides/sentinel-2-msi/overview
[34] ESA [Internet]: 2024 [cited 2024 april 20]. Spatial Resolution. Available from: https://sentinels.copernicus.eu/web/sentinel/user-guides/sentinel-2-msi/resolutions/spatial 20.04.2024
[35] ESA [Internet]: 2024 [cited 2024 april 20]. Level-2A. Available from: https://sentinels.copernicus.eu/web/sentinel/user-guides/sentinel-2-msi/product-types/level-2a
[36] Hashim H. Abd Latif Z. Adnan NA. (2019). Urban vegetation classification with NDVI threshold value method with very high resolution (VHR) Pleiades imagery. The International Archives of the Photogrammetry, Remote Sensing and Spatial Information Sciences. 2019;42:237-240.
[37] Tempa K, Ilunga M, Agarwal A, Tashi N. Utilizing Sentinel-2 satellite imagery for LULC and NDVI change dynamics for Gelephu, Bhutan. Applied Sciences. 2024;14(4):1578.
[38] Aryal J, Sitaula C, Aryal S. NDVI threshold-based urban green space mapping from Sentinel-2A at the local governmental area (LGA) level of Victoria, Australia. Land. 2022;11(3):351.

[39] Rouse JW, Haas RH, Schell JA, Deering DW. Monitoring vegetation systems in the Great Plains with ERTS. In: Third Earth Resources Technology Satellite-1 Symposium; 1973 Dec 10–14; Washington, DC. Washington (DC): NASA; p. 309–17.
[40] Shekhar S, Aryal J. Role of geospatial technology in understanding urban green space of Kalaburagi city for sustainable planning. Urban Forestry & Urban Greening. 2019;46:126450.
[41] Johnson B, Jozdani S. Identifying generalizable image segmentation parameters for urban land cover mapping through meta-analysis and regression tree modeling. Remote Sensing. 2018;10(1):73.
[42] Kotaridis I, Lazaridou M. Object-based image analysis of different spatial resolution satellite imageries in urban and suburban environment. Int Arch Photogramm Remote Sens Spatial Inf Sci. 2020;XLIII-B3:105–12.
[43] Kuang W, Dou Y. Investigating the patterns and dynamics of urban green space in China's 70 major cities using satellite remote sensing. Remote Sensing. 2020;12(12):1929.
[44] Zhu Y, Ling GHT. Spatio-temporal changes and driving forces analysis of urban open spaces in Shanghai between 1980 and 2020: An integrated geospatial approach. Remote Sensing. 2024;16(7):1184.
[45] Atasoy M. Monitoring the urban green spaces and landscape fragmentation using remote sensing: a case study in Osmaniye, Turkey. Environmental Monitoring and Assessment. 2018;190(12).
[46] Kowe P, Mutanga O, Dube T. Advancements in the remote sensing of landscape pattern of urban green spaces and vegetation fragmentation. International Journal of Remote Sensing. 2021;42(10):3797–832.
[47] Dahu BM, Alaboud K, Nowbuth AA, Puckett HM, Scott GJ, Sheets LR. The role of remote sensing and geospatial analysis for understanding COVID-19 population severity: A systematic review. International Journal of Environmental Research and Public Health. 2023;20(5):4298.
[48] Olgun R. Orta ölçekli kentler için kentsel yeşil alan sistem önerisi: Niğde kenti örneği. Artium. 2019;7(1):57–69.

Appendices

Appendix A. 2017-2023 populations of the neighborhoods
Appendix B . Neighbourhoods and UGSI
Appendix C . Neighbourhoods and PCGS

Appendix A. 2017-2023 populations of the neighborhoods

ID	Neighbourhood	Population						
		2017	2018	2019	2020	2021	2022	2023
01	Altındağ	8501	8434	8410	8226	8478	8481	8319
02	Bahçelievler	6144	6083	6209	6272	6265	6230	5892
03	Balbey	1056	1029	999	962	1026	1072	992
04	Barbaros	187	187	183	171	159	174	164
05	Bayındır	8806	8616	8796	8719	8870	8853	8612
06	Çağlayan	25376	26280	27282	27586	28543	28768	27732
07	Çaybaşı	7923	8111	8399	8445	8585	9965	8782
08	Cumhuriyet	11401	11172	11314	11410	11383	11641	11420
09	Demircikara	5090	5104	5177	5283	5398	5301	5153
10	Deniz	7189	7021	6983	6952	7031	6981	6730
11	Doğuyaka	4387	4669	4928	5010	5068	5188	5220
12	Dutlubahçe	10732	10708	10979	11115	11230	11344	11296
13	Elmalı	843	868	929	894	931	962	876
14	Ermenek	6800	6936	7033	7067	7081	7075	7160
15	Etiler	13884	14081	14602	14603	14621	14704	14547
16	Fener	17292	17415	17753	17631	17957	18058	17175
17	Gebizli	6876	7737	8757	9376	9859	10121	10238
18	Gençlik	6662	6568	6578	6508	6444	6360	6014
19	Güvenlik	13333	13246	13454	13517	13617	13816	13804
20	Güzelbağ	4282	4316	4630	4701	4962	4979	4951
21	Güzeloba	31125	32897	35220	34807	37424	39354	37074
22	Güzeloluk	8547	8669	8906	9005	9101	9156	8846
23	Haşimişcan	1544	1542	1543	1574	1550	1483	1463
24	Kılınçarslan	441	463	459	450	447	425	428
25	Kırcami	2748	2782	2755	2769	2719	2731	2835
26	Kışla	3621	3482	3504	3333	3488	3521	3167
27	Kızılarık	17915	18684	20162	20916	21856	22223	22035
28	Kızılsaray	4615	4577	4633	4596	4606	4734	4621
29	Kızıltoprak	21506	22562	23953	24469	25323	25814	25707
30	Konuksever	20597	20620	21211	21412	21268	21407	21237
31	Mehmetçik	1796	1870	1896	1957	2008	2037	2058
32	Meltem	12307	12246	12370	12234	12281	12158	11916
33	Memurevleri	7626	7484	7443	7409	7493	7414	7119
34	Meydankavağı	27632	28280	28908	29373	29583	29692	28558
35	Muratpaşa	12194	12410	12934	12985	12966	12943	12765
36	Sedir	8511	8478	8617	8610	8480	8509	8346
37	Selçuk	129	127	122	115	119	105	87
38	Sinan	7990	7956	8056	8097	8087	8099	7826
39	Şirinyalı	18315	18537	18793	18724	18430	18227	17683
40	Soğuksu	10546	10404	10635	10811	10803	10797	10547
41	Tahılpazarı	1937	1971	2038	1940	1988	2131	1999
42	Tarım	1794	1760	1809	1783	1818	1781	1701
43	Topçular	1024	1394	1260	1414	1321	1198	1019
44	Tuzcular	63	63	63	63	63	63	100
45	Üçgen	10729	10386	10454	10242	10286	10062	10002
46	Varlık	10133	10062	10240	10131	9980	9976	9818
47	Yenigöl	1645	1639	1526	1533	1625	1459	1462
48	Yenigün	21918	23167	23822	24066	24843	25045	24557
49	Yeşilbahçe	17647	17235	17153	17091	16836	16546	16124
50	Yeşildere	4846	4950	5280	5389	5529	5556	5705
51	Yeşilova	2892	2807	2871	2886	2915	2946	2855
52	Yıldız	9285	9174	9276	9287	9325	9333	9251
53	Yüksekalan	8583	8844	9124	9166	9231	9341	9112
54	Zerdalilik	7816	7892	8295	8324	8281	8345	8100
55	Zümrütova	1611	1613	1622	1597	1569	1580	1500

Appendix B. Neighbourhoods and UGSI

ID	Neighbourhood	Population		UGSI* (2017)	UGSI* (2023)
		2017	2023		
01	Altındağ	8501	8319	12.76	12.42
02	Bahçelievler	6144	5892	51.67	44.23
03	Balbey	1056	992	39.18	31.92
04	Barbaros	187	164	58.17	31.81
05	Bayındır	8806	8612	33.43	28.89
06	Çağlayan	25376	27732	34.34	37.28
07	Çaybaşı	7923	8782	28.68	23.56
08	Cumhuriyet	11401	11420	16.83	13.13
09	Demircikara	5090	5153	71.20	60.45
10	Deniz	7189	6730	33.95	25.21
11	Doğuyaka	4387	5220	64.38	65.89
12	Dutlubahçe	10732	11296	17.38	14.38
13	Elmalı	843	876	4.80	6.53
14	Ermenek	6800	7160	59.99	66.26
15	Etiler	13884	14547	18.58	16.82
16	Fener	17292	17175	52.47	47.50
17	Gebizli	6876	10238	23.21	19.34
18	Gençlik	6662	6014	31.12	28.84
19	Güvenlik	13333	13804	18.16	11.84
20	Güzelbağ	4282	4951	52.33	51.31
21	Güzeloba	31125	37074	47.06	52.29
22	Güzeloluk	8547	8846	54.51	54.80
23	Haşimişcan	1544	1463	62.10	54.25
24	Kılınçarslan	441	428	59.20	40.61
25	Kırcami	2748	2835	73.35	67.19
26	Kışla	3621	3167	21.29	19.62
27	Kızılarık	17915	22035	38.17	29.63
28	Kızılsaray	4615	4621	15.41	11.30
29	Kızıltoprak	21506	25707	30.24	25.02
30	Konuksever	20597	21237	20.36	16.98
31	Mehmetçik	1796	2058	76.66	74.25
32	Meltem	12307	11916	66.94	58.30
33	Memurevleri	7626	7119	10.09	7.24
34	Meydankavağı	27632	28558	36.27	27.59
35	Muratpaşa	12194	12765	15.99	16.58
36	Sedir	8511	8346	42.53	34.98
37	Selçuk	129	87	59.74	52.53
38	Sinan	7990	7826	19.04	12.56
39	Şirinyalı	18315	17683	59.01	44.56
40	Soğuksu	10546	10547	31.69	23.42
41	Tahılpazarı	1937	1999	10.77	12.17
42	Tarım	1794	1701	72.49	71.23
43	Topçular	1024	1019	55.06	61.34
44	Tuzcular	63	100	27.16	16.05
45	Üçgen	10729	10002	23.47	20.80
46	Varlık	10133	9818	24.25	18.32
47	Yenigöl	1645	1462	51.08	45.78
48	Yenigün	21918	24557	26.88	22.15
49	Yeşilbahçe	17647	16124	56.14	44.07
50	Yeşildere	4846	5705	46.23	29.85
51	Yeşilova	2892	2855	53.75	55.88
52	Yıldız	9285	9251	15.11	12.83
53	Yüksekalan	8583	9112	37.49	33.65
54	Zerdalilik	7816	8100	29.70	23.12
55	Zümrütova	1611	1500	71.77	70.66

**Values are %*

Appendix C. Neighbourhoods and PCGS

ID	Neighbourhood	Population		PCGS** 2017	PCGS** 2023
		2017	2023		
01	Altındağ	8501	8319	4.41	4.39
02	Bahçelievler	6144	5892	40.80	36.42
03	Balbey	1056	992	69.98	60.69
04	Barbaros	187	164	245.45	153.05
05	Bayındır	8806	8612	25.64	22.65
06	Çağlayan	25376	27732	36.13	35.90
07	Çaybaşı	7923	8782	18.26	13.54
08	Cumhuriyet	11401	11420	13.13	10.23
09	Demircikara	5090	5153	87.45	73.32
10	Deniz	7189	6730	14.54	11.53
11	Doğuyaka	4387	5220	285.84	245.86
12	Dutlubahçe	10732	11296	7.67	6.03
13	Elmalı	843	876	6.88	9.02
14	Ermenek	6800	7160	449.85	471.87
15	Etiler	13884	14547	9.72	8.40
16	Fener	17292	17175	63.34	57.72
17	Gebizli	6876	10238	20.40	11.42
18	Gençlik	6662	6014	21.27	21.83
19	Güvenlik	13333	13804	7.70	4.85
20	Güzelbağ	4282	4951	517.59	438.96
21	Güzeloba	31125	37074	235.65	219.84
22	Güzeloluk	8547	8846	291.06	282.76
23	Haşimişcan	1544	1463	80.96	74.64
24	Kılınçarslan	441	428	203.63	143.93
25	Kırcami	2748	2835	590.03	523.88
26	Kışla	3621	3167	13.01	13.70
27	Kızılarık	17915	22035	26.17	16.52
28	Kızılsaray	4615	4621	8.13	5.95
29	Kızıltoprak	21506	25707	20.03	13.87
30	Konuksever	20597	21237	8.84	7.15
31	Mehmetçik	1796	2058	403.01	340.67
32	Meltem	12307	11916	121.21	109.02
33	Memurevleri	7626	7119	2.69	2.06
34	Meydankavağı	27632	28558	21.03	15.48
35	Muratpaşa	12194	12765	7.70	7.63
36	Sedir	8511	8346	29.01	24.32
37	Selçuk	129	87	603.88	787.36
38	Sinan	7990	7826	8.10	5.46
39	Şirinyalı	18315	17683	62.64	48.99
40	Soğuksu	10546	10547	16.43	12.15
41	Tahılpazarı	1937	1999	11.51	12.61
42	Tarım	1794	1701	580.82	601.94
43	Topçular	1024	1019	652.54	730.52
44	Tuzcular	63	100	174.60	65.00
45	Üçgen	10729	10002	9.65	9.17
46	Varlık	10133	9818	13.27	10.35
47	Yenigöl	1645	1462	5402.25	5448.43
48	Yenigün	21918	24557	12.45	9.15
49	Yeşilbahçe	17647	16124	41.16	35.36
50	Yeşildere	4846	5705	49.28	27.03
51	Yeşilova	2892	2855	631.60	665.15
52	Yıldız	9285	9251	6.44	5.49
53	Yüksekalan	8583	9112	24.75	20.92
54	Zerdalilik	7816	8100	15.60	11.72
55	Zümrütova	1611	1500	562.26	594.73

***Values are m^2*

Volume 14, Issue 3, Page 218-225, 2025 https://doi.org/10.46810/tdfd.1753513 Research Article

BİNGÖL UNIVERSITY

Türk Doğa ve Fen Dergisi
Turkish Journal of Nature and Science
www.dergipark.gov.tr/tdfd

Investigation of Water Quality and Molecular Analysis (16s rRNA) of Bacterial Community Structure in a Rural Geothermal Spring: Ucler Hill (Azat Village), Kars, Türkiye

Orhan ULUÇAY[1*]

[1]Kafkas University, Faculty of Engineering and Architecture, Department of Bioengineering, Kars, Türkiye
Orhan ULUÇAY ORCID No: 0000-0002-0820-5372

**Corresponding author: orhanulucay@gmail.com*

(Received: 29.07.2025, Accepted: 16.09.2025, Online Publication: 26.09.2025)

Keywords
Natural drinking water source, Microbial diversity, Rural water security, Chemical water quality, 16S rRNA sequence analysis

Abstract: This study was carried out to evaluate the chemical and microbiological properties of a natural water source located in Azat Village (Ucler hill) of Kars province and used as drinking water by the surrounding villagers. Water samples taken from three different sampling points were analyzed for pH, electrical conductivity, total hardness, alkalinity, nitrogenous compounds (NO_2^-, NO_3^-, NH_4^+), metal contents (Fe, Cu, Al, Pb), sulfate and chloride levels. The data obtained were compared with World Health Organization (WHO) drinking water standards and one-sample t-test was applied for each parameter. Statistically significant differences were found in total hardness, NO_3^-, Fe, Cu, SO_4^{2-} and Cl^- parameters ($p < 0.05$), while other parameters were found to be compatible with WHO reference values. In microbiological analyses, a total of eight different bacterial species were isolated by culture-dependent methods. These species were identified by 16S rRNA gene sequencing analysis and all of them were determined to be non-pathogenic environmental microorganisms. The identified species included *Microbacterium* spp., *Bacillus subtilis*, *Corynebacterium* spp., *Lactobacillus* spp., *Rhodococcus* spp., *Pseudomonas putida*, *Leuconostoc* spp. and *Aeromonas* spp. Although some species have the potential to be opportunistic pathogens, the overall microbiological profile was considered to be within acceptable limits for natural sources.

Kırsal Bir Jeotermal Kaynakta Su Kalitesi ve Moleküler Analiz (16s rRNA) ile Bakteriyel Topluluk Yapısının İncelenmesi: Üçler Tepesi (Azat Köyü), Kars, Türkiye

Anahtar Kelimeler
Doğal içme suyu kaynağı, Mikrobiyal çeşitlilik, Kırsal su güvenliği, Kimyasal su kalitesi, 16S rRNA dizi analizi

Öz: Bu çalışma, Kars ilinin Azat Köyü'nde (Üçler tepesi) bulunan ve çevre köylüler tarafından içme suyu olarak kullanılan doğal bir su kaynağının kimyasal ve mikrobiyolojik özelliklerini değerlendirmek amacıyla gerçekleştirilmiştir. Üç farklı örnekleme noktasından alınan su örnekleri pH, elektriksel iletkenlik, toplam sertlik, alkalinite, azotlu bileşikler (NO_2^-, NO_3^-, NH_4^+), metal içerikleri (Fe, Cu, Al, Pb), sülfat ve klorür seviyeleri açısından analiz edilmiştir. Elde edilen veriler Dünya Sağlık Örgütü (WHO) içme suyu standartları ile karşılaştırılmış ve her parametre için tek örneklem t-testi uygulanmıştır. Toplam sertlik, NO_3^-, Fe, Cu, SO_4^{2-} ve Cl^- parametrelerinde istatistiksel olarak anlamlı farklılıklar bulunurken ($p<0.05$), diğer parametreler WHO referans değerleriyle uyumlu bulunmuştur. Mikrobiyolojik analizlerde, kültüre bağlı yöntemlerle toplam sekiz farklı bakteri türü izole edilmiştir. Bu izolatlar 16S rRNA gen dizileme analizi ile tanımlanmış ve patojen olmayan çevresel mikroorganizmalar olduğu belirlenmiştir. Tanımlanan türler arasında *Microbacterium* spp., *Bacillus subtilis*, *Corynebacterium* spp., *Lactobacillus* spp., *Rhodococcus* spp., *Pseudomonas* putida, *Leuconostoc* spp. ve *Aeromonas* spp. yer almaktadır. Bazı türler fırsatçı patojen olma potansiyeline sahip olsa da, genel mikrobiyolojik profilin doğal kaynaklar için kabul edilebilir sınırlar içinde olduğu düşünülmüştür.

1. INTRODUCTION

Freshwater resources are vital for both drinking and agricultural irrigation, especially for rural communities [1]. However, the sustainable and safe use of these resources is directly related not only to their quantity but also to their microbiological and chemical quality [2, 3]. Especially Kars province, which is located in the east of Turkey and has various geological structures, has a significant potential in terms of natural spring waters [4]. Azat village and its surroundings, which are discussed in this study, offer a remarkable research area due to their geographical location and hydrogeological characteristics. Ucler locality, which is close to the central district of Kars, where Azat Village is located, has a volcanic crater form with its topographical structure. Satellite images and field observations show that this region bears the traces of volcanic activities that occurred in the historical process. The flattened area in the center of the crater structure and the surrounding elevations suggest that the hydrogeochemical processes in this region are effective on the groundwater regime (Figure 1). In areas with volcanic rocks, the interaction of water with various minerals during its passage through the subsurface may create an environment that is both enriched in terms of ionic composition and suitable for the development of unique microbial communities [5].
In this context, remarkable differences can be observed in physicochemical parameters such as pH, conductivity and organic matter content as well as metals such as iron, manganese, sulfate and aluminum in water resources of volcanic origin. In fact, previous studies in these regions have reported critical values for human health, especially excessive iron and copper content, high ammonium and nitrite levels [6-8]. However, the fact that natural springs in such geological structures have been preferred by the public as drinking and utility water for many years brings with it the risk of ignoring possible microbiological threats.

From a microbiological point of view, natural mineralized waters formed by volcanic structures allow the development of bacterial communities adapted to harsh environmental conditions such as extreme temperature, pH changes and high ionic stress [9, 10]. These microorganisms are mostly saprophytes, but occasionally pathogenic species such as members of *Enterobacteriaceae*, *Pseudomonas* spp., *Staphylococcus* spp. and *Listeria* spp. have been reported [4, 11-13]. These bacteria may pose a risk of infection, especially for immunocompromised individuals and animals [12, 14]. In addition, the antibiotic resistance and heavy metal tolerance of bacteria also indicate the potential for significant public health problems in the long-term use of such resources.

This study aims to investigate both chemical parameters and microorganisms isolated by culture-based methods from a natural water source located in Azat Village of Kars province and used directly as a drinking water source by local people. In addition, identification of the bacterial isolates obtained at the molecular level by 16S rRNA gene region sequencing analysis will be carried out. Thus, the possible microbial risks, metal tolerance, diversity level and public health impact of natural water resources in the region will be revealed in a multidimensional way.

The results of this study will provide important information not only for the Kars region but also for the identification and control of environmental microorganisms that may threaten public health in rural areas with similar geological structures.

2. MATERIAL AND METHOD

2.1. Biological Material

The water samples analyzed in this study were collected from a natural water source located within the borders of Azat Village in the central district of Kars province, which is widely preferred by the local people for drinking and utility water. The spring is located in the center of an old volcanic structure at approximately 40.511855 °N latitude and 43.139596 °D longitude (Figure 1). This geological structure is characterized by its crater-like morphology and offers unique conditions for the mineral content and microbial load of the water. The sampling points on the map are marked in Figure 1. Sampling was conducted in June 2025 under moderate weather conditions; the season, date, time, and local observations (including limited animal activity around the source and moderate water flow) were recorded to provide context for the one-time sampling. A total of three different sampling points were identified; these points were taken from the main outlet near the center of the water source, from the middle zone downstream and from the expansion area approximately 50 meters beyond the outlet. Two samples were taken from each point, one from the surface (0-10 cm) and one from the bottom (20-30 cm), for a total of six water samples. Water samples were filled into sterile glass bottles and sealed to minimize contact with air during sampling [15]. The samples were transported to the laboratory of the Department of Bioengineering, Kafkas University within a maximum of 6 hours using ice-reinforced portable boxes. A constant temperature of less than 4°C was maintained during transportation of the samples, and the box was kept sterile to prevent external contamination. All samples were immediately separated for microbiological and chemical analyses upon arrival at the laboratory. During field studies, physical parameters such as water temperature, pH and electrical conductivity were measured and recorded instantly in the field with portable measuring devices [16]. At the same time, sampling coordinates, environmental observations and risk factors (animal mobility, agricultural activities, soil structure, vegetation cover, etc.) were documented in detail with a GPS device.

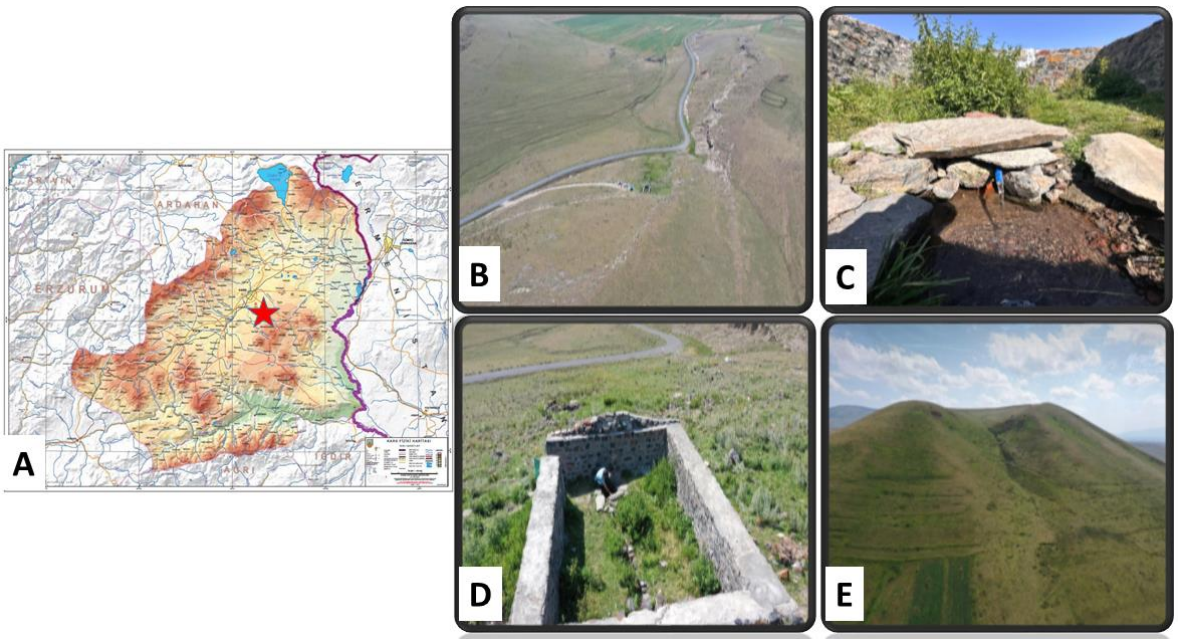

Figure 1. Visual components of the study area. (A) Location of the water source (indicated by the red star) on the physical map of Turkey-Kars province obtained from the General Directorate of Mapping [17]. (B) General view of the vicinity of the water source taken by drone from an altitude of approximately 350 m. (C) Stone structure and water outlet point in the inner region used directly as drinking water by local people. (D) View of the water source from upper elevations and surrounding settlement structure. (E) Topographic view of the northern slope of the volcanic mountain where the water source is located

2.2. Water Quality Assessment Based on Chemical Indicators

Within the scope of the research, chemical evaluation of water samples collected from three different points in Azat Village was carried out using internationally accepted standard analysis methods. In these analyses, physical parameters such as pH, conductivity, total hardness and alkalinity were first measured; then the levels of chemical components such as nitrite (NO_2^-), nitrate (NO_3^-), ammonium (NH_4^+), iron (Fe), aluminum (Al), copper (Cu), lead (Pb), sulfate (SO_4^{2-}) and chloride (Cl^-) were determined. All analyses were carried out in a laboratory approved by the Ministry of Agriculture and Forestry, based on Turkish Standards Institute (TSE) and World Health Organization (WHO) drinking water quality criteria [18]. The data obtained were presented in a tabular form to allow comparison of the parameters with the limit values and their compliance status was also evaluated. Thus, it was objectively revealed whether the water source carries a potential risk in terms of potability. All chemical analyses were performed in an accredited laboratory in accordance with TSE and WHO standard protocols [18]. Device calibration, blind sample and standard use, and repeat measurements were performed to ensure quality assurance/quality control (QA/QC) and the reliability of the results.

2.3. Isolation and Cultivation of Environmentally Brought Bacteria

Bacterial isolation from water samples was carried out using culture-based classical microbiological methods. After the samples arrived at the laboratory, they were subjected to serial dilutions from 10^{-1} to 10^{-6} under aseptic conditions [15]. Each dilution was inoculated into Nutrient Agar (NA) medium by the surface spreading method using sterile pipettes. Incubation in Petri dishes was performed at 37°C under aerobic conditions for 24 to 72 hours. Colonies exhibiting different colony morphologies were selected and reseeded by drawing method to obtain pure culture. The purified isolates were stored at -20 °C in liquid medium containing 15% glycerol for storage as stock cultures [19]. This approach provides a baseline for the preliminary identification of the dominant bacterial species naturally found in environmental water sources. Isolates were subjected to preliminary classification by observing colony morphology, color, size and margin structure. The pure cultures obtained were transferred to the next stages to be used for further molecular analyses [20].

2.4. DNA Preparation Protocol for Molecular Analyses

Genomic DNA extraction from pure cultures obtained as a result of bacterial isolations was carried out based on the phenol-chloroform-based classical method described in the literature [21]. Firstly, the isolates were incubated in liquid medium overnight and then the cells were precipitated by centrifugation. The cell pellets obtained were treated with lysis buffer and cell walls were lysed. Proteinase K and SDS were applied to remove protein structures, then DNA was extracted with phenol: chloroform: isoamyl alcohol (25:24:1). DNA samples precipitated with isopropanol were washed with 70% ethanol, dried and dissolved in TE buffer [15]. The purity and integrity of the DNA were checked by NanoDrop spectrophotometer and 1% agarose gel electrophoresis [22, 23]. Suitable samples were stored for further molecular analysis.

2.5. 16S rRNA profiling of culture-based isolates

The high purity genomic DNA samples obtained were subjected to PCR analysis targeting the 16S rRNA gene region for bacterial species identification. Amplification was performed using universal primers 27F (5′-AGA GTT TGA TCC TGG CTC AG-3′) and 1492R (5′-GGT TAC CTT GTT GTT ACG ACT T-3′) [24]. The PCR reaction was prepared in a total volume of 25 µL and included Taq DNA polymerase, dNTP mix, $MgCl_2$, primers and template DNA. Reactions were run in thermal cycles using standard temperature cycles and the PCR products obtained were visualized and verified on a 1% agarose gel [4]. Cleaned amplicons were sequenced by Sanger sequencing using a commercial sequencing service. The sequences were converted to FASTA format and analyzed by BLASTn searches in the NCBI GenBank database for species-level identification. Matches with 98% or more similarity were considered for taxonomic matching.

2.6. Assessment of Molecular Analysis

To reveal the similarities between the bacterial species isolated in this study, sequences belonging to the 16S rRNA gene region were amplified by PCR. The sequence analysis results were organized in FASTA format, and the closest matching culture reference species were determined by BLASTn search [25]. Sequences from environmental or undescribed species were not included in the evaluation.

2.7. Statistical Analyses

The chemical parameter data obtained in the study were evaluated in comparison with the drinking water standards recommended by the World Health Organization (WHO) [18]. Three repeated measurements were made for each parameter and mean values were calculated together with standard deviations. One-sample t-test was performed on the obtained data to evaluate whether the measured values showed a statistically significant difference with the reference limits. The significance level was accepted as $p<0.05$. All calculations were carried out using Microsoft Excel and IBM SPSS Statistics software and the results were supported by relevant graphs and tables [26]. This numerical evaluation aimed to increase the scientific reliability of both chemical and microbiological results.

3. RESULTS

3.1. General Characteristics of the Sampling Area and Water Quality Indicators

This study was carried out in a natural water source located in Azat Village of Kars province and used as drinking water by the public. The water temperature of the spring was approximately 35 °C and the pH value was measured as 7.4. The water is in the neutral pH range and has natural spring characteristics. In the chemical analysis, 13 different parameters were evaluated. All of these parameters such as pH, conductivity, total hardness, alkalinity, NO_2^-, NO_3^-, NH_4^+, Al, Pb, SO_4^{2-} and Cl^- were found to comply with the limit values set by the World Health Organization for drinking water. However, Fe (0.32 mg/L) and Cu (2.05 mg/L) levels were slightly above the limit values (Fe ≤ 0.3, Cu ≤ 2.0). Therefore, these two parameters were evaluated as “above the limit, therefore non-compliant”. This can be explained by the effect of the geological structure through which the water passes. Overall, the chemical quality of the Azat Village water source is largely suitable for drinking (Table 1).

Table 1. Mean values, standard deviations, WHO drinking water limit values and compliance status of chemical parameters measured in samples taken from the Azat Village water source.

Parameter	Average Value (X̄)	Standard Deviation (±)	WHO Limit	Compliance
pH	7.4	0.1	6.5 – 8.5	Compliance
E.C. (mS/cm)	2.4	0.05	<2.5	Compliance
Total Hardness (mg/L $CaCO_3$)	290.0	10.0	0 – 500	Compliance
Alkalinity (mg/L)	180.0	8.0	0 – 200	Compliance
NO_2^- (mg/L)	0.48	0.03	≤0.5	Compliance
NO_3^- (mg/L)	45.5	1.5	≤50	Compliance
NH_4^+ (mg/L)	0.48	0.02	≤0.5	Compliance
Fe (mg/L)	0.32	0.01	≤0.3	**Non-compliant**
Al (mg/L)	0.19	0.01	≤0.2	Compliance
Cu (mg/L)	2.05	0.04	≤2.0	**Non-compliant**
Pb (mg/L)	0.009	0.002	≤0.01	Compliance
SO_4^{2-} (mg/L)	120.0	4.3	≤250	Compliance
Cl^- (mg/L)	41.0	1.2	≤250	Compliance

3.2. Morphological Characterization of Isolates

The bacteria were isolated from water samples and analyzed by Gram staining method. In microscopic analysis, mostly Gram positive rod and cocci form bacteria were observed (Figure 2 and Table 2). All of these bacteria are among the non-pathogenic species commonly found in drinking and environmental waters in the literature. As a result of the morphological examinations, bacteria similar to the following were identified among the identified species: *Microbacterium spp., Bacillus subtilis, Corynebacterium spp., Lactobacillus spp., Rhodococcus spp., Pseudomonas putida, Leuconostoc spp. and Aeromonas spp.* These species are described as generally harmless aquatic bacteria with high environmental tolerance in natural waters and do not show pathogenicity.

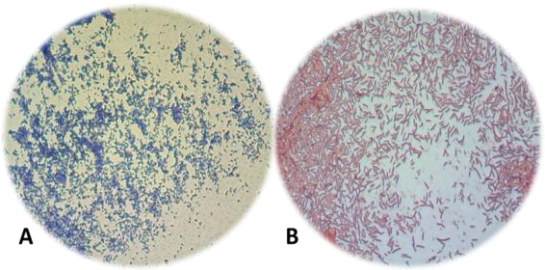

Figure 2. Gram staining micrographs of isolated bacterial species. **(A)** Gram-positive, short rod morphology *Microbacterium* spp. AZ1 is characterized by blue-purple stained cell structure. **(B)** Microscopic image of a Gram-negative, pink-colored long rod-shaped *Pseudomonas putida* AZ6. Both images were taken with immersion oil at 1000× magnification

3.3. 16S rRNA Gene Regions of the Isolates

In order to identify the bacteria isolated in the study at species level, genomic DNA of each isolate was obtained following appropriate protocols. Then, the 16S rRNA gene region was successfully amplified and sequenced using universal primers (Figure 3). The sequences obtained were compared with the NCBI GenBank database and species with 98% or more similarity were identified (Table 2). According to the molecular identification results, a total of 8 different species were identified. The majority of these species are non-pathogenic bacteria that are frequently encountered as environmental saprophytes in natural drinking water sources. These results indicate that the bacteria present in the water source are largely of environmental origin and non-pathogenic in character. These molecular level analyses provided an important overview of the microbial content of the water.

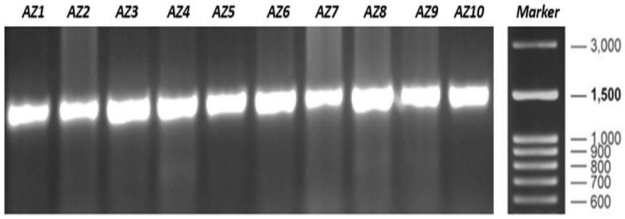

Figure 3. Agarose gel image of PCR amplification of the 16S rRNA gene region of bacteria isolated from water samples from Azat Village. The bands approximately 1500 bp long were observed in all isolates.

Table 2. Optimum pH and temperature ranges of bacterial species isolated from the Azat Village water source. All isolates grew in the pH range of 7.0–7.5, and temperature tolerances varied among species.

Isolate	Identified	pH	Temperature Range / T_{opt} (°C)	Gram Staining	Form
AZ1	*Microbacterium* spp.	7.0–7.5	20–45 / 37	+	*Bacilli*
AZ2	*Bacillus subtilis*	7.0–7.5	35–50 / 40	+	*Bacilli*
AZ3	*Corynebacterium* spp.	7.0–7.5	20–40 / 30	+	*Bacilli* (irregular form)
AZ4	*Lactobacillus* spp.	7.0–7.5	20–45 / 37	+	*Bacilli*
AZ5	*Rhodococcus* spp.	7.0–7.5	25–45 / 37	+	*Cocco bacil*
AZ6	*Pseudomonas putida*	7.0–7.5	25–45 / 37	-	*Bacilli*
AZ7	*Leuconostoc* spp.	7.0–7.5	15–35 / 30	+	*Cocci*
AZ8	*Aeromonas* spp.	7.0–7.5	20–42 / 35	-	*Bacilli*
AZ9	*Bacillus* sp.	7.0–7.5	35–50 / 40	+	*Bacilli*
AZ10	*Pseudomonas* sp.	7.0–7.5	25–45 / 37	-	*Bacilli*

3.4. The Chemical Parameters of the Water Samples

The comparative analysis of the chemical parameters of the water samples taken from Azat Village with the drinking water limit values determined by the World Health Organization (WHO) was carried out by one-sample t-test. Three repeated measurements were taken for each parameter and statistical validity was tested by calculating the mean value and standard deviation. The Total Hardness, expressed as mg/L $CaCO_3$, was found to be significantly less than the WHO upper limit of 500 mg/L in the cases under concern ($p = 0.0004$). This indicates the natural low hardness level of water in the region but within acceptance. Except for these, parameters such as pH, conductivity, alkalinity, NO_2^-, NO_3^-, NH_4^+, Al, Pb, SO_4^{2-}, and Cl^- showed mean values which were not significantly different from the WHO limit ($p > 0.05$). The results imply that, in general, the chemical composition of the water is safe for drinking purposes. However, the measured mean values of Fe (mg/L) and Cu (mg/L) parameters were slightly above the WHO recommended limit values, and these differences were found to be statistically significant ($p < 0.05$).

Table 3. One-sample t-test results for comparing chemical parameters obtained from Azat Village water samples with World Health Organization (WHO) drinking water standard values. Mean value, standard deviation, reference value, t-statistic, and p-value are given for each parameter, and significance was assessed at $p < 0.05$.

Parameter	Average	Standard Deviation	WHO Reference	t-statistic	p-value
pH	7.4	0.1	7.5	0.121	0.9151
Electrical Conductivity (mS/cm)	2.4	0.05	2.5	-2.41	0.1376
Total Hardness (mg/L $CaCO_3$)	290.0	10.0	500.0	-50.483	0.0004
Alkalinity (mg/L)	180.0	8.0	200.0	-3.675	0.0667
NO_2^- (mg/L)	0.48	0.03	0.5	0.964	0.4368
NO_3^- (mg/L)	45.5	1.5	50.0	-4.94	0.0386
NH_4^+ (mg/L)	0.48	0.02	0.5	0.121	0.9151
Fe (mg/L)	0.32	0.01	0.3	7.711	0.0164
Al (mg/L)	0.19	0.01	0.2	0.121	0.9151
Cu (mg/L)	2.05	0.04	2.0	5.813	0.0283
Pb (mg/L)	0.009	0.002	0.01	1.386	0.3001
SO_4^{2-} (mg/L)	120.0	4.3	250.0	-73.843	0.0002
Cl^- (mg/L)	41.0	1.2	250.0	-438.024	0.0

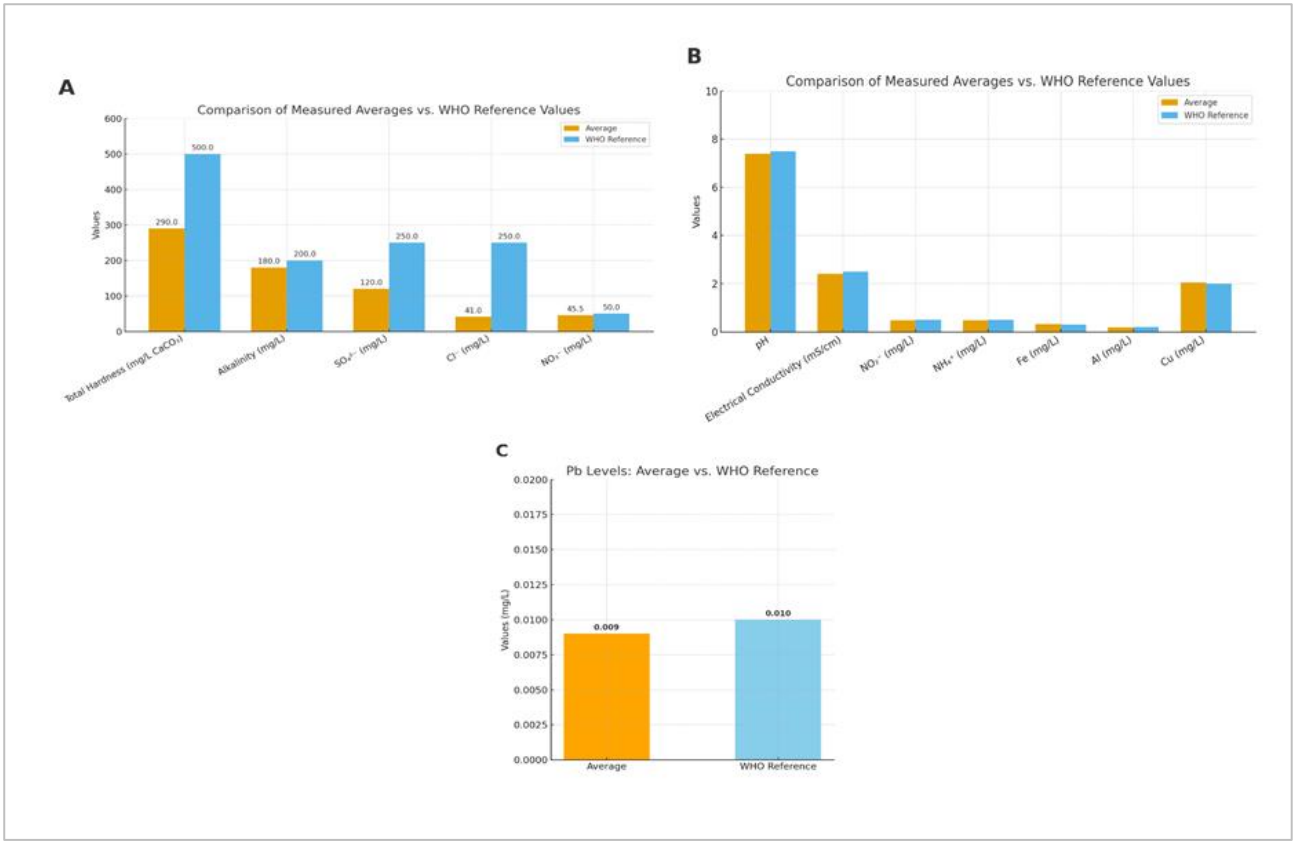

Figure 4. Comparison of average measured values of chemical parameters with the WHO drinking water standards. **(A)** Total Hardness, Alkalinity, SO_4^{2-}, Cl^-, and NO_3^- concentrations; **(B)** pH, Electrical Conductivity, NO_2^-, NH_4^+, Fe, Al, and Cu values; **(C)** Pb levels.

4. DISCUSSION

In this study, a natural water source located in Azat Village of Kars province and preferred by local people for drinking and utilization purposes was evaluated chemically and microbiologically. The results show that the spring water is safe for drinking to a large extent, but some parameters have reached limits that require caution. In this context, the results are important not only for regional public health but also for shaping rural water security policies.

From the chemical analyses, 11 out of 13 parameters fell within the prescribed limits for potable water as per WHO standards [18]. Thus, water specimens were under permissible limits for pH, conductivity, total hardness, alkalinity, nitrite (NO_2^-), nitrate (NO_3^-), ammonium (NH_4^+), aluminum (Al), lead (Pb), sulfate (SO_4^{2-}), and chloride (Cl^-). This indicates that the water in Azat Village comes from a geologically stable composition and is insulated from sources of external contamination. Especially nitrate and ammonium are below the limits, which means that the source is comparatively protected from agrarian pollution and livestock effluent [27, 28].
Here is a noteworthy observation: Whereas Fe and Cu levels were ever so slightly above the WHO limits, the mean value for iron is 0.32 mg/L against WHO limit of 0.3 mg/L and 2.05 mg/L for copper, while the limit value was 2.0 mg/L [18]. The one-sample t-test showed that the differences for both parameters were statistically significant ($p < 0.05$). Still, these slight differences warrant long-term monitoring. This result may be attributed to the low measurement variations and limited number of samples. The fact that both parameters were very close to the limit indicates that they should be monitored carefully, especially for long-term use. On the contrary, the solubility of these metals in water might be associated with the rock structure lying around the source and some geothermal activity effects [29]. Copper, in particular, is among the elements that can pass into water from soils and rocks of volcanic origin [30]. As a result of microbiological analyses, a total of eight different bacterial species were isolated by culture-based methods and identified at molecular level by 16S rRNA gene sequencing. These bacteria include *Microbacterium* spp., *Bacillus* spp., *Corynebacterium* spp., *Lactobacillus* spp., *Rhodococcus* spp., *Pseudomonas* spp., *Leuconostoc* spp. and *Aeromonas* spp. All these taxa are delineated in the scholarly corpus as saprophytic and generally non-pathogenic microorganisms associated with environmental aquatic systems [4, 31-34]. These observations, corroborated by Gram staining and morphological assessments, suggest that the microbial quality of the water is at an acceptable standard. Nevertheless, the identification of opportunistic pathogenic taxa such as *Aeromonas* and *Pseudomonas*, even at minimal concentrations, is significant as they may present a potential hazard for individuals with compromised immune systems [35-37].

An important contribution that is being made by this study is the detailed examination of a remote water source existing in a geologically and climatically unique geography of Kars, chemically, and microbiologically.

One thing that the literature report clearly states is that the number of scientific data on natural water resources in and around Kars is very limited. Therefore, the product of this research will help raise awareness among the local people in the context of water safety, hygiene, and public health, apart from providing scientific input to local governments for preparing monitoring and improvement strategies. On the other hand, the study also faces some constraints. It remained as a single episode sampling with limited repetitions. Considering the effects of seasonal differences on chemical and microbiological parameters, it is recommended that such studies be repeated periodically throughout the year in the future. In addition, revealing a wider microbial diversity through non-culture-dependent methods such as metagenomic analysis will provide a more comprehensive perspective on the microbiological safety of water.

5. CONCLUSIONS

This study evaluated the chemical and microbiological quality of the natural drinking water source in Azat Village, Kars province. As a result of the analyses, it was determined that most chemical parameters were in compliance with the World Health Organization (WHO) drinking water standards. However, iron and copper levels were very close to the limit values and it should be emphasized that they should be monitored regularly for long-term use.

A total of eight bacterial species were identified in the microbiological analyses, most of which were environmental and non-pathogenic. However, the presence of some opportunistic species reveals a situation that needs to be carefully monitored.

In conclusion, although the Azat Village water source is generally potable, periodic chemical and microbiological controls are recommended, taking into account seasonal changes. In the future, more comprehensive microbial diversity screening with metagenomic analysis will make important contributions to water safety. In addition, the data obtained are also instructive for the studies to be carried out for other natural resources in the region.

Acknowledgement
The author used tools such as Grammarly, ChatGPT, DeepL, Google Translate, and Quillbot to improve spelling and readability, and personally reviewed and edited the final content. No funding has been provided for this work.

REFERENCES

[1] Mishra, R.K., Fresh water availability and its global challenge, British Journal of Multidisciplinary and Advanced Studies 4(3) 2023; 1-78.
[2] Till, D., G. McBride, A. Ball, K. Taylor, E. Pyle, Large-scale freshwater microbiological study: rationale, results and risks, Journal of Water and Health 6(4) 2008; 443-460.
[3] Verma, S., S. Verma, R. Ramakant, V. Pandey, A. Verma, Comprehensive Assessment of Physico-Chemical and Biological Parameters in Water Quality Monitoring: A Review of Contaminants, Indicators, and Health Impacts, International Journal of Horticulture, Agriculture and Food science 9(2) 2025; 611019.
[4] Ulucay, O., Potential Health Risks of the Çakmak Village Thermal Spring (Turkey, Kars) for Grazing Animals: Characterization of Bacterial Communities and Water Quality, Journal of Environmental Chemical Engineering 2025; 118059.
[5] Reysenbach, A.-L., E. St. John, J. Meneghin, G.E. Flores, M. Podar, N. Dombrowski, A. Spang, S. L'Haridon, S.E. Humphris, C.E.J. De Ronde, Complex subsurface hydrothermal fluid mixing at a submarine arc volcano supports distinct and highly diverse microbial communities, Proceedings of the National Academy of Sciences 117(51) 2020; 32627-32638.
[6] Uluçay, O., A. Görmez, C. Öziç, Determination of Physical, Chemical Properties of the Hot Springs Waters and Comparison of Bacteria: Hot Springs in the East and Southeast Anatolia Region of Turkey, Journal of Agriculture 4(1) 2021; 24-29.
[7] Hamilton, T.L., E. Koonce, A. Howells, J.R. Havig, T. Jewell, J.R. de la Torre, J.W. Peters, E.S. Boyd, Competition for ammonia influences the structure of chemotrophic communities in geothermal springs, Appl Environ Microb 80(2) 2014; 653-661.
[8] Dippong, T., M.-A. Resz, Heavy metal contamination assessment and potential human health risk of water quality of lakes situated in the protected area of Tisa, Romania, Heliyon 10(7) 2024.
[9] Lynch, R.C., A.J. King, M.E. Farías, P. Sowell, C. Vitry, S.K. Schmidt, The potential for microbial life in the highest-elevation (> 6000 masl) mineral soils of the Atacama region, Journal of Geophysical Research: Biogeosciences 117(G2) 2012.
[10] Smrhova, T., K. Jani, P. Pajer, G. Kapinusova, T. Vylita, J. Suman, M. Strejcek, O. Uhlik, Prokaryotes of renowned Karlovy Vary (Carlsbad) thermal springs: phylogenetic and cultivation analysis, Environmental Microbiome 17(1) 2022; 48.
[11] Arvanitidou, M., A. Papa, T.C. Constantinidis, V. Danielides, V. Katsouyannopoulos, The occurrence of Listeria spp. and Salmonella spp. in surface waters, Microbiological Research 152(4) 1997; 395-397.
[12] Ghilamicael, A.M., H.I. Boga, S.E. Anami, T. Mehari, N.L.M. Budambula, Potential human pathogenic bacteria in five hot springs in Eritrea revealed by next generation sequencing, PLoS One 13(3) 2018; e0194554.
[13] Rahel, C., R. Adriyani, H.A. Nurfitria, Health risk in hot springs: A literature review, Journal of Health Science and Prevention 5(2) 2021; 88-99.
[14] Deza, M.A., M. Araujo, M.J. Garrido, Inactivation of Escherichia coli, Listeria monocytogenes, Pseudomonas aeruginosa and Staphylococcus aureus on stainless steel and glass surfaces by neutral electrolysed water, Lett Appl Microbiol 40(5) 2005; 341-346.

[15] Ulucay, O., A. Gormez, C. Ozic, Identification, characterization and hydrolase producing performance of thermophilic bacteria: geothermal hot springs in the Eastern and Southeastern Anatolia Regions of Turkey, Antonie van Leeuwenhoek 2022; 1-18.
[16] Uluçay, O., & Öziç, C. (2025). Molecular identification and phylogenetic profiling of keratinolytic bacteria isolated from goose and chicken farms in a cold region of Türkiye. International Journal of Agriculture Environment and Food Sciences, 9(2), 436-445. https://doi.org/10.31015/2025.2.17
[17] Kars Maps, 2025. https://www.harita.gov.tr/urun/kars-fiziki-il-haritasi/382. (Accessed 25.06.2025 2025).
[18] Edition, F., Guidelines for drinking-water quality, WHO chronicle 38(4) 2011; 104-8.
[19] Oztas Gulmus, E., A. Gormez, Identification and characterization of novel thermophilic bacteria from hot springs, Erzurum, Turkey, Curr Microbiol 77(6) 2020; 979-987.
[20] Ahmadpour, A., Y. Ghosta, Z. Alavi, F. Alavi, L.M. Hamidi, P.H. Rampelotto, Morphological and Molecular Characterization of a New Section and Two New Species of Alternaria from Iran, Life 15(6) 2025; 870.
[21] Javadi, A., M. Shamaei, L.M. Ziazi, M. Pourabdollah, A. Dorudinia, S.M. Seyedmehdi, S. Karimi, Qualification study of two genomic DNA extraction methods in different clinical samples, Tanaffos 13(4) 2014; 41.
[22] Elkins, K.M., Determination of Quality and Quantity of DNA Using Agarose Gel Electrophoresis, Forensic DNA Biology. Oxford, USA: Elsevier Inc 2013; 53-57.
[23] Gurcan, K., F. Demirel, M. Tekin, S. Demirel, T. Akar, Molecular and agro-morphological characterization of ancient wheat landraces of turkey, Bmc Plant Biol 17(Suppl 1) 2017; 171.
[24] Chen, C., P.H. Qu, Q. Gu, B. Huang, W.Z. Zhang, X.P. Mu, L. Zhang, M.R. Chen, L.X. Wang, Y.J.Y. E Sm, Application of broad-spectrum PCR amplification and direct sequencing for identification of the infrequent bacterial cultures from clinical sources, targeting the bacterial 16S rRNA gene with universal primers, Chin J Lab Med 35 2012; 612-619.
[25] Drancourt, M., C. Bollet, A. Carlioz, R. Martelin, J.-P. Gayral, D. Raoult, 16S ribosomal DNA sequence analysis of a large collection of environmental and clinical unidentifiable bacterial isolates, Journal of clinical microbiology 38(10) 2000; 3623-3630.
[26] Meyers, L.S., G.C. Gamst, A.J. Guarino, Performing data analysis using IBM SPSS, John Wiley & Sons2013.
[27] Sahoo, P.K., K. Kim, M.A. Powell, Managing groundwater nitrate contamination from livestock farms: implication for nitrate management guidelines, Current Pollution Reports 2(3) 2016; 178-187.
[28] Lawniczak, A.E., J. Zbierska, B. Nowak, K. Achtenberg, A. Grześkowiak, K. Kanas, Impact of agriculture and land use on nitrate contamination in groundwater and running waters in central-west Poland, Environmental monitoring and assessment 188(3) 2016; 172.
[29] Crerar, D., S. Wood, S. Brantley, A. Bocarsly, Chemical controls on solubility of ore-forming minerals in hydrothermal solutions, The Canadian Mineralogist 23(3) 1985; 333-352.
[30] Zampella, M., P. Adamo, L. Caner, S. Petit, D. Righi, F. Terribile, Chromium and copper in micromorphological features and clay fractions of volcanic soils with andic properties, Geoderma 157(3-4) 2010; 185-195.
[31] Farrar Jr, W.E., Serious infections due to "non-pathogenic" organisms of the genus bacillus: Review of their status as pathogens, The American journal of medicine 34(1) 1963; 134-141.
[32] Hajmeer, M.N., D.Y.C. Fung, Infections with other bacteria, Foodborne Infections and Intoxications (3rd Ed.) Elsevier, UK 2006; 341-367.
[33] Oliveira, A., L.C. Oliveira, F. Aburjaile, L. Benevides, S. Tiwari, S.B. Jamal, A. Silva, H.C.P. Figueiredo, P. Ghosh, R.W. Portela, Insight of genus Corynebacterium: ascertaining the role of pathogenic and non-pathogenic species, Frontiers in microbiology 8 2017; 1937.
[34] Ivshina, I.B., M.S. Kuyukina, A.V. Krivoruchko, E.A. Tyumina, Responses to ecopollutants and pathogenization risks of saprotrophic Rhodococcus species, Pathogens 10(8) 2021; 974.
[35] Janda, J.M., S.L. Abbott, The genus Aeromonas: taxonomy, pathogenicity, and infection, Clinical microbiology reviews 23(1) 2010; 35-73.
[36] Fernández-Bravo, A., M.J. Figueras, An update on the genus Aeromonas: taxonomy, epidemiology, and pathogenicity, Microorganisms 8(1) 2020; 129.
[37] De Bentzmann, S., P. Plésiat, The Pseudomonas aeruginosa opportunistic pathogen and human infections, Environmental microbiology 13(7) 2011; 1655-1665.

Volume 14, Issue 3, Page 226-232, 2025 https://doi.org/10.46810/tdfd.1587969 Review

BİNGÖL UNIVERSITY

Türk Doğa ve Fen Dergisi
Turkish Journal of Nature and Science
www.dergipark.gov.tr/tdfd

Considering the Health Effects of Climate Change: A Scoping Review

Emine Didem EVCİ KİRAZ[1], Kübra Ecem TURGUTKAYA[1*], Eda ÇELİK[1], Onur TOPÇU[1], İsmail ÇEVİK[1], Dilara ŞAHİN[1], Murat EĞİLMEZ[1], Kübra SOFUOĞLU[1], Tolga Hüseyin ATIŞ[1]

[1] Aydın Adnan Menderes University, Faculty of Medicine, Public Health Department, Aydın, Türkiye
Emine Didem EVCİ KİRAZ ORCID No: 0000-0003-0090-5590
Kübra Ecem TURGUTKAYA ORCID No: 0000-0002-0697-336X
Eda ÇELİK ORCID No: 0009-0009-1942-7921
Onur TOPÇU ORCID No: 0009-0003-6479-2967
İsmail ÇEVİK ORCID No: 0000-0002-3797-4461
Dilara ŞAHİN ORCID No: 0000-0002-4499-8533
Murat EĞİLMEZ ORCID No: 0000-0002-9279-2038
Kübra SOFUOĞLU ORCID No: 0009-0000-9710-2326
Tolga Hüseyin ATIŞ ORCID No: 0000-0002-1533-4877

**Corresponding author: kturgutkaya@adu.edu.tr*

(Received: 20.11.2024, Accepted: 02.08.2025, Online Publication: 26.09.2025)

Keywords
Climate change, Health impacts, Public health, Scoping review

Abstract: The consequences of climate change significantly affect human health. The purpose of this review is to outline the progress of studies in the field of climate and health to date and to shed light on future research. The PRISMA-ScR (Preferred Reporting Items for Systematic Reviews and Meta-Analyses extension for Scoping Reviews) checklist was used to guide the study. A literature search was conducted on September 13, 2024, using PubMed and Google Scholar, covering the period from 2019 to 2024. Of the included studies, 65(40.12%) were from Europe, 43(26.54%) from Asia, and 34 (20.98%) from North America. The most commonly used research types included were reviews (%31.48) and modelling studies (%20.37). The most frequently used climate change evidence category in the included studies were “extreme weather events and heat/cold air waves”. The most frequently obtained health effects category in the compiled studies was "diseases related to heat and cold". This review summarizes research conducted in the past five years on the health impacts of climate change, identifying knowledge gaps and research priorities. Future studies should combine quantitative and qualitative methods to better understand the health impacts of climate change, assess health risks, and develop effective interventions.

İklim Değişikliğinin Sağlık Etkilerinin Ele Alınması: Kapsam Derlemesi

Anahtar Kelimeler
İklim değişikliği, Sağlık etkileri, Halk sağlığı, Kapsam derlemesi

Öz: İklim değişikliğinin sonuçları insan sağlığını önemli ölçüde etkilemektedir. Bu derlemenin amacı, iklim ve sağlık alanındaki çalışmaların bugüne kadarki ilerlemesini özetlemek ve gelecekteki araştırmalara ışık tutmaktır. PRISMA-ScR (Sistematik İncelemeler ve Meta-Analizler için Tercih Edilen Raporlama Öğeleri) kontrol listesi çalışmayı yönlendirmek için kullanılmıştır. 13 Eylül 2024 tarihinde, PubMed ve Google Scholar kullanılarak 2019'dan 2024'e kadar olan dönemi kapsayan bir literatür taraması gerçekleştirilmiştir. Derlenen çalışmaların 65'i (%40,12) Avrupa'dan, 43'ü (%26,54) Asya'dan, 34'ü (%20,98) Kuzey Amerika'dandı. Derlenen çalışmalar arasında en sık kullanılan araştırma türleri derleme (%31,48) ve modelleme çalışmaları (%20,37) olmuştur. Derlenen çalışmalarda en sık kullanılan iklim değişikliği kanıt kategorisi “aşırı hava olayları ve sıcak/soğuk hava dalgaları” olmuştur. Derlenen çalışmalarda en sık elde edilen sağlık etkileri kategorisi “sıcak ve soğuğa bağlı hastalıklar” olmuştur. Bu derleme, son beş yılda iklim değişikliğinin sağlık üzerindeki etkilerine dair yapılan araştırmaları özetlemekte ve bilgi boşlukları ile araştırma önceliklerini belirlemektedir. Gelecekteki çalışmalar, iklim değişikliğinin sağlık üzerindeki etkilerini daha iyi anlamak için nicel ve nitel yöntemleri birleştirerek, sağlık risklerini ölçmeli ve etkili müdahaleler geliştirilmelidir.

1. INTRODUCTION

According to the Lancet Countdown 2024: Health and Climate Change Report, Europe faced record-breaking temperatures during the summer of 2023, with extreme heat waves affecting the southern half of the continent, causing temperatures to exceed 45°C in some regions. In Europe, temperatures are rising twice as fast as the global average, posing a threat to public health across the continent. The 2024 report emphasizes the negative impacts of climate change on human health and highlights the delays in climate action by European countries [1].

The World Health Organization (WHO) predicts that between 2030-2050, climate change will lead to approximately 250,000 additional deaths annually due to malaria, malnutrition, heat stress and diarrhea [2,3]. More than half of these additional deaths are expected to occur in Africa by 2050 [4].

At COP 24, for the first time, a special report on health and climate change was published [5]. The COP 24 Special Report on Health and Climate Change identified climate change as the greatest public health issue of the 21st century. COP 28 is a turning point for climate and health. For the first time, "Health Day" was celebrated at this COP, and the "Climate and Health Declaration" was published [6,7].

The Alliance for Action on Climate Change and Health (ATACH) initiative is another significant effort in the field of climate and health. ATACH is introduced as an initiative that takes on the responsibilities of facilitating international change on priority issues, monitoring, quality assurance, coordinating access to financing, information sharing, and technical assistance. It has legal status granted by the WHO, and its secretariat is operated by the WHO [8].

The results of climate change significantly affect human health. The three most common health effects are infectious diseases, mortality and respiratory, cardiovascular or neurological outcomes [9]. However, in studies related to climate change, the impact of climate change on health has remained in the background [10]. In 2010, the WHO, in collaboration with the United Nations Development Programme (UNDP), introduced the first global project for public health adaptation to climate change [11]. Through the Climate Promise Project, carried out by the UNDP, work has been conducted with more than 120 countries and regions to reduce greenhouse gas emissions and cope with the challenges posed by climate change. Türkiye is one of these countries. In Türkiye, the 'İklimin', 'İklimi Duy', 'İklimce Sohbetler' and 'İklime Uyum' Projects have been carried out, becoming pioneers in their fields [12-14].

Efforts are accelerating to reduce and adapt to the impacts of climate change on public health.In the U.S., the Centers for Disease Control and Prevention (CDC) developed and launched the Building Resilience Against Climate Effects (BRACE) framework to support local efforts to adapt to the impacts of climate change [15]. The CDC's work on climate and health began in 2006, the climate and health program was launched in 2009, and Türkiye's climate and health strategy efforts started in 2010. In 2015, Türkiye published the Strategy and Action Plan on the Adverse Effects of Climate Change on Human Health, which is the main outcome of the work carried out by the Republic of Türkiye Ministry of Health in collaboration with the World Health Organization [16].

In 2022, Türkiye's Health and Climate Change Profile was published on the World Health Organization's website, highlighting Türkiye's opportunities, strengths, weaknesses, and expected future threats in the face of climate change. Türkiye's 2024-2030 Climate Change Mitigation and Adaptation Strategy and Action Plans have been prepared. The impacts of climate change on public health and ways to combat them have been included in these national reports [17].

The 'Climate and Health Journal,' specifically targeting the study of climate and health research, was first published in 2021, followed by 'The Journal of Climate Change and Health,' which began publication in the same year [18,19].

The field of climate change is increasingly attracting the attention of researchers. As mentioned above in Turkiye there is a noticeable effort to hold awareness through the academic community by researchers. However, studies related to the health effects of climate change remain limited. The weak evidence base in the field of climate and health affects the development of health-centered international and national policies. The purpose of this review is by outlining the progress of studies in the field of climate and health to date to identify existing knowledge gaps regarding the relationship between climate change and health. Thus, it is aimed to provide comprehensive guidance for future research, from topic selection to methodological approaches, and to encourage an increase in studies addressing the effects of climate change on health.

2. MATERIAL AND METHOD

2.1. Protocol

We utilized the Preferred Reporting Items for Systematic Reviews and Meta-Analyses extension for Scoping Reviews (PRISMA-ScR) checklist to direct our research [20]. Our process was informed by Arksey and O'Malley's five-stage framework [21]. These stages include formulating research questions, identifying relevant studies, selecting studies, synthesizing and interpreting essential information (referred to as "charting the data"), and compiling, summarizing, and presenting the findings.

2.2. Search Criteria

A literature search was conducted using PubMed and Google Scholar on September 13, 2024, covering the period from 2019 to 2024.

The subsequent keywords and their combinations were employed for the literature search on PubMed: (climate change[Title/Abstract]) AND ((health impact[Title/Abstract]) OR (diseases related to heat[Title/Abstract]) OR (diseases related to cold[Title/Abstract]) OR (side effects of ultraviolet radiation[Title/Abstract]) OR (health problems caused by changes in air quality[Title/Abstract]) OR (diseases related to food[Title/Abstract]) OR (diseases related to water[Title/Abstract]) OR (changing infectious disease agents[Title/Abstract]) OR (vector related diseases[Title/Abstract]) OR (mental health issues[Title/Abstract]) OR ("re-emerging diseases"[Title/Abstract]) OR (new diseases[Title/Abstract]))

The same words or sequences of words were searched in Turkish in Google Scholar in Turkish. Since some words or sequences of words can have similar meanings in Turkish but with different spellings, more words were included in the search than in English. The English and Turkish keywords we searched for are shown in Table 1.

Table 1. The keywords in English and Turkish.

	English Keywords		Turkish Keywords
1.	Climate change	1.	İklim değişikliği
2.	Health impact	2.	Sağlık etkisi
3.	Diseases related to heat	3.	Sıcağa bağlı hastalıklar, sıcak ile ilişkili hastalıklar, sıcakla ilişkili hastalıklar
4.	Diseases related to cold	4.	Soğuğa bağlı hastalıklar, soğuk ile ilişkili hastalıklar, soğukla ilişkili hastalıklar
5.	Side effects of ultraviolet radiation	5.	Ultraviyole radyasyonun yan etkileri, uv radyasyonun yan etkileri
6.	Health problems caused by changes in air quality	6.	Hava kalitesindeki değişikliklerin neden olduğu sağlık sorunları, hava kalitesindeki değişikliklerin neden olduğu sağlık problemleri, hava kalitesindeki değişikliklerin neden olduğu hastalıklar, hava kalitesinin bozulmasına bağlı sağlık sorunları, hava kalitesinin bozulmasına bağlı sağlık problemleri, hava kalitesinin bozulmasına bağlı hastalıklar, hava kalitesinin bozulması ile ilişkili sağlık sorunları, hava kalitesinin bozulması ile ilişkili sağlık problemleri, hava kalitesinin bozulması ile ilişkili hastalıklar
7.	Diseases related to food	7.	Gıda ile ilgili hastalıklar, gıdayla ilgili hastalıklar, gıda ile ilişkili hastalıklar, gıdayla ilişkili hastalıklar
8.	Diseases related to water	8.	Suyla ilgili hastalıklar, su ile ilgili hastalıklar, su ile ilişkili hastalıklar, suyla ilişkili hastalıklar
9.	Changing infectious disease agents	9.	Değişen bulaşıcı hastalık etkenleri
10.	Vector related diseases	10.	Vektörlerle ilgili hastalıklar, vektörlerle ilişkili hastalıklar
11.	Mental health issues	11.	Ruhsal sorunlar, ruhsal sağlık sorunları, mental sağlık sorunları, mental sorunlar
12.	Re-emerging diseases	12.	Yeniden ortaya çıkan hastalıklar
13.	New diseases	13.	Yeni hastalıklar

The keywords and combinations listed below were utilized for the literature search on Google Scholar in Turkish: “iklim değişikliği” AND “sağlık etkisi” OR “sıcağa bağlı hastalıklar” OR “sıcak ile ilişkili hastalıklar” OR “sıcakla ilişkili hastalıklar” OR “soğuğa bağlı hastalıklar” OR “soğuk ile ilişkili hastalıklar” OR “soğukla ilişkili hastalıklar” OR “ultraviyole radyasyonun yan etkileri” OR “UV radyasyonun yan etkileri” OR “hava kalitesindeki değişikliklerin neden olduğu sağlık sorunları” OR “OR “hava kalitesindeki değişikliklerin neden olduğu sağlık problemleri” OR “hava kalitesindeki değişikliklerin neden olduğu hastalıklar” OR “hava kalitesinin bozulmasına bağlı sağlık sorunları” OR “hava kalitesinin bozulmasına bağlı sağlık problemleri” OR “hava kalitesinin bozulmasına bağlı hastalıklar” OR “hava kalitesinin bozulması ile ilişkili sağlık sorunları” OR “hava kalitesinin bozulması ile ilişkili sağlık problemleri” OR “hava kalitesinin bozulması ile ilişkili hastalıklar” OR “gıda ile ilgili hastalıklar” OR “gıdayla ilgili hastalıklar” OR “gıda ile ilişkili hastalıklar” OR “gıdayla ilişkili hastalıklar” OR “suyla ilgili hastalıklar” OR” su ile ilgili hastalıklar” OR “su ile ilişkili hastalıklar” OR “suyla ilişkili hastalıklar” OR “değişen bulaşıcı hastalık etkenleri” OR “vektörlerle ilgili hastalıklar” OR “vektörlerle ilişkili hastalıklar” OR “ruhsal sorunlar” OR “ruhsal sağlık sorunları” OR “mental sağlık sorunları” OR “mental sorunlar” OR “yeniden ortaya çıkan hastalıklar” OR “yeni hastalıklar”

2.3. Selection Criteria and Screening

Publications written in English or Turkish from the last five years (2019-2024) were included in the review. No restrictions were placed on the type of research or publication.

During the initial selection phase, the abstract of each study was reviewed and assessed. Papers that did not meet the following criteria were excluded from our review:

- Studies that do not examine the effects of climate change on human health.
- Studies not published in English or Turkish.
- Studies for which the full text is not available.

2.4. Data Extraction

The selected studies were analyzed and recorded for the following details: first author, publication date, journal name, type of research, location (country and continent),

climate signal examined, primary health effects associated with the climate signal, and any limitations of the study.

2.5. Data Analysis

In the full texts of the studies, qualitative analysis was conducted using the MaxQDA program, and the results were visualized with tables and a word cloud. The data extracted from the studies and transferred to an Excel table were analyzed using mixed methods with the MaxQDA program. Graphs were created using Excel.

3. RESULTS

The detailed results of the study selection are presented in Figure 1.

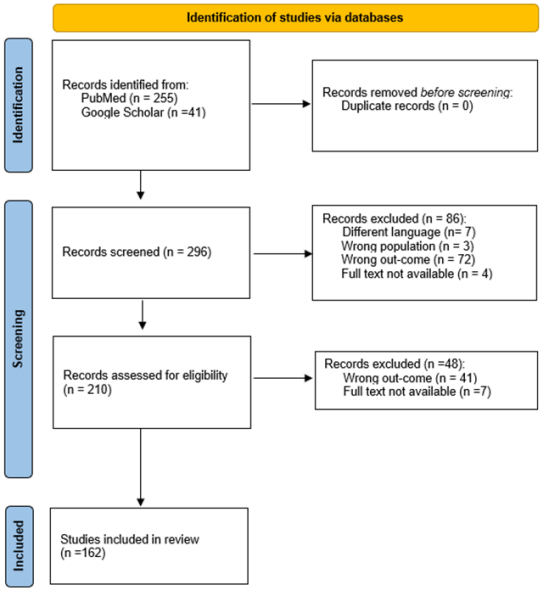

Figure 1. The selection process of the studies included in the Scoping Review-2024 according to the PRISMA-ScR flowchart [22]

A total of 296 studies were identified through a literature search, with 255 from PubMed and 41 from Google Scholar. Based on the inclusion and exclusion criteria, 7 studies were excluded due to being in a different language, 3 were excluded because they involved the wrong population, and 72 were excluded for reporting irrelevant outcomes. As a result, 210 full-text articles were assessed. A total of 189 English studies and 21 Turkish studies were evaluated according to the inclusion and exclusion criteria. Five English studies were excluded because their full text was not accessible, and 34 studies were excluded for not being related to the health impacts of climate change. Similarly, two Turkish studies were excluded due to inaccessible full texts, and 7 were excluded for not being related to the health impacts of climate change. In total, 162 studies were included in the scoping review, consisting of 150 English studies and 12 Turkish studies.

The distribution of studies included in the Scoping Review by 2024 is presented in Figure 2. The distribution of the included studies by country is shown on a world map in Figure 3. The highest number of studies was conducted in 2021, within the 2019-2024 range. Of the included studies, 65 (40.12%) were from Europe, 43 (26.54%) from Asia, 34 (20.98%) from North America, and the remaining studies were conducted by authors from Africa, Oceania, and South America.

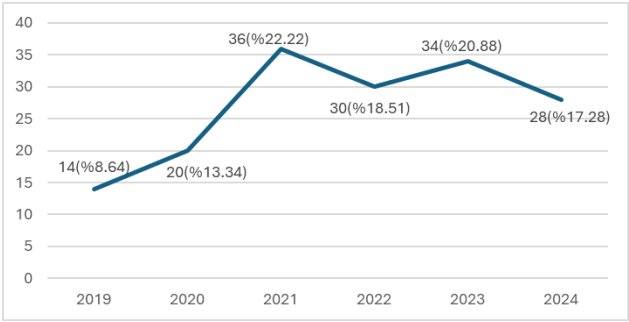

Figure 2. The distribution of the studies included in the Scoping Review-2024 by year

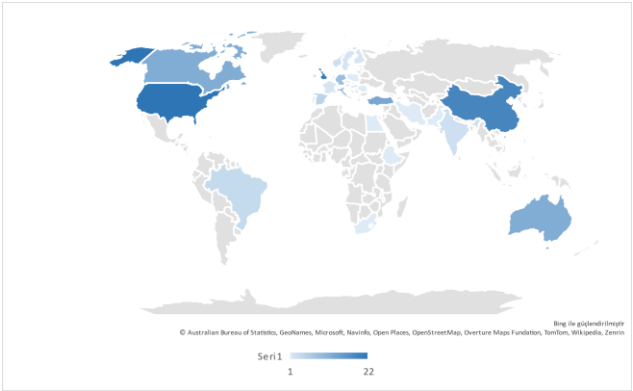

Figure 3. The distribution of the studies included in the Scoping Review-2024 by country

The most commonly used research types among the included studies were reviews (%31.48) and modelling studies (%20.37). The climate change evidences, and health impacts were categorized [23]. These categories are presented in Table 2.

Table 2. The climate change evidences, and the health impacts are categorized [23]

Climate Change Evidences	Health Impacts
Extreme weather events	Diseases related to heat and cold
Changes in water resources	Side effects of ultraviolet radiation
Heat/cold air waves	Health issues caused by air pollution
Rising sea levels	Food and waterborne diseases
Changes in air quality	Changing infectious disease agents
Increase in ultraviolet radiation	Vector-borne diseases
	Mental health issues
	Emerging and re-emerging diseases

The climate change evidences in the included studies were categorized as extreme weather events, changes in water resources, heat/cold air waves, rising sea levels, changes in air quality, increase in ultraviolet radiation and general climate change. These categories are presented in Table 3. The most frequently used climate change evidences category in the included studies were “extreme weather events and heat/cold air waves”.

Table 3. The distribution of the studies included in the Scoping Review-2024 by climate change evidences

Climate Change Evidences	Frequency	Percent (%)
Extreme weather events	66	29.86
Changes in water resources	2	0.90
Heat/cold air waves	65	29.41
Rising sea levels	9	4.07
Changes in air quality	47	21.26
Increase in ultraviolet radiation	2	0.90
General climate change	30	13.57
Total	221	100.00

The health impacts obtained from the included studies were classified as diseases related to heat/cold, side effects of ultraviolet radiation, health issues caused by air pollution, food and waterborne diseases, changing infectious disease agents, vector-borne diseases, mental health issues, emerging and re-emerging diseases. These categories are presented in Table 4. The most frequently obtained health effects category in the compiled studies was "diseases related to heat and cold".

Table 4. The distribution of the studies included in the Scoping Review-2024 by health impacts

Health Impacts	Frequency	Percent
Diseases related to heat and cold	70	24.39
Side effects of ultraviolet radiation	2	0.69
Health issues caused by air pollution	58	20.20
Food and waterborne diseases	38	13.24
Changing infectious disease agents	25	8.71
Vector-borne diseases	33	11.49
Mental health issues	51	17.77
Emerging and re-emerging diseases	10	3.48
Total	287	100.00

The word analysis conducted on the full texts of the included studies shows that the 30 most frequently used words are presented in a word cloud in **Figure 4.**

Figure 4: The 30 most frequently used words in the studies included in the Scoping Review-2024

4. DISCUSSION AND CONCLUSION

This scoping review summarizes research published between 2019 and 2024 on the health impacts of climate change and evaluates the findings in light of the current literature. Most of the 162 studies included in this review originate from Europe, North America, and Asia. This indicates a growing recognition among researchers of the link between climate change and public health. Similarly, the Lancet Countdown 2024 report emphasizes that temperatures in Europe are rising twice as fast as the global average, highlighting significant public health risks across the continent [1]. The IPCC Sixth Assessment Report also details the multidimensional health effects of climate change (IPCC, 2023) [24].

In this review, extreme weather events and heat/cold waves were the most frequently cited evidence of climate change. This finding aligns with previous studies showing that heatwaves are associated with increased cardiovascular and respiratory diseases and higher mortality rates [25]. The Lancet Countdown and WHO reports also highlight that heatwaves pose serious risks, especially for the elderly, children, and those with chronic illnesses [26]. Similarly, cold spells have been shown to increase acute health problems and mortality risk [27].

Degradation of air quality emerged as another significant category in this review. Climate change increases levels of pollutants such as ozone and particulate matter, which in turn raise the incidence of asthma, COPD, and other respiratory diseases [26]. Furthermore, Koder et al. (2023) suggest that air pollution caused by climate change could be linked to an additional 250,000 deaths per year between 2030 and 2050 [2]. These findings are in full agreement with current literature.

Vector-borne diseases and food- and water-borne infections also appeared as significant health impacts in this review. As indicated in the IPCC (2023) report, climate change alters the geographic distribution of vectors such as mosquitoes and ticks, increasing the spread of diseases like malaria, dengue, and Lyme disease [24]. In tropical and subtropical regions, rising temperature and humidity increase the prevalence of vector-borne diseases [28]. Additionally, the incidence of water- and food-borne diseases is also rising with climate change [29].

Mental health effects are a topic that has been increasingly emphasized in recent literature and also emerged as a significant category in this review. Increased stress, anxiety, and depression due to climate-related disasters, displacement, and loss of livelihoods have been frequently reported in recent studies (Koder et al., 2023) [2]. Berry et al. (2010) state that the mental health impacts of climate change can have serious consequences at the community level [30]. Therefore, it is essential to integrate mental health services into climate adaptation strategies.

The findings of this review also point to some important gaps in the literature. Notably, there is a lack of studies on the health impacts of climate change in low- and middle-income countries, despite higher exposure and more fragile health systems in these regions [24]. There is also limited research on the long-term health consequences of ecosystem changes [31].

The results support the need for health-focused climate policies, as emphasized in the WHO 2024 report [26].

Health systems should be strengthened to manage the disease burden associated with climate change, early warning systems should be expanded, and health infrastructure should be made more resilient The health sector should also play an active role in combating climate change, supporting the transition to clean energy, reducing greenhouse gas emissions, and promoting sustainable agriculture [31].

This review provides a comprehensive overview of scientific research conducted over the past five years investigating the impacts of climate change on human health, identifying knowledge gaps and potential research priorities in this field. While research on climate change is rapidly expanding, studies on the health effects of climate change remain limited, leaving significant knowledge gaps. Existing research predominantly relies on reviews and modeling studies with limited empirical evidence. The current literature primarily focuses on infectious diseases as health outcomes, including vector-borne diseases, waterborne and foodborne illnesses, zoonotic infections, and emerging infectious diseases. However, the effects of climate change on other health areas remain understudied. Specifically for Türkiye, the number of scientific studies on how climate change impacts health is significantly lower compared to the global research volume.

Future research should use quantitative and qualitative methods together to more accurately assess the impacts of climate change on various health outcomes and develop evidence-based response strategies to mitigate these consequences. Measuring the health risks associated with climate change together with climate signals, their hazards, their effects, and vulnerability analyses will enable us to better understand the geographical distribution, temporal trends and effects of these risks on different demographic groups. This will facilitate the development of targeted and effective interventions to mitigate the health effects of climate change.

REFERENCES

[1] Van Daalen, Kim R et al. The 2024 Europe report of the Lancet Countdown on health and climate change: unprecedented warming demands unprecedented action. The Lancet Public Health, Volume 9, Issue 7, e495 - e522

[2] Koder J, Dunk J, Rhodes P. Climate Distress: A Review of Current Psychological Research and Practice. Sustainability [Internet]. 16 Mayıs 2023;15(10):8115. Available from: https://www.mdpi.com/2071-1050/15/10/8115,

[3] Climate change [Internet]. [cited 2024 Oct 30]. Available from: https://www.who.int/news-room/fact-sheets/detail/climate-change-and-health

[4] Calvin K, Dasgupta D, Krinner G, Mukherji A, Thorne PW, Trisos C, vd. IPCC, 2023: Climate Change 2023: Synthesis Report. Contribution of Working Groups I, II and III to the Sixth Assessment Report of the Intergovernmental Panel on Climate Change. IPCC, Geneva, Switzerland. [Internet]. 2023 [cited 2024 october 2]. Available from: https://www.ipcc.ch/report/ar6/syr/

[5] COP24 Special Report: Health and Climate Change [Internet]. World Health Organisation; 2018. [cited 2024 october 2]. Available from: https://unfccc.int/sites/default/files/resource/WHO COP24 Special Report_final.pdf

[6] Evci Kiraz ED. Sağlık, Bir Sektör Tanımlamasına Sığmayacak Kadar "Her Şeydir".ekoİQ [Internet]. 2023;109(COP28 Kazanım mı Hezimet mi?). Erişim adresi: https://www.ekoiq.com/wp-content/uploads/2023/12/ekoiq-yayina-109_web.pdf

[7] COP28 Health Day [Internet]. Available from:https://www.who.int/news-room/events/detail/2023/12/03/default-calendar/cop28-health-day

[8] Alliance for action on climate change and health (ATACH) [Internet]. [cited 2024 october 2]. Available from: https://www.who.int/initiatives/alliance-for-transformative-action-on-climate-and-health

[9] Rocque RJ, Beaudoin C, Ndjaboue R, et al. Health effects of climate change: an overview of systematic reviews. BMJ Open 2021;11:e046333. DOI:10.1136/ bmjopen-2020-046333

[10] Tol, Richard S J. 2009. "The Economic Effects of Climate Change." Journal of Economic Perspectives 23 (2): 29–51. DOI: 10.1257/jep.23.2.29

[11] Piloting climate change adaptation to protect human health [Internet]. UNDP, WHO; 2010 [cited 2024 Oct 30]. Available from: https://info.undp.org/docs/pdc/Documents/H21/3248%20Global%20Health%20-%20WHO%20prodoc%20signature.pdf

[12] İklim değişikliğinin insan sağlığına etkileri. [Internet]. 2019. [cited 2024 october 2]. Available from: https://www.iklimin.org/egitimmateryalleri/Sa%C4%9Fl%C4%B1k_DEK.pdf

[13] İklim değişimine uyum eğitimi [Internet]. 2019. [cited 2024 october 2]. Available from: https://www.iklimiduy.org/belediye-personelleri-icin-hazirlanan-iklim-degisikligine-uyum-egitimleri-tamamlandi/screenshot-1319/

[14] İklimce sohbetler-Sağlık [Internet]. 2022. [cited 2024 october 2].Available from: https://iklimce.undp.org.tr/saglik/

[15] Climate Models and the use of climate projections [Internet]. 2022. [cited 2024 october 2]. Available from: https://www.cdc.gov/climate-health/media/pdfs/Climate_Models_and_Use_of_Climate_Projections_1.pdf

[16] İklim Değişikliğinin Sağlık Üzerine Olumsuz Etkilerinin Azaltılması Ulusal Programı ve Eylem Planı [Internet]. 2015. [cited 2024 october 2]. Available from: https://hsgm.saglik.gov.tr/depo/birimler/cevre-sagligi-db/Dokumanlar/Sunumlar/Iklim_Degisikligi_Eylem_Plani.pdf

[17] Türkiye'nin İklim Değişikliği Eylem Planı ve İklim Değişikliği Uyum Stratejisi ve Eylem Planı

[Internet]. 2015. [cited 2024 october 2]. Available from: https://iklim.gov.tr/eylem-planlari-i-19
[18] Climate and health journal [Internet]. 2021. [cited 2024 october 2]. Available from: https://climateandhealthj.org/index.php/ch
[19] The Journal of Climate Change and Health 2021. [cited 2024 october 2]. Available from: https://www.sciencedirect.com/journal/the-journal-of-climate-change-and-health
[20] Tricco AC, Lillie E, Zarin W, O'Brien KK, Colquhoun H, Levac D, et al. PRISMA Extension for Scoping Reviews (PRISMA-ScR): Checklist and Explanation. Ann Intern Med. 2018; 169(7):467-73.
[21] Arksey, H, O'Malley L. Scoping studies: Towards a methodological framework. International Journal of Social Research Methodology. 2005; 8(1):19–32.
[22] Page MJ, McKenzie JE, Bossuyt PM, Boutron I, Hoffmann TC, Mulrow CD, et al. The PRISMA 2020 statement: an updated guideline for reporting systematic reviews. BMJ. 2021; 372:n71.
[23] Kiraz E. İklim Değişikliğinin İnsan Sağlığına Etkileri. Ankara: İklim Değişikliği Eğitim Modülleri Serisi; 2019.
[24] IPCC, 2023: Climate Change 2023: Synthesis Report. Contribution of Working Groups I, II and III to the Sixth Assessment Report of the Intergovernmental Panel on Climate Change. IPCC, Geneva, Switzerland.
[25] Gasparrini A, et al. Mortality risk attributable to high and low ambient temperature: a multicountry observational study. The Lancet. 2015;386(9991):369-375.
[26] World Health Organization (WHO). Climate change and health. Fact sheet.
[27] Anderson BG, Bell ML. Weather-related mortality: how heat, cold, and heat waves affect mortality in the United States. Epidemiology. 2009;20(2):205-213.
[28] Ryan SJ, Carlson CJ, Mordecai EA, Johnson LR. Global expansion and redistribution of Aedes-borne virus transmission risk with climate change. PLoS Negl Trop Dis. 2019;13(3):e0007213.
[29] Smith KR, Woodward A, Campbell-Lendrum D, et al. Human health: impacts, adaptation, and co-benefits. In: Climate Change 2014: Impacts, Adaptation, and Vulnerability. Part A: Global and Sectoral Aspects. Contribution of Working Group II to the Fifth Assessment Report of the Intergovernmental Panel on Climate Change. Cambridge University Press; 2014.
[30] Berry HL, Bowen K, Kjellstrom T. Climate change and mental health: a causal pathways framework. Int J Public Health. 2010;55(2):123-132.
[31] Watts N, et al. The 2021 report of the Lancet Countdown on health and climate change: code red for a healthy future. The Lancet. 2021;398(10311):1619-1662.

Volume 14, Issue 3, Page 233-241, 2025 https://doi.org/10.46810/tdfd.1694044 Review

BİNGÖL UNIVERSITY

Türk Doğa ve Fen Dergisi
Turkish Journal of Nature and Science
www.dergipark.gov.tr/tdfd

Melatonin: The Multifaceted Hormone

Beyzanur ŞİMŞEK[1], Esra AYDEMİR[1], Bülent KAYA[1*]

[1] Department of Biology, Faculty of Science, Akdeniz University, Antalya TR-07058, Turkey
Beyzanur ŞİMŞEK ORCID No: 0000-0003-3086-6836
Esra AYDEMİR ORCID No: 0000-0002-5206-7333
Bülent KAYA ORCID No : 0000-0002-0491-9781

**Corresponding author: bkaya@akdeniz.edu.tr*

(Received: 07.05.2025, Accepted: 05.09.2025, Online Publication: 26.09.2025)

Keywords
Cancer, Circadian rhythm, Hormone, Melatonin,

Abstract: Melatonin is a hormone secreted by the pineal gland and its main biological function is to regulate the circadian rhythm. Melatonin synthesis varies according to light and dark conditions. While melatonin production is suppressed in the light environment, melatonin production increases in the dark environment. Melatonin acts through different mechanisms. One of these mechanisms is receptor-dependent signal transduction mechanism. Two types of receptors have been identified as melatonin receptor, melatonin receptor 1 and melatonin receptor 2. Through these mechanisms of action, in addition to circadian rhythm regulation, melatonin has various physiological and pathophysiological roles, including sleep cycle regulation, antioxidant and anti-inflammatory effects, immune system modulation, effects on cancer, cardiovascular system, central nervous system and neurodegenerative diseases. In this review, it is aimed to examine the roles of melatonin in physiological and pathophysiological processes.

Melatonin: Çok Yönlü Bir Hormon

Anahtar Kelimeler
Kanser, Sirkadiyen ritim, Hormon, Melatonin,

Öz: Melatonin, epifiz bezi tarafından salgılanan bir hormondur ve temel biyolojik işlevi sirkadiyen ritmi düzenlemektir. Melatonin sentezi, aydınlık ve karanlık ortam koşullarına göre değişmektedir. Aydınlık ortamda, melatonin üretimi baskılanırken, karanlık ortamda melatonin üretimi artmaktadır. Melatonin farklı mekanizmalar aracılığıyla etki göstermektedir. Bu mekanizmalardan biri reseptöre bağımlı sinyal iletim mekanizmasıdır. Melatonin reseptörü olarak melatonin reseptörü 1 ve melatonin reseptörü 2 olmak üzere iki tip reseptör tanımlanmıştır. Bu etki mekanizmaları aracılığıyla sirkadiyen ritim düzenlenmesinin yanı sıra uyku döngüsünün düzenlenmesi, antioksidan ve anti-inflamatuar etkileri, immün sistem modülasyonu, kanser, kardiyovasküler sistem, santral sinir sistemi ve nörodejeneratif hastalıklar üzerine etkileri olmak üzere çeşitli fizyolojik ve patofizyolojik rolleri bulunmaktadır. Bu derlemede genel olarak melatoninin fizyolojik ve patofizyolojik süreçlerdeki rollerinin incelenmesi amaçlanmaktadır.

1. INTRODUCTION

Melatonin was first isolated from the bovine pineal gland by Aaron B. Lerner in 1958 [1]. The chemical structure of melatonin with the molecular formula $C_{13}H_{16}N_2O_2$ is shown in Figure 1. This indoleamine, also known as N-acetyl-5-methoxytryptamine, is primarily synthesised by the pineal gland in the human body, although other organs such as the bone marrow, retina, skin and gastrointestinal system also secrete melatonin. Notably, melatonin secreted by the pineal gland represents the most systemically significant source, while production by other structures is considered less impactful at the systemic level [3]. Melatonin is widely distributed in nature, and its mechanism representing one of the phylogenetically oldest biological signaling systems. This molecule has been found in all major taxa of organisms, including bacteria, unicellular eukaryotes and macroalgae. Additionally, it is found in various parts of plants such as roots, stems, flowers, and seeds and in both invertebrate and vertebrate species. This wide distribution suggests that melatonin has been conserved throughout evolution [4,5]. The synthesis and secretion of melatonin are regulated by light and darkness. While light suppresses melatonin production, darkness enhances it. Thus, melatonin is known as the 'hormone of darkness' [6]. Although important insights into the role of melatonin in human physiology and pathophysiology have been gained

in recent years, many of the functions and effects of this hormone are still not fully understood. Melatonin is recognised not only as a hormone but also as a cellular protector. It has demonstrated significant effects on biological processes such as oxidative stress, immune modulation, sleep, and circadian rhythm regulation. Moreover, melatonin plays a critical role in the treatment of various conditions, including depression, insomnia, epilepsy, Alzheimer's disease, diabetes, obesity, alopecia, migraine, cancer, immune disorders, and cardiovascular diseases (Figure 3) [3,6]. In this review, the physiological and pathophysiological roles of melatonin are explored.

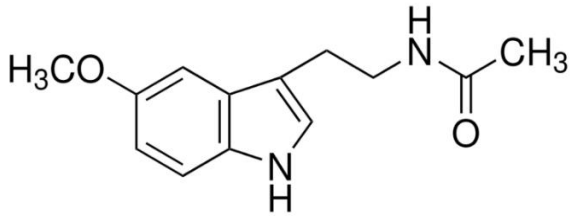

Figure 1. Chemical Structure Of Melatonin (N-acetyl-5-methoxytryptamine) [2]

2. MELATONIN METABOLISM

2.1. Biosynthesis

Melatonin biosynthesis in humans begins with tryptophan, an essential amino acid that serves as a precursor in this process. Tryptophan is absorbed from the plasma by the pineal gland and subsequently hydroxylated by the enzyme tryptophan hydroxylase within the pinealocytes. This reaction produces the first intermediate metabolite, 5-hydroxytryptophan, which then undergoes decarboxylation by the enzyme decarboxylase to form 5-hydroxytryptamine, commonly known as serotonin. Serotonin is acetylated by the enzyme NAT (N-acetyl transferase) and converted to N-acetylserotonin. Finally, acetylserotonin O-methyltransferase (ASMT), also known as hydroxy-indole O-methyltransferase (HIOMT), converts N-acetylserotonin to melatonin (Figure 2) [7,8].

Melatonin synthesis is a complex process regulated by light and dark cycles, and serum concentrations vary according to these cycles. This production in the pineal gland aligns with the 24-hour light/dark rhythm governed by the suprachiasmatic nucleus (SCN), where synthesis and release are elevated at night while inhibited by light during the day. Neural impulses to the pinealocytes via postganglionic sympathetic neurons play a critical role in regulating the melatonin rhythm.During the night, increased electrical activity in the SCN triggers melatonin production. The pineal gland functions as a neuroendocrine transformer, converting these electrical signals into hormonal secretions that elevate melatonin levels during darkness [9]. The enzyme N-acetyltransferase (NAT), a key regulator of melatonin synthesis, exhibits low activity during daylight hours but increases significantly in the dark, underscoring the dependency of this process on the light-dark cycle.At night, norepinephrine binds to α and β adrenergic receptors and causes an increase in intracellular calcium (Ca^{2+}). This increase potentiates the activation of enzymes such as protein kinase C (PKC) and calcium-calmodulin kinase (CaM kinase), which in turn increases cAMP levels and the phosphorylation of rate-limiting enzymes (AANAT and ASMT) in melatonin synthesis [10].

In summary, melatonin synthesis begins with the hydroxylation and decarboxylation of serotonin, a process regulated by cAMP-dependent transcription factors and photoperiodic conditions. Light inhibits melatonin synthesis by transmitting signals from the retina to the SCN and other structures in the hypothalamus. In darkness, norepinephrine released from postganglionic sympathetic fibres binds to β1 receptors and releases serotonin and NAT into the cell. This biochemical signalling cascade accelerates melatonin production and ensures its regular synthesis and release in accordance with the day-night rhythm [10,11].

2.2. Secretion

The amphiphilic structure and small molecular size of melatonin enable it to easily permeate cell membranes, allowing it to reach various biological fluids and tissues, including saliva, urine, cerebrospinal fluid (CSF), preovulatory follicles, sperm, amniotic fluid, and milk. These characteristics imply that melatonin is not stored in pinealocytes but is instead released immediately upon synthesis. The dense vascular network of the pineal gland and its dorsal and posterior attachment to the wall of the third ventricle allow melatonin to be released into the central nervous system, particularly the CSF and bloodstream, during the night [3,8]. The half-life of melatonin in the body ranges between 20 and 40 minutes, and after secretion, it rapidly disperses into the blood and CSF. Approximately 60-70% of melatonin in the bloodstream is bound to albumin. However, the distribution of melatonin in the body is not homogenous; the concentration of melatonin in the CSF is higher than in the blood. Blood melatonin levels typically range from a few pg/mL during the day to 50-100 pg/mL during the night, reflecting overall systemic concentrations. Age significantly influences melatonin levels. In the first three months of life, these levels are relatively low but begin to rise between three and six months, leading to the development of a day-night rhythm. Nocturnal melatonin concentrations are approximately 250 pg/mL in children aged 1-5 years, decrease to 65 pg/mL between 5-15 years, and further decline to 20 pg/mL in individuals aged 50-70 years. In adults, average plasma melatonin levels range between 50-70 pg/mL during the night [12,13].

2.3. Catabolism

The liver is the primary organ responsible for clearing more than 90% of circulating melatonin and is the central site of melatonin metabolism [14]. Melatonin is primarily metabolised to 6-hydroxymelatonin in the liver by cytochrome P450 isoforms, particularly CYP1A2, CYP1A1 and CYP1B1 enzymes. Subsequently, this metabolite undergoes conjugation and is excreted in urine as the major metabolite, 6-sulfatoxymelatonin (aMT6S).

Urinary aMT6S levels closely reflect plasma melatonin concentrations. Melatonin in the CSF is metabolised by neurons and glial cells via cleavage of the pyrrole ring, resulting in the formation of N-acetyl-N-formyl-5-methoxyquinuramine (AFMK). AFMK is the primary metabolite formed through oxidation of melatonin, which is subsequently converted to N-acetyl-5-methoxyquinuramine (AMK). Both AFMK and AMK exhibit potent free radical scavenging properties. Notably, AMK interacts with reactive oxygen and nitrogen species, generating a range of metabolites [15,16].

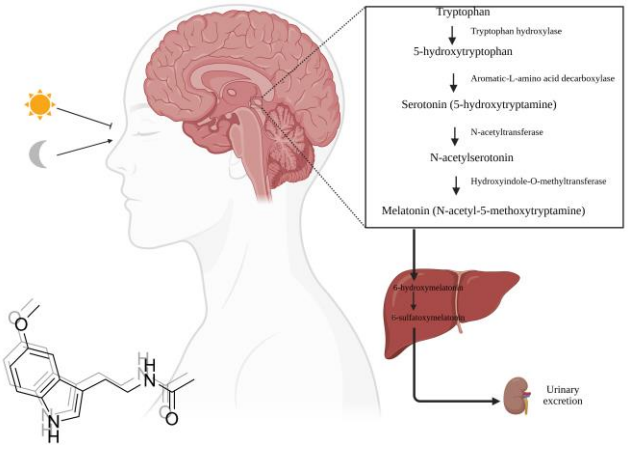

Figure 2. Synthesis of Melatonin (Created in BioRender license: https://BioRender.com/gde2tmi)

3. PHYSIOLOGICAL AND PATHOPHYSIOLOGICAL ROLES OF MELATONIN

3.1. Antioxidant and Anti-inflammatory Actions

Oxidative stress is defined as the disruption of cellular homeostasis as a result of the increase in reactive oxygen species (ROS) generated during cellular metabolism and the inadequacy of antioxidant defence mechanisms. This condition arises due to an excessive accumulation of free radicals and a deficiency of both enzymatic and non-enzymatic antioxidants. As a consequence, oxidative stress exerts harmful effects on key biomolecules, including lipids, proteins, and DNA. Reactive oxygen species (ROS) and reactive nitrogen species (RNS) accumulate in cells as a result of exposure to various stressors such as inflammation, infection, ultraviolet (UV) and ionising radiation. While low levels of ROS play a crucial role in physiological processes such as cell proliferation, apoptosis, and immune response, excessive ROS production induces significant cellular damage, leading to DNA mutations and severe pathological conditions, including cancer [3,17]. Moreover, the disruption of metal homeostasis contributes to DNA damage, lipid peroxidation, and protein modification. Research has reported that metals such as iron, copper, chromium, and cobalt contribute to free radical formation. Among these, cobalt is a potent inducer of oxidative stress, primarily through the generation of free radicals. Studies have shown that metals cause oxidative damage and melatonin has been shown to reduce this damage [18,19]. The body tries to prevent the effects of oxidative stress through the action of endogenous and exogenous antioxidants. Oxidative stress has been implicated in numerous chronic diseases, including cardiovascular disease, diabetes, rheumatoid arthritis, cancer, and neurodegenerative disorders. This condition highlight the significance of maintaining a balance between oxidants and antioxidants in the prevention and treatment of such diseases. To sustain this balance, antioxidant-rich diets, dietary supplements, and phytotherapeutic approaches have been highlighted as essential strategies [20].

Melatonin is a widely distributed compound in nature that plays a crucial role in various biological processes. While its fundamental physiological function is hormonal properties, one of its most notable properties is its potent antioxidant activity. The antioxidant property of melatonin is based on the pyrrole ring in its structure. Moreover, due to its solubility in both aqueous and lipid phases, melatonin effectively protects cellular components, including the cell membrane, organelles, and nucleus, from oxidative damage [3,21]. Melatonin neutralises free radicals by providing electrons directly to oxidant substances and also shows an indirect effect by activating endogenous antioxidant systems. The ability to neutralise harmful reactive oxygen species, such as superoxide, hydroxyl radical, hydrogen peroxide and peroxynitrite is shown as an example of the direct effect of melatonin. In addition, melatonin mitigates oxidative stress indirectly by upregulating the expression of antioxidant enzymes, including superoxide dismutase, catalase, glutathione peroxidase, and glutathione reductase. In conditions of high oxidative stress, melatonin produces antioxidant metabolites, such as 6-hydroxymelatonin, 2-hydroxymelatonin, 4-hydroxymelatonin, N-acetyl-N-formyl-5-methoxykynuramine (AFMK), N-acetyl-5-methoxykynuramine (AMK), and cyclic 3-hydroxymelatonin, which are reported to exert a protective role against free radicals [3,22]. One of the distinctive properties of melatonin is that it does not convert into prooxidant compounds after exerting its effects, and its intermediates also exhibit antioxidant activity. Due to this characteristic, melatonin is regarded as a ‘terminal antioxidant,’ in contrast to other antioxidants [22].

3.2. Effects on Sleep and Regulation of Circadian Rhythm

Circadian rhythms are approximately 24-hour cycles that regulate various biological processes, including sleep-wake cycles, hormone secretion, cognitive function, and emotional states. These biological rhythms can range from short-term cycles to long-term cycles lasting years. Circadian rhythms play a crucial role in regulating physiological processes such as body temperature, hormone secretion and sleep patterns. Disruptions of these rhythms can lead to varying degrees of health problems. Moreover, external factors such as light exposure, physical activity, dietary habits, and pharmacological interventions can either enhance or disrupt circadian rhythm function [23,24]. The suprachiasmatic nucleus (SCN), located in the hypothalamus, is the central pacemaker that regulates these rhythms. In mammals, the SCN regulates optimal physiological and behavioural

rhythms by synchronising internal biological clocks with external environmental signals, particularly cycles of light and darkness. Through its connections with other hypothalamic nuclei, the SCN ensures that endogenous biological processes are aligned with environmental changes. This synchronisation is crucial for survival of organisms and the maintenance of healthy daily activities [23,25].

Melatonin serves as an endogenous synchroniser that balances and strengthens the bodily rhythms and is therefore called a 'chronobiotic', i.e. a molecule that regulates the timing of the biological clock. It is the primary marker that regulates the circadian rhythm by responding to light-dark cycles. Moreover, this hormone plays a crucial role in maintaining homeostatic balance through the epigenetic regulation of clock genes in cells. Additionally, melatonin contributes to the reduction of body temperature during the night, thereby facilitating the transition to sleep [4,9,25]. Melatonin production follows a distinct cycle as part of the circadian rhythm. Light exposure reaches the suprachiasmatic nucleus (SCN) through signals from the retina and inhibits melatonin synthesis in the pineal gland. Melatonin secretion peaks during the night, typically reaching its highest levels between 02:00 and 04:00. In summary, melatonin and the circadian rhythm contribute to the regulation of various physiological functions depending on the body's internal clock [24]. The sleep-wake cycle is one of the most prominent circadian rhythms and is tightly regulated by neurochemical processes. Sleep fulfils many critical functions of the brain, such as energy regeneration, switching off external stimuli and processing learning and memory. These processes are crucial for brain development as well as mental and physical health. Melatonin is a hormone long known for its role in regulating sleep, with its sleep-promoting effects typically associated with its secretion 1-2 hours before sleep time. The ability of melatonin to facilitate the transition to sleep and regulate the sleep cycle has led to its investigation in the treatment of insomnia and sleep disorders. Especially in individuals with chronic insomnia, other psychiatric disorders such as depression and anxiety are also common. This condition is more prevalent in older individuals due to the age-related decline in melatonin production. This decrease in melatonin levels is thought to be one of the main causes of insomnia. This hormone regulates the sleep cycle by working in harmony with circadian phase markers and synchronising with other biological functions, thus playing a crucial role in the treatment of sleep disorders [25,26].

3.3. The Role of Melatonin in Cancer

Cancer is the second leading cause of death globally, following cardiovascular disease [27]. It is a genetic disorder resulting from defects in cellular DNA, leading to the abnormal expression of genetic information. Cancer typically develops due to the activation of genes that regulate critical cellular functions such as growth, survival, and invasion/motility, alongside the repression of genes that limit these functions. However, these characteristics alone are insufficient for cancer formation. The hallmarks of cancer such as sustaining proliferative signaling, evading growth suppressors, ability to evade programmed cell death, enabling replicative immortality, inducing angiogenesis, activating invasion and metastasis, genome instability and mutation, tumor-promoting inflammation, reprogramming energy metabolism and evading immune destruction are also integral to this process. The fundamental mechanism underlying cancer is typically linked to the accumulation of mutations. However, epigenetic changes, particularly DNA methylation, are increasingly playing a central role in cancer development [28,29].

Studies conducted by Bergmann and Engel between 1935 and 1952 demonstrated that pineal gland extracts slowed growth in experimental animals, suggesting a potential inhibitory effect on cancer progression. Additionally, some epidemiological studies have reported an increased risk of breast cancer among occupational groups engaged in night shift work, particularly female healthcare professionals, pilots, and flight attendants. Experimental studies in mice have reported that circadian disruption promotes tumour growth [22,30]. Melatonin has been identified as an effective and safe agent against various types of cancer, with this indoleamine targeting multiple mediators that regulate cancer metabolism at both transcriptional and post-transcriptional levels. Epidemiological studies have demonstrated that melatonin exhibits significant oncostatic (tumour growth-inhibiting) effects across various types of cancer. Furthermore, both *in vitro* and *in vivo* experiments have indicated that melatonin can suppress tumour growth. Findings suggest that reduced melatonin levels may accelerate tumour progression, whereas lung and colorectal cancer patients receiving melatonin treatment demonstrate improved quality of life and higher remission rates [31,32].

Processes such as tumour development, growth, invasion, and metastasis can be regulated by the actions of melatonin. Early studies have reported that melatonin reduces the likelihood of healthy cells undergoing malignant transformation by suppressing growth factors, including insulin-like growth factor-1 (IGF-1), epidermal growth factor receptor (EGFR), hepatocyte growth factor (HGF), transforming growth factor (TGF), and platelet-derived growth factor (PDGF). As the tumour progresses, the proliferative and invasion potential of cancer cells increases rapidly. During this process, melatonin not only inhibits cancer cell proliferation but also prevents invasion and metastasis by suppressing factors such as matrix metalloproteinase 9 (MMP-9) and fibroblast growth factor 19 (FGF19) [33,34,35]. Melatonin is known to have antiproliferative effects on many types of cancer through melatonin receptors (MT1 and MT2). These effects are mediated by different molecular mechanisms involving the activation of membrane-specific G protein-coupled receptors. The melatonin receptors are called MT1 and MT2, with MT1 exhibiting high affinity and MT2 low affinity. These receptors have different pharmacological properties and chromosomal arrangements and bind to α, β, and γ subunits of G proteins in intracellular signaling pathways. Stimulation

of MT1 receptors inhibits the adenylate cyclase pathway, whereas MT2 receptor activation induces phospho-inositides hydrolysis. MT1 receptors are widely distributed in the anterior pituitary, hypothalamus, and various brain regions, while MT2 receptors are primarily concentrated in the retina, hippocampus, and cerebellum. Additionally, melatonin receptors are also found in tissues, including the ovaries, blood vessels, immune cells, kidneys, and pancreas [32,35]. In addition to directly interacting with cancer cells via these receptors, melatonin regulates T helper cells by activating natural killer (NK) cells and stimulating the release of cytokines such as IL-2 and IFN-γ [35].

Epithelial-mesenchymal transition (EMT) is a process that plays a crucial role in the initiation of cancer metastasis. During this process, epithelial cells lose their polarity and intercellular adhesion properties, acquiring mesenchymal stem cell characteristics, which enhance their motility and invasiveness and enable their differentiation into various cell types. Research has demonstrated that melatonin suppresses the migration and invasion of prostate cancer cells by inhibiting EMT. Angiogenesis is a critical process in tumour growth and metastasis. Vascular endothelial growth factor (VEGF) is a potent pro-angiogenic factor that induces endothelial cell proliferation and increases vascular permeability. Several data suggest that anti-VEGF therapy inhibits tumour progression and extends progression-free survival in patients. Additionally, melatonin has been reported tohave an important regulatory effects on angiogenesis. Interestingly, melatonin may have different effects on neovascularisation depending on pathological and physiological conditions; while it supports angiogenesis in some physiological conditions, it may suppress this process in tumours and in hypoxic environments [33,36]. While melatonin functions as a potent apoptotic agent, particularly in cancer cells, it supports anti-apoptotic processes in normal cells. Melatonin can activate both intrinsic and extrinsic apoptotic pathways. Within the intrinsic pathway, it stimulates caspase-3, caspase-8, and caspase-9, increases cytochrome c levels in the cytosol, suppresses the anti-apoptotic Bcl-2 protein, and upregulates the pro-apoptotic Bid protein. In the extrinsic apoptotic pathway, melatonin accelerates cell death by enhancing Fas and Fas ligand (FasL) expression. These mechanisms demonstrate that melatonin effectively promotes programmed cell death in cancer cells. Furthermore, melatonin can induce genetic modifications through various mechanisms, including epigenetic alterations, oncogene suppression, and the regulation of long non-coding RNAs (LncRNAs) and microRNAs (miRNAs). These processes allow melatonin to inhibit cancer cell proliferation, migration, and invasion, while also enhancing the sensitivity of these cells to radiotherapy and chemotherapy. Additionally, several studies indicate that melatonin exhibits oncostatic properties against cancers in various tissues, including the breast, prostate, ovary, liver, kidney, lung, pancreas, colorectal, skin, and gastrointestinal tract [31,37,38].

3.4. Effects on Neurodegenerative Diseases

Neurodegeneration is associated with progressive central nervous system disorders, which are defined clinically, morphologically, and biochemically. The human brain, with its high levels of polyunsaturated fatty acids (PUFAs), increased oxygen demands, elevated ascorbate and iron accumulation in certain regions, and limited antioxidant defense capacity, is vulnerable to damage caused by reactive oxygen species (ROS). Excessive elevation of ROS levels leads to mitochondrial imbalance in brain cells during aging and neurodegenerative processes, resulting in the dysfunction of the electron transport chain [39]. These diseases cause a slowly progressive loss of neurons in the central or peripheral nervous system, leading to impairments in movement or cognitive function. They include Alzheimer's, Parkinson's, Huntington's disease, and amyotrophic lateral sclerosis (ALS), but may also be associated with neurodevelopmental disorders and psychiatric conditions such as schizophrenia. These diseases can lead to progressive loss of brain function, causing severe disability and death in older people. Moreover, neurodegenerative diseases share similar clinical features and molecular mechanisms, such as cognitive deficits, motor disorders, and sleep disturbances [40,41].

Circadian rhythm disturbances and alterations in sleep-wake cycles are frequently observed in neurodevelopmental disorders. This highlights the need to investigate melatonin metabolism in these conditions, given its crucial role in regulating circadian rhythms, synchronisation of sleep-wake cycles and supporting neural development. Melatonin production significantly decreases with age and in neurodegenerative diseases such as Alzheimer's and Parkinson's, suggesting that melatonin deficiency may contribute to the onset or progression of these diseases. In patients with Alzheimer's disease, low levels of melatonin have been detected in both blood and cerebrospinal fluid, even in the early stages of the disease [40,42,43]. The protective effects of melatonin on neurological diseases include mechanisms such as reducing oxidative stress, regulating inflammatory responses, preventing cellular apoptosis and supporting the neurogenesis process. Melatonin can positively affect the differentiation and migration processes of neural stem cells by promoting the survival, proliferation and maturation of neural stem cells without causing toxic side effects [44]. In addition, melatonin supplementation has been shown to be beneficial in improving cognitive and motor function in neurodegenerative diseases, as well as alleviating sleep disorders. The age-related decline in melatonin synthesis may contribute to the acceleration of neurodegenerative processes. Studies have reported that melatonin reduces the DNA damage response (DDR) in neuronal cells of humans, and female mice with accelerated aging. In conclusion, melatonin deficiency is a significant factor that contributes to increased oxidative damage and the development of age-related neurodegenerative diseases [39,40,45].

3.5. Effects on Cardiovascular System

Cardiovascular disease (CVD) is one of the leading causes of death worldwide, particularly affecting the elderly population. According to the World Health Organization (WHO), 17.9 million people died from CVDs in 2019. These diseases, which encompass conditions such as coronary heart disease, myocardial infarction, heart failure, cardiomyopathy, arrhythmias, congenital heart disease, peripheral vascular disease, and hypertensive heart disease, continue to represent a significant public health problem. Modifiable risk factors, including physical inactivity, obesity, smoking, and poor dietary habits, play a crucial role in the development of CVD [46,47].

Melatonin is recognized for its potential protective effects against cardiovascular disease. It exerts its protective actions through both receptor-mediated and receptor-independent mechanisms. Melatonin receptors are distributed across both central and peripheral tissues, and the distribution and types of these receptors determine the physiological effects of melatonin. The MT1 and MT2 receptors within the cardiovascular system underscore melatonin's cardioprotective properties. Activation of MT1 receptors induces a vasoconstrictive effect by regulating vascular tone, and provides protection against oxidative damage by increasing the production of antioxidant enzymes. This mechanism safeguards endothelial cells from damage caused by reactive oxygen species and helps prevent vascular disease. MT2 receptors, on the other hand, cause vasodilation by stimulating the production of nitric oxide. This property regulates blood flow and plays a key role in reducing blood pressure. Additionally, melatonin’s antioxidant properties support vascular health by preventing damage caused by oxidative stress. Melatonin significantly supports cardiovascular health through mechanisms such as vasodilation, antioxidant and anti-inflammatory effects, blood pressure regulation and modulation of lipid metabolism. These multifaceted effects position melatonin as a promising therapeutic agent for the treatment of cardiovascular disease [48,49,50].

4. LIMITATIONS AND FUTURE PERSPECTIVES

Melatonin, as a versatile hormone with minimal toxicity, can be effective in many physiological and pathophysiological processes. However, its application as an anticancer agent is constrained by several challenges, including low bioavailability, inconsistent measurement methods, and uncertain dosage regimens and routes of administration. The pharmacokinetics of exogenous melatonin are not fully understood; interindividual differences in absorption, metabolism, and elimination lead to high variability in bioavailability. Indeed, Fourtillan et al. reported bioavailability to be between 1% and 37% [51], while DeMuro et al. reported it to be 15% [52]. Although oral administration is the most common route, bioavailability is low and highly variable. In a systematic review, Zetner et al. evaluated the effects of various routes of administration, including intranasal, transdermal, oral transmucosal, and subcutaneous [53]. According to their findings, intranasal administration results in higher bioavailability than oral melatonin. Melatonin's low solubility, poor chemical stability, and short half-life exacerbate this problem. Therefore, developing biocompatible carrier systems that increase solubility and bioavailability is important. In particular, nanoparticle-based systems are attracting attention due to their potential to increase therapeutic efficacy, reduce side effects, and improve quality of life. For instance, delivering melatonin with doxorubicin (DOX) via magnetic Fe_3O_4 nanoparticles has increased apoptosis in osteosarcoma cells and demonstrated synergistic antitumor effects in nanoformulations [33,54]. Findings regarding melatonin levels in epidemiological studies are often inconsistent. This may be due to differences in sample types (e.g., urine, plasma, or serum), variable collection times, and diverse assessment methods. Circadian rhythm-dependent variation in melatonin levels also contributes to this situation. Therefore, future studies should standardize the sample type and collection time and adopt the most reliable assessment approach by comparing existing methods. These changes would reduce inconsistencies in the literature and yield more accurate results regarding the therapeutic level of melatonin [38,55]. Current findings indicate that melatonin can be used as both an adjuvant and a protective agent in cancer treatment. When used as an adjuvant, it can enhance the therapeutic effects of chemotherapy and radiotherapy while also mitigating the adverse side effects caused by these treatments. Furthermore, clinical studies have reported that melatonin improves the efficacy of anticancer drugs, enhances sleep patterns, and contributes to an improved quality of life. However, inconsistencies arising from different doses and application durations necessitate the development of a standard treatment protocol [3,38]. The safety profile of new treatments in oncology is of great importance. Melatonin has not exhibited significant toxicity, even at high doses, and has not been linked to serious adverse effects in clinical studies. In fact, it has been reported to reduce some adverse effects caused by radiotherapy and chemotherapy. Melatonin has also been found to be safe when taken in doses ranging from 10-50 mg per day, which is above the recommended dose of 0.5-5 mg per day [56]. Furthermore, it has been reported that melatonin may increase survival rates, accelerate response rates to antitumor treatments, and alleviate both treatment-related toxicities and malignancy-related symptoms [57]. To enhance melatonin's anticancer potential, it is suggested that more stable and effective analogues be developed through chemical modifications [58]. In particular, it is thought that derivatives exhibiting multi-target effects could provide potent antitumor results by simultaneously interfering with different pathways in tumors. However, for melatonin to be used as a clinical agent, a better understanding of its molecular mechanisms and comprehensive clinical studies are required. Current findings support the idea that melatonin, either alone or in combination with other anticancer agents, could be a promising therapeutic option.

Figure 3. Biological Effects of Melatonin

5. CONCLUSIONS

Melatonin is widely distributed in nature and is present in a diverse range of organisms, from unicellular organisms to humans. This molecule plays a critical role in fundamental physiological functions, including circadian rhythm regulation, sleep cycle management, and antioxidant and anti-inflammatory properties. Moreover, it exerts significant effects in pathological conditions such as neurodegenerative diseases, cancer, and cardiovascular diseases. Melatonin triggers receptor-dependent signal transduction mechanisms by binding to membrane receptors while also demonstrating receptor-independent effects. Due to these multifaceted mechanisms of action, melatonin is gaining attention as a potential agent both in maintaining physiological homeostasis and in the treatment of various diseases. Further research is needed to elucidate its therapeutic potential by providing a more in-depth understanding of its role in these diverse processes.

REFERENCES

[1] Claustrat B, Leston J. Melatonin: physiological effects in humans. Neurochirurgie. 2015;61(2-3):77-84.

[2] Merck KgaA [Internet]. Melatonin [cited 2025 May 02]. Available from: https://www.sigmaaldrich.com/TR/en/substance/melatonin2322873314

[3] Talib WH, Alsayed AR, Abuawad A, Daoud S, Mahmod AI. Melatonin in cancer treatment: current knowledge and future opportunities. Molecules. 2021;26(9):2506.

[4] Pandi-Perumal SR, Srinivasan V, Maestroni GJM, Cardinali DP, Poeggeler B, Hardeland R. Melatonin: nature's most versatile biological signal?. The Febs Journal. 2006;273(13):2813-2838.

[5] Cipolla-Neto J, Amaral FGD. Melatonin as a hormone: new physiological and clinical insights. Endocrine Reviews. 2018;39(6):990-1028.

[6] Singh M, Jadhav HR. Melatonin: functions and ligands. Drug Discovery Today. 2014;19(9):1410-1418.

[7] Günhan R.S. Melatonin ve önemi. Biological Diversity And Conservation. 2021;14(2):342-350.

[8] Amaral FGD, Cipolla-Neto J. A Brief review about melatonin, a pineal hormone. Archives Of Endocrinology And Metabolism. 2018;62:472-479.

[9] Salt A, Çenesiz M, Çenesiz S. Melatonin, etkileri ve kullanım alanları. Etlik Veteriner Mikrobiyoloji Dergisi. 2017;28(1):7-12.

[10] Albreiki M. Characteristic, synthesis, and non-photic regulation of endogenous melatonin. In Melatonin-Recent Updates. 2022;Intechopen.

[11] Şener G. Karanlığın hormonu: melatonin. Marmara Pharmaceutical Journal. 2010;14(3):112-120.

[12] Ferlazzo N, Andolina G, Cannata A, Costanzo MG, Rizzo V, Currò M, et al. Is melatonin the cornucopia of the 21st century?. Antioxidants. 2020;9(11):1088.

[13] Atasoy ÖB, Erbaş O. Melatonin hormonunun fizyolojik etkileri. İstanbul Bilim Üniversitesi Florence Nightingale Tıp Dergisi. 2017;3(1):52-62.

[14] Claustrat B, Brun J, Chazot G. The basic physiology and pathophysiology of melatonin. Sleep Medicine Reviews. 2005;9(1):11-24.

[15] Hassell KJ, Reiter RJ, Robertson NJ. Melatonin and ıts role in neurodevelopment during the perinatal period: a review. Fetal And Maternal Medicine Review. 2013;24(2):76-107.

[16] Talib WH. Melatonin and cancer hallmarks. Molecules. 2018;23(3):518.

[17] Morvaridzadeh M, Sadeghi E, Agah S, Nachvak SM, Fazelian S, Moradi F, et al. Effect of melatonin supplementation on oxidative stress parameters: a systematic review and meta-analysis. Pharmacological Research. 2020;161:105210.

[18] Jomova K, Valko M. Advances ın metal-induced oxidative stress and human disease. Toxicology. 2011;283(2-3):65-87.

[19] Ertuğrul H, Yalçın B, Güneş M, Kaya B. Ameliorative effects of melatonin against nano and ıonic cobalt ınduced genotoxicity ın two *in vivo* drosophila assays. Drug And Chemical Toxicology. 2020;43(3):279-286.

[20] Aydın S. Melatonın as an antıoxıdant and ıts protectıve effects on neurodegeneratıve dıseases. Health And Lıfe Wıth Dıfferent Aspects. Ankara; 2023. p. 89-124.

[21] Atasoy N. Melatonin ve antioksidan etkileri. Düzce Üniversitesi Sağlık Bilimleri Enstitüsü Dergisi. 2019;9(3):196-201.

[22] Topal T, Öter S, Korkmaz A. Melatonin ve kanserle ilişkisi. Journal Of General Medicine. 2009;19(3):137-143.

[23] Verma AK, Khan MI, Ashfaq F, Rizvi SI. Crosstalk between aging, circadian rhythm, and melatonin. Rejuvenation Research. 2023;26(6):229-241.

[24] Albreiki M. Characteristic, synthesis, and non-photic regulation of endogenous melatonin. In Melatonin-Recent Updates. 2022;Intechopen.

[25] Zisapel N. New perspectives on the role of melatonin ın human sleep, circadian rhythms and their regulation. British Journal Of Pharmacology. 2018;175(16):3190-3199.

[26] Megha KB, Arathi A, Shikha S, Alka R, Ramya P, Mohanan PV. Significance of melatonin ın the regulation of circadian rhythms and disease management. Molecular Neurobiology. 2024;61(8):5541-5571.
[27] Deniz EB. Kanser epidemiyolojisi. Turkey Health Literacy Journal. 2022;3(2):102-111.
[28] Hanahan D, Weinberg RA. Hallmarks of cancer: the next generation. Cell. 2011;144(5):646-674.
[29] Nenclares P, Harrington KJ. The biology of cancer. Medicine. 2020;48(2):67-72.
[30] Çimen A, Akbaş Y, Erbaş O. Uyku, melatonin ve kanser ilişkisi. İstanbul Bilim Üniversitesi Florence Nightingale Transplantasyon Dergisi. 2019;3(1-2):38-41.
[31] Moloudizargari M, Moradkhani F, Hekmatirad S, Fallah M, Asghari MH, Reiter RJ. Therapeutic targets of cancer drugs: modulation by melatonin. Life Sciences. 2021;267:118934.
[32] Putta CL, Eswar K, Rengan AK. Melatonin: avenues ın cancer therapy and ıts nanotechnological advancements. Medcomm–Biomaterials And Applications. 2023;2(3): E58.
[33] Wang L, Wang C, Choi WS. Use of melatonin ın cancer treatment: where are we?. International Journal Of Molecular Sciences. 2022;23(7):3779.
[34] Wang L, Su Y, Choi WS. Melatonin suppresses oral squamous cell carcinomas migration and ınvasion through blocking FGF19/FGFR 4 signaling pathway. International Journal Of Molecular Sciences. 2021;22(18):9907.
[35] Maleki M, Khelghati N, Alemi F, Younesi S, Asemi Z, Abolhasan R, et al. Multiple ınteractions between melatonin and non-coding rnas in cancer biology. Chemical Biology and Drug Design. 2021;98(3):323-340.
[36] Mehrzadi S, Pourhanifeh MH, Mirzaei A, Moradian F, Hosseinzadeh A. An updated review of mechanistic potentials of melatonin against cancer: pivotal roles ın angiogenesis, apoptosis, autophagy, endoplasmic reticulum stress and oxidative stress. Cancer Cell İnternational. 2021;21:1-28.
[37] Samanta S. Melatonin: an endogenous miraculous ındolamine, fights against cancer progression. Journal Of Cancer Research And Clinical Oncology. 2020;146:1893-1922.
[38] Li Y, Li S, Zhou Y, Meng X, Zhang JJ, Xu DP, et al. Melatonin for the prevention and treatment of cancer. Oncotarget. 2017;8(24):39896.
[39] Verma AK, Singh S, Rizvi SI. Therapeutic potential of melatonin and ıts derivatives ın aging and neurodegenerative diseases. Biogerontology. 2023;24(2):183-206.
[40] Chen D, Zhang T, Lee TH. Cellular mechanisms of melatonin: ınsight from neurodegenerative diseases. Biomolecules. 2020;10(8):1158.
[41] Dailah HG. Potential of therapeutic small molecules ın apoptosis regulation ın the treatment of neurodegenerative diseases: an updated review. Molecules. 2022;27(21):7207.
[42] Feybesse C, Chokron S, Tordjman S. Melatonin in neurodevelopmental disorders: a critical literature review. Antioxidants. 2023;12(11):2017.
[43] Kopustinskiene DM, Bernatoniene J. Molecular mechanisms of melatonin-mediated cell protection and signaling in health and disease. Pharmaceutics. 2021;13(2):129.
[44] Potes Y, Cachán-Vega C, Antuña E, García-González C, Menéndez-Coto N, Boga JA, et al. Benefits of the neurogenic potential of melatonin for treating neurological and neuropsychiatric disorders. International Journal Of Molecular Sciences. 2023;24(5): 4803.
[45] Majidinia M, Sadeghpour A, Mehrzadi S, Reiter RJ, Khatami N, Yousefi B. Melatonin: a pleiotropic molecule that modulates dna damage response and repair pathways. Journal Of Pineal Research. 2017;63(1): E12416.
[46] Pourhanifeh MH, Dehdashtian E, Hosseinzadeh A, Sezavar SH, Mehrzadi S. Clinical application of melatonin ın the treatment of cardiovascular diseases: current evidence and new insights ınto the cardioprotective and cardiotherapeutic properties. Cardiovascular Drugs And Therapy. 2022;36(1):131-155.
[47] Tobeiha M, Jafari A, Fadaei S, Mirazimi SMA, Dashti F, Amiri A, et al. Evidence for the benefits of melatonin ın cardiovascular disease. Frontiers In Cardiovascular Medicine. 2022;9:888319.
[48] Ozkalayci F, Kocabas U, Altun BU, Pandi-Perumal S, Altun A. Relationship between melatonin and cardiovascular disease. Cureus, 2021;13(1).
[49] Mendes L, Queiroz M, Sena CM. Melatonin and vascular function. Antioxidants. 2024;13(6):747.
[50] Abdulqader BK. Effect of endogenous melatonin hormone on cardiovascular system: a review of literature. Ann Coll Med Mosul. 2023;45(1):84-91.
[51] Fourtillan JB, Brisson AM, Gobin P, Ingrand I, Decourt JP, Girault J. Bioavailability of melatonin in humans after day-time administration of D7 melatonin. Biopharmaceutics and Drug Disposition. 2000;21(1):15-22.
[52] DeMuro RL, Nafziger AN, Blask DE, Menhinick AM, Bertino Jr JS. The absolute bioavailability of oral melatonin. The Journal of Clinical Pharmacology. 2000;40(7):781-784.
[53] Zetner D, Andersen LPH, Rosenberg, J. Pharmacokinetics of alternative administration routes of melatonin: a systematic review. Drug Research. 2016;66(04):169-173.
[54] Niu G, Yousefi B, Qujeq D, Marjani A, Asadi J, Wang Z, Mir SM. Melatonin and doxorubicin co-delivered via a functionalized graphene-dendrimeric system enhances apoptosis of osteosarcoma cells. Materials Science and Engineering:C. 2021;119:111554.
[55] Gurunathan S, Qasim M, Kang MH, Kim JH. Role and therapeutic potential of melatonin in various type of cancers. OncoTargets and Therapy. 2021; 2019-2052.

[56] Foley HM, Steel AE. Adverse events associated with oral administration of melatonin: A critical systematic review of clinical evidence. Complementary Therapies in Medicine. 2019;42:65-81.
[57] Seely D, Wu P, Fritz H, Kennedy DA, Tsui T, Seely AJ, Mills E. Melatonin as adjuvant cancer care with and without chemotherapy: a systematic review and meta-analysis of randomized trials. Integrative Cancer Therapies. 2012;11(4):293-303.
[58] Cao Y, Zhang H, Chen X, Li C, Chen J. Melatonin: a natural guardian in cancer treatment. Frontiers in Pharmacology. 2025;16:1617508.